Light Induced Local Structure Changes and Dynamics of the Photoreceptor PYP Studied by Thiocyanate as IR Label

Dissertation
zur Erlangung des Doktorgrades
der Naturwissenschaften

vorgelegt beim Fachbereich Physik
der Johann Wolfgang Goethe-Universität
in Frankfurt am Main

von Larissa Blankenburg
aus Mosbach

Frankfurt 2020
(D 30)

vom Fachbereich Physik der

Johann Wolfgang Goethe-Universität als Dissertation angenommen.

Dekan: Prof. Dr. Michael Lang

Gutachter: Prof. Dr. Jens Bredenbeck
Prof. Dr. Josef Wachtveitl

Datum der Disputation: 07. Dezember 2020

Light Induced Local Structure Changes and Dynamics of the Photoreceptor PYP Studied by Thiocyanate as IR Label

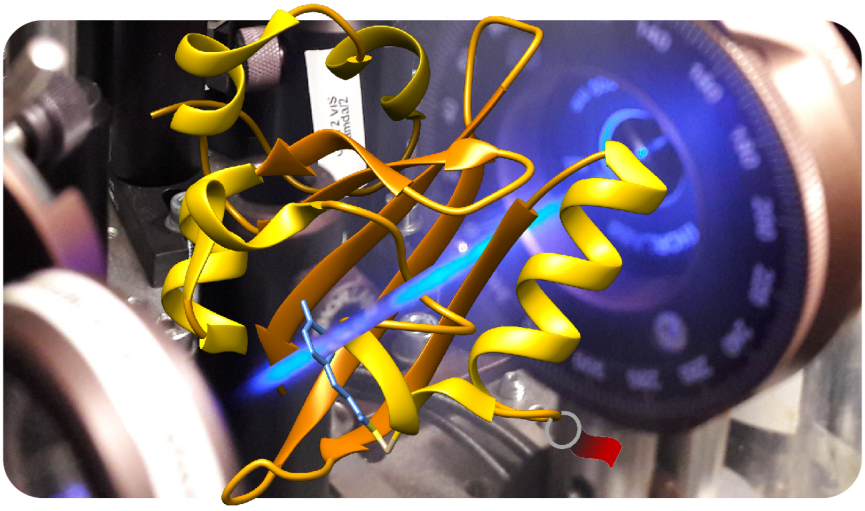

Dissertation by Larissa Blankenburg
Frankfurt, 2020

"Trying to determine the structure of a protein by UV spectroscopy was like trying to determine the structure of a piano by listening to the sound it made while being dropped down a flight of stairs."

– Francis Crick (1916 - 2004)

Contents

Motivation

To gain a better understanding of the function and mechanism of biological processes, investigation of protein structure and dynamics are of large interest for the research field of biomolecular dynamics. Proteins play a crucial role for many biological functions like catalysis, signal transduction, transport within the organism, or DNA transcription. Over the last decades it became clear that protein dynamics cover many orders of magnitude in time ranging from femtoseconds (10^{-15} s) to many hours making their investigation in a native environment challenging. NMR spectroscopy has proven to be a powerful method to resolve protein structure in the solution phase on an amino acid level, but it is limited to timescales slower than 10 ms and therefore not feasible to track fast protein dynamics [1, 2]. A high time resolution (tens of femtoseconds) with a sufficiently high structural sensitivity at the same time can be achieved by pump-probe spectroscopic techniques that probe the time evolution of electronic or vibrational modes of the protein.

A protein class that was intensively studied in the last decades due to its biological significance are photoreceptors like rhodopsins, phytochromes, xanthopsins, or cryptochromes [3]. These light-sensitive proteins are involved in a manifold of signal transduction pathways in many biological systems as response to light. Of large interest are the dynamical structure changes after photon absorption by the chromophore leading to the formation of different photocycle intermediates, which are often identified and investigated by time-resolved pump-probe methods.

Historically, many of the first photocycle models were derived by transient UV/vis pump-probe spectroscopy - for example for Photoactive Yellow Protein (PYP) of the xanthopsin family [4, 5], the protein that is studied in this thesis - and comprised only a few intermediates. With UV/vis spectroscopy only the electronic states of the chromophore can be investigated, resulting in information about the changes in the chromophore structure and the influence of its direct environment [4, 6–9]. More intermediates were found thereafter by applying time-resolved infrared (IR) spectroscopy which is more sensitive for information about the protein structure [10–14]. However, in infrared spectroscopy, too, the site-selectivity is limited to the chromophores and some specific side chains that are involved in hydrogen bonding interactions or proton transfer processes [15], while the majority of the protein contributes to broad bands (in particular the amide I signal) in congested regions of the vibrational spectrum. The incorporation of infrared labels at almost every desired position within the protein makes much more site-specific information from different parts of the protein available [15–19]. Thus, more detailed information about the structure of known intermediates can be obtained and may even lead to the discovery of new photocycle intermediates.

The focus of this thesis is on investigating the structural changes and dynamics during the photocycle of the photoreceptor PYP by means of the infrared label thiocyanate (SCN). Hence SCN-labeled protein mutants are studied under equilibrium (steady-state) and non-

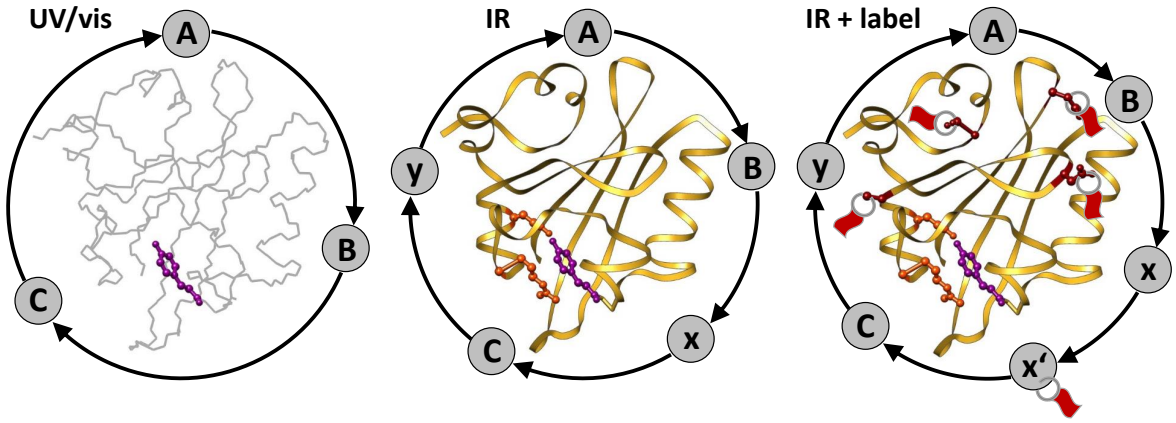

Figure 1: *Schematic photocycle models obtained by different spectroscopic techniques. With transient UV/vis spectroscopy only a few intermediates (A, B, C) are found since only the electronic state of the chromophore (purple) can be probed. Time-resolved IR spectroscopy is sensitive to the overall protein structure (backbone in yellow) leading to the discovery of additional intermediates (x, y), but site resolution is only provided by the chromophore (purple) and a few special side chains (orange). The implementation of IR labels (marked by the red tags at different positions) increases the local resolution significantly and may result in new photocycle intermediates (x').*

equilibrium conditions. PYP is a small, stable protein with a para-hydroxycinnamic acid as covalently bound chromophore that enters a reversible photocycle after excitation with blue light. During the photocycle *trans-cis*-isomerization and protonation of the chromophore as well as partial unfolding of the protein take place, resulting in intermediate states that are formed and populated on timescales ranging from femtoseconds up to seconds [20]. To probe these changes of the structure locally, the SCN moiety is inserted at different locations in the protein *via* cyanaylation of cysteine [21, 22]. The label's CN stretch vibration is highly sensitive to solvent polarity and hydrogen bonding and spectrally well separated from the overlapping protein absorptions [23–25].

First, steady-state experiments are performed on different labeled mutants in the dark state of PYP showing the influence of various local environments on the label. Under constant illumination with blue light the signaling state is populated and the label responds significantly to the structural changes depending on its location. These steady-state conditions are examined on the one hand by FTIR spectroscopy with central wavenumber and lineshape of the SCN absorption serving as observables, on the other hand by ultrafast IR-pump-IR-probe experiments with the vibrational lifetime of the label as observable for solvent exposure.

The transient structures of PYP's photocycle are investigated by time-resolved IR spectroscopy following the kinetics of the SCN label. With transient fs-to-ms vis-pump-IR-probe experiments on the SCN-labeled PYP mutants it is possible to follow most part of the photocycle from chromophore isomerization (ps) and protonation (µs) to the conformational changes of the protein structure (ms). The available time range is further extended up to tens of milliseconds by step-scan FTIR spectroscopy. Depending on the location of the SCN label different transitions of the photocycle are probed. Labels that are located distant from the chromophore respond only on a hundreds of microsecond timescale, when the proton transfer processes and structural rearrangements of the protein occur. Labels close to the chromophore or to the glutamate (E46), which is involved in stabilization of the

binding pocket and proton transfer processes, already sense changes due to the electronic excitation and the isomerization of the chromophore and detect alterations in the binding pocket throughout the entire photocycle.

The aim of this thesis is to demonstrate how the usage of the site-specifically incorporated infrared label thiocyanate enhances the information that are obtained by infrared spectroscopic techniques for the investigation of protein structure, dynamic processes and electrostatic effects. Further, the label allows to gain insight into the photo-induced structural kinetics of PYP with high spatial and temporal resolution.

Part I

Introduction

1 Theoretical Background

1.1 Vibrational Spectroscopy

The following chapter is mainly based on the books of N. Colthup *Introduction of Infrared and Raman Spectroscopy* [26] and P. Larkin *IR and Raman Spectroscopy: Principles and Spectral Interpretation* [27].

Vibrational spectroscopy is a widely used technique to investigate the structure of molecules and their dynamics. The interaction with light raises the energy of a molecule from the ground state to the excited state. The energy difference ΔE between these two states depends on the vibrational frequency ν, the wavenumber $\tilde{\nu}$ or the wavelength λ of the light and can be described as

$$\Delta E = h\nu = hc\tilde{\nu} = h\frac{c}{\lambda} \tag{1.1}$$

where h is the Planck constant and c is the speed of light in vacuum.

Infrared (IR) spectroscopy is a non-invasive method to study the vibrational modes in molecules. In contrast to Raman spectroscopy, a different method for investigating molecular vibrations which is based on inelastic scattering, IR spectroscopy uses the resonant absorption of the light. In IR spectroscopy mostly wavenumbers are used, as they provide the advantage of being proportional to the energy difference between two states (see equation (1.1)). The mid-IR region that is sensitive to molecular vibrations spans from 400 to 4000 cm^{-1}.

As for all absorption spectroscopies the IR absorption is described by the Lambert-Beer law which sets the intensities of the incident light I_0 and the transmitted light I into relation and shows their dependency on the concentration and kind of the molecule as well as the frequency of the absorbed light:

$$A = -logT = log\frac{I_0}{I} = c\epsilon d \tag{1.2}$$

with T as transmission, c as concentration of molecules, ϵ as frequency-dependent extinction coefficient of the molecule and d as pathlength of the sample. The Lambert-Beer law only applies for the absorption in cases where no scattering or reflection of light occurs, otherwise only the extinction is described [28].

The characteristic vibrations of molecules lead to molecular motion that can be defined by internal degrees of freedom. Every molecule with N atoms has in total 3N degrees of freedom with three degrees of translation and three degrees of rotation. In general, a non-linear molecule with more than two atoms has 3N−6 normal modes of vibration, including symmetric and asymmetric stretching and bending vibrations, but a linear molecule has 3N−5 modes, because rotation about the molecular axis cannot be observed.

In a simple model, that can be derived from classical mechanics, the atoms of the molecule are represented by point masses (*e.g.* m_1 and m_2) that are connected by massless springs. The vibrational frequency ν for such a diatomic molecule is dependent of the reduced mass μ of the two atoms and the force constant k as a measure of bond energy:

$$\nu = \frac{1}{2\pi}\sqrt{\frac{k}{\mu}} \text{ with } \mu = \frac{m_1 m_2}{m_1 + m_2}. \tag{1.3}$$

The energy of the vibrational modes can be described by the classical harmonic oscillator by assuming states of equidistant energy levels. These energies are calculated by

$$E_\mathrm{v} = h\nu(\mathrm{v} + \frac{1}{2}), \quad \mathrm{v} = 0, 1, 2, 3... \tag{1.4}$$

with Planck constant h, vibrational frequency ν and energy levels v. Vibrational spectroscopy probes the transition of the molecule from one of the energy states to another. In case of the harmonic oscillator only transitions of $\Delta\mathrm{v} = \pm 1$ are allowed.

For real vibrations transitions of $\Delta\mathrm{v} > 1$ are additionally allowed. If the transition is only slightly higher, *e.g.* $\Delta\mathrm{v} = 2$, it can still be described nicely by the harmonic approximation, but with increasing $\Delta\mathrm{v}$ the interactions with other nuclei and surroundings increase, as well, and therefore include deviations from the harmonic description. These transitions appear as overtones and combination bands in IR spectroscopy and are better represented by an anharmonic oscillator that is described by the Morse potential:

$$V = D_e(1 - e^{a(r-r_e)})^2 \tag{1.5}$$

with D_e as dissociation energy that is required to dissociate the molecule from equilibrium, a as a constant varying the width of the potential, r as internuclear distance and r_e as equilibrium distance where the energy is at a minimum.

The spacing between the energy levels in an anharmonic oscillator becomes smaller with higher energies until they reach the dissociation limit:

$$E_\mathrm{v} = h\nu_0(\mathrm{v} + \frac{1}{2}) - \frac{h^2\nu^2}{4D_e}(\mathrm{v} + \frac{1}{2})^2, \quad \mathrm{v} = 0, 1, 2, 3... \tag{1.6}$$

where the factor $\frac{h\nu}{4D_e}$ is called anharmonicity constant and the vibrational frequency ν is defined as

$$\nu = \frac{a}{2\pi}\sqrt{\frac{2D_e}{m}}. \tag{1.7}$$

To observe absorption bands in IR spectroscopy not only the light frequency and vibrational frequency have to coincide, but it is required that the vibrations induce a change of dipole moment in the molecule as well. The intensity of the absorption is proportional to the square of the change in the transition dipole moment.

IR spectroscopy shows a high sensitivity to structural changes and therefore is a powerful method for the investigation of conformational changes, the interactions between molecules, stability of molecules and solvation effects.

1.2 Time-resolved Pump-Probe Spectroscopy

Many processes in physics, chemistry and molecular biology take place on timescales faster than one second. A schematic overview of typical timescales for selected processes is given in figure 1.1. The fastest ones occur in a sub-femtosecond ($< 10^{-15}$ s) to picosecond (10^{-12} s) regime and are too fast to be measured by any detector in real time so far. To overcome this limitation in time resolution, indirect measurement methods have to be used. One of the most common techniques is the ultrafast pump-probe spectroscopy method. In this case the time resolution only depends on the pulse duration that can be as short as femtoseconds and not on the time response of the detector [29–31].

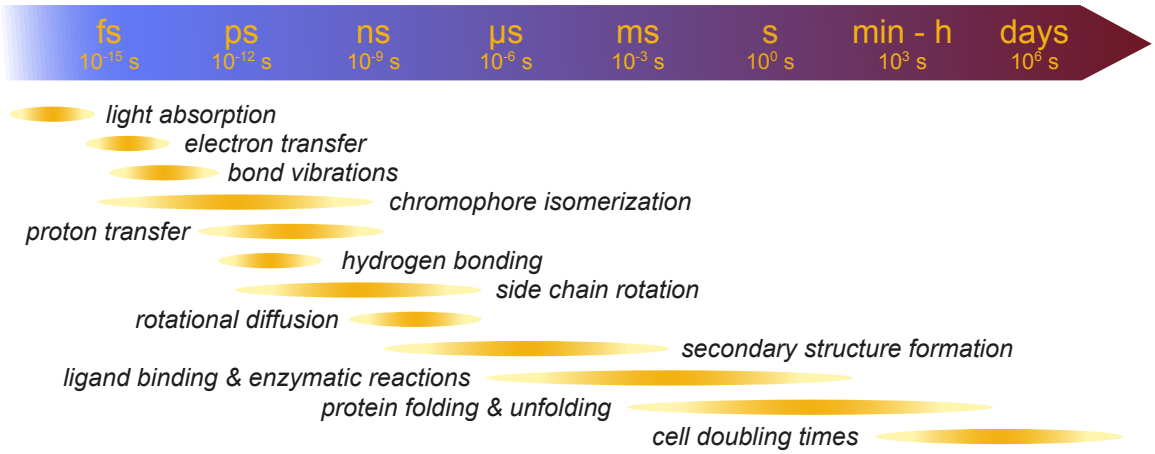

Figure 1.1: *Timescales for selected processes in physics, chemistry and molecular biology ranging from sub-femtoseconds to many hours or days. Inspired by [32–34].*

In time-resolved pump-probe spectroscopy an ultrashort pump pulse interacts with the sample and excites the molecules. This pump pulse is followed by an ultrashort infrared probe pulse with a certain time delay Δt. The delay time Δt is typically adjusted by a difference in the optical path length that the pump pulse travels - here a path difference of approximately 0.3 mm equals a time delay of 1 ps [31]. A schematic sketch of a pump-probe experiment is depicted in figure 1.2A on the following page.

Depending on the frequency of the applied pump pulse, one distinguishes between visible-pump-IR-probe experiments (also referred to as vis-pump-IR-probe) and IR-pump-IR-probe experiments (often referred to as 2D-IR spectroscopy). The visible pump pulse promotes the transition from a lower to a higher electronic state leading to a disturbed equilibrium of the investigated molecule (see figure 1.2B and figure 1.2D on the next page). The infrared pump pulse excites the vibrational states in the molecules inducing no real disturbance of the molecule's equilibrium (depicted in figure 1.2C and figure 1.2E on the following page). In both cases the IR probe pulse that is delayed with respect to the pump pulse

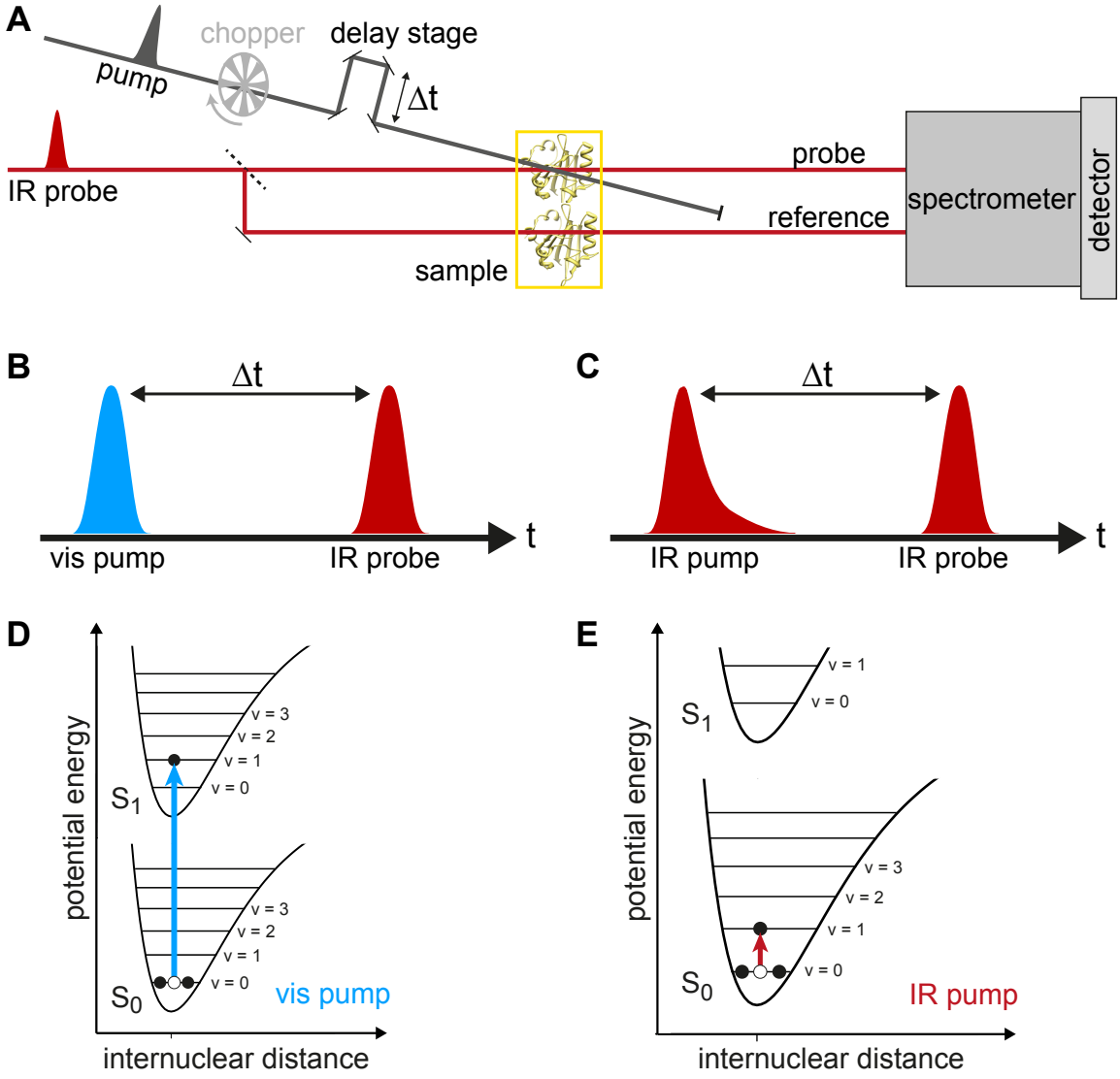

Figure 1.2: *(A) Schematic sketch of a typical pump-probe experiment with a pump pulse (gray) that travels over a movable delay stage to adjust the time delay Δt with respect to the probe pulse (red) before both hit the sample at the same spot. The chopper is used to block every second pump pulse. The IR pulse is split into probe and reference beam which are sent through the sample at spatially separated positions and are both dispersed by a spectrometer onto a detector afterwards. (B) Pulse sequence for a visible-pump-IR-probe experiment with ultrashort visible pump (blue) and mid-IR probe (red) pulses. (C) Pulse sequence for an IR-pump-IR-probe experiment with a spectrally narrow mid-IR-pump pulse (dark red) that is therefore elongated in time (≈ 1 ps) and an ultrashort mid-IR probe pulse (red). (D) Representation of an exemplary electronic transition from the electronic ground state (S_0) to the first electronically excited state (S_1) after excitation with a visible pump pulse. (E) Representation of an exemplary vibrational transition from the vibrational ground state to the first vibrationally excited state (corresponding to a transition of Δ v = 1) after excitation with a mid-IR pump pulse.*

monitors the alterations of the vibrational modes caused by the excitation resulting in absorption changes between the ground state and the excited state of the molecule. These absorption differences ΔA are calculated by subtracting the unperturbed absorption from the perturbed one by applying a mechanical chopper (as shown in figure 1.2A) in the pump beam path to block every second pulse. Additionally, the probe pulse can be divided into

two paths (probe and reference) before it reaches the sample, whereby the reference pulse interacts with the sample spatially separated from probe and pump pulse to correct for intensity fluctuations of the laser system [31, 35].

1.2.1 Vis-Pump-IR-Probe Spectroscopy

The disturbance of the equilibrium by applying an ultrafast visible pump excitation to the molecule initiates dynamic processes like photoreactions, structural rearrangements or energy transfer. These processes evolve over time and the transient species are probed by the ultrafast IR pulse. As the population of molecules in the ground state is reduced after excitation to an electronically excited state, the IR probe pulse absorbs less photons at the frequencies of the vibrational modes in the ground state resulting in a bleached difference absorption signal ($\Delta A < 0$). The molecules that were promoted to the excited state thus absorb at characteristic frequencies different to the ones of the ground state contributing to a positive absorption feature ($\Delta A > 0$). Consequently, inspection of the spectral changes (peak position and band width) reveals information about different transient species after visible excitation [31, 36, 37].

The formation of these transient species that is triggered by the visible pump pulse, *e.g.* the photocycle intermediates of a photoreceptor protein, can span a broad time range. However, the delays obtained in a typical pump-probe experiment with the pump pulse being delayed by changing the beam path length (so called "mechanical" delays) are limited to 3 ns. Previously, only step-scan FTIR techniques were available to exceed the time range to longer delays with the drawback of a time resolution that is limited to tens of nanoseconds [38, 39]. To cover the measurement gap in the low nanosecond range Bredenbeck *et al.* [40] introduced the synchronization of two fs-laser systems, which delay the two pulses electronically with respect to each other. This technique provides the advantage of a high temporal resolution of tens of picoseconds, while at the same time very long delays can be achieved, only limited by the repetition rate of the laser systems. Combination of the different pump-probe methods allows to follow dynamics on timescales of multiple orders of magnitude with high temporal resolution. For IR-pump-IR-probe experiments such long measurement times are not required since the vibrationally excited modes typically only live for tens of picoseconds [41].

1.2.2 IR-Pump-IR-Probe Spectroscopy

In the IR-pump-IR-probe experiments the pump pulse is often narrowed in the frequency domain (by a Fabry Perot etalon) to guarantee excitation of specific vibrational modes, however, the high resolution in frequency causes an elongation in time domain to approximately 1 ps (represented by the exponentially decaying tail of the IR pump pulse in figure 1.2C on the facing page) and therefore a lower time resolution for the experiment [42]. Excitation of selected vibrational modes and probing of a broad spectrum of infrared frequencies is widely used to study vibrational relaxation dynamics, spectral diffusion, energy transfer to other vibrational modes or chemical exchange after triggering a chemical reaction. This method is highly sensitive for molecular structure and interactions of the vibrational modes with their local environment [41, 42].

Interaction with the infrared pump pulse leads to excitation of some molecules to a vibrationally excited state and the probe pulse senses the depletion of the ground state. This exhibits a negative absorption in the difference spectrum referred to as ground state bleach. Additionally, stimulated emission contributes to the negative signal when the probe pulse interacts with some molecules in the excited state triggering the emission of photons to the ground state [35, 41]. The excited-state absorption is responsible for a positive signal since molecules that were promoted to an excited state by the pump pulse are further excited to higher states. Due to the anharmonicity between the pumped and the probed mode it is possible to measure a 2D-IR signal, where the excited-state absorption is red-shifted compared to ground state bleach and stimulated emission [43].

In this thesis the IR-pump-IR-probe experiments focus on the investigation of vibrational relaxation dynamics, also referred to as vibrational lifetimes of the studied modes. After excitation the vibrational mode distributes the excess energy to other modes in its proximity either *via* intra- or intermolecular energy transfer until it returns to the vibrational ground state. When applying an IR probe pulse of corresponding frequency at proceeding delay times one can follow the exponential decay dynamics of the vibration and the vibrational lifetime τ_{vib} can be described by contributions of the intra- and intermolecular decay rates k

$$\tau_{vib} = \frac{1}{k_{vib}} = \frac{1}{k_{intra} + k_{inter}}. \tag{1.8}$$

For small molecules or decoupled vibrational modes the intramolecular decay rate vanishes and the energy is only transferred to acceptor states of the surrounding molecules. This intermolecular decay rate depends on the coupling to the energy-accepting states (*e.g.* of the solvent) and their density and can be described by Fermi's Golden Rule [43–45]. Hence the vibrational lifetime is highly sensitive to it surrounding environment.

1.3 Photosensor Photoactive Yellow Protein

In this thesis IR spectroscopy was applied to the small blue-light photoreceptor Photoactive Yellow Protein (PYP) to study its protein structure by steady-state experiments with FTIR and time-resolved IR-pump-IR-probe spectroscopy and its dynamics by transient vis-pump-IR-probe experiments. The protein was discovered in 1985 in the extremophilic purple bacterium *Halorhodospira halophila* by T.E. Meyer [4]. Since then similar proteins have been found in a number of phototrophic bacteria. As chromophore a para-hydroxycinnamic acid also called p-coumaric acid (pCA) is covalently bound to PYP. The visible absorption maximum is at 446 nm and responsible for the yellow color which is eponymous for the protein [20, 46, 47].

PYP is supposed to participate in a signaling transduction cascade that leads to negative phototaxis to prevent the bacterium from photo-damage due to UV-light exposure near the water surface [48]. Later van der Horst *et al.* [49] discovered in *Idiomarina loihiensis* that PYP also takes part in regulation of biofilm formation. The water soluble protein has a small size of 125 amino acids and a molecular weight of 14 kDa. PYP shows high physicochemical stability under various conditions like changes in pH value, temperature,

high salt concentrations and light radiation, especially in the visible range [20, 46]. Due to these favorable properties, the comparably fast photocycle and its reversibility, quickly established the photoreceptor as model system for kinetic and structural investigations with a large variety of measurement techniques.

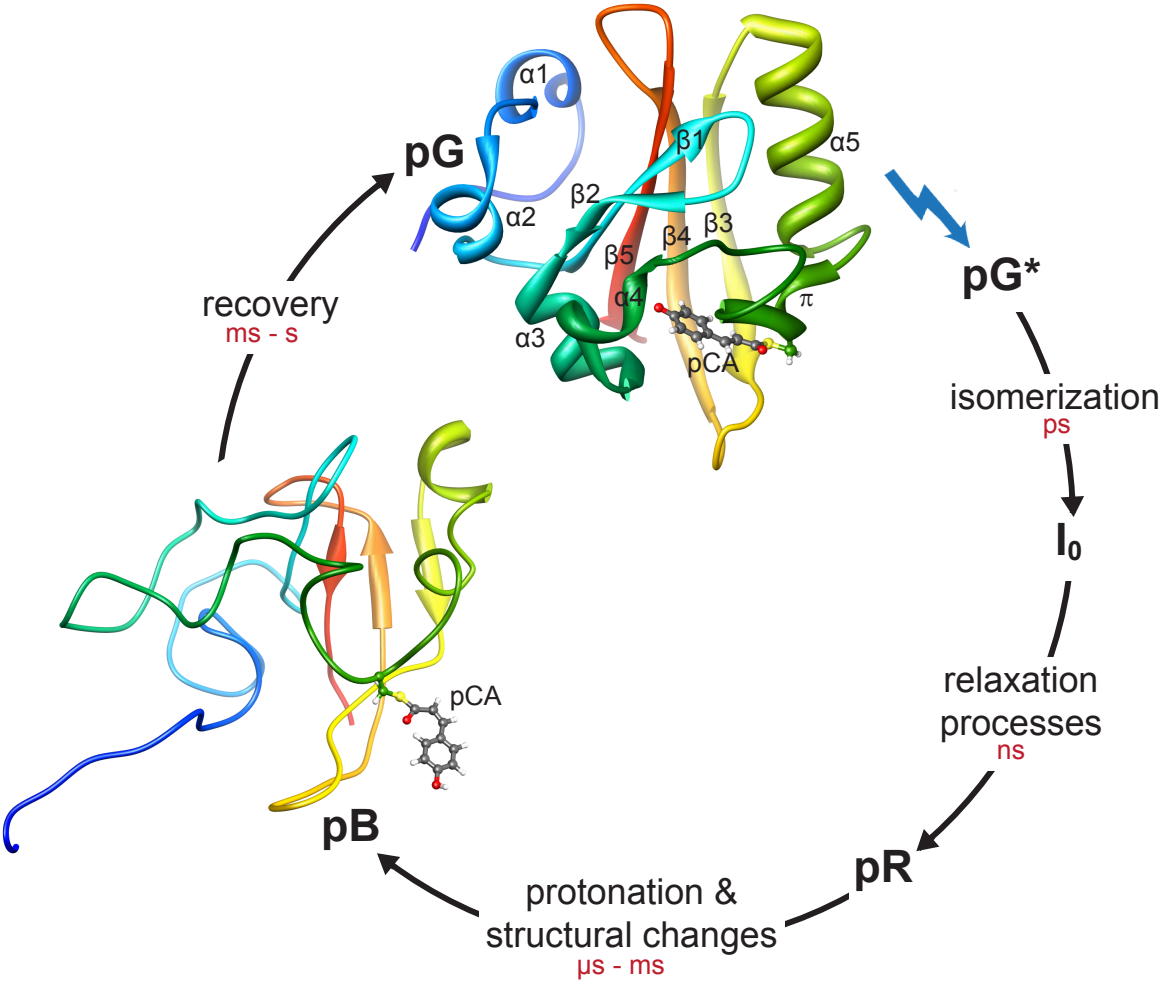

Figure 1.3: *Schematic photocycle model of PYP [46, 50]. Dark state pG (pdb entry 1NWZ by X-ray crystallography) and signaling state pB (pdb entry 2KX6 structure model based on DEER, NMR and TR-SAXS/WAXS) structures are shown in rainbow color code from blue (N-terminus) to red (C-terminus) following the residue number.[1] The chromophore (pCA) is depicted as ball-and-stick model in both structures. The designation of the secondary structure elements in pG is based on the PDB structure 1NWZ by [51].*

The dark state (pG) structure of PYP features a central core built by antiparallel β-sheets surrounded by α-helices (for structure see figure 1.3). The hydrophobic binding pocket for the chromophore is embraced by a long loop region and adjacent to a π-helix that guarantees high flexibility. The pCA chromophore is covalently bound to C69 (Cys69) via a thiol ester linkage [20, 46, 47]. Kyndt *et al.* [52, 53] discovered that two enzymes are responsible for production and incorporation of the chromophore *in vivo*. One enzyme is the Tyrosine ammonia lyase (TAL) which catalizes the conversion of L-tyrosine to p-coumaric acid. The second enzyme, p-hydroxycinnamyl:CoA ligase (pCL), is expected to catalyze the activation of the chromophore by binding the p-coumaric acid to Coenyme A (CoA) whereby

[1]The structure images were created by using Chimera 1.6.2.

ATP (Adenosine triphosphate) is hydrolyzed to AMP (Adenosine monophosphate). Afterwards the activated chromophore binds to the cysteine side chain of the apo-protein and releases the CoA [52, 53].

In the dark state the chromophore is in *trans*-configuration and deprotonated as shown in the first panel of figure 1.4. It is stabilized by a hydrogen bonding network mainly from its phenolate oxygen to the hydroxyl groups of Y42 (Tyr42) and E46 (Glu46) and the positively charged R52 (Arg52) nearby that stabilizes the anionic chromophore electrostatically and protects it against influences of the surrounding environment [54, 55].

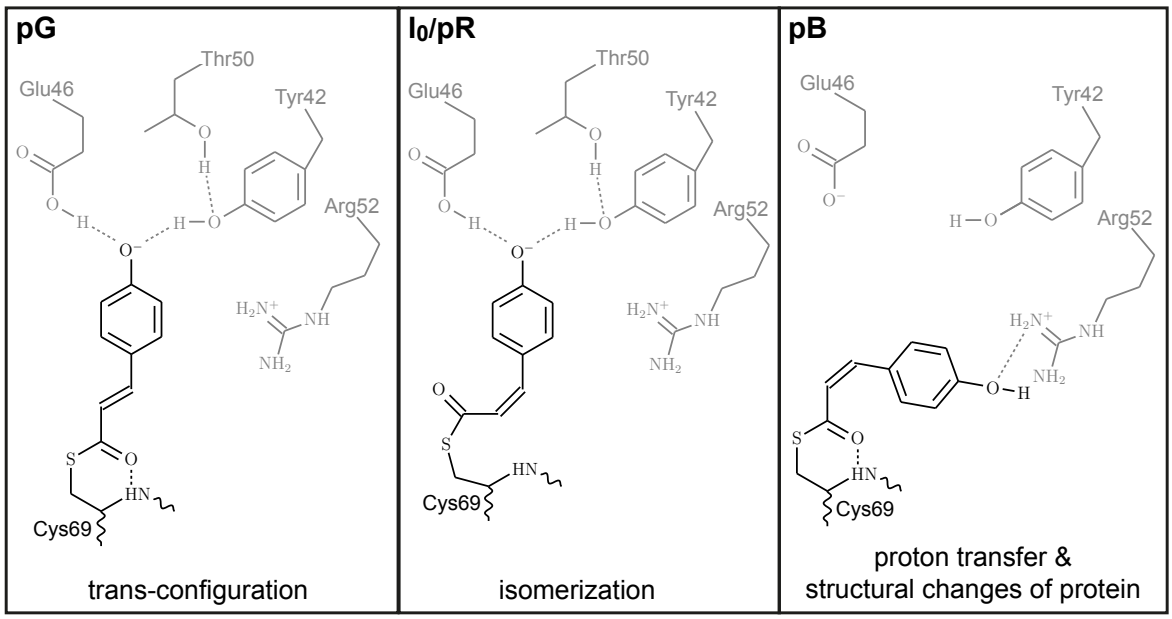

Figure 1.4: *Schematic representation of the p-coumaric acid chromophore (black) and some of the sourrounding amino acids (gray), that stabilize the chromophore by hydrogen bonding. Conformations of the dark state pG, the intermediates after isomerization (I_0/pR) and the signaling state pB are depicted [14, 56, 57].*

Irradiation of PYP with blue light leads to isomerization of the chromophore from *trans*- to *cis*-configuration due to rotation around the C_7=C_8 vinyl double bond as depicted in figure 1.4 [58, 59]. With this step, the protein enters a reversible photocycle (schematically shown in figure 1.3 on the preceding page) where the isomerization is followed by relaxation, intramolecular proton transfer to the chromophore, large structural changes and finally the recovery of the ground state (dark state). These processes occur on timescales from femtoseconds to seconds [46, 60] and were studied in the past three decades with many time-resolved techniques like spectroscopic methods as transient UV/vis absorption, vis-pump IR-probe, step-scan FTIR, stimulated Raman and transient grating spectroscopy, but also by pump-probe X-ray crystallography and solution scattering. The reviews [20, 50, 60] give an overview of the different photocycle intermediates that are discussed in the following. Note that many different notations for the intermediates exists, often depending on the method that was applied for investigation. Here, two of the most used notations in visible and infrared spectroscopy studies are given for completion.

Before the chromophore isomerizes, the hydrogen bonds in its surrounding are weakened in hundreds of femtoseconds after excitation. The transition from *trans*- to *cis*-configuration of the chromophore and formation of the red-shifted intermediate I_0 (λ_{max} = 500 nm) occur

on a picosecond timescale and are caused by breaking of the hydrogen bond between the chromophore's carbonyl and the backbone amide group of C69 [9, 12, 13, 46, 61–67]. The isomerization is followed by relaxation processes of the chromophore and the hydrogen bonding network in its surrounding leading to formation of the semi-stable intermediate pR/I_1 (λ_{max} = 465 nm) in 1 - 3 ns [8, 12, 14, 62, 68–70].

Protonation of the pCA chromophore and deprotonation of amino acid E46, as it is shown in panel 3 in figure 1.4 on the preceding page, was determined to occur in approximately 100 µs to 600 µs and is preliminary to large structural rearrangements of the protein on a millisecond timescale that result in the signaling state pB/I_2' (λ_{max} = 355 nm) [7, 10, 11, 70–75]. In the signaling state PYP is partially unfolded while the N-terminus folds away from the protein body [11, 75–81] and the chromophore moves out of the binding pocket in a more solvent exposed environment [82, 83]. These conformational changes lead to an increased radius of gyration for the protein [55, 84].

During the return to the ground state the chromophore is deprotonated again and isomerizes back to its original *trans*-configuration. Further the structural changes have to fold back to the ground state conformation. These processes are mostly described to follow biphasic kinetics on a hundreds of ms up to one second timescale [4, 5, 70, 72–75, 85].

Initially, only the three intermediates pG, pR and the signaling state pB were observed and defined the first photocycle models [4, 5]. As the time resolution improved the early intermediate I_0 was discovered by transient absorption spectroscopy [9, 61]. All these intermediates have in common that they can be easily detected by widely used UV/vis spectroscopic techniques as their absorption spectra are clearly distinguishable [5, 20, 74, 86]. However, there are further intermediates (not shown in the simple photocycle model in figure 1.3 on page 9) that either do not show such favorable spectroscopic properties so that different methods have to be applied for identification or their existence is controversially discussed.

In-between the isomerization of the chromophore (I_0, 2 ps) and formation of pR (3 ns) after various relaxation processes, an intermediate was observed with transient absorption spectroscopy that is formed in 220 ps [8, 9, 87, 88]. Spectroscopically $I_0^\ddagger$ displays similar absorption characteristics to those of I_0, only deviating in the absorptivity. The transition from I_0 to $I_0^\ddagger$ is suggested to arise from fast relaxation processes of the protein in the proximity of the chromophore. The decay of $I_0^\ddagger$ on a nanosecond timescale involves further relaxation processes of protein, chromophore and the surrounding hydrogen bonding network [8]. Resonant Raman spectroscopy, however, implies that the changes between I_0 and $I_0^\ddagger$ are localized on the chromophore's phenolate ring [88]. On the other hand even the existence of this intermediate is disputed since no evidence was found in pump-dump-probe experiments [62] and ultrafast vis-pump-IR-probe measurements [13] performed later on.

Many studies revealed dynamics on an early microsecond timescale implying the existence of two sub-states for intermediate pR, which is characterized by an isomerized chromophore in *cis*-configuration that is still deprotonated, although the interpretation of the structural differences between pR_1 and pR_2 is ambiguous [73, 75, 89–92]. Since both substates pR_1 and pR_2 cannot be distinguished by their visible absorption spectra, some studies suggested a structurally similar chromophore and assigned the formation of the second sub-state to conformational changes of the protein far away from the chromophore [73, 92].

Based on Raman spectroscopy in combination with DFT calculations and solution scattering, however, the two sub-states were attributed to different hydrogen bonding patterns of the chromophore. While one population features two intact hydrogen-bonds between the chromophore and the residues E46 and Y42, the hydrogen-bond with E46 is broken in the other one [75, 90]. Regardless of the investigation method, both pR states were found to be followed by the protonation process of the chromophore.

The first photocycle models already postulated an additional intermediate (later assigned to pB') in the transition from pR to pB as it was found to be bi-exponential, but it was not possible to distinguish this species spectroscopically from pB due to the similar electronic state of the chromophore [4, 5]. Therefore other investigation methods like time-resolved FTIR spectroscopy had to be applied to resolve the differences between the two intermediates as it was first carried out by Xie *et al.* [11]. In pB'/I_2 the chromophore is protonated prior to the large conformational changes of the protein that finally lead to PYP's signaling state pB. Moreover, the existence and properties of the pB' intermediate were confirmed by time-resolved resonant Raman spectroscopy [93] and a detailed kinetic analysis of visible absorption data [74]. Simultaneously with the protonation process of the chromophore, deprotonation of the nearby E46 residue appears indicating a proton transfer from the glutamate to the chromophore [10, 11, 93–95], whereas other studies suggest that water molecules, that are able to penetrate into the binding pocket, serve as proton source [96–98]. Despite the fact that it has not yet been conclusively determined whether deprotonation of E46 directly leads to chromophore protonation or not, it seems to play a crucial role in triggering the large movements of the protein backbone since the negative charge of E46 is buried in a highly hydrophobic environment in pB' resulting in strong destabilizing effects on the structure of PYP [11, 99].

For the recovery of the ground state pG from the signaling state pB, the chromophore has to be re-isomerized in its *trans*-configuration and the structural rearrangements have to be reversed. These processes are initiated by deprotonation of the chromophore. The intermediate pB^{deprot} that originates from proton transfer to presumably a hydroxyl ion, shows very similar absorption characteristics in the UV/vis to the signaling state [74, 100]. In contrast to the thermal recovery of the ground state, that appears spontaneously in the dark, the light-induced recovery, that can be triggered by absorption of UV light in the pB' or pB state, is an order of magnitude faster because the rate-limiting step of chromophore deprotonation is omitted before its re-isomerization [86].

1.4 Site-specific Infrared Labels in Proteins

Vibrational spectroscopy has proven to be a highly sensitive method providing a spatial resolution on the level of single atom bonds with a temporal resolution appropriate to resolve even the fastest chemical and physical processes occuring on a femtosecond timescale. When applied to proteins, however, it is nearly impossible to gain any site-specific information about structure and dynamics of the system from the intrinsic infrared modes since the majority of the vibrations contribute to signals in the same crowded spectral region. Only isotope labeling or some special structure elements like protonable or hydrogen-bonded side chains or changes affecting chromophores may provide limited local resolution. These challenges can be overcome by the usage of infrared labels that are applicable at almost any

desired position within the protein and have a well separated absorption frequency aside from other protein and solvent absorptions in the infrared spectrum [16, 17], as it is shown for SCN and the isotope-labeled $S^{13}C^{15}N$ in figure 1.5.

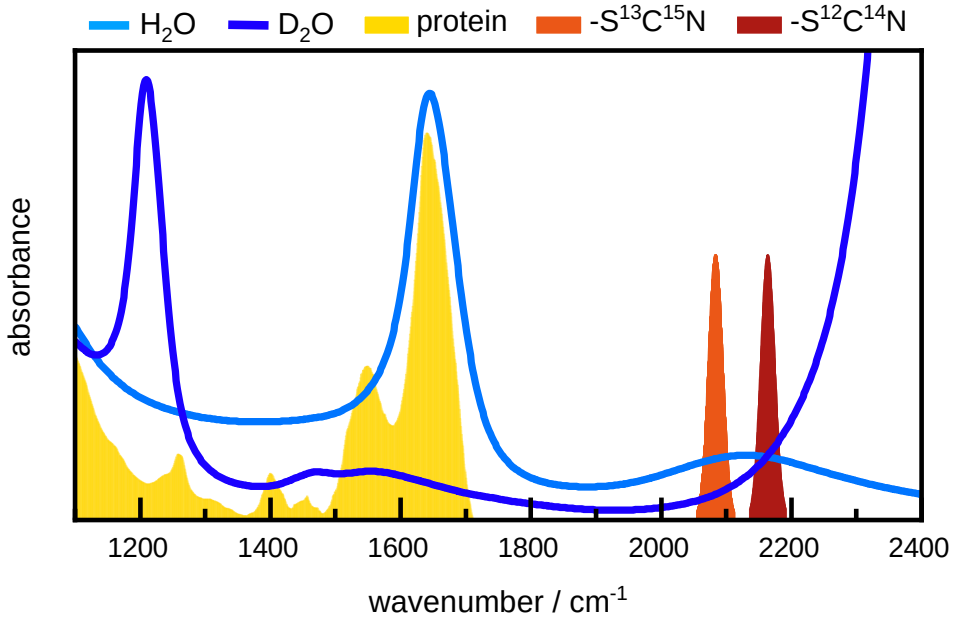

Figure 1.5: *Typical infrared absorptions of proteins (yellow), the solvents H_2O (light blue) and D_2O (dark blue), and of isotope-labeled $S^{13}C^{15}N$ (orange) and $S^{12}C^{14}N$ (red) in proteins in the spectral window of interest.*

Over the last years the field of infrared labels developed rapidly. Due to their site-specific incorporation, they provide high spatial and temporal resolution for local processes enabling a detailed investigation of protein structure and kinetics. There are several requirements that the labels have to fulfill, namely a clearly defined absorption in an uncongested spectral window with a suitably strong transition dipole moment, high sensitivity to variations in their environment and no perturbation of protein structure, stability and function [16–18, 101]. Widely used probes, that meet most of these criteria, are nitriles (*e.g.* cyanophenylalanines [102–105], thiocyanates [23, 24, 106, 107] or cyanotryptophans [108]) or azido functional groups (*e.g.* azidophenylalanines [109, 110] or azidohomoalanines [111, 112]). For detailed reviews about vibrational labels see references [16], [17], and [18].

The focus of this thesis is on the infrared label thiocyanate as it is a small moiety that can be easily inserted into proteins posttranslationally by a chemical reaction with cysteine as depicted in figure 1.6 on the following page [21, 22].

The nitrile stretch vibration is located in a transparent spectral region (2140 - 2170 cm^{-1}) of the infrared spectrum where no protein absorption bands occur and typical solvent absorption (H_2O and D_2O) is relatively low [17]. Isotope-labeling of the SCN shifts the absorption to approximately 2080 cm^{-1} which is favorable for measurements in D_2O due to its smaller extinction coefficient in this spectral region (see figure 1.5). The SCN itself has an extinction coefficient of approximately 50 - 100 $cm^{-1}M^{-1}$ in the infrared [16, 24].

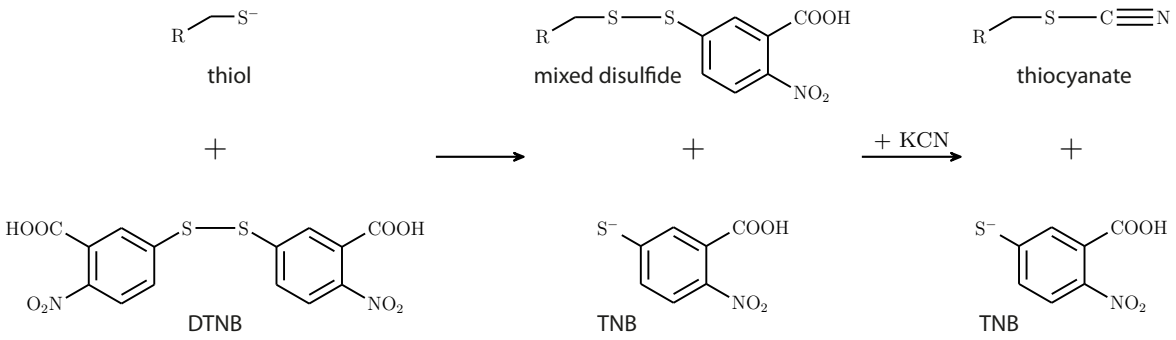

Figure 1.6: *Reaction scheme of cysteine cyanylation. When DTNB (5,5'-dithiobis(2-nitrobenzoic acid) or Ellman's reagent) is added to a protein that contains a cysteine, the thiol breaks the disulfide bond in the DTNB followed by a nucleophilic substitution. This results in a mixed disulfide and the anionic byproduct TNB (2-nitro-5-thiobenzoate). To form a thiocyanate, potassium cyanide (KCN) reacts with the mixed disulfide and another TNB molecule is released [21, 22].*

In FTIR studies of methylthiocyanate (MeSCN) in different solvents, a strong dependency of the nitril vibration on the hydrogen bonding strength and the electrostatic environment was observed (see figure 1.7A on the facing page) [23–25]. Therefore changes in the vibrational frequency can be directly assigned to changes in the local surrounding of the label. Unfortunately, interpretation of the spectra is complicated by competing effects of hydrogen bonding interactions and polarity on the peak position of the label. Besides the vibrational frequency, additional observables facilitate the conclusions about the label's immediate environment. Thiocyanate has a large anharmonicity and an exceptionally long vibrational lifetime of tens of picoseconds compared to other infrared labels (typically only a few picosecond [111, 113, 114]) making it a favorable label also for IR-pump-IR-probe and 2D-IR spectroscopy [16, 24, 115]. The vibrational lifetime is especially sensitive to solvent exposure of the thiocyanate label since the heavy sulfur atom blocks internal energy transfer to other protein modes by the thermal insulation effect and hence it is dominated by intermolecular relaxation to solvent molecules [115].

Due to the aforementioned characteristics, thiocyanate has proven to be a suitable IR label for detecting changes in structure and following kinetics and was used for many applications in protein systems recently (reviewed by [19]). Using SCN as infrared label, insight into the catalytic activity of enzymes [116–118], ligand binding [119–121], protein-protein interactions [122–124], or structure and function of macromolecules [24, 25, 106, 125, 126] was revealed.

Thiocyanate is a sensitive reporter of electrostatics in the protein environment. The influence of local electric fields on the nitrile vibration can be theoretically described by the Vibrational Stark Effect (VSE) [18, 19, 127, 128]. The VSE spectroscopy directly relates changes in the transition frequency $\Delta\tilde{\nu}_{probe}$ of the vibrational probe to differences in the local electrostatic field $\Delta\vec{F}_{protein}$ upon perturbation given by

$$hc\Delta\tilde{\nu}_{probe} = -\Delta\vec{\mu}_{probe} \cdot \Delta\vec{F}_{protein} \tag{1.9}$$

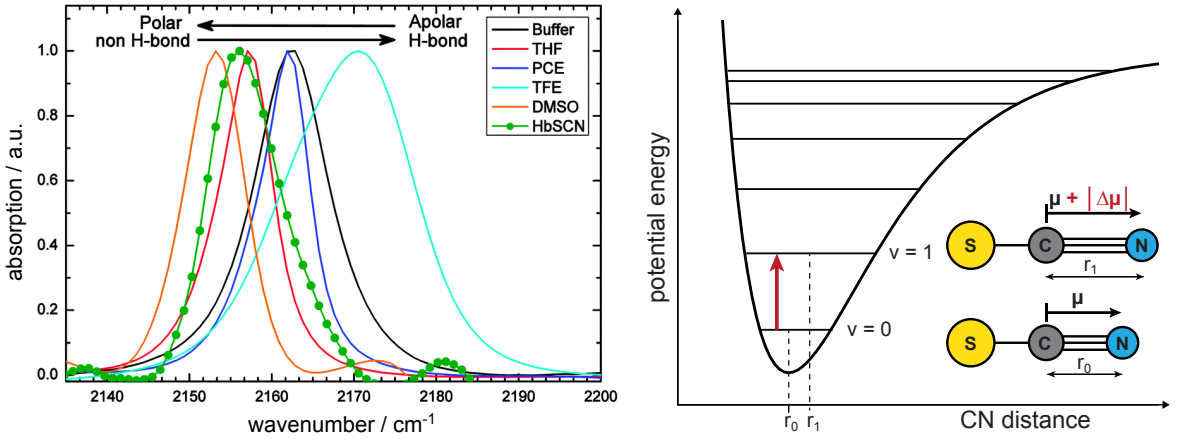

Figure 1.7: *(A) Environment dependent absorption signals of methylthiocyanate (MeSCN) in different solvents and of SCN-labeled hemoglobin (green). Frequency shifts are caused by varying polarity and hydrogen bonding interactions. The figure was adapted with permission from [24] - Published by the PCCP Owner Societies. (B) Schematic depiction of the Stark tuning rate $|\Delta\mu|$. Excitation from the ground state to an excited vibrational state (indicated by the red arrow) changes the bond length of the C≡N vibration from r_0 to r_1 and therefore increases the dipole moment μ by a factor that corresponds to the Stark tuning rate $|\Delta\mu|$. The figure was inspired by [119, 127].*

with the Planck constant h, the speed of light c and $\Delta\vec{\mu}_{probe}$ as difference in the dipole moment between the ground and excited vibrational state, also referred to as Stark tuning rate $|\Delta\mu|$ [116, 129]. Due to the anharmonicity of the nitrile bond, a large increase in dipole moment for the vibrational transition occurs leading to a high electric field sensitivity of the probe as depicted in figure 1.7B. Typical Stark tuning rates for the SCN label are measured to be 0.5 - 3 $cm^{-1}/(MV/cm)$ corresponding to a frequency shift of 0.5 - 3 cm^{-1} for an electric field of 1 MV/cm experienced by the probe along its vibrational axis [17, 19, 127].

However, additional to the sensitivity to electrostatic fields thiocyanate is also very sensitive to hydrogen bonding interactions as it is a relatively good hydrogen bond acceptor that can form hydrogen bonds towards water or donors in the protein. The competing effects of the different interactions with the probe impede a straightforward interpretation of the vibrational spectrum. Therefore the contributions of the hydrogen bonding interactions on the vibrational frequency have to be separated from the ones described by the VSE. Several methods are usually applied to detect the presence of H-bonds such as high-resolution crystallography [102, 116] and molecular dynamics simulations [118, 130] which are highly elaborate or the comparison of the nitrile frequencies to ^{13}C chemical shifts from NMR experiments which is limited to certain hydrogen bond geometries [102, 131]. Another easily accessible approach without the aforementioned limitations is the measurement of the frequency-temperature line slope (FTLS) which utilizes the dependence of the hydrogen bonding strength on the temperature resulting in frequency shifts of the nitrile vibration. Changes in the FTLS allow measuring the degree of hydrogen bonding of the probe even in the intricate protein environment [17, 125, 132].

2 Experimental Setup and Methods

2.1 Sample Preparation

In this chapter mutagenesis of the PYP DNA, expression and purification of the proteins and cyanaylation of the mutants are described. The vectors encoding for PYP-WT (pET15b(pyp)) and the biosynthetic and maturation enzymes TAL and pCL (pACYC(talpcl)) were provided by Kyndt *et al.* [53]. Mutagenesis, expression and protein purification were supported by Florian Habenstein during his master thesis, Hans-Werner Müller and Sabrina Oesteritz.

2.1.1 Mutagenesis

A construct including the start methionine (atg), a 6x histidine-tag (His-tag, DNA sequence: cat cac cat cac cat cac) and a TEV (Tobacco Etch Virus) protease cleavage site (sequence: Glu-Asn-Leu-Tyr-Phe-Gln-Gly) was inserted into the original expression vector pET15b(pyp) at the N-terminal end of the pyp gene to facilitate protein purification. The 5'-end PCR primer contained a NcoI restriction site and the aforementioned construct, the 3'-end primer a BamHI restriction site. All mutagenetic primers were ordered from Invitrogen. PCR was performed with *Phusion High-Fidelity* DNA Polymerase (New England Biolabs). The PCR product was extracted from a 1 % agarose gel and digested with NcoI and BamHI. Afterwards the digested PCR product and the pET15b(pyp) vector, that was digested by the two enzymes and extracted from a 1 % agarose gel as well, were ligated by T4 DNA Ligase (*Quick Ligation Kit* by New England Biolabs). The DNA was transformed into *E.coli* cloning strain DH5α by electroporation, selected by ampicillin resistance and isolated with the *NucleoBond Xtra Midi* kit by Macherey-Nagel.

Site-directed mutagenesis of the pET15b(pyp/His) vector[1] was used to obtain the cysteine mutants L23C, A30C, A44C, D48C, V57C, M100C and V122C. The PCR was performed either with *Phusion High-Fidelity* DNA Polymerase (New England Biolabs) or the *GeneArt Site-Directed Mutagenesis System* by Invitrogen. All mutated vectors were transformed into *E.coli* cloning strain DH5α by electroporation, selected by ampicillin resistance and isolated with the *NucleoBond Xtra Midi* kit by Macherey-Nagel or by Miniprep using isopropanol precipitation.

All DNA sequences were confirmed by sequencing with the customary T7 sequencing primer by Eurofins MWG.

[1] The vector encoding PYP with the inserted His-tag construct.

2.1.2 Protein Expression and Purification

For expression of holo-PYP (protein with covalently bound chromophore pCA) the pACYC(talpcl) vector, encoding for the two enzymes responsible for *in vivo* synthesis and incorporation of the chromophore as it is described in section 1.3 on page 8, and the pET15b(pyp/His) vector encoding for either the WT' or one of the mutants were successively transformed into the *E.coli* expression strain BL21(DE3) by electroporation and selected by chloramphenicol and amplcillin resistance, respectively.

Protein expression was performed in LB (lysogeny broth) medium with 100 µg/ml ampicillin and 60 µg/ml chloramphenicol (both Carl Roth) either in chicane flasks or a flask that was purged with air to ensure a sufficient supply of oxygen. The culture was inoculated with 2 - 3 % overnight culture and grown at 37 °C until it reached an optical density of 0.7 - 0.8 at 600 nm to induce it with a final concentration of 1 mM IPTG (isopropyl-β-D-thiogalactopyranoside, by Carl Roth).

The induced cells were grown for another 18 - 20 h at room temperature before they were harvested and resuspended in buffer (50 mM Tris/HCl, 100 mM NaCl, pH 8). After cell lysis by sonification, genomic DNA was precipitated with 0.5 % streptomycin sulfate on ice and debris was removed by centrifugation with a *L7 Ultracentrifuge* by Beckman.

The cell lysate was purified by affinity chromatography using a Ni^{2+}-nitrilotriacetic acid (Ni-NTA) column that bound the His-tagged protein. In a first step, the column was washed with 10 mM imidazole in buffer (50 mM Tris/HCl, 100 mM NaCl, pH 8) before the His-tagged protein was eluated with 250 mM imidazole buffer. The washing step with 10 mM imidazole is not mandatory since it was found that leaving it out resulted in similarly purified eluate.

To optimize the yield of holo-protein, especially for the mutants, an additional step of chemical reconstitution with the activated chromophore, as described in the dissertation of J. Hendriks (2002) [133], was introduced. The activated chromophore was obtained by mixing p-coumaric acid (Sigma) in dry DMF (N,N-dimethylformamide, Fluka Chemie) with CDI (1,1'-carbonyldiimidazole, Sigma Aldrich) in dry DMF. Under stirrig, 200 µl of the activated chromohphore were slowly mixed to the eluate from the first purification step, changed into 100 mM borate buffer and concentrated to a small volume. The protein solution was filled up to 40 ml volume with 50 mM Tris/HCl, 100 mM NaCl buffer (pH 8) supplemented with 1 mM DTE (dithioerythritol). To remove the His-tag 4 ml TEV protease (c = 3 mg/ml) were added and incubated over night at room temperature followed by a second purification step with the Ni-NTA column. To increase the yield of holo-PYP this chemical reconstruction was first tested on eluate containing solely apo-PYP that was expressed without the pACYC(talpcl) vector. But since the results were similar to the ones obtained for the *in vivo* incorporation, both methods were applied together.

For the separation of holo-PYP from apo-PYP the protein was changed into 20 mM Tris/HCl buffer (pH 9) and an anionic exchange chromatography was performed with a *Source Q* column (GE Healthcare Life Science). The protein was eluated with a gradient running from 0 to 150 mM NaCl. The holo-PYP was eluated at lower salt concentrations than the apo-PYP.

Unfortunately, there were many fractions collected containing a mixture of holo- and apo protein. With a second purification step by anionic exchange chromatography it was also not possible to further separate the two species in these fractions.

All purification steps were monitored and the purity of the holo-PYP was confirmed with a 10 % Schaegger polyacrylamide gel electrophoresis (PAGE) as it is shown in an exemplary way for PYP-WT in figure 2.1. The amount of holo-PYP was determined by using the ratio of absorptions between 446 nm (chromophore absortion) and ca. 280 nm (absorption of aromatic amino acids in protein backbone). Kyndt *et al.* [53] calculated a ratio of 2.2 for 446 nm to 280 nm for fully separated holo-protein of the PYP-WT which can be seen in figure 2.2 on the following page as well. In general, only fractions with an amount of > 90 % holo-PYP were collected and used for measurements, only exception was M100C for which often only an amount of 50 - 60 % holo-protein was achieved.

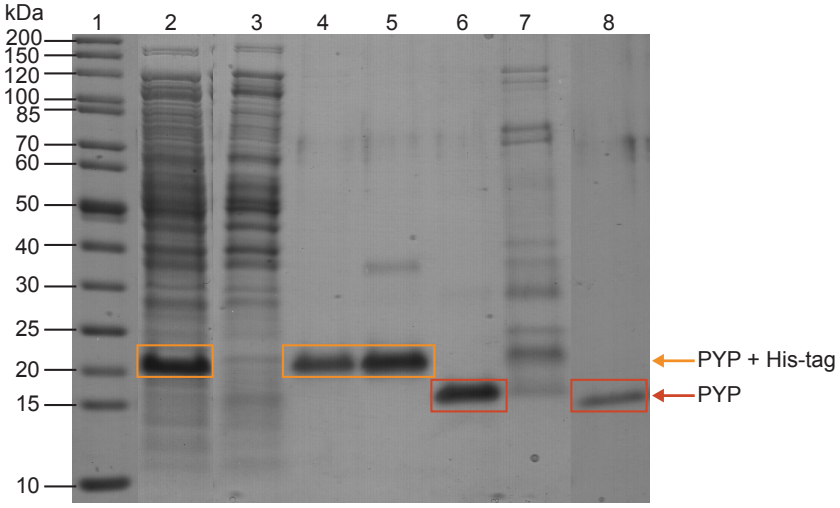

Figure 2.1: *10 % Schaegger PAGE of PYP-WT. Trace 1: PageRuler Unstained Protein Ladder 200 to 10 kDa (ThermoFisher Scientific); 2: cytosol after lysis of BL21(DE3) after expression of PYP-WT; 3: flow-through of 1st Ni-NTA purification; 4: wash step with 10 mM imidazole of 1st Ni-NTA purification; 5: eluate (250 mM imidazole) of 1st Ni-NTA purification; 6: flow-through of 2nd Ni-NTA purification after cleavage of the His-tag; 7: eluate (250 mM imidazole) of 2nd Ni-NTA purification; 8: purified PYP after anionic exchange chromatography. The bands of PYP with the His-tag construct are marked in orange, the ones without the His-tag construct (cleaved by TEV protease) are marked in red.*

The aforementioned WT' was actually a PYP mutant with the mutation M1G, due to the inserted TEV cleavage site that was used to separate the His-tag from the protein. This mutation was also present in all the cysteine mutants as well and therefore this protein was used for comparison reasons and is referred to in the following as PYP-WT'.

The actual WT that is expressed with the original pET15b(pyp) vector described by Kyndt *et al.* [53] was prepared, too. Expression and cell lysis were performed with the same protocol as described above. For purification, in the first step the anion exchange column *Q Sepharose High Performance* (GE Healthcare) was used with a 50 mM Tris/HCl buffer (pH 9) and a gradient from 0 to 300 mM NaCl for elution. As second purification step size exclusion chromatography with a *Sephacryl S100* (GE Healthcare) and 50 mM Tris/HCl (pH 8) as running buffer was carried out. The purity of the protein was verified by PAGE and UV/vis spectroscopy as well and the amount of holo-PYP was about 100 %.

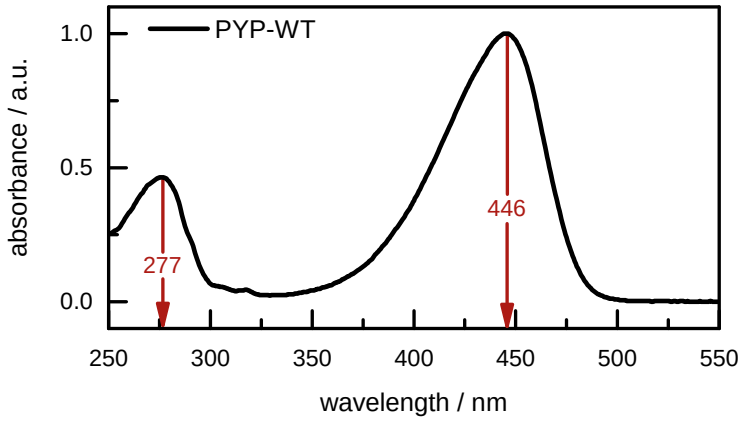

Figure 2.2: *Typical UV/vis absorption spectrum of PYP (WT). A ratio of 2.2 [53] for the absorbance between 446 nm and 277 nm (approx. 280 nm) indicates a fully separated holo-protein.*

2.1.3 Protein Cyanylation

The thiocyanate label (SCN) was introduced into the PYP mutants *via* a cyanylation reaction of the cysteines. This protocol was adapted over the last years due to slight improvements in the procedure. In the following the current state of the protocol is given. As buffer for the cyanylation 100 mM Tris/HCl (pH 7) was used in all steps.

To reduce intermolecular disulfide bridges that may have formed approximately 10 mM TCEP (tris(2-carboxyethyl)phosphine) were added to the purified holo-PYP ($\sim$ 30 - 50 mg protein in total per reaction) and washed with buffer to reduce the concentration of the reducing agent by centrifugation in *Vivaspin 2* (Satorius Stedim Biotech) with 5 kDa cut-off or *Amicon Ultra-15 Centrifugal Filter Devices* (Merck) with 3 kDa cut-off.

Afterwards predissolved DTNB (5,5'-dithiobis(2-nitrobenzoic acid), Sigma Aldrich) was added in a two-fold excess in a falcon and incubated for 1 h at room temperature while it was shaking. The yellow byproduct TNB (2-nitro-5-thiobenzoate) was washed out with the buffer by centrifugation until the flow-through was colorless again. For cyanylation isotopic-labeled potassium cyanide ($K^{13}C^{15}N$, Sigma Aldrich), predissolved in buffer, was added in excess and incubated shaking for 30 - 60 minutes at room temperature. TNB and remaining KCN were removed by washing with the buffer until the flow-through got colorless. In the end the buffer was exchanged either to 50 mM sodium phosphate (pH 8) or 50 mM sodium phosphate (pD 8). A successful incorporation of thiocyanate was examined by FTIR absorption spectroscopy and ESI mass spectrometry by Rene Zangl (AK Morgner, Uni Frankfurt).

FTIR absorption spectroscopy and ESI mass spectrometry revealed that labeling of the mutants V57C ($<$ 10 % labeled) and V122C ($\approx$ 50 % labeled) had a low efficiency. As both side chains point into the interior of the protein and therefore are probably not easy accessible for DTNB and KCN, both mutants were labeled under high urea concentrations as it was done for Calmodulin [134]. In principle the cyanylation reaction followed the protocol described before, but before adding DTNB and potassium cyanide, respectively, the protein solution was concentrated to a small volume ($\sim$ 0.5 - 1 ml) and filled up to 7 ml with 9 mM urea buffer (100 mM Tris/HCl, pH 7). After incubation the urea concentration

was diluted by a factor of two with buffer, before it was given into the centricon for the washing procedure. In the end the samples had to be checked with UV/vis spectroscopy if all protein was folded back properly (unfolded protein shows a peak at 346 nm). For V57C the labeling efficiency increased drastically with this procedure, for V122C there was no significant difference in efficiency observed.

Additionaly, labeling under constant irradiation was tested for V57C as the protein structure is known to become less compact in the signaling state. After adding DTNB and KCN, respectively, the protein solution was shaken in a 15-ml falcon tube (approximately 10 ml of solution) and in doing so it was illuminated with a 450 nm-LED for 2-3 hours. However, FTIR absorption spectroscopy revealed no increased labeling efficiency. Maybe a smaller sample volume has to be used, stirred with a small stirring bar and instead of the LED, that illuminated a relatively large area with low power, the continuous wave diode laser (*LDM-445-1600*, Lasertack), that was used in the steady-state infrared experiments and has a beam diameter of approximately 4 x 4 mm with high intensities, could irradiate the sample.

2.2 UV/vis Spectroscopy

UV/vis spectra were recorded with a Hitachi *U-2000 Spectrophotometer*. The measurements were performed with a quartz cuvette of 1 cm path length. Fully demineralized water was taken as background for the protein measurements. The samples were diluted to have a maximum absorption of OD 1.0. All spectra were taken at room temperature with the spectrometer scan speed set to 400 nm/min and a step size of 0.5 nm. The extinction coefficient of PYP's chromophore that was used to calculate the (holo-)protein concentration by Lambert-Beer law (see equation (1.2) on page 3) is ε = 45500 $M^{-1}cm^{-1}$ at 446 nm [135]. The given extinction coefficient was determined for the WT, but was applied to the mutants as well, although there could be some variations in the value for the mutants especially when they are near the chromophore.

2.3 CD Spectroscopy

CD measurements of WT, WT' and the SCN-labeled mutants were performed with a Jasco *J-720 spectropolarimeter*. For the measurements the protein samples in aqueous buffer (50 mM sodium phosphate, pH 8) were brought between to calcium fluoride (CaF_2) windows with a path length of 5.8 µm. Near UV/vis spectra were recorded at a concentration of approximately 2 mM in a region from 250 to 550 nm, far UV spectra at a concentration lower than 15 µM from 180 to 250 nm. As reference for the background the same buffer was used. The measurements were taken at room temperature. Spectra were recorded with a scanning speed of 200 nm/min and a band width of 1.0 nm. In both regions 20 single spectra were accumulated to increase the signal-to-noise-ratio.

2.4 Steady-state FTIR Spectroscopy

FTIR spectra in the steady-state were recorded with a *Tensor 27* spectrometer by Bruker equipped with a photoinductive mercury cadmium telluride (MCT) detector. PYP samples were either measured in phosphate buffer (50 mM NaPi, pH 8) or deuterated phosphate buffer (50 mM NaPi, pD 8). Absorption spectra and especially difference spectra in the SCN label region were taken in D_2O at a path length of 50 µm and protein concentrations of 6 - 12 mM, difference spectra especially in the amide and chromophore region were taken in H_2O at a path length of 10 µm and concentrations of 2 - 8 mM. The path length was determined by the thickness of a PTFE (polytetrafluoroethylene) spacer (Goodfellow Cambridge Limited) that separated to CaF_2 windows (Crystal GmbH) and were mounted in a self-built sample cell that was also used for all laser measurements. All spectra were recorded with a aperture of 1 mm and 1 cm^{-1} resolution for absorption spectra or 2 cm^{-1} resolution for difference spectra.

For the absorption measurements air was used as background, whereas for the difference spectra, the spectrum of PYP in its dark state (pG) was measured as background and subtracted from the PYP spectrum under constant irradiation with blue light (signaling state pB). The temperature for all measurements was set to 8 °C by using a circulating water bath (*Julabo F-25*) for temperature control. To accumulate the signaling state (pB) constant irradiation with blue light of 445 nm was used. Therefore a continuous wave diode laser (*LDM-445-1600*, Lasertack) was coupled into the spectrometer and directed to the sample by two enhanced aluminum mirrors (Thorlabs). The irradiation power was approximately 300 mW at the sample position.

For the FTLS measurements absorption spectra were recorded at different temperatures for 50 mM MeSCN in THF or D_2O with a 50 µm spacer and for A30C*, A44C* and V57C* in deuterated phosphate buffer (50 mM NaPi, pD 8) with a protein concentration of 8 mM and 100 µm path length. The circulating water bath mentioned above was used to set the temperatures at approximately 5 °C, 12 °C, 20 °C, 25 °C, 30 °C and 39 °C measured directly at the sample cell with a digital thermometer. At each temperature the sample was equilibrated for approximately 15 min and measured in the dark and under constant irradiation with blue light.

To correct for the solvent background, all measured SCN spectra were fitted with a polynomial of fifth order excluding the region of the signal. The fit was subtracted from the raw data.

The absorption wavenumbers of the SCN bands in the absorption spectra were determined in two different ways. On the one hand, the second derivative of the SCN signal was taken and smoothed with a Savitzky-Golay filter. The negative minima of the second derivative marked the band positions. This method is also sensitive to find pronounced subpopulations. The absorption wavenumbers obtained by the second derivative are referred to as $\tilde{\nu}_{sd}$. On the other hand, the first central moment of the entire band was used to get the mean wavenumber $\tilde{\nu}_{mean}$ of the SCN absorption as shown in the following equation

$$\tilde{\nu}_{mean} = \frac{\int_{2060}^{2100} d\tilde{\nu} I(\tilde{\nu}) \tilde{\nu}}{\int_{2060}^{2100} d\tilde{\nu} I(\tilde{\nu})} \tag{2.1}$$

with wavenumber $\tilde{\nu}$ and absorbance I($\tilde{\nu}$) [134].

2.5 SASA Calculations

SASA (solvent accessible surface area) calculations of all residues that were chosen for mutation and of all SCN-labeled PYP mutants were performed by Bartosz Błasiak (currently at Wrocław University of Science and Technology, Department of Physical and Quantum Chemistry, Poland) applying umbrella sampling molecular dynamics simulations. For the dark state structure pdb-file 1NWZ and for the signaling state structure pdb-file 2KX6 were used. A detailed methodological description of the calculations can be found in Blankenburg *et al.* [136] and Schmidt-Engler and Blankenburg *et al.* [121]. The SASA approach probes the accessibility of residues by rolling a water sphere of a given radius (here 1.4 Å) along the van der Waals surface of the protein [137].

2.6 nESI Mass Spectrometry

nESI (nano electrospray ionization) mass spectra of WT-PYP and the SCN-labeled mutants were recorded and analyzed by Rene Zangl and Jan Hoffmann from Nina Morgner's group (Institute of Physical and Theoretical Chemistry). The proteins were brought into gas phase *via* the ESI process resulting in highly charged ions which were analyzed by a time-of-flight mass analyzer. Labeling efficiencies were calculated for all samples that were used in the time-resolved vis-pump-IR-probe experiments.

Ion mobility separation (IMS) data were measured under non-illuminated and illuminated conditions. With this method it was possible to separate the gas phase ions according to their charge state and collision cross section (CCS). Depending on the exposed surface area both parameters change allowing predictions about the shape and conformational state of the investigated protein [138]. To obtain molecules in the illuminated state, the sample reservoir was irradiated with a blue (445 nm) cw diode laser in the nESI tip.

2.7 Ultrafast IR-Pump-IR-Probe Experiments

The ultrafast IR-pump-IR-probe experiments were performed to determine the vibrational lifetime of the SCN label in different PYP mutants in the dark and signaling state. The measurements and their analysis were carried out together with Julian Schmidt-Engler. In this chapter the structure and operating principle of the setup as well as the implementation of the measurements are described.

2.7.1 Setup

To carry out ultrafast IR-pump-IR-probe studies, a new 2D mid-IR spectroscopy setup was constructed during this thesis combining the probe light path with the pump light path and sending both beams through a sample and over a spectrometer on the mid-IR detector. A schematic drawing of the whole setup is depicted in figure 2.3 on the following page.

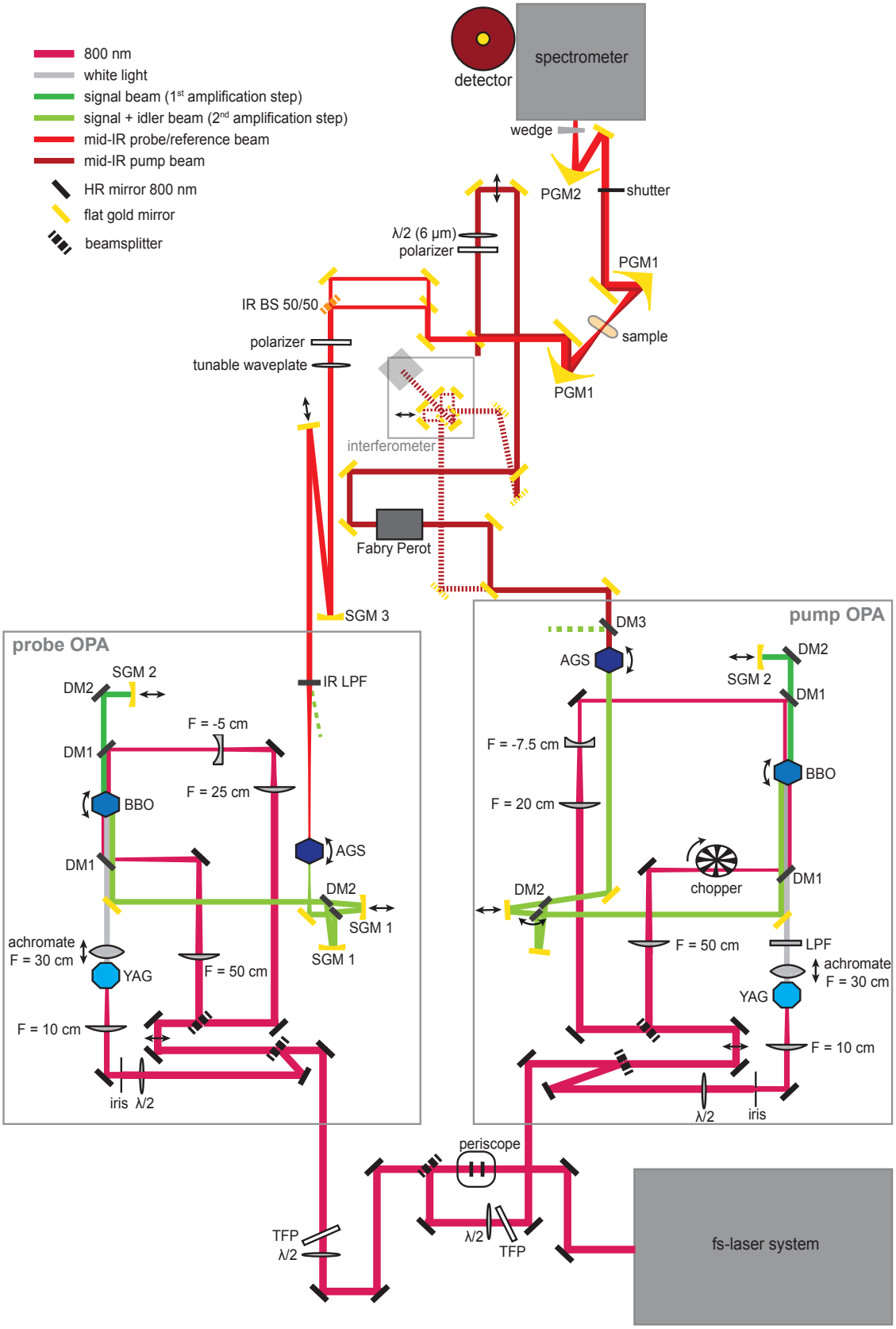

Figure 2.3: *Schematic drawing of the new-built 2D mid-IR spectroscopy setup that was used for the ultrafast IR-pump-IR-probe study of SCN-labeled PYP. TFP = thin film polarizer, LFP = long pass filter, BS = beamsplitter. The specifications for the dichroic mirrors (DM1-3), the spherical gold mirrors (SGM1-3), the parabolic gold mirrors (PGM1+2), the YAG disk and the BBO and AGS crystals are given in table 2.1 on the facing page.*

Table 2.1: *Specifications of selected optics that were built into the 2D setup and are depicted in figure 2.3 on the facing page.*

Label	Optic	Manufacturer
DM1	dichroic mirror, Infrasil S1: ARr(45°, 1200-2700 nm)<2 % S2: HRp(45°, 780-820 nm)>99.7 % + Rr(45°, 1200-2700 nm)<10 %	Layertec
DM2	dichroic mirror, Infrasil S1: uncoated S2: HRs(45°, 1220-1560 nm)>99.7 % + Rp(45°, 1620-2500 nm)<10 %	Layertec
DM3	dichroic mirror, ZnSe S1: HRs(45°, 1280-1500 nm)+ HRp(45°, 1710-2180 nm) + HTp(45°, 3000-18000 nm) S2: AR(45°, 3000-18000 nm)	Altechna
SGM1	spherical gold mirror F=−50 cm 6N-BK7	Laseroptik
SGM2	spherical gold mirror F=−25 cm 6N-BK7	Laseroptik
SGM3	spherical gold mirror F=−100 cm 6N-BK7	Laseroptik
PGM1	off-axis parabolic gold mirror F=101.6 mm, 30°, Ø50.8 mm	Edmund Optics
PGM2	off-axis parabolic gold mirror F=127 mm, 30°, Ø50.8 mm	Edmund Optics
YAG	$Y_3Al_5O_{12}$ crystal, undoped, orientation (111), 4 mm	Crystal GmbH
BBO	β-BaB_2O_4 crystal, Θ=27°, φ=30°, type II, 4 mm	Castech
AGS	$AgGaS_2$ crystal, Θ=40°, φ=45°, type II, S2 wedged 0.5°, 4 mm	Eksma Optics

For generation of mid-IR light two OPAs (optical parametric amplifiers) - one high-power for the pump beam and one low-power for the probe beam - were used. These two OPAs had been built by Tim Vogt und Katharina Eberl. Besides the different input powers - 1.5 mJ for the high-power OPA and 200 µJ for the low-power OPA, both were constructed almost identically according to the design of Hamm *et al.* [139].

The OPAs were operated by 800 nm fs-pulses produced by a *Spitfire Ace* system from Spectra Physics with a repetition rate of 1 kHz (5 mJ, 90 fs pulses). Later the repetition rate was increased to 3 kHz.[2] This 5 W system was pumped by an *Empower 45* laser and used a *Mai Tai SP* laser as oscillator. The output energy of the laser system was 5 mJ. To adjust the height of the 800 nm beam to 145 mm above the laser table, a periscope was used. Afterwards the beam was split by a 80/20-beamsplitter[3] (84/16 for 3 kHz) to separate light for the low-power and the high-power OPA. The input power in both OPAs was regulated by a half-wave plate and thin film polarizer (TFP) combination. This allowed for corrections of differences in day-to-day power fluctuations. The length of the beam paths before the OPAs had to be adjusted during construction of the pump-probe setup to keep the path length of mid-IR light as short as possible.

In the OPA a very small portion of the incoming beam was reflected by a beamsplitter for generation of a white light continuum [140]. The transmitted light was used as pump light. Initially, the 800 nm light was p-polarized. To pump the white light generation the

[2]Only mentioned for completeness as all measurements shown in this thesis were performed at 1 kHz.
[3]Ratios for beamsplitters are always given as % reflection/% transmission.

polarization was rotated by a half-wave plate. Then the s-polarized light was focused into a 4 mm thick YAG-crystal. Third-order nonlinear effects in the material led to extreme spectral broadening of the pulses [140, 141].

The white light was focused into the BBO (β-barium borate) crystal by an achromatic lens (F = 30 cm). To get rid of short wavelength components, which were not needed for the amplification process, a long-pass filter (LPF) was used.

While the white light served as seed beam, a portion of the fundamental 800 nm light was used as first pump beam. It was separated by a second beamsplitter and focused into the BBO with a convex lens (F = 50 cm). If the seed and the pump pulse were spatially and temporally overlapping in the BBO crystal, preamplification took place.

The resulting near-IR signal beam was isolated from the idler using dichroic mirrors (DM1 and DM2) as filters and collimated by a spherical gold mirror (SGM2, F = -25 cm). Then it traveled back to the BBO crystal where it was mixed with the second pump beam. This intense pump light was the transmitted light of the second beamsplitter and therefore the majority of the fundamental 800 nm beam. To fit the size of the BBO crystal, its beam size was reduced by an implemented telescope (plano-convex lens with F = 25 cm in the probe and F = 20 cm in the pump OPA, plano-concave lens with F = -5 cm (probe) or F = -7.5 cm (pump)). In this second amplification stage an amplified signal beam and an idler beam were generated.

To generate mid-IR light a second non-linear process was necessary. Therefore signal and idler beam were separated by a dichroic mirror (DM2) and led through an interferometer. In the high-power OPA two flat gold mirrors and in the low-power OPA two spherical gold mirrors with F = -50 cm were used in the interferometer. One of the two gold mirrors was mounted on a delay stage to adjust not only the spatial but also the temporal overlap of the signal and idler beam. Afterwards both collinear beams traveled through a silver thiogallate ($AgGaS_2$, short AGS) crystal. In the crystal the non-linear process of difference frequency generation (DFG) of the near-IR signal and near-IR idler created mid-IR light, if the phase matching condition was met. Due to the type I-phase matching in the AGS crystal, the resulting mid-IR light was p-polarized. By setting different combinations of rotational angles for the BBO and AGS crystals a spectral tuning range from 3 - 6 µm was achieved. After the high-power OPA another dichroic mirror (DM3) and after the low-power OPA an infrared long-pass filter (LPF) were used to get rid of the transmitted near-IR light, before the mid-IR light from the two OPAs was sent into the so called 2D-setup.

As in the low-power OPA's interferometer two concave mirrors with F = -50 cm were used to focus the beam into the AGS crystal, a telescope was applied to collimate the mid-IR beam. Therefore the beam was first sent to a flat gold mirror on a delay stage to adjust the path length and then to a concave mirror with F = -100 cm. Afterwards the collimated beam traveled through a tunable waveplate and polarizer combination that was used to vary the intensity, before the beam was split into a probe and a reference beam by a 50/50 mid-IR beamsplitter. The probe beam was adjusted to a height of 135 mm over the table, the reference beam to a height of 145 mm in order to be spatially separated at the sample position later on. Both beams were focused into the sample with a parabolic gold mirror (PGM1, F = 108.89 mm). The focus size was about 85 x 80 µm (FWHM of diameter) for the probe and 85 x 75 µm for the reference beam at 4620 nm. In the sample, probe and

reference beam were separated in height by approximately one millimeter. To collimate the beams a second parabolic gold mirror with identical focal length was implemented after the sample position. A third parabolic mirror (PGM2, F = 136.1 mm) focused the probe and reference beam into the spectrometer.

To guarantee an individual frequency dispersion for probe and reference beam to the mercury cadmium telluride (HgCdTe, short MCT) array detector with 2 x 64 pixels (Infrared Associates), the two beams were focused to different focus points in the spectrometer. Therefore they were made parallel to each other by passing two BaF_2 wedges (7.7°) in front of the spectrometer's entrance slit.

As the OPAs produced a relatively broad mid-IR spectrum, a Fabry-Pérot filter was placed in the pump beam path to create a spectrally narrow pump pulse. Thus it was possible to excite only a narrow selected part of the IR-spectrum and to reduce solvent excitation. Drawback of this method was a very broad pulse in the time domain (as it is narrow in the frequency domain). Therefore fast times after excitation (< 1 ps) could not be measured. Alternatively, a second pathway for the pump beam was used running through a Mach-Zehnder interferometer[4] that was implemented by Julian Schmidt-Engler (shown in dashed lines in Figure 2.3) [142]. The interferometer operated in the time domain and as it used the broadband spectrum of the OPA, it made faster times accessible, but lacking the selective excitation. For suppression of scattering an oscillating ZeSn Brewster window (wobbler) was used in the interferometer path.

The pump beam traveled over a motorized translation stage (Physik Instrumente (PI)) to control the time delay between pump and probe pulse in the sample and to measure time-resolved spectra. A polarizer was placed in the pump path to rotate the polarization of the pump pulse. To reach spatial overlap between pump and probe pulse, the pump pulse was focused to the same spot in the sample as the probe using the same parabolic mirrors. The focus size of the pump beam is about 110 x 110 µm. To avoid pump light on the detector, the pump beam was blocked by a shutter in front of the entrance slit of the spectrometer.

An optical chopper (Thorlabs) is placed in the first 800 nm pump beam of the pump OPA and runs at 500 Hz to prevent every second mid IR pump pulse from reaching the sample. This allows to collect data with alternating pump on and pump off which are used to calculate difference absorption spectra ($pump_{on}$ - $pump_{off}$).

2.7.2 Experiment

For the ultrafast IR-pump-IR-probe experiments the OPAs were operated at $\lambda_0 \approx 4810$ nm and delivered approximately 2 µJ for the low-power probe OPA and over 12 µJ for the high-power pump OPA. The broadband pump pulses were narrowed by a Fabry-Pérot filter to 12 cm^{-1} bandwidth (6th order, 1.2 ps pulse duration). The polarization of the pump pulse was set to 54.7 ° (magic angle) with respect to the probe pulse to cancel out the contribution of rotational diffusion from the measured dynamics.

[4]Only mentioned for completeness as all IR-pump-IR-probe measurements shown in this thesis were performed with the Fabry-Pérot filter.

For dispersion onto the MCT detector a 300 l/mm grating was used resulting in a resolution of 1 cm^{-1} for the recorded difference absorption spectra. The detector was cooled with liquid nitrogen and the dewar was refilled by an automatic liquid nitrogen refilling system [143] to guarantee continuous data acquisition. The 2D-setup was purged with dry air during the measurements.

Protein samples of the cyanylated PYP mutants were measured in H_2O or D_2O buffer (50 mM sodium phosphate, pH 8 or pD 8). The same buffers were used for the methyl thiocyanate sample (Sigma Aldrich) that was prepared at a final concentration of 200 mM. A drop of sample (7.5 µl) was brought between two CaF_2 windows (Crystal GmbH) separated by a PTFE spacer (Goodfellow Cambridge Limited) with a thickness of 100 µm for H_2O samples and 150 µm for D_2O samples (M100C*). Protein concentrations ranged from 10 to 18 mM. The temperature of the sample was kept at 8 °C by a circulating water bath (*Julabo F-25*) that was connected to the sample cell holder.

For measurements of the signaling state (pB) the sample was constantly irradiated by 445 nm light of 300 mW by using a cw diode laser (*LDM-445-1600*, Lasertack).

Data were recorded from −40 to 300 ps. The spectrum of the first time point (−40 ps), with the probe pulse arriving at the sample before the pump pulse, was used for background correction. Global analysis was performed on all data using the Globe Toolbox [144]. For the global fit a parallel model was applied fitting the data with six or seven exponential functions - three or four sub-ps components to fit during the temporal overlap of pump and probe pulse (< 1 ps after excitation), one fast component that could be attributed to solvent excitation, one component corresponding to the vibrational lifetime of the SCN label and one "long lived" component that exceeded the timescale of the experiment (> 300 ps). All components are depicted in figure E.5 on page 197 and figure E.6 on page 198 in the appendix.

2.8 Transient Vis-Pump-IR-Probe Experiments

The transient vis-pump-IR-probe measurements of SCN-labeled PYP and their evaluation were accomplished together with Luuk van Wilderen. The measurements were performed in two experiments to follow the photocycle dynamics of PYP up to almost 1 ms with a high temporal resolution (600 fs). In this chapter the experimental setup for the ps-to-ms experiments (electronic delays) with the two synchronized laser systems, the Lissajous scanner for translation of the sample cell, the chopper divider scheme that was introduced to lower the repetition rate of the pump pulses and the implementation of the measurements are illustrated. Further the setup of the fs-to-ns experiments (mechanical delays), which were conducted to add the very fast dynamics of the PYP photocycle with a resolution of several hundred femtoseconds to the synchronized vis-pump-IR-probe experiments, is described.

2.8.1 Setup Electronically Delayed Vis-Pump-IR-Probe Experiments

To extend the delay time between pump and probe pulse and to follow dynamics up to almost one millisecond, two synchronized fs-laser systems were used for vis-pump-IR-probe experiments. In contrast to conventional time-resolved laser experiments the delay between the two pulses is not modulated by the mechanical change of optical path length - limiting the delay time to several nanoseconds - but is controlled electronically. The system for synchronizing the two 1 kHz fs-lasers was first described by Jens Bredenbeck and Jan Helbing [40] and introduced in our lab by Manuel Pescher and Luuk van Wilderen [145].

The first fs-laser system that served as master oscillator and for probe pulse generation was a 3 W laser/amplifier system by Spectra Physics. A passively modelocked Ti:Sapphire oscillator (*Tsunami*, 80 MHz) was pumped by a diode-pumped, solid-state cw-laser (*Millennia Pro*). For pulse amplification a Ti:Sapphire regenerative amplifier (*Spitfire Pro*) was used that was pumped by a Q-switched Nd:YLF laser (*Empower*). The laser system ultimately generated 3 mJ of output power at 800 nm with a pulse duration of 100 fs and a repetition rate of 1 kHz and an output energy of 3 mJ.

As slave oscillator and for pump pulse generation a 5 W laser/amplifier system by Coherent was used. A modelocked Ti:Sapphire oscillator (*Mira 900*, 80 MHz) was pumped by a diode-pumped, solid-state cw-laser (*Verdi*) and seeded the 1 kHz Ti:Sapphire amplifier (*Legend Elite*) with integrated, Q-switched Nd:YLF pump laser (*Evolution*). This produced 800 nm pulses of 100 fs duration with a repetition rate of 1 kHz and an average output power of 4.5 mJ.

The master oscillator delivered the reference frequency and set the clock for the other oscillator, the so called slave, to synchronize the pulses in both systems in phase and frequency. The pulse trains of both oscillators were monitored with photodiodes, converted into a sinusoidal waveform and sent into an electronic circuit that mixed the signals and allowed to introduce a phase shift between the two signals. The output of that circuit provided a DC voltage that steered a piezo-mounted mirror in the slaves's oscillator, providing delay times up to 12.5 ns - the round trip time of the pulses in the oscillator. Besides the fine adjustment with the piezo actuator, the cavity length could additionally be controlled *via* the cavity end mirror that was moved by a motorized micrometer actuator. For delay times longer than 12.5 ns, the amplifier triggers (Q-switch and pockels cells) of the slave were electronically delayed relative to the master by multiples of the oscillator round trip time. To scan continuously up to 750 µs, a combination of both methods was employed. An overview diagram outlining the principle of synchronization of two laser systems is shown in figure 2.4 on the next page [40, 145].

As control unit for the synchtonization of the two oscillators, the so called synchrobox (in figure 2.4 on the following page labeled with "trigger generation") was used. It is depicted in figure 2.5 on page 31 with a schematic drawing of the whole synchro setup. A detailed description of the used setup is given in the following.

The master oscillator provided the 800 nm pulses for probe pulse generation. To obtain mid-IR light in a range from 4720 to 6450 nm, 350 µJ of the 800 nm light (regulated by an half-wave plate/thin film polarizer (TFP) combination) were led into an OPA with a white light seeded two-stage BBO to generate near-IR signal and idler pulses that were mixed

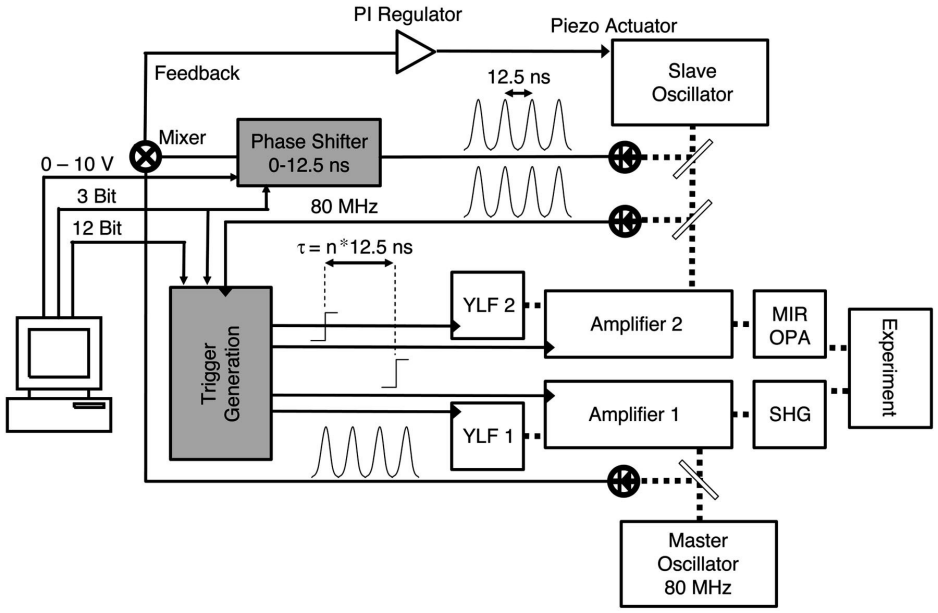

Figure 2.4: *Diagram of synchronization of two fs-laser systems. The phase shifter modulates the delay times from 0 to 12.5 ns by shifting the phase of the slave oscillator's pulse train with respect to the phase of the master oscillator. The trigger generation is used to delay the trigger for the slave amplifier by multiples of 12.5 ns. The figure was adapted with permission from [40] - Published by Review of Scientific Instruments, American Institute of Physics.*

in an AGS crystal for difference frequency generation (DFG). As the probe OPA in the 2D mid-IR setup, described in section 2.7 on page 23, had been identically constructed as this OPA, it is not depicted in detail in figure 2.5 on the next page (indicated as probe OPA).

As the OPA's interferometer had two concave mirrors (F = −50 cm) to focus signal and idler beam into the AGS crystal, the mid-IR beam had to be collimated by a concave gold mirror (SGM1, F = −7.5 cm) after the OPA. An IR long pass filter (LPF) was used to separate remaining signal and idler from the mid-IR light. The diameter of the mid-IR beam was decreased by a telescope consisting of two spherical gold mirrors with F = −10 cm (SGM2) and F = −15 cm (SGM 3). The mid-IR beam was split into probe and reference beam by an 50/50 IR beamsplitter (IR BS). Due to the polarization of the mid-IR light (p-polarized) more of the light was transmitted through the beamsplitter than reflected (50/50 refers to unpolarized light), therefore the intensity of the reference beam was further reduced by a second IR beamsplitter (65 % transmission) and was manually adjustable by a polarizer to match the intensity of the probe beam.

Afterwards both beams were led the same path at different heights and were focused into the sample by a parabolic gold mirror (PGM1, F = 101.6 mm) with the reference beam approximately 1 mm above the probe beam. The focus size of probe and reference beam was about 90 x 80 µm (FWHM of diameter) at a wavelength of 6 µm. A second parabolic gold mirror with the same focal length was used to collimate probe and reference beam behind the sample.

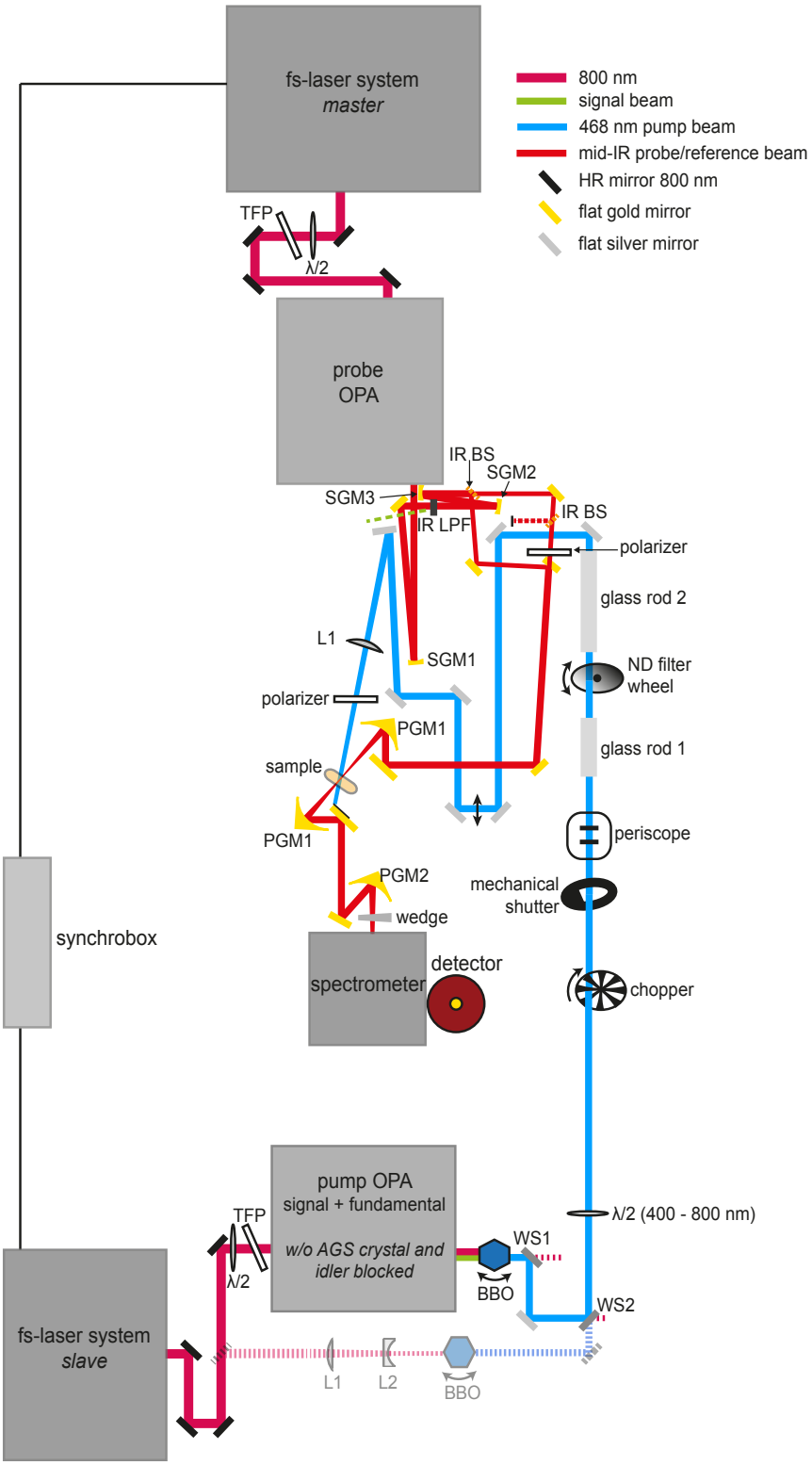

Figure 2.5: *Schematic drawing of the vis-pump-IR-probe spectroscopy setup with two synchronized fs-laser systems that was used to measure the dynamics of SCN-labeled PYP up to 750 µs. The pump beam was generated by mixing the fundamental with the signal beam to produce 468 nm (continuous lines), or doubling the fundamental to produce 401 nm (dashed lines). TFP = thin film polarizer, LFP = long pass filter, BS = beamsplitter. The specifications for the spherical gold mirrors (SGM1-3), the parabolic gold mirrors (PGM1+2), the lenses in the pump path (L1+2), the BBO crystal and the wavelength separators (WS1+2) are given in table 2.2.*

Table 2.2: *Specifications of selected optics that were built into the synchronized vis-pump-IR-probe setup and are depicted in figure 2.5 on the previous page.*

Label	Optic	Manufacturer
SGM1	spherical gold mirror F=−7.5 cm 6N-BK7	Laseroptik
SGM2	spherical gold mirror F=−10 cm 6N-BK7	Laseroptik
SGM3	spherical gold mirror F=−15 cm 6N-BK7	Laseroptik
PGM1	off-axis parabolic gold mirror F=101.6 mm, 30°, Ø50.8 mm	Edmund Optics
PGM2	off-axis parabolic gold mirror F=127 mm, 30°, Ø50.8 mm	Edmund Optics
BBO	β-BaB_2O_4 crystal, Θ=29.2°, φ=0°, 4 mm	unknown
WS1	wavelength separator, fused silica S1: ARr(45°, 600-1100 nm)<1.5 % S2: HRs(45°, 470-570 nm)>99.9 % + Rs+p(45°, 700-1100 nm)<5 %	Layertec
WS2	wavelength separator, fused silica S1: ARp(45°, 800-950 nm)<0.2 % S2: HRs(45°, 320-470±5 nm)>99.7 % + Rp(45°, 600-950 nm)<2 %	Layertec
L1	plano-convex lens F=25 cm UV fused silica, uncoated, 185-2100 nm	Thorlabs
L2	plano-concave lens F=−7.5 cm N-BK7, AR-coating, 650-1050 nm	Thorlabs

The frequencies of probe and reference beam were dispersed individually to the two arrays of 31 pixels of the MCT detector (Infrared Associates) by focusing the two beams to different spots in the spectrometer with a parabolic gold mirror (PGM2) with F = 127.0 mm. Two BaF_2 wedges (7.7°) in front of the spectrometer's entrance slit made the two beams parallel to each other.

For pump pulse generation the slave oscillator was used. Part of the 800 nm output was directed to the pump OPA whose input energy was regulated to 1.69 mJ by a half-wave plate and TFP combination. The OPA was constructed in an analogous manner as the pump OPA described in section 2.7 on page 23. Additionally, a 40/60-beamsplitter was placed after the telescope in the path of the 800 nm pump beam that was used for the second amplification stage. The reflected light was guided over a mechanical delay stage and sent over a dichroic mirror (HR 45° 800 ± 40 nm, AR 45° 1200 - 2700 nm <2 %) to a second BBO crystal (Θ = 29.2°, φ = 0°) that is shown in figure 2.5 on the previous page.

The signal beam of the optical parametric amplification process was sent through the interferometer as described for all OPAs before, but instead of mixing it with the idler beam in an AGS crystal for DFG, the idler was blocked and the signal (near-IR) was mixed with the fundamental in the aforementioned BBO crystal for sum frequency generation (SFG). The delay stage in the fundamental was used to adjust the temporal overlap. A half-wave plate was placed after the stage to optimize the polarization of the fundamental for the mixing process. The BBO crystal was mounted on two rotational mounts to allow variation of the crystal angles in three different planes with respect to the incoming beams. The SFG process generated about 22 µJ light of 468 nm (measured after WS2 in figure 2.5 on the preceding page).

As not all photons of fundamental and signal beam are converted in the non-linear process, wavelengths separators were used to separate the visible beam from the initial beams. First, a separator that reflected 470 - 570 nm and had an anti-reflective coating for 600 - 1100 nm (WS1, Layertec 101938) was implemented in the beam path, afterwards a separator that reflected 320 - 470 nm with an anti-reflective coating for 600 - 950 nm (WS2, Layertec 104582) was employed.

The pump beam was led over a periscope to adjust the beam height and through two glass rods that stretched the pulse duration to 900 fs in total (300 fs in glass rod 1 and 600 fs in glass rod 2) to lower the excitation density in the sample to prevent irreversible sample changes like adherence to the CaF_2 windows. An ND filter wheel was placed in the beam path to set the pump power according the requirements. The pump beam size at the sample position was aligned to be 180 x 180 µm at 468 nm by a focusing lens with F = 25 cm and a distance of 28.5 cm to the sample. A polarizer for 350 - 700 nm (GL15-A, Thorlabs) in front of the sample holder and a half-wave plate (400 - 800 nm, Thorlabs) that was already placed behind the second wavelength separator (WS2 in figure 2.5 on page 31) were used to set the pump light polarization and to optimize for maximum power at the sample, respectively.

An optical chopper (HMS) was placed in the pump beam path to block some of the pump pulses (*e.g.* every second pulse when running at 500 Hz) to calculate difference absorption spectra between pumped and unpumped sample ($pump_{on}$ - $pump_{off}$). Before the measurement the phase of the chopper (triggered by the Coherent slave system) had to be checked for the full range of delay times as the trigger pulses for the chopper tended to shift. For this purpose the relative phase of two TTL pulses (1 kHz master trigger vs. the 500 Hz output signal of the trigger electronics) was monitored on a scope as the output, used to trigger the data acquisition, may undesirably flipped its sign while electronically scanning the delay. Additionally, a mechanical shutter (Thorlabs) was installed to block the pump light if needed.

Although the time delays between pump and probe pulse were shifted electronically with the two synchronized lasers, the pump beam was guided over a mechanical delay line to determine for example time zero (when probe and pump pulse arrive simultaneously in the sample) in the semiconductor gallium arsenide (GaAs) and thus the jitter of the synchronization with a high femtosecond time resolution. The jitter is the instability of the relative timing between pump pulse and probe pulse mainly caused by the used electronics. The jitter determines the time resolution that is achievable in the pump-probe experiment. The signal from the GaAs rises after excitation with the visible light. The first derivative of this slope was fitted by a Gaussian function whose FWHM gave the jitter of the synchronization. The determined jitter was dependent on the spot at the GaAs and varied up to several tens of picoseconds (*e.g.* measured to be 15 - 40 ps for the same settings) when the spot was changed. To minimize the jitter the "gain" and "control" settings of the piezo control unit at the synchrobox were adjusted to vary the slope and proportion factor of the difference ferquency and the relative phase shift between master and slave oscillator [145].

At the beginning, when setting up the synchronization of the two laser systems, the temporal overlap between the pulses of the two laser systems was best found with a fast (400 MHz to 2 GHz) digital oscilloscope (*WaveRunner Xi-A*, borrowed from AK Dörner, Institute of Experimental Atomic Physics) using two photodiodes (model DET10A/M, Thorlabs).

Instead of creating pump light of 468 nm by SFG with signal and fundamental, there was an alternative way implemented for 401 nm light generation implied by the fainted dashed lines in pink and blue in figure 2.5 on page 31. In this case, a small part of the fundamental 800 nm was separated by a beamsplitter before the pump OPA and reduced in beam size by a telescope with a plano-convex lens of F = 25 cm and a plano-concave lens of F = −7.5 cm. In a BBO crystal ($\Theta = 27°$, $\varphi = 30°$) the fundamental was doubled by SFG. Afterwards the emerged 401 nm pump beam traveled the same path as the 468 nm pump beam using the same mirrors and lenses and resulting in a focus size at the sample of 140 x 140 µm.

Lissajous scanner

The sample cell was moved during the measurement to prevent adherence of the sample on the one hand and to excite a fresh sample spot with every laser shot - giving the previously excited molecules time to relax to the ground state before exciting them again - on the other. Therefore we designed a cell holder that moved the sample cell in a Lissajous pattern (see figure 2.6). The cell holder and the round sample cells were constructed in the Workshop for High-frequency and Optical Precision Mechanics of the Institute of Physical and Theoretical Chemistry. The design is a more compact and improved version of a similar device that was kindly provided by Chavdar Slavov from Joseph Wachtveitl's group (Institute of Physical and Theoretical Chemistry). The overall footprint was reduced, the sample holder was changed to accommodate the sample cell, the vertical stage was spring loaded to achieve a smoother returning motion, and stronger motors were installed. The electronics and the code to steer the motors were also designed and build together with Luuk van Wilderen (see appendix figure F.1 on page 199 and appendix F.1.2 on page 200). Pictures of the scanner are shown in figure 2.7 on the facing page.

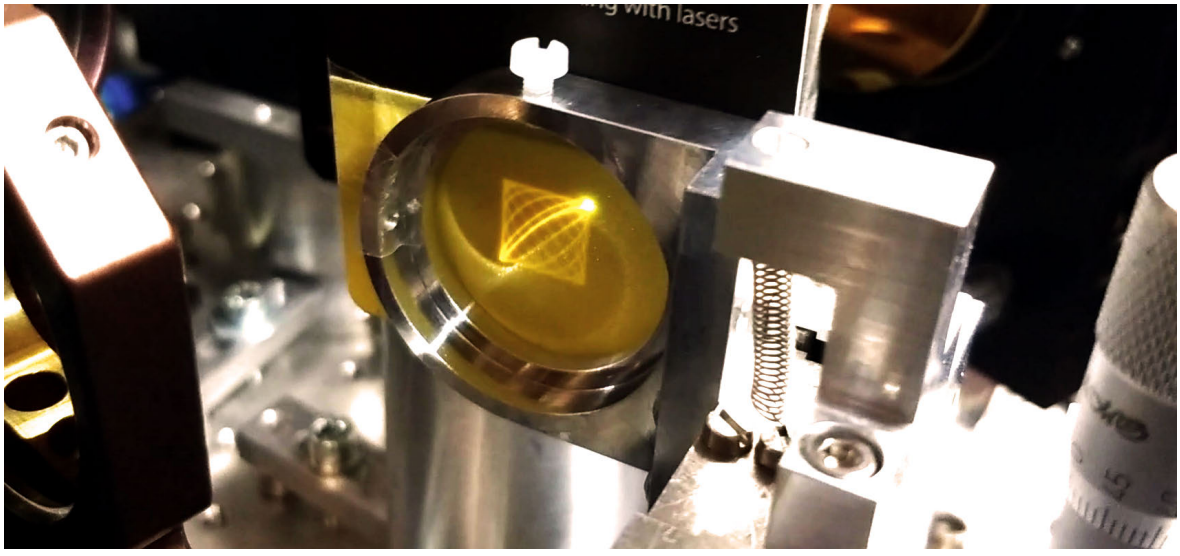

Figure 2.6: *Picture of an exemplary Lissajous pattern as it was used for rastering the sample during the experiment. For visualization of the pattern a laser detector card (VRC1: 250 - 540 nm, Thorlabs) was moved with the Lissajous scanner during illumination with the 401 nm pump beam. The pattern is visible due to the long emission time of the coating. The curved light to the left of the illuminated square pattern is a reflection from the aluminum holder.*

The Lissajous scanner was built with a base plate (1) at the bottom that allowed to fix the scanner to the laser table. It consisted of three mechanical delay stages which could be moved individually by a millimeter screw in x-, y- and z-direction - with x (2) horizontal to the table in the direction of motion of the first motor (4), with y (6) perpendicular to the table (up and down) in the direction of motion of the second motor (7) and z (3) horizontal to the table but in the direction of the traveling beams. First, the delay stage for movement in the x-direction (2) was mounted on the base plate (1). On top was the z-delay stage (3) mounted, this one was only moved to place the sample in the beam waist of the probe beam focus. When moved, both stages relocated the whole Lissajous scanner atop. Next came a plate on which the first motor (4) and the slide (5), that was driven by it over a rotation arm, were mounted. This motor was responsible for the horizontal movement. The y-delay stage (6) was attached perpendicular on the moving part of the slide. At the delay stage the second slide (8) that was driven vertically by the second motor (7) was fixed. The moving part of this slide was connected to the sample cell holder (9) shown in figure 2.7 with the cell (golden color) inserted.

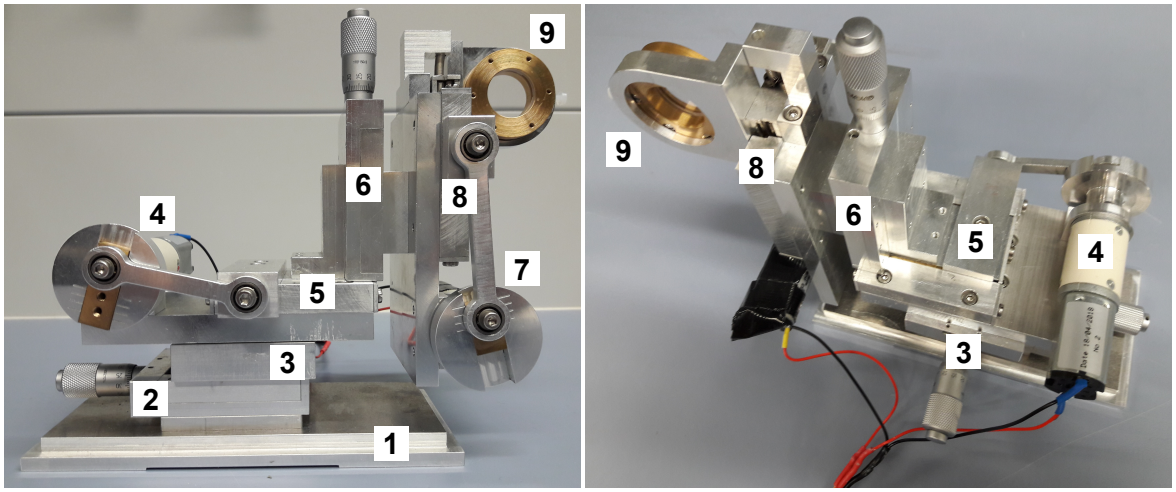

Figure 2.7: *Lissajous scanner as sample holder shown from two perspectives with inserted sample cell. 1: base plate; 2: x-delay stage; 3: z-delay stage; 4: motor 1; 5: slide driven by motor 1; 6: y-delay stage; 7: motor 2; 8: slide driven by motor 2; 9: cell holder with sample cell (golden color).*

As motors, two Canon iron core DC motors DN22 (24 VDC/1.4 W/0.1 A/5400 rpm) were used together with the gearhead GPP22.0014 (Trident Engineering) which reduced the engine speed by 14:1 to 485 rpm. The rotation arms were placed off the axis of the motor. The amplitude of the Lissajous pattern could be adjusted by relocating the position of the rotation arm with respect to the motor axis. The rotation arms were fixed with small messing blocks to the axis. These messing blocks were optimized in length to minimize the measurement noise. Additionally the whole Lissajous scanner was electrically disconnected from the laser table. With this provisions the running Lissajous scanner gave only minor contribution to the measurement noise.

To control both motors, a motor drive board module L298N was controlled by an Arduino Nano (Rev3.0)[5]. Motor driver and Arduino were supplied by an external PSU (power supply unit) *via* a voltage regulator (Recom R-78E5.0-0.5). The speed of the motors could

[5]This design was based on https://howtomechatronics.com/tutorials/arduino/arduino-dc-motor-control-tutorial-l298n-pwm-h-bridge/, accessed 05/08/19.

be steered independently with two potentiometers (10 kΩ). A detailed circuit diagram of the electronics that drove the motors and the code for the Arduino can be found in the appendix figure F.1 on page 199 and appendix F.1.2 on page 200.

Chopper divider

To artificially decrease the repetition rate of the pump pulses - while leaving the laser repetition rate untouched at 1 kHz - and to slow down the rate with which the sample is excited, an alternative chopper pattern had to be applied. Typically, the chopper runs at 500 Hz with a uniformly distributed pattern of holes and closed parts, blocking every second pump pulse as it is shown on top in figure 2.8. In this case, two pulse pairs (of

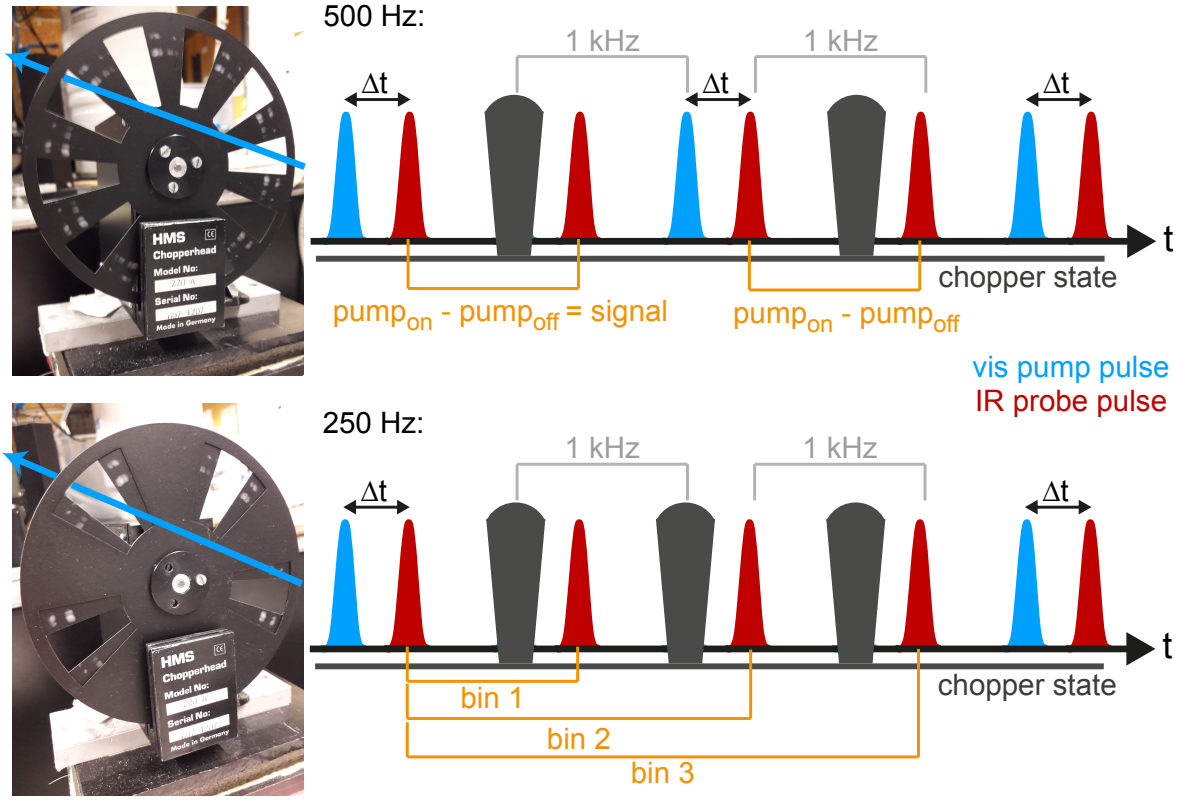

Figure 2.8: *Pulse pattern of a vis-pump-IR-probe experiment for different chopper schemes. On top the chopper scheme for a frequency of 500 Hz is shown, below the chopper scheme for 250 Hz can be seen. The visible pump pulses are shown in blue, the IR probe pulses in red. The grey trapezoids symbolize the closed chopper state corresponding to the solid parts between the holes of the chopper wheel (shown on the left). The repetition rate of the lasers generating the pump and probe pulses is 1 kHz.*

pump and probe) were used to calculate the difference absorption signal. The first pulse pair, for which the pump pulse as well as the probe pulse reached the sample, gave the absorption of the excited sample pump$_{on}$. In the second pulse pair only the probe pulse reached the sample as the pump pulse was blocked by the chopper wheel. This gave the absorption of pump$_{off}$. The signal was calculated by the difference of pumped and unpumped absorption (pump$_{on}$ - pump$_{off}$) with the probe beam always on.

For a decreased repetition rate, the so called "chopper divider" was used. Here the chopper ran with a reduced frequency of 250 Hz with the chopper wheel blocking three pump pulses for every pulse that passed (see bottom figure 2.8 on the preceding page). In contrast to the 500 Hz scheme, four pulse pairs were used to calculate the three signals named "bin 1", "bin 2" and "bin 3". Bin 1 was calculated by $pump_{on}$ - $pump_{off}$, with the probe pulse that arrived after the first blocked pump pulse was taken into account. As $pump_{on}$ for bin 2 the same probe pulse that probed the pumped sample for bin 1 was used, but $pump_{off}$ was measured with the probe pulse that hit the sample after the second blocked pump pulse (arriving 1 ms later than the one of bin 1). For bin 3, again the same $pump_{on}$ was taken for the calculation of the signal, but this time the probe pulse of the third blocked pump pulse was subtracted. So, the three bins differed in the unpumped absorption while using the same pumped one. The different probe pulses detected different states of the molecules after excitation with the first pump pulse as each one followed at a longer time span after the excitation. This allowed to move the sample slowly, to avoid moving the excited molecules out of the probe spot even for long delays (Δt) between pump and probe pulse, without pumping the previously excited molecules a second time as there was sufficient time until the next pump pulse arrives at the sample (4 ms after the first pump pulse).

The best speed to move the sample with the Lissajous scanner and the chopper divider applied was judged by the signal at negative times (-7.5 ns), where the probe pulse hit the sample before the corresponding pump pulse, and therefore all signals that were detected, could be attributed to the excitation of the previous pump pulse (that arrived at the sample and was not blocked by the chopper). In the ideal case the Lissajous scanner was moved so slow that the background signal completely vanished in bin 3 - but was still partially visible in the signals of bin 1 and 2 with the probe pulses arriving earlier - since then there were no previously excited molecules in the probe spot.

The measurement routines (Visual Basic) for displaying the signal on the screen, for scanning of time zero and for measuring the vis-pump-IR-probe spectra had to be accommodated for calculating and saving the three bin signals with the chopper divider.

2.8.2 Setup Mechanically Delayed Vis-Pump-IR-Probe Experiments

For the fs-to-ns vis-pump-IR-probe only the Spectra Physics fs-laser system that served as master oscillator in the synchronized measurements with a pulse duration of 100 fs, a repetition rate of 1 kHz and an output energy of 3 mJ was used to generate mid-IR probe and visible pump pulses with its 800 nm fundamental. In contrast to the synchronized setup the delay times were not controlled electronically but mechanically by a movable delay line and therefore were limited to approximately 1 ns. However, the time resolution was not limited by some electronics but merely by the pulse length that was stretched to 600 fs by using one glass rod of 15 cm length ($\approx$150 fs without glass rod) to prevent potential "burn spots" by reducing the intensity per time unit.

For mid-IR generation the same probe OPA as in the synchronized vis-pump-IR-probe experiments was used and probe and reference beams traveled exactly the same paths as described in section 2.8.1 on page 29 and therefore are not explained here in more detail. Nevertheless the beam paths are represented together with the pathway of the pump pulses in figure 2.9 on the next page.

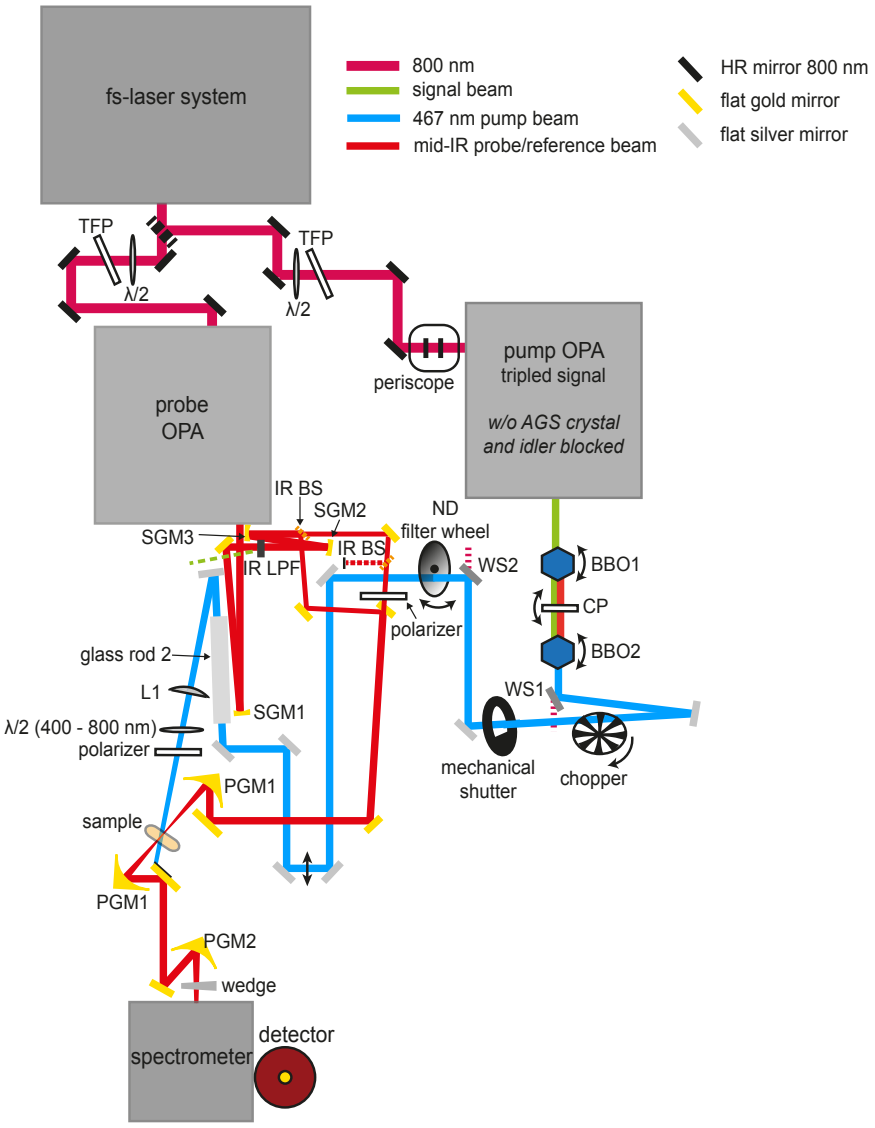

Figure 2.9: *Schematic drawing of the femtosecond vis-pump-IR-probe spectroscopy setup that was used to measure the dynamics of SCN-labeled PYP with a resolution of several hundreds of femtoseconds. The pump beam was generated by tripling the signal beam of the OPA. TFP = thin film polarizer, LFP = long pass filter, BS = beamsplitter. The specifications for the dichroic mirrors (DM1+2), the spherical gold mirrors (SGM1-3), the parabolic gold mirrors (PGM1+2), the pump lens (L1), the BBO crystals (BBO1+2), the calcite plate (CP) and the wavelength separators (WS1+2) are given in table 2.3 on the next page.*

Table 2.3: *Specifications of selected optics that were built into the femtosecond vis-pump-IR-probe setup and are depicted in figure 2.9 on the preceding page.*

Label	Optic	Manufacturer
SGM1	spherical gold mirror F=−7.5 cm 6N-BK7	Laseroptik
SGM2	spherical gold mirror F=−10 cm 6N-BK7	Laseroptik
SGM3	spherical gold mirror F=−15 cm 6N-BK7	Laseroptik
PGM1	off-axis parabolic gold mirror F=101.6 mm, 30°, Ø50.8 mm	Edmund Optics
PGM2	off-axis parabolic gold mirror F=127 mm, 30°, Ø50.8 mm	Edmund Optics
BBO1	β-BaB_2O_4 crystal, Θ=20.5°, φ=90°, type I, 2.5 mm	Eksma Optics
CP	natural calcite plate, Θ=38°, 0.5 mm	Eksma Optics
BBO2	β-BaB_2O_4 crystal, Θ=31.6°, φ=0°, type II, 0.5 mm	Eksma Optics
WS1	wavelength separator, fused silica S1: ARr(45°, 600-1100 nm)<1.5 % S2: HRs(45°, 470-570 nm)>99.9 % + Rs+p(45°, 700-1100 nm)<5 %	Layertec
WS2	wavelength separator, fused silica S1: ARp(45°, 800-950 nm)<0.2 % S2: HRs(45°, 320-470±5 nm)>99.7 % + Rp(45°, 600-950 nm)<2 %	Layertec
L1	plano-convex lens F=25 cm UV fused silica, uncoated, 185-2100 nm	Thorlabs

Most of the 800 nm light was reflected by a beamsplitter directly after the laser exit and was directed to the pump OPA over a periscope to adapt the beam height. A half-wave plate and TFP combination regulated the input energy of the pump OPA to 1.6 mJ. Since the OPA had been built in the same way as the pump OPA in the 2D mid-IR setup described in section 2.7 on page 23, it is not shown in detail in figure 2.9 on the preceding page. Unlike in the 2D mid-IR setup, the AGS crystal that was used for mid-IR generation was removed and the idler beam was blocked in the interferometer in order to employ the signal beam for 467 nm generation. For this process a so called tripler was used that tripled the wavelength of the signal beam. The tripler was composed of two BBO crystals and one calcite plate (Eksma Optics). The first BBO crystal (Θ = 20.5°, φ = 90°, type I) doubles the wavelength of a fraction of the signal beam by second harmonic generation (SHG). To control the temporal overlap between remaining signal beam and doubled signal a calcite time delay compensator was placed behind the first BBO crystal. Afterwards a second BBO crystal (Θ = 31.6°, φ = 0°, type II) was implemented to mix signal and doubled signal by sum frequency generation (SFG). The resulting 467 nm pump beam was led over to wavelength separators (WS1 and WS2) to separate the blue light from not converted signal and doubled signal photons.

Again the optical chopper (HMS) was placed in the beam path running at 500 Hz to block every second pump pulse and also the mechanical shutter (Thorlabs) was used in order to block the pump beam from exciting the sample while the delay line was moving. The pump pulse traveled the same path over the mechanical delay stage (Physik Instrumente) as in the synchronized measurements, but in this case the stage was used to vary the delay times between pump and probe pulses during the experiment. For the ultrafast vis-pump-IR-probe measurements only the longer one of the two glass rods was left in the beam path stretching the pulse duration to approximately 600 fs. The pump beam size was reduced

by a lens with a focal length of F = 25 cm that was placed 28 cm before the sample leading to a beam size of 140 x 140 µm in the sample. A half-wave plate for 400 to 800 nm and a polarizer were used in front of the sample to set the pump beam polarization.

2.8.3 Experiment

The transient vis-pump-IR-probe experiments were achieved for WT, WT' and the SCN-labeled mutants A30C*, A44C*, V57C*, M100C*, V122C* and V122C[6]. Three spectral windows were measured - the amide I region with the probe OPA centralized at $\lambda_0 \approx 6200$ nm (1613 cm^{-1}), the C=O region in which the proton transfer of the Glu46 could be seen with $\lambda_0 \approx 5770$ nm (1733 cm^{-1}) and in case of the labeled mutants the SCN region with $\lambda_0 \approx 4790$ nm (2088 cm^{-1}). In the amide I and C=O region a 150 l/mm grating was used for dispersion on the MCT detector resulting in a resolution of 4 cm^{-1} for the recorded spectra. In the SCN region a 300 l/mm grating was used giving a resolution of 2 cm^{-1}. The detector was cooled with liquid nitrogen and an automatic liquid nitrogen refilling system [143] ensured a continuous data acquisition. The setup was purged with dry air during the measurements.

For the electronic delays the PYP samples were excited by visible pump pulses of 468 nm or 401 nm[7], respectively. Spectra of the pump pulses are shown in figure 2.10 on the facing page. In the amide I and C=O region pump energies of 3 - 5 µJ at the sample position, in the SCN region energies of 7 - 9 µJ were used. For the mechanical delays only 467 nm pump pulses (see figure 2.10) of 3 - 5 µJ in the amide I and C=O region and 6 - 12 µJ in the SCN region were applied. The polarization of the pump pulses was set to magic angle (54.7° with respect to probe pulses) to suppress the contribution of rotational diffusion on the molecule dynamics.

Temporal overlap of probe and pump pulse was determined in the semiconductor GaAs as described above. For adjusting the spatial overlap the phosphorescent organic molecule 4CzIPN (2,4,5,6-tetra(carbazol-9-yl)benzene-1,3-dicarbonitrile) in DCM (dichloromethane) was used as it provided a big signal in all measured spectral regions at 0.1 ns.

All protein samples were measured in D_2O buffer (50 mM NaPi, pD 8) and WT, WT' and A44C* samples were additionally recorded in H_2O buffer (50 mM NaPi, pH 8)[8]. The sample thickness was determined by the PTFE spacer (Goodfellow Cambridge Limited) separating the two CaF_2 windows (Crystal GmbH) in the sample cell. In the amide I and C=O region a sample thickness of 50 µm (25 µm for M100C*) for samples in D_2O and a thickness of 10 µm for samples in H_2O was applied. Protein concentrations lay between 4 and 5 mM. In the SCN region samples were measured with a spacer thickness of 150 µm for D_2O and 100 µm for H_2O with protein concentrations of 9.5 to 12 mM. All measurements were performed at room temperature.

[6] With V122C additionally the unlabeled mutant was measured as labeling efficiency was only about 50 % in the electronically delayed experiments.

[7] The 401 nm pulses were only applied on WT (amide I/C=O region), A44C* (amide I/C=O/SCN region) and M100C* (SCN region).

[8] For the mechanical delays only the WT was measured in H_2O buffer.

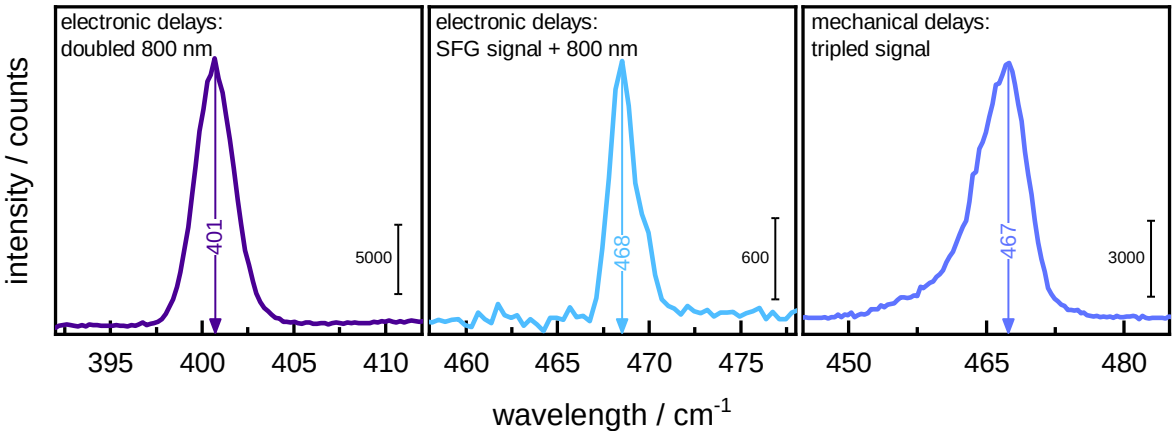

Figure 2.10: *UV/vis spectra of visible pump pulses from transient vis-pump-IR-probe experiments. The pulses for the electronic delays were obtained either by doubling the 800 nm fundamental (401 nm, left) or by SFG of the signal beam with the 800 nm fundamental (468 nm, middle) and for the mechanical delays by mixing part of the original signal beam with the doubled signal beam (467 nm, right). The spectra of the 467 nm and 468 nm pulses were recorded directly after the OPAs that were used for their generation, the 401 nm pulse was recorded in front of the sample cell.*

For translation of the sample cell, it was moved by the Lissajous scanner with an amplitude in horizontal and vertical direction of 1.3 cm. The pattern was adjusted *via* the speed of the two motors in a way that it returned to the starting point after 18 to 40 s. All samples were measured with the chopper running at 500 Hz, the chopper divider (250 Hz) was only additionally applied for WT, A44C* and M100C* in the ps-to-ms experiments. For the mutants A30C* and M100C* the mechanical shutter in figure 2.5 was programmed to block the pump beam after every measured time point for 5 s or 15 s, respectively, to give the protein more time to recover its ground state. When using the mechanical shutter, 300 shots were recorded for each time point, otherwise 500 shots were taken. Electronic delay times were measured from −7.5 ns up to 750 µs. The jitter of the laser synchronization and therefore the temporal resolution of the experiment was determined in the semiconductor GaAs (see section 2.8.1 on page 29) to be 15 to 30 ps. Mechanical delay times were measured from −20 ps to 850 ps. The instrument response function (IRF) was determined in the semiconductor GaAs and gave a resolution of 400 to 800 fs with the long glass rod in. For V57C* the glass rod was taken out and the IRF was measured to be 150 to 300 fs. For background correction the first time point (−7.5 ns or −20 ps, repectively) was subtracted from all other time points.

For analysis the overlapping spectral windows (overlap approximately 4 - 5 pixels between 1659 cm^{-1} and 1670 cm^{-1}) of the amide I and the C=O region were merged, adapting the intensities by multiplication of the C=O window with a constant factor. The merged spectrum will be referred to as CC/CO region from now on. The SCN region was analyzed separately.

Global analysis (also global lifetime analysis or short GA) was performed on all data using the Globe Toolbox [144]. A sequential model with 11 components was applied to the merged CC/CO region and with 9 or 10 components to the SCN region of the electronic or mechanical delays, respectively. Depending on the sample one to three components were necessary to fit the data within the jitter of the ps-to-ms experiment and within the temporal

overlap of pump and probe pulse of the fs-to-ns experiment for both spectral windows. The other components could be assigned to either photocycle transitions in the CC/CO region and changes in the labels environment in the SCN region or to underlying water dynamics. Additionally, at least one "long lived" component exceeding the timescale of the experiment (> 750 µs) had to be applied. All components and their errors are depicted in figures F.15–F.21 in the appendix.

Since the signal size in the SCN region was relatively small, a pixel-dependent spike-like structure appeared in the data. This structure was effectively corrected with a 3 point moving mean of the collected spectra referred to as "denoised" data. Other correction methods were applied as well to remove the spike-like structure, but the 3 point moving mean proved to be most reliable for all SCN spectra of the different mutants without effecting the shape of the SCN signal to an appreciable extent. Furthermore, the correction did neither influence the time-dependence of the data nor their interpretation as it is shown in a comparison of global analysis spectra of raw and denoised data in figures F.10–F.14 in the appendix.

In addition to global analysis, in which the spectra and their associated lifetimes were obtained by correlating the kinetics at multiple spectral positions *via* application of a sequential model, a model-free analysis technique that focuses on the representation of changes in the complex transient data was applied. In the lifetime density analysis (LDA) method a quasi-continuous distribution of exponential lifetimes was fitted to the data, independently for each pixel. The amplitudes of the resulting lifetime density maps (LDMs) correlate with the changes of the exponential pre-factors obtained by these fits [146–151]. For LDA the OPTIMUS toolbox [146] was used. For regularization the Tikhonov regularization method (or ridge regression) was applied and the optimal regularization factor determined by finding the point of maximum curvature for the "L-curve" (*i.e.* a log-log plot of the smoothing norm of the regularization *vs.* the residual norm) averaged for all fitted pixels [146]. For the mechanically delayed data, a distribution of 220 lifetimes was fitted between 10^{-4} ns and 25 ns and for the electronically delayed data the same amount of lifetimes was fitted between 0.04 ns and $2.6*10^{7}$ ns, in both cases the fitted time range is extended with respect to the measured one by at least a factor of four. Before applying the LDA to the data, global lifetime analysis of the OPTIMUS toolbox was used to determine the instrument response function (IRF) and the dispersion of the data sets in order to apply them to the data used in the LDA.

To suppress artificial oscillations from the LDMs, standardization of the raw data was required [152]. For standardization the z-score method was used (MATLAB function zscore, v. R2017a), entailing centering the time trace of each pixel by setting the time-average to zero and setting the standard deviation to one [152]. In the LDMs of the standardized data, however, features near to the end of the measured time range are artificially shifted to earlier lifetimes. Features appearing earlier in time are not affected. The lifetimes resulting from global analysis (performed also by the Globe toolbox [144]) are, however, accurate over the full measured time range, and thus used as reference lifetime values.

As alternative method to the Tikhonov regularization, the Lasso regression (Least Absolute Shrinkage and Selection Operator) was also tested, producing more narrow pre-exponential amplitudes in time [147]. This method proved to remove the oscillations, which occur when the Tikhonov regularization is used (especially without standardization), effectively, but the

resulting lifetimes are consistently shorter than expected for delays beyond halve the end of the measured time window. Analysis of a synthetic data set that modeled a single exponential decay demonstrated that both methods produce an accurate time estimation of the lifetime, but in combination with a second lifetime (for instance representing a growth and decay lifetime) it was found that the corresponding features in the LDMs were artificially pushed apart in time in case the lifetimes were set too close to each other. Since such errors of the obtained lifetimes were larger for Lasso regression than for Tikhonov regularization, only the latter was used for the analysis and interpretation of the transient vis-pump-IR-probe data described in this thesis.

The datasets of different samples measured in the same spectral region under the same conditions were merged (*e.g.* all CC/CO regions for electronic delays or all SCN regions of the mutants for mechanical delays in D_2O) and analyzed simultaneously. For the LDMs in the SCN region, a linear baseline between the first and last pixel of each mutant was subtracted for each time point. For the mechanical delays, the subtraction was performed before LDA, for electronic delays afterwards. The sign of the features originally obtained from LDA was revered for all LDMs, so that a negative feature (blue) corresponds to decreasing values of the difference absorption bands and a positive feature to increasing values, *i.e.* an ingrowing bleach causes a negative LDM feature, in the same way as a vanishing positive band, conversely, a positive band that increases and a bleach that vanishes result in a positive feature.

2.9 Step-scan FTIR Measurements

The step-scan FTIR measurements were performed in collaboration with Lea Schröder and Tilman Kottke at Bielefeld University, Physical and Biophysical Chemistry.

Step-scan FTIR spectra were recorded with an *IFS 66v* spectrometer by Bruker in combination with a photoconductive MCT detector. The spectral measurement range was limited to 1129 - 2256 cm^{-1} by a combination of an infrared long-pass filter (*LP-4500*, Spectrogon) and two CaF_2 windows in front of the detector. This minimized the number of mirror positions for data acquisition to 316 by undersampling. A spectral resolution of 8 cm^{-1} was obtained.

PYP-WT' and the SCN-labeled mutant PYP-A44C* were measured. 2.5 µl of sample were placed between two CaF_2 windows without spacer. The windows were sealed immediately without drying the sample. These samples gave an absorbance in the amide I region at 1650 cm^{-1} of 0.9 to 1.1 OD. The samples were well hydrated judged by the ratio of absorbance between amide I/water band (1650 cm^{-1}) and amide II band (1550 cm^{-1}) that was about 2.0 to 2.3.

For generation of 450 nm excitation pulses with a duration of 10 ns an optical parametric oscillator (OPO) by Opta was pumped by a Nd:YAG laser (*Quanta Ray*, Spectra Physics). The pulse energy was set to 10 mJ. An optical shutter (LSTXY, nm Laser Products) was used to reduce the excitation rate from 10 Hz to 0.5 Hz allowing the protein to recover the dark state.

A time resolution of 10 µs was reached for the experiment. The time range of the measurements was up to 18.9 ms. At each mirror position three coadditions were averaged. For each sample it was possible to excite up to 5700 times until the sample bleached out and had to be replaced by fresh sample. For PYP-WT′ 21 representative experiments were averaged, for PYP-A44C* 24 experiments were used. The data were averaged on a logarithmic timescale and to correct for the water background at around 1650 cm^{-1} previously acquired time-resolved spectra of water were subtracted [153].

Part II

Characterization of SCN-labeled PYP Mutants

3 Selection of Mutation Sites

PYP from *halorhodospira halophila* is an excellent candidate for incorporation of the thiocyanate label. It contains one single cysteine (at position 69), which is covalently bound to the pCA-chromophore and therefore not available for the cyanylation reaction. This allows for site-specific labeling by introducing a second cysteine at distinct positions in the protein. The mutation sites were chosen at positions that are of interest during the photocycle but at the same time do not affect integrity and function of the protein and are expected to have only minor influences on the photocycle kinetics. For these reasons, amino acids were selected which are not in the direct vicinity of the chromophore when pointing into the chromophore binding pocket and are not involved in hydrogen bonds of the network that stabilizes the binding pocket. Other amino acids were chosen as they were oriented towards the solvent. The positions of all selected mutation sites in the protein are highlighted in the dark state (pG) and signaling state (pB) structures in figure 3.1.

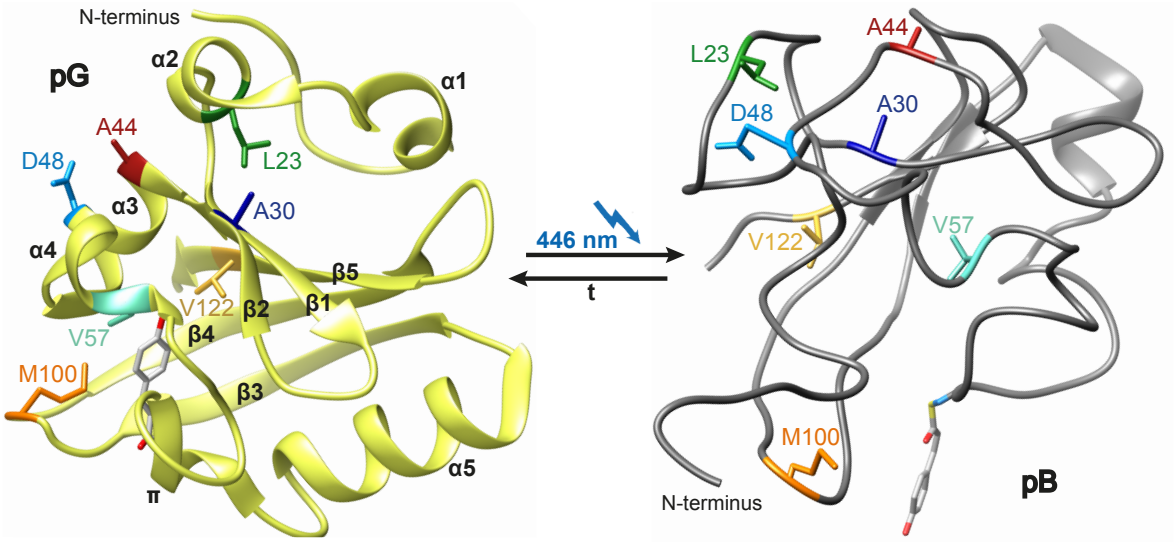

Figure 3.1: *Structure representation of PYP with the selected cysteine mutation sites highlighted. On the left the dark state structure pG (pdb entry 1NWZ: X-ray crystallography), on the right the signaling state structure pB (pdb entry 2KX6: structure model based on DEER, NMR and tr-SAXS/WAXS) are shown. The chromophore is colored in light gray and red.*[1] *The designation of the secondary structure elements in pG is based on the PDB structure 1NWZ by [51].*

The selection is also based on a study by Philip *et al.* [85], who performed an alanine scanning on PYP and replaced every residue discretely by alanine (alanine residues were replaced by glycine). That way they investigated expression level, active site properties,

[1]The structure images were created by using Chimera 1.6.2.

functional kinetics and stability with respect to the wild type [85]. The outcomes of this study gave an additional impression how the mutation of a particular residue influences the protein.

Two solvent exposed residues at the surface of the protein were selected for mutation and labeling. A44 and D48 (red and light blue in figure 3.1 on the previous page) are both located in the α3-helix, which flanks the chromophore binding pocket. An H-D-exchange study by Brudler *et al.* [154] indicated destabilization and partial unfolding of this helix during the photocycle, as they measured a slightly increased exchange rate of the protein backbone in the pB state compared to the pG state. Literature also predicts that D48 moves, together with other nearby amino acids (residues 42, 45 to 51), into the binding pocket, that was left empty by the chromophore in the pB state [82, 83, 154]. In contrast to other residues in the α3-helix, like E46 and T50, A44 and D48 are not known for contributing to the hydrogen bonding network that stabilizes the chromophore and its binding pocket in the pG state and thus mutation is not expected to have a great impact [20, 46]. Furthermore, replacement of A44 by glycine and D48 by alanine performed by Philip *et al.* [85] revealed no measurable effect on the function or stability of the protein.

To probe the N-terminal movement away from the protein body, the residues L23 and A30 were chosen [11, 55, 75, 77, 79, 81, 83]. L23 (green in figure 3.1 on the preceding page) is located in the α2-helix of the N-terminus and is pointing towards the protein body. The leucine was exchanged for an alanine by Harigai *et al.* [155] as well as by Philip *et al.* [85]. The former confirmed that the mutation does not perturb the structure of the protein using UV/vis and FTIR difference spectroscopy. However, an 8-times slower decay of PYP to the pG state was observed with respect to the wild type when measuring time-resolved UV/vis spectra [155]. In the second study the same method revealed a decay time that was only slower by a factor of 3 compared to the wild type [85].

The mutation site A30 (dark blue in figure 3.1 on the previous page) is located in the β1-sheet. In the pG sate it is oriented towards L23 and into the cavity that is formed by the N-terminus and the protein body. Therefore it is expected to sense the movement of the N-terminus and the opening of the cavity enclosed by it as well.

Three residues were chosen for mutation and SCN labeling that point into the chromophore binding pocket and are expected to probe some chromophore dynamics as well as the collapse of the binding pocket during the structural rearrangements towards the pB state [20, 46, 83, 154]. Residue V57, which is part of the α4-helix and is shown in cyan in figure 3.1 on the preceding page, was selected as it possibly probes when the chromophore moves out of the binding pocket, but also has some distance to the chromophore to not perturb the chromophore's direct environment by mutation and labeling. Philip *et al.* [85] observed a small decrease in the folding stability for alanine substitution indicated by a smaller ΔG_U that is measured *via* Gdm-HCl titration, but the protein kinetics remained unaffected.

The decision to label V122 in the β5-sheet at the protein's C-terminus was made as there are only minor changes predicted for the backbone in this region [83, 154]. Brudler *et al.* [154] noticed only a slight increase in the deuteration level of the β5-sheet backbone in the

pB state. However, the side chain of V122 is orientated towards the chromophore and is part of the amino acids forming the hydrophobic binding pocket [50]. Therefore it might sense changes in the cavity during the photocycle.

The residue closest to the chromophore, that was substituted and labeled, was M100. Located in the flexible loop that encompasses the chromophore binding pocket, M100 is at a position within the protein where it should sense the structural changes of the chromophore on the one hand, but also undergoes movements during the photocycle itself. Mutation of the methionine is known to have a large impact on the photocycle kinetics without influencing the structure as judged by UV/vis and CD spectroscopy on different mutants [85, 156–159]. Several studies observed a considerably reduced decay rate to the pG state after exchanging the methionine. For the mutants M100A, M100K and M100L the recovery was slowed down by a factor of 500 to 2000 compared to the wild type, for M100E it was only 20-times slower [85, 156–159]. An explanation was given by Kumauchi *et al.* [156] who suggested that methionine has some electron-donating properties that accelerate recovery to the pG state by weakening the interaction between R52 and the chromophore facilitating the *cis-trans*-isomerization of the latter as depicted in figure 1.4 on page 10 of the theoretical introduction. These properties get lost when exchanging the methionine especially by neutral residues.

4 Characterization of PYP Mutants

Although the residues for mutation had been chosen carefully to not disturb the correct folding, the stability, and the functionality of PYP, as described above, it had to be ensured that exchange of the amino acids and their labeling with thiocyanate did not alter the secondary or tertiary structure of the protein or its ability to undergo the photocycle. This characterization in comparison to WT' was performed by UV/vis, FTIR difference and CD spectroscopy. At this point a short notation for the $S^{13}C^{15}N$-labeled cysteine mutants shall be introduced, in which an asterisk marks the labeled form of the protein, *e.g.* M100C* for M100C-$S^{13}C^{15}N$ and analogous for all other mutants.

Changes in the direct environment of the chromophore can be observed by UV/vis spectroscopy. Due to altered conditions, the visible absorption of the chromophore shifts during the photocycle from 446 nm in the pG state to 510 nm after isomerization (intermediate I_0) and to 355 nm in the pB state, when the chromophore moves out of the hydrophobic binding pocket [5, 20, 82, 83, 154]. Examination of the UV/vis spectra of all mutants, that are shown in appendix figure A.1 on page 181, revealed that the absorption maxima lie between 443.5 nm (for V122C*) and 446 nm (WT' and M100C*). These findings indicate that the chromophore environment was hardly influenced by the substitutions of the amino acids and cyanylation of the cysteines.

CD spectroscopy is generally used to gain information about the secondary and tertiary structure of proteins. With this method the difference in the absorption of left and right circularly polarized light is determined. Distinct secondary structure elements lead to different transitions of the peptide bonds due to their geometry, especially when measured in the far-UV region (180 to 240 nm) [160–162]. In the far-UV CD spectra of PYP-WT' and the SCN-labeled mutants, that are depicted in figure 4.1A on the next page, a positive peak at 190 nm and a negative feature at 222 nm with a shoulder at 205 nm are observed. This represents a typical protein structure that is dominated by α-helical and β-sheet motifs.

The signals in the near-UV/visible region (from 260 nm on) originate from the side chains of aromatic amino acids and chromophores (*e.g.* flavins and heams) and reflect their altering environments [163]. In the near-UV/visible spectra of PYP, shown in figure 4.1A on the following page, the positive peak at 446 nm is assigned to the electronic transition of the pCA chromophore analogous to the UV/vis absorption spectrum, which was measured with linearly polarized light. The features around 310 nm, that exhibit some substructure, are also assumed to arise from transitions of the chromophore [158, 164]. The negative signal in the near-UV at 272 nm is assigned to aromatic amino acids, especially tyrosines and tryptophan (Y42, Y118 and W119) in the case of PYP which are buried in the interior of the protein [79].

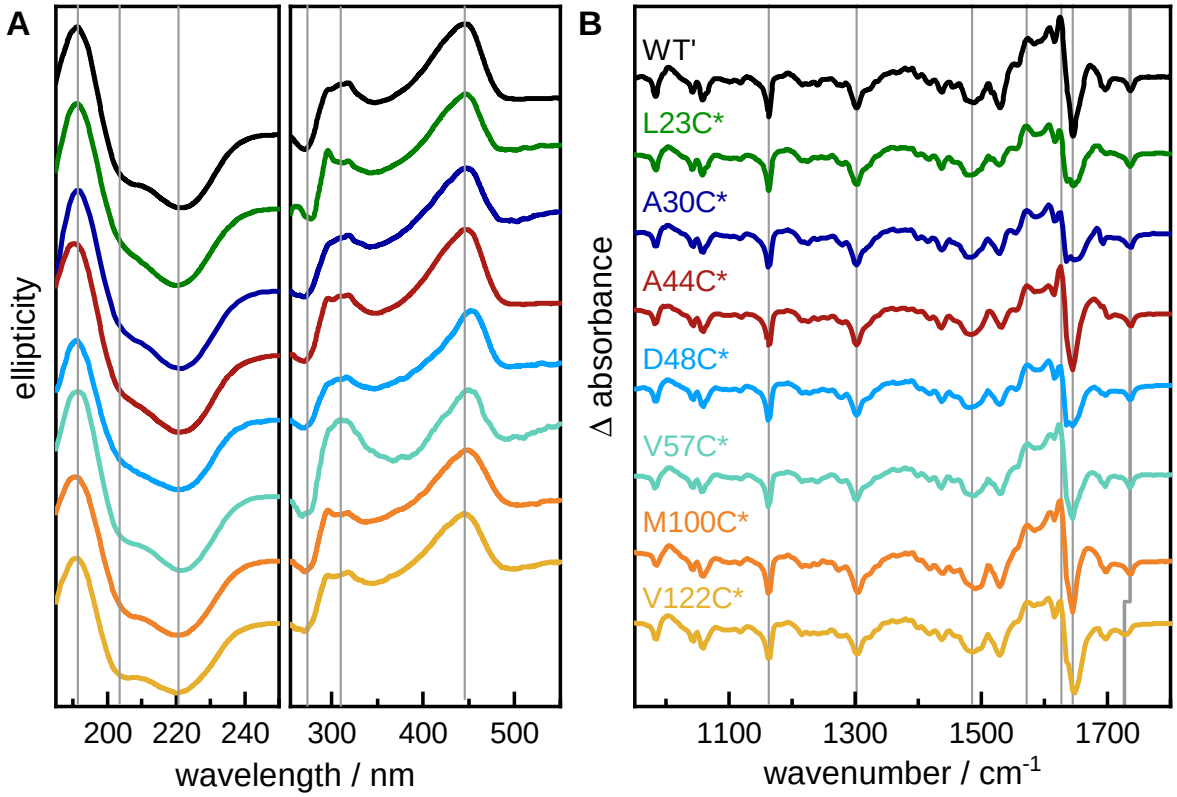

Figure 4.1: *(A) Far-UV and near-UV/vis CD spectra of PYP-WT' and all SCN-labeled mutants. (B) FTIR difference spectra between pG state and pB state in the protein/chromophore region. The color coding is the same for both figures. Gray lines indicate prominent features. All spectra were measured in H_2O buffer with a sample thickness of 5.8 µm for CD and 10 µm for FTIR experiments.*

In the CD spectra both spectral regions are comparable for WT' and all mutants indicating that the secondary as well as the tertiary structure of PYP are maintained after substitution of the residues and SCN-labeling. The spectra are also consistent with PYP spectra given in literature [4, 79, 158, 164].

Changes of the vibrational modes of the peptide backbone and the chromophore due to photocycle dynamics are investigated by FTIR difference spectroscopy. The differences between pG state and the illuminated pB state (spectra shown in figure 4.1B) are markers for the *trans-cis*-isomerization of the chromophore, protonation and deprotonation processes and rearrangements of secondary structure (amide I). A typical *trans-cis* marker band can be found at 1302 cm^{-1}, whereas the modes at 1161 cm^{-1}, 1487 cm^{-1}, and 1574 cm^{-1} indicate a protonated chromophore [10, 11]. Many of these features overlap with contributions of the protein, for instant the aromatic ring vibration at 1574 cm^{-1} that is superimposed by vibrations of various polar side chains, which occur in the region between 1560 cm^{-1} and 1610 cm^{-1} [11]. The most prominent feature in the spectra is the amide I band at 1624 cm^{-1} and 1645 cm^{-1}, respectively, that is associated with changes of the protein backbone. Deprotonation of E46 resulted in a negative feature at 1734 cm^{-1} in an otherwise rather transparant spectral region [10, 14, 97].

Comparison between WT′ and the labeled mutants reveals that they all exhibit the same spectral features besides small variations in the relative intensities of the peaks. Hence the protein is still functional even after cysteine mutation and cyanylation and follows the photocycle kinetics into the pB state.

There is one small deviation in the spectrum for V122C*, though (yellow in figure 4.1B on the facing page). The carboxyl stretching vibration of E46 is red-shifted by 8 cm^{-1} compared to WT′ and the other six mutants. For better visualization the FTIR absorption spectra of the C=O vibration in WT′, V122C* and V122C (not SCN-labeled mutant) in the pG state are depicted in figure 4.2. Here the absorption of E46 in V122C* is also shifted, but it becomes clear that the difference with respect to the wild type does not originate from SCN-labeling but from the substitution of valine by a cysteine as the spectra of the labeled and the unlabeled mutant resemble each other. Investigation of the crystal structure (pdb: 1NWZ) revealed that the side chains of E46 and V122 are very close in the pG state with a distance of approximately 3.6 Å as it is shown on the right in figure 4.2.

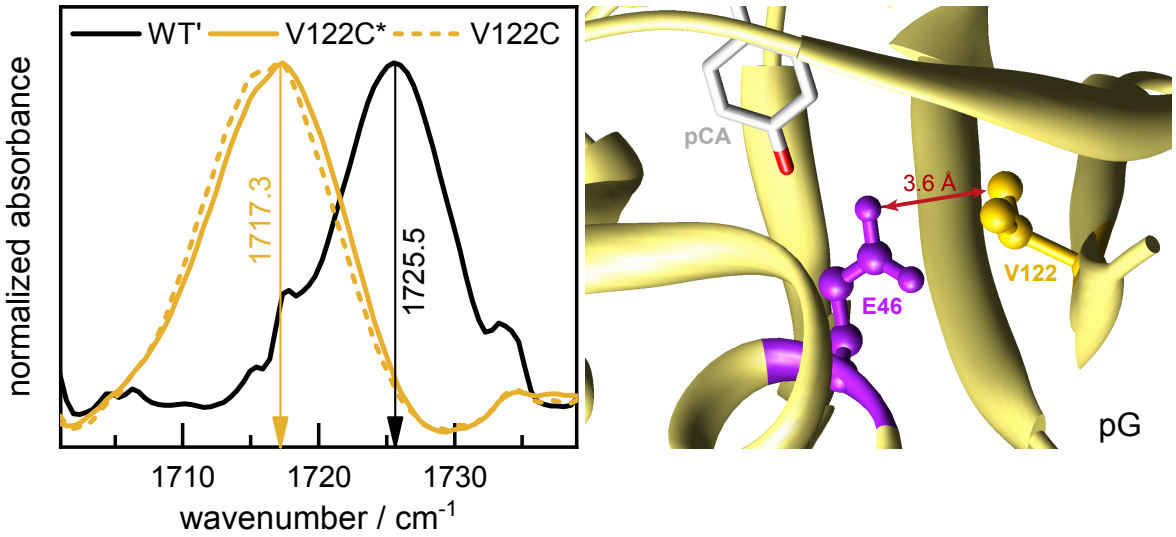

Figure 4.2: *Left: Comparison of the FTIR absorption spectra of E46's C=O band for V122C* (with SCN label) and V122C (without label) both in yellow with WT′ (black) in the pG state. Right: Detail of the PYP structure in the pG state (pdb: 1NWZ) with E46 in purple, V122 in yellow, the chromophore in gray and red and the distance between E46 and V122 side chains given with 3.6 Å.*[1]

An explanation can be found in literature. Borgstahl *et al.* [165] observed that the $C_{\gamma 2}$ of V122 is engaged in hydrophobic interactions with E46 as it is located in a distance of 3.7 Å and also Xie *et al.* [11] described that the carboxylic group of E46 is buried in a very hydrophobic environment defined by the side chains of I31, I49 and V122, which are known to be relatively rigid and non-polar. Therefore the substitution of the highly hydrophobic valine by cysteine probably led to changes in the environment of the E46 carboxyl, although the cysteine side chain was found to have hydrophobic properties as well, however, not as strong as for valine [166, 167]. Moreover, the orientation of the cysteine side chain towards the E46 can play a crucial role for the hydrophobic interactions and possibly differs from the orientation of the side chain of valine.

[1]The structure image was created and the distance between E46 (atom OE1) and V122 (atom CG2) determined with Chimera 1.6.2.

Part III

Structural Investigation of PYP by Steady-state Experiments

5 Steady-state FTIR Measurements

This chapter discusses the steady-state FTIR measurements of the SCN-labeled PYP mutants in the pG and the pB state in detail and is mainly based on data published in "Following local light-induced structure changes and dynamics of the photoreceptor PYP with the thiocyanate IR label" by Blankenburg *et al.* [136].

Depending on the position in the protein, the thiocyanate label senses different environments in the pG state. This leads to varying wavenumbers and lineshapes of the SCN absorption spectra. Under constant irradiation with blue light the photocycle intermediate pB is accumulated. In this intermediate the chromophore isomerized from *trans*- to *cis*-configuration and was protonated, furthermore large rearrangements of the protein backbone took place resulting in a more unfolded structure [20, 46]. Local changes in polarity and the hydrogen bonding interactions give rise to shifts in the SCN wavenumber and variations in the lineshape of the SCN absorption compared to the pG state.

5.1 Results and Discussion

5.1.1 SCN Absorption Changes

The FTIR spectra shown in this chapter are all corrected for the broad underlying D_2O background by subtracting a higher order polynomial fit from the data. The raw absorption spectra and the applied fits are shown in figure B.1 on page 183 in the appendix. The measured difference spectra between pG and pB were corrected the same way to obtain a flat baseline.

Unless stated otherwise, the wavenumbers discussed in the following for the SCN absorption are the wavenumbers $\tilde{\nu}_{sd}$ that are obtained from the negative minima of the second derivative of the FTIR absorption spectra (see figure B.2 on page 184 in the appendix). These wavenumbers display the wavenumbers of pronounced subpopulations, as well. As second method, the mean wavenumber $\tilde{\nu}_{mean}$ of the absorbance is calculated representing the first central moment of the absorption band. When only one subpopulation is present, the values for $\tilde{\nu}_{sd}$ and $\tilde{\nu}_{mean}$ are close, if more subpopulations appear, $\tilde{\nu}_{mean}$ is located in-between the wavenumbers of $\tilde{\nu}_{sd}$ as the first moment depends on all subpopulations. All wavenumbers are given in table 5.1 on the next page.

To determine the solvent exposure of the SCN labels in the two different states, SASA (solvent accessible surface area) calculations of all native residues in WT-PYP that were chosen for mutation and of all SCN-labeled cysteine mutants were performed with umbrella sampling MD simulations of the pG (pdb: 1NWZ) and pB (pdb: 2KX6) structures. A comparison between the native side chains and the SCN-labeled ones in figure C.1 on

Table 5.1: *Wavenumbers $\tilde{\nu}_{sd}$ and $\tilde{\nu}_{mean}$ for the SCN absorption in pG and pB state of all labeled mutants.*

mutant	pG state		pB state	
	$\tilde{\nu}_{sd}$ / cm^{-1}	$\tilde{\nu}_{mean}$ / cm^{-1}	$\tilde{\nu}_{sd}$ / cm^{-1}	$\tilde{\nu}_{mean}$ / cm^{-1}
L23C*	2080.0	2081.1	2081.3	2081.4
A30C*	2079.9	2080.0	2078.4	2079.8
A44C*	2085.2	2083.7	2076.3/2084.0	2080.1
D48C*	2084.3	2083.8	2083.4	2082.8
V57C*	2080.2	2080.4	2080.6	2080.9
M100C*	2069.8/2077.1	2074.3	2082.7	2082.8
V122C*	2079.9/2084.7	2081.0	2078.4	2079.2

page 187 in the appendix reveals that they show similar solvent accessibilities for each position. Moreover, these similarities indicate that the inserted label is oriented more or less like the side chains of the native amino acids of WT-PYP. For a clear conclusion, however, a detailed comparison of the angles formed by the SCN groups obtained by MD simulations with the angles formed by the side chains in WT-PYP would be required. In the following only the SASA values for the SCN-labeled residues are discussed.

Measuring solvent exposure at the protein surface: A44C* and D48C*

In the pG state, the SCN-labeled mutant A44C* yields the highest wavenumber for the C≡N stretching vibration of all positions investigated in this study as shown in the absorption spectrum of pG in figure 5.1 on the next page. With 2085.2 cm^{-1} the wavenumber is even higher than for the model compound MeSCN in H_2O (2162.4 cm^{-1}, 2083.2 cm^{-1} with isotope shift) determined by van Wilderen *et al.* [24, 25] and representing the fully solvent exposed nitrile. The wavenumber $\tilde{\nu}_{mean}$ (2083.7 cm^{-1}) is a bit lower than the one determined with the second derivative and hence matching MeSCN in water. Anyway, this high wavenumber indicates a solvent exposed label as it was expected for A44 positioned at the protein surface with its side chain pointing into the solvent. These observations are also supported by the SASA calculations of the SCN-labeled mutant, which show a high solvent accessibility for A44C* in the pG state (see figure 5.1 on the facing page on the right).

Two subpopulations are observed for the SCN absorption of A44C* in the pB state, evident by the clearly non-Gaussian line shape of the spectrum and depicted by the red arrows at the wavenumbers obtained from the second derivative of the spectrum. Both subpopulations are red-shifted compared to the pG state. The higher wavenumber is only shifted by 1.2 cm^{-1} compared to the pG state, the lower wavenumber which represents the fraction with the higher intensity is shifted to 2076.3 cm^{-1}.[1] SASA calculations suggest only a small decrease in solvent accessibility which is in good agreement with the slightly red-shifted subpopulation. However, the shift of the main part of the absorption band is too big to be only caused by less solvent exposure as it shifts to a wavenumber lower than MeSCN in THF (2156.9 cm^{-1}, 2077.9 with isotope shift [24, 25]), an aprotic and apolar solvent which has a similar dielectric constant as the interior of a protein. Therefore other effects like

[1] In comparison to $\tilde{\nu}_{mean}$ (2083.7 cm^{-1}) in pG there is no shift observed for the higher wavenumber component ($\tilde{\nu}_{sd}$ = 2084.0 cm^{-1}) of A44C* in pB.

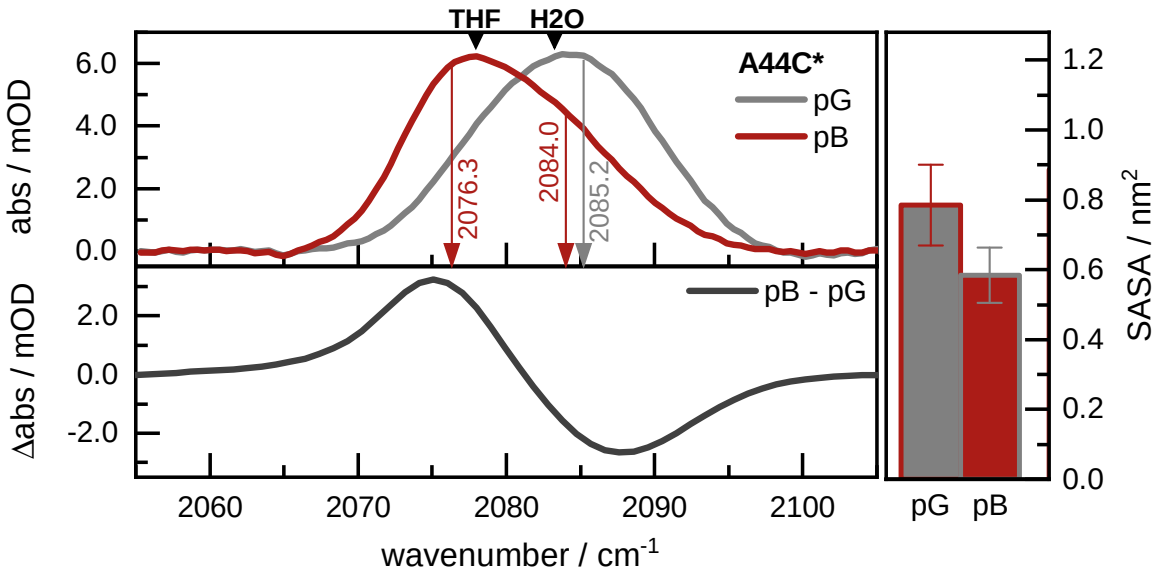

Figure 5.1: *FTIR absorption spectra (top panel) of SCN in A44C* in pG (gray) and pB (red) and the measured difference spectrum between pB and pG (bottom panel). The sample concentration was 11.6 mM at 50 µm path length. Arrows indicate the wavenumbers $\tilde{\nu}_{sd}$. Small black arrows mark the absorption of MeSCN in THF and H_2O buffer [24, 25]. Right panel: SASA values for the SCN-labeled A44C* in pG (gray) and pB (red) with error bars.*

changes in the electrostatic field, that are detected by the label, have to be considered. Maybe the proximity of A44 to E46, which becomes deprotonated and therefore negatively charged in the pB state [46], plays some role. Further insight into the influence of E46 on the label and whether its deprotonation is responsible for the large red-shift in A44C* will be obtained in the transient vis-pump-IR probe experiments discussed later in this thesis.

The second mutant that was expected to be solvent exposed in the pG state is D48C*. Indeed, a high wavenumber of 2084.4 cm^{-1} is observed for the SCN absorption of D48C*, as shown in figure 5.2 on the next page, that matches the wavenumber of MeSCN in H_2O and indicates a high solvent accessibility. This is confirmed by SASA calculations which exhibit similar values for D48C* and A44C* in the pG state.

Under irradiation the wavenumber of the SCN absorption is red-shifted by less than 1 cm^{-1}. In contrast to the SASA calculations which propose a slightly higher solvent accessibility in the pB state, the observations for the SCN label hint to a small decrease in exposure. However, Genick *et al.* [82] and Brudler *et al.* [154] suggested a partial unfolding of the α3-helix in the pB state and the movement of D48 into the empty cavity after the chromophore moved outwards. These structural changes could be assumed to result in a more shielded environment at position 48, which would be in good agreement with the measured data.

Investigating the N-terminal movement: L23C* and A30C*

The wavenumber of the SCN absorption of L23C* in the pG state is 2080.0 cm^{-1} (see figure 5.3 on page 61) and hence lower than for the two solvent exposed mutants discussed earlier, indicating fewer contacts with water molecules or a more polar environment. The

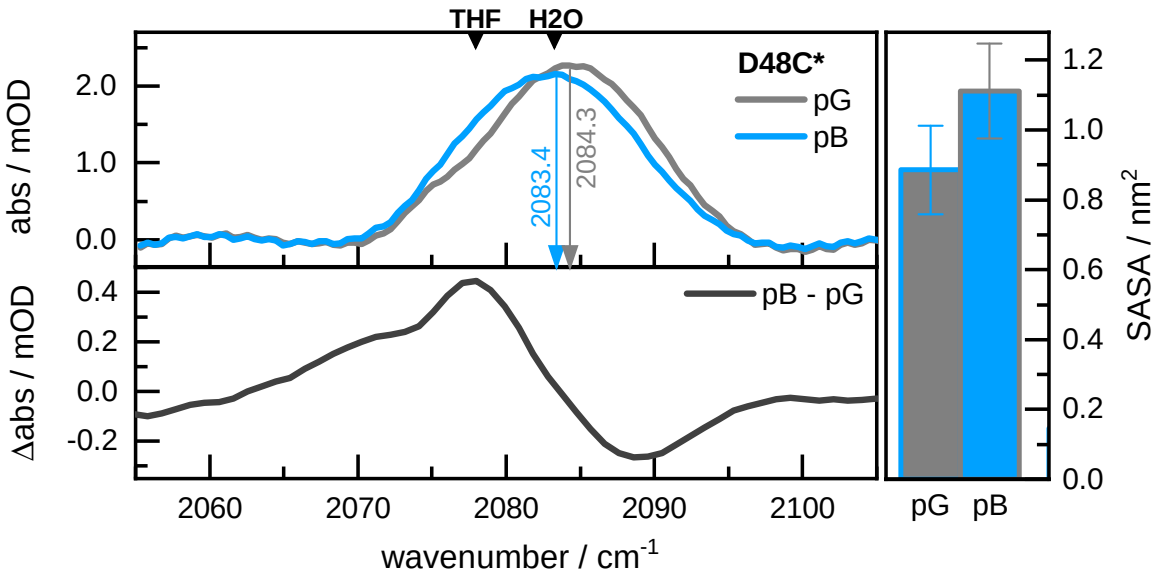

Figure 5.2: *FTIR absorption spectra (top panel) of SCN in D48C* in pG (gray) and pB (light blue) and the measured difference spectrum between pB and pG (bottom panel). The sample concentration was 11 mM at 50 µm path length. Arrows indicate the wavenumbers $\tilde{\nu}_{sd}$. Small black arrows mark the absorption of MeSCN in THF and H_2O buffer [24, 25]. Right panel: SASA values for the SCN-labeled D48C* in pG (gray) and pB (light blue) with error bars.*

location of L23 in the N-terminal region with its side chain oriented into the hydrophobic cavity that is formed between the N-terminus and the rest of the protein gave reason to expect an environment that barely exposed the SCN label to the solvent. These expectations are supported by the SASA calculations that reveal a very low accessibility in the pG state compared to A44C* and D48C*. Nevertheless, taking these structural predictions into account, the SCN absorption should be comparable to the wavenumber of the model compound MeSCN in THF (2156.9 cm^{-1}, 2077.9 with isotope shift [24, 25]) mimicking the water-shielded interior of a protein, though it was measured to be blue-shifted by approximately 2 cm^{-1}. The sensitivity of the SCN label to polarity and H-bonding, which have competing effects on the direction in which the absorption is shifted, has always to be taken into account when discussing these data. However, in this particular case structural changes in the mutant are considered to be responsible for the unexpectedly high wavenumber. Probably the cavity is not as narrow as predicted due to substitution of the leucine and/or labeling with the thiocyanate and solvent molecules were able to partly access the space between the N-terminus and the protein.

This hypothesis is supported by measurements of the gas phase ion structure of L23C* under dark and illuminated conditions that were performed with ESI-IMS mass spectrometry (see figure D.3 on page 191 in the appendix). Examination of the ion mobilograms for WT reveals that in pG signals occur only at low charge states with a collision cross section (CCS) of about 2000 $Å^2$. This indicates a compact protein structure as it is expected for the natively folded PYP in pG. Upon illumination of the molecules at the nESI tip, the signals shift to a distribution of higher charge states resulting in an averaged CCS of about 3000 $Å^2$ as it is typical for an partially unfolded protein that exhibits a larger surface area [138]. While the other labeled mutants that were investigated show comparable results

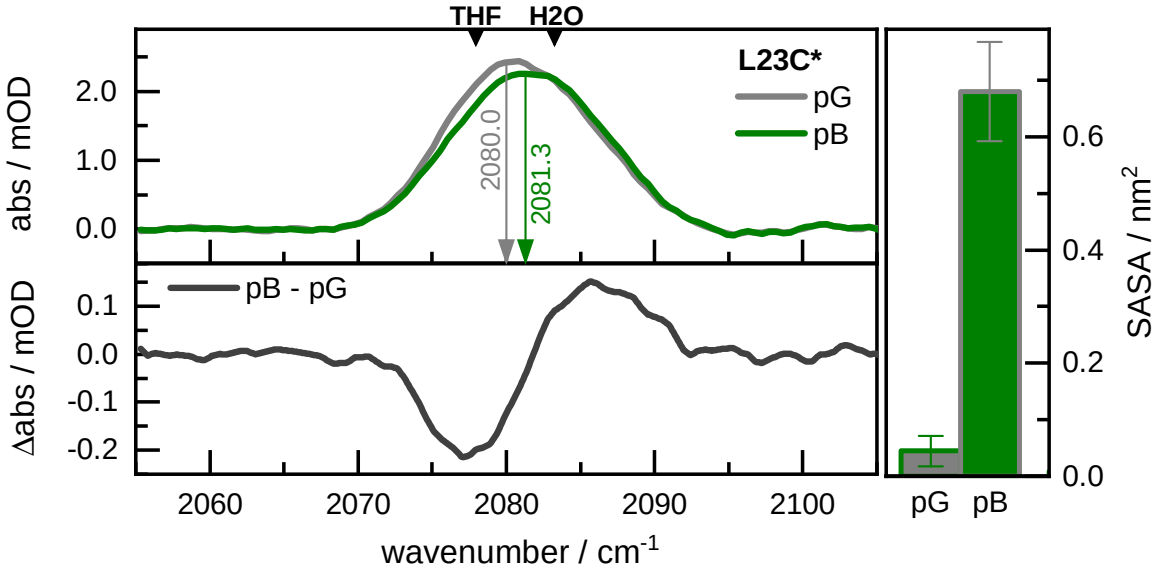

Figure 5.3: *FTIR absorption spectra (top panel) of SCN in L23C* in pG (gray) and pB (green) and the measured difference spectrum between pB and pG (bottom panel). The sample concentration was 10 mM at 50 µm path length. Arrows indicate the wavenumbers $\tilde{\nu}_{sd}$. Small black arrows mark the absorption of MeSCN in THF and H_2O buffer [24, 25]. Right panel: SASA values for the SCN-labeled L23C* in pG (gray) and pB (green) with error bars.*

under similar conditions, L23C* also exhibits in pG a large charge state distribution and the effects caused by illumination are negligible corresponding to an enlarged surface area already in pG, which is similar to the one of the illuminated state. Therefore it can be concluded that mutation and/or labeling of L23 led to a destabilization of the N-terminal region in pG resembling a protein conformation as expected for pB. Furthermore, in a cristallography study [91] the involvement of L23 in a hydrogen bond to N43 in the α3-helix is described, which connects the N-terminus to the protein body. Although it is the oxygen of the leucine's backbone carbonyl that forms the hydrogen bond, substitution of the amino acid and labeling could lead to a weaker or lost binding of the N-terminus due to structural variations. In CD and FTIR difference spectroscopy of the protein region (see figure 4.1 on page 52), which were used to evaluate the structural integrity of the protein mutants, the detachment of the N-terminus is not observable as both techniques are only sensible to changes in the secondary structure contributions.

The upshift that is observed for the SCN absorption in the pB state is rather low with only 1.3 cm^{-1}, although L23 should be involved in large structural rearrangements during the photocycle when the N-terminus flips away from the rest of the protein and the N-terminal α-helices unfold [11, 55, 75, 77, 79, 81, 83]. However, the wavenumber of the absorption (2081.3 cm^{-1}) matches the absorption of MeSCN in H_2O closely indicating a solvent accessible environment. The SASA calculations also reveal a high solvent exposure for L23C* in the pB state with a value that is comparable to other solvent exposed mutants. This is interpreted in a way that, indeed, the SCN is less shielded in the pG state, but senses the expected water exposure due to the movement of the N-terminus in the pB state.

For A30C* (see figure 5.4) that is located opposite of L23C* at the protein body with the side chain pointing towards the N-terminus into the cavity, a similar wavenumber as for L23C* in the pG state is observed. As discussed above, this could be evidence that some water molecules were able to penetrate into the cavity and partially expose the SCN label to solvent, although in contrast to L23, A30 is not known to be involved in some interactions with the N-terminus that could be perturbed. Moreover, the SCN absorption of A30C* features a very narrow, Lorentzian-like line shape which implies a rather confined environment as it would be expected for a label buried in the protein interior. The SASA calculations show in this case the lowest solvent accessibility for all labeled mutants.

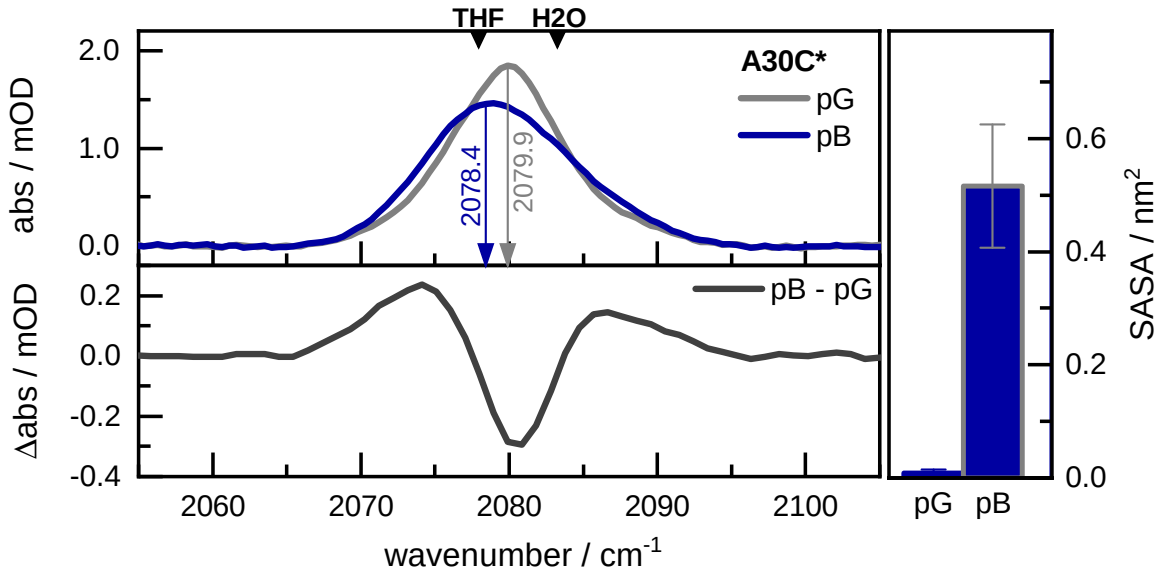

Figure 5.4: *FTIR absorption spectra (top panel) of SCN in A30C* in pG (gray) and pB (dark blue) and the measured difference spectrum between pB and pG (bottom panel). The sample concentration was 6 mM at 50 µm path length. Arrows indicate the wavenumbers $\tilde{\nu}_{sd}$. Small black arrows mark the absorption of MeSCN in THF and H_2O buffer [24, 25]. Right panel: SASA values for the SCN-labeled A30C* in pG (< 0.01 nm^2) and pB (dark blue) with error bars.*

In the pB state the SCN absorption for A30C* red-shifts by 1.5 cm^{-1} to 2078.4 cm^{-1} resembling the wavenumber for MeSCN in THF. This observation contradicts the expectations that the SCN label becomes more solvent exposed in the pB state when the N-terminus protrudes as described in literature [11, 55, 75, 77, 79, 81, 83] and can be also seen in the SASA calculations where the solvent accessibility increases considerably. However, the line shape of the absorption band changes significantly under irradiation from the narrow Lorentzian to a broadened Gaussian one. Contrary to the observation that was made for the wavenumber shift, this could be an effect of more contacts to the solvent as this usually leads to a less homogeneous environment with the label sensing a manifold of different microenvironments. Besides inhomogeneous broadening, additional effects have to be considered that influence the line shape such as lifetime broadening or motional narrowing due to fast dynamics (picoseconds). To examine the factors contributing to the line shape and the unexpectedly low wavenumber in the pB state further studies have to be applied including 2D-IR spectroscopy and simulations. Investigation of the vibrational lifetimes of the SCN label, discussed in the following chapter, reveal further information about the solvent exposure in the two different states.

Probing changes of chromophore and binding pocket: V57C*, V122C* and M100C*

The SCN absorption of V57C* (see figure 5.5) in the pG state is located at 2080.2 cm^{-1} between the absorption assigned to the fully solvent exposed case, represented by MeSCN in H_2O (2162.4 cm^{-1}, 2083.2 cm^{-1} with isotope shift [24, 25]), and a fully shielded environment, represented by MeSCN in THF (2156.9 cm^{-1}, 2077.9 with isotope shift [24, 25]). The SASA calculations show a rather low value that indicates a mainly solvent protected environment, although the value is higher than for L23C* and A30C* in the pG state as discussed above. Considering the structure of pG, a low solvent accessibility and therefore a lower wavenumber than observed would be expected since V57 is pointing into the hydrophobic chromophore binding pocket. However, one explanation for the blue-shifted absorption compared to the fully solvent protected label, could be a hydrogen bond of the SCN towards a confined water molecule in the protein interior. Indeed, in the MD simulations it is observed that a water molecule is able to penetrate into the binding pocket and to bind to V57C*. Further insight into hydrogen bonding is obtained by temperature-dependent FTIR measurements with the FTLS approach [125, 132, 168] which also suggest a hydrogen-bonded SCN in the pG state as discussed in detail in section 5.1.2 on page 68.

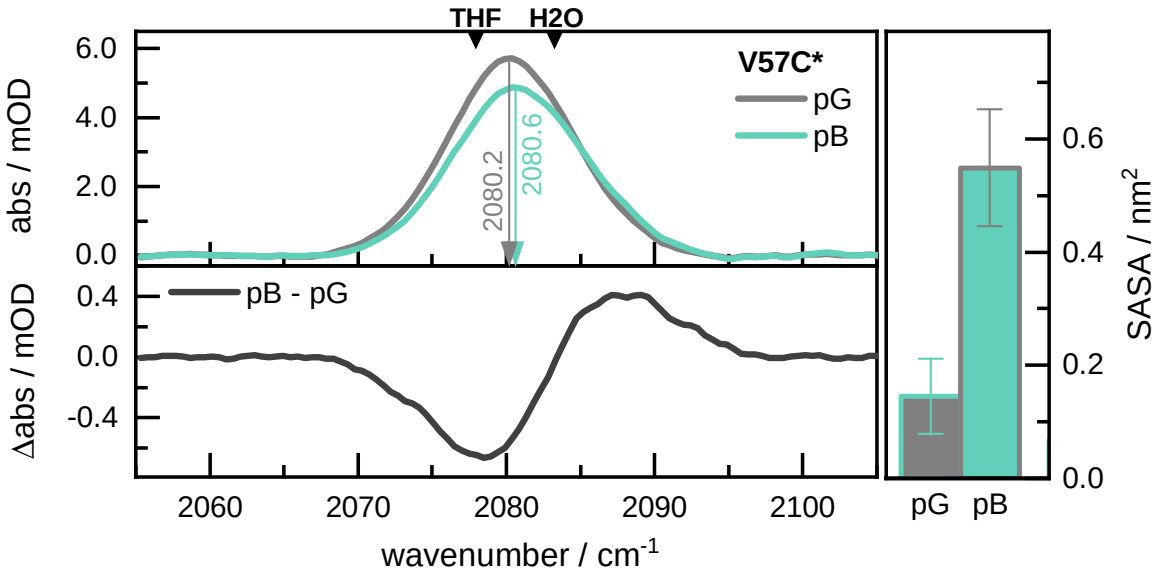

Figure 5.5: *FTIR absorption spectra (top panel) of SCN in V57C* in pG (gray) and pB (cyan) and the measured difference spectrum between pB and pG (bottom panel). The sample concentration was 8 mM at 50 µm path length. Arrows indicate the wavenumbers $\tilde{\nu}_{sd}$. Small black arrows mark the absorption of MeSCN in THF and H_2O buffer [24, 25]. Right panel: SASA values for the SCN-labeled V57C* in pG (gray) and pB (cyan) with error bars.*

The chromophore binding pocket is known to collapse during the photocycle, when the chromophore moves outwards and large structural rearrangements take place [20, 46, 83, 154]. These changes are reflected by the SASA calculations for V57C* in the pB state as they exhibit a significantly increased solvent accessibility, whereas the FTIR measurements show only a very small blue-shift of less than 1 cm^{-1} for the SCN absorption. This wavenumber of 2080.6 cm^{-1}, however, indicates an environment that is well accessible for water molecules.

The reason for the small shift compared to the large structural changes is probably the already quite high wavenumber of the pG absorption, that was most likely caused by the binding of an internal water molecule.

As V122 is located at the end of the C-terminus in the β5-sheet pointing into the hydrophobic cavity that surrounds E46 (see figure 4.2 on page 53) and is part of the chromophore binding pocket, only little solvent contacts were expected. The SCN absorption spectrum for the pG state of V122C* in figure 5.6 features two subpopulations that are both located further to the blue part of the spectral region than expected for low solvent accessibility as predicted by the SASA calculations. The lower subpopulation is identified at 2079.9 cm^{-1} and is comparable to the wavenumbers of L23C*, A30C* and V57C* in the pG state. The upshift compared to a fully solvent protected environment of this subpopulation could perhaps be explained by the competing effect of polarity and hydrogen bonding on the nitrile stretch vibration. While more hydrogen bonds lead to a blue-shift of the absorption, the same effect is caused by a decreased polarity [23, 24]. In most of the cases examined so far, the position of the absorption is more likely influenced by the hydrogen bonding interactions to the solvent than by polarity. In this case, however, in which the label senses a very hydrophobic surrounding (with the hydrophobic amino acids I31 and I49 nearby) it might be that the decreased polarity induced a shift to higher wavenumbers although the SCN is shielded from the solvent. The wavenumber of the blue-shifted subpopulation lies at 2084.7 cm^{-1} and therefore resembles the solvent exposed environment that is sensed in the pG state by the SCN label of the two residues A44C* and D48C* on the protein surface. It is assumed that this subpopulation reflects a second confirmation with the labeled cysteine oriented somehow to the solvent.

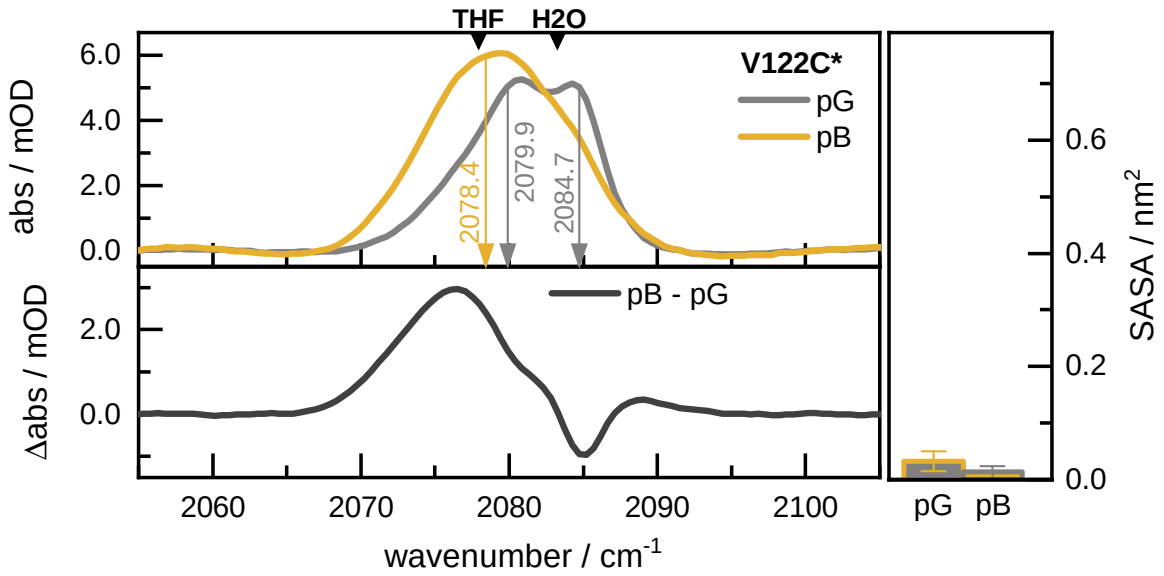

Figure 5.6: *FTIR absorption spectra (top panel) of SCN in V122C* in pG (gray) and pB (yellow) and the measured difference spectrum between pB and pG (bottom panel). The sample concentration was 10 mM at 50 µm path length. Arrows indicate the wavenumbers $\tilde{\nu}_{sd}$. Small black arrows mark the absorption of MeSCN in THF and H_2O buffer [24, 25]. Right panel: SASA values for the SCN-labeled V122C* in pG (gray) and pB (yellow) with error bars.*

The SASA calculations suggest an even lower solvent accessibility for V122C* in the pB state than in the pG state. This matches the observed FTIR spectrum where the SCN absorption is red-shifted to 2078.4 cm^{-1} close to the absorption of MeSCN in THF. Contrary to the pG state, only one single population is observed here. Obviously the label stays in a solvent protected environment during irradiation. However, the strong influence of the polarity on the nitrile vibration seems to be lost perhaps due to structural alterations of the hydrophobic cavity.

The SCN absorption spectrum of M100C* in the pG state features two prominent subpopulations (see figure 5.7) with the lowest wavenumbers of all SCN-labeled PYP mutants. The subpopulation with the higher intensity is found at 2077.1 cm^{-1}, which is similar to the wavenumber of MeSCN in THF and corresponds to a shielded environment. This is in good agreement with the SASA calculations that show a low accessibility for the pG state and meet the expectations for a residue pointing into the binding pocket towards the chromophore. The second subpopulation reveals an extremely red-shifted wavenumber of 2069.8 cm^{-1} (corresponding to 2148.5 cm^{-1} for SCN without isotope shift), which is distinctly lower than the absorption for the model compound MeSCN in the polar, non-H-bonding solvent DMSO (2153.1 cm^{-1}, 2074.2 cm^{-1} with isotope shift [24, 25]). To my knowledge this is the lowest wavenumber for an SCN label in proteins that was observed to date.

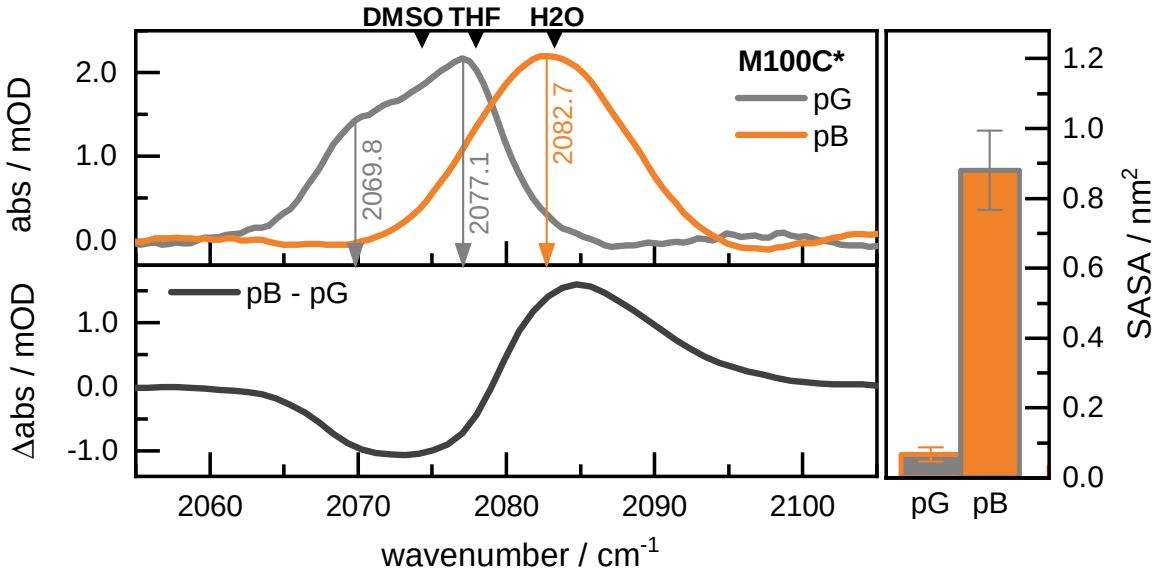

Figure 5.7: *FTIR absorption spectra (top panel) of SCN in M100C* in pG (gray) and pB (orange) and the measured difference spectrum between pB and pG (bottom panel). The sample concentration was 8 mM at 50 µm path length. Arrows indicate the wavenumbers $\tilde{\nu}_{sd}$. Small black arrows mark the absorption of MeSCN in DMSO, THF and H_2O buffer [24, 25]. Right panel: SASA values for the SCN-labeled M100C* in pG (gray) and pB (orange) with error bars.*

To get a feeling for the strength of the electrical field that was induced by the SCN and corresponds to the measured wavenumber, the Stark tuning rate from the Onsager model for thiocyanate in aprotic solvents from van Wilderen *et al.* [24, 25] was used, assuming that there were no interactions of hydrogen bonds involved. This led to an estimated field of approximately -100 MV/cm for the low wavenumber subpopulation which is considerably stronger than the solvent fields that were calculated for MeSCN in different aprotic

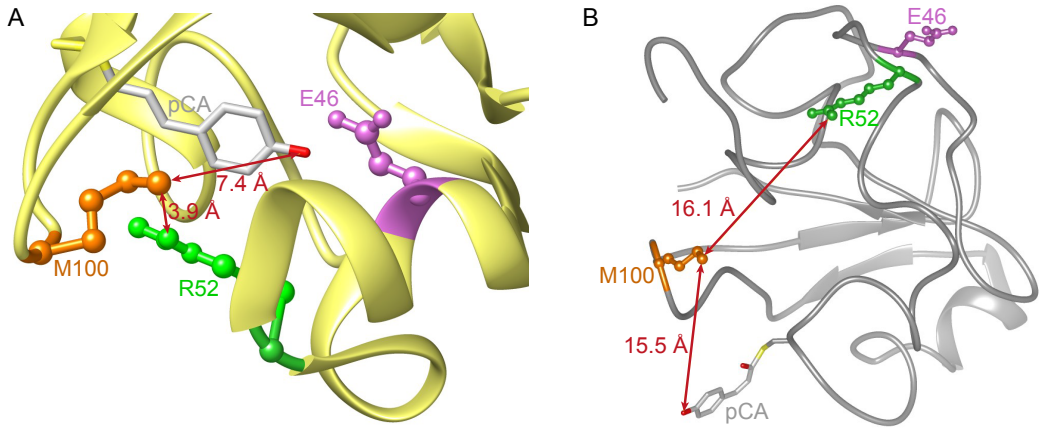

Figure 5.8: *Protein environment of M100. (A) Zoom into the surrounding environment of M100 in pG (pdb: 1NWZ) with M100 in orange, the pCA chromophore in gray and red, R52 in green and E46 in purple. The distance between M100 and the side chain of R52 is 3.9 Å and between M100 and the chromophore's carbonyl oxygen 7.4 Å. (B) Protein structure of pB (pdb: 2KX6) with the same amino acids colored as in pG. The distance between M100 and the side chain of R52 increased to 16.1 Å and between M100 and the chromophore to 15.5 Å.*[2]

solvents by van Wilderen *et al.* covering a range from -22 MV/cm (CCl_4) to -57 MV/cm (DMSO). Responsible for this extreme shift could be the vicinity to charged side chains like the nearby R52 (positively charged) in a distance of 3.9 Å and/or the deprotonated chromophore that is negatively charged in the pG state and 7.4 Å away from the side chain of M100 (see figure 5.8A).

Under irradiation the SCN absorption of M100C* is shifted by 5.6 cm^{-1} to the blue with respect to the higher wavenumber subpopulation in the pG state and hence resembles the absorption of MeSCN in H_2O. This indicates a higher accessibility of water molecules into the surrounding of the label, which is also supported by the SASA calculations. In the pB state the absorption spectrum exhibits only one single band. These observations can be explained by the collapse of the binding pocket after protonation and movement of the chromophopre which exposed the residue and the label to the solvent. Moreover, the positively charged residue R52 increased its distance to the side chain of M100 by a factor of four (see figure 5.8B).

An overview of the wavenumbers $\tilde{\nu}_{sd}$ of all labeled mutants for the pG and the pB state is shown in figure 5.9 on the next page demonstrating the range of wavenumbers accessible with the SCN label at different positions in the PYP due to altering environments.

Wavenumber-SASA correlation

To get a better measure how the solvent exposure influences the shifts of the SCN absorption, a linear correlation plot between mean wavenumber $\tilde{\nu}_{mean}$ and SASA values for all seven mutants in pG and pB was created. The plot is depicted in figure 5.10 on page 68.

[2]The structure image was created and the distance between M100 (atom CE) and R52 (atom NH1) as well as pCA (atom O4) were determined with Chimera 1.6.2.

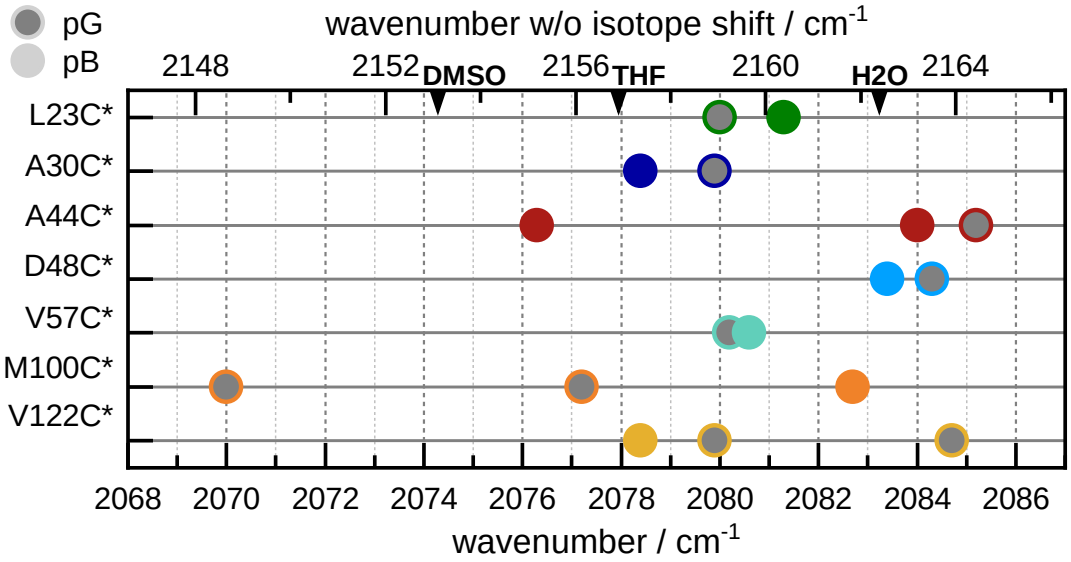

Figure 5.9: *Comparison of the wavenumbers $\tilde{\nu}_{sd}$ of the SCN absorption for all mutants in pG (gray with colored rim) and pB (closed colored circles). Small black arrows mark the absorption of MeSCN in DMSO, THF and H_2O buffer [24, 25]. On the top axis wavenumbers corrected for the isotope shift are given for better comparison with the literature. They are calculated with the experimentally determined factor of 1.038 [136].*

The mean wavenumber $\tilde{\nu}_{mean}$ was chosen instead of $\tilde{\nu}_{sd}$ - that was discussed more comprehensively above - because it describes a mean value of the wavenumbers of all subpopulations and the SASA values consider only one population for each mutant, as well. For M100C* in the pG state, additionally $\tilde{\nu}_{sd}$ of the higher wavenumber subpopulation is shown (orange square), as $\tilde{\nu}_{mean}$ is far red-shifted due to the second subpopulation, which exhibits an extremely low wavenumber ($\tilde{\nu}_{sd}$ = 2069.8 wn) probably caused by nearby charges and not by protection from the solvent. Therefore $\tilde{\nu}_{sd}$ of the higher wavenumber subpopulation was allowed for the linear fit instead of $\tilde{\nu}_{mean}$ for M100C* in pG.

The plot demonstrates the trend that high solvent accessibility as given by high SASA values leads to a blue-shifted absorption for the thiocyanate. Nevertheless, the correlation is not particularly high (r = 0.73) with many $\tilde{\nu}_{mean}$ that deviate from the expected SASA values. This can be taken as evidence that there are additional effects besides the solvent environment that contribute to the position of the absorption band. Such effects can be hydrogen bonds to nearby residues or to confined water molecules inside the protein as it was suspected for V57C* in the pG state. Furthermore, electrostatic fields by polar or charged groups in the proximity of the label can have a notable effect on the vibration frequency. This is presumably observed for M100C*, which is surrounded by the positively charged R52 and the negatively charged chromophore in the pG state, and also for A44C* located close to E46 that becomes deprotonated and negatively charged during the photocyle. A further role can be played by conformational heterogeneities as it was assumed for the higher wavenumber subpopulation of V122C* in the pG state possibly corresponding to a second conformation oriented towards the solvent. However, for the comparison with the SASA calculations in pB one has to bear in mind that these values emerge from a structure model (pdb: 2KX6) based on different methods like DEER, NMR and tr-SAXS/WAXS [83] and therefore could result in variations from the real solution structure.

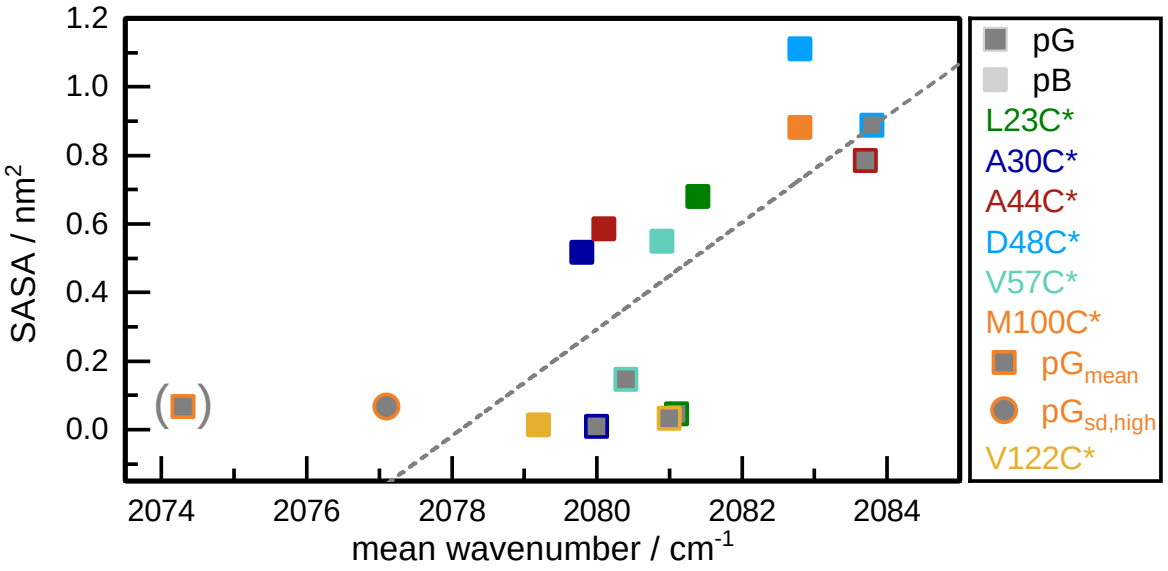

Figure 5.10: *Linear correlation plot between mean wavenumbers $\tilde{\nu}_{mean}$ and SASA values for all mutants in pG (gray squares with colored rim) and pB (closed colored squares). As $\tilde{\nu}_{mean}$ for M100C* pG was relatively low due to the extremely red-shifted subpopulation ($\tilde{\nu}_{sd}$ = 2069.8 wn), additionally $\tilde{\nu}_{sd}$ of the higher wavenumber subpopulation is depicted (orange closed circle) and was allowed instead for the linear fit. The gray dashed line displays the linear fit (correlation coefficient r = 0.73)*[3].

5.1.2 FTLS Measurements

For the thiocyanate labels the interpretation of spectral shifts in the FTIR is complicated due to competing effects of polarity and hydrogen bonding interactions. With the temperature dependent absorption measurements Adhikary *et al.* [125] introduced a simple method to investigate the microenvironment of nitriles that is especially useful to distinguish whether a nitrile is engaged in hydrogen bonding or not. This distinction is based on the influence of the temperature on the strength of hydrogen bonds and thus on the frequency of the C≡N vibration, whereas electrostatic effects are not affected by variations in temperature. The resulting frequency-temperature line slope (FTLS) is a direct measure for hydrogen bonding interactions [125, 132].

FTLS measurements were performed for the model compound MeSCN in the aprotic solvent THF, which was used to mimic an H-bond free environment as it can occur in the protein interior, and for MeSCN in D_2O resembling a fully solvent exposed nitrile label. Three PYP mutants were chosen for investigation, for which the FTIR experiments revealed that their SCN-labels probed potentially three different environments in the pG state. A44C* was expected to provide a solvent exposed environment with the label engaged in hydrogen bonds towards the bulk water and A30C* was found to be placed most likely inside the protein, shielded from the solvent. For V57C* SASA calculations predicted a relatively low solvent accessibility, whereas the FTIR absorption showed a quite high wavenumber that implies a hydrogen bond to an internal water molecule. With the FTLS approach this contradicting behavior of the label might be explained. Furthermore, FTLS were measured for all three mutants in the pB state. The temperature range for all measurements reached

[3] Linear regression was performed with OriginPro 2018G. Correlation coefficient r represents the "Pearson R" of the fit.

from 5 °C to 39 °C, and the mean wavenumber $\tilde{\nu}_{mean}$ (except for A44C* pB where $\tilde{\nu}_{sd}$ was used) was taken to calculate the wavenumber/frequency shifts (see temperature-dependent absorption spectra for the mutants in pG in the top row of figure 5.11 and for MeSCN and the mutants in pB in the appendix in figure B.3 on page 185).

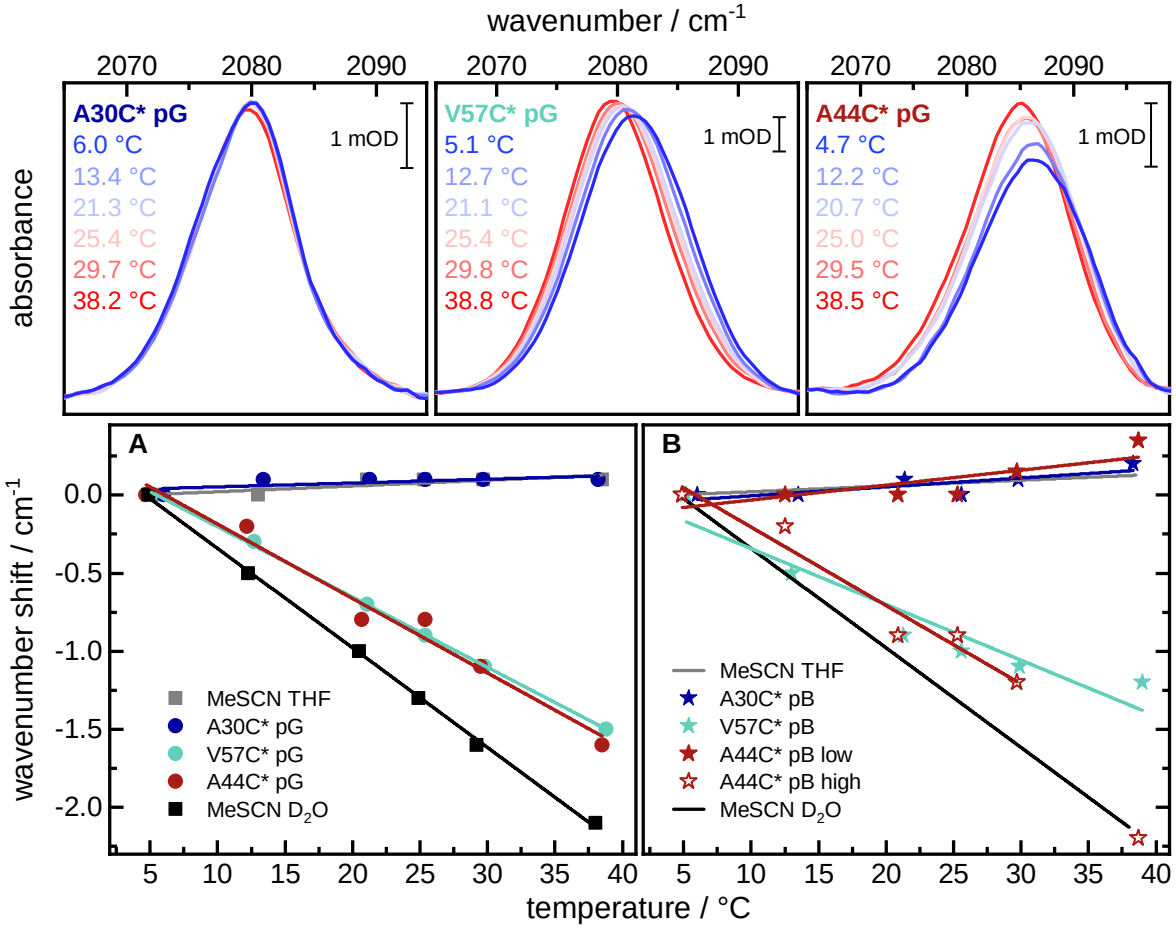

Figure 5.11: *Temperature-dependent FTIR absorption spectra and FTLS of SCN. Top row: Temperature-dependent FTIR absorption spectra of SCN for A30C*, V57C* and A44C* in pG. For the spectra of MeSCN and the mutants in pB see figure B.3 on page 185 in the appendix. Bottom row: (A) FTLS of MeSCN in THF (gray squares) and in D_2O (black squares), the pG states of A30C* (blue dots), V57C* (cyan dots) and A44C* (red dots). The linear fits are shown as solid lines in corresponding colors. (B) FTLS of the pB states of A30C* (blue stars), V57C* (cyan stars) and A44C* with the two subpopulations pB_{low} (closed red stars) and pB_{high} (open red stars). The linear fits are shown as solid lines in corresponding colors. For A44C* pB_{high} the value at 39 °C was excluded from the linear fit as $\tilde{\nu}_{sd}$ could not be extracted from the second derivative reliably (see figure B.3). The fitted FTLS of MeSCN in THF/D_2O (gray/black solid line are depicted for comparison.*

In figure 5.11A the FTLS for MeSCN in THF (gray) and D_2O (black) are shown. The non-H-bonded MeSCN in THF exhibits a slightly positive slope (0.0037 $cm^{-1}K^{-1}$), whereas the fully solvent exposed MeSCN that is able to engage in hydrogen bonding interactions has a clearly negative slope (-0.06379 $cm^{-1}K^{-1}$). The measurements of A30C* (blue in figure 5.11A) in the pG state yield approximately the same FTLS as for MeSCN in THF implying that the label does not form any hydrogen bonds. This is in good agreement with the steady-state FTIR measurements, in which a very narrow line shape of the SCN absorption was

observed and led to the conclusion that the label is buried in a homogeneous environment. Additionally, these findings are supported by the SASA calculations that predicted a completely solvent protected position.

For A44C* in the pG state a large FTLS (red in figure 5.11A on the previous page) is found, only a bit smaller than for MeSCN in D_2O, indicating a high hydrogen bonding strength. The high absorption wavenumber of the SCN in the FTIR (similar to MeSCN in water [24, 25]) suggested already a high solvent exposure. It is interesting to note that the temperature-dependent FTIR absorption spectra of SCN for A44C* (figure 5.11 on the preceding page) show an significant increase in the extinction coefficient with weakening of the hydrogen bonds due to higher temperatures. V57C* (cyan in figure 5.11A on the previous page) exhibits a slope similar to the one observed for A44C*. That demonstrates that the SCN label in V57C* is indeed engaged in hydrogen bonding interactions in the pG state, most likely to a confined water molecule that was able to penetrate through the protein surface.

The measurements of the three mutants in the pB state are depicted in figure 5.11B on the preceding page. For these measurements the errors of the linear fits are larger than in the pG state as small heating effects due to illumination could not be measured with the temperature sensor placed at the outside of the sample cell. Nevertheless, we observe a linear behavior between wavenumber shift and temperature. In case of A30C* the obtained slope is nearly identical with the slope in the pG state. That implies that A30C* does not take part in hydrogen bonding interactions in neither state. These findings are contradictory to the SASA calculations as the SASA values suggested a change to higher solvent accessibility in pB. However, the changes of the SCN absorption in the steady-state FTIR were not unambiguous. The broadening of the absorption band under irradiation was interpreted as a loss of the label's homogeneous microenvironment due to higher solvent exposure, but the small red-shift that was observed could indeed hint to an even more protected environment. Further observables, like the vibrational lifetime that is discussed in chapter 6 on page 75, are necessary to better understand the structural changes.

The FTLS of V57C* in the pB state differs hardly from the slope in pG indicating a similar hydrogen bonding strength. This is in good agreement with the absorption spectra which showed only a tiny blue-shift for pB, although the SASA calculations predicted a significantly increased solvent exposure. If the hydrogen bonding in the pG state is caused by an internal water molecule and in the pB state by contacts to the surrounding solvent, the FTLS cannot distinguish, at least in this measurement, between hydrogen bonds to single solvent molecules or to the bulk water. This result is somehow unexpected as First *et al.* [132] observed in their study with nitrile labels at many distinct positions in GFP that the nitriles at each location showed a very unique FTLS due to a manifold of different hydrogen bonding interactions.

For A44C* in the pB state two subpopulations are observed in the absorption spectra (see figure 5.1 on page 59), one major population around 2076 cm^{-1} (henceforth referred to as pB_{low}) and a minor population around 2084 cm^{-1} (henceforth referred to as pB_{high}). To investigate both subpopulations independently, the second derivative of the absorption spectra at each temperature is taken and the wavenumber shifts of both $\tilde{\nu}_{sd}$ correlated separately with the temperature (closed red stars for pB_{low} and open red stars for pB_{high} in figure 5.11B on the previous page). The slope of pB_{high} is very similar to the one of

A44C* in the pG state representing a solvent exposed label. This is consistent with the observation that there is only a small red-shift of the absorption spectrum from the pG state to the minor population of the pB state. To exclude that pB_{high} is some ground state population, an irradiation titration was performed for A44C* as discussed in section 5.1.3 on the following page. The very large red-shift (9 cm^{-1}) of the major population was previously explained to be caused rather by changes in the electrostatic field, probably due to the proximity to the deprotonated E46 in the pB state, than to less solvent exposure, especially as the SASA calculations suggested a solvent accessibility that is only a little lower as in pG. However, the FTLS of pB_{low}, that is comparable to MeSCN in THF which implies a completely non-H-bonded SCN label, supports the interpretation that, indeed, the movement into an environment that is shielded from the solvent is responsible for the shift to very low wavenumbers.

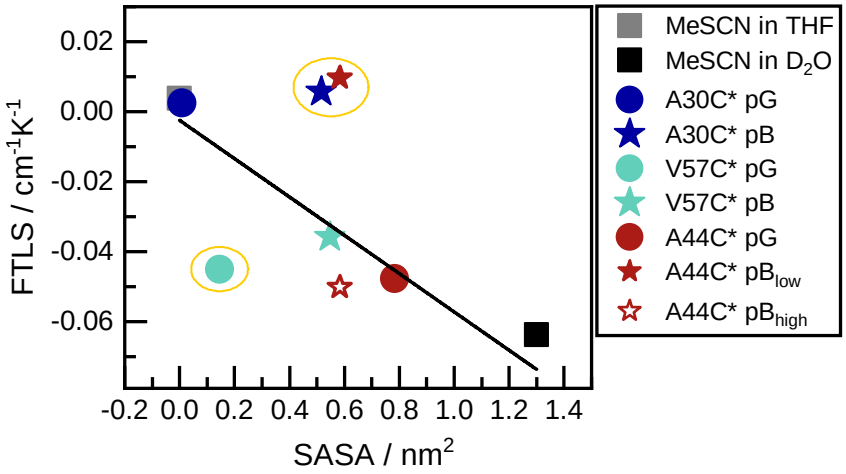

Figure 5.12: *Linear correlation plot between FTLS and SASA values. The SASA value for MeSCN in THF was set to zero as there are no hydrogen bonding interactions expected. The data points in yellow circles were excluded from the linear fit. The black line displays the linear fit (correlation coefficient r = -0.95).*

Whereas the FTLS is sensitive to all kinds of hydrogen bonding interactions either with the bulk solvent, with confined water molecules, or with the protein itself, SASA can only probe the engagement in hydrohen bonds towards the bulk water [125, 132]. Nonetheless, both are a good measure for solvent exposure of the SCN label. In figure 5.12 the correlation between FTLS and SASA for the investigated systems is depicted. In general there is a linear relation between both methods displayed by the black line in figure 5.12. However, not all slopes that were determined for the SCN at different positions match the calculated SASA values for the mutants (indicated by a yellow circle in figure 5.12 and not considered for the linear fit). V57C* pG has an FTLS that is too steep to fit the relatively low SASA value. This can be explained by an internal water molecule that engages in a hydrogen bond to the SCN and is sensed by the FTLS, but not by the SASA as it is buried inside the protein. In case of A30C* pB and A44C* pB_{low}, SASA calculations[4] reveal medium solvent accessibility, whereas with the FTLS no hydrogen bonding interactions are detected.

[4]There is only one SASA value for A44C* pB not distinguishing between the two subpopulations that were observed in the FTIR spectra.

5.1.3 Irradiation Titration of A44C*

To ensure that the complete population is shifted to the pB state and to identify the minimal amount of blue light that has to be applied on the PYP samples to completely accumulate the pB intermediate, an irradiation titration was performed with varying power of the diode laser. The test was exemplarily carried out on the SCN-labeled A44C*. Different FTIR methods and observables were applied to find the minimum required irradiation power. FTIR difference spectra in the spectral region of the chromophore and protein backbone absorption on the one hand, and for the SCN absorption on the other were investigated. Furthermore, alterations in the position of the SCN absorption spectra are examined. In figure 5.13 on the facing page all spectra and a comparison of the different methods is depicted.

In the FTIR difference spectra of both the chromophore/protein region (figure figure 5.13A on the next page) and the SCN region (figure figure 5.13B on the facing page) it is apparent that already with the lowest amount of light that was used in the experiments (3 mW, purple line) large spectral changes occur and the signal amplitude reaches approximately 70 % of the final intensity. When the irradiation power is further increased, the signal intensity also increases until it reaches saturation around 150 mW. For higher power no further gain in intensity can be observed.

These results are confirmed by the investigation of the SCN absorption spectra (figure 5.13C on the next page), which shift in position when the irradiation power is increased. In the pG state the mean wavenumber of the absorption lies at 2083.7 cm^{-1}. Even for the lowest irradiation power, the red-shift is already 2.2 cm^{-1}. The saturation and therefore a fully accumulated pB state is reached between 150 and 200 mW with the mean wavenumber shifted to 2079.9 cm^{-1}. With further increasing power up to 1355 mW the absorption spectrum experiences no significant changes anymore. This additionally indicates that the second subpopulation in the pB state with $\tilde{\nu}_{sd}$ = 2084.0 cm^{-1}, which is less pronounced than the subpopulation at 2076.3 cm^{-1}, is not a remnant of the pG intermediate despite the similar wavenumbers and FTLS, but represents a second spectral feature of the pB state. Furthermore, the blue-shifted UV/vis spectra of the pB state have no significant absorption at the excitation wavelength of 445 nm [5, 20, 74, 86]. Thus it can be conclude that, if enough irradiation power is used, the population is mostly shifted to the pB state and the contributions of pG become negligible.

The exponential fits of the correlated signal amplitudes or positions with the irradiation power were normalized and are compared in figure figure 5.13D on the facing page. In all four cases a very similar curve is observed with beginning saturation around 150 mW. This value is a good measure for the minimal irradiation power that has to be used to completely accumulate the pB state. However, all experiments in this thesis under permanent irradiation with blue light were performed with an irradiation power that was at least twice as high.

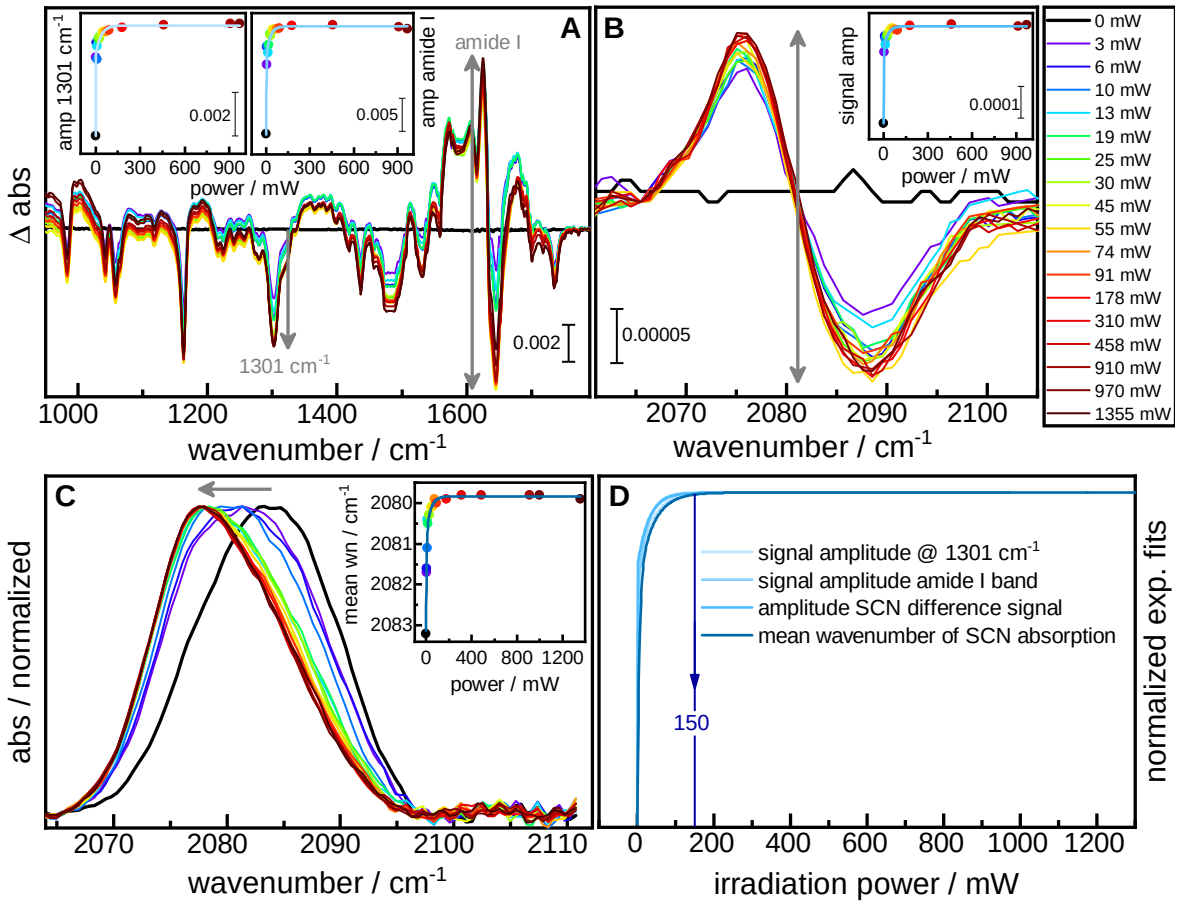

Figure 5.13: *Irradiation titration of PYP-A44C*. (A) FTIR difference spectra between pB and pG of the chromophore and protein region at irradiation powers from 0 mW to 970 mW (H_2O buffer, pathlength 5 µm). The insets depict the changes of the signal amplitudes (indicated by gray arrows) of the chromophore's C-C mode at 1301 cm^{-1} (left) and the amide I band between the maximum at 1626 cm^{-1} and the minimum at 1646 cm^{-1} (right) with varying irradiation powers. (B) FTIR difference spectra between pB and pG of the SCN signal at irradiation powers from 0 mW to 970 mW (H_2O buffer, pathlength 5 µm, background correction of each spectrum by subtraction of a polynomial fit of 5^{th} order). The inset shows the change of the signal amplitude (indicated by the gray arrow) with increasing irradiation power. (C) FTIR absorption spectra of SCN at irradiation powers from 0 mW (pG, black) to 1355 mW (D_2O buffer, pathlength 150 µm, background corrected). In the inset the change of the mean wavenumbers (indicated by the gray arrow), which represents the first central moment of the absorption band, with increasing irradiation power can be seen. (D) Comparison of the exponential fits (blue lines in the insets of panels A-C, normalized) of the correlation between signal amplitude or spectral position and irradiation power. Saturation of the pB state was reached at approximately 150 mW irradiation power.*

5.2 Conclusion

In the steady-state FTIR study of SCN-labeled PYP, variations in the thiocyanate absorption were observed depending on the position of the label within the protein and between the photocycle intermediates pG and pB. In general, a blue-shifted absorption indicated a solvent exposed environment with the wavenumber resembling the wavenumber of the model compound MeSCN in H_2O as measured by van Wilderen *et al.* [24, 25]. A red-shifted absorption was related to a buried label comparable to MeSCN in the aprotic, apolar

solvent THF that mimicked the properties of the protein interior [24, 25]. Therefore it was concluded that mainly the hydrogen bonding environment of the solvent influenced the observed SCN absorptions, as an increase in hydrogen bonding interactions leads to a blue-shift whereas an increase in polarity causes a red-shift [23–25, 130]. This conclusion was supported by the SASA calculations, a measure of solvent exposure, which exhibited in most cases a higher accessibility for blue-shifted species. However, there were additional effects besides interactions with the solvent that shifted the absorption of the thiocyanate. Among these effects were polarity of the surrounding, electrostatic fields of charged groups and internal hydrogen bonds. Temperature-dependent measurements of the FTLS helped to distinguish between the different contributions as they indicate the engagement of the label in hydrogen bonding interactions.

The measured variations in the surrounding of the label allowed to draw some conclusions on local structural changes of PYP that occurred during the photocycle. Although A44C* and D48C* are both solvent exposed in the pG state and located in the same helix (α3), the SCN labels sensed different changes between intermediates pG and pB. A44C*, which is located close to E46, detected the proton transfer from the glutamate since the electrostatic field changed due to the negative charge of deprotonated E46. On the other hand, D48C* seemed not to sense the deprotonation process, but a movement into a more solvent protected environment as it was provided by the hydrophobic binding pocket, which was left empty by the chromophore in the pB state. M100C* that is positioned in the proximity of positively charged R52 and the deprotonated chromophore in the pG state perceived the large structural rearrangements during the photocycle that drastically increased the distance between the SCN label and R52 as well as the chromophore, that was protonated in the meanwhile and flipped out of the binding pocket. This movement of the chromophore and the expansion of the whole protein was additionally sensed by V57C* which is facing into the chromophore binding pocket and became more solvent exposed since more water molecules were able to penetrate into the protein interior in the pB state. Further, L23C* and A30C*, both oriented into the cavity between the N-terminal region and the rest of the protein, were chosen to follow the movement of the N-terminus during the photocycle that was predicted in literature. L23C* was not able to detect this movement most likely due to a structure with an already detached N-terminus in the pG state caused by mutation and/or labeling. However, this higher solvent accessibility for the space between the N-terminus and the protein body was observed for A30C*. Whereas the change in position of the SCN absorption did not indicate an increased solvent exposure in the pB state, the altered line shape of the absorption band suggested this assumption.

Steady-state FTIR spectroscopy with the thiocyanate-labeled PYP mutants revealed a first impression on how irradiation of the protein led to local variations in the protein structure, but further insight has to be gained by several other methods to fully understand the connection between spectral and structural changes. With detailed MD simulations the spectroscopic observables can be calculated based on the protein structures. 2D-IR spectroscopy will help to further characterize the vibrational mode by investigation of the vibrational lifetime, anisotropy or spectral diffusion. Exact information on the structure of the mutants and the label's environment can be obtained by X-ray crystallography of the SCN-labeled mutants at least for the pG intermediate. The steady-state data can be supported by time-resolved measurements which give insight into local protein dynamics and therefore into structural changes towards the pB state as discussed during this thesis.

6 Ultrafast IR-Pump-IR-Probe Experiments

In this chapter the ultrafast IR-pump-IR-probe experiments for investigation of the vibrational lifetimes of the thiocyanate label in the PYP mutants in pG and pB are discussed. The results are based on data published in "Vibrational lifetime of the SCN protein label in H_2O and D_2O reports site-specific solvation and structure changes during PYP's photocycle" by Schmidt-Engler and Blankenburg *et al.* [121].

After investigating the spectral position and line shape of the SCN absorption and their changes upon formation of pB in the infrared, examined in detail in the previous chapter, a new observable was applied to improve the interpretation of the local structural alterations. The vibrational lifetime of the SCN incorporated in proteins was found to be highly sensitive to its surrounding as intramolecular energy relaxation is blocked by the heavy sulfur atom that decouples the C≡N vibration from other protein modes [115]. Therefore changes of the vibrational lifetime are an excellent indicator for variations in the label's environment [23–25].

To distinguish unambiguously between solvent effects and influences of the protein on the lifetime the experiments were carried out in the solvents D_2O and H_2O as published in [121]. Due to different spectral densities of energy-accepting modes and coupling to the C≡N vibration, the lifetime varies in the two isotopological solvents [43]. A difference of Δ = 16 ps between the lifetimes of the model compound MeSCN in D_2O and H_2O, respectively, was observed. The investigation of the labeled proteins in both solvents and comparison to the model compound and structural predictions for the different labeling sites allowed to draw conclusions on the solvent exposure of the label. In the following, only the SCN lifetimes obtained for the different mutants in H_2O will be used to facilitate the interpretation of the steady-state FTIR data.

6.1 Results and Discussion

The vibrational lifetimes of SCN in all seven mutants, that have been examined in the steady-state FTIR measurements, were extracted from the time dependent experiments for pG and pB state. The measurements discussed here were carried out in H_2O buffer[1]. The IR pump pulses were centered at the wavenumbers of maximum absorption in the FTIR spectra, except for M100C* in pG where it was centered at the left (2068 cm^{-1}, pG_{low}) and the right (2080 cm^{-1}, pG_{high}) flank, respectively, of the SCN absorption spectrum to excite the two observed subpopulations separately (depicted in figure E.2 on page 194 in the appendix). The absorption of the SCN label was almost not influenced by exchange from D_2O (as used in the FTIR study) to H_2O buffer as it can be seen for absorption spectra of

[1] As M100C* pG could only be measured in D_2O buffer, the data for the pB state are discussed in both solvents.

MeSCN in both solvents in figure E.1 on page 193 in the appendix. The vibrational lifetimes of SCN at all different labeling sites are depicted in figure 6.1 on the next page (except for M100C* that is separately shown in figure 6.2 on page 81) along with their corresponding decay-associated difference spectra from global analysis. The spectra of all components from global analysis are shown in figure E.5 on page 197 in the appendix.

For MeSCN in H_2O the lifetime was determined to be 36 ps (depicted as gray arrow and line in the bar plots of figure 6.1 on the facing page). A similar lifetime for the SCN corresponds to a fully solvent exposed label and deviations from this value indicate less solvent accessibility.

Buried in the protein interior: V122C*

In V122C* pG a lifetime of 53 ps was measured as depicted in figure 6.1 on the next page. This lifetime is remarkably longer than the lifetime for a solvent exposed label (36 ps for MeSCN). This deviation implies clearly an SCN label that is buried inside the protein. In the FTIR two subpopulations were identified for pG with $\tilde{\nu}_{sd}$ at 2079.9 cm^{-1} and 2084.7 cm^{-1} and relatively narrow bandwidth for both. In the IR-pump-IR-probe experiment it was not possible to distinguish between both populations due to the width of the pump pulse that was determined to be 12 cm^{-1} (FWHM). Therefore the lifetime reflects a mixture of both subpopulations, but is predominantly influenced by the red-shifted population as the pump pulse was centered in its maximum (2080 cm^{-1}). From the FTIR measurements and the SASA calculations a solvent protected label was predicted, placed in the hydrophobic E46 cavity, although the wavenumber of 2079.9 cm^{-1} was higher than it would be expected for a fully shielded label (indicated by MeSCN in THF at 2077.9 cm^{-1} after correction of the isotope shift [24, 25]). This deviation was explained by effects of the highly hydrophobic environment as a decreased polarity leads to an upshifted SCN absorption. Indeed, this interpretation is strongly supported by the vibrational lifetime, which indicates a label without solvent contacts.

Under irradiation the lifetime of V122C* remains almost unchanged at 55 ps. Consequently, the label stays in its buried environment in pB. The downshift that is displayed for the decay-associated difference spectrum of the component from global analysis corresponding to the vibrational lifetime, as shown in figure 6.1 on the facing page, implies that there are changes in the surrounding though the lifetime is unaffected. Thus the spectral shift is not caused by changes in the solvent accessibility, but by variations in the polarity or the electrostatics as they are very likely to occur after E46, that is nearby in pG, gets deprotonated and moves out of the hydrophobic cavity in the pB state observed by examination of the pB structure (pdb: 2KX6). Overall, these findings are in good agreement with the changes in the FTIR study.

Large environmental changes: A30C* and V57C*

With 57 ps A30C* exhibits a quite long lifetime in the pG state, which is similar to those found for V122C* in pG and pB as shown in figure 6.1 on the next page, hence the label is solvent protected in the pG state. This confirms the conclusion drawn from the steady-state FTIR experiments. There the very narrow line shape of the SCN absorption was interpreted

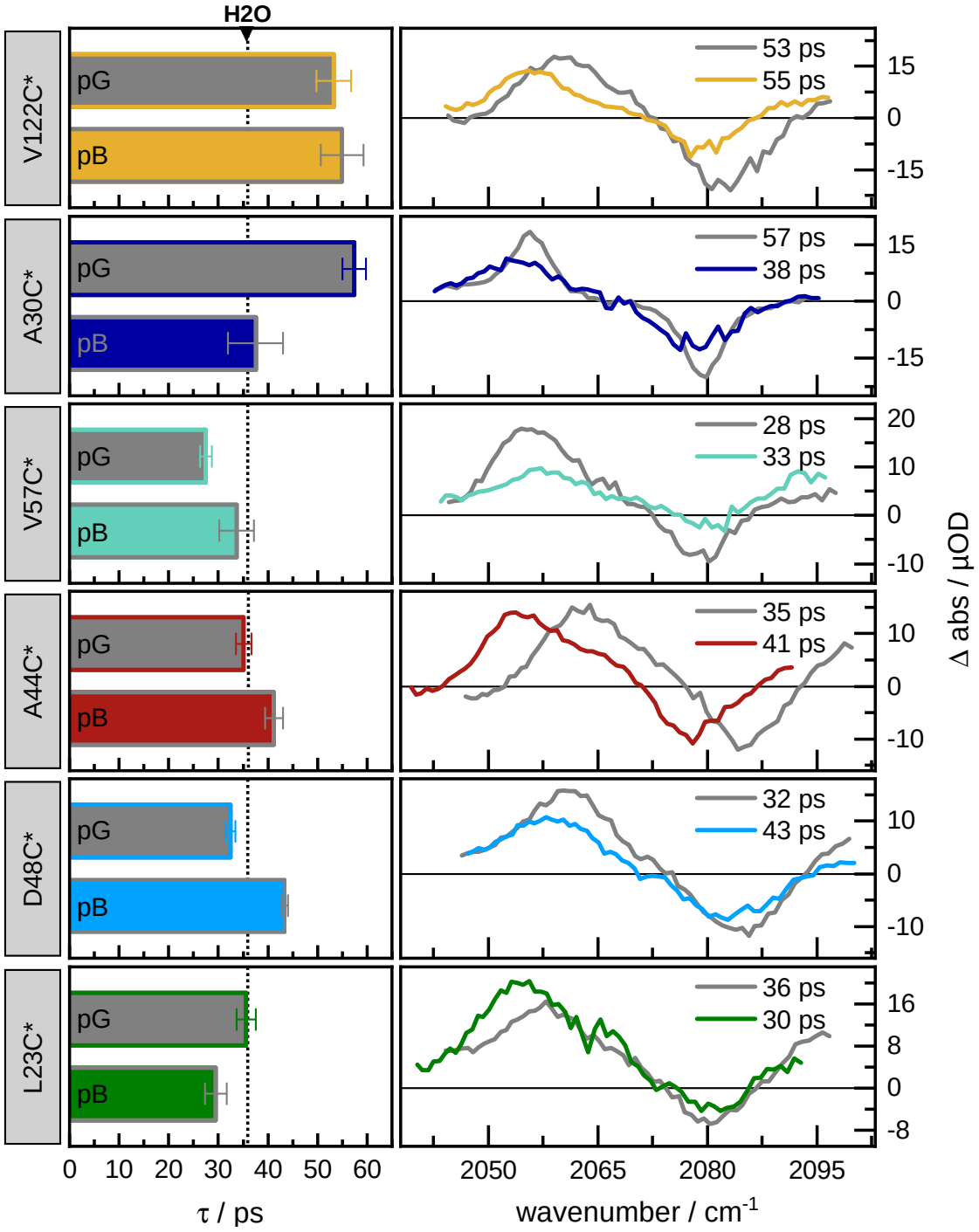

Figure 6.1: *Vibrational lifetimes of SCN at different labeling sites for pG (gray) and pB (colored corresponding to the mutant) in H_2O buffer. The bar plots (left) represent the vibrational lifetimes of SCN, the lifetime of MeSCN in H_2O is indicated by a black arrow and the dashed black line. On the right the decay-associated difference spectra of the component corresponding to the vibrational lifetime from global analysis of the IR-pump-IR-probe data are shown. The sub-ps component, the one corresponding to solvent excitation and the long lived component are omitted here, but shown in figures E.5 and E.6 in the appendix.*

as homogeneous environment provided by the interior of the protein despite the slightly blue-shifted wavenumber compared to a fully shielded label. The narrow line shape of the FTIR absorption spectrum is reflected in the decay-associated difference spectra of the vibrational lifetime of the SCN component as well.

In the pB state the lifetime of A30C* decreases drastically to 38 ps revealing the largest difference of lifetimes (Δ = 19 ps) between pG and pB for all investigated labeling positions. The lifetime in the pB state resembles the lifetime of MeSCN in the same solvent indicating a full accessibility of water molecules to the label. Therefore large structural changes of the protein can be assigned to the transition from pG to pB resulting in a solvent exposed environment for the SCN in the pB state of A30C*. However, the interpretation of the FTIR absorption spectra was contradictory. While the significant broadening of the line shape (see FTIR absorption spectra in figure 5.4 on page 62 and decay-associated difference spectra in figure 6.1 on the previous page) implied a more inhomogeneous environment due to more solvent contacts, the slightly red-shifted absorption (1.5 cm^{-1}) suggested a more shielded surrounding. The temperature-dependent FTLS measurements, as shown in figure 5.11B on page 69, revealed that there are no hydrogen bonding interactions in the pB state while featuring a slope similar to the one in the pG state. Using the vibrational lifetime as additional observable these findings can be unambiguously explained. In the pG state the SCN label of A30C* senses the solvent protected environment of the cavity that is formed by the N-terminus and the rest of the protein, but upon formation of the pB state the N-terminus moves away and water is able to penetrate into the cavity leading to a fully solvent exposed label. This is also supported by the SASA calculations that show a very low value in pG and a high value in pB. It can be concluded that the downshift that is observed for the pB spectrum is not caused by hydrogen bonding interactions towards the solvent but rather by other effects on the label.

The shortest lifetime of all mutants appears in the pG state of V57C* with the label pointing into the chromophore binding pocket. With 28 ps it is 8 ps shorter than the lifetime of the model compound MeSCN in H_2O representing the fully exposed label (see figure 6.1 on the previous page). Based on a combination of SASA calculations and FTIR experiments, especially the temperature-dependent FTLS measurements which exhibited that the SCN is engaged in strong hydrogen bonding interactions (see figure 5.11A on page 69), it was proposed that the label most likely forms a hydrogen bond to a confined water molecule inside the protein. These findings could as well explain the remarkably short lifetime of the label. This result emphasizes that the vibrational lifetime is sensitive to the kind of hydrogen bonding interaction it is involved in, distinguishing between contacts to the bulk water or to single water molecules.

In pB the lifetime of V57C* increases to 33 ps matching the lifetime of the label in a solvent exposed environment. This is in good agreement with the SASA calculations that predicted a high solvent accessibility in the pB state. Considering the spectral properties, there are only minor changes between pG and pB (see figure 5.5 on page 63 and figure 6.1 on the preceding page) including an almost negligible upshift of the SCN absorption (< 1 cm^{-1}). Taking only the spectra into account, it is hardly possible to draw any conclusion about the local structural changes sensed by the label in V57C*. The vibrational lifetime in combination with structural examination of the labeling site (*e.g.* by SASA calculations), however, allow a clear interpretation of the changes during the photocycle. While in pG the label is

buried inside the protein with only contacts to a single enclosed water molecule, it becomes solvent exposed in pB when the chromophore binding pocket collapses after the movement of the chromophore as described in literature [83, 85, 154].

Small changes of solvent contacts: A44C*, D48C* and L23C*

The SCN lifetime that is obtained for A44C* in the pG state is 35 ps as shown in figure 6.1 on page 77. This lifetime perfectly matches the lifetime of MeSCN in H_2O indicating that the label is highly exposed to the surrounding solvent in pG. Thus, the observations from the FTIR experiment are confirmed. There, one of the highest wavenumbers of all investigated SCN labels ($\tilde{\nu}_{\mathrm{mean}}$ = 2083.7 cm^{-1}, see table 5.1 on page 58 and figure 5.1 on page 59) was determined that resembled the wavenumber (corrected for the isotope shift) of the model compound MeSCN in water. The vibrational lifetime as well as the absorption spectrum endorse the conclusion that the SCN label in A44C* pG is in direct contact to the bulk water as further suggested by the high SASA value that was calculated for the pG state structure (see appendix figure C.1 on page 187).

The measurements in the pB state reveal a 6 ps longer lifetime (41 ps) compared to the pG state. The extended lifetime implies that the influence of the protein environment on the label increases. This is in good agreement with the SASA calculations that yielded a lower solvent accessibility in pB. The decay-associated difference spectra of the lifetime component from the global analysis in figure 6.1 on page 77 show that the pB spectrum is clearly downshifted compared to the pG spectrum. An analogous behavior was observed for the FTIR spectra which exhibited a red-shift of approximately 9 cm^{-1} from pG to pB for the major subpopulation (see figure 5.1 on page 59). Note here, that for the IR-pump-IR-probe experiment under constant irradiation the pump pulse (FWHM = 12 cm^{-1}) was centered at 2078 cm^{-1} and therefore excited to a large extent the major subpopulation leading to an negligible influence of the minor subpopulation on the obtained lifetime.

The interpretation of the FTIR absorption spectrum in the pB state, however, was not unambiguous. The red-shift indicated indeed a less hydrogen bonding environment, though the extent of the shift contradicted the expectations from the SASA calculations that predicted only a small decrease in solvent exposure. Accordingly the changes were attributed to be mainly caused by variations in the electrostatic environment due to the proximity to deprotonated E46 in the pB state. The temperature dependent FTLS measurements, however, revealed that the major subpopulation of A44C* pB (referred to as pB_{low} in figure 5.11 on page 69) was not engaged in any hydrogen bonding interactions which would be the case in the protein interior. Considering the vibrational lifetime, the deviation from the lifetime of MeSCN in the solvent is by far not as large as it is for labels that were found to be completely solvent protected (*e.g.* A30C* pG, V122C* pG and pB) as discussed above (compare figure 6.1 on page 77). This supports the interpretation of a label that moved in a surrounding that has a slightly decreased solvent accessibility, but the main shift of its absorption is caused by altered electrostatics.

In the pG state D48C* exhibits a lifetime of 32 ps which is a few picoseconds shorter than for MeSCN (36 ps) and A44C* pG (35 ps) as depicted in figure 6.1 on page 77. The shortened lifetime could be a sign for hydrogen bonds to other protein residues, but no such interactions were observed in the MD simulations (see table C.1 on page 188 in the

appendix). Therefore the label is most likely in contact with surrounding water molecules, supporting the conclusion obtained by investigation of the FTIR absorption spectrum that revealed a wavenumber typical for a solvent exposed SCN ($\tilde{\nu}_{sd}$ = 2084.3 cm^{-1}, see figure 5.2 on page 60).

Under constant irradiation the lifetime of the label increases by 11 ps to 43 ps and approaches the lifetimes that were observed for SCN in the protein interior. Since it is similar to the lifetime of A44C* in pB, the label most likely senses a still solvent exposed environment, but with larger influences of other parts of the protein on the SCN. The steady-state FTIR experiment showed an absorption that was red-shifted less than 1 cm^{-1} (compare figure 5.2 on page 60), also implying the movement into a less accessible surrounding, whereas the SASA calculations predicted an increased accessibility with the highest SASA value of all investigated sites (see appendix figure C.1 on page 187). In literature a partial unfolding of the α3-helix was described followed by the movement of parts of the helix, including D48, into the collapsed binding pocket [82, 154], confirming the observations of the FTIR and IR-pump-IR-probe measurements.

The lifetime of L23C* pG resembles the lifetime of MeSCN in water (both 36 ps as shown in figure 6.1 on page 77) implying an exposed label. This is contradictory to the expectations due to the known structure visible in a relatively low value for the SASA calculations. There it is suggested that L23 is protected from the solvent as it is positioned in the N-terminal region and oriented into the hydrophobic cavity that is formed with the rest of the protein [46]. Furthermore, it is pointing towards the residue of A30 whose label features a lifetime that is 21 ps longer in pG and displays the lifetime of a label buried inside the protein. However, the absorption spectrum of L23C* in the pG state was shifted to higher wavenumbers than expected for a solvent protected label (see figure 5.3 on page 61) and IMS mass spectrometry indicated that the N-terminus is already detached in the pG state due to mutation and labeling of L23 and possibly weakening or disruption of an hydrogen bond towards the protein body [91] allowing water molecules to penetrate into the cavity. This assumption is now further supported by the observed lifetime.

In pB the lifetime is 6 ps shorter than in pG, supposedly still representing a label of high water exposure. Comparison to the lifetime measured in D_2O buffer as shown in [121] confirms this interpretation since the lifetime of L23C* pB matches the lifetime of MeSCN in the D_2O, too. These observations coincide with the FTIR measurement and the SASA calculations, both predicting a solvent accessible label in the pB state. Consequently, there are only minor changes in the solvent exposure of the SCN during the photocycle.

Variations in electrostatics and solvent exposure: M100C*

For M100C* the two subpopulations, that were observed in the pG state (see figure 5.7 on page 65) and referred to as pG_{low} and pG_{high} in the following, were excited separately in the ultrafast measurements. Unfortunately, the signal size in H_2O buffer was too small to obtain reliable results for the two subpopulations, therefore the data measured in D_2O buffer are represented and discussed here.

The low wavenumber population pG_{low} of M100C* reveals a vibrational lifetime of 70 ps (shown in light gray in figure 6.2). This is by far the longest lifetime measured for all SCN labels in PYP (also compared to the other lifetimes in D_2O not discussed here, see [121]). Such a long lifetime indicates that the vibration of the SCN is not influenced by any hydrogen bonding interactions neither to water molecules nor to the protein environment. Accordingly, the FTIR experiments exhibited the lowest absorption wavenumber (2069.8 cm^{-1}, see figure 5.7 on page 65) of an SCN label incorporated into a protein observed to date. It was assumed that this extreme red-shifted absorption is caused by strong electrostatic effects of the charged amino acid R52 and the deprotonated chromophore nearby on the label that is buried in the hydrophobic binding pocket.

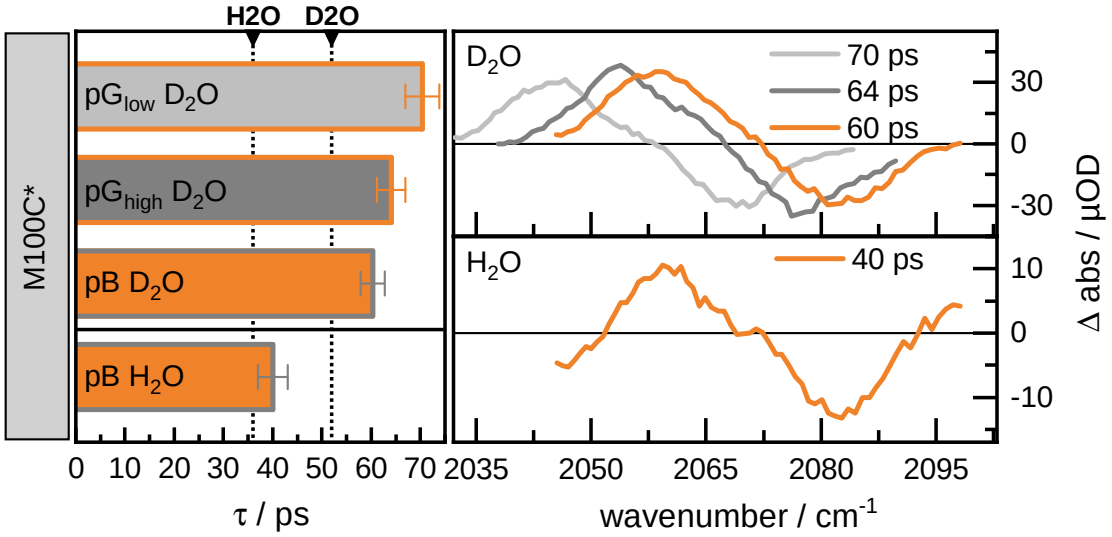

Figure 6.2: *Vibrational lifetimes of SCN in M100C* for pG_{low} (light gray, pump centered at 2068 cm^{-1}), pG_{high} (dark gray, pump centered at 2080 cm^{-1}) and pB (orange) in D_2O (top) and pB in H_2O buffer (bottom). The bar plots (left) represent the vibrational lifetimes of SCN, the lifetimes of MeSCN in D_2O and H_2O are indicated by black arrows and the dashed black lines. On the right the decay-associated difference spectra of the component corresponding to the vibrational lifetime from global analysis of the IR-pump-IR-probe data are shown.*

Although the lifetime of pG_{high} is 6 ps shorter than the one of the down-shifted subpopulation, it is still longer than the lifetimes of V122C* pG (53 ps) and pB (55 ps) and A30C* pG (57 ps) in H_2O that were found to be in a highly solvent protected environment (compare figure 6.1 on page 77). The spectral features appear at lower wavenumbers than in case for the aforementioned labeling sites as well and slightly red-shifted compared to the model compound MeSCN in THF [24, 25], which mimics the hydrogen bond free interior of a protein. In the MD simulations, the majority of hydrogen bonds that involved the SCN groups of the investigated mutants in pG and pB were found to come from water, either in a bulk-like form or from molecules trapped inside the protein. Even in the case of buried labels, the hydrogen bonds with proteins residues were a minor part of the total hydrogen bonding interactions. Only exception is M100C* in the pG state, for which the average number of hydrogen bonds towards the SCN label is slightly higher for protein residues than for water molecules (see table C.1 on page 188 in the appendix). This implies that the red-shifted absorption has to be caused by electrostatic effects. Considering the vibrational lifetime, the FTIR absorption and the SASA calculations, which predicted a low solvent

accessibility for the pG state, the conclusion that the label in M100C* in pG is located in a confined environment with no contacts to the solvent, but senses the electric fields of charged groups in close proximity, is strongly supported.

In the pB state the lifetime of the label in M100C* decreases further to 60 ps in the D_2O measurement, representing still a quite long lifetime. However, the comparison to the lifetime obtained in H_2O that is 40 ps and therefore similar to the one of MeSCN in the solvent reveals that the SCN in pB reacts noticeably to the exchange of solvents, a sign for a well exposed label. These findings are in good agreement with the FTIR study where a large blue-shift of the absorption to 2082.7 cm^{-1} (see figure 5.7 on page 65) was observed. This large shift indicated significant changes in the labels environment with variations in the electrostatics on the one hand, and accessibility for water molecules on the other. In conclusion, the SCN label in the flexible loop region encompassing the chromophore binding pocket moved from the completely water shielded interior to a highly exposed environment after the collapse of the binding pocket in pB.

6.2 Conclusion

The ultrafast IR-pump-IR-probe experiments in aqueous buffer yielded vibrational lifetimes for the SCN label at different positions in the protein in pG and pB state that spanned a range from 28 ps to 70 ps, when also taking the data of M100C* measured in D_2O into account. This broad range reflects the sensitivity of the lifetimes to the surrounding environment, especially probing solvent exposure. The comparison to the lifetime of the model compound MeSCN in the solvent, serving as measure for a fully exposed label, supported the interpretation of the water accessibility of the label and therefore of the local protein structure.

The vibrational lifetime of the thiocyanate label proved itself to be a beneficial observable in addition to the infrared absorption spectra for the examination of local structural changes during PYP's photocycle. Especially due to competing effects of polarity and hydrogen bonding interactions on the position of the SCN absorption, it is sometimes difficult to obtain unambiguous information about these changes from the steady-state FTIR experiments alone. For some labeling sites the lifetimes facilitated the interpretation obtained from the absorption spectra, for others the drawn conclusions were endorsed.

Investigation of the lifetimes revealed that the label in V122C* is buried inside the protein in both the pG and pB state and that the deviations in the SCN absorption had to be caused by changes in the electrostatic environment. In the ultrafast experiments it became clear that the thiocyanate in A30C* sensed the transition from a completely solvent shielded to a highly accessible surrounding, while this was reflected particularly by the change of the line shape and not the position of the SCN absorption in the FTIR spectra. For V57C* further evidence was found that the label is hydrogen-bonded to a confined water molecule inside the protein in the pG state, but becomes solvent exposed after the collapse of the chromophore binding pocket.

The lifetimes supported the conclusion that the labels in A44C* and D48C* in pG are fully exposed towards the solvent and loose some of the contacts to the water molecules upon formation of the pB state as the influence of the protein increases. Additionally,

the results indicated that the large red-shift of the SCN absorption in A44C* pB was not caused by remarkable changes in the solvent accessibility, but rather due to alterations of the local electric field. The observation that the SCN label in L23C* is solvent exposed in both photocycle intermediates, since the N-terminus occurs to be already detached in the pG state due to mutation and labeling, was confirmed by the ultrafast experiments. It was found that the two subpopulations of M100C* in the pG state, which exhibited the lowest wavenumbers of all SCN absorptions, revealed at the same time the longest lifetimes measured in this experiment. This showed that the label is placed in an extremely confined microenvironment in both conformations, whereas the structural changes of the hydrophobic binding pocket in the pB state led to high solvent exposure as it was predicted by the absorption spectra.

With its long vibrational lifetimes the thiocyanate also appears to be a promising label for 2D-IR experiments where spectral diffusion and chemical exchange can further support the structural investigation of local PYP dynamics.

Part IV

Kinetic Investigation of PYP's Photocycle by Time-resolved IR Spectroscopy

7 Transient Vis-Pump-IR-Probe Experiments

In this chapter the transient vis-pump-IR-probe experiments, that allowed to follow the transient photocycle species of WT-PYP (and WT', which features a M1G mutation) and its SCN-labeled mutants from the femtosecond to the millisecond timescale, are discussed. This investigation of almost the complete photocycle was enabled by combination of "mechanically" and "electronically" delayed pump pulses with respect to the probe pulses. To obtain the fast delay times from hundreds of femtoseconds up to 1 ns the pump pulse was delayed *via* a mechanical translation stage by varying the optical path length as it is widely used for time-resolved pump-probe experiments. The time resolution was only limited by the pulse length. For the electronic delays two synchronized fs-laser systems were used increasing the achievable time range up to 1 ms while providing simultaneously a high time resolution of tens of picoseconds.

To extract the main features of the large amount of data spanning nine decades in time over a broad spectral range, a combination of global analysis (GA) and lifetime density maps (LDMs) was applied facilitating the understanding of global and local changes during PYP's photocycle. The spectral region from approximately 1550 cm^{-1} to 1800 cm^{-1} (referred to as CC/CO region in the following) provides information about changes in protein (backbone) structure, the chromophore's configuration, protonation state and environment, and hydrogen bonding or protonation states of specific residues (*e.g.* E46) after photoexcitation. With the SCN label it is possible to site-specifically resolve the locations that are involved in the changes during the photocycle.

7.1 Results and Discussion

In the transient vis-pump-IR-probe experiments the laser-induced absorption difference was measured for varying delay times. The collected raw data of all samples in all spectral windows are shown in figures F.2–F.5 in the appendix as spectral slices at selected time points. To follow the actual dynamics during the photocycle, global analysis was performed on all data using a sequential model resulting in species-associated difference spectra (SADS). In figure 7.2 on page 91 the SADS for WT and WT' in the CC/CO region for mechanical and electronic delays are depicted. SADS for all investigated samples can be found in the appendix in figures F.6–F.9 for the CC/CO region and figures F.10–F.14 for the SCN region.

Additionally, LDMs were computed to obtain a comprehensive overview of spectral differences and the corresponding kinetics (see exemplarily figure 7.2 on page 91 for WT and WT'). For the LDMs the data were fitted with a quasi-continuous distribution of exponential lifetimes. Since the amplitude of the LDMs correlates with the exponential pre-factor, the LDMs indicate where *changes* occur in the measured data, but do not show a difference

signal that is continuously present without alterations. Therefore they are comparable to decay-associated difference spectra (DADS) from global analysis that result from using a simple sum-of-exponentials. All LDMs shown in this chapter were standardized by using a z-score before the analysis was performed. The standardization centers the time trace of each pixel to have a mean value of zero and a standard deviation of one. This is necessary to suppress unwanted oscillations (alternating pattern of positive and negative features), which complicate the interpretation of the LDMs due to additional artifacts. Unfortunately, the standardization shifts the features at the end of the measurement range to earlier lifetimes. These shifts seem though to occur uniformly for all pixels in such a way that the values, especially in the hundreds of microseconds range of the electronically delayed data, cannot be taken unquestionably as actual lifetimes, but still allow a qualitative comparison for the appearance of different features with respect to each other. The LDMs calculated without previous standardization are shown in figures F.28–F.34 in the appendix.

Due to the small signal size of the SCN vibration, a pixel-dependent spike-like structure is observed in the data[1], which could effectively be corrected by taking a three point moving mean of the raw spectra. This filter method is found to neither influence the time-dependent dynamics nor the interpretation of the data. Hence, only the denoised data are shown here to simplify the examination of the SCN signals. A comparison of raw and denoised data is given in figures F.10–F.14 in the appendix.

Contour plots of the SCN data provide an overview over the evolution of the SCN signals over all timescales for all labeled mutants as depicted in figures 7.6–7.10. In the same figures the SADS resulting from global analysis of the denoised data are shown above and below for the corresponding time ranges. The LDMs of the SCN region allow insight into the response of the label to changes in its environment in the course of the photocycle. In reality these LDMs are superimposed on large baseline dynamics caused by a broad water absorption band which changes continuously during the time span of the experiment. For a better visibility of the small SCN signals, the water dynamics were suppressed by subtracting a linear baseline between the first and the last pixel for each time point. Following the baseline shifts allows conclusions on the dynamics of water heating. Besides, these dynamics also appear as broad featureless baseline dynamics in several SADS resulting from a global analysis. Altogether the analysis with both methods provides a consistent interpretation with the SCN features observed in the LDMs fairly matching the globally fitted lifetimes and their associated spectral changes.

7.1.1 Photocycle Intermediates

Upon excitation with blue light PYP enters a photocycle with a manifold of intermediates evolving on a broad range of timescales (see figure 7.1 on the facing page) [20, 50, 60]. The electronically excited state pG* is formed hundreds of femtoseconds after photon absorption accompanied by weakening of hydrogen bonds in the surrounding of the chromophore facilitating its *trans-cis*-isomerization on a picosecond timescale [9, 12–14, 62]. If the hydrogen bond between the chromophore and the protein backbone is broken during

[1] This structure is possibly caused by slightly different responsivities and/or by interference within the half-wave plate that is used to attenuate the reference beam.

isomerization, intermediate I_0 is formed and PYP successfully enters the photocycle [12, 14, 93, 169]. Otherwise the so called ground state intermediate (GSI) appears from which the protein directly decays into its dark state in about 6 ps [14].

Following the isomerization of the chromophore, fast relaxation processes in the nearby protein structure are controversially discussed to lead to formation of intermediate $I_0^{\ddagger}$ in 220 ps [8, 13, 62, 87]. Less controversial is the relaxation of the chromophore itself and the surrounding hydrogen bonding network on an early nanosecond timescale in the form of intermediate pR [8, 12, 14, 62, 68–70]. Several studies suggest the existence of two substates of pR (pR_1 and pR_2) which differ either in protein conformation far away from the chromophore or in the hydrogen bonding state of the chromophore. Independent from the interpretation of the structural differences between the two states, their dynamics are observed in the microsecond range [5, 70, 73–75, 89–92, 170].

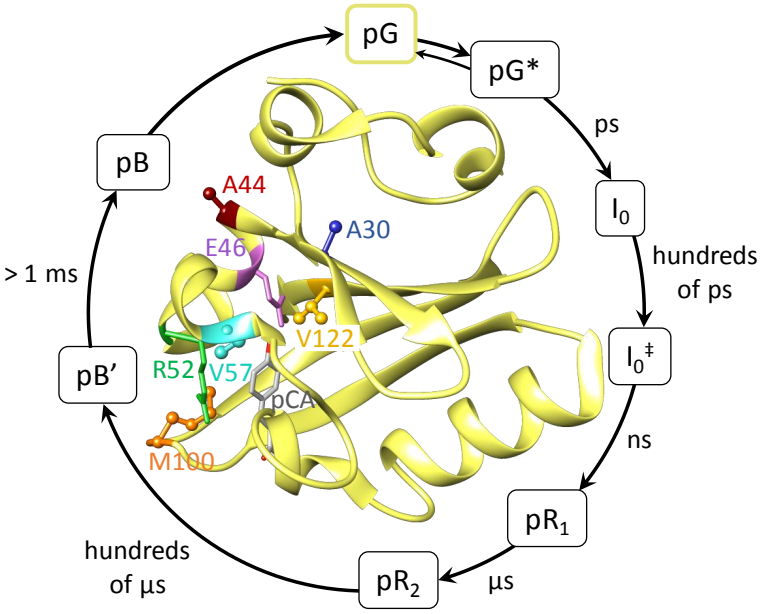

Figure 7.1: *Photocycle model and pG structure (pdb: 1NWZ) of PYP for the intermediates and locations investigated in the transient vis-pump-IR-probe experiments. The timescales given for the photocycle transitions were proposed in previous studies. In the pG structure the residues A30 (blue), A44 (red), V57 (cyan), M100 (orange), and V122 (dark yellow), at which the SCN labels were introduced, and the residues E46 (purple) and R52 (green), which play a crucial role during the photocycle, are highlighted. The pCA chromophore is shown in gray and red.*

One of the most crucial events during the photocycle is the protonation of the chromophore in hundreds of microseconds, although it is not unambiguously solved yet whether the proton is donated by the nearby E46 or by water molecules that are able to penetrate the chromophore binding pocket. Anyway, in the pB' state the chromophore is protonated and E46 deprotonated triggering large conformational changes of the protein and formation of the signaling state pB on a millisecond timescale [4, 5, 10, 11, 74, 93]. Afterwards, the long-living signaling state recovers to the dark state with a decay time of about hundreds of ms to one second, meanwhile the chromophore becomes deprotonated again and re-isomerizes to the *trans*-configuration [4, 5, 70, 72–75, 85].

To analyze the photocycle transitions measured in the transient laser experiments, close inspection of the data and comparison to the literature assignments are carried out. However, especially the CC/CO region is crowded - even in the LDMs - due to overlapping contributions originating from vibrations of the chromophore and the protein backbone. For simplification, prominent features in the LDMs were marked with squares and an overview for WT-PYP, WT' and all labeled mutants in all investigated spectral windows is given in figure 7.4 on page 105. It is striking to observe narrow horizontal lines in the protein CC/CO window and a similar pattern in the other windows that can be assigned to the transitions of the photocycle. Since the features in the amide I region are comparable regardless of the mutation, this indicates that the formation of the different photocycle intermediates is not influenced to a large extent by exchange of the amino acids and labeling.

The lifetimes obtained by global analysis and the lifetimes of the prominent features in the LDMs, that are also indicated by the dashed yellow lines in the LDMs for WT and WT' in figure 7.2 on the facing page, match the transitions described in literature remarkably well. The intermediates are discussed in detail for the WT and compared to WT' in the following. Later on the SCN data are described with help of the WT assignments.

Early photocycle transitions

The spectral window investigated in the laser experiments was limited to the region between 1555 cm^{-1} and 1800 cm^{-1} lacking several marker bands of PYP's vibrational spectrum that appear down to 950 cm^{-1}. Nevertheless, it was possible to assign the observed decays in the picosecond to nanosecond time range, obtained from global analysis and LDMs, to the early transitions of the photocycle known from literature. These transitions on a very fast timescale were studied in the infrared by Groot *et al.* [12], Heyne *et al.* [13] and van Wilderen *et al.* [14] *via* transient laser experiments and changes regarding the chromophore were studied by resonance Raman spectroscopy by Unno *et al.* [90, 169] and Zhou *et al.* [88]. Additionally, there are several studies probing the visible dynamics on the fast timescale [8, 9, 61, 87, 171].

Although the first transition after photon uptake resulting in the formation of the excited state pG* lay within the instrument response of the mechanical delay experiment (approximately 600 fs), the vibrational spectrum typical for the pG* intermediate could be recorded. It is characterized by a large upshift of E46's COOD group from 1725 cm^{-1} to 1745 cm^{-1} due to the weakening of the hydrogen bond between the glutamate and the phenolate ring of the chromophore [13]. Especially in the GA of the WT and WT' data (see figure 7.2 on the next page) these features are prominent, since the sub-ps component shows an instantaneous bleach at 1725 cm^{-1} and an induced absorption at 1745 cm^{-1}. Further, the C=C stretch vibration of the chromophore at 1621 cm^{-1} (positiv band) and C=O stretch vibration at 1660 cm^{-1} (negative band) are typical for the infrared difference spectrum of the pG* state [12] being also visible in the SADS of the sub-ps component.

However, the dynamics of the excited state are complex as only part of the excited molecules (20 - 60 % depending on the investigation method) enters the photocycle successfully, while the rest directly returns to the dark state. Therefore the kinetics are described with multiple decay times in literature [9, 12, 13, 61, 62, 87, 171]. Larsen *et al.* [62] suggested three lifetimes for the pG* decay in pump-dump-probe experiments of 600 fs, 2.8 ps and 40 ps,

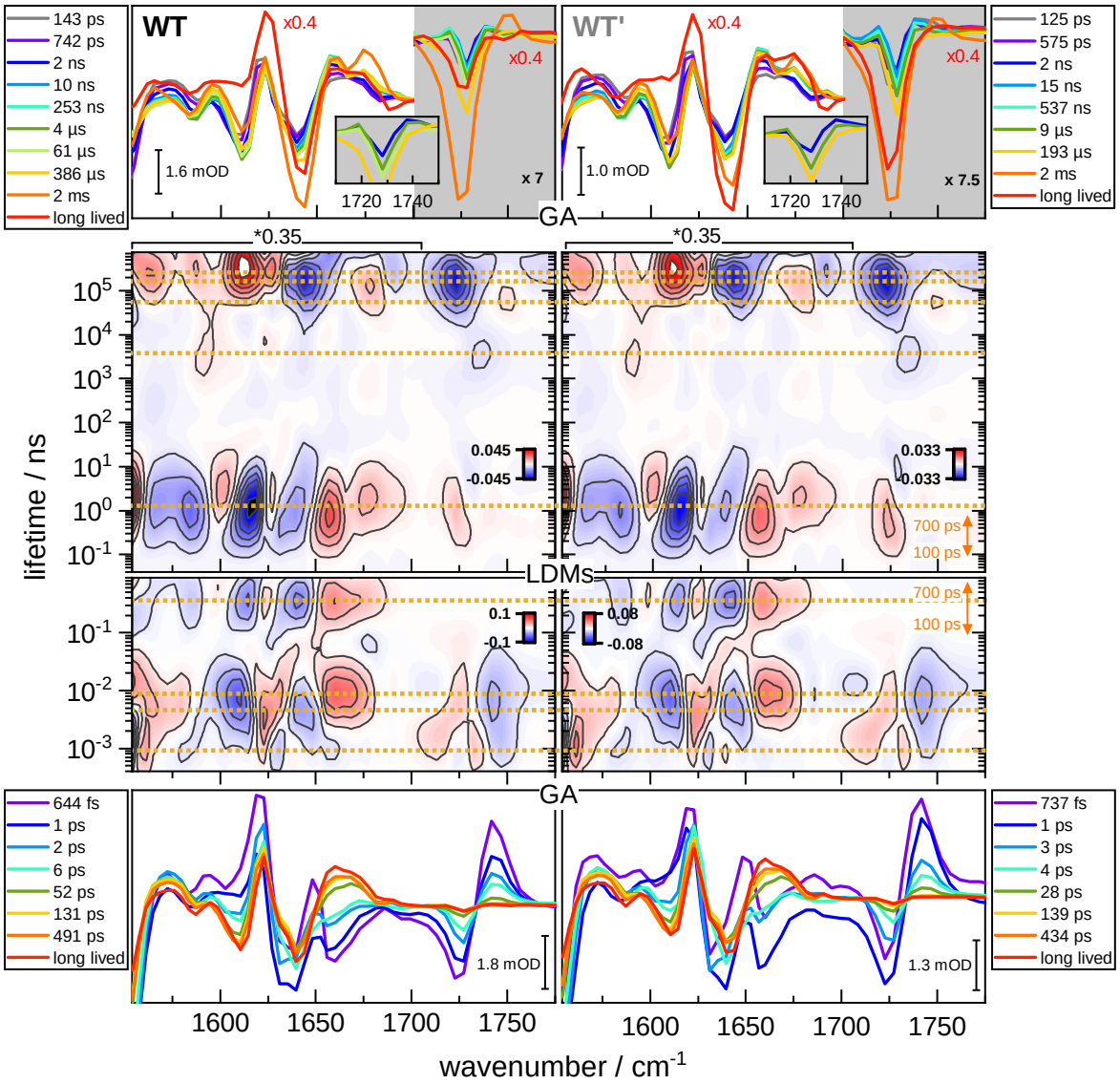

Figure 7.2: *Comparison of SADS from global analysis (GA, first and fourth row) and LDMs (second and third row) for WT (left) and WT′ (right) in the CC/CO region for mechanical (lower two rows) and electronic delays (top two rows). For the SADS only components > 600 fs for mechanical delay data (bottom) and > 50 ps for electronic delay data (top) are shown. In the electronic delay spectra the long lived component is scaled with a factor 0.4 for WT and WT′ and the ordinates for the CO regions of E46 (from 1700 cm^{-1} to 1775 cm^{-1}, shaded in gray) are enlarged by a factor of 7 for WT and 7.5 for WT′ for better visualization. The insets show a zoom into the CO region of E46 with a reduced number of spectra (only 2 ns, 4 µs, 61 µs, and 386 µs for WT and 2 ns, 9 µs, and 193 µs for WT′). All LDMs are plotted with 11 major and 5 minor contour levels. The corresponding L-curves are depicted in figure F.36 in the appendix. The orange arrows display the same time window. For better visualization the intensity of the amide I region in the electronic delay plots is scaled by a factor of 0.35. Yellow dashed lines at 900 fs, 4 ps, 8 ps, 350 ps (mechanical delays) / 1 ns, 4 µs, 60 µs, 170 µs, and 260 µs (electronic delays) highlight prominent features in the LDMs appearing in both samples.*

with the longest one only occurring to a very small extent. In transient vis-pump-IR-probe experiments Groot *et al.* [12] described biexponential kinetics of 2 ps and 9 ps for the decay of pG*. An explanation for these complicated dynamics is given by Heyne *et al.* [13],

who suggested that the multiple time constants not necessarily originate from multiexponential decays of the excited state, but might also emerge from intramolecular vibrational redistribution or vibrational cooling processes of "hot" dark and I_0 states.

In good agreement with the observation of multiple decays for pG* in literature, the GA reveals four components in the sub- and early picosecond time range with 644 fs, 1 ps, 2 ps and 6 ps for WT-PYP (737 fs, 1 ps, 3 ps and 4 ps for WT'). The species-associated difference spectra derived for the first two components differ mainly in the intensity, but show similar spectral features implying that they correspond to different decay times of the excited state. The most obvious differences of the spectrum at 6 ps (4 ps; cyan in figure 7.2) compared to the two earliest ones (purple and dark blue) are an ingrowing negative feature at 1610 cm^{-1}, an upshift and narrowing of the bleached absorption from 1635 cm^{-1} to 1639 cm^{-1}, the vanishing of the depleted absorption around 1660 cm^{-1} and a proceeding disappearance of the difference signal above 1700 cm^{-1}. The 2 ps (3 ps; light blue) component seems to be a mixture of the early spectra and the 6 ps (4 ps) component resembling the early spectra in the negative band around 1635 cm^{-1}, whereas the other aforementioned features are more similar to the following spectrum.

Intermediate I_0 is assumed to form in a few ps when the pCA chromophore isomerizes from *trans*- to *cis*-configuration [12–14, 62]. Since the strength of the hydrogen bond between E46 and chromophore recovers after isomerization, this transition is accompanied by the disappearance of the COOD signal of E46 [13]. A typical marker mode for the chromophore in *trans*-configuration is the C=C stretch vibration at 1607 cm^{-1}. With the chromophore in *cis*-configuration the absorption at this position decreases significantly resulting in a prominent bleach. Additionally, the C=O vibration of the chromophore upshifts from about 1640 cm^{-1} to 1663 cm^{-1} when the hydrogen bond between the chromophore's C=O group and C69 is broken [12, 93, 169]. The disappearance of the E46 C=O vibration, the bleaching of the *trans*-marker band at 1607 cm^{-1} and especially the upshifted absorption at 1663 cm^{-1} are observed in the SADS from global analysis corresponding to delay times of 52 ps, 131 ps and 491 ps in the mechanically delayed data for the WT (28 ps, 139 ps and 434 ps for WT') and 143 ps, 742 ps and 2 ns in the electronically delayed data (125 ps, 575 ps and 2 ns for WT'). They all match the typical spectra observed in literature for intermediate I_0 [12, 14] and are nearly indistinguishable except for very small intensity changes.

In literature a ground state intermediate (GSI) is proposed which forms simultaneously with I_0 from pG* and also exhibits an isomerized chromophore, but since the hydrogen bond between the carbonyl and C69 stays intact, PYP is not able to enter the photocycle, instead the chromophore re-isomerizes and the protein was found to decay back to the dark state in several picoseconds [14, 62]. Since the component in figure 7.2 that decays with 6 ps (4 ps) shows similar spectral features as the I_0 spectrum, except for a missing induced absorption around 1663 cm^{-1}, which arises from the breaking of the aforementioned hydrogen bond, it is tempting to attribute it to the GSI. However, van Wilderen *et al.* [14] applied a target analysis on their data with a parallel decay of pG* to both GSI and I_0, the latter further decaying to pR, while the data presented here were analyzed with a sequential model. Thus, the obtained spectra are not directly comparable. For this reason it cannot clearly be resolved whether the deviating spectral features arise due to the different applied models or because the 6 ps (4 ps) component from the sequential model does not describe the decay of the GSI. Differences are observed mainly around 1640 cm^{-1}, where the

target analysis exhibits a positive feature for the spectrum assigned to the GSI, and a bleach in the I_0 spectrum due to the upshifted absorption of the chromophore C=O, while the latter is already present for the SADS of the 6 ps (4 ps) component shown here, and around 1660 cm^{-1}, where a broad negative band similar to the one observed for pG* is obtained by target analysis, but not present in the sequential model. To describe such branched dynamics and unambiguously resolve the existence of the GSI, it would be necessary to perform a target analysis of the data presented here, as well.

The early changes of spectral features can be also observed in the LDMs of the mechanical delay experiments in figure 7.2 on page 91 highlighted by yellow dashed lines at lifetimes of 900 fs, 4 ps and 8 ps. In contrast to the global analysis spectra, that were discussed before, the LDMs represent a parallel model and all pixels are analyzed independently. Moreover, it has to be noted that the sign of the LDM features is reversed with respect to the one obtained originally from LDA, now resulting in negative features for decreasing intensities (*e.g.* increasing bleach or vanishing positive band) and positive features for increasing intensities. The earliest features (matching the 1 ps component in the GA) appear at 1629 cm^{-1}, corresponding to the in-growing bleached absorption, and in the C=O region of E46. At 4 ps further decay of the C=O vibration of E46 occurs and in the CC region a positive feature at 1624 cm^{-1} indicates an increasing induced absorption of the C=C vibration of the chromophore, while the negative feature at 1643 cm^{-1} can be assigned to changes of the chromophore's C=O vibration. For a lifetime of 8 ps mainly the disappearence of the *trans*-marker band of pCA at 1607 cm^{-1} (negative feature) and the upshift of the chromophore's C=O vibration at 1664 cm^{-1} (positive feature), that occurs when the hydrogen bond towards C69 is broken, arise, implying that the chromophore isomerizes on this timescale and intermediate I_0 is formed. Additionally, the hydrogen bond between chromophore and E46 recovers its strength, depicted by the red (1726 cm^{-1}) and blue (1742 cm^{-1}) features at 8 ps, which indicate the vanishing of the C=O vibration of E46. In the LDMs no unambiguous evidence for the existence of the GSI is found. It needs to be mentioned that no clear GSI markers were identified in the DADS from GA with a parallel model by van Wilderen *et al.* [14] either, but they only became evident after applying the target model. The LDMs here are thus in principle consistent with the DADS shown in [14]. This leads to the conclusion that the early ps-components indeed arise from relaxation processes of the electronically excited state. While it is not possible to distinguish whether the faster dynamics correspond to the relaxation to pG or arise from different decay times towards the I_0 state, the latest of the ps-features in the LDMs can clearly be assigned to the formation of I_0.

For the decay of I_0 mainly two transitions are described in previous studies. Either intermediate I_0 decays directly into pR on a nanosecond timescale (700 ps [14], 0.9 - 1 ns [12], 1.5 ns [62]) or the still debated intermediate $I_0^{\ddagger}$ is formed in 220 ps [8, 87] before decaying to pR (in 3 ns [8]). To identify the transitions that are really related to the decay of I_0, the global analysis data are compared to the corresponding LDMs. Here the number of decays, at which spectral changes occur, is reduced and prominent features are only observed at one lifetime in the fs-to-ns LDMs (350 ps) and one lifetime in the ps-to-ms LDMs (1 ns) for the time range in question. It is striking to see that the observed features for mechanical and electronic delays in the investigated time ranges that overlap between 50 ps and 860 ps do not show similar lifetimes in both experiments as it would be expected. The electronic delays are lacking the 350 ps component that appears in the LDMs of the mechanical delays. Comparing the features from both experiments, it occurs that the features at 350 ps

(mechanical delays) are identical to the ones at 1 ns (electronic delays). One reason could be that the features at 350 ps are at the limit of the achievable time range of the mechanical delay experiment and therefore fitting with the exponential lifetimes could be erroneous. As mentioned before, standardization of the data before calculation of the LDMs was observed to shift the features at the end of the measured time range to faster lifetimes. Comparison with the not-standardized LDMs (see figure F.28 on page 228 in the appendix) reveals, though, that in this case the same features appear likewise at hundreds of picoseconds for mechanical delays and at a few nanoseconds for electronic delays. However, when relying on the electronic delays for lifetimes slower than 100 ps, the only features appear on the ns timescale giving no indication for the formation of the $I_0^‡$ intermediate in the LDMs.

This is in good agreement with transient IR measurements and pump-dump-probe experiments, in which no hint was found for the existence of the $I_0^‡$ intermediate so far [13, 62]. However, after its observation in time-resolved UV/vis experiments, the $I_0 \rightarrow I_0^‡$ transition was assigned to relaxation processes of the protein in the vicinity of the chromophore [8, 87]. Heyne *et al.* [13] suggested that the appearance in UV/vis but not in IR spectroscopy might be due to changes that arise from alterations of amino acids in the binding pocket that are not involved in hydrogen bonding interactions and therefore the changes in the vibrational spectrum are negligible. When comparing the SADS from GA for 131 ps (yellow in figure 7.2 on page 91 and the long lived spectrum (red) of the mechanical delays and for 143 ps (gray) and 2 ns (dark blue) of the electronic delays, which would match the expected lifetime for $I_0^‡$ formation, only small spectral changes are observed (for easier comparison see also figure F.6 and figure F.8 in the appendix). The most obvious one is the increased absorption of the chromophore C=O at 1660 cm^{-1}, while the higher wavenumber part of the broad absorption band stays unchanged. The increased absorption of the C=O might be the result of two slightly different C=O conformations absorbing at 1659 cm^{-1} and 1672 cm^{-1}, as suggested by pH-dependent Raman experiments, with the lower wavenumber population featuring only one intact hydrogen bond between chromophore and the nearby Y42, while in the other population it is additionally H-bonded towards E46 [90]. The two populations are discussed in more detail when having a closer look at the pR states in section 7.1.1 on the next page. Further changes appear for the chromophore's C=C stretch vibration resulting in a slightly narrowed positive band at 1621 cm^{-1} and a reduced absorption of the phenolate ring mode around 1575 cm^{-1}.

Formation of pR occurs in about 1 - 3 ns, when the chromophore structure and the surrounding hydrogen bonding network relax, no matter if it emerges directly from I_0 or *via* intermediate $I_0^‡$. With respect to the I_0 spectrum, the negative feature of the chromophore's C=O mode at about 1635 - 1640 cm^{-1} is described to become narrower and to upshift a little, whereas the induced absorption at 1666 cm^{-1} increases further [12, 90, 93]. Moreover, the absorption of the phenolate ring mode at 1580 cm^{-1}, that originated from charge translocation of the phenolic oxygen over the chromophore upon excitation [12, 14], decreases. In the LDMs many features can be seen in the protein CC/CO region at a lifetime of 1 ns (highlighted by a yellow dashed line in figure 7.2) corresponding to changes in the phenolate ring modes and the chromophore's C=C and C=O stretch vibrations. The SADS from global analysis are almost indistinguishable for decay times of 10 ns, 253 ns, 4 µs and 61 µs for the WT (15 ns, 537 ns and 9 µs for WT'). Most likely, multiple components are needed to fit the data properly due to some underlying water dynamics. To have a closer

look into the spectral changes during the transition from $I_0/I_0^{\ddagger}$ to pR the SADS at 2 ns(dark blue in figure 7.2) was compared to the later ones corresponding to the pR intermediate. Here a further increase in absorption of the low wavenumber component (1659 cm^{-1}) of the chromophore's C=O can be observed and also the absorption of the higher wavenumber component (1676 cm^{-1}) increases, resulting in two slightly separated bands. Additionally, the phenolate ring mode at 1575 cm^{-1} nearly vanishes as predicted in literature. Note that intensity changes between the two intermediates are relatively small. The narrowing and small upshift of the bleach, assigned to the chromophore's carbonyl, from 1635 cm^{-1} to 1639 cm^{-1}, that occurs in the SADS shown in [12], is not observed in the $I_0 \rightarrow I_0^{\ddagger} \rightarrow$ pR transition, but seems to appear already on an early picosecond timescale as it can be seen in the mechanical delay spectra. However, the intensity of the bleach increases a bit in the transition to the pR state. Additionally, a small increase in the bleach of the E46 carboxyl at 1728 cm^{-1} can be observed (see insets in the plots of GA spectra in figure 7.2 on page 91), that might result from changes in the strength of the hydrogen bond between the glutamate and the chromophore.

So far the small band shift from 1587 cm^{-1} to 1595 cm^{-1} that becomes already visible on a picosecond timescale and significantly increases for longer delay times (> 2 ns) was not discussed. In other infrared studies, that were mostly performed in H_2O, this feature was not present, but instead a similar upshift of 8 cm^{-1} was found from 1685 cm^{-1} to 1693 cm^{-1}, which is missing in the D_2O data shown here. This band shift was assigned to the C=N stretch vibration of R52 [12, 172]. Deuteration seems to shift this difference feature dramatically to lower wavenumbers, consistent with the observations found for a deuterated guanidine group [173, 174]. Further, the temporal dynamics that were observed in D_2O for the difference feature, were also detected in the same laser experiments performed in H_2O for the feature around 1690 cm^{-1} (data not shown here, but see comparison between D_2O and H_2O data in section 7.1.5 on page 134). The small difference signal at early times was associated to changes of the electron distribution or polarization of the chromophore [12, 172]. The large increase of the signal proceeding the formation of pR on a nanosecond timescale (with its maximum from µs to ms) was explained by the movement of the R52 residue, which is known to shield the chromophore in the hydrophobic binding pocket from contacts with the solvent in the dark state [82, 172]. The motion leads to an exposed chromophore allowing for proton absorption from the solvent as it will be discussed in more detail for the pR $\rightarrow$ pB' transition.

Overall, the early transitions in PYP's photocycle and their time constants observed in the transient vis-pump-IR-probe experiments are in good agreement with those identified in previous studies.

Multiple pR states

The pR state, that is formed in about 2 ns after photoexcitation, is characterized by a still deprotonated *cis*-isomerized chromophore. In many studies evidence for the existence of a mixture of (two) sub-states for the pR intermediate was found [5, 70, 73–75, 89–92, 170]. However, the structural differences leading to the various sub-states are still debated. The absence of a signal that could be assigned to a second pR state in the transient visible absorption measurements was interpreted by conformational relaxation processes of the

protein distant from the chromophore and thus not contributing to the electronic spectrum [73, 74, 92]. Resonance Raman studies and time-resolved X-ray solution scattering and crystallography indicated that changes in the hydrogen bonding network from the chromophore to nearby amino acids cause the differences between the two sub-states [70, 75, 90]. A third interpretation suggested changes in the interactions of the chromophore with aromatic or charged residues in the hydrophobic binding pocket as possible reason [89]. All experiments had in common that a kinetic component in the short microsecond time range was observed giving evidence for a second pR species (1.3 µs [73], 2 µs [74], 5/10 µs [89], 10 µs [75], 30 µs [70], 2 µs (mutant E46Q) [91], and 3.1 µs (mutant E46Q) [92]). It is still ambiguous, though, if the pR states are formed simultaneously before decaying to pB' on different timescales [68, 70, 75, 90] or if it is a sequential transition $pR_1 \rightarrow pR_2 \rightarrow pB'$ with the first pR state converting into the second one before the chromophore gets protonated [73, 75, 92, 170]. From the presented data no conclusions can be drawn at this point.

Time-resolved solution scattering [75] and crystallography [70] favored the model describing a parallel formation of pR_1 and pR_2 on a nanosecond timescale. In both studies one species (pR_2) with two intact hydrogen bonds of the chromophore towards E46 and Y42 similar to the dark state was observed, while in the second species (pR_1) the hydrogen bond towards E46 was broken and only the one with Y42 remained. Later on in the pB' (and pB) intermediate both hydrogen bonds are broken. Thus, Kim *et al.* [75] found the parallel model more realistic since the sequential model, although fitting their data just as well as the parallel one, would involve alternating breaking and formation of the aforementioned hydrogen bonds and they found in addition that the orientation of the phenolic ring in pR_1 resembles the one in pB', whereas it is twisted in pR_2. Hence, the observed 10 µs component (30 µs for [70]) was assigned to the $pR_1 \rightarrow pB'$ transition in the parallel model (the time constant for $pR_2 \rightarrow pB'$ is approximately 10 times slower). Due to the similar chromophore orientation and hydrogen bonding network in both pR_1 and pB', they stated that this transition is likely to cause only small signals in the transient visible absorption and infrared measurements explaining why no short microsecond component was detected with those methods so far. However, in both studies no remarks were made concerning the proton transfer process during this transition, which is known to accompany the formation of pB'. In MD simulations [175] and a time-resolved resonance Raman study [93] only evidence for one pR conformation was found with two intact hydrogen bonds towards Y42 and E46 similar to the structure of the previously discussed pR_2 state [175].

Further resonance Raman experiments in combination with DFT calculations [90], on the other hand, supported the structural interpretation for the two pR states. In a pH-dependent study, two different structures with slightly different chromophore C=O conformations were identified. The low wavenumber population (absorption band at 1655 cm^{-1}) is stated to lack the hydrogen bond between the chromophore and E46 (like pR_1) and is suggested to be an "active structure" that promotes the protonation of the chromophore, whereas the high wavenumber population (absorption band at 1672 cm^{-1}) should contain two intact hydrogen bonds towards Y42 and E46 (like pR_2) and was interpreted as a direct photointermediate from the dark state.

The µs-dynamics were first discovered by measuring volume and enthalpy changes with transient grating spectroscopy [73]. Since the structural changes of and around the chromophore are completed within several ns creating the pR state (pR_1), as observed in pre-

vious experiments, these dynamics were attributed to other protein parts far from the chromophore, which were still moving and forming the second pR state pR_2, that finally evolves to intermediate pB'. In contrast to the studies discussed before, here a sequential model for formation of the two sub-states was applied. The structure changes distant from the chromophore seem to explain the lack of indications for the pR_2 intermediate in light absorption techniques quite well, since the visible absorption is dependent on alterations of the chromophore structure or its direct microenvironment [5, 8, 9] and the infrared absorption might be influenced only to a small extent, which would cause only tiny intensity changes in the amide I region, that are hardly detectable [10, 11]. However, Hendriks *et al.* [74] were able to measure the $pR_1 \rightarrow pR_2$ transition with visible absorption techniques (laser-flash photolysis), although the absorption spectra of both states are very similar and only differ in their extinction coefficient. Nevertheless, the lifetime observed for this transition (2 µs) is in good agreement with the ones from the transient grating experiments.

In the ps-to-ms LDMs of WT and WT' (see figure 7.2 on page 91) for the experiments performed in this thesis, two rather small features appear at a lifetime of about 4 µs as highlighted by a yellow dashed line. One arises at 1592 cm^{-1} and was previously assigned to changes in the C=N vibration of R52. The other one, which is even smaller since the intensities below 1705 cm^{-1} were scaled by a factor of 0.35, occurs in the CO region of E46 at 1736 cm^{-1} associated with changes of the C=O vibration of the glutamate. Also in the GA a component of 4 µs (9 µs for WT') is found (dark green SADS in figure 7.2). There are additional spectra with decay times of 10 ns and 253 ns (15 ns and 537 ns for WT') that are spectrally almost indistinguishable from the µs-spectrum and therefore assigned to dynamics of the solvent. Note here that to properly fit the dynamics following the fast µs-decay for the WT data two components of 61 µs and 386 µs were necessary whereas the WT' data were fitted with one single component of 193 µs that lay in between the components obtained for the WT. As the LDMs look very similar for WT and WT' in this time range, it is assumed that the dynamics of both proteins are similar. A detailed comparison between WT and WT' dynamics is given in section 7.1.2 on page 104. For investigation of the transition on the µs timescale the spectrum with a decay time of 4 µs/9 µs (dark green SADS), that was assigned to pR before (corresponding to pR_1 in a sequential model), is compared with the spectrum decaying in 386 µs/193 µs (yellow SADS) that would correspond to intermediate pR_2.

In good agreement with the ps-to-ms LDMs, global analysis shows only minimal changes in the amide I region. More obvious are the intensity changes in the CO region, with the bleach of the E46 carboxyl increasing and the small positive shoulder at the high wavenumber flank of the bleach at 1741 cm^{-1} disappearing (see insets in the plots of GA spectra in figure 7.2) corresponding to the small negative feature observed in the LDMs. The increase of the C=O bleach might be due to alterations in the hydrogen bonding strength or beginning changes of the deprotonation state of E46. The positive shoulder is most likely a remnant of the upshifted absorption that appeared directly after photoexcitation in pG*. This shift of the C=O frequency of E46 from 1725 cm^{-1} to higher wavenumbers (1745 cm^{-1}) was caused by the weakening of the hydrogen bond of the COOD group with the phenolate ring of the chromophore, either due to a small increase in the distance between E46 and chromophore or partial localization of the glutamates proton closer to the phenolic oxygen. In the following transition to the I_0 intermediate the difference signal was observed to decrease quickly as the strength of the hydrogen bond recovered [12, 13]. Indeed, in

literature the positive peak seems to have vanished after tens of picoseconds [13] and is not present in the spectra corresponding to later photocycle intermediates [12]. The GA of the fs-to-ns data shows as well that the induced absorption decreases quickly on a tens of picoseconds timescale to an intensity approximately one order of magnitude smaller than in the spectrum assigned to the pG* state (see purple SADS in the fs-to-ns GA plot in figure 7.2), but afterwards the signal persists with almost unchanged intensity until it finally disappears in several microseconds as it can be seen in the ps-to-ms data. Additionally, a small increase of the positive band at 1596 cm^{-1} is observed, coinciding with the positive feature in the LDMs at about 4 µs and previously assigned to the movement of R52, which opens the gateway between chromophore binding pocket and the solvent [82, 172], as already discussed for the nanosecond timescale.

It cannot be solved yet, whether the increase of the E46 C=O bleach and vanishing of its positive shoulder result from alterations of the protonation state of the glutamate or from changes in the hydrogen bonding strength. The latter would argue against the interpretation that the microsecond component represents the $pR_1 \rightarrow pB'$ transition since the involvement of proton transfer steps are crucial for formation of pB'. No evidence for protonation of the chromophore in this time range was found, though, that would lead to an increase of the absorption band at 1565 cm^{-1}, which was identified as marker band for chromophore protonation [58]. Instead the assignment of an increasing hydrogen bonding strength and the possibility of an associated reduction of the distance between E46 and the chromophore would favor a consecutive course of events, where first pR_1 is formed in several nanoseconds after isomerization of the chromophore and then the slight movement of the glutamate in several microseconds leads to formation of the intermediate state pR_2, which prepares the proton transfer to the chromophore on a hundreds of microseconds timescale in the transition to pB'.

The two conformations of the C=O stretch vibration of the chromophore at 1656 cm^{-1} and 1674 cm^{-1}, that were assigned to the two pR states differing in their hydrogen bonding pattern with one or two intact hydrogen bonds from the chromophore towards nearby residues (Y42 and E46) [90], do not change during the microsecond decay (no obvious difference between the dark green (4 µs/9 µs) and the yellow SADS (386 µs/193 µs) in this spectral region, see figure 7.2). They rather appeared already within the 2 ns lifetime of the $I_0 \rightarrow pR$ transition (from the dark blue spectrum (2 ns) to later SADS), which might indicate a simultaneous formation of both pR states as suggested by the parallel model in several studies [68, 70, 75, 90]. In this case the changes in the CO region on the microsecond timescale (see insets in the plots of the GA spectra and the negative feature in the LDMs at about 4 µs), that possibly arise from deprotonation of E46, might correspond to a fast proton transfer from E46 to the phenolate of the chromophore as it could occur in the transition from pR_1 to pB' (10 µs or 30 µs assigned to this transition by [75] and [70], respectively). The missing marker band for chromophore protonation in the LDMs around 1565 cm^{-1} might be explained by the low intensity of all changes that occur on this microsecond time range.

Examination of the data measured for the labeled mutant M100C* revealed some indications that maybe a branched model for the formation and decay of the two pR sub-states could be applied. The replacement of the methionine might favor the formation of the pR_1 state and therefore the majority of the molecules probably follows E46 deprotonation

and chromophore protonation dynamics on a tens of microseconds timescale ($pR_1 \rightarrow pB'$), while only a few molecules show these processes in hundreds of microseconds assigned to the $pR_2 \rightarrow pB'$ transition, as it mainly occurs for the WT. This discussion will be expanded later on in section 7.1.3 on page 119 *ff.* when looking at M100C* in more detail.

In conclusion, the measured data clearly show the existence of multiple pR states in good agreement with the microsecond dynamics proposed in many previous studies. This is, to my knowledge, the first time these dynamics were observed in an infrared study. As already mentioned, not so much the existence, but rather the structure and kinetics of the second pR state are debated in literature, especially regarding different interpretations of where the changes between the two states appear and whether they are formed concurrently or in sequence. Unfortunately, the data of WT-PYP, analyzed here, cannot provide an unambiguous answer to the model that has to be applied because hints were found supporting both interpretations. A schematic representation of the two possible ways for pR formation (parallel or sequential) is shown in the two photocycle models suggested for WT-PYP in figure 7.3 on page 103. Further insight will be gained, however, when examining the SCN-labeled mutants. With the combination of the LDMs and global analysis it was possible, though, to pinpoint the main changes on this timescale to residues in the chromophore binding pocket, namely R52 and E46, which are known to play a crucial role in the photocycle dynamics.

Proton transfer and chromophore binding pocket dynamics during pR $\rightarrow$ pB'

Besides the *trans-cis*-isomerization of the chromophore, its protonation is one of the crucial steps during the photocycle for signaling state formation. The proton transfer process was found to occur on a few hundred microseconds timescale and to be accompanied by a distinct color change in the visible spectrum (λ_{max} = 355 nm) [20]. In the pB' intermediate the hydrogen bonds between the chromophore and the nearby residues Y42 and E46 are broken [57, 75, 82, 93]. The chromophore protonation is preliminary to the large structural rearrangements leading to signaling state pB [4, 6, 77, 78]. However, the origin of the proton is still under debate whether it is donated intermolecularly by the nearby residue E46 that gets deprotonated on a similar timescale [10, 11, 93, 94, 97] or is transferred by surrounding solvent molecules that are able to invade the binding pocket [6, 96, 98].

Previous time-resolved FTIR studies suggested a direct proton transfer from E46 to the phenolate oxygen of the chromophore based on the simultaneous appearance of marker bands indicating E46 deprotonation and chromophore protonation. They observed that the bleach of the COOD stretch vibration of E46 at 1726 cm^{-1} (COOH at 1736 cm^{-1}), an indicator for glutamate deprotonation, follows the same kinetics as the ring vibration of the chromophore at 1498 cm^{-1}, that decreases in 260 µs with protonation of the phenolate [11] or the stretch vibration of the chromophore's aromatic ring at 1575 cm^{-1}, that is typical for a protonated chromophore [10]. Although the synchronous dynamics are strong evidence for intermolecular proton transfer during the $pR_2 \rightarrow pB'$ transition, there are observations contradicting this interpretation.

In mutation studies with E46Q, in which the putative proton donor E46 is absent, the chromophore still gets protonated even though the dynamics of the process are accelerated about 5-times compared to WT-PYP [11, 96]. The protonation process in the mutant is fol-

lowed by global conformational changes, too. Therefore an alternative proton source has to be taken into account. Of course, the E46Q mutation could have altered the photocycle in a way that other protonation pathways were created, which do not exsist in the WT, but that seems rather unlikely. Transient absorption spectroscopy with pH-indicator dyes proofed that protonation of the chromophore appears simultaneously with proton absorption, that was monitored by pH-dependent changes in the absorption of the dye. This led to the conclusion that the proton has to be donated from water molecules in about 540 µs [96]. This interpretation is further supported by investigation of the protein structure which revealed that on the one hand the movement of residue R52 opens the gateway of the chromophore binding pocket allowing water molecules to penetrate towards the chromophore and on the other hand the aromatic ring of the chromophore moves towards the protein surface [82]. In a pH-dependent study of the deuterium exchange effect, the data supported an intermolecular proton transfer from E46, but could be equally well explained by assuming a water molecule as proton donor [74].

In the LDMs resulting from analysis of the electronic delay data a prominent feature appears at a lifetime of about 170 µs for the deprotonation of the carboxyl group of E46 at 1725 cm^{-1} as shown in figure 7.2 on page 91 for WT and WT' (highlighted by a yellow dashed line). This lifetime is in good agreement with values found in literature ranging from 100 - 600 µs [10, 11, 71, 72, 92, 96]. Since the lifetimes in this time range of the LDMs were shifted due to standardization, the lifetimes have to be compared to the ones obtained from global analysis, time traces of the raw spectra (see figure F.22 on page 223 in the appendix) or the features in the not-standardized LDMs (see figure F.28 on page 228 in the appendix). By these methods lifetimes for E46 deprotonation of 386 µs (193 µs for WT'), 276 µs, and 360 µs were obtained respectively. Simultaneously with E46 deprotonation spectral changes in the amide I region (especially for the bleach at 1643 cm^{-1}) and around 1675 cm^{-1}, corresponding to the C=O stretch vibrations of the chromophore, are observed (highlighted by the yellow dashed line at 170 µs in figure 7.2). In the hundreds of µs time range a positive feature at 1565 cm^{-1} (1575 cm^{-1} in H_2O) is found which can be associated with the protonation of the chromophore [10, 58] and was described to follow the same kinetics as the deprotonation process of E46 leading to the conclusion that the proton is directly transferred from the glutamate to the chromophore [10]. However, in the LDMs it seems to occur delayed with respect to the E46 C=O bleach by almost 100 µs (marked by the yellow dashed line in figure 7.2 at 260 µs). Also, the investigation of the time traces of the raw data (figure F.22) revealed a lifetime of 690 µs for chromophore protonation, which is significantly slower than the deprotonation process. It has to be mentioned here, though, that the aromatic ring vibration of the chromophore at 1565 cm^{-1}, that serves as marker band for the protonation process, overlaps with other protein vibrations, which can affect the obtained lifetime.

For better comparison of the kinetics for both features at 1725 cm^{-1} and 1565 cm^{-1}, time course slices through the LDMs of WT and WT' are depicted in figure F.23 on page 224 in the appendix. Only one single feature is observed in the traces of both spectral positions for time constants above 100 µs, indicating that they show kind of a single exponential behavior. Technically speaking, the peaks in the LDMs are always representations of exponential disributions, thus the Tikhonov regularization artifically broadens even a model curve having a single exponential lifetime. Anyway, it is striking to see that chromophore protonation appears notably later than deprotonation of the glutamate. Despite that, the lifetimes are

still consistent with the ones found in the time-resolved step-scan FTIR study by Brudler *et al.* [10] that reported lifetimes of 113 µs (for the major population of molecules) and 1.5 ms with which the proton transfer process can occur (assuming a branched model as discussed in detail later). The lifetimes found in the LDMs lie in between those two that resulted from a global fit of the full spectrum, whereas the LDM lifetimes are resolved for single spectral features. In the spectra revealed by global analysis of the transient vis-pump-IR-probe data the 61 µs and 386 µs (193 µs for WT'; light green and yellow spectra in figure 7.2) components show the synchronous spectral changes correlating with E46 deprotonation and chromophore protonation, while the succeeding 2 ms component (orange spectrum) displays mainly changes in the amide I region that are assigned to movements of the protein backbone. These observations are in good agreement with the dynamics reported by Xie *et al.* [11] (data analyzed by global fitting as well).

An explanation for the absence of differentiation between the kinetics for the two proton transfer processes in the global analysis can be found when thinking about how the global lifetime components are obtained. In the time range under investigation, the lifetimes are dominated by the larger spectral changes in the amide I region, which additionally feature a higher signal-to-noise ratio. Since all spectral changes are correlated by the associated spectra *via* the lifetimes, the changes of single features are less weighted in the fit and therefore the dynamics of these features make only a small contribution to the global lifetime. Hence a global lifetime can be described by the composition of many smaller contributions emerging during a relatively short time window, so that they are correlated but do not have to appear necessarily at exactly the same time. This would coincide with the photocycle following not a smoothed but a more rugged potential energy landscape involving multiple small steps as it is described theoretically for the process of protein folding [176, 177].

The analysis of the LDMs that revealed different lifetimes for the deprotonation and the protonation process, indicates that the proton is most likely not transferred directly from E46 towards the chromophore, although they are located in close proximity within the binding pocket. These observations imply, indeed, that the proton for protonation of the chromophore's phenolate oxygen originates from another proton source, such as an external water molecule as it was suggested by transient absorption measurements with a pH-sensitive dye [96]. However, this is, to my knowledge, the first direct kinetic evidence that proofs that E46 is not the proton donor for the proton accepted by the chromophore. When inspecting the data from the previous step-scan FTIR study by Xie *et al.* [11] closely, it might be possible that the bleach of E46 also appears slightly earlier in time than the ring vibration of the chromophore serving as protonation marker. Although the difference looks similar to the shift observed here, they interpreted the kinetics as simultaneous appearance of the E46 signal with the chromophore protonation process. Additionally, after examination of different studies in a detailed review [98], it was concluded as well that the proton is transferred from the solvent to the chromophore, consistent with the results found here.

The LDMs show that changes in the chromophore C=O region around 1670 cm^{-1} (positive feature) occur a little earlier than deprotonation of E46. As discussed earlier, the C=O vibration (with the hydrogen bond towards C69 broken) is sensitive to changes in the chromophore's conformation resulting from altering hydrogen bonding interactions of the

phenolate towards nearby residues, namely Y42 and E46. While in pR_2 probably both hydrogen bonds of the chromophore are still intact (or at least the one towards Y42 for pR_1), it is known that in pB′ both H-bonds are broken leading to a relaxed chromophore structure [57, 75, 82, 93]. Apparently, disruption of the hydrogen bonding interactions and structural changes of the chromophore appear prior to deprotonation of E46 and protonation of the chromophore (compare also figure F.23). Actually, the structural rearrangements of the chromophore might even facilitate the proton transfer from the solvent as the phenolate oxygen becomes more accessible [82].

In addition to the proton transfer processes, the $pR_2 \rightarrow pB'$ transition is accompanied by structural dynamics of the chromophore binding pocket. Preceding the appearance of the E46 bleach, an upshifted feature of the C=O vibration can be observed at 1750 cm^{-1} (1759 cm^{-1} in H_2O). This induced absorption is found in the LDMs at a lifetime of about 60 µs (highlighted by a yellow dashed line) and is also present in the spectrum from global analysis that corresponds to the pB′ intermediate (orange in figure 7.2). In the SADS it arises synchronously with the spectral features that indicate chromophore protonation and glutamate deprotonation at 386 µs for the WT (193 µs for WT′). It is assigned to the protonated E46 [10, 11, 84] coinciding with the observation that the signal arises before E46 becomes deprotonated as it is easily visible in the time slices through the LDMs that are depicted in figure F.23 on page 224. Previous time-resolved FTIR studies suggested that the upshift of the absorption[2] is caused by the movement of E46 into a more hydrophobic environment [10, 11].

The existence of the induced absorption is for Brudler *et al.* [10] reason to suggest a branched model for the photocycle. Due to the smaller integral of the upshifted band compared to the bleached absorption of E46, the minor population of molecules ($\approx$ 25 %) was associated to the ones in which E46 first moves into a more hydrophobic environment with 113 µs, followed by deprotonation of the glutamte in 1.5 ms. Concurrently E46 becomes directly deprotonated in the major population of molecules ($\approx$ 75 %) in 113 µs and the millisecond lifetime was assigned to overall conformational changes of the protein. If the movement of E46 leads to an increased distance between chromophore and glutamate, direct proton transfer from the latter would become less likely. However, the data shown here suggest a consecutive course of events during the $pR_2 \rightarrow pB'$ transition due to the different time constants observed for E46 movement, E46 deprotonation and chromophore protonation. At first, E46 shifts into a hydrophobic pocket to allow deprotonation towards the solvent. This process is followed with some delay by the arrival of a proton, possibly from the solvent, at the chromophore and is probably facilitated by the movement of E46 away from the chromophore. The generally accepted photocycle transition from pR_2 to pB′ can now be subdivided in multiple steps as indicated in both photocycle models in figure 7.3 on the next page. Later it will be possible to highlight the individual steps by the SCN label's at different positions in the protein.

An indispensable step for the proton transfer from the solvent to the chromophore is the movement of nearby residue R52, which prevents the intrusion of water molecules into the binding pocket in the dark state. As mentioned earlier the difference band around 1590 cm^{-1} in the GA spectra can be assigned to the C=N vibration of R52 [12, 172]. It was observed that large changes occur already on a nanosecond timescale implying that R52

[2] Xie *et al.* [11] observed the upshifted absorption only in PYP crystals.

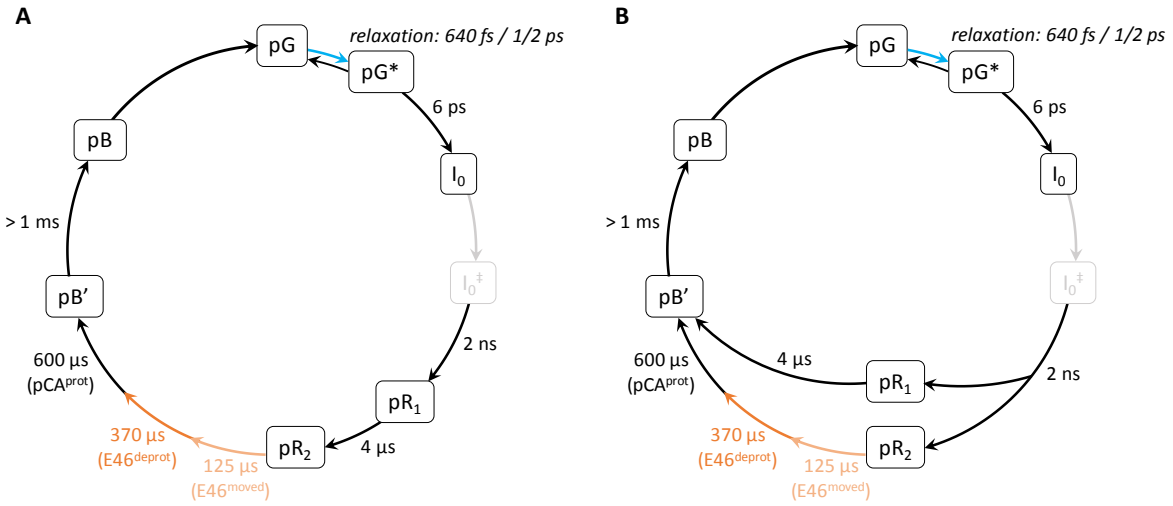

Figure 7.3: *Photocycle models for WT-PYP derived from transient vis-pump-IR-probe experiments with a consecutive model for the two pR states (A) or a parallel formation of pR_1 and pR_2 (B). Lifetimes were obtained by global analysis from components that have corresponding features in the LDM. For the $pR_2 \rightarrow pB'$ transition the lifetimes were taken from the not-standardized LDM, since they are known to be shifted for the standardized data, and the global analysis is not able to distinguishing between the slightly different kinetics of the movement of E46 into a more hydrophobic environment ($E46^{move}$; faint orange), the deprotonation of E46 ($E46^{deprot}$; orange) and the protonation of the chromophore (pCA^{prot}; black) revealing only one component for all three processes. The $I_0^{\ddagger}$ is depicted in gray as it was proposed in (some) literature and was discussed previously, but no clear evidence for its existence was found by examination of the WT data. The 650 fs, 1 ps and 2 ps lifetimes were assigned to relaxation processes of pG*, but whether it relaxes back to the ground state or with multiple components to I_0 cannot be judged in this case.*

started moving long before chromophore protonation. But also in the further course the signal increases persistently which can be interpreted as the steady opening of the gateway to the solvent [82, 172] allowing solvent molecules to penetrate in the proximity of the chromophore's phenolic oxygen [178].

Structural rearrangements during signaling state formation

The pB' $\rightarrow$ pB transition is characterized by large structural rearrangements of the protein [4, 5, 10, 11, 74, 93]. The driving force for these conformational changes was found to be the movement and deprotonation of E46 and the concomitant formation of a buried charge in a highly hydrophobic environment which has a strongly destabilizing effect on the structure of the protein [11, 93, 99]. Thus, the large changes of the protein backbone lead to a large increase of the amide I signal (1623/1643 cm^{-1}) in the vibrational spectrum as it can be observed in the SADS of the long lived component that is formed on a millisecond timescale[3] (shown in red in figure 7.2 on page 91 with the signal size decreased to 40 % for better visualization).

[3]Note that the lifetime of 2 ms already exceeds the measured time range (last data point at 750 µs), but is given to differentiate this component from the long lived one. Thus, the value for the lifetime can only be seen as an approximation.

Further spectral changes are observed in the region between 1560 cm^{-1} and 1610 cm^{-1}, in which on the one hand marker bands for polar side chain groups with double bonds appear in the pB spectrum [11] due to changes in the environment of these groups and on the other hand positive bands at 1574 cm^{-1} and 1606 cm^{-1} were assigned (in part) to the aromatic ring and the vinyl group of the chromophore (coupled C–C and C=C stretch vibrations) [10, 179] indicating variations of the chromophore structure. Additionally, the pB′ $\rightarrow$ pB transition gives rise to a negative band at 1689 cm^{-1} in the global analysis spectra originating from a ND-containing side chain group (arginine, asparagine or glutamine in D_2O) implying that large changes in the environment of this side change take place when the protein structure changes dramatically [11].

In time-resolved resonance Raman experiments [93] the new formation of a hydrogen bond with the chromophore's carbonyl oxygen was observed. Structural investigation of pB suggested the backbone amide of C69 as potential hydrogen bonding donor [82]. This would involve considerable structural rearrangements of the chromophore including a flip of the phenolate ring. Spectroscopically the change in the hydrogen bonding state was observed by a shift of the C=O stretch vibration from 1660 cm^{-1} to 1651 cm^{-1} [93], this shift is not visible in the SADS from global analysis shown here. Anyway, a detailed kinetic analysis of the pB′ $\rightarrow$ pB transition with the data presented here is not possible as only a few time points capture the formation of the signaling state.

In conclusion, the photocycle transitions and corresponding lifetimes found for WT-PYP are generally consistent with the ones observed in previous studies. The combination of mechanical and electronic delays in the transient vis-pump-IR-probe experiments enabled the reconstruction of the photocycle intermediates starting with the electronically excited state pG* after hundreds of femtoseconds until the formation of the signaling state pB on a millisecond timescale. In between the formation of I_0 accompanied by isomerization of the chromophore could be resolved, but no clear indications for the existence of the short living ground state intermediate and the debated $I_0^{\ddagger}$ intermediate were found. Further a short microsecond component that was suggested to correspond to multiple pR states was measured. It was not possible to conclusively clarify which kinetic model should be best applied, but the changes that occur during this transition can now be located to the chromophore binding pocket especially to E46 and R52. Further first direct kinetic evidence was found that E46 can be excluded as proton donor for chromophore protonation in the formation of pB′. Moreover, this transition consists of individual consecutive steps including E46 movement and deprotonation as well as chromohphore protonation.

7.1.2 Comparison of the Dynamics WT and WT′

WT and WT′ differ only in the first position of the amino acid chain, where the methionine in WT was replaced by a glycine in WT′ due to the cleavage site for the TEV protease that is necessary to remove the His-tag inserted for simplification of the purification (the same procedure is used for all mutants that all contain the M1G mutation). This mutation was expected to be minimally invasive.

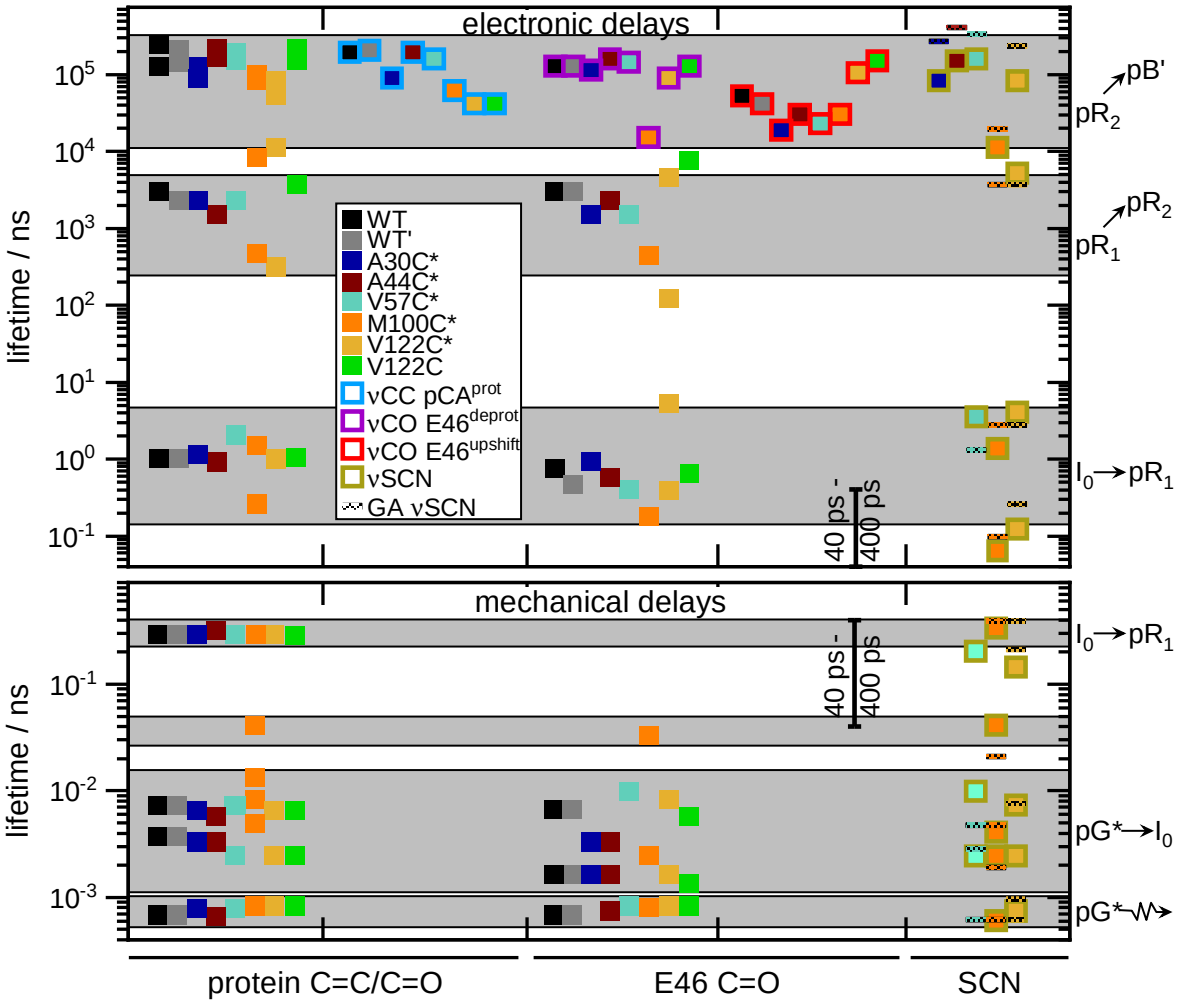

Figure 7.4: *Overview over the lifetime density analysis of PYP-WT, WT' and all studied mutants. Each square represents a characteristic feature at one lifetime that was observed in a specific spectral range of the LDMs of mechanical (bottom) and electronic delays (top). The vertical black lines represent the same time window. On the left the features of every investigated sample in the CC/CO region of the protein (up to 1705 cm^{-1}) are depicted, in the middle features of the CO region of E46 and on the right features in the SCN region for the labeled mutants. The outlined squares highlight prominent features of chromophore protonation (blue), E46 deprotonation (purple), the upshifted absorption of E46 (red) and the SCN signals (yellow). The gray horizontal bars outline roughly the features that correspond to one photocycle transition. The shaded thin bars in the SCN spectral region represent fitted lifetimes resulting from global analysis (GA) that correspond to spectral changes of the SCN difference signal. If an SCN signal was present from the beginning in GA a small bar was set at 650 fs, the approximate resolution of the experiments.*

Comparison of the LDMs as well as the SADS from GA in figure 7.2 on page 91 demonstrates that the kinetics and spectral features for WT and WT' are very similar during the early photocycle dynamics, except for small variations in the intensity ratio of different vibrational modes.

For the µs-component global analysis of WT' revealed a decay time of 9 µs, twice as long as for WT (4 µs). In the LDMs of both samples, however, no remarkable differences are found for the features below 100 µs. The deviation in the lifetime could result from the

additional component of 61 µs that is needed to fit the electronic delay data of the WT properly. Here instead of one component of 193 µs as for WT', two components of 61 µs and 386 µs are necessary. The 61 µs spectrum looks very similar to the 4 µs spectrum varying more conspicuously only at 1739 cm^{-1}, where it resembles rather the following spectrum with the positive absorption band vanished (compare insets in figure 7.2 on page 91). Both spectra (at 386 µs for WT and 193 µs for WT', yellow SADS), which are assigned to the pR_2 intermediate, are comparable for both samples. The features in the LDMs also appear at similar lifetimes for WT and WT' in this time range. Only close inspection of the time slices through the ps-to-ms LDMs in figure F.23 on page 224 in the appendix revealed a sligthly faster movement of E46 in a more hydrophobic environment for WT' (traces of induced absorption at 1747 cm^{-1}), whereas the other three investigated traces for chromophore protonation (1565 cm^{-1}), changes of the chromophore's C=O conformation (1678 cm^{-1}), and E46 deprotonation (1724 cm^{-1}) can be considered as equal for both samples within the accuracy of the analysis method. Thus, it is concluded that the replacement of the first methionine by a glycine does not significantly influence the protein dynamics.

7.1.3 SCN Dynamics

By investigation of the CC/CO spectral region of WT-PYP, an overview of the photocycle kinetics was obtained, now facilitating a detailed interpretation of the SCN label's response to the structural transitions. Thus, site-specific information about the different transitions are available depending on the location at which the label is inserted. Whereas the difference signals of A30C* and A44C* appear only in hundreds of microseconds, the labels for V57C*, M100C* and V122C* show an immediate response on the ultrafast timescale (see overview figure 7.4 on the preceding page and figure 7.5 on the next page). The latter two are subject to frequent perturbations by changes in their structural and electrostatic environment. V57C*, however, follows the changes of the chromophore and its surrounding until the ns-transition and then only responds again after hundreds of microseconds.

In addition to the SCN dynamics, specific characteristics of chromophore and protein kinetics for the different mutants are discussed, as well. Overall they proofed to be relatively consistent with the ones of WT' as it is shown in figure 7.4, but especially in the pR $\rightarrow$ pB' transition there seem to appear some variations for the proton transfer processes of E46 and the chromophore.

Detecting proton transfer and N-terminal movement: A44C* and A30C*

A44C* is located in the α3-helix at the protein surface, pointing into the solvent in pG. In the signaling state pB the helix is predicted to partially unfold and move further towards the empty chromophore binding pocket [82, 154], but the influence of the protein environment on the SCN label does merely change as it was observed in the study of vibrational lifetimes leaving the residue mostly solvent-exposed also in pB (see chapter 6 on page 75 and [121]). The steady-state FTIR spectra (see figure 5.1 on page 59 and [136]), however, show a large red-shift for the SCN absorption from pG to pB indicating significant changes

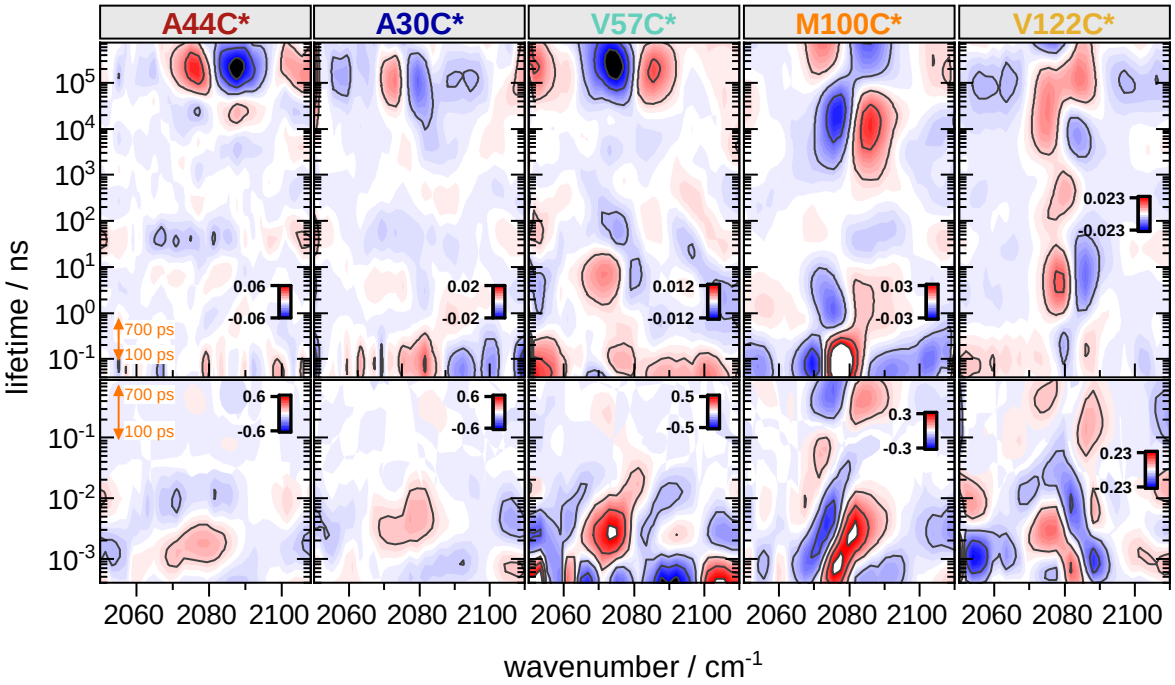

Figure 7.5: *Overview of all LDMs in the SCN region from transient vis-pump-IR-probe measurements with mechanical (bottom) and electronic delays (top). All LDMs are plotted with 5 major and 5 minor contour levels. The corresponding L-curves are depicted in figure F.37 in the appendix. The orange arrows display the same time window. A linear baseline between the first and last pixel of each mutant was subtracted for each time point before LDA for mechanical delays and after LDA for electronic delays.*

in the electrostatics. Since these alterations are most likely caused by changes of the ionization state of the nearby E46, A44C* might prove as potential sensor for the deprotonation process.

In the time-resolved vis-pump-IR-probe measurements the only difference signal arises on a hundreds of microseconds timescale when the SCN absorption is down-shifted as shown in figure 7.6 on the following page. The long lived spectrum (red) from the GA[4], associated with the pB' state and forming in 445 µs, resembles the difference spectra between pG and pB in the FTIR and the IR-pump-IR-probe experiments remarkably well (compare figure 5.1 on page 59 and figure 6.1 on page 77). Note that in the GA of the mechanical delays a tiny difference signal appears in the long lived spectrum, which is also present in the spectral slices at late delay times (see figure F.2 on page 203 in the appendix), but is neither visible in the GA spectra nor the spectral slices at early electronic delays (see figure F.4 on page 205 in the appendix). Therefore this signal is likely caused by slight misalignment of the the mechanical delay stage since the path length changes about 25 cm between the first and the last measured time points (which are subtracted from each other to obtain the difference absorption signal). This makes the experiment vulnerable for alterations in beam pointing, although the stage was tested beforehand for constant light intensity on a photo diode over

[4]Whereas in the GA of the CC/CO region an additional millisecond component was necessary to fit the data properly, in the SCN region for all labeling sites only one component (long lived) was needed to fit the data exceeding the time span of the experiment comprising both pB' and pB fractions.

the whole range. Because no such beam pointing issue can occur for the electronic delays and there no difference signal is present at early times for these data, it is concluded that this signal is an artifact of the measurement method.

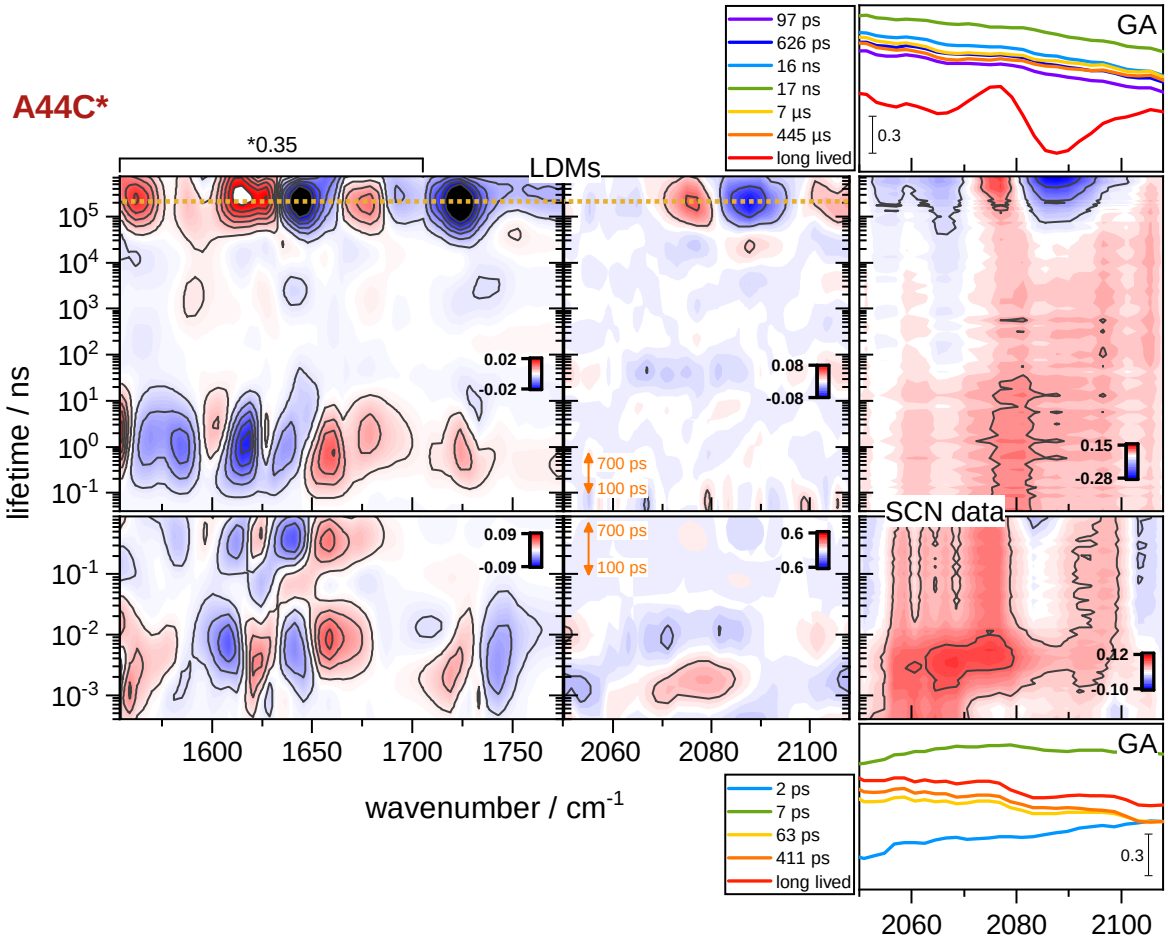

Figure 7.6: *Overview of transient vis-pump-IR-probe measurements with mechanical (bottom) and electronic delays (top) for A44C* in the CC/CO and SCN region. LDMs in the CC/CO region (first column, contour plot with 11 major levels) and the SCN region (second column, contour plot with 5 major levels, linear baseline subtracted) are shown. The corresponding L-curves are depicted in figures F.36 and F.37 in the appendix. The orange arrows display the same time window. The intensity of the amide I region in the electronic delay plot is scaled by a factor of 0.35. The yellow dashed line at 220 µs highlights features that appear simultaneously with changes in the SCN signal. Third column: Contour plot (5 major levels, linear baseline subtracted) of denoised data in the SCN region. For the SADS obtained from global analysis (GA) of the denoised SCN data only components > 600 fs for mechanical delay data (bottom) and > 50 ps for electronic delay data (top) are shown.*

When examining the LDMs of the SCN region, it becomes clear that the only spectral changes appear in the hundreds of µs time range (approximately 220 µs, highlighted by the yellow dashed line in figure 7.6), while the small patterns in the rest of the LDMs (for mechanical and electronic delays) originate from background noise and remnants of the large underlying water background[5]. However, this lifetime is twice as fast as the one obtained from GA (445 µs), since the essential standardization of the data before lifetime

[5]The LDMs of the SCN region were corrected for the water background dynamics by subtracting a linear baseline between the first and last pixel of the spectral window from each time point.

density analysis led to a shift of the features near the end of the measurement range to faster lifetimes as it was already discussed previously. It is striking to observe that the SCN features arise simultaneously with the negative feature assigned to the C=O bleach of E46 at 1724 cm^{-1} and features in the amide I region and of the chromophore C=O vibration around 1670 cm^{-1} indicated by the yellow dashed line in figure 7.6. Note here that in the LDM of the not-standardized data (see figure F.30 on page 230 in the appendix) the SCN signal appears at 450 µs matching the lifetime from GA (445 µs). Nonetheless, the features that arise at the same lifetime in the not-standardized LDM of the CC/CO region are equal to the ones observed after standardization resulting in the same conclusion. This observation proves that the qualitative comparison of features in the standardized LDMs is valid despite the shifted lifetimes.

The synchronous appearance of those features in the CC/CO region is analogous to spectral changes observed for WT-PYP (see figure 7.2 on page 91), that were assigned to the deprotonation of E46 as discussed above. Although one cannot distinguish from the LDMs alone if the SCN response is influenced by changes in the electrostatic field due to proton transfer or by conformational rearrangements that accompany the deprotonation process, combination with structural investigation of the labeling site and the steady-state experiments, it seems very likely that the shift of the SCN signal of A44C* is induced by the formation of a negatively charged E46 in its proximity and thus follows the deprotonation process.

The LDMs show that the marker band for chromophore protonation at 1565 cm^{-1} (positive feature) arises only slightly after the C=O bleach of E46 on a microsecond timescale (compare also the time slices trough the ps-to-ms LDM figure F.24 on page 225 in the appendix). For closer inspection of the kinetics of both proton transfer processes, the time traces of the raw data were fitted with exponential functions (above 100 ns) and revealed lifetimes of 650 µs for the chromophore protonation and 345 µs for the corresponding E46 deprotonation (see figure F.22 on page 223 in the appendix) implying that in A44C*, as well as in WT, the glutamate is deprotonated well before the proton arrives at the chromophore. Therefore the SCN signal reacts on a timescale that is more similar to the decay time of the C=O bleach of E46. Furthermore the distance between residue and chromophore makes a direct response of the label on protonation of the chromophore unlikely.

Whereas A44C* seems to stay solvent exposed during the complete photocycle, A30C* was found in steady-state experiments to be buried inside the protein in pG, but to become highly accessible for water molecules in pB (figure 5.1 on page 59 and figure 6.1 on page 77). A30C* is positioned in the β1-sheet and oriented into the cavity that is formed between the N-terminus and the protein body in pG. The detachment of the N-terminus in pB allows water molecules to penetrate into the former cavity and form contacts with the SCN label.

Similar to the data for A44C*, the SCN signal in A30C* arises only very late in the photocycle at hundreds of µs (see figure 7.7 on the next page). The tiny difference signal results from a very small downshift of the absorption and is only present in the long lived spectrum (red) from global analysis forming in about 290 µs. In the LDM of the SCN region a real feature, corresponding to the observed difference signal in the contour plot and GA, appears only at a lifetime of approximately 110 µs (200 µs for not standardized data), highlighted by the yellow dashed line. A comparison with the CC/CO region reveals that the SCN responds simultaneously with protonation of the chromophore which

appears slightly faster than deprotonation of E46 in A30C* in contrast to the WT. Further changes start to arise in the amide I region at a similar lifetime. However, it is not possible to conclude from these data which of these changes during the $pR_2 \rightarrow pB'$ transition are ultimately sensed by the SCN label. Thus, the position of A30C* within the protein structure is closely inspected.

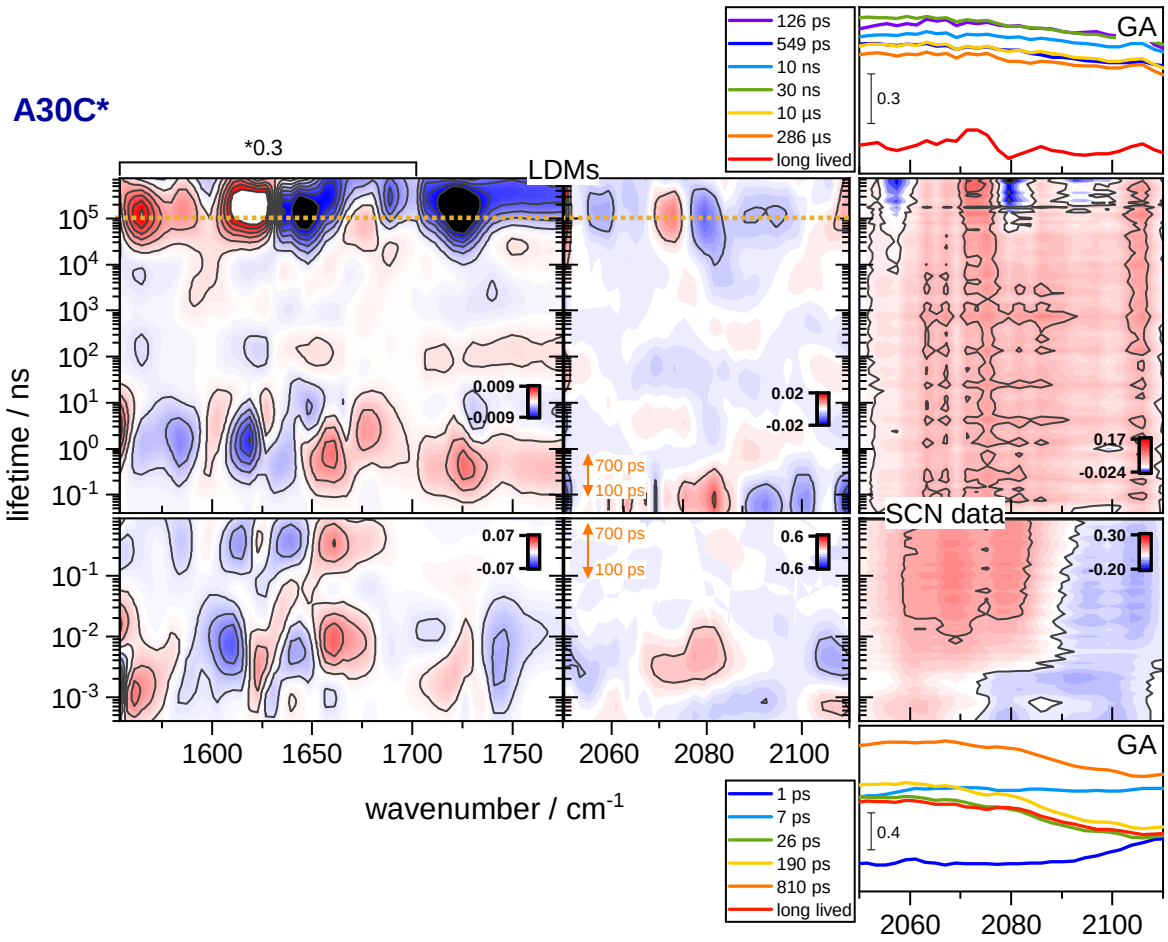

Figure 7.7: *Overview of transient vis-pump-IR-probe measurements with mechanical (bottom) and electronic delays (top) for A30C* in the CC/CO and SCN region. LDMs in the CC/CO region (first column, contour plot with 11 major levels) and the SCN region (second column, contour plot with 5 major levels, linear baseline subtracted) are shown. The corresponding L-curves are depicted in figures F.36 and F.37 in the appendix. The orange arrows display the same time window. The intensity of the amide I region in the electronic delay plot is scaled by a factor of 0.3. The yellow dashed line at 110 µs highlights features that appear simultaneously with changes in the SCN signal. Third column: Contour plot (5 major levels, linear baseline subtracted) of denoised data in the SCN region. For the SADS obtained from global analysis (GA) of the denoised SCN data only components > 600 fs for mechanical delay data (bottom) and > 50 ps for electronic delay data (top) are shown.*

Examination of the distances[6] between the methyl group (atom CB) of A30's side chain and the oxygen (atom OE2) of E46 that is deprotonated in pB' and the phenolate oxygen (atom O4') of the chromophore revealed 8.3 Å and 9.7 Å, respectively, for the crystal structure of the pB' intermediate (pdb entry 1TS0) and very similar distances in pG (pdb entry 1NWZ), while the side chain of A30 is oriented away from the binding pocket towards the

[6]The distances were determined with Chimera 1.6.2.

N-terminus. In the structure model for pB the distances between A30 and E46 as well as the chromophore increased dramatically. With these findings, it seems very unlikely that one or both proton transfer processes contribute to the formation of the SCN signal. The changes in the labels environment are rather caused by alterations of the N-terminal region that lead to higher solvent accessibility as indicated by the steady-state experiments, discussed before. This hypothesis is supported by several studies that investigated the conformational changes of the N-terminus during the photocycle. There it was observed that the N-terminus already starts to unfold and protrude during the $pR_2 \rightarrow pB'$ transition prior to the global conformational changes of the protein [75, 170, 180]. Transient spectroscopy with dye-labeled PYP revealed that part of the N-terminus is perturbed already on a 200 µs timescale [180] and transient grating experiments showed changes of protein diffusion with 170 µs due to unfolding of the N-terminal α-helices [170] (all measured in H_2O). These kinetics match the observed lifetime of the SCN label implying that, indeed, the structural changes and movement of the N-terminus are responsible for the appearance of the SCN signal.

Conversely, the usage of the SCN label reveals site-specific information about changes during pB' formation, since it is now possible to assign the signal changes in the amide I region that accompany the proton transfer processes on a sub-millisecond timescale at least partially to the unfolding of the N-terminus.

When closely looking into the LDMs of A30C*, E46 deprotonation and chromophore protonation occur almost simultaneously with the protonation step even slightly earlier, in contrast to WT' where both processes are separated by about 100 µs (compare figure F.24 on page 225 and figure F.23 on page 224 in the appendix). Exponantial fitting of the time traces from the raw spectra (see figure F.22 on page 223 in the appendix), however, revealed that the deprotonation process (196 µs) is still a little faster compared to chromophore protonation (225 µs), which is significantly faster than protonation in WT, WT' and A44C*, though. From the location and orientation of the residue one would not expect that modification and labeling would have such significant impact on the mechanism of the proton transfer that chromophore protonation in A30C* occurs almost at the same time as deprotonation of E46, particularly given that the processes during the other photocycle transitions were not disturbed by the mutation (see also figure 7.4 on page 105).

In conclusion, the SCN signals of the two investigated labeling sites A44C* and A30C* both appear only on a hundreds of microseconds timescale showing a down-shifted absorption, albeit the two labels detect different processes during the $pR_2 \rightarrow pB'$ transition. While A44C* senses the deprotonation process of E46, A30C* responds most likely to early conformational changes of the N-terminal region, both crucial precursors for signaling state formation.

Probing alterations in the chromophore binding pocket: V57C*

The third mutant investigated with transient vis-pump-IR-probe spectroscopy was V57C*. This residue is located in the α4-helix oriented into the chromophore binding pocket with a distance of 6.5 Å to the chromophore[7] and therefore expected to sense changes of the

[7]Distance calculated from one methyl group of V57 (atom CG2) to the phenolate oxygen of pCA (atom O4') in 1NWZ (pG state) using Chimera 1.6.2.

chromophore and the binding pocket during the photocycle. Steady-state experiments showed that V57C* is buried inside the protein in pG, but probably hydrogen-bonded to a confined water molecule, and becomes solvent exposed in pB when the hydrophobic cavity collapses (see chapter 5 on page 57, chapter 6 on page 75 and ref. [121, 136]).

In the global analysis of the transient vis-pump-IR-probe data in figure 7.8 on the facing page an SCN signal is observed already for very early time constants (there is also a difference signal visible in the SADS corresponding to a delay time of 500 fs[8], see figure F.18 on page 219 in the appendix). This indicates that the label reacts to the electronic excitation of the chromophore directly after photon absorption. With a decay time of 3 ps (dark blue to light blue SADS in figure 7.8) the SCN absorption shifts and further changes are observed for a decay time of 5 ps. In the LDMs features appear at 3 ps and 12 ps in the SCN region. These spectral changes correlate with the features in the LDM of the CC/CO region that were previously assigned to the relaxation of pG*, which involves formation of the I_0 intermediate and possibly recovery of pG. In I_0 the chromophore isomerized from *trans*- to *cis*-configuration and the hydrogen bond towards C69 is successfully broken indicated by the negative feature at 1610 cm^{-1} and the positive one at 1665 cm^{-1} that appear at about 12 ps in the LDM and with 5 ps in the GA of the CC/CO region (see figure F.7 on page 208). Consequently, the SCN label of V57C* is a suitable reporter of the early photocycle events including weakening of the hydrogen bonding network around the chromophopre in pG* and the isomerization process of the chromophore.

At about 5 ns a pronounced positive and a small negative features appear in the ps-to-ms LDM of the SCN region, indicating a response of the label on a nanosecond timescale. Close inspection of the spectra from global analysis for electronic delays reveals that for the 3 ns component a small spectral change (from the light blue (3 ns) to the dark green SADS (46 ns) in figure 7.8) can be observed, as well. Thereby, mainly the induced absorption of the difference signal broadens, in good agreement with the positive feature at 2072 cm^{-1} in the LDM. Comparison to the LDM of the CC/CO region shows that the SCN label reacts to changes of the protein previously assigned to the $I_0 \rightarrow pR_1$ transition. Hence, the label in V57C* senses the relaxation processes of the chromophore and the surrounding binding pocket, although the impact on the SCN signal and therefore the direct environment of the label is rather small. Subsequently, the SCN signal persists up to hundreds of µs unaltered. In global analysis only changes of the baseline are observed in this time range. The persisting signal indicates that the label still senses the environmental changes caused by the chromophore isomerization and following relaxation processes, but does not detect the early µs-kinetics assigned to the decay of pR_1, implying that the changes associated with this transition involve neither structural changes of the chromophore nor arise in the protein environment close to the label.

On a hundreds of microseconds timescale the SCN signal is upshifted as it can be clearly seen in both the GA and the LDM of the SCN region. In the data from global analysis the spectral change is observed for the formation of the long lived spectrum (red SADS in figure 7.8) corresponding to the pB' intermediate with 357 µs. Comparing the LDMs for SCN and CC/CO regions reveals that the SCN feature appears simultaneously with the bleach of the C=O vibration of E46 at 1726 cm^{-1}, the positive feature that arises with

[8] For the mechanical delays of V57C* the IRF was approximately 200 fs as no glass rod was used in the pump beam path to stretch the pulse length.

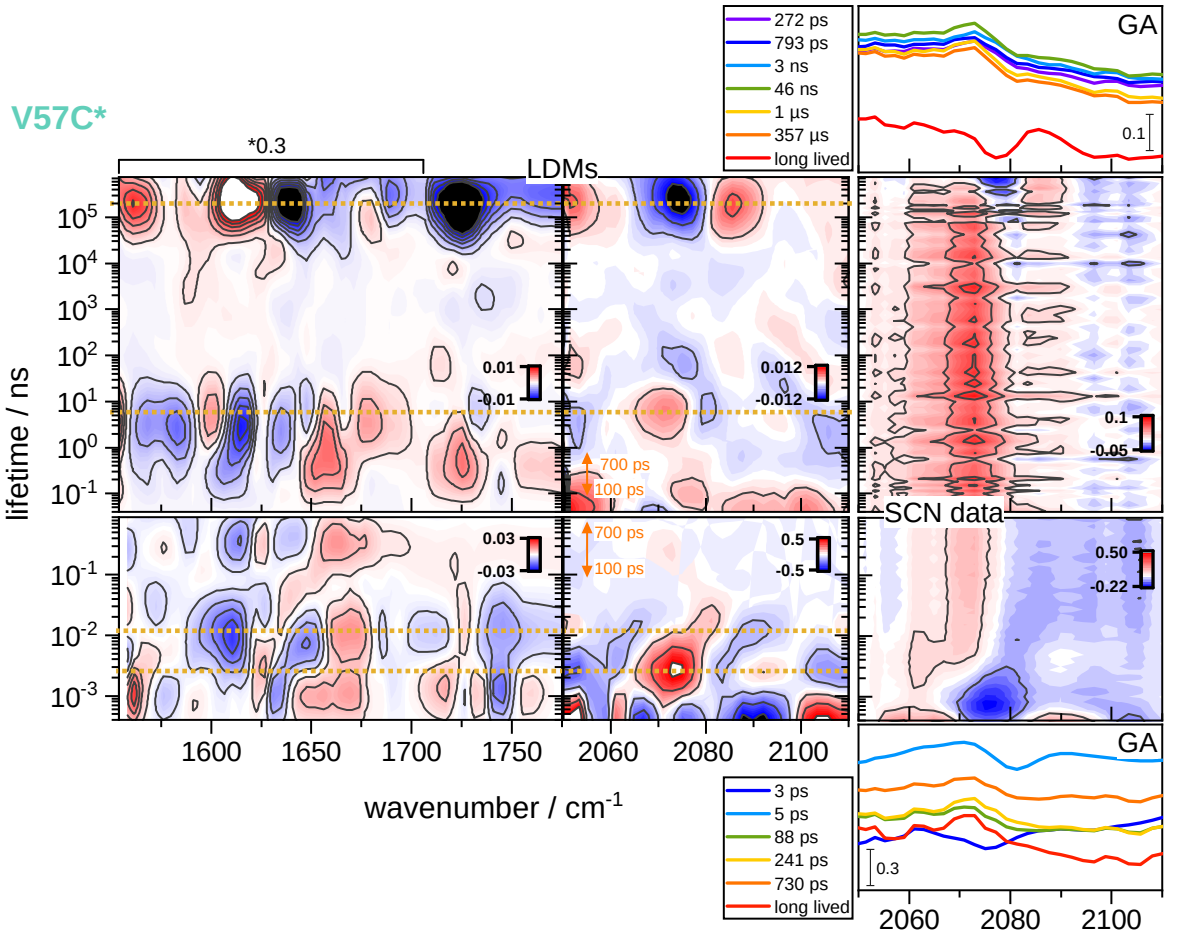

Figure 7.8: *Overview of transient vis-pump-IR-probe measurements with mechanical (bottom) and electronic delays (top) for V57C* in the CC/CO and SCN region. LDMs in the CC/CO region (first column, contour plot with 11 major levels) and the SCN region (second column, contour plot with 5 major levels, linear baseline subtracted) are shown. The corresponding L-curves are depicted in figures F.36 and F.37 in the appendix. The orange arrows display the same time window. The intensity of the amide I region in the electronic delay plot is scaled by a factor of 0.3. The yellow dashed lines at 3 ps, 12 ps / 5 ns, and 220 µs highlight features that appear simultaneously with changes in the SCN signal. Third column: Contour plot (5 major levels, linear baseline subtracted) of denoised data in the SCN region. For the SADS obtained from global analysis (GA) of the denoised SCN data only components > 600 fs for mechanical delay data (bottom) and > 50 ps for electronic delay data (top) are shown.*

chromophore protonation at 1563 cm^{-1}, and the features in the amide I region that accompany the (de-)protonation processes highlighted by the yellow dashed line in figure 7.8 at 220 µs. Since the LDMs indicate that the chromophore is protonated almost at the same time as E46 is deprotonated in V57C* (see also figure F.24 on page 225 in the appendix for a detailed comparison), it is not possible to ascertain which of these processes influences the response of the SCN label eventually. Also, examination of the time traces of the raw data (see figure F.22 on page 223 in the appendix) cannot clearly identify to which process the response of the SCN corresponds, since the time constant obtained for E46 deprotonation is with 265 µs faster than the formation of the SCN signal with 357 µs, while for protonation of the chromophore a slower time constant of 410 µs was received. Based on the proximity of the label to the chromophore and the fact that it senses the sturctural changes

at early times during the photocycle, it is assumed that V57C* reacts most likely to chromophore protonation and to possible rearrangements in the surrounding binding pocket. These structure changes include among others a higher accessibility of the hydrophobic cavity for solvent molecules due to the movement of R52 [82, 172], as discussed before for WT-PYP. This is also supported by the increased solvent exposure for the pB state that was demonstrated in the steady-state experiments presented in this thesis.

Observation of the SCN kinetics in V57C* revealed that the alterations in the chromophore binding pocket are quite extensive during excited state formation directly after photon absorption and, of course, during the chromophore's isomerization. The following relaxation processes in the binding pocket have only small impact on the label and the decay of pR_1 is not sensed at all, since the changes, mainly assigned to E46 and R52, seem to occur too far away from the position of V57C* in the binding pocket. Hence, the SCN signal persists unberturbed until the electrostatically relevant proton transfer processes and beginning larger conformational changes take place during the $pR_2 \rightarrow pB'$ transition.

Detecting multiple photocycle transitions close to the chromophore: M100C*

In M100C* the label is placed close to the chromophore in the binding pocket and near the positively charged R52 in a flexible loop region. The steady state experiments revealed for M100C* in pG the lowest wavenumber of all SCN absorptions (see figure 5.7 on page 65) and the longest SCN lifetime of all investigated mutants (see figure 6.2 on page 81) probably due to the shielded environment and the proximity to charged side chains. Upon irradiation, M100C* becomes highly solvent exposed in pB and the influence of charged groups is lost resulting in a large blue-shift in the FTIR spectrum.

M100 mutations were found to slow down the $pB \rightarrow pG$ transition dramatically [85, 156–159]. Additionally, it was found in a transient visible absorption study of M100A that not only the dark state recovery is influenced by replacement of M100, but also the formation of pB' [157]. For this transition they proposed a lifetime < 1 µs (faster than the resolution of their experiment) which is significantly accelerated compared to WT-PYP. This faster decay to pB' is supported by the findings from low-temperature spectroscopy studying the early photocycle transitions of M100A [181]. Unfortunately, there were, to my knowledge, no studies performed at room temperature that further investigated the kinetics of M100 mutants in the sub-ms time regime to achieve additional information about the influence on earlier photocycle transitions, since all mutation studies focus on the decelerated kinetics of the $pB \rightarrow pG$ transition. Due to these potential influences of the M100C* mutation on the photocycle dynamics, first the CC/CO region is closely examined and compared to the WT' assignments before describing the SCN data.

Examination of the global analysis spectra in the CC/CO region in the fs-to-ns time range for M100C* (see figure F.7 on page 208 in the appendix) revealed that both spectra corresponding to the 1 ps (light blue) and 6 ps component (cyan) show the spectral features typical for the excited state pG*, characterized in particular by the bleached absorption around 1661 cm^{-1}. In contrast to the WT and all other labeled mutants no additional early ps component appears (*e.g.* 6 ps spectrum for WT) that exhibits almost no absorption change compared to the dark state in this spectral region besides a small upshift of the negative band around 1635 cm^{-1} to 1640 cm^{-1}. The LDM of the CC/CO region for the early

transitions measured with the mechanical delays (figure 7.9) also exhibits some differences to the features that were observed for WT and WT' (figure 7.2 on page 91). At about 1 ps a positive feature occurs at 1623 cm^{-1} associated with changes of the chromophore's C=C vibration and a negative feature at 1664 cm^{-1} indicating depletion of the C=O vibration of the chromophore. Furthermore, small features in the CO region of E46 appear with an inverted sign compared to the WT on this timescale. These changes match the spectral changes that were found for formation of the electronically excited state pG*. At 5 ps mainly a negative feature at 1639 cm^{-1} arises which can be assigned to the upshift of the bleached absorption from 1635 cm^{-1}, consistent with the change observed with 6 ps in the SADS from GA (figure F.7).

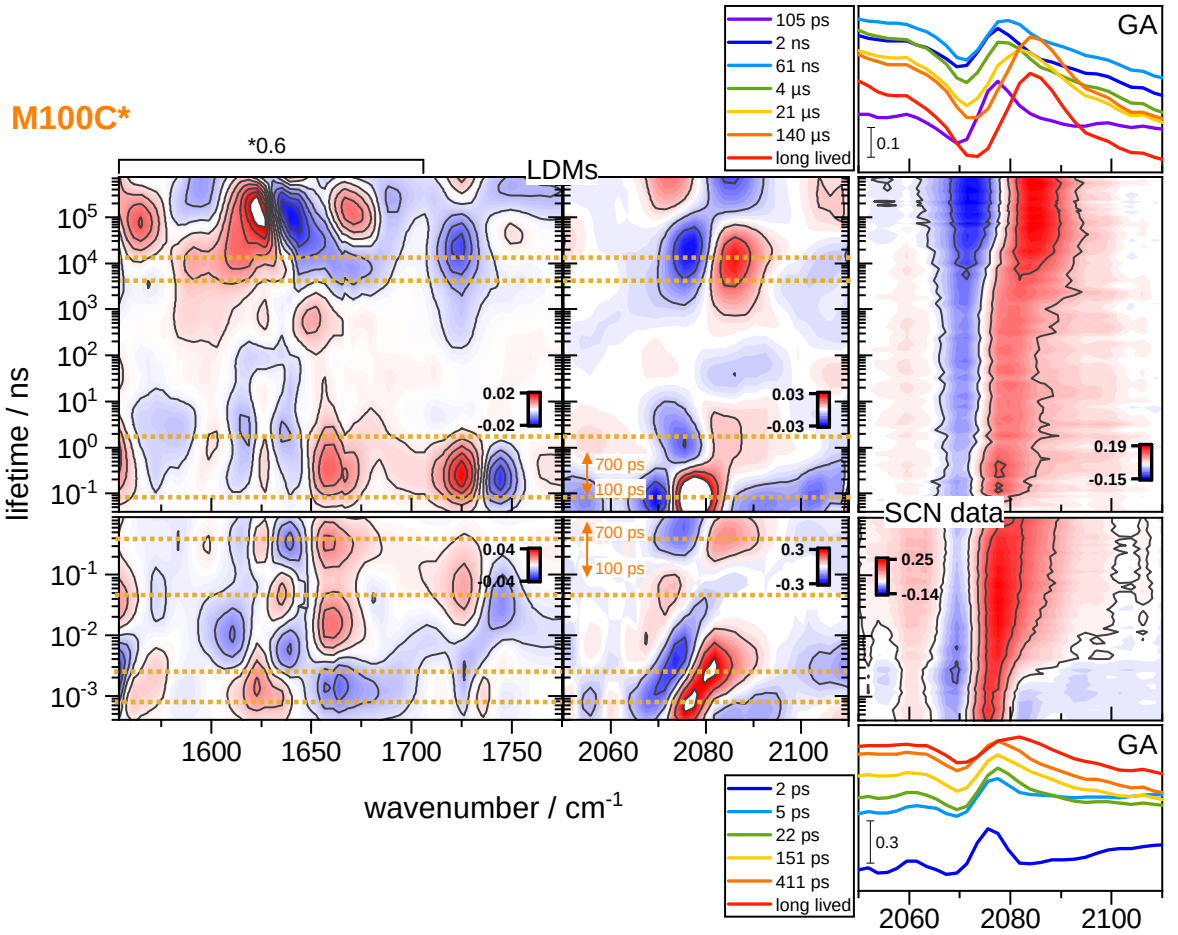

Figure 7.9: *Overview of transient vis-pump-IR-probe measurements with mechanical (bottom) and electronic delays (top) for M100C* in the CC/CO and SCN region. LDMs in the CC/CO region (first column, contour plot with 11 major levels) and the SCN region (second column, contour plot with 5 major levels, linear baseline subtracted) are shown. The corresponding L-curves are depicted in figures F.36 and F.37 in the appendix. The orange arrows display the same time window. The intensity of the amide I region in the electronic delay plot is scaled by a factor of 0.6. The yellow dashed lines at 800 fs, 3 ps, 50 ps, 380 ps / 80 ps, 2 ns, 4 µs, and 14 µs highlight features that appear simultaneously with changes in the SCN signal. Third column: Contour plot (5 major levels, linear baseline subtracted) of denoised data in the SCN region. For the SADS obtained from global analysis (GA) of the denoised SCN data only components > 600 fs for mechanical delay data (bottom) and > 50 ps for electronic delay data (top) are shown.*

The feature that corresponds to the *trans-cis* marker band at 1610 cm^{-1} appears at 10 ps implying the isomerization of the chromophore on this timescale. Whereas in the WT and the other mutants the isomerization marker and the rise of the chromophore's C=O absorption band at 1660 cm^{-1}, which indicates the disruption of the carbonyl's hydrogen bond towards the backbone, appear almost simultaneously, the latter is delayed for M100C* and occurs only at about 16 ps. This difference can be observed in the SADS from global analysis as well. While the bleach at 1610 cm^{-1} grows already in with 6 ps, the broad positive band at 1660 cm^{-1} appears with a lifetime of 25 ps (see figure F.7). Therefore formation of the I_0 intermediate seems to be slower in M100C* with respect to the WT and the events that are indispensable for the successful entry into the photocycle occur not concurrently, but with different lifetimes.

The features in the CO region of E46 (positive feature around 1726 cm^{-1} and negative feature around 1745 cm^{-1}) that show the recovery of the hydrogen bonding strength between E46 and the phenolate of the chromophore typically occurring in a few picoseconds, arise at about 50 ps in the fs-to-ns LDM of M100C* (highlighted by a yellow dashed line in figure 7.9). Global analysis revealed also a slower disappearance of the difference signal of the E46 carboxyl group resulting in a significant contribution that is still visible in the spectrum with a lifetime of 77 ps and even some signal in the hundreds of picoseconds component (yellow and orange SADS in figure F.7 on page 208). It cannot clearly be distinguished if these alterations in the kinetics of the E46 C=O correspond to a slow strengthening of the hydrogen bond after I_0 formation or to a decelerated recovery of the dark state. However, previous studies showed that the replacement of the methionine influences the relaxation dynamics of the pB $\rightarrow$ pG transition dramatically [85, 156–159], because the methionine catalyzes the *cis-trans*-isomerization of the chromophore due to its electron-donating properties by weakening the interactions between R52 and the chromophore [156, 157, 159]. These findings might hint that replacement of M100 with cysteine also leads to a decelerated decay to the dark state, not only during the relaxation of the signaling state, but also at the beginning of the photocycle. Except for the still relatively large C=O signal of E46, due to an apparently slowed down decay, the SADS of the 77 ps component (yellow) in figure F.7 exhibits the typical spectral features for the I_0 intermediate. In combination with the observations from the LDM of the mechanical delays, where the features corresponding to I_0 formation appear prior to the ones indicating the disappearance of the E46 CO signal, it can be assumed that the chromophore is probably isomerized before it slowly returns to pG. This might hint to the existence of a GSI, as it was suggested by van Wilderen *et al.* [14], but, as it has already been emphasized, without applying a target model to the data, it cannot be clearly distinguished between GSI and I_0 formation, that would occur simultaneously.

Surprisingly, the SADS with 75 ps lifetime (gray spectrum in figure F.9 on page 210 in the appendix) from GA of the electronic delays looks rather like the SADS with 25 ps lifetime (dark green SADS) than the one with 77 ps (yellow SADS) of the mechanical delays, especially due to the missing positive band that corresponds to the chromophore's C=O vibration in a not-hydrogen-bonded conformation. However, the spectral slice taken at 50 ps of the electronically delayed raw data (see figure F.3 on page 204 in the appendix) features already a slightly positive absorption band around 1660 cm^{-1}. Nevertheless, the

SADS of M100C* that decays with 3 ns is similar to the one observed for WT′ with a decay of 2 ns (see figure F.8 on page 209 in the appendix) implying that the formation of pR occurs with comparable dynamics in both samples.

In the ps-to-ms LDM (figure 7.9) the positive and negative feature corresponding to the difference signal in the CO region of E46 is very prominent at early lifetimes in contrast to WT and the other mutants. It appears, though, shifted to later delays with respect to the fs-to-ns LDM at approximately 200 ps. In the LDMs of the not-standardized data the difference for the appearance of these features between mechanical and electronic delays is significantly smaller (see figure F.32 on page 232). Further, the positive feature at 1660 cm^{-1} arises prior to the other features on the early nanosecond timescale in the electronic delay LDM. For mechanical delays, however, where these features were previously found to occur in general shifted to faster lifetimes, the feature at 1660 cm^{-1} appears simultaneously with the other features in the CC region. For WT′ a synchronous appearance was observed in both LDMs. For these differences in the lifetimes of single features no explanation was found so far. However, at about 2 ns the features which are typical for the formation of the pR_1 state are present analogous to WT′ and in good agreement with the spectral changes obtained by global analysis.

At about 600 ns features appear in the LDM for M100C* that are not present in the LDMs of WT and WT′. The most obvious feature at this timescale is observed at 1651 cm^{-1} and further changes at 1595 cm^{-1}, assigned to the C=N vibration of R52, and at 1724 cm^{-1} for depletion of the E46 C=O absorption. Comparison to the global analysis spectra revealed that there a component of 531 ns (cyan in figure F.9) was obtained, as well. At 1651 cm^{-1} only a slight broadening of the difference absorption band centered at 1657 cm^{-1}, which is assigned to the low wavenumber component of the chromophore's C=O vibration that is most likely associated with a conformation with only one intact hydrogen bond towards Y42, occurs. The more obvious changes, though they are small as well, arise at 1595 cm^{-1} and 1726 cm^{-1} perfectly matching the two other features observed in the LDM. For WT and WT′ also hundreds of nanosecond components are found, but here hardly any changes occur in the spectra and no features are observed in the LDMs, so that these components are rather assigned to dynamics of the solvent background. These changes that are visible in M100C*, however, resemble the changes observed for the early µs-component in the other samples quite well implying that this transition (probably $pR_1 \rightarrow pR_2$) is accelerated in M100C*.

The bleached absorption of the carboxyl group of E46 already grows in with a lifetime of 14 µs at 1725 cm^{-1} (dark green to yellow SADS in figure F.9). Examination of the LDM reveals that there is a negative feature visible at 1724 cm^{-1} for a lifetime of 20 µs, implying a accelerated deprotonation process of E46 with respect to WT, WT′ and the mutants A44C*, A30C*, and V57C*, which were examined previously and showed deprotonation dynamics on a hundreds of microseconds timescale. Large changes of the marker band for chromophore protonation at 1565 cm^{-1}, however, appear in the global analysis only in the subsequent transition with a lifetime of 67 µs (yellow to orange SADS). Also in the LDM the positive feature at 1565 cm^{-1} occurs significantly faster than for WT-PYP at about 80 µs. Analogous to the observations for WT′, the protonation of the chromophore is delayed with respect to the deprotonation process. This is also supported by the exponential fits of the time traces from raw data shown in figure F.22 on page 223 in the appendix, which exhib-

ited delay times of 31 µs for E46 deprotonation and 80 µs for chromophore protonation. In the LDM, the changes in the amide I region are more distinct on the timescale on which the proton is transferred towards the chromophore. The upshifted absorption of the C=O vibration of E46 at 1750 cm^{-1}, assigned to the movement of E46, was observed to occur prior to the deprotonation process for WT, WT' and the mutants discussed so far. In M100C*, however, the corresponding feature appears delayed with respect to the E46 bleach, but before chromophore protonation arises. In the global analysis it is observed that this feature grows in with the 67 µs component synchronous to the protonation marker band. Additionally, the conformational changes of the chromophore that are indicated by spectral changes of the chromophore's C=O vibration around 1670 cm^{-1} seem to arise as slowest process during pB' formation as it can clearly be seen in the time slices through the LDM in figure F.25 on page 226 in the appendix. Altogether the formation of pB' is significantly accelerated after replacement of the methionine in good agreement with predictions of previous studies [157, 181]. However, this is the first direct kinetic evidence under physiologic conditions that showed these fast proton transfer processes for an M100 mutant.

The LDM of the electronically delayed data in the CC/CO region of M100C* demonstrates that the standardization improved the quality of the LDM dramatically by suppressing the unwanted oscillations (compare standardized LDM in figure 7.9 on page 115 and not-standardized LDM in figure F.32 on page 232 in the appendix) and has generally to be applied to the data. However, the drawback of the standardization is, as mentioned earlier, that especially the features at the end of the measured time range are shifted to faster lifetimes, which could lead to a loss of separation between features. This could be the case for M100C* where in the LDM of the not-standardized data possibly a second deprotonation and protonation process appear at hundreds of µs as shortly discussed in the following.

Examination of the not-standardized LDM for electronic delays of M100C* (see figure F.32 on page 232) reveals that there is also a negative feature visible at 1724 cm^{-1} for a lifetime of about 20 µs comparable to the standardized LDM. Perhaps a second feature appears, though, at 500 µs, but with a considerably lower intensity. If this additional feature does not arise as artifact from the alternating pattern of the oscillations that are very severe for this LDM, it could imply that two deprotonation processes of E46 take place with the majority of the molecules donating their E46 proton on the faster timescale. There are also two features at 1565 cm^{-1}, but with similar intensities, indicating that in one part of the molecules the chromophore is protonated with a lifetime of 60 µs, in the other molecules the proton transfer occurs with approximately 600 µs. In both cases the protonation of the chromophore is delayed with respect to the corresponding deprotonation processes. The changes in the amide I region that accompany the early proton transfer processes are rather small compared to the ones that occur in the same time range as the later (de)protonation step. Slightly preceding the appearance of the negative feature for the bleached absorption of E46 occurs a positive feature at 1590 cm^{-1} which can be assigned to the movement of R52. These changes of R52 and E46 on an early microsecond timescale are similar to the ones observed for WT' and the other investigated mutants. However, neither in the standardized nor in the not-standardized LDMs of WT' (or the mutants) indications for an early protonation process are found, which resulted in the conclusion that probably a sequential model with $pR_1 \rightarrow pR_2$ should be favored for WT-PYP. It is likely, though, that

not only the intensity of the E46 bleach is significantly lower with respect to M100C*, but also the intensity of the positive feature corresponding to the protonation marker band which thus could be too small to be detected.

The upshifted absorption at 1750 cm^{-1} that most likely corresponds to a movement of E46 into a more hydrophobic environment [10] is only visible at 110 µs. In global analysis it is observed that this feature grows in with the 67 µs component coincident with the chromophore protonation band (see figure F.9). Additionally, the SADS from global analysis show a very high absorption of the low wavenumber population at 1655 cm^{-1} in the C=O region of the chromophore that was previously assigned to a conformation with only one intact hydrogen bond of the phenolate to Y42 [90] and a hardly pronounced high wavenumber population at 1674 cm^{-1} probably corresponding to a conformation with two intact hydrogen bonds contrary to the 9 µs spectrum in WT'. As discussed earlier for WT-PYP, the population with only one intact hydrogen bond can most likely be associated to the pR_1 state, whereas the other hydrogen bonding conformation is assigned to pR_2 [75]. Therefore the large difference between the low and high wavenumber populations might indicate that in M100C* the formation of pR_1 is possibly favored over the formation of pR_2.

These observations would support a parallel model for formation and decay of pR_1 and pR_2 as it was suggested in literature [70, 75, 90] and discussed for WT-PYP beforehand. In this model both pR states are formed simultaneously on a nanosecond timescale. The difference between both states is suggested to be the conformation of the chromophore's C=O that is probably influenced by varying hydrogen bonding configurations of the phenolate ring towards Y42 and E46 [75, 90]. Comparison of the global analysis spectra with an early µs decay imply already that in M100C* most likely formation of pR_1 is favored, whereas in the the other samples investigated so far the formation of the pR_2 intermediate seems to be dominating. Further evidence for this hypothesis can be found when examining the transition to the pB' intermediate. For the parallel model it was suggested that pR_1, which is supposed to exhibit only one intact hydrogen bond with Y42, promotes this transition since the structure of the chromophore is more similar to the one in pB' (especially the fact that only one hydrogen bond has to be broken instead of two). Therefore the µs component was assigned to a shortcut for the pB' formation. In M100C* it is now observed that, most likely, two deprotonation processes of E46 and two protonation processes of the chromophore occur on different timescales. The fast proton transfer processes at 20 µs (deprotonation) and 60 µs (protonation) would thus correspond with the accelerated $pR_1 \rightarrow$ pB' transition, while the later steps at 500 µs and 600 µs, respectively, can be assigned to the $pR_2 \rightarrow$ pB' transition with the lifetimes in good agreement with the ones observed previously for the other samples. The fact that in M100C* the majority of the molecules follows the accelerated proton transfer processes, but only tiny signals were found for this fast transition for the WT, would match the interpretation that in M100C* the formation of pR_1 is favored and in the others, however, predominantly pR_2 is formed and therefore most of the molecules pass the $pR_2 \rightarrow$ pB' transition. This is supported by a transient fluorescent study that suggested that for WT-PYP in solution at alkaline pH[9] only the pR_2 state with two intact hydrogen bonds is present [68]. It is noticeable, though, that the movement of E46 (only of molecules with still protonated E46?) into a more hydrophobic environment seems only to occur during the decay of pR_2 prior to the slow proton transfer

[9] For the experiments presented here a slightly alkaline pD of 8 was used.

processes and that only in this case larger changes in the amide I region arise resulting from alterations of the protein structure. Why the replacement of the methionine would lead to a shifted equilibrium favoring the pR_1 state and a possibly promoted pB' formation is not resolved yet.

The bi-exponential fit of the time traces for chromophore protonation and E46 deprotonation of the raw data in the µs time range (fitted from 100 ns to the last measured time point at 750 µs) in figure F.22 on page 223 in the appendix revealed two lifetimes for the kinetics of the E46 bleach of 1.2 µs and 31 µs and one lifetime for the chromophore protonation band of 80 µs in the investigated time range. The second lifetime for protonation was $\gg$ 1 ms which could indicate a further, slower component and therefore a second protonation process. Close inspection of the traces shows that there could possibly a third slow component for deprotonation, as well.

In the standardized LDM in figure 7.9, changes of R52 and E46, which are similar to the ones observed for WT' and the other mutants on an early microsecond timescale, were found to appear at about 600 ns and were previously interpreted as an accelerated $pR_1 \rightarrow pR_2$ transition. The positive feature at 1590 cm^{-1} and the negative one at 1724 cm^{-1} are probably also in the not-standardized LDM (figure F.32) at about 550 ns present, although they can hardly be distinguished from the background noise caused by the oscillations. If, indeed, a parallel model for the formation of the two pR states would be applied with pR_1 directly decaying to pB' with sped up dynamics, the question arises what transition is correlated to the changes occurring in hundreds of nanoseconds influencing R52 and E46. Since there are still some open questions and the LDA of the not-standardized data suffers from severe artifacts, the following discussion will be based on the results of the standardized LDM further on, assuming for simplicity reasons a sequential model for the $pR_1 \rightarrow pR_2 \rightarrow pB'$ transitions as discussed before.

After discussing the photocycle kinetics of M100C* based on the protein and chromophore signals, the changes are investigated site-specifically by looking at alterations of the SCN labels local environment. In the contour plots of the SCN data (see figure 7.9 on page 115) it becomes visible that the SCN difference signal, which is already present within the IRF of the mechanical delays experiment, senses a successive blue-shift throughout the measured time range. The bleached absorption shifts by approximately 5 cm^{-1} and the induced absorption even by 8 cm^{-1} from the electronically excited state to 750 µs.

In the first SADS from global analysis with a decay time of 2 ps (dark blue in figure 7.9), an upshifted absorption of the SCN label is observed. This spectrum corresponds most likely to pG* which results from electronic excitation of the chromophore due to absorption of blue light involving relocalization of the electronic charge with changes in the chromophore's dipole moment and weakening of the hydrogen bond between E46 and the phenolate [12, 13, 95, 182]. As explained above, a blue-shift of the SCN absorption can either be caused by an increase in hydrogen bonding interactions of the label or a decrease of the polarity in its surrounding. The latter seems to be the more obvious reason for the upshifted absorption of pG*, since the structures of the chromophore and the protein are almost not influenced by the excitation, but charge redistribution most likely changes the electrostatic properties of the chromophore's direct environment and can thus be detected by the nearby label of M100C*. During the relaxation of pG* in 2 ps this signal shifts slightly further to higher wavenumbers.

In the LDM of the mechanical delays, SCN features are already visible at about 800 fs[10] matching the features in the LDM of the CC/CO region around 1 ps that might arise from the formation of the pG* state. For a decay rate of 2 ps the second features appear in the LDM (highlighted by the second yellow dashed line from below) which are not well separated from the first ones but clearly show a further upshift of the absorption demonstrating further changes of the SCN signal that can be assigned to one of the multiple relaxation processes of pG*. With global analysis yet another upshift of the induced absorption is observed for the 5 ps component (light blue SADS in figure 7.9). In the LDM, the elongated features in the early ps time range might also indicate a further upshift or broadening at about 5 ps, but they are not clearly separated from the features appearing at 2 ps. From examination of the CC/CO region at this lifetime mainly a negative feature at 1639 cm^{-1} occurs belonging most likely to further relaxation processes of pG*. The SADS from global analysis show though, that the bleach at 1610 cm^{-1}, which serves as marker band for *trans-cis*-isomerization of the chromophore, grows already in with 6 ps, whereas the corresponding feature in the LDM arises slightly shifted at a lifetime of about 10 ps. Anyways, the label in M100C* seems to respond to the isomerization of the chromophore.

In contrast to WT' and the other mutants discussed so far, the appearance of the positive band in the chromophore's C=O region around 1660 cm^{-1}, that indicates the rupture of the hydrogen bond between chromophore and C69 during formation of the I_0 intermediate, is delayed with respect to the isomerization process for M100C*. It occurs with a decay time of 25 ps in the global analysis (see figure F.3 on page 204 in the appendix) and at a lifetime of about 16 ps in the fs-to-ns LDM of the CC/CO region. On the same timescale (22 ps in GA of mechanical delays, dark green SADS in figure 7.9) small changes of the SCN signal take place as well, where mainly the induced absorption is broadened on the blue site of the signal. These observations demonstrate that the SCN label in M100C* is highly sensitive to the different changes that lead to formation of I_0 after photon absorption including mainly alterations of the chromophore's electron distribution and structure.

The 151 ps component from global analysis of the mechanical delays and especially the 105 ps component of the electronic delays reveal a significant decrease of the SCN signal size (about 35 % for the decay time of 105 ps; purple (105 ps) to dark blue SADS (2 ns) in figure 7.9) without obvious shifts of the absorption. This partial disappearance of the difference signal could mean that the SCN label of a part of the molecules returns into an environment identical to the one they sensed in the dark state. This is in good agreement with the findings for the CC/CO region. There the features in the CO region of E46, that correspond to the disappearance of the upshifted C=O vibration due to recovery of hydrogen bonding strength after weakening during pG* formation, occur at 50 ps in the fs-to-ns LDM and at 200 ps in the ps-to-ms LDM. These observations were assumed to indicate a decelerated recovery of pG subsequent to the isomerization process. The interpretation of the changes of the SCN signals from the LDMs is difficult, though. For the mechanical delays only tiny features (a more pronounced positive one and a very faint negative one) appear at about 50 ps (highlighted by a yellow dashed line in figure 7.9 on page 115) simultaneously with the changes of the E46 C=O. Since the sign of the features seems to be inverted with respect to the ones that occur at earlier lifetimes, they could indeed indicate

[10]The sub-ps component from GA is not shown since it was a bit faster than 600 fs, which was found to be approximately the resolution of the experiment, but it also showed an upshifted SCN signal (see figure F.19 on page 220 in the appendix).

a decreased signal size. In the LDM of the electronic delays relatively prominent features arise at about 80 ps in the SCN region, however, with a negative feature at 2069 cm^{-1} and a positive feature at 2077 cm^{-1}, which would rather imply an increasing intensity for the bleach and the induced absorption, respectively. Hence they show an opposite behavior than the SCN signal in the global analysis for the same time range. Presumably this is an artifact of the LDA for early electronic delay times due to the convolution with the IRF. Furthermore, these SCN features are slightly prior to the features in the CO region of E46 in the ps-to-ms LDM, which appear at approximately 200 ps. However, the SCN label seems to respond to the slow recovery of the dark state after unsuccessful entry into the photocycle that is caused by the replacement of the methionine.

In the ps-to-ms LDM of the SCN label, features appear at about 2 ns with a negative sign at 2074 cm^{-1} and a positive sign at 2084 cm^{-1}. Comparison with the fs-to-ns LDM reveals that these features have the same characteristics as the features that arise with 400 ps for the mechanical delays (both highlighted by yellow dashed lines). This matches earlier observations in which the features in the nanosecond time range were shifted to faster times when analyzing the mechanical delay data with LDA. The investigated LDM features are in good agreement with the global analysis of the electronic delays that shows an upshift of the SCN signal in about 2 ns. Simultaneously with the SCN signal, the same features appear in the LDM of the CC/CO region that were previously assigned to pR_1 formation. During this transition the chromophore structure and the surrounding hydrogen bonding network relax, which is likely to influence the microenvironment of the label. For the 61 ns component (light blue) from global analysis only changes of the baseline arise leaving the SCN signal unperturbed, supported by the LDM of the SCN region, in which no features appear at this lifetime.

For the early µs time range two components were obtained by global analysis of the SCN data. With a lifetime of 4 µs the SCN signal shifts considerably to higher wavenumbers and the signal size increases (green to yellow SADS) and with 21 µs it upshifts even more with the amplitude growing further (shift to orange SADS). Especially the induced absorption experiences a large blue-shift of 6 cm^{-1} between the maximum of the spectrum that decays with 4 µs at 2079 cm^{-1} and the one that is formed in 21 µs (maximum at 2085 cm^{-1}), while the amplitude is almost doubled. Examination of the LDM of the SCN region shows very prominent features at about 14 µs (negative around 2076 cm^{-1}, positive around 2086 cm^{-1}) matching the observed spectral change from GA. The feature corresponding to the 4 µs component (green) from global analysis is not clearly detectable, although the features with their maximum at 15 µs look a bit elongated towards faster lifetimes (highlighted by yellow dashed lines at 4 µs and 14 µs in figure 7.9). In the LDM of the not-standardized data (figure F.32 on page 232) the features for the two lifetimes are also not properly separated, but it seems that the larger features at 20 µs have a red-shifted tail (especially the positive one) at earlier lifetimes about 6 µs.

Comparison with the LDM of the CC/CO region at 4 µs shows that no separated features appear there either, but the features at 1590 cm^{-1}, assigned to the movement of R52, and at 1723 cm^{-1}, corresponding to changes of the C=O vibration of E46, are also stretched to faster lifetimes down to hundreds of nanoseconds. In the GA spectra of the CC/CO region, however, no additional component was found between the 531 ns component, that was interpreted as accelerated $pR_1 \rightarrow pR_2$ transition, and the 14 µs component, which

is associated with the deprotonation process. Investigation of the time traces of the raw data (figure F.22 on page 223 in the appendix) revealed an additional lifetime of 1.2 µs for the E46 bleach, besides the 31 µs lifetime that corresponds to E46 deprotonation. If the SCN kinetics on an early microsecond timescale are indeed real, they would presumably describe the decay of the pR_1 intermediate since the spectral changes of the protein and chromophore region as well as the decay time resemble the ones observed for WT-PYP. In this case it has to be inquired if the hundreds of nanosecond dynamics, that have no corresponding response of the SCN label, arise from a second accelerated pR_1 decay or have to be associated to another transition. Inspection of the time trace through the LDM at 1591 cm^{-1} and 1725 cm^{-1} (see figure F.26 on page 226 in the appendix) reveals only a small maximum around 500 ns before the major signal size is reached at approximately 11 µs for the R52 movement and at about 23 µs for E46 deprotonation.

The prominent SCN features at about 15 µs arise simulatenously with changes of the absorption band at 1590 cm^{-1} (positive feature), assigned to R52, and a bit faster than the bleach of E46 (negative feature at 1724 cm^{-1}) accompanied by small changes in the chromophore's C=O and the amide I region. Due to its proximity to R52, the label certainly senses the movement of this residue. In the transition from pR to pB' the distance between M100 and the charged side chain of R52 increases dramatically from approximately 4 Å to 10.5 Å.[11] The SCN signal is probably not only influenced by the alterations of the electrostatics due to the positive charge moving away, but with this movement it becomes more likely that water molecules are able to penetrate into the binding pocket when the gateway between binding pocket and solvent opens. Both the loss of a charged residue nearby and the potentially higher solvent exposure would lead to a blue-shifted absorption of the SCN [19, 23, 127] as it is observed here. Whether the label additionally detects the deprotonation of E46, which is further away, cannot be definitively resolved from the data, but seems to be rather unlikely. Protonation of the chromophore during this transition was found to be delayed with respect to E46 deprotonation appearing at approximately 80 µs, the SCN, however, does not show a response at this lifetime. Examination of the protein structure revealed that the distance between M100 and the phenolate oxygen of the chromophore is similar to the distance to the oxygen of E46, that becomes deprotonated (about 8 Å, calculated for pdb-file 1TS7). But seemingly, the label senses neither of both proton transfer processes, although they should have a large effect on the electrostatic environment. Besides the distance to the label, also the relative orientation of the nitrile group's dipole moment with respect to the induced electric fields, which vary with changes in the ionization state of E46 and the chromophore, could be responsible for the label not detecting these changes. To evaluate the relative orientations of the dipole moments, though, structural information about the labeled mutants and MD simulations would be necessary.

From the time-resolved experiments it can be concluded that the large blue-shift that was observed for the steady-state FTIR measurements between dark and signaling state (see figure 5.7 on page 65) arises already during the pB' formation and is not caused by the following global rearrangements of the protein. Besides it was found that the SCN label responds on the movement of the nearby charged residue R52 additionally allowing for penetration of solvent molecules into the chromophore binding pocket.

[11] For the pR states pdb-file 1TS7 (chain #2) and for pB' pdb-file 1TS6 (chain #2) were used [70]. Distances were calculated between atom CE of M100 and atom NH1 of R52 using Chimera 1.6.2.

On earlier timescales the label reacts to almost all transitions that are mainly localized at the chromophore or in its close environment. Hence, it senses the formation of the electronically excited state after photon absorption and relaxation processes of this intermediate, isomerization and other structural rearrangements of the chromophore leading to formation of I_0 and the relaxation processes in the chromophore binding pocket that result in the pR_1 state. Moreover, the significant decrease in signal size of the SCN label on a 100 ps timescale supports the observation that in M100C* the recovery of the dark state for the molecules that are not able to successfully enter the photocycle is dramatically delayed.

Following changes in the proximity of E46: V122C*

V122C* is located in the β5-sheet at the C-terminus and part of the residues forming the small hydrophobic cavity for E46. Characterization of the mutant revealed already that replacement of the valine by a cysteine led to a shift of the C=O mode of E46 (compare figure 4.2 on page 53) due to an altered hydrophobicity of its environment. Otherwise the mutation did not seem to influence structure, stability and function of PYP to a larger extent. Investigation of the vibrational lifetimes of SCN in V122C* (figure 6.1 on page 77) resolved that the label stays buried in the protein interior for the dark and the signaling state. Hence, V122C* was expected to be a good sensor for variations of the interactions between E46 and the chromophore and especially the deprotonation process of E46 during pB' formation.

The SCN label in V122C* responds directly to the formation of the electronically excited state pG* indicated by a difference absorption signal that is already present within the instrument response of the experiment. The first spectrum from global analysis with a lifetime > 600 fs (1 ps component in figure 7.10 on the next page) shows and increased absorption at 2083 cm^{-1} and a tiny bleach at either site that might be arise from narrowing of the absorption band. In the steady-state FTIR measurements two subpopulations were observed in pG with $\tilde{\nu}_{sd}$ at 2080 cm^{-1} and 2085 cm^{-1} (compare figure 5.6 on page 64). The narrowing of the absorption band in the pG* spectrum could hint to the movement in a more homogeneous environment where only one population exists.

For the 1 ps decay (light blue to green SADS in figure 7.10) mainly a decrease in the intensity of the difference signal, but no change in frequency is observed. This can be interpreted as partial recovery of the dark state because the absorption shifts back to the same position and shape as before photon absorption. In the LDM of the label this transition is split into two lifetimes that appear at 800 fs and 3 ps. The features at 800 fs can be interpreted with the narrowing of the SCN signal as the intensity at 2083 cm^{-1} increases (resulting in the positive feature in the middle) and the intensities of the two bleaches on either site become more negative (resulting in two negative features at 2076 cm^{-1} and 2089 cm^{-1}). Whereas the LDM features at 3 ps, with the positive feature at 2076 cm^{-1} and the negative one at about 2084 cm^{-1}, match a partial disappearance of the SCN difference signal, since the lower wavenumber bleach vanishes and the positive band of the spectrum decreases. This is in good agreement with the changes observed for the 1 ps decay from global analysis. The features at the red and blue end of the shown spectral window are caused by changes in the background signal and can be neglected in the interpretation. Comparison to the CC/CO region in the LDM reveals that both components arise simultaneously with the spectral

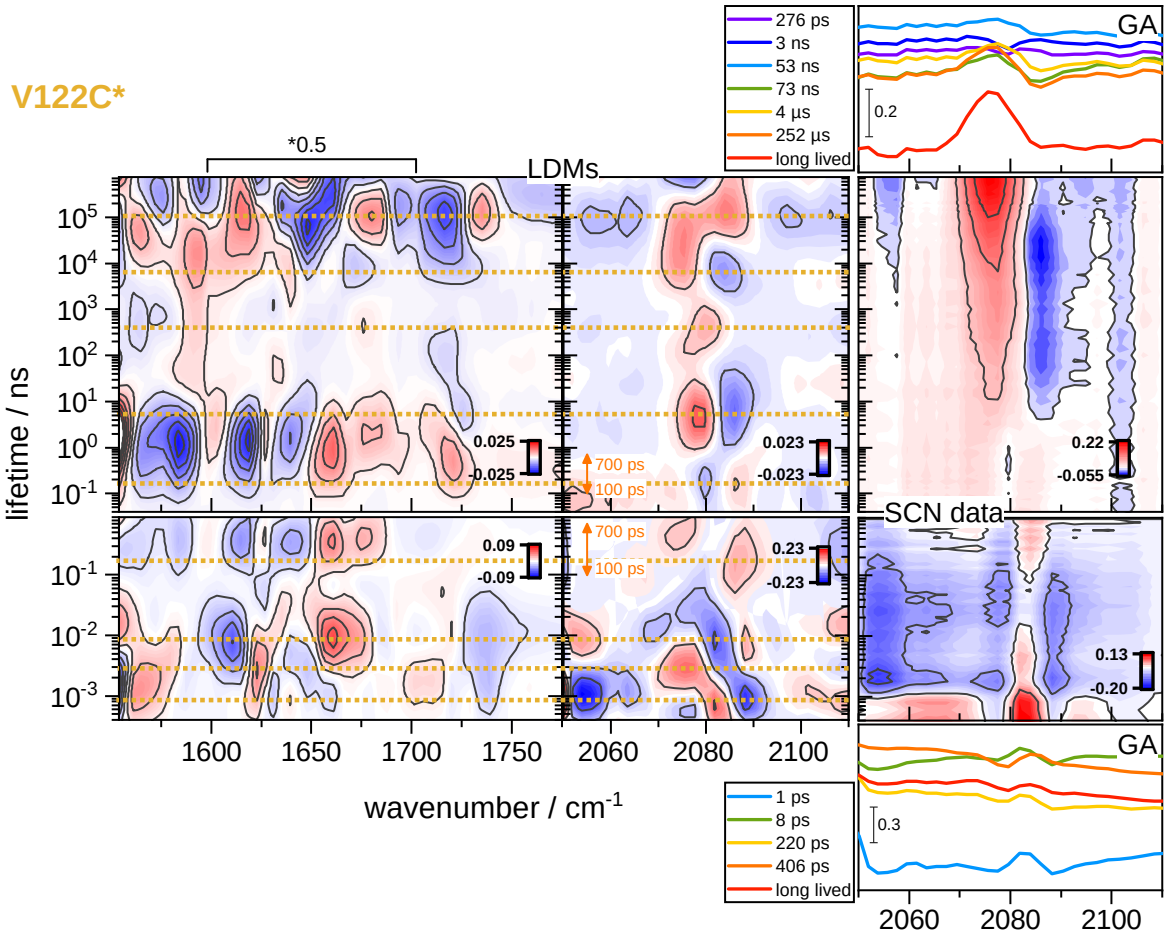

Figure 7.10: *Overview of transient vis-pump-IR-probe measurements with mechanical (bottom) and electronic delays (top) for V122C* in the CC/CO and SCN region. LDMs in the CC/CO region (first column, contour plot with 11 major levels) and the SCN region (second column, contour plot with 5 major levels, linear baseline subtracted) are shown. The corresponding L-curves are depicted in figures F.36 and F.37 in the appendix. The orange arrows display the same time window. The intensity of the amide I region in the electronic delay plot is scaled by a factor of 0.5. The yellow dashed lines at 800 fs, 3 ps, 9 ps, 170 ps / 170 ps, 5 ns, 430 ns, 7 µs, and 110 µs highlight features that appear simultaneously with changes in the SCN signal. Third column: Contour plot (5 major levels, linear baseline subtracted) of denoised data in the SCN region. For the SADS obtained from global analysis (GA) of the denoised SCN data only components > 600 fs for mechanical delay data (bottom) and > 50 ps for electronic delay data (top) are shown. Comparison of the CC/CO region with and without SCN label for the mutant V122C is depicted in figure 7.11 on page 130.*

changes that were previously assigned to the multiple decays of pG*. This is further supported by global analysis of the CC/CO region[12] where the 725 fs and 2 ps components in figure F.7 on page 208 in the appendix both show the typical features of a pG* spectrum comparable to WT-PYP. These multiple decays of pG* lead either to isomerization of the chromophore forming I_0 or to a direct return to pG as discussed for the WT [12, 13, 62]. Hence, photon absorption and relaxation of the electronically excited state seem to affect the hydrophobic cavity comprising E46.

[12]Note here that the shifted absorption of the C=O vibration of E46, that was already observed in the FTIR measurements, leads to the appearance of the difference signal of E46 at 1715 cm^{-1} / 1735 cm^{-1} for mechanical delays.

The following component with a decay time of 8 ps (green) in the GA of the SCN region exhibits a further decrease of the difference signal. At a corresponding lifetime (9 ps; highlighted by a yellow dashed line in figure 7.10) a negative feature also appears in the LDM at 2083 cm^{-1} and a small positive one at higher wavenumbers possibly indicating a decrease in signal size. Simultaneously, the features assigned to the isomerization marker band at 1607 cm^{-1} and the chromophore's C=O vibration at 1660 cm^{-1}, that arises when the hydrogen bond towards the protein backbone is broken, occur in the CC/CO region. This indicates that the label detects the isomerization process that leads to formation of the I_0 intermediate. However, it is unexpected that this tranisition causes a decrease in signal size of the SCN difference signal. One explanation could be an altered orientation of the E46 in pG* due to the weakening of the hydrogen bond towards the phenolate of the chromophore, that changes back to its original conformation during I_0 formation when the hydrogen bonding strength recovers as it is implied by the decreasing difference signal of the E46 C=O vibration.

During the 220 ps decay the SCN difference signal is shifted to higher wavenumbers (yellow to orange SADS for fs-to-ns GA). This upshift of about 2 cm^{-1} is also observed in the global analysis of the electronic delays with a time constant of 276 ps (purple to dark blue SADS). In the LDMs a corresponding feature appears at 175 ps for electronic delays and maybe at the same lifetime for mechanical delays although there is only a positive feature visible at the same wavenumber (2086 cm^{-1}) as the positive feature in the ps-to-ms LDM. Examination of the CC/CO region with global analysis (see figures F.7 and F.9) revealed, however, only tiny changes on a 89 ps (93 ps for electronic delays) timescale. These changes mainly appear for the phenolate ring modes at 1575 cm^{-1}, the chromophore's C=O vibration around 1660 cm^{-1}, the chromophore's C=C vibration at 1607 cm^{-1}/1621 cm^{-1}, and the C=O vibration of E46 (only visible for the mechanical delays when zoomed in). In the LDMs in figure 7.10, it is not possible to distinguish corresponding features from the ones of the pR formation occurring at 1 ns for electronic delays and shifted to earlier times (around 360 ps) in the LDM for mechanical delays. The features in the ps-to-ms LDM resemble the ones observed for WT' quite well.

Whereas the interpretation of the tiny spectral changes of protein and chromophore bands made the existence of the intermediate $I_0^{\ddagger}$ rather unlikely, the occurrence of changes in the label's environment is a clear indication for the formation of another intermediate besides I_0 and pR_1. These findings support the studies which suggested that $I_0^{\ddagger}$ is formed in about 200 ps [8, 87], while others found no evidence for its existence [13, 62]. The small alterations in the CC/CO region indicate changes of the chromophore structure probably due to relaxation processes and the further decrease of the E46 C=O signal implies changes in the strength of the hydrogen bond towards the chromophore. It is very likely that the SCN in the proximity of E46 detects relaxation processes that might lead to changes in the orientation of the glutamate. Thus, the strengthening of the hydrogen bonding interaction between E46 and chromophore probably results in a smaller distance between the two of them and therefore in a slightly altered orientation of E46. The upshifted SCN signal suggests an environment that becomes more hydrophobic at about 250 ps due to the movement of E46. This observation agrees with the interpretation from transient visble absorption studies assuming that the $I_0 \rightarrow I_0^{\ddagger}$ transition is caused by changes in the interaction between chromophore and protein [8, 87].

On the early nanosecond timescale a large red-shift of the SCN signal is observed in the SADS (dark blue to light blue). Whereas the bleach and induced absorption of the difference signal in the $I_0^‡$ intermediate were positioned at 2079 cm^{-1} and 2086 cm^{-1}, respectively, they flipped their order and appear at 2086 cm^{-1} (bleach) and 2077 cm^{-1} (induced absorption) within 3 ns. This downshifted feature is also present in the LDM of the SCN region at 5 ns. A cautious comparison with the LDM in the CC/CO region reveals that most features that were prviously assigned to the $I_0/I_0^‡ \rightarrow pR_1$ transition arise already at about 1 ns and simulatneously with the SCN signal mainly a small negative feature at 1725 cm^{-1}, corresponding to the C=O vibration of E46, appears. Global analysis of V122C* also revealed that there are two early nanosecond components at 1.6 ns and 4.5 ns (see figure F.9 on page 210 in the appendix). The latter shows a slightly positive absorption band at about 1720 cm^{-1} in the CO region of E46, where typically the bleach of E46 is observed, and which does not appear in WT' or any other mutant, but is also present in the unlabeled V122C (see figure F.9). This positive signal might hint to changes in the hydrogen bonding strength compared to the dark state and therefore variations in the orientation of the carboxylic group following the relaxation processes during pR formation. The replacement of V122 seems to influence conformational changes of the glutamate on this timescale, which is not surprising since it also has an effect on the environment of E46 indicated by the shift of the C=O vibration that occurs already in the dark state. Therefore the SCN label probably responds to changes in its environment that might be unique for the V122C mutants, but are likely to be triggered by the relaxation processes of chromophore and hydrogen bonding network during the pR_1 formation.

For the subsequent two decay times at 53 ns and 73 ns (light blue to green to yellow in figure 7.10) obtained by global analysis only an increase in the signal size of the SCN occurs. In the LDM of the SCN region no features appear on a similar time range. However, at about 430 ns a positive feature occurs in the LDM at 2079 cm^{-1} (highlighted by a yellow dashed line in figure 7.10), lacking a negative corresponding feature, that could indicate a broadening of the higher wavenumber flank of the positive absorption band. On this timescale hardly any protein and chromophore dynamics are observed in the GA spectra (see figure F.9 on page 210) and in the LDM of the CC/CO region only small changes around 1565 cm^{-1} (negative feature), at 1590 cm^{-1} (positive feature), which is assigned to changes of R52, and maybe in the C=O region of the chromophore and of E46 can be found.

With a lifetime of 4 µs in the global analysis and at 7 µs in the LDM a small red-shift of the SCN signal is observed. In the same time range significant changes of the protein occur at 1596 cm^{-1} associated with the movement of R52 which allows water molecules to penetrate into the chromophore biding pocket and at 1720 cm^{-1} implying changes in the hydrogen bonding strength or deprotonation of E46 similar to the changes observed in WT' in the early µs time range. The appearance of alterations in the SCN label's environment on this timescale supports the findings that the $pR_1 \rightarrow pR_2$ transition (in a sequential model) clearly involves changes affecting E46. If the red-shift of the SCN signal would be caused by deprotonation of E46 and the consequent formation of a negatively charged side chain this could be some evidence that probably a parallel model should be applied for formation of the two pR states and this early deprotonation process corresponding to the fast $pR_1 \rightarrow pB'$ transition. However, since it cannot be excluded that the shift is caused by changes in the orientation of the glutamate, the question which model has to be applied still remains.

In the last transition that appears in the global analysis, the induced absorption of the difference signal at 2076 cm^{-1} increases drastically with a decay time of 252 µs, while the bleach at the blue side of the signal vanishes. The features that are visible in the LDM, highlighted by a yellow dashed line at 100 µs in figure 7.10 on page 125, are consistent with the observed spectral changes. On the same timescale many features arise in the LDM of the CC/CO region. The induced absorption of the C=O vibration of E46 which was assigned to the movement of the glutamate into a more hydrophobic environment appears in V122C* at 1735 cm^{-1} (positive feature) and, in contrast to all other investigated samples, not prior to the deprotonation step of the $pR_2 \rightarrow pB'$ transition, but simultaneously with the C=O bleach (negative feature). Additionally, changes in the chromophore C=O region indicating conformational variations of the chromophore and in the amide I region arise. It is not possible to clearly distinguish which of these synchronous processes finally influence the SCN response, but certainly the movement and deprotonation of E46 play a crucial role. The increase in signal size hints towards an increased extinction coefficient, which was found to be sensitive to changes in the electric field environment [23–25].

Comparison between the long lived SCN spectrum (red) from global analysis of the time-resolved data and the difference spectrum between pG and pB from the steady-state FTIR measurements (see figure 5.6 on page 64) yields that the spectra look quite similar except for the missing small bleach at the higher wavenumber side of the spectrum. Since this feature is relatively narrow, it might have disappeared due to the lower resolution of 2 cm^{-1} in the pump-probe experiments. Besides the pixel-dependent spike-like structure on the data is very distinct for the SCN spectra of V122C* as it can be seen in figure F.14 on page 215 in the appendix, so that the small bleach could vanish in this structured noise and cannot be brought out with the three point moving mean denoising method.

In V122C* the positive feature assigned to chromophore protonation at 1565 cm^{-1} appears in between the changes of the E46 C=O vibration on a fast microsecond timescale, that might be caused by deprotonation, and the later deprotonation step at hundreds of µs. The time traces of the the raw data revealed, as well, that the trace at 1725 cm^{-1} decays with two components of 14 µs and 260 µs, whereas the protonation band arises with about 70 µs (see figure F.22 on page 223 in the appendix). In WT' and the other mutants, the chromophore protonation occurred mostly subsequent, but never prior to E46 deprotonation. This might indicate that, indeed, a fast and a slow pathway (or population) of pB' formation exist, as suggested by the parallel model, with part of the molecules following the accelerated $pR_1 \rightarrow pB'$ transition and the rest the $pR_2 \rightarrow pB'$ transition, which is predominant in WT-PYP. However, it has to be mentioned that for the slow pB' formation step no feature corresponding to the protonation of the chromophore, typically appearing at 1565 cm^{-1}, is found in the LDM. This might, of course, be due to a delayed proton transfer to the chromophore that does not arise in the investigated time range anymore, but also in the global analysis spectra of the CC/CO region (see figure F.9 on page 210 in the appendix) it seems that the changes for this absorption band are less pronounced in the SADS of the last two components than for the other samples that were analyzed. On the other hand, if the protonation step corresponding to the slow E46 deprotonation process is indeed missing, this could indicate that the parallel model is not supported by the data. Another explanation for the fast protonation step could then be that due to possibly different conformations of

E46 resulting from the mutation of V122, protonation of the chromophore is facilitated and does not depend on the movement of E46 into a more hydrophobic environment and its deprotonation to be triggered.

In the standardized LDM of the CC/CO region, the features on the early microsecond timescale are not clearly separated from the following features, especially for the E46 C=O. Thus they are compared to the LDM of the not-standardized data (see figure F.33 on page 233 in the appendix). There the features corresponding to the R52 movement and the changes of E46 occur at 17 µs and are nicely distinguishable from the features arising in the hundreds of µs time range and corresponding to the $pR_2 \rightarrow pB'$ transition.

In conclusion, the SCN label in V122C* reacts mainly to changes that involve E46 as it was expected due to the close proximity between the label and the glutamate. Therefore it responds to the formation of pG* and its relaxation processes as well as I_0 formation, which all comprise changes in the strength of the hydrogen bond between E46 and the phenolate of the chromophore and probably influencing the orientation of E46. The small upshift of the SCN signal around 250 ps, which appears in a time range that cannot be associated to any noticeable changes of the protein or the chromophore, hints towards the existence of the $I_0^{\ddagger}$ intermediate that is still under debate in literature. Further the label reacts slightly delayed to the ns-kinetics of the pR_1 formation, possibly to changes of E46 that only occur after replacement of V122. Since the $pR_1 \rightarrow pR_2$ and the $pR_2 \rightarrow pB'$ transitions involve significant changes of E46, especially its deprotonation during the latter, both transitions are detected by the SCN label. Furthermore, the question is raised once again if not a concurrent model should be favored with the simultaneous formation of both pR states and two different pathways leading to pB'.

Since determination of the labeling efficiency with mass spectrometry revealed that only about 50 % of V122C* were labeled (at least for the measurement of the electronic delays), additional measurements for the unlabeled mutant V122C were performed in the CC/CO region to investigate if the kinetics with and without SCN label differ from each other. In figure 7.11 on the following page the LDMs of V122C* and V122C are compared. The global analysis results for both are depicted in figure F.7 on page 208 for the mechanical delays and in figure F.9 on page 210 for the electronic delays. The features observed in the LDMs at early lifetimes up to the nanosecond time range are very consistent for the labeled and the unlabeled mutant. In the GA spectra assigned to pG* the depleted absorption at 1696 cm^{-1} is more pronounced for V122C* than for V122C or the other samples. In calculations it was found that this frequency might be associated with the C=O stretch vibration of a chromophore with relaxed planar geometry which is present in the I_0 state [13]. If the absorption could also occur from an extremely red-shifted C=O vibration of E46 is rather questionable since the typical wavenumber range for Glu-COOD is located between 1706 cm^{-1} and 1775 cm^{-1} [183]. However, in the electronically excited state, in which the hydrogen bond between E46 and the phenolate of the chromophore is weakened, this C=O vibration is influenced to a small extent by the incorporation of the SCN label. The small feature in the CO region of E46 that appears at about 5 ns in the LDM for the labeled mutant and is associated with a red-shift of the SCN label, is not visible in the LDM of V122C. Comparison of the GA spectra shows, however, that also in V122C, besides

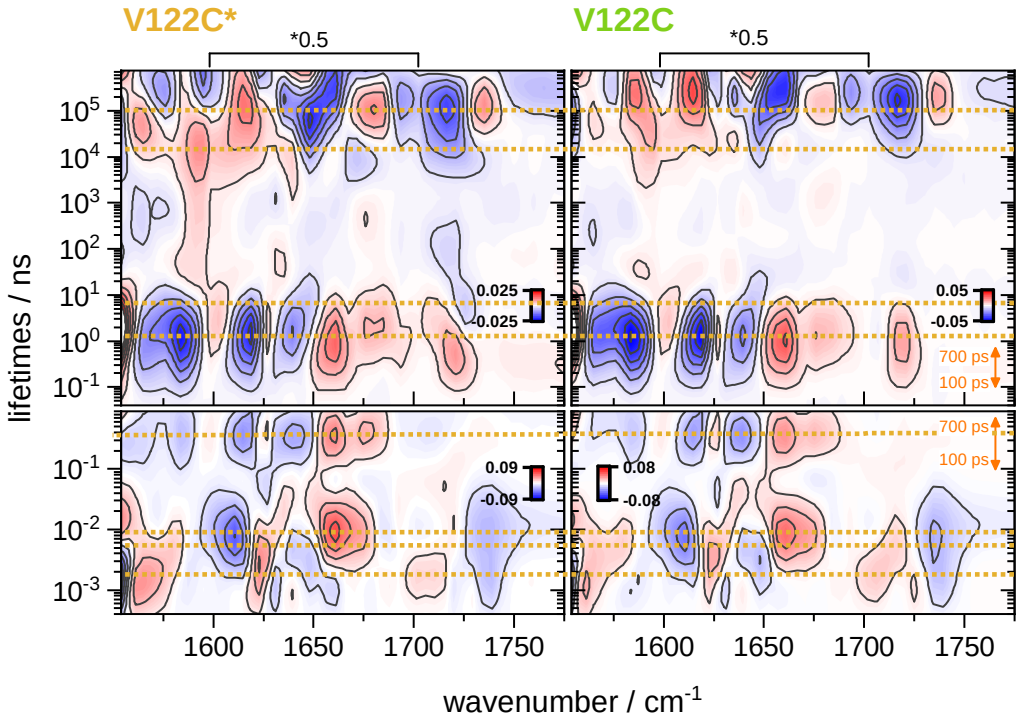

Figure 7.11: *Comparison of the LDMs in the CC/CO region (contour plots with 11 major levels) of V122C* and unlabeled V122C for mechanical (bottom) and electronic delays (top). The corresponding L-curves are depicted in figure F.36 in the appendix. The orange arrows display the same time window. The intensity of the amide I region in the electronic delay plot is scaled by a factor of 0.5 for both samples. The yellow dashed lines at 1 ps, 3 ps, 9 ps, 370 ps / 1 ns, 6 ns, 15 µs, and 120 µs highlight prominent features.*

the 1 ns component, a component with a decay time of 5 ns (light blue SADS in fig: GA mechanical pump-probe 2 appendix) appears which displays the the small positive band of the C=O vibration of E46 around 1720 cm^{-1} similar to V122C*.

On the microsecond timescale the kinetics of V122C* and V122C slightly differ. In the labeled mutant components of 13 µs, 69 µs and 311 µs are observed with GA, while the unlabeled one shows a 3 µs, 34 µs and 410 µs component indicating that the faster processes are decelerated for the labeled mutant and the slower process becomes accelerated. Examination of the time traces from the raw spectra (see figure F.22 on page 223 in the appendix) reveals, though, that the changes of the C=O vibration of E46 on the early microsecond timescale, that corresponds to the decay of the pR_1 state, are similar for both V122C mutants, but appear slightly delayed with respect to WT' and the other mutants. Further, the accelerated protonation of the chromophore occurs with similar lifetimes of 70 µs (V122C*) and 80 µs (V122C). Hence, both kinetics seem not to be influenced by labeling of the V122C mutant. For the slower deprotonation step and movement of E46, on the other hand, this is different. Here, indeed, a faster deprotonation is observed for V122C* with a decay time of 260 µs obtained by fitting the time traces, while for V122C the decay time is 320 µs. In the LDMs it is also visible that the E46 deprotonation is slightly delayed for the unlabeled mutant and the upshifted absorption of E46 at 1735 cm^{-1}, which is attributed to the movement of E46 into a more hydrophobic environment, appears a little later, as well. Overall the differences in the measured kinetics between the labeled V122C* and the unlabeled V122C appear mainly during pB' formation for changes that are directly related to E46, but they

are relatively small when comparing them to the differences between various mutants and the WT/WT', concluding that the lower labeling efficiency does not alter the protein and chromophore dynamics of V122C* significantly.

Site-specific photocycle model

After the dynamics of several photocycle transitions were identified by investigation of WT-PYP, local structural information of the transitions were resolved due to the response of the SCN label at different locations within the protein. Hence a "site-specific" photocycle model could be derived as shown in figure 7.12 on the following page with each colored arrow representing the changes of the SCN label in the corresponding mutant that could be assigned to the respective transitions.

Excitation of PYP with blue light is probed by the labels in V57C*, M100C* and V122C*. All three labels are located in the chromophore binding pocket and thus are sensitive to changes of the chromophore's polarization and hydrogen bonding interactions that are altered in the electronically excited state pG*. Therefore the labels also react to relaxation processes of pG* decaying back to the dark state or towards the following intermediate in the photocycle. Due to their proximity to the chromophore or to residues that are involved in the stabilization of the chromophore structure, the labels of all three mutants respond to the *trans-cis*-isomerization of the chromophore and the related structural changes in the binding pocket resulting in the intermediate I_0. For M100C* a significantly delayed recovery of the dark state is detected most likely after isomerization, for molecules that are probably not able to enter the photocycle successfully.

All three labels in V57C*, M100C* and V122C* also sense the following relaxation processes of the chromophore structure and the surrounding hydrogen bonding network, although the influence on V57C*, which is located further away from the chromophore and E46 is rather small. With the label in V122C* strong evidence was found that the postulated $I_0^{\ddagger}$ intermediate probably exists. This intermediate is formed in between I_0 and pR_1 resulting from relaxation processes that influence the proximity of E46, which is connected to the phenolate of the chromophore *via* a hydrogen bond, and could not be found by examination of protein and chromophore vibrations. The decay of pR_1 that leads to formation of pR_2, when assuming a consecutive model, is definitely sensed by the label in V122C* further encouraging the observation that this transition involves changes in the environment of E46 next to changes that most likely occur for the residue R52 in the binding pocket. Latter supports the interpretation that the kinetics observed for the SCN label in M100C* with a few microseconds possibly correspond to the same transition since the label is close to the positively charged side chain of R52. However, investigation of the protein vibrations rather implies an accelerated $pR_1 \rightarrow pR_2$ transition of about hundreds of nanoseconds that is not detected by the label.

The subsequent formation of pB' is the first transition that is sensed by the SCN label in all investigated mutants. Depending on the location, though, the label responds to different processes during this transition. Due to the replacement of the methionine, M100C* was found to have a significantly accelerated $pR_2 \rightarrow pB'$ transition compared to WT-PYP or the other mutants. The label seems, albeit in the proximity of the chromophore, not to react to the proton transfer processes, but to the movement of the nearby R52 and probably

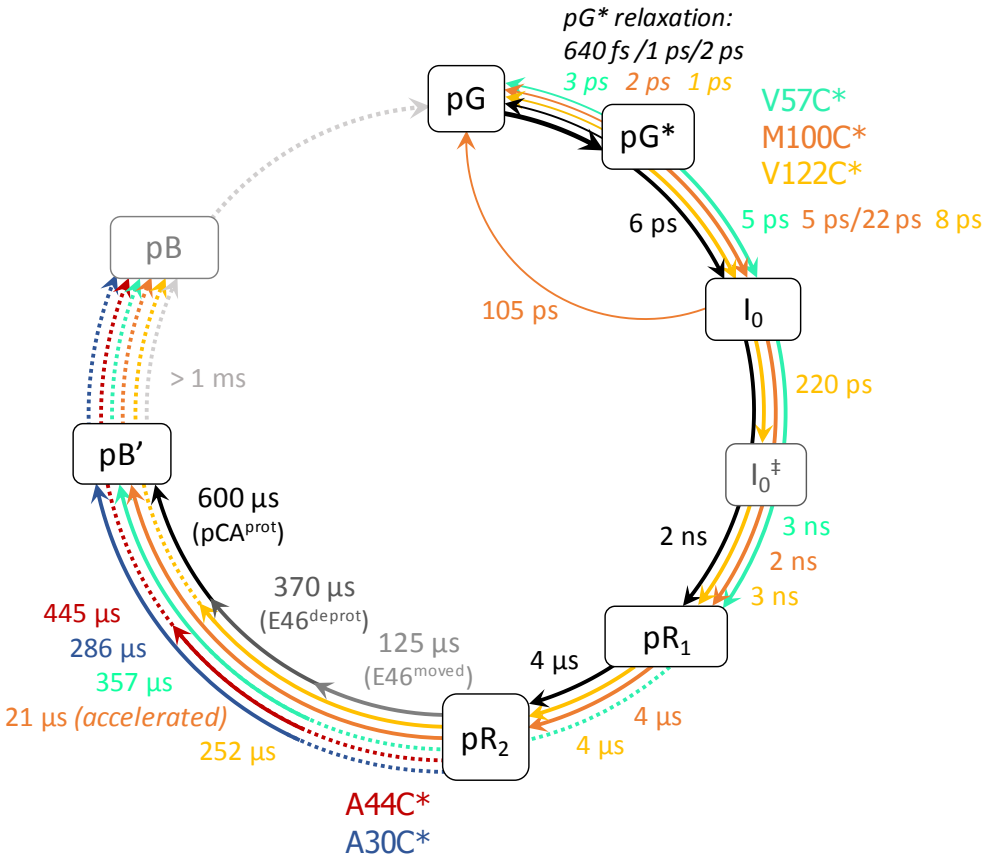

Figure 7.12: *Site-specific photocycle model obtained by the kinetics of the SCN label for all investigated mutants. Each colored arrow represents changes detected by the SCN label for the corresponding mutant. Dotted lines are used when the SCN signal is present during a transition, but does not sense any changes. The given lifetimes for the different transitions were obtained by GA of the SCN data. The lifetimes given for "pG* relaxation" could correspond to the decay to pG as well as to I_0 (multiple formation steps). The formation of pB' is accelerated in M100C* and the SCN label detects probably non of the kinetics associated with the three steps depicted here, but rather the movement of R52. In black and gray the photocycle model (sequential) that was previously derived for WT-PYP is shown. The lifetimes of the WT-kinetics for the $pR_2 \rightarrow pB'$ transition including the movement of E46 into a more hydrophobic environment ($E46^{move}$; light gray), the deprotonation of E46 ($E46^{deprot}$; dark gray) and the protonation of the chromophore (pCA^{prot}; black) were taken from the not-standardized LDM (figure F.28), the other lifetimes were obtained by GA (figure 7.2). All lifetimes given here were determined in D_2O.*

the resulting penetration of water molecules into the binding pocket that also accompanies the pB' formation. This higher solvent accessibility of the binding pocket is possibly also detected by the label in V57C*, but cannot clearly be distinguished from other structural changes which could influence the label's environment as well. The SCN labels in V122C* and A44C* respond to the deprotonation of E46, which was found to be most likely not the proton source for chromophore protonation due to its delayed occurrence. In V122C* it additionally senses the movement of E46 into a more hydrophobic environment, which occurs simultaneously with deprotonation in this mutant. Because of its orientation away from the chromophore binding pocket into the cavity between N-terminus and the rest of

the protein, it is assumed that the label in A30C* detects the movement of the N-terminal region appearing prior to the overall conformational changes of the protein and leading to a higher accessibility of the aforementioned cavity.

Since the time-resolved vis-pump-IR-probe experiments allowed only to measure up to 750 µs, it was not possible to follow the dynamics of the pB' $\rightarrow$ pB transition. However, the steady-state experiments, that were discussed earlier, in this thesis showed the spectral changes occurring for the SCN labels in the signaling state pB. Essentially, the changes in the environment of the investigated labels are rather small for the proceeding dynamics until pB is formed.

7.1.4 Solvent Dynamics

Global analysis of the protein and chromophore vibrations as well as the SCN signals reveal additional lifetime components that show hardly any spectral changes and therefore exhibit no corresponding features in the LDMs. Moreover, in the SCN region, where the signals are rather small, broad features are observed in the LDMs of the electronic delays[13] when not suppressed by subtraction of a linear baseline connecting the first and last pixel of the spectrum as it is depicted in figure F.27 on page 227 in the appendix. These continuously changing baseline dynamics are most likely caused by the underlying broad water (D_2O) absorption band. The baseline shifts provide information about the timescales of water heating resulting from the deposition of energy into the chromophore by the visible pump pulse and its subsequent distribution to the protein and its surrounding water. Here only a rough overview about these heating dynamics in PYP is given by briefly comparing them to the ones observed in literature. For a more detailed insight into the water dynamics, a more sophisticated data analysis with possibly additional measurements and calculations should be applied, but this is beyond the scope of this thesis.

For the heat transfer of excess energy from a protein's chromophore to its direct solvent environment, two different processes with time constants of a few picoseconds and tens of picoseconds were found in previous studies (*e.g.* for myoglobin and hemoglobin in D_2O) [184, 185]. The faster process is suggested to arise from non-diffusive energy transfer probably due to collective motions of the protein, whereas the slow process is assigned to diffusion of heat through the protein. In the range between 100 ps to 2 ns a thermal equilibrium at the higher average temperature was reached [184]. Examination of the mechanical delay data revealed several components in the 1 - 3 ps time range that were attributed to relaxation processes of pG*. Since the spectral changes are partially rather small it might be that also non-diffusive energy transfer to the solvent contributes to the relaxation. Further, a time constant between 15 ps and 60 ps was obtained by global analysis of the CC/CO region of all investigated samples and also in the SCN region for the mutants. The GA spectra show only very small spectral changes and in the LDMs no corresponding features are observed implying that these lifetimes could indeed arise from solvent dynamics due to heating of the water by energy diffusion.

[13] For the mechanical delay data the linear baseline had to be subtracted beforehand to obtain proper LDMs.

Particularly striking in the transient vis-pump-IR-probe experiments are the lifetimes in the nanosecond time range. While the first ns-component of about 1 - 3 ns can unambiguously be associated to the spectral changes of pR_1 formation, additional components occur around 10 ns and in hundreds of nanosecond, timescales on which no features appear in the LDMs at all for WT-PYP and most of the mutants. In temperature jump experiments in D_2O, Petty and Volk [186] observed similar time constants after increasing the temperature by 1 K. They assigned an 8 ns component to structural relaxation of the protein backbone after heating and assumed that the 200 ns component was caused by relaxation processes of helical structure elements. However, these processes are accompanied by changes of the amide I band. Close inspection of the spectra in the CC/CO region obtained from global analysis show that there might be tiny changes in the amide I region, but they are probably too small to appear in the LDMs. Cooling of the sample due to heat diffusion out of the probe region is found to occur on a 100 µs to 10 ms timescale [184, 186].

7.1.5 Photocycle Dynamics in H_2O

Most of the transient vis-pump-IR-probe experiments presented in this thesis were carried out in D_2O due to its better transmittance in the spectral windows of interest with respect to H_2O allowing for larger sample thicknesses and thus larger signal sizes. However, since the step-scan FTIR measurements, that are discussed later on, and also some IR spectroscopy studies in literature were performed in H_2O, samples of WT, WT' and A44C* were additionally examined in H_2O (at least for electronic delays) for better comparison. SADS from global analysis of all investigated samples are shown in the appendix in figure F.39 on page 239 for the CC/CO region and in figure F.41 on page 241 for the SCN region of A44C*.

Spectrally two of the most prominent differences between D_2O and H_2O are the frequency of the C=O vibration of E46 and the C=N vibration of R52 as shown in figure 7.13 on the facing page, which compares the mechanical and electronic delays for WT in both solvents[14]. The bleached absorption of E46 is upshifted by 10 cm^{-1} to 1736 cm^{-1} for COOH. The band shift from 1587 cm^{-1} to 1595 cm^{-1} that was identified to correspond most likely to the movement of R52 in D_2O, was proposed in previous IR studies to appear from 1685 cm^{-1} to 1693 cm^{-1} in H_2O [12, 172]. Further differences occur for the C=O vibration of the chromophore that shifts from 1643 cm^{-1} to 1660 cm^{-1} after excitation similarly for both solvents, but especially the depleted absorption seems to be less pronounced in H_2O. This is also apparent for the mechanical delays, which were only measured for WT. The smaller intensities of features in the spectral window around 1643 cm^{-1} are most likely caused by superposition of the broad H_2O absorption band, as it is shown in the introduction in figure 1.5 on page 13, whereas D_2O has a significantly lower absorption in this region.

For the fast photocycle processes, the dynamics found in H_2O resemble the ones in D_2O. Relaxation of the electronically excited state pG* occurs with a time constant of 2 ps in global analysis (light blue SADS in figure 7.13), particularly characterized by the vanishing of the depleted absorption around 1664 cm^{-1}, which is associated with the chromophore's C=O vibration, and the decrease of the difference signal of the carboxyl group of E46

[14] The LDMs for electronic delays of WT' in H_2O and D_2O are compared in figure F.38 on page 238 in the appendix.

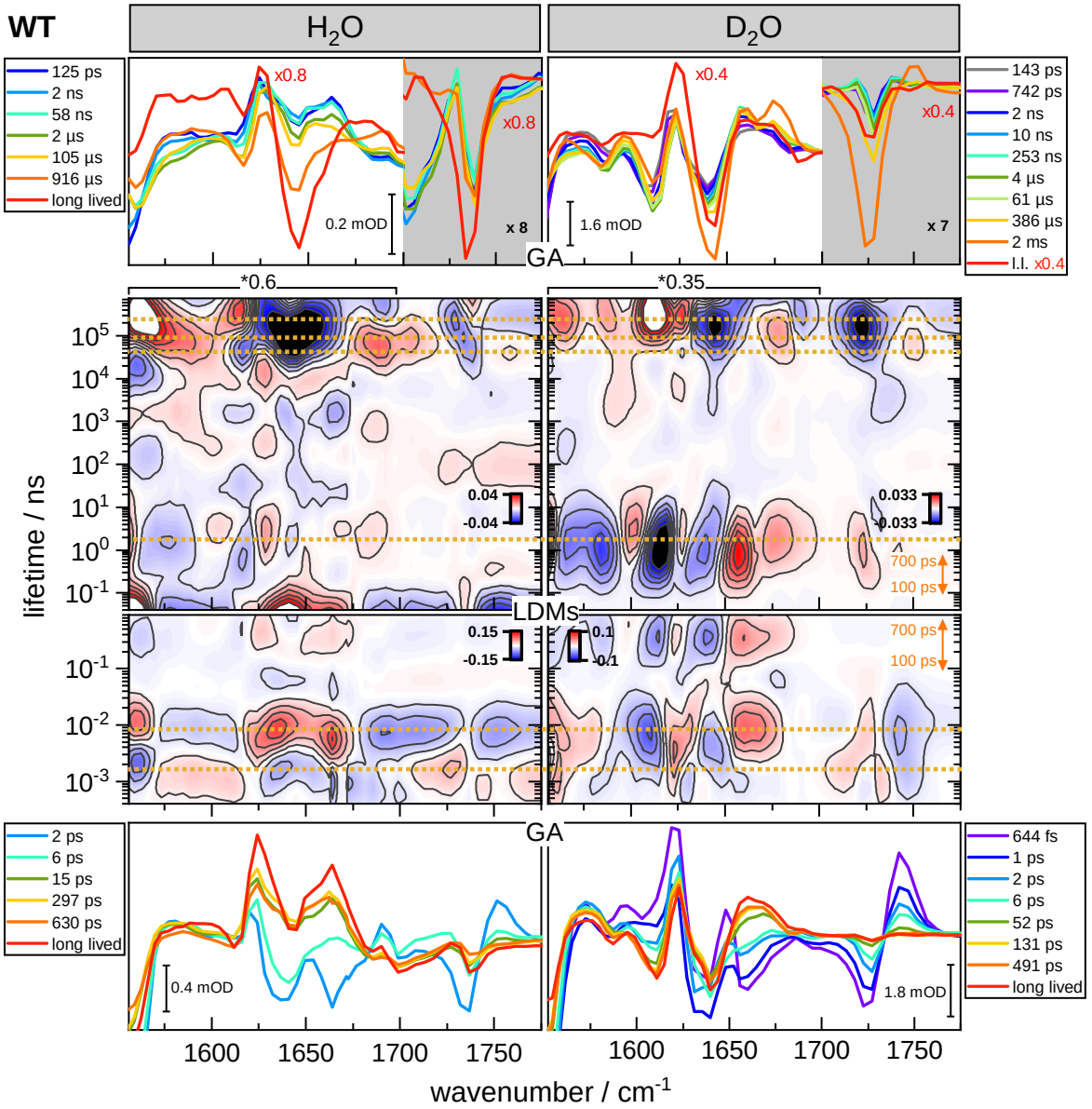

Figure 7.13: *Comparison of SADS from global analysis (GA, top and bottom row) and LDMs (second and third row) for WT in H_2O (left) and D_2O (right) in the CC/CO region for mechanical (lower two rows) and electronic delays (top two rows). For the SADS only components > 600 fs for mechanical delay data (bottom) and > 50 ps for electronic delay data (top) are shown. In the electronic delay spectra the long lived component is scaled with a factor of 0.8 for H_2O and 0.4 for D_2O and the ordinates for the CO region of E46 (from 1700 cm^{-1} to 1775 cm^{-1}, shaded in gray) are enlarged by a factor of 8 and 7, respectively, for better visualization. All LDMs are plotted with 11 major and 5 minor contour levels. The corresponding L-curves are depicted in figures F.36 and F.44 in the appendix. The orange arrows display the same time window. For better visualization the intensity of the amide I region in the electronic delay plots is scaled by a factor of 0.6 for H_2O and 0.35 for D_2O. Yellow dashed lines at 2 ps, 9 ps (mechanical delays) / 2 ns, 45 µs, 90 µs, and 240 µs (electronic delays) highlight prominent features appearing in H_2O.*

due to recovery of the hydrogen bond towards the chromophore. The I_0 intermediate is formed in 6 ps (cyan SADS for both solvents), the same time constant that was observed for WT-PYP in D_2O (compare figure 7.2 on page 91), indicated by the emergence of the broad positive absorption band around 1660 cm^{-1}, that appears with the disruption of

the hydrogen bond between the chromophore's C=O and C69. The changes in the *trans-cis*-isomerization marker band at about 1610 cm^{-1} are not as pronounced as in the D_2O spectra, probably due to the large H_2O background in this spectral region. However, in the LDM of the mechanical delays a negative feature at this frequency is also visible in H_2O, arising simultaneously with the positive feature around 1665 cm^{-1} corresponding to hydrogen bond breaking at about 9 ps.

Not only the early photocycle transitions, but also the formation of pR_1 appear at similar times in H_2O and D_2O. Global analysis revealed a time constant of 2 ns for this transition (light blue SADS for H_2O and dark blue for D_2O for electronic delays in figure 7.13) and in the LDMs of both solvents similar features occur at this lifetime, although the smaller intensity in H_2O complicates the distinction from the background noise. On the early microsecond timescale a lifetime of 2 µs is obtained by global analysis (dark green SADS). The spectral changes are rather small as found in D_2O as well. The most obvious changes occur at about 1690 cm^{-1}, which is assigned to the C=N vibration of R52 and is in good agreement with the observations in D_2O that R52 moves during the relaxation of pR_1, most likely slowly opening the gateway that separates the surrounding water from the binding pocket [12, 82, 172]. The chromophore's C=O vibration is downshifted in H_2O with respect to D_2O with the low wavenumber population occurring at about 1651 cm^{-1} (instead of 1659 cm^{-1} in D_2O) and the high wavenumber population at about 1663 cm^{-1} (instead of 1674 cm^{-1}). Due to the shift and the large underlying H_2O background, the intensity ratio of both populations changed after solvent exchange. Additionally, small variations in the spectra are observed in the spectral region around 1590 cm^{-1}, possibly arising from alterations of various polar side chain groups [11]. In contrast to the measurements in D_2O, almost no changes occur in the CO region of E46 for the µs-component. Either the spectral changes are too small to be detected, have a significantly faster time constant in H_2O, or E46 is less effected by theses structural changes in H_2O. The latter two are however unlikely, as no earlier spectral changes are detected and the deuteration is not expected to significantly alter the structural changes occurring during the photocycle transitions. The LDM does not help to facilitate the interpretation in this case, since the spectral features in this time range cannot unambiguously be assigned to the $pR_1 \rightarrow pR_2$ transition due to their low intensity and a high background noise.

The processes occurring during the $pR_2 \rightarrow pB'$ transition were found to take place on a hundreds of microseconds timescale. Global analysis revealed a 105 µs component for WT and WT' (see figure F.39 on page 239 in the appendix and yellow SADS in figure 7.13), that is faster than the lifetimes obtained in D_2O involving the main changes of this transition (386 µs for WT and 193 µs for WT' as shown in figure 7.2 on page 91). On this timescale protonation of the chromophore appears, indicated by the rise of the positive band at 1578 cm^{-1} in the SADS (the positive feature around 1580 cm^{-1} in the LDM of H_2O appears earlier in time than in D_2O), which is assigned to the phenolate ring modes of the chromophore. The upshifted absorption of the C=O vibration of E46 at 1756 cm^{-1} occurs in the same SADS (in the LDM the small red feature has its maximum shifted to later times in D_2O), implying the movement of the glutamate into a more hydrophobic environment. Surprisingly, for the E46 bleach, which appeared with the same component than the aforementioned processes in D_2O, almost no changes are observed at 105 µs, but it increases only with the ms-component (which already exceeds the time range of the experiment) accompanied by a small downshift and broadening of the bleach. Considering the kinetic

isotope effect one would expect faster proton transfer processes in H_2O than in D_2O including chromophore protonation as well as deprotonation of E46, since the heavier mass of the deuterium atom theoretically slows down the reaction by a factor of about 1.4 [74, 187]. In a previous H/D-exchange study of PYP an accelerated formation of pB' was observed accordingly, however not discriminating between the different proton transfer steps [74].

Examination of the deprotonation dynamics with the time traces of the raw data for WT and WT' (see figure F.40 on page 240 in the appendix) shows that the dynamics of the E46 bleach (followed at 1734 cm^{-1} for H_2O and 1728 cm^{-1} for D_2O) in both samples seem to be slower in H_2O than in D_2O, but clearly arising on a hundreds of microseconds timescale and not within milliseconds. The fitting of the traces in H_2O is relatively error-prone though, as the data quality is lower and the absorption band slightly shifts. Besides there might be possibly a second, faster process as revealed by the 100 µs component for WT'. For WT a similar kinetic is observed, but it was not possible to fit it properly by multiple exponentials[15].

The LDMs of the electronic delays in figure 7.13 on page 135 for the WT and figure F.38 on page 238 for WT' show that the negative feature in the CO region of E46 seems to be composed of at least two features, one at 1734 cm^{-1} at about 90 µs or faster and a shifted one at 1729 cm^{-1} around 240 µs. The first feature could correspond to a slight broadening of the bleach that can be seen for a lifetime of 105 µs by close inspection of the SADS from global analysis. The later one matches the disappearance of the narrow positive feature at 1729 cm^{-1} in the global analysis, that is caused by the downshift of the bleached absorption, although the time constant of 916 µs is distinctly slower than the lifetime observed in the LDM. Because of the difficult interpretation of the negative feature in the CO region of E46 in the standardized LDMs, further complicated by the shift of the signals at the end of the measurement range to earlier lifetimes, the not-standardized LDMs (see figure F.42 on page 242) are additionally examined. The not-standardized LDMs show only one negative feature at 1734 cm^{-1}, corresponding to an increasing bleach of E46 and therefore, most likely, indicating deprotonation, that appears at about 360 µs. However, the oscillations are very pronounced for the not-standardized data making them less reliable.

The small positive feature in the standardized ps-to-ms LDM in figure 7.13 that corresponds to the upshifted absorption of E46 at 1756 cm^{-1}, highlighted by the yellow dashed line at 45 µs, was assigned to the movement of E46 and is apparently slightly accelerated compared to the D_2O measurements. This is in good agreement with the observations from global analysis where the upshifted absorption occurs with 105 µs in H_2O and only with 386 µs in D_2O (for WT' 105 µs in H_2O and 193 µs in D_2O are observed, see figure F.39 on page 239 in the appendix). Possibly the slightly blue-shifted part of the stretched, negative feature in the CO region of E46 in the standradized LDM, which appears in less than 100 µs, coincides with this upshifted E46 absorption exhibiting a distinct kinetic isotope effect with faster dynamics in H_2O than D_2O. The second, later part at about 240 µs, that is shifted to lower frequencies, might correspond to a decelerated deprotonation process in H_2O. This would admittedly contradict the expectations for the kinetic isotope effect, but would be generally consistent with the interpretation of the deprotonation dynamics in

[15] For the time traces in D_2O a faster component was found, too (compare figure F.22 on page 223 in the appendix), albeit on a few microseconds timescale and therefore clearly corresponding to the $pR_1 \rightarrow pR_2$ transition

H_2O by Brudler *et al.* [10]. In their IR study, they also investigated the bleached absorption of the C=O vibration in H_2O in terms of E46 deprotonation and found two time constants of 113 µs and 1.5 ms. Hence, they suggested two possible interpretations for the observed dynamics. In the first one, the movement of E46, indicated by the upshifted absorption at 1759 cm^{-1}, occurrs with 113 µs followed by deprotonation in 1.5 ms. The second interpretation suggested a parallel model, which they considered more likely, in which a part of the molecules follows the dynamics described before, but the other (major) part becomes already deprotonated in 113 µs and the 1.5 ms time constant was assigned to structural changes.

However, the deviating dynamics obtained by the different analysis methods for the bleached absorption of the COOH group of E46, whose changes were previously assigned to the deprotonation of the glutamate [10, 11, 97], might hint that this feature cannot unambiguously be used as marker band for the deprotonation process. The bleach arises when the dark state's C=O vibration of the COOH group vanishes. This was found to be the case for deprotonation to a COO^- group leading to an extreme shift of the C=O vibration of about 150 - 400 cm^{-1} (to around 1570 cm^{-1} and 1400 cm^{-1} as suggested for PYP by [11] or 1500 cm^{-1} and 1350 cm^{-1} for the symmetric and asymmetric stretching vibrations as found by [188]). Since these downshifted vibrations are superimposed by other protein and chromophore vibrations, their assignment and interpretation are very complicated or even impossible so that they are usually not applied for analyzing the proton transfer from E46 [97]. However, without the possibility to simultaneously examine the formation of the product band of the COO^-, the bleached absorption alone cannot be taken as deprotonation marker unquestioned. An increase of the bleach could also arise due to other effects besides ionization of E46, *e.g.* changes of the vibration's extinction coefficient would lead to an altered intensity without occurrence of a product band.

Whereas the analysis of the deprotonation dynamics is complicated in H_2O, the interpretation of the chromophore protonation by means of the previously identified marker band around 1575 cm^{-1} is more straightforward. As already mentioned before, global analysis revealed a faster protonation process in H_2O (105 µs) than in D_2O (386 µs for WT, 193 µs for WT'). These findings are supported by the time traces of the raw data, that follow the protonation of the chromophore at 1578 cm^{-1} in H_2O and at 1565 cm^{-1} in D_2O (see figure F.40 on page 240 in the appendix), and show that these kinetics are significantly accelerated in H_2O in good agreement with the kinetic isotope effect. In the LDMs of the electronic delays in figure 7.13 on page 135 for the WT and figure F.38 on page 238 for WT', the positive feature, that is associated with the chromophore protonation, is only visible as shoulder near 1580 cm^{-1} of the main feature at 1560 cm^{-1} (corresponding to the disappearance of the large bleach in the spectrum). It occurs at a lifetime of approximately 90 µs (highlighted by the yellow dashed line in figure 7.13) and therefore much faster than in the LDMs of the D_2O data. Due to the difficult assignment of the deprotonation process of E46 in H_2O, no clear answer can be found whether E46 can be excluded as proton donor as suggested by the measurements in D_2O or whether the proton could not actually be transferred intermolecularly from E46 to the chromophore as proposed in some previous studies (not exclusively for H_2O) [10, 11, 93, 94, 97].

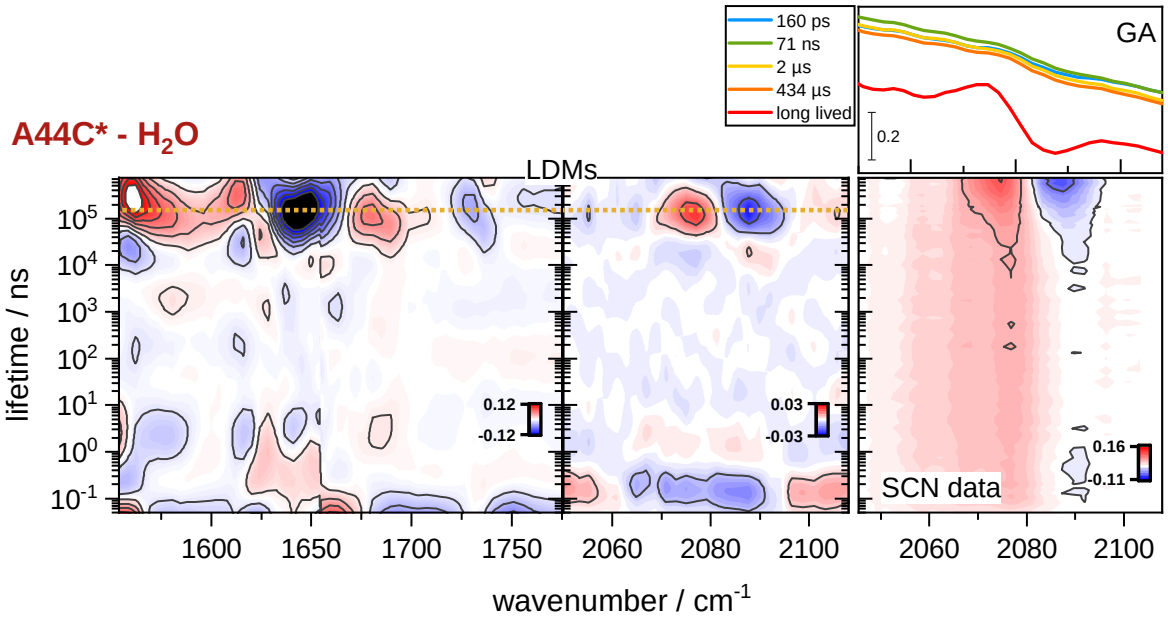

Figure 7.14: *Overview of transient vis-pump-IR-probe measurements with electronic delays for A44C* in H_2O in the CC/CO and SCN region. LDMs in the CC/CO region (first column, contour plot with 11 major levels) and the SCN region (second column, contour plot with 5 major levels, linear baseline subtracted) are shown. The corresponding L-curves are depicted in figure F.44 in the appendix. The yellow dashed line at 150 µs highlights features that appear simultaneously with changes in the SCN signal. Third column: Contour plot (5 major levels, linear baseline subtracted) of denoised data in the SCN region. For the SADS obtained from global analysis (GA) of the denoised SCN data only components > 50 ps are shown.*

In addition to the CC/CO regions in WT and WT', the CC/CO and SCN regions of A44C* were investigated in H_2O. Since the measurements in D_2O revealed that the label responds only on a hundreds of microseconds timescale, just the electronic delays were examined for the mutant. Comparable to the observations in D_2O, the SCN signal appears only in the long lived spectrum obtained by global analysis, as it is shown in figure 7.14 (comparison of raw and denoised data in figure F.41 on page 241 in the appendix), and is formed with a lifetime of 434 µs, which is very similar to the lifetime of 445 µs found for the D_2O experiment. Although the identification of the deprotonation process in H_2O is inconclusive, the LDM features of the downshifted SCN absorption (highlighted by the yellow dashed line at 150 µs in figure 7.14) seem to appear on a similar timescale as the negative feature assigned to the C=O vibration of E46 around 1728 cm^{-1} in the LDM of the CC/CO region. This might indicate that despite the unambiguous assignment of the deprotonation of E46 the label in H_2O also senses this process equally to the observations in D_2O. In fact, it could be also interpreted the other way round: From the steady-state experiments and structural investigation of the labeling site, it was concluded that the large red-shift of the label's absorption is caused by deprotonation of E46, which drastically changes the electrostatic properties in its surrounding. Investigation of the dynamics in D_2O supported this hypothesis as well, since the SCN signal was found to arise simultaneously with the bleached feature associated with deprotonation of E46 (see figure 7.6 on page 108). Therefore the response of the SCN label in the H_2O measurements could provide information about the occurrence of the deprotonation process.

Comparison of the LDMs of the SCN region in both solvents, shown in figure 7.15, revealed that the SCN absorption appears slightly faster in H_2O (150 µs, highlighted by the yellow dashed line) than in D_2O (220 µs). This observation is supported by the time traces of the SCN kinetics (amplitude from the maximum to the minimum of the difference absorption signal), which are shown in the same figure. Here time constants of 320 µs in H_2O and 440 µs in D_2O were obtained by fitting with single exponential functions (between 100 ns and 750 µs). Since both LDMs and time traces indicated accelerated kinetics in H_2O, it seems surprising that similar lifetimes were observed for the formation of the SCN signal in global analysis. This might be explained by the underlying dynamics of the large water background, which follow different kinetics for the two solvents and possibly influence the global lifetimes. The difference between the lifetimes in H_2O and D_2O, that was observed in the LDMs and the time traces, matches the difference expected for the kinetic isotope effect remarkably well implying that the SCN indeed responds to changes sensitive for H/D exchange, as it is the case for proton transfer processes. Hence, the measured SCN kinetics prompt that deptotonation of E46 should occur accelerated in H_2O compared to D_2O. However, in the LDMs of A44C* the feature assigned to the protonation of the chromophore (the shoulder at 1580 cm^{-1} of the large positive feature) also seems to appear on a similar timescale as the SCN feature and thus almost simultaneously with deprotonation of E46. Therefore the investigation of the labeled mutant in H_2O facilitates the identification of the deprotonation dynamics, but is not able to discriminate the proton donor for the protonation process.

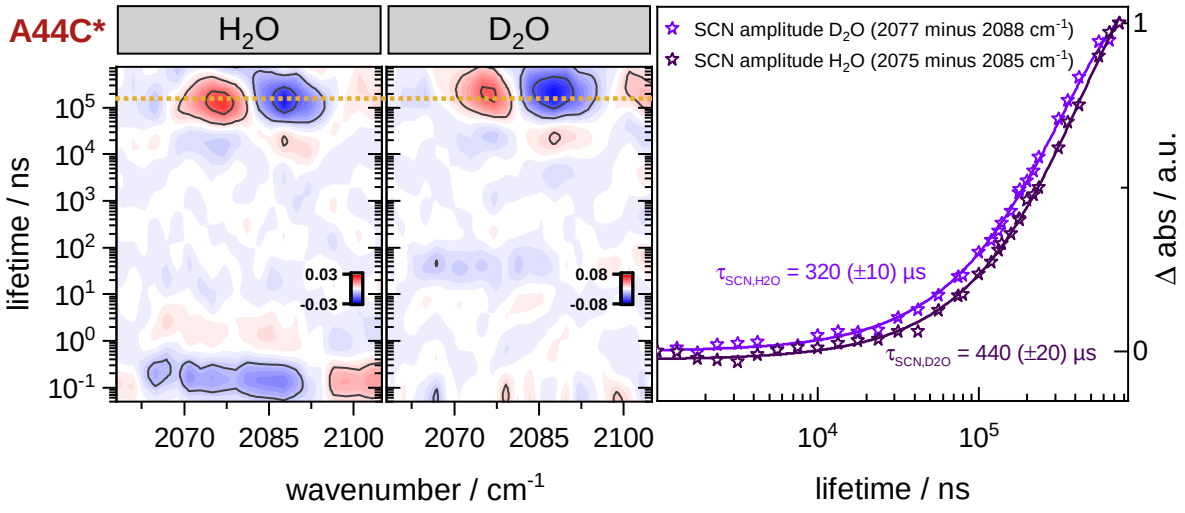

Figure 7.15: *Comparison of the SCN signals in the LDMs of A44C* in H_2O and D_2O (left). The corresponding L-curves are depicted in figures F.37 and F.44 in the appendix. Normalized time traces of the raw data of the SCN amplitude of A44C* in H_2O (purple) and D_2O (dark purple) are compared (right). The kinetics of the SCN amplitudes are fitted with a single exponential function (solid line) between 100 ns and the last time point for both solvents.*

7.1.6 Decreasing the Pump Pulse Rate *via* the Chopper Divider

The electronic delay of the probe pulses with respect to the pump pulses allowed to extend the delay time almost to the repetition rate of the two laser systems[16]. This makes the measurements challenging because each laser shot needs to excite a fresh laser spot. Therefore, the sample has to be moved slow enough to still have excited molecules in the probe spot, even when the probe pulse arrives long after the pump pulse, but at the same time the sample has to be exchanged fast enough to excite fresh molecules with the next pump pulse, that hits the sample, at the very same spot. To defer the arrival of the next pump pulse at the sample, the pump pulse's repetition rate was artificially decreased by introducing the so called chopper divider routine. The principle of the chopper divider is explained in detail in figure 2.8 on page 36 in the introduction. In short, a chopper wheel is used that runs at 250 Hz and lets only every fourth pump pulse pass, instead of a chopper wheel that is typically used in pump-probe experiments running at 500 Hz and blocking only every second pulse. Thus, it takes 4 ms until the next pump pulse arrives at the sample, when using the chopper divider routine, allowing to move the sample twice as slow as normally done (see also figure 2.8 on page 36).

To see if there are still some molecules in the probe spot that were excited by the previous pump pulse, a background signal is recorded first. This signal is obtained when the pulse order of pump and probe is interchanged and the probe pulse arrives at the sample before it was excited by the pump pulse. For the experiments presented here, a delay of -7.5 ns was measured as background, which is later on subtracted from the other time points, and is exemplarily plotted in figure 7.16 on the next page for the three different bins of the CO region of WT and the SCN region of A44C*. The background spectra in figure 7.16 show that the speed of the Lissajous scanner was adjusted properly with a large signal in bin 1 and almost no signal in bin 3. The optimal speed to move the sample with the Lissajous scanner would result in a pronounced difference signal of the background for bin 1, because this implies that the speed is slow enough to have many excited molecules still in the probe spot after 1 ms, which would approximately match the delay of the last time point in the measurement. Further a completely vanished signal in bin 3 would be ideal corresponding to a speed fast enough to have none previously excited molecules left in there after 3 ms, which is less time than two subsequent pump pulses need to arrive at the sample. Note that the absorption of the spectra in figure 7.16 is flipped due to the reversed pulse order.

To investigate the effects of the chopper divider routine on the actual data, the background corrected spectra and spectral changes of the three different bins at 250 Hz and for the chopper running at 500 Hz are compared for both the CO region of WT and the SCN region of A44C* as shown in figure 7.17 on page 143. For the CO region of WT, that was measured with electronic delays in D_2O, global analysis was performed for the data of each bin and the 500 Hz data[17] and they were additionally analyzed with LDA. Comparison of the spectra and lifetimes from global analysis for the three chopper divider bins reveals that they are very similar. For the 500 Hz data comparable lifetimes were obtained as

[16] The last delay of the measurements performed here is at 750 µs, the repetition rate at 1 kHz, which is equivalent to 1 ms.

[17] The data in the CO region of WT were only analyzed up to 360 µs due to problems with the chopper phase, that occurred for the last four time points when the chopper was running at 250 Hz.

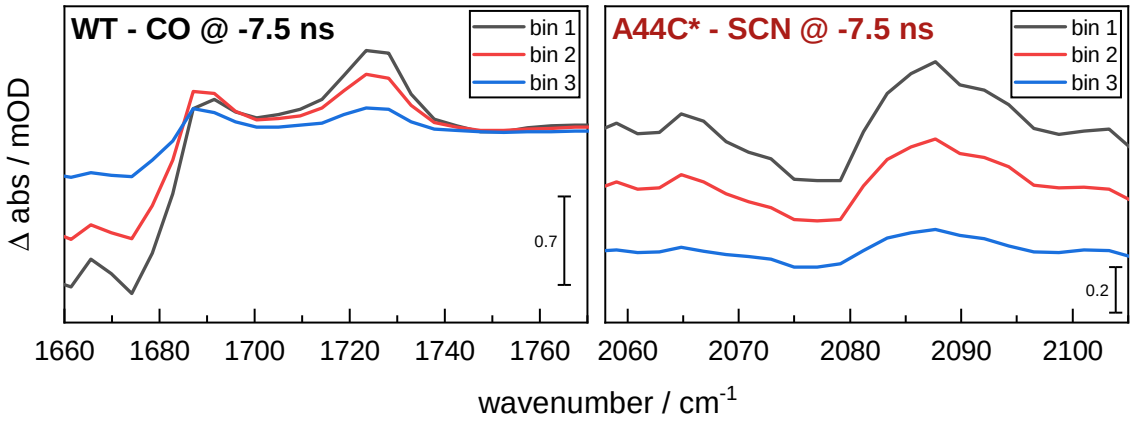

Figure 7.16: *Background spectra at −7.5 ns of the three bins from the chopper divider routine for the CO region of WT (left) and the SCN region of A44C* (right), both in D_2O, recorded with the chopper running at 250 Hz. The absorption of the spectra is flipped due to the reversed pulse order with the probe pulse arriving 7.5 ns earlier at the sample than the corresponding pump pulse and therefore detecting the remaining excitation of the previous pump pulse.*

well, except for an additional component of 37 µs in between the early µs-component, previously assigned to the relaxation of pR_1, and the 300 µs component which is clearly associated with E46 deprotonation. A similar component (61 µs) was observed in the analysis of the merged CC/CO region for these data, but no corresponding lifetime was found for WT'. Since the spectra of this additional component and the prior component are almost indistinguishable and no matching feature occurred in the LDMs of the CC/CO regions neither, it was concluded that on this timescale no relevant changes of the protein take place. In the LDM for the CO region presented here also no indication for changes on a tens of microseconds timescale was found that would differ from the LDMs of the data recorded at 250 Hz.

In general, the features that appear in the LDMs of the CO region show a close resemblance for the three bins and the 500 Hz data. The features assigned to the $pR_1 \rightarrow pR_2$ and the $pR_2 \rightarrow pB'$ transitions appear simultaneously at about 2 ns and 160 µs, respectively, as indicated by yellow dashed lines in figure 7.17. For the features that are highlighted by the yellow dashed line at 150 ps, small deviations between the data recorded at 250 Hz and the ones recorded at 500 Hz are visible. Due to different jitters in both experiments, that were fitted with differing instrument response functions, large features at earlier times may shift features on slightly longer delays, similar to the effect that was observed at late times, where the oscillations at the end pushed earlier features to earlier delays. Moreover the dynamics of the SCN label in A44C* were analyzed with the LDMs for the three chopper bins and the 500 Hz data (all analyzed simultaneously). Here, as well, it is obvious that the changes of the SCN signal occur almost simultaneously in all four LDMs at about 190 µs.

These measurements of the WT CO region and the SCN region of A44C* demonstrate that the dynamics are not influenced by the time between the first excitation of the sample and the subsequent one, at least as long as it is longer than the longest measured delay time. This also implies that it does not play a crucial role if there is a background signal present or not, like for the first two bins of the chopper divider and, of course, also for the 500 Hz measurement. Since the majority of the background dynamics results from the recovery

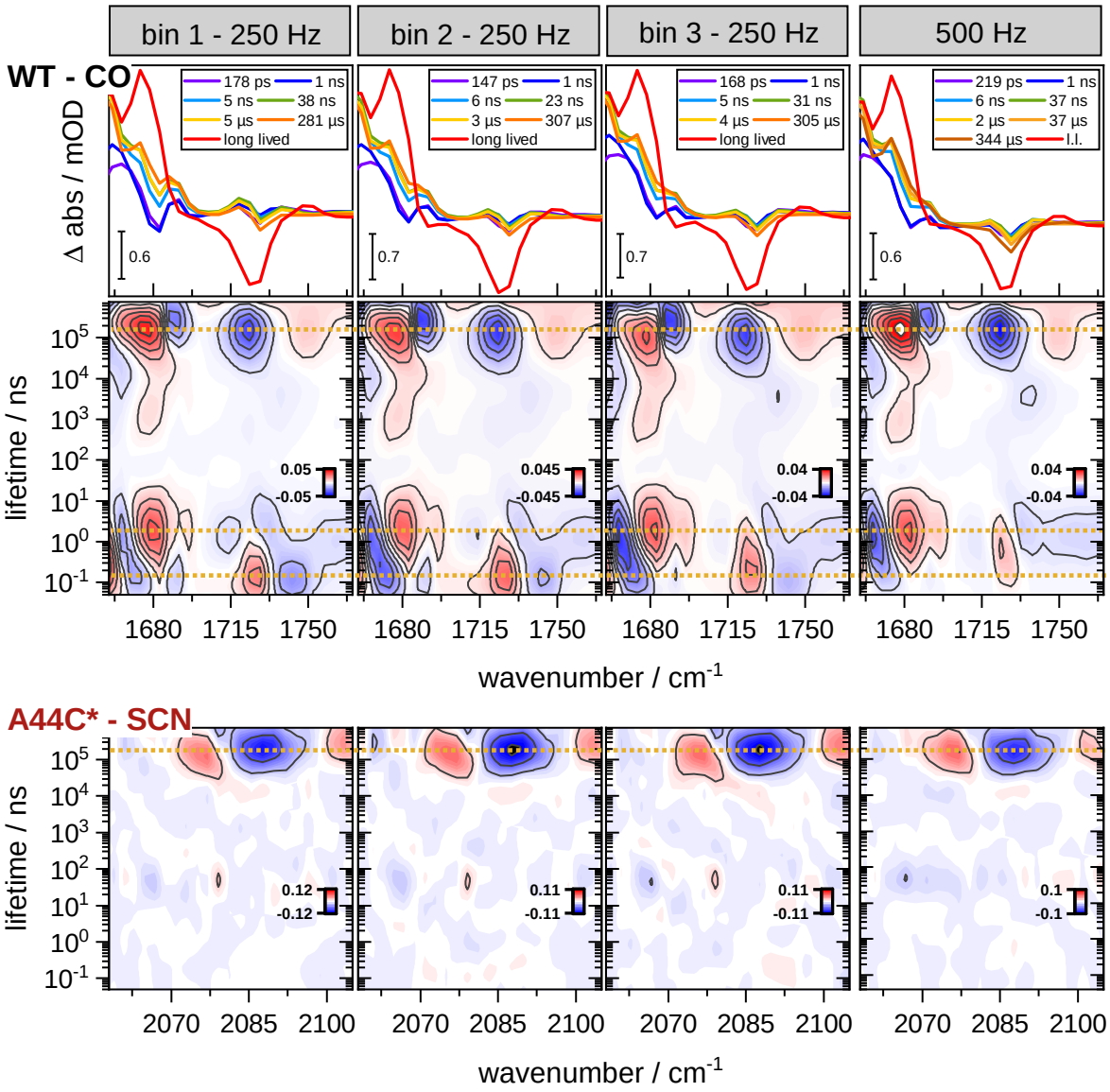

Figure 7.17: *Comparison of GA spectra and LDMs (all standardized) from different bins of the chopper divider routine at 250 Hz with the chopper running at 500 Hz. The SADS obtained by GA with a sequential model of 9 components for the CO region of WT measured in D_2O with electronic delays are depicted in the top row (only components > 50 ps). The corresponding LDMs are shown in the second row (plotted with 11 major and 5 minor levels). The corresponding L-curves are depicted in figure F.45 in the appendix. The yellow dashed lines indicate prominent features in all LDMs at 150 ps, 2 ns and 160 µs. The LDMs of the SCN region of A44C* at 250 Hz and 500 Hz are shown in the bottom row (plotted with 5 major and 5 minor levels, linear baseline subtracted) with the yellow dashed line at 190 µs.*

of the dark state pG, which is known to occur in hundreds of milliseconds to seconds [4, 5, 74], they decay on a much slower timescale than the investigated dynamics (< 1 ms). Therefore, the background signal can be considered as almost constant during the entire measured time range and for all bins (which are recorded within a few milliseconds) so that it can be subtracted without changing the detected kinetics. The deviations between the background signals of the three different bins shown in figure 7.16 on the preceding page, however, result from the movement of the sample cell. Thus different spots in the sample are probed containing less and less previously excited sample.

For long electronic delays, sign flips of the chopper phase were noticed during the experiment, as it was observed for the CO region of WT when using the chopper divider routine. These phase flips may probably arise due to the large step size at the end of the measurement range and the delays being close to the repetition rate of the laser. The trigger for the chopper was provided by the slave oscillator and thus from the so called synchrobox, which shifts the trigger of the Pockels cells every time it changes the electronic delays. If the set time steps are large (*i.e.* > 100 µs), the chopper needs more time to adjust to the shifted trigger and stabilize there. At 250 Hz the chopper is more sensitive to such sign flips, probably due to the larger inertia of the chopper wheel (two stacked wheels are used for the chopper divider, only one wheel is used for 500 Hz), which increases the time that is needed to follow suit. Since no significant differences were found in the dynamics, but the chopper proved to operate more reliable especially at long time delays when it runs at 500 Hz, the transient vis-pump-IR-probe-experiments were performed with this setting instead of using the chopper divider routine. An additional advantage is that more laser shots can be collected in less time, because even if the data from all three bins can be averaged, the background is only averaged at a 250 Hz repetition rate.

An alternative method to slow down the repetition rate of the pump pulses at the sample was applied for the measurements of M100C* (and A30C* but only with little benefit). While the dark state of PYP is typically recovered in about 1 s, the replacement of M100 prolongs the lifetime of the signaling state pB to several minutes [85, 156–159]. The pattern of the Lissajous scanner, which moved the sample cell, was chosen in a way that it returns to the same spot in tens of seconds. This is sufficient for most of the investigated samples to fully recover the dark state of the excited molecules when once moved out of the probe spot, except for M100C*. Due to the considerably decelerated dynamics of the pB′ → pG transition in the latter, a lot of molecules have not fully recovered to pG when the same spot in the sample is reached again, so that the amount of molecules which can be excited again by the pump pulse is decreased leading to a noticeably smaller signal (because the visible absorption spectrum shifts away from the used excitation wavelength for the different transient species). This was prevented by additionally inserting a mechanical shutter in the pump path, that was closed after each recorded time point to block the pump pulses for several seconds to give the protein more time to relax to pG. A closing time of 15 s was experimentally determined to obtain a favorable ratio between measurement time and signal size. This method reduced the total amount of pump pulses arriving at the sample substantially, although within one recorded time point the pump pulse rate is still at 500 Hz, analogous to the measurements discussed before. Thus the closing of the shutter improved the signal size significantly without influencing the dynamics.

7.1.7 PYP Dynamics After Excitation with 468 nm and 401 nm Light

In the first transient vis-pump-IR probe experiments performed during this dissertation, 401 nm pump pulses were used for visible excitation. The creation of light in this wavelength range is convenient, because it only involves sum frequency generation (SFG) in a BBO crystal leading to a doubled 800 nm fundamental with no further non-linear mixing processes (and therefore no OPAs) being necessary. However, the measured spectra and dynamics in the CC/CO region seemed not to resemble the ones observed in previous IR studies [10, 11]. Moreover, the detection of an SCN signal appeared to be not possible,

although steady-state FTIR difference spectra (excitation at 445 nm) of the same samples indicated that a sufficiently large SCN signal should be expected. After red-shifting the wavelength of the pump pulses to 468 nm by performing SFG of the 800 nm fundamental mixed with the near-IR signal from the first amplification step in an OPA (for the electronic delays), similar results to those in literature were obtained as discussed in detail above.

First evidence for differences depending on the excitation wavelength can be found when examining the UV/vis spectra of PYP in the dark state pG (yellow) and the signaling state pB (gray) as schematically depicted in figure 7.18. While the 468 nm pulse (light blue) is on the red side of the PYP absorption maximum (446 nm) of pG, the 401 nm pulse (purple) is located on the blue side. Further it can be noticed that the pump pulse at 401 nm would not only excite the molecules in the dark state, but can also excite some molecules of the blue-shifted pB state, which has its absorption maximum at 355 nm [7, 9, 86]. This additional photon absorption of preexcited molecules could result in different dynamics for PYP.

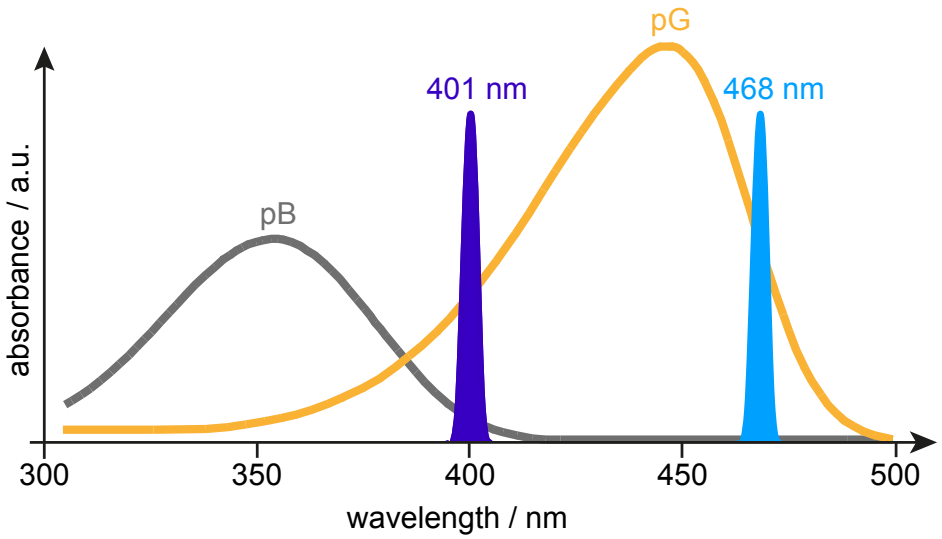

Figure 7.18: *Schematic representation of UV/vis spectra for PYP in the pG (yellow) and pB state (gray) [7, 86]. Two narrow Gaussians represent the two visible pump pulses at 401 nm (purple) and 468 nm (blue) that were used for excitation in the transient vis-pump-IR-probe experiments.*

Previous transient visible absorption studies investigated the effect of excitation with different wavelength on the early photocycle dynamics [9], but also the photoinduced recovery of the dark state from different intermediates with a second pump pulse [72, 86]. Devanathan *et al.* [9] suggested that an alternative excitation pathway is initiated when exciting with 395 nm light instead of 460 nm. This pathway is assumed to involve different vibrational and conformational properties of the chromophore in the electronically excited state pG* [9]. In the vis-pump-IR-probe experiments performed here, the excitation with 401 nm was only applied for the electronic delays not detecting the very early photocycle transitions. Therefore these deviations in excitation and photochemistry of pG* could not be directly observed here, but it is not unlikely that this alternative pathway will affect later photocycle dynamics as well.

In the double flash (pump-dump-probe or pump-repump-probe) experiments, the PYP sample was first excited by 446 nm [86] or 430 nm [72] pump pulses, before exciting it again after a certain delay with 355 nm pump pulses. When the 355 nm photons were

absorbed by molecules in the signaling state, the chromophore was isomerized back from *cis*- to *trans*-configuration leading to a considerably accelerated recovery of the dark state in hundreds of µs with respect to the thermal relaxation process that occurs on a hundreds of milliseconds to seconds timescale. Due to this long lifetime of pB, it is easily possible to excite the molecules a second time with a pump pulse arriving several milliseconds later at the sample. Examination of the background spectra (at −7.5 ns) in the previous chapter (see figure 7.16 on page 142) indicated that on the timescale on which the pump pulses arrive at the sample still some molecules are in the probe spot that were excited priorly.

To better understand the differences resulting from the two excitation wavelength, single spectra of selected time points in the CC/CO region of WT are compared in figure 7.19. The most prominent differences between the 468 nm and 401 nm excitation appear in the CO region of E46, the amide I region around 1640 cm^{-1}, and for the C=O vibration of the chromophore.

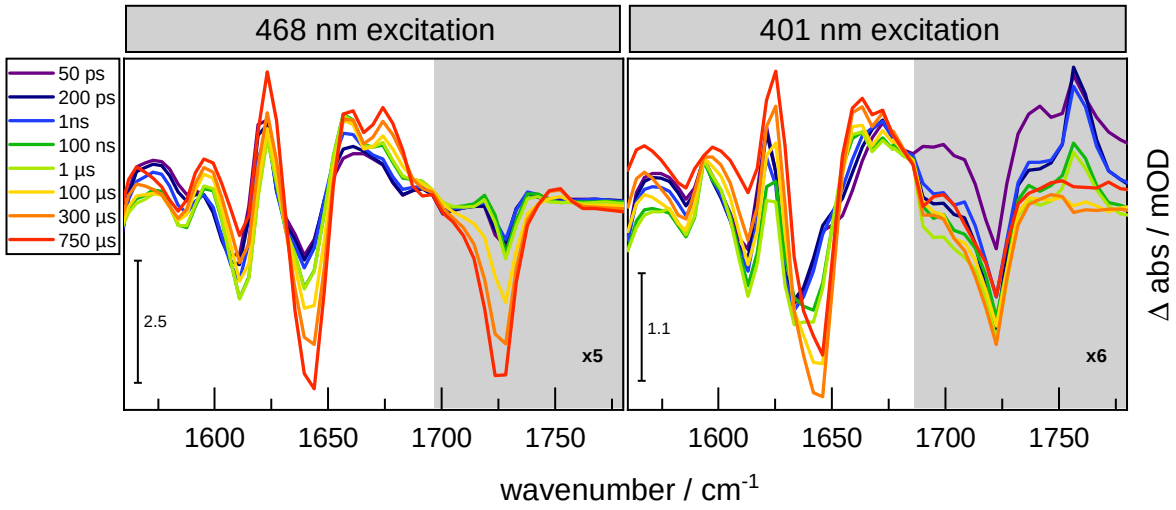

Figure 7.19: *Comparison of excitation with 468 nm (left) and 401 nm pump pulses (right) by single spectra at selected time points for the CC/CO region of WT measured with electronic delays. The CO region of E46 (highlighted in gray) is enlarged by a factor of 5 for 468 nm excitation and a factor of 6 for 401 nm excitation for better visualization. The data for 468 nm excitation were measured in D_2O with 500 Hz, while for 401 nm excitation they were measured in D_2O with the chopper divider routine (250 Hz, bin 1 shown).*

After excitation with 468 nm, a small bleach of the C=O vibration at 1727 cm^{-1} is already present at the beginning of the measurements and increases considerably in the hundreds of µs time range (yellow, orange, and red spectrum in figure 7.19). The increase of the bleach was previously assigned to deprotonation of E46. The upshifted absorption of the C=O vibration at about 1750 cm^{-1}, that was associated with the movement of E46 in a more hydrophobic environment, occurs only in the late spectra (> 100 µs, orange and red). When excited with 401 nm light however, the E46 bleach at 1722 cm^{-1} is also present in the first spectra, but in contrast to 468 nm excitation it persists almost unaltered during the full time range of the measurement. Only in the last spectrum (at 750 µs, red in in figure 7.19) it might have even decreased a little. The spectra for 401 nm excitation exhibit a significantly larger upshift of the C=O vibration of E46 to 1758 cm^{-1}, which is only observed in the early spectral slices (purple, dark blue, blue, and dark green) and vanishes in hundreds of nanoseconds. On a microsecond timescale however, a new small positive feature around

1740 cm^{-1} may be seen, similar to that observed after 468 nm excitation. The protonation marker band of the chromophore at 1568 cm^{-1} seems to follow comparable kinetics for both excitation wavelengths.

In the amide I region the difference signal of the amide I band (1621/1643 cm^{-1}) mainly increases after 468 nm excitation, besides a very small upshift of the negative band at late time points (> 1 µs), corresponding to structural changes and partial unfolding of the PYP. When excited with 401 nm light, however, the signal in the amide I region shows a more pronounced upshift on a microsecond timescale (from light green (1 µs) to yellow (100 µs) in figure 7.19), especially for the negative band, which shifts from about 1634 cm^{-1} to 1643 cm^{-1}. Surprisingly, this shift bears a resemblance to the shift that is observed for the very fast photocycle kinetics within a few picoseconds measured with the mechanical delays after 468 nm excitation (compare figure F.2 on page 203 in the appendix). The last noticeable spectral variations occur in the CO region of the chromophore around 1665 cm^{-1}. In the spectra for the 468 nm excitation, the broad absorption band is already present on a tens of picoseconds timescale (purple spectrum). Afterwards, the low wavenumber population (1659 cm^{-1}) of the band grows in quickly (< 100 ns), whereas the high wavenumber population (1674 cm^{-1}) increases only in the late spectra. For 401 nm excitation, the absorption band is also present from the beginning, however, the low wavenumber population at about 1660 cm^{-1} is hardly developed, but instead the high wavenumber population at about 1673 cm^{-1} exhibits already a pronounced absorption (see purple, dark blue, and blue spectrum in figure 7.19). While the band at 1673 cm^{-1} hardly changes during the experiment, the low wavenumber population increases significantly with kinetics that are comparable to the ones of the high wavenumber population after 468 nm excitation.

Considering the observed differences between the two excitation wavelength, two hypothesis can be developed, that might explain the altering dynamics. First, it might be assumed that two dark state conformers exist that follow different photocycles. Alternatively, there could be only one pG population, but the 401 nm pump pulse is able to repump or dump a fraction of the transient population. In both cases a detailed analysis of the dynamics after excitation with pump pulses of 401 nm is complicated, since a mixture of molecules either following different pathways or passing different phases of the photocycle is present in the sample at the same time. Anyway, this reduction of molecules following the regular photocycle simultaneously could be the reason why it was not possible to observe any SCN signal, since it probably leads to a very small signal size of the SCN.

If the dynamics are influenced by the usage of a blue-shifted excitation wavelength that can be absorbed by the signaling state, also depends on the time delay with which the pump pulses arrive at the sample. In time-resolved step-scan FTIR experiments, Brudler *et al.* [10] applied an excitation wavelength of 395 nm to the sample, but observed dynamics similar to the ones of the measurements with 468 nm excitation performed here. While in the latter the interval between the pump pulses was < 4 ms, Brudler's sample was excited only every 4 s in the step-scan FTIR experiments. On this timescale all the previously excited molecules should be completely relaxed to the dark state, so that exclusively molecules in pG get excited independent of the excitation wavelength. Based on these observations the existence of different dark states species seems rather unlikely, since they would lead to altered spectral changes independent from the repetition rate of the pump pulses. Hence

one is inclined to conclude that the second hypothesis is more plausible. Moreover, the repumping or dumping of a transient population would coincide with the double flash experiments performed in previous studies [72, 86].

7.2 Conclusion

The combination of mechanical and electronic delays in the transient vis-pump-IR-probe experiments allowed to cover a time range of nine orders of magnitude from hundreds of femtoseconds to almost 1 ms. Hence it was possible to follow most part of PYP's photocycle. The concurrent use of global analysis and lifetime density analysis was established as powerful tool for the investigation of such a broad time range and a multitude of protein and chromophore vibrations, although the shifted lifetimes in the LDMs of standardized data complicated the interpretation at some points. The protein and chromophore dynamics measured here are in good agreement with the dynamics observed in previous studies of the photocycle of WT-PYP. With the incorporation of the SCN label at five selected positions within the protein, different dynamics during the photocycle could additionally be probed with local structural resolution.

For the early photocycle dynamics, multiple lifetimes for relaxation of the electronically excited state pG* were found. Isomerization of the chromophore and thus formation of intermediate I_0 occurred a few picoseconds after photon absorption. These early transitions including excitation and isomerization of the chromophore were detected by the SCN labels in V57C*, M100C* and V122C*, which are all located in the chromophore binding pocket. M100C* additionally showed a significantly slower return to the dark state in almost 100 ps, comparable to the decelerating effect that was observed for the relaxation dynamics of the signaling state after replacement of this methionine [85, 156–159].

The existence of the $I_0^{\ddagger}$ intermediate, which was suggested to form in about 220 ps possibly due to relaxation processes in the vicinity of the chromophore [8, 87], could not be confirmed by investigation of the protein and chromophore kinetics. But the response of the SCN label in V122C* in about 220 ps indicated changes in the proximity of the label, involving probably the nearby E46, which is also hydrogen-bonded to the chromophore and might be influenced by the relaxation processes after chromophore isomerization. Therefore the occurrence of changes in the SCN signal could most likely be assigned to the formation of $I_0^{\ddagger}$.

Further structural relaxation processes of the chromophore and the surrounding hydrogen bonding network appeared in a few nanoseconds resulting in the formation of the pR state and were sensed by the labels in V57C*, M100C* and V122C*, as well. The µs-dynamics, that were assigned to the existence of two pR sub-states in literature [70, 73–75, 89, 91, 92], were observed for the first time in time-resolved IR experiments. Furthermore, it was possible to localize the changes in the chromophore binding pocket, especially involving E46 and R52, which moves to open the gateway between chromophore and surrounding solvent [12, 172]. These findings for the protein and chromophore dynamics, were supported by the response of the SCN labels in V122C*, which is close to E46, and (most likely) in M100C*, which is in the neighborhood of the positively charged side chain of R52. However, it was not possible to unambiguously determine whether the two states are formed

concurrent on a nanosecond timescale or subsequently with pR_1 relaxing to pR_2 in a few microseconds. Examination of the protein and chromophore vibrations of M100C* with the LDM of not-standardized data might imply that the two pR states are formed in parallel with the mutant favoring the formation of pR_1, which follows an accelerated transition to pB'. Otherwise only evidence for an accelerated pB' formation in general was found for M100C*. In this case, the SCN label did not help to distinguish between both models.

Evidence was found indicating intermolecular proton transfer, presumably from the solvent, for chromophore protonation during pB' formation. E46, which is often suggested as proton source [98], seemed not to be deprotonated simultaneously with the protonation of the chromophore making intramolecular proton transfer unlikely. This is the first direct kinetic evidence that E46 does not serve as proton donor for the chromophore. Additionally, the upshifted absorption of the C=O vibration of E46, that was previously interpreted as movement of E46 in a more hydrophobic environment [10, 11], was found to appear prior to the proton transfer processes, indicating that multiple consecutive steps are necessary to form pB'. So far, these steps were always observed as a single step process in literature. With the aid of LDA it was possible to distinguish the nature of the pR $\rightarrow$ pB' transition in detail, which in fact consisted of multiple small consecutive structural rearrangements that ultimately led to pB'. While most of the photocycle dynamics were hardly influenced by the exchange of D_2O with H_2O, the different steps during pB' formation showed some response. The movement of E46 and protonation of the chromophore seemed to be accelerated in H_2O due to the kinetic isotope effect. The dynamics of the E46 bleach were, however, complicated in H_2O making the interpretation of the deprotonation process difficult. Therefore E46 could not be excluded as proton donor, when only taking the measurements in H_2O into account.

The formation of pB' is the only transition in the photocycle that was detected by all five SCN labels. Albeit, the labels responded to different structure changes, that occurred during the $pR_2 \rightarrow$ pB' transition, due to their various locations within the protein. The label in V122C* probed most likely the movement of E46 and deprotonation of E46, which occurred simultaneously in this mutant, as it was expected by their proximity to this residue. The deprotonation process was also detected by the SCN label in A44C*. This observation was strongly supported by the steady-sate measurements, which indicated the influence of a charged group, like the carboxylate anion formed by deprotonation of E46, on the label. Hence investigation of the SCN dynamics of A44C* in H_2O supported the interpretation of the deprotonation kinetics of E46 implying that this process became possibly also accelerated when changing the D_2O solvent for H_2O, which could not be unambiguously observed by the C=O vibration of E46 alone. The label in A30C* probably detected the conformational changes of the N-terminus, that take already place during pB' formation [75, 170, 180]. In M100C*, the label reacted to the movement of the nearby R52 and presumably to the associated intrusion of water molecules into the chromophore binding pocket. For V57C*, it could not clearly be distinguished which alterations of the binding pocket finally affect the label during this photocycle transition.

Besides investigation of the overall protein dynamics and site-specific information about structural changes during the photocycle, additionally some technical requirements were examined during the transient vis-pump-IR-probe experiments. Measurements with the chopper divider routine, which decreased the pump pulse rate artificially by a factor of

two, revealed that its application was not required, since the sample could be moved slow enough to measure up to 750 µs without leaving the probe spot even when the interval of pump pulses arriving at the sample was not reduced. This was possible since the previously excited molecules, that might be still in the probe spot when the following pump pulse arrived, only contributed to a background signal with distinctly slower dynamics (hundreds of milliseconds to seconds) and therefore, it could be considered as constant within the investigated time range and could be subtracted from each time point easily. However, this was only applicable if the pump pulse could not be absorbed by the long-living signaling state with its absorption maximum at about 355 nm. When the excitation was chosen too far at the blue end of the visible spectrum, for instance at 401 nm, the pump pulse was most likely able to repump or dump a fraction of a transient species leading to a mixture of dynamics from molecules in different phases of the photocycle. Consequently, the experiments were performed with the chopper running at 500 Hz, blocking every second pump pulse and leading to a delay of 2 ms between two pulses that arrive at the sample, and an excitation wavelength of 468 nm, which is clearly separated from the absorption of the signaling state.

8 Time-resolved Step-scan FTIR Experiments

To further extend the timescale on which photocycle dynamics can be followed, step-scan FTIR experiments were applied to WT′ and A44C* in H_2O. These experiments allow to measure the spectral range from 1200 cm^{-1} to 2200 cm^{-1} synchronously up to 19 ms, but have a limited time resolution of 10 µs. Therefore, additional information about pB′ formation and especially insights into the formation of the signaling state pB can be obtained, that are not covered by the transient vis-pump-IR-probe experiments, since it occurs in several milliseconds. The results discussed in this chapter were based on data published in "Following local light-induced structure changes and dynamics of the photoreceptor PYP with the thiocyanate IR label" by Blankenburg *et al.* [136].

8.1 Results and Discussion

Analogous to the transient pump-probe data, the step-scan FTIR data were analyzed by global analysis and lifetime density analysis. Single spectra for WT′ and A44C* are shown in figure G.1 on page 245 in the appendix. First, the CC/CO regions of both samples are compared with the dynamics obtained by the previously discussed time-resolved experiments. In figure 8.1 on the next page the SADS from global analysis with a sequential model of three components for WT′ and A44C* are shown. Moreover, the LDMs of the not-standardized data are depicted. Unlike in the previous chapters, here are not mainly the LDMs of the standardized data discussed. The reason is that in the standardized LDM some of the features indicate changes for which no equivalent can be observed in the GA or single raw spectra, *e.g.* a negative feature (indicating decreasing intensity in the difference signal) appears around 1370 cm^{-1} at 250 µs for WT′ or at 570 µs for A44C*, although the absorption in the GA and single spectra is steadily increasing (which would correspond to a positive LDM feature). The standardized LDMs are shown in the appendix in figure G.2 on page 246.

Global analysis yielded three components of 70 µs, 640 µs, and a long lived one for WT′ and 36 µs, 530 µs, and a long lived component for A44C*. The spectra look similar to the ones measured by Brudler *et al.* [10], although they found two slower lifetimes of 113 µs and 1.5 ms in addition to two lifetimes that exceed the time range accessible in the experiments shown here, *i.e.* 189 ms and 583 ms. For the fast component, which is only slightly higher than the resolution of the experiment, relatively small changes are observed in the spectra. The most obvious changes occur around 1660 cm^{-1}, corresponding to the chromophore's C=O vibration, and at 1690 cm^{-1}, where the absorption band assigned to the C=N vibration of R52 grows in, implying the movement of the arginine and opening of the chromophore binding pocket for water molecules on this timescale [12, 172]. The alterations in the C=O region of E46 or of other protein and chromophore bands are minor, especially for WT′.

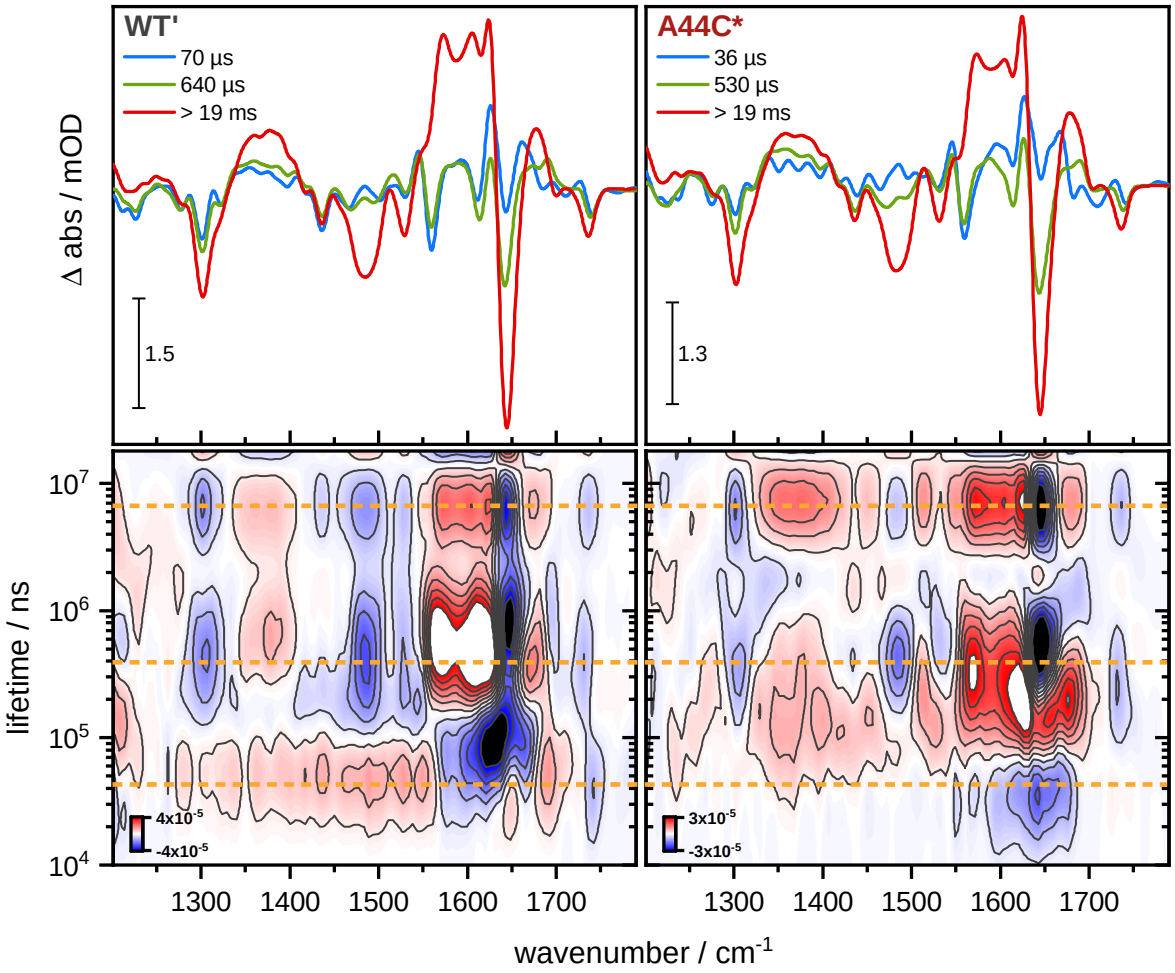

Figure 8.1: *SADS from global analysis (top) and not-standardized LDMs (bottom) of time-resolved step-scan FTIR data of WT′ (left) and A44C* (right). GA spectra were obtained by fitting with a sequential model of 3 components. The not-standardized LDMs are shown, since they better match the spectral changes observed in the GA spectra than the standardized ones (compare figure G.2 in the appendix). The corresponding L-curve is depicted in figure G.3 in the appendix. The yellow dashed lines highlight prominent features at 45 µs, 400 µs, and 7 ms. Only the region of protein and chromophore vibrations is shown, since in this representation no signals can be resolved in the SCN region.*

In the LDMs the early features that appear below 100 µs describe the changes that occur with respect to time zero, at which no difference spectrum was detected, and are hence not interpreted in detail.

Except for the early component, global analysis revealed only one further lifetime within the time range of the measurement. Examination of this component shows that the dynamics of A44C* (530 µs) are slightly accelerated compared to WT′ (640 µs). The spectra, that look very similar for both samples, resemble the difference spectrum recorded at 450 µs by Brudler *et al.* [10] under comparable conditions. In the LDMs, however, two regions were identified, in which features appear at the same time range. One occurs on a hundreds of microseconds timescale and the other one around 7 ms. This meets the expectations that in the investigated measurement window the formation of pB′ and the the subsequent

pB′ → pB transition should occur [10, 11]. Since the dynamics on a hundreds of microseconds timescale, most likely corresponding to the pR_2 → pB′ transition, are rather complex, they will be closely examined in the following.

Due to the limited spectral window in the transient pump-probe experiments, chromophore protonation could only be followed by the marker band at 1575 cm^{-1}, which is in part assigned to coupled C–C and C=C modes of the chromophore's aromatic ring, but overlaps with other protein absorptions [10, 179]. The step-scan FTIR data provide an additional marker band, since the phenolate ring vibration of the ionized chromophore at 1487 cm^{-1} (1498 cm^{-1} in D_2O) is upshifted to 1514 cm^{-1} after protonation [11]. In the LDMs the features at 1487 cm^{-1} appear almost simultaneously for WT′ and A44C* at about 400 µs (the yellow dashed line in figure 8.1 marks a lifetime of 400 µs), while the features for the other protonation marker at 1575 cm^{-1} occur significantly delayed for WT′ at 560 µs, but slightly accelerated for A44C* at 330 µs. These differences might be caused by the underlying kinetics of the protein modes, which probably differ between the two investigated samples.

For better comparison of the protonation dynamics, the time traces of the raw data for the corresponding peaks are depicted in figure 8.2 on the next page. The time constants, that were obtained by fitting the traces with three exponential functions, serve rather as orientation, because their errors are relatively large, especially for the fast and long lived (> 19 ms) components. For WT′ the dynamics of the trace at 1486 cm^{-1} (red circles) seem indeed a bit faster than the dynamics at 1572 cm^{-1} (dark red triangles), but for A44C* almost no difference can be observed. Overall, the time traces also indicate that the protonation process is a bit accelerated in the labeled mutant with respect to WT′. In the same figure the time traces of the C=O bleach of E46 at 1736 cm^{-1} (blue squares) are additionally shown. Although the transient pump-probe experiments in H_2O demonstrated that the kinetics of this spectral feature cannot be used to follow the deprotonation dynamics of the glutamate unequivocally, they were considered here in absence of another option. At first glance the deprotonation process seems to be faster than chromophore protonation in WT′, but the fitted time constants indicate similar dynamics for both processes (when comparing the 1736 cm^{-1} trace with the one at 1486 cm^{-1}). In A44C* the deprotonation seems to be in fact a little accelerated compared to the proton transfer to the chromophore. Here as well, E46 is faster deprotonated in the mutant than in WT′. These findings are supported by the results from the LDMs, in which the feature corresponding to the E46 deprotonation appears at 400 µs for WT′ and at 230 µs for A44C*. Therefore the feature for WT′ occurs simultaneously with the one of the phenolate ring vibration at 1487 cm^{-1}, while the one for A44C* arises prior to the features assigned to chromophore protonation. However, due to the complicated interpretation of the C=O bleach as marker band for E46 deprotonation, the comparison of the proton transfer processes has to be considered with caution. Nevertheless, the occurrence of these features on the hundreds of microseconds timescale confirms clearly that this transition can be assigned to the formation of pB′.

Besides the features corresponding to the proton transfer steps, further prominent features appear in the LDMs at the same time range. For example, the feature that is associated with the chromophore's C=O vibration at 1676 cm^{-1} occurs at a lifetime of about 390 µs for WT′ and 210 µs for A44C*, resulting from changes in the chromophore conformation. These changes were previously recognized to precede the chromophore protonation during the

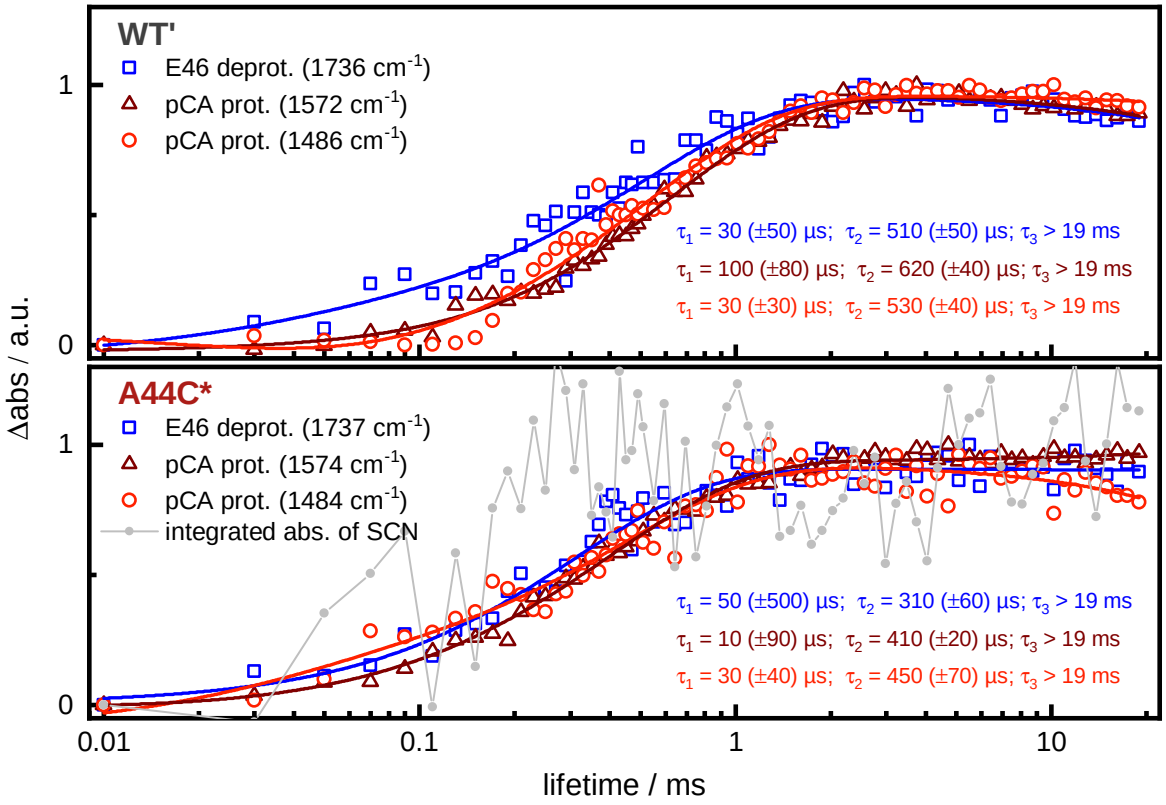

Figure 8.2: *Normalized time traces of E46 deprotonation (E46 deprot., blue squares) and chromophore protonation (pCA prot., dark red triangles and light red circles) marker bands for WT′ (top) and A44C* (bottom) in the step-scan FTIR data. The dynamics of the chromophore protonation marker band at about 1574 cm^{-1} (dark red triangles) is superimposed by the dynamics of polar side chain groups of the protein [11]. Note that the assignment of the trace around 1736 cm^{-1} to E46 deprotonation is not unambiguous in H_2O. All traces were normalized and fitted with three exponential functions, however, the errors especially of the first and long lived component are quite high. In the figure of A44C*, additionally the trace of the integrated absorption of the SCN signal (see more details in figure 8.4 on page 157) is shown in light gray for comparison.*

$pR_2 \rightarrow pB'$ transition, possibly to facilitate the proton transfer from water molecules in the binding pocket to the phenolate of the chromophore. The most pronounced features occur in the amide I region, indicating conformational changes of the protein. It is noticeable that the positive feature at 1624 cm^{-1} and the negative feature at 1644 cm^{-1} of the backbone absorption do not appear simultaneously. This might be due to the overlap of different contributions from protein absorptions in this spectral region. For both WT′ and A44C* the positive feature appears prior to the negative one. The structural changes though, seem to be significantly faster in A44C* with lifetimes of 210 µs and 550 µs for the positive and the negative feature, respectively, while for WT′ lifetimes of 510 µs and 820 µs are obtained. The appearance of a feature corresponding to the C–C modes of the chromophore at 1301 cm^{-1} on a similar timescale as the protonation is probably caused by structure changes of the chromophore. This negative absorption is also used as *trans-cis* marker band [14], but its existence already in the first single spectra (see figure G.1 on page 245 in the appendix) indicates that the chromophore is in *cis*-configuration during the complete measured time range.

The LDM features on the millisecond timescale appear all approximately at the same lifetime of 7 ms in WT′ as well as A44C*, highlighted by the yellow dashed line in figure 8.1. It is striking to see that the features occur at almost the same spectral positions and with the same signs like the ones on the hundreds of microseconds timescale, implying that these changes are only caused by a further increase in signal size. This matches the spectral changes observed in global analysis between the 640 µs/530 µs component and the long lived spectrum, that decays with > 19 ms, since most of the bands only grow larger in intensity without distinct frequency shifts. The long lived spectrum concurs with the difference spectrum measured by Brudler *et al.* [10] at 10 ms that was assigned to I_2, which corresponds to pB in the nomenclature used here. Due to the missing millisecond component in the global analysis, the interpretation of the changes at a lifetime of 7 ms is complicated, but the comparison to previous step-scan FTIR studies [10, 11] and the significant increase of the features in the amide I region imply that they originate from the large conformational changes of the protein backbone during the signaling state formation. Essentially, the protein and chromophore dynamics obtained by time-resolved step-scan FTIR spectroscopy are in very good agreement with the ones observed in the transient vis-pump-IR-probe experiments, that were discussed before for the same samples in H_2O and D_2O.

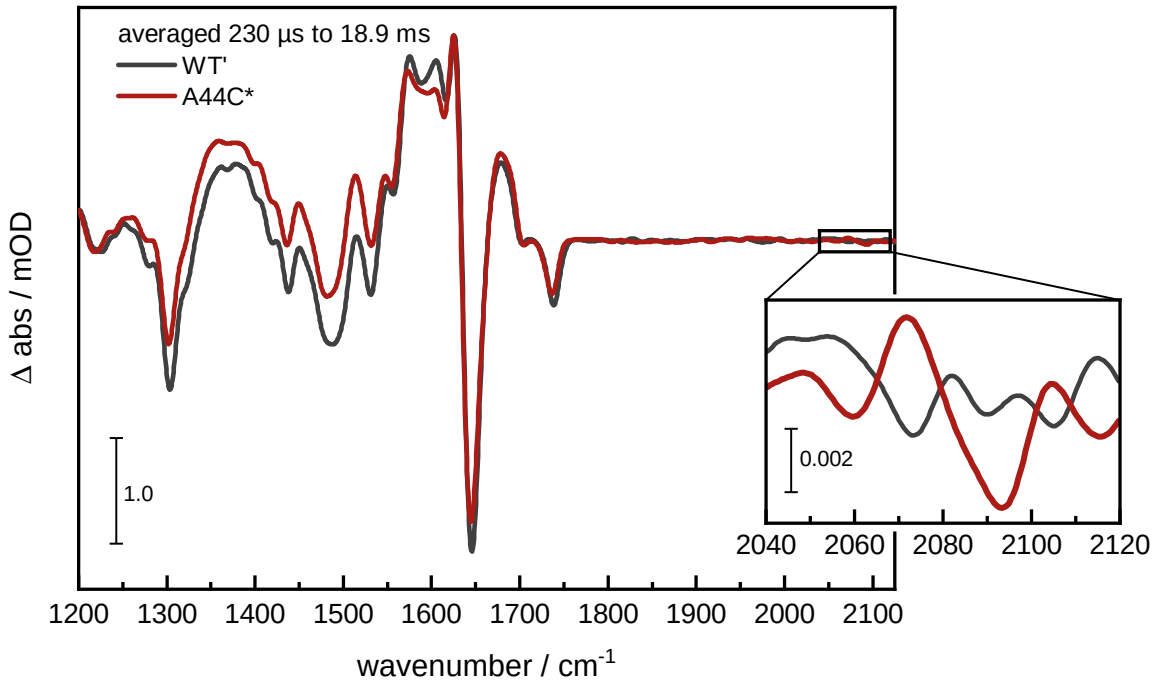

Figure 8.3: *Time-resolved step-scan FTIR spectra of WT′ (dark gray) and A44C* (red) were averaged from 230 µs to 18.9 ms, the time range in which the SCN signal reached the largest amplitude (compare figure 8.4 on page 157). The inset shows a zoom into the spectral region of the SCN signal, that is present in A44C* (red), but not in WT′ (dark gray).*

To spectrally resolve the difference signal of the SCN label in A44C*, the step-scan FTIR spectra between 230 µs and 18.9 ms had to be averaged. In this time range the SCN signal was found to reach its maximum absorption as it can be seen in the SCN time trace in figure 8.4 on page 157. A comparison between the averaged WT′ and A44C* spectra is shown in figure 8.3. As already discussed before, the protein and chromophore absorptions of both samples agree markedly well. The inset in figure 8.3, which provides

an enlarged representation of the SCN region, clearly shows the signal of the SCN label (red), despite its very small amplitude of only 6 µOD. Form and position of the label match the ones observed in the steady-state FTIR experiments (compare figure 5.1 on page 59). The tiny signal size results from the very thin sample thickness, since in the step-scan FTIR measurements no spacer was used, whereas in the transient pump-probe experiments in H_2O a 100 µm thick spacer was applied.

To investigate the kinetics of the SCN label, the so called integrated absorption was used, where time traces with a positive SCN signal (between 2082 cm^{-1} and 2101 cm^{-1}) were added up and the traces with a negative signal (2082 cm^{-1} and 2101 cm^{-1}) were subtracted. For better comparison, the signal of WT' in this spectral region was calculated by treating the time traces in the same way (adding up the traces in the same spectral range and subtracting the same traces). Both resulting time traces are plotted in figure 8.4 on the facing page. It is clearly visible that for A44C* the SCN signal grows in (panel in the middle), while the time trace for WT' (panel at the top) fluctuates around an absorption of zero, with larger deviations especially below 100 µs where the density of time points is low and the noise relatively high. The dashed lines in both plots in figure 8.4 illustrate the fits obtained from global analysis of the entire measured spectral range, that were summed up analogous to the raw data. As the overall protein kinetics, that are represented by the GA fit with three lifetimes of 36 µs, 530 µs, and > 19 ms, do not coincide very well with the dynamics of the SCN label, the SCN trace was additionally fitted with a single exponential function with a lifetime of 100 µs, which seems to describe the dynamics considerably better (solid red line in figure 8.4).

However, this time constant is remarkably faster than the one observed for the SCN dynamics in the transient vis-pump-IR-probe experiments of A44C* in H_2O, that revealed a lifetime of 320 µs when fitting the time traces of the SCN kinetics (or 434 µs in global analysis). To exclude that the deviations in the lifetimes result from the fits, the time traces of the SCN signal's raw data from both experiments are contrasted in the third panel of figure 8.4. For the kinetics from the pump-probe measurements the amplitude of the SCN signal (from the maximum to the minimum) is applied, while for the step-scan FTIR data the integrated absorption is depicted again. With this comparison it is obvious that the SCN dynamics measured by step-scan FTIR spectroscopy are indeed faster than the ones obtained in the pump-probe experiments, although the conditions were quite similar apart from the significant difference in the sample thickness, which is not expected to influence any dynamics. Besides, examination of the protein and chromophore dynamics showed that they are alike in both experiments as it was discussed before. Therefore no obvious reason can be found so far that would explain the apparently accelerated SCN kinetics in the step-scan FTIR measurements.

The steady-state experiments in combination with the structural investigation of A44C* suggested that the SCN label responds to deprotonation of the nearby E46 during signaling state formation and also the kinetics found in the transient pump-probe experiments in D_2O agreed with these findings since the label followed E46 deprotonation in the $pR_2 \rightarrow pB'$ transition. In H_2O however the interpretation was more difficult due to the unclear assignment of the E46 deprotonation process, but the SCN kinetics (and therefore probably the deprotonation as well) were found to be slightly accelerated with respect to the measurements in D_2O. Based on these observations, the time trace of the integrated ab-

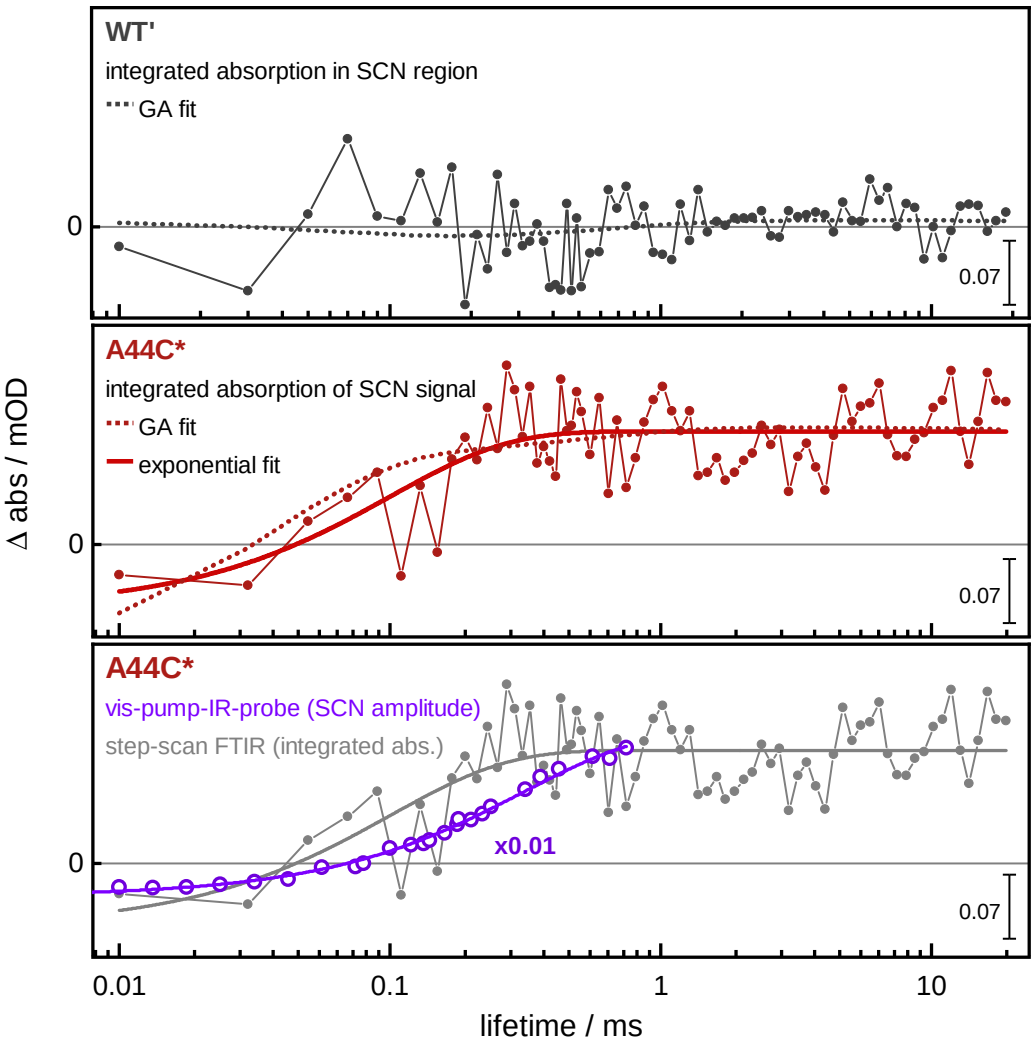

Figure 8.4: *Time traces of WT′ (first panel) and A44C* (second panel) in the SCN region for time-resolved step-scan FTIR measurements and comparison with SCN kinetics from transient vis-pump-IR-probe experiments of A44C* in H_2O (third panel). The signal for A44C* was calculated by taking the integral absorption between 2062 cm^{-1} and 2081 cm^{-1} (induced absorption of SCN signal corresponding to pB) minus the integral absorption between 2082 cm^{-1} and 2101 cm^{-1} (bleach of the SCN signal) of the raw data (line-symbol), for WT′ the signal was calculated in the same way. This "integration" method is only valid for signals which do not shift, as it is the case here. Note that the amplitude for the SCN time trace obtained by the integrated absorption is approximately 20-times larger than the real signal size of the SCN (compared at the last time point) due to the summation of the amplitudes of the different time traces. The dashed lines (gray for WT′ and red for A44C*) represent the fits obtained from global analysis that were summed up in the same way as the raw data. The SCN kinetics of A44C* were additionally fitted by a single exponential function (solid red line in the second panel) with τ = 100 (±30) µs. In the third panel the integrated SCN signal of A44C* and the corresponding single exponential fit for the step-scan data are depicted in light gray. The SCN signal amplitude (max(2075 cm^{-1}) − min(2085 cm^{-1})) from the transient vis-pump-IR-probe data of A44C* in H_2O is shown as purple circles and was scaled by a factor of 0.01 to match the amplitude of the step-scan data. The data were also fitted by a single exponential function (purple solid line) with τ = 320 (±10) µs. Global analysis revealed a lifetime of 434 µs for the SCN signal.*

sorption of the SCN signal from the step-scan FTIR measurements is compared to the time traces of E46 deprotonation and chromophore protonation in A44C*, shown in figure 8.2 on page 154. Although the noise level of the SCN trace is very high due to its tiny signal size, the comparison implies that the kinetics of the SCN label are significantly faster than the kinetics of the proton transfer processes. The exponential fits of both, the SCN signal and E46 deprotonation, suggest as well that the label dynamics observed here are about three times faster than the deprotonation dynamics. Unfortunately, the SCN signal is too small to resolve its changes in the LDM of the step-scan FTIR data (SCN region not shown). Nevertheless, the step-scan FTIR measurements, which expanded the accessible measurement range to lifetimes longer than 1 ms, confirm that the SCN label reacts to changes during the $pR_2 \rightarrow pB'$ transition and not to the subsequent formation of the signaling state pB.

8.2 Conclusion

The time-resolved step-scan FTIR measurements extended the investigated time range with respect to the transient vis-pump-IR-probe experiments, discussed in the previous chapter, and additionally allowed to probe the formation of the signaling state pB. A further advantage was the broad spectral window that could be detected in one measurement and provided additional information about protein and chromophore kinetics.

In the step-scan FTIR measurements similar dynamics were found for WT' and A44C* as observed in the transient pump-probe experiments in H_2O on a hundreds of microseconds timescale. This transition could clearly be assigned to the pB' formation, but also here, like in the previously performed H_2O experiments, it was not possible to distinguish unambiguously whether chromophore protonation and E46 deprotonation occurred simultaneously or delayed with respect to each other. It was observed though, that the proton transfer processes in A44C* were slightly accelerated compared to WT'. Besides dynamics at about 7 ms corresponding to the formation of pB were observed, but could only be resolved by lifetime density analysis. However, the features in the LDMs indicated that the $pB' \rightarrow pB$ transition is mainly accompanied by conformational changes. Although an early millisecond component is missing in the results obtained from global analysis, the long lived spectra were in good agreement with the steady-state difference spectra between pB and pG presented before (see figure 4.1 on page 52) and the spectrum assigned to the pB state in previous step-scan FTIR measurements [10].

Despite the tiny signal size of about 6 µOD, it was possible to resolve the response of the SCN label in A44C*. Investigation of the kinetics revealed that the label seemed not to follow the overall protein dynamics, but rather grew in with a lifetime of about 100 µs. This means that these SCN dynamics are remarkably faster than the ones obtained for the label in A44C* by the pump-probe measurements (320 µs in H_2O) under comparable conditions. Thus, the kinetics of the label were also significantly accelerated compared to the proton transfer processes, which occurred on a similar timescale as in the pump-probe experiments. This difference in the SCN dynamics, while the protein and chromophore dynamics were similar for both methods, might possibly be caused by the very small signal size of the SCN vibration, which is hardly larger than the background noise level, or could be influenced by the integrated absorption, that was used to present the kinetics. In spite of everything, it was clearly resolved that the label reacted to changes during pB' and not

during signaling state formation. For a more detailed analysis of the SCN dynamics, a larger signal size would be necessary. This could be reached by the usage of D_2O instead of H_2O, which would allow to increase the thickness of the sample significantly. Then it would probably also be possible to measure the kinetics of the labels in other mutants, that mostly showed smaller SCN signals than the one in A44C*.

Part V

Summary

9 Summary and Outlook

During the course of this work it was impressively demonstrated that the application of the IR label thiocyanate provides a powerful method to investigate local protein dynamics of the photoreceptor PYP in a native environment. The successful insertion of the SCN label at selected positions in PYP allowed to study structural changes and dynamics during the photocycle with high spatial resolution by using various IR spectroscopic techniques. With steady-state experiments, the influence of the local environment on the label and alterations of the protein structure due to formation of the signaling state pB were investigated for the different labeling sites using the central wavenumber and line shape of the SCN absorption as well as the vibrational lifetime of the label as observables. Time-resolved methods facilitated following the protein dynamics throughout most part of the photocycle up to tens of ms with high temporal resolution (hundreds of fs). While IR spectroscopy reveals site-specific information usually only on the chromophore and potentially a few side chains, the response of the SCN labels to chromophore isomerization (ps), structural relaxation within the binding pocket (ns), proton transfer processes (µs), and conformational changes (ms) of the protein structure [20] provided information about when and how selected locations in the protein changed during the photocycle.

Examination of the changes in the SCN absorption for different labeling sites and between the pG and pB state by steady-state FTIR spectroscopy showed that the SCN absorption is mainly sensitive to hydrogen-bonding interactions leading to a blue-shifted absorption [23–25]. This influence of solvent exposure on the central wavenumber of the absorption was supported by SASA calculations from MD simulations, which provided a good measure for the solvent accessibility of the label at different positions within PYP in both states [121, 136]. Besides the hydrogen-bonding interactions with the solvent, however, other effects were found to influence the SCN absorption like the polarity of the label's surrounding, charged groups in the proximity, or hydrogen bonds to confined water molecules in the protein interior. The sometimes competing effects on the SCN absorption could make a straightforward conclusion about the label's environment difficult. Temperature dependent FTIR measurements indicated whether the SCN label was engaged in hydrogen bonds or not, helping to simplify the interpretation. Ultrafast IR-pump-IR-probe measurements made an additional observable for investigation of PYP in the steady-state available: The vibrational lifetime of the C≡N vibration at different labeling sites in PYP was observed to cover a broad range of lifetimes (28 ps to 70 ps) reflecting the high sensitivity of this observable to the surrounding environment, especially to solvent exposure. Comparison to the lifetime of the model compound MeSCN in water (36 ps), which represents the fully exposed label, revealed insights into the influence of bulk water and the protein environment on the label. Therefore, the vibrational lifetimes facilitated the interpretation of the absorption spectra from the FTIR experiments significantly, because they were not affected by the competing effects of polarity and hydrogen-bonding interactions observed for the SCN absorption.

The photocycle dynamics were investigated by time-resolved vis-pump-IR-probe spectroscopy. Combination of mechanically delayed pump pulses, created by changes in the optical path length, and electronically delayed pump pulses, obtained by synchronization of two fs-laser systems [40, 145], made it possible to cover a time range of nine orders of magnitude from hundreds of femtoseconds to almost 1 ms. Especially the synchronization of the two laser systems was applied for the first time to a comprehensive study of dynamics in proteins. Therefore several technical requirements had to be adjusted to allow for the measurement of the slow dynamics. The application of the Lissajous scanner improved the performance of the experiments and the data quality significantly (in comparison to the usage of a flow cell), whereas lowering the repetition rate of the pump pulses by the chopper divider routine was found to be not required. The transient pump-probe experiments enhanced the local structural resolution of the photocycle dynamics by probing the SCN kinetics in five different labeled PYP-mutants and provided, in addition, new insights into the overall protein and chromophore dynamics. In general the observed dynamics were in good agreement with previous studies. Depending on the position of the label within the protein, different transitions during the photocycle could be detected. While some of the labels already reacted on the electronic excitation of the chromophore directly after photon absorption and its subsequent isomerization, others only sensed the proton transfer processes or structural rearrangements during pB' formation on a hundreds of microseconds timescale. The combination of global analysis [144], which simultaneously analyzes the entire investigated spectral region by applying a model (in this case: sequential), and lifetime density analysis [146], where a quasi-continuous contribution of exponential functions is fitted to each wavenumber individually to obtain only the time-dependent changes in the measured data, proved to be essential for investigation of such a broad time range and multitude of different protein, chromophore and SCN vibrations. The measurement range was further extended up to 20 ms by time-resolved step-scan FTIR spectroscopy, that allowed to additionally probe the partial unfolding of PYP during the formation of pB for WT-PYP and one of the labeled mutants (A44C*). One advantage of these measurements with respect to the transient pump-probe experiments was the synchronous recording of an extremely broad spectral window providing additional information about protein and chromophore kinetics due to further detected vibrational modes.

The mutation sites for the cysteines were selected in a way to neither affect integrity nor function of the protein, but at the same time being at locations that potentially provide interesting insights into the structural changes during the photocycle. Hence, two mutation sites at the protein surface (A44, D48), two for probing the kinetics of the N-terminus (L23, A30), and three within the chromophore binding pocket (V57, M100, V122) were chosen. Function and structure of the proteins after mutation and labeling were characterized by various spectroscopic methods, *i.e.* UV/vis, CD and FTIR difference spectroscopy, and ESI-IMS mass spectrometry. The latter was used to investigate the gas phase ion structure and therefore the surface exposure of the mutants revealing information about the folding state of the proteins. Overall, the structure of the proteins and the ability to form the signaling state were hardly influenced by replacement of the native residues and cysteine cyanylation. However, for some mutants local changes occurred past mutation and/or labeling. The FTIR spectra of V122C* and the unlabeled V122C showed that the carboxyl vibration of E46 was significantly red-shifted with respect to WT-PYP and the other mutants. This could be explained by the close proximity of V122 to the glutamate and its involvement

in hydrophobic interactions [11, 165]. The replacement of the rigid, non-polar valine by a cysteine probably led to changes in the highly hydrophobic environment of the carboxylic group of E46. Another mutant, that was slightly disturbed by mutation and/or labeling, was L23C*, which was found to have already in pG a detached N-terminal region as it was only expected for pB. In CD and FTIR difference spectroscopy, this alteration was not observed, since both methods are mainly sensitive to changes in the secondary structure, but the gas phase ion structure as probed by ion mobility mass spectrometry revealed a similar charge state distribution for both dark and illuminated conditions indicating an enlarged surface area due to destabilization of the N-terminal region. Possibly the hydrogen bond, that is formed between the backbone of L23 and N43 in the α3-helix [91], was altered or broken after substitution with cysteine or perturbed by insertion of the SCN. From previous studies it was already known that the replacement of the methionine at position 100 dramatically decelerates the recovery of the pG state [85, 156–159] due to the loss of the electron-donating properties of methionine, which facilitated the re-isomerization of the chromophore [156]. Nevertheless, this mutation site was chosen for cyanylation, since the structure was found to be not disturbed by mutation and to investigate the influence of the mutation on the other photocycle transitions. Moreover, the position close to the chromophore was expected to reveal interesting insights into changes of the chromophore and the environment of the surrounding binding pocket.

Investigation of the SCN labels at the selected locations in the protein *via* the different IR techniques revealed site-specific information about structure changes in the steady-state and photocycle dynamics of PYP. The label in A44C*, located in the α3-helix and exposed to the solvent in pG, exhibited a large red-shift of the SCN absorption of about 9 cm^{-1} under illumination. This shift seemed quite large considering the SASA calculations, which showed only a small decrease in solvent accessibility, and the vibrational lifetimes deviating only a little in pB from the fully solvent exposed case, that was observed in pG. Therefore the steady-state experiments indicated the influence of changes in the electrostatic field on the label, most likely caused by deprotonation of the nearby E46. This assumption was further supported by the time-resolved measurements, since the label at the surface of the protein responded only during the $pR_2 \rightarrow pB'$ transition simultaneously with deprotonation of E46. In H_2O the SCN kinetics were slightly accelerated consistent with the kinetic isotope effect, which was expected to influence the proton transfer processes. Since the interpretation of the deprotonation dynamics by looking at the C=O vibration of E46 was complicated in H_2O, the investigation of the SCN kinetics in A44C* supported the assignment of the deprotonation process. In the time-resolved step-scan FTIR experiments a tiny SCN signal of about 6 µOD was resolved. However, the kinetics of the SCN label were markedly faster (about 100 µs) than observed in the pump-probe experiments (about 320 µs) under similar conditions, while the protein and chromophore dynamics were comparable for both methods. Presumably the difference was caused by the low signal-to-noise ratio of the SCN in the step-scan FTIR measurements. Nevertheless, these measurements proved as well that the label did not follow the overall protein dynamics during pB formation, but already responded to changes during the $pR_2 \rightarrow pB'$ transition.

Although located in the same helix as A44C* and also solvent exposed in the pG state, the label in D48C* sensed only a very small red-shift of the SCN absorption. The vibrational lifetimes were similar to the ones for A44C* indicating a fully exposed label in pG, which lost some of its contacts to the bulk water when the influence of the protein increased in

pB. This implied the partial movement into the more solvent protected environment of the hydrophobic chromophore binding pocket after the chromophore moved outwards in pB as suggested by previous studies for this residue [82, 154]. Due to the very small difference signal of SCN in the steady-state measurements, this mutant was anticipated to produce signals that were not detectable in the time-resolved experiments and thus was not further investigated.

In A30C* the label was oriented into the cavity between the N-terminal region and the rest of the protein. The SCN absorption in pG showed a very narrow, Lorentzian-like line shape, that was interpreted as homogeneous environment as it was expected for a label buried inside the protein. This was in good agreement with the SASA calculations, where also a very low solvent accessibility was predicted for pG. The vibrational lifetime suggested a shielded label inside the protein, too, that became highly accessible in pB with the expected movement of the N-terminus, indicated by a decrease in the vibrational lifetime to a similar one as for MeSCN in water, which represented the fully solvent exposed SCN. In the FTIR spectra the transition into an exposed environment was not so much reflected by the change of the central wavenumber, but the change of the line shape which broadens significantly in pB. The time-resolved measurements revealed that the changes probed by the SCN label occurred already during pB' formation and were probably associated with conformational changes of the N-terminus, that were found to take place in about 200 µs [75, 170, 180] resembling the kinetics detected for the SCN label in A30C*.

In addition, L23C* was selected to probe the movement of the N-terminus, but due to destabilization of the N-terminal region even in pG, the influence of the photocycle dynamics on the label's environment could not be detected. Both the SCN absorption and the vibrational lifetime indicated a solvent exposed SCN label in the pG and pB state. Because of the altered conformation resulting in an almost identical central wavenumber for the SCN absorption, the difference signal was very small and therefore the SCN dynamics were not examined by the time-resolved pump-probe experiments.

The label in V57C* was located in the chromophore binding pocket, but with some distance to the chromophore and E46. Although it was buried in the protein interior and the SASA calculations predicted a low accessibility in pG, the SCN absorption was shifted to a relatively high central wavenumber. The results of the temperature dependent FTIR measurements indicated the engagement of the label into hydrogen-bonding interactions. Further, the extremely short vibrational lifetime for V57C* pG of only 28 ps suggested a strong hydrogen bond with another hydrogen bond donor than the bulk water, which would lead to lifetimes of about 36 ps for the label. These observations in combination with the MD simulations, which revealed that most of the hydrogen bonds of the SCN in V57C* were formed with water molecules instead of the protein environment in pG, led to the conclusion that the label was hydrogen-bonded to a confined water molecule inside the protein. Under illumination, the vibrational lifetime assimilated to one of the fully exposed label. This was in good agreement with the expected collapse of the hydrophobic binding pocket, which would allow the invasion of water molecules. In the spectral shift of the SCN absorption, this change from solvent protected to solvent accessible in pB was not well represented, since the central wavenumber was already blue-shifted in pG. Due to its position in the chromophore binding pocket, the label detected the electronic excitation and isomerization of the chromophore on a sub-ps and ps timescale, respectively, after absorp-

tion of a blue photon. The subsequent ns-relaxation processes of the chromophore and the surrounding hydrogen-bonding network had only small impact on the SCN label. During the following transition the SCN signal persisted unaltered, until it reacted on a hundreds of µs timescale. It was not clearly distinguishable which of the processes occurring during the $pR_2 \rightarrow pB'$ transition in the chromophore binding pocket were sensed by the label, but an increased accessibility for water molecules after movement of R52 seems reasonable.

The SCN absorption of V122C* featured two conformations of the label in the pG state. The exact structural differences between these two conformations could not be resolved yet. However, in pB only one slightly red-shifted conformation was observed. The long vibrational lifetime of the two pG conformers (not measured separately) was hardly changing between pG and pB indicating a buried label in both investigated states. This was further supported by the SASA calculations, that showed very low solvent accessibilities for pG and pB. Hence, the deviations in the SCN absorption were probably caused by changes in the polarity of the surrounding. In the time-resolved measurements the label in V122C* was found to already respond to the early photocycle transitions, similar to the one in V57C*, but rather to changes involving E46, which is hydrogen-bonded to the chromophore and close to the label, than to alterations of the chromophore itself. With the response of the SCN label in V122C* at 220 ps, evidence for the existence of the $I_0^{\ddagger}$ intermediate was found, which was proposed in some studies to be formed with the same time constant and was related to relaxation processes of the protein in the vicinity of the chromophore [8, 87]. While apparently the protein and chromophore vibrations did not respond to this transition, probably due to the very small impact on the protein structure, the label even made a "visualization" of the changes upon $I_0^{\ddagger}$ formation in the proximity of E46 possible. The subsequent relaxation processes during pR_1 formation in a few nanoseconds were detected by the label in V122C* as well. The response of the SCN label on an early µs timescale supported the observations from WT-PYP, as discussed later on, that indeed a second pR sub-state (pR_2) exists involving changes of E46 with respect to pR_1. During the $pR_2 \rightarrow pB'$ transition, V122C* probed the deprotonation of E46 and its movement into a more hydrophobic environment with both processes occurring simultaneously in this mutant.

In the pG state the label in M100C* was positioned in the proximity of the positively charged side chain of R52 and the deprotonated chromophore. The pronounced shoulder in the SCN absorption indicated the existence of two subpopulations in pG. The influence of the charged groups was most likely responsible for the occurrence of the lowest wavenumber observed for SCN in proteins so far (2069.8 cm^{-1}, corresponding to 2148.5 cm^{-1} without isotope shift, for the red-shifted subpopulation). Furthermore, the SCN absorption of both subpopulations in the pG state indicated a solvent protected environment. At the same time, the longest vibrational lifetimes (70 ps and 63 ps) were obtained for the two subpopulations implying that the vibration of the label was not influenced by any hydrogen bonds towards the solvent or, most likely, neither the protein. Under illumination a large blue-shift of the SCN absorption was observed corresponding to the large conformational rearrangements occurring during the photocycle, which drastically increased the distance between the charged groups and the label, and led to the solvent exposure of the label as not only indicated by the SCN wavenumber, but also by the changes in the vibrational lifetime. The time-resolved measurements showed that already the electronic excitation of the chromophore after photon absorption had a large influence on the SCN label, probably due to changes of the electrostatic properties of the chromophore. The structural rear-

rangements of the chromophore during *trans-cis*-isomerization were sensed by the label as well. The significant decrease of the SCN signal size at about 100 ps indicated a slow return to pG after isomerization of the chromophore for the molecules that were not able to successfully enter the photocycle (possibly *via* a ground state intermediate GSI [14]). This observation is comparable to the effect that was found for the relaxation dynamics of pB in previous studies after replacement of the methionine [85, 156–159]. On a few nanoseconds timescale the label probed the relaxation processes of the chromophore resulting in the formation of pR_1. Presumably the SCN label also sensed the early µs-dynamics that were assigned to the $pR_1 \rightarrow pR_2$ transition in a sequential model, in good agreement with the findings that R52, which is close to M100C*, was involved in this transition. The pB' formation was found to appear accelerated in M100C* in tens of µs. The SCN label reacted simultaneously with changes of the R52 absorption, prior to the proton transfer processes, sensing the movement of the positively charged R52 and the intrusion of water molecules into the binding pocket. Thus, the large blue-shift of the SCN absorption was observed during this transition.

Besides the site-specific information from the SCN labels, the time-resolved experiments also allowed new insight into the photocycle dynamics of WT-PYP. Consistent with previous studies [12–14, 62], multiple relaxation processes of the electronically excited state pG* were observed after photon absorption followed by *trans-cis*-isomerization of the chromophore and loss of the hydrogen bond between the chromophore's carbonyl and residue C69 in a few picoseconds. The existence of intermediate $I_0^{\ddagger}$ could not unambiguously be identified in WT, only the SCN kinetics in V122C* on a hundreds of ps timescale indicated its formation. The pR intermediate was found to form in a few nanoseconds with changes mainly involving the chromophore. The transient vis-pump-IR-probe experiments presented in this thesis, provided the first evidence for the early µs-dynamics in an IR study, that were previously assigned to the existence of two pR states by various studies, *i.e.* using transient grating spectroscopy or X-ray scattering techniques [70, 73–75, 89, 92]. It was not only possible to detect these dynamics, but also to localize the corresponding structural changes to residues in the chromophore binding pocket, namely E46 and R52, which were interacting with the chromophore *via* a hydrogen bond and electrostatic interactions, respectively. In literature, however, the differences leading to the two sub-states were still under debate suggesting either relaxation processes of the protein structure distant from the chromophore [73, 74, 92], changes of the hydrogen-bonding network of the chromophore with nearby amino acids [70, 75, 90], or interactions with aromatic or charged residues [89] as origin. Neither investigation of the native amino acid and chromophore bands nor of the SCN bands could solve conclusively, however, whether the formation of the two sub-states followed a consecutive model with pR_1 relaxing to pR_2 on the µs timescale or a parallel model with both sub-states formed simultaneously in a few ns and then decaying to pB' on different timescales (pR_1 in a few µs and pR_2 in hundreds of µs).

In this thesis first direct kinetic evidence was found excluding E46, which became deprotonated during pB' formation, as proton donor for the chromophore, since the deprotonation process did not appear simultaneously but prior to the protonation of the chromophore in the hundreds of µs time range. Instead it seems to be more likely that water molecules, which were able to penetrate into the binding pocket, enabled intermolecular proton transfer [98]. While most of the photocycle dynamics were hardly influenced by the exchange of D_2O with H_2O, the proton transfer processes during pB' formation exhibited a kinetic

isotope effect. While the deprotonation of E46 seems to be slower in H_2O than in D_2O, the movement of E46 and the protonation of the chromophore were clearly accelerated. The interpretation of the deprotonation dynamics was, however, not straightforward and comparison of the SCN kinetics in A44C* even suggested an accelerated deprotonation process, which would be more consistent with the expected kinetic isotope effect. Thus it was not possible to exclude E46 as proton donor, when only taking the measurements in H_2O into account. In both solvents, the upshifted absorption of the carboxylic group of E46, that was assigned to the movement into a more hydrophobic environment [10, 11], preceded the proton transfer processes. Therefore, the generally accepted photocycle transition $pR_2 \rightarrow pB'$ could be subdivided into multiple steps indicating a consecutive course of E46 movement, E46 deprotonation and chromophore protonation. Whereas global analysis alone was not able to distinguish between these different steps, the analyses with both the LDA and fitting of the time traces pointed to this interpretation independently. With the SCN labels at various positions in the protein, it was possible to follow individual steps of this photocycle transition. The time-resolved step-scan FTIR measurements suggested that the signaling state pB was formed in about 7 ms, matching kinetics found in previous IR studies [10, 11].

Examination of the protein and chromophore dynamics of the SCN-labeled mutants revealed that they commonly equaled the dynamics of WT-PYP for all investigated photocycle transitions. One exception was V122C*, which showed concurrent deprotonation and movement of E46 proceeding the protonation of the chromophore. The other one was M100C* showing a slow relaxation to pG on the hundreds of ps timescale after unsuccessful entry into the photocycle and a significantly accelerated formation of pB' occurring in tens of µs.

Using the SCN in form of cyanylated cysteines as IR label at selected positions in PYP allowed to gain insights into the protein environment in steady-state and its changes during the photocycle with high spatial resolution on a single side chain level. In the following several approaches are discussed that could further improve the interpretation of the conclusions drawn in this thesis and could provide additional information about PYP and its photocycle. First, the lifetime density analysis could be improved. It is essential to solve the problem of the shifted lifetimes that occurs after standardization. Therefore one has to look at the influence of the regularization factor in the Tikhonov regression method on the LDA of each individual pixel. Furthermore, different regularization methods could be applied [147, 189, 190].

Simulations of the line shape and frequency of the SCN absorption from FTIR measurements for all investigated mutants in pG and pB, analogous to the one performed for SCN-labeled calmodulin by [191], would facilitate the understanding of the effects that influence the SCN absorption and therefore more precise conclusions about the label's direct surrounding could be drawn. To gain an even more detailed insight into the orientation and environment of the SCN label, crystallography of the labeled mutants, at least in pG, is necessary. The crystal structures would provide information about the orientation of the SCN towards the surrounding residues, solvent exposure, and the involvement into hydrogen-bonding interactions to both the solvent and the protein. An additional observable for the investigation of the protein structure in the steady-state can be obtained with

2D-IR spectroscopy of the label. The temporal evolution of the 2D line shape probes spectral diffusion and can reveal insight into the equilibrium dynamics involved at the label's protein environment [192].

One aim in the future should be to measure all transient species of PYP's photocycle from the early picosecond to the tens of milliseconds timescale with one setup in one single measurement. For that reason, the jitter of the electronically delayed pulses in the vis-pump-IR-probe experiments has to be improved to 1 ps, which is technically achievable [40], making the mechanical delay experiments redundant. Moreover, the performance of the laser synchronization has to be adapted in a way to allow the extension of the accessible measurement range to tens of ms, which also enables recording of the pB formation. The application of ultra-broadband measurements (tens of fs pulses) would allow to measure a much broader spectrum at once providing more spectral features simultaneously for interpretation. Furthermore, it would be beneficial to increase the signal size of the SCN label in the time-resolved step-scan FTIR experiments. This can easily be achieved by an increase of the sample thickness, when using D_2O instead of H_2O as solvent. Hence it would be possible to also measure the SCN signals in other mutants, where the signal size of the SCN was mostly even smaller than in A44C*, up to tens of milliseconds. A larger SCN signal would also facilitate the interpretation of the kinetics in A44C*.

Eventually, the examination of additional SCN-labeled mutants could enhance the understanding of protein structure and photocycle dynamics of PYP. A large number of labeling sites might even provide benchmark studies for MD simulations to develop models for the influence of local fields and hydrogen-bonding interactions on the spectral shifts of the SCN absorption. Ultimately, with a high precision of these simulations, experiments would be no longer required to predict the surrounding structure of the labels. One interesting location for a new label could be a residue in the N-terminus for example, whose mutation and labeling does not perturb the structure, but allows the label to sense the movement of the N-terminal region. Further locations, that should be investigated, are residues far away from the binding pocket, which can detect influences on the distant protein structure during the photocycle.

After the SCN label demonstrated its ability in investigating the photocycle dynamics in PYP in this comprehensive study, it could also assist in unraveling dynamics in multiple other proteins and could help to gain local insights *e.g.* into ligand docking in proteins or protein-protein interactions by means of IR spectroscopy.

10 Zusammenfassung

Proteine haben eine unentbehrliche Funktion in vielen biologischen Prozessen, wie Enzymkatalyse, Signalübertragung, Transportprozesse oder DNA Transkription. Daher ist es wichtig ihre Funktionsweise und Arbeitsmechanismen zu verstehen. Aus diesem Grund wurden in den letzten Jahrzehnten sowohl die Struktur als auch die Dynamik vieler Proteine eingehend untersucht. Eine große Herausforderung für die Untersuchung von Proteinen in ihrer natürlichen Umgebung ist dabei die lange Zeitskala, auf der sich die verschiedenen oben genannten Prozesse abspielen und die sich von wenigen Femtosekunden (10^{-15} s) bis zu vielen Stunden erstreckt. Spektroskopische Methoden bieten die Möglichkeit Proteinstruktur und -dynamik mit sehr hoher Zeitauflösung und ausreichend guter Strukturauflösung zu beobachten, indem man die zeitliche Entwicklung von elektronisch und vibronisch angeregten Moden verfolgt.

Aufgrund ihrer Relevanz für eine Vielzahl von Signalübertragungswegen in biologischen Systemen, ist die Untersuchung von Photorezeptorproteinen, wie dem Photoactive Yellow Protein (PYP), von großem Interesse. Hierbei spielen vor allem die Identifikation von Photozyklusintermediaten und die Beobachtung von dynamischen Strukturänderungen nach der Absorption eines Photons durch den Chromophor eine wichtige Rolle. Die ersten Photozyklusmodelle wurden mit Hilfe transienter UV/Vis-Spektroskopie erstellt. Mit dieser Technik können jedoch nur die elektronischen Zustände des Chromophors erfasst werden, was die verfügbaren Informationen auf die Struktur des Chromophors und die Auswirkungen auf dessen direkte Umgebung beschränkt [4, 6–9]. Weitere Intermediate konnten später mit zeitaufgelöster Infrarotspektroskopie identifiziert werden, die deutlich detailliertere Informationen über die Proteinstruktur liefert. Allerdings ist die Ortsauflösung auch hierbei auf den Chromophor und einige bestimmte Seitenketten, die in H-Brücken und Protonentransferprozesse involviert sind, beschränkt, während die restliche Proteinstruktur zu einer breiten Absorptionsbande (Amid-I-Bande) beiträgt [15]. Der Einbau von IR-Sensoren an nahezu allen gewünschten Positionen innerhalb des Proteins ermöglicht es ortsaufgelöste Informationen über verschiedene Regionen des Proteins zu erhalten [15–19]. Dies kann zu der genaueren Beschreibung bereits bekannter Photozyklusintermediate beitragen oder sogar zur Entdeckung neuer Intermediate führen.

In dieser Arbeit wurden die Strukturänderungen und Dynamiken, die während des Photozyklus des Photorezeptorproteins PYP auftreten, mit Hilfe des IR-Sensors Thiocyanat (SCN; hier wurde das isotopenmarkierte $S^{13}C^{15}N$ verwendet) sowohl im Gleichgewichtszustand als auch nach einer Störung zeitaufgelöst untersucht. Bei PYP handelt es sich um ein kleines, stabiles Protein mit einem kovalent gebundenen Chromophor, das als Reaktion auf die Anregung mit blauem Licht einen reversiblen Photozyklus durchläuft. In dessen Verlauf treten die *trans-cis*-Isomerisierung des Chromophors, sowie dessen Protonierung auf, gefolgt von großräumigen Strukturänderungen, die zur teilweisen Entfaltung des Proteins im Signalzustand führen. Die Änderungen während des Photozyklus finden auf ei-

ner Zeitskala von hunderten Femtosekunden bis hin zu einer Sekunde statt [20]. Um diese Strukturänderungen ortsaufgelöst verfolgen zu können, wurde der SCN-Sensor durch die Cyanylierung von Cysteinen an unterschiedlichen Positionen im Protein eingebaut [21, 22]. Die CN-Schwingung des Sensors reagiert sehr empfindlich auf Veränderungen der Polarität in seiner direkten Umgebung oder sich ändernde H-Brücken und kann abseits der restlichen Proteinabsorptionen detektiert werden [23–25].

Untersuchung von Strukturänderungen im Gleichgewichtszustand

Zunächst wurden Messungen im Gleichgewichtszustand durchgeführt, wobei die Absorption der SCN-Sensoren an sieben ausgewählten Positionen untersucht wurde. Der Einfluss der verschiedenen lokalen Umgebungen auf das SCN ließ sich im Dunkelzustand (pG) von PYP messen, während der Sensor unter dauerhafter Beleuchtung des Proteins mit blauem Licht auf die Strukturänderungen in Folge der Bildung des Signalzustands (pB) reagierte, die erheblich von der untersuchten Position abhingen. Als Observablen dienten hierbei die Zentralwellenzahl und die Bandenform der SCN-Absorption, die in FTIR (Fourier-transformierte Infrarot) Messungen in beiden Zuständen ermittelt wurden, und die Schwingungslebensdauer aus ultraschnellen IR-Pump-IR-Probe Experimenten, die sich besonders als Indikator für den Kontakt zum Lösungsmittel eignet. Die Absorptionsspektren und Lebenszeiten für SCN an den unterschiedlichen Positionen im Dunkel- und Signalzustand sind in Abbildung 10.1 zusammengefasst.

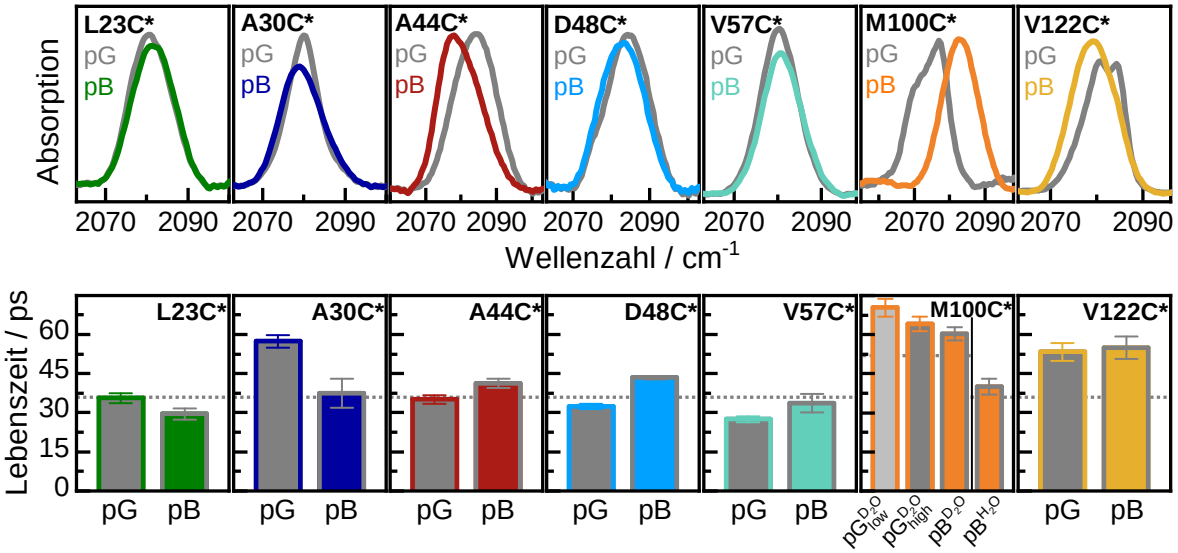

Abbildung 10.1: *Absorptionsspektren (oben) und Schwingungslebenszeiten (unten) des SCN-Sensors an ausgewählten Positionen innerhalb des Photorezeptorproteins PYP im Dunkelzustand (pG) und im Signalzustand (pB).*

Die FTIR Messungen im Gleichgewichtszustand haben gezeigt, dass die Veränderungen in der SCN-Absorption je nach Position des Sensors und Zustand des PYP, hauptsächlich von der Ausbildung von H-Brücken zu den umgebenden Wassermoleküle abhängen. Daher deutet eine Blauverschiebung der Absorption auf SCN an der Proteinoberfläche hin, das im Kontakt zur Lösungsmittelumgebung steht, während eine Rotverschiebung meist auf SCN, das im Proteininneren verborgen ist, verweist. Die Zugänglichkeit der SCN-Sensoren

für Wassermoleküle wurde zusätzlich mit SASA (*solvent accessible surface area*) Berechnungen aus Molekulardynamik (MD) Simulationen an PYP im pG und pB Zustand untersucht. Neben den Wechselwirkungen über H-Brücken zum umgebenden Wasser, wurden weitere Effekte beobachtet, die für eine Verschiebung der SCN-Absorption verantwortlich waren, so zum Beispiel die Polarität der Umgebung des Sensors, geladene Seitenketten anderer Aminosäuren in der Nähe oder H-Brücken zu Wassermolekülen, die im Proteininneren eingeschlossen sind. Da die verschiedenen Einflüsse die SCN-Absorption teilweise in unterschiedliche Richtungen verschieben können, wird eine eindeutige Interpretation der SCN-Umgebung in einigen Fällen erschwert. Mit Hilfe temperaturabhängiger FTIR Messungen ließ sich die Beteiligung des SCN an H-Brücken erkennen, was zu einer Vereinfachung der Interpretation beitragen konnte. Die Schwingungslebensdauern im Gleichgewichtszustand konnten zusätzliche Informationen über die lokalen Strukturen in der Nähe des Sensors liefern. Die Lebenszeiten, die für verschiedene Positionen im PYP in den beiden Zuständen pG und pB gemessen wurden, decken einen breiten Zeitbereich ab (28 ps bis 70 ps). Der Vergleich zur Lebenszeit der Modelverbindung MeSCN (36 ps), die ein vollständig wasserexponiertes SCN repräsentiert, bietet Einblicke in den Einfluss des umgebenden Wassers und der direkten Proteinumgebung auf den SCN-Sensor.

Die Untersuchung des SCN-Sensors an ausgewählten Positionen im Protein, lieferte ortsaufgelöste Informationen über die Struktur und deren Änderungen im Gleichgewichtszustand von PYP. Obwohl A44C* und D48C* beide in der α3-Helix an der Oberfläche des Proteins liegen und in pG exponiert zum umgebenden Wasser sind, nahmen die beiden Sensoren unterschiedliche Änderungen in der Umgebung zwischen pG und pB wahr. Das SCN in A44C* (dritte Spalte in Abb. 10.1), das in der Nähe zu E46 liegt, hat wahrscheinlich die Deprotonierung dieser Aminosäure während der Bildung des pB Zustandes detektiert, was sich in einer deutlichen Rotverschiebung der SCN-Absorption zeigt. Der Sensor in D48C* (vierte Spalte in Abb. 10.1) hat hingegen nur sehr kleine Veränderungen erfahrem, die vermutlich durch die Bewegung dieser Proteinregion in die hydrophobere Umgebung der Chromophorbindetasche nach teilweiser Entfaltung der α3-Helix in pB hervorgerufen werden [82, 154]. Die SASA Berechnungen haben für beide Mutanten gezeigt, dass der Sensor in beiden Zuständen gut für Wassermoleküle zugänglich ist. Auch die Schwingungslebensdauern des SCN deuten darauf hin, dass dieses in beiden Mutanten in pG nahezu vollständig wasserexponiert ist und unter Beleuchtung der Einfluss der Proteinumgebung auf die Sensoren nur leicht zunimmt.

A30C* und L23C* wurden ausgewählt um die Bewegung des N-Terminus weg vom restlichen Protein während des Photozyklus zu verfolgen. Die Sensoren in beiden Mutanten zeigen von gegenüberliegenden Seiten in den Zwischenraum, der von N-Terminus und Protein gebildet wird. Für die SCN-Absorption und die Schwingungslebenszeiten des SCN in L23C* (erste Spalte in Abb. 10.1), konnten kaum Veränderungen zwischen pG und pB gemessen werden, obwohl die SASA Berechnungen eine deutliche Zunahme der Wasserzugänglichkeit in pB vorhergesagt hatten. Vermutlich hatte sich der N-Terminus, bedingt durch die Mutation und/oder den Einbau des SCN, bereits in pG vom restlichen Protein wegbewegt, sodass das SCN in beiden Zuständen Kontakt zum umgebenden Wasser hat. Diese Strukturänderung in pG konnte vor allem durch Messungen der Ionenstruktur in der Gasphase mit ESI-IMS Massenspektrometrie ermittelt werden, die für L23C* eine vergleichbare Verteilung der Ladungszustände unter unbeleuchteten und beleuchteten Bedingungen ergaben. Dies deutet auf eine vergrößerte Proteinoberfläche aufgrund der

Destabilisierung des N-Terminus hin. Für die SCN-Absorption von A30C* (zweite Spalte in Abb. 10.1) in pG wurde eine sehr schmale Bandenform gemessen. Diese deutet auf eine homogene Umgebung des IR-Sensors hin, wie es im Inneren des Proteins der Fall ist. Unter Beleuchtung verbreiterte sich die Absorptionsbande sichtbar, auch wenn keine größere Verschiebung der Bandenposition zu beobachten war, was als Zunahme der Zugänglichkeit für Wassermoleküle interpretiert werden kann. Diese Annahme wird nicht nur durch die SASA Berechnungen unterstützt, sondern auch die Messung der Schwingungslebensdauern ergab einen Verlust der geschützten Proteinumgebung. Während in pG die Lebenszeit deutlich länger ist als für MeSCN, gleicht sich diese in pB nahezu an, was auf mehr Kontakt zum umgebenden Wasser hindeutet. Diese Strukturänderungen sind auf die Bewegung des N-Terminus weg vom restlichen Protein zurückzuführen, welche den Zwischenraum und damit das SCN für Wassermoleküle zugänglich machen.

Die SCN-Absorption von V57C* (fünfte Spalte in Abb. 10.1) in pG ist zu relativ hohen Wellenzahlen verschoben, obwohl sich der Sensor im Proteininneren in der hydrophoben Chromophorbindetasche befindet. Die temperaturabhängigen FTIR Messungen deuten auf eine Beteiligung des SCN an H-Brücken hin. Die außergewöhnlich kurze Schwingungslebensdauer von nur 28 ps in pG legt ebenfalls nahe, dass das SCN eine starke H-Brücke zu einem Donor formt, der nicht das umgebende Lösungsmittel sein kann, da sonst die Lebenszeit der des MeSCN gleichen müsste. Diese Beobachtungen in Verbindungen mit den durchgeführten MD Simulationen, die darauf hindeuten, dass ein Wassermolekül an diese Stelle im Proteininneren vordringen konnte, legen den Schluss nahe, dass das SCN an einer H-Brücke zu einem internen Wassermolekül beteiligt ist. Die Ergebnisse aller Messungen im Gleichgewichtszustand haben gezeigt, dass der Sensor in pB exponierter für das umgebende Wasser ist, da die hydrophobe Bindetasche während des Photozyklus ihre abschirmende Funktion verliert und Wassermoleküle eindringen können. V122C* befindet sich ebenfalls in der Bindetasche, allerdings in der unmittelbaren Nähe von E46, das über eine Wasserstoffbrücke mit dem Chromophor verknüpft ist und in pB deprotoniert vorliegt. Anhand der SCN-Absorption (siebte Spalte in Abb. 10.1), die andeutet, dass es in pG möglicherweise zwei unterschiedliche SCN-Konformationen gibt und die Absorption in pB eine Rotverschiebung erfährt, ließen sich keine eindeutigen Informationen über die SCN-Umgebung und die Strukturänderungen in dieser ableiten. Die Schwingungslebensdauern ergaben jedoch, dass sich der Sensor sowohl in pG als auch in pB in einer geschützten Umgebung im Proteininneren ohne Kontakt zum umgebenden Wasser befindet. Dies deutet darauf hin, dass die Verschiebung der SCN-Absorption in pB nicht auf Änderungen in der Wasserzugänglichkeit, sondern auf Änderungen der Polarität in der direkten Umgebung durch die Deprotonierung von E46 zurückzuführen ist.

Der SCN-Sensor in M100C* befindet sich in einer flexiblen Schleife in der Nähe der positiv geladenen Seitenkette von R52 und des Chromophors, der in pG deprotoniert ist. Der Einfluss dieser beiden geladenen Gruppen ist wahrscheinlich für die extreme Rotverschiebung der SCN-Absorption in pG verantwortlich (siehe sechste Spalte in Abb. 10.1). Diese weist zwei Teilpopulationen auf, wobei für die am weitesten rotverschobene Teilpopulation mit 2069.8 cm^{-1} (dies entspricht 2148.5 cm^{-1} ohne die Verschiebung durch Isotopenmarkierung) die niedrigste, je in einem Protein gemessene SCN-Absorption beobachtet wurde. Gleichzeitig wurden für die beiden Teilpopulationen in pG auch die längsten Schwingungslebensdauern ermittelt. Dies deutet auf eine geschützte Umgebung im Inneren des Proteins in pG hin, in der das SCN weder durch H-Brücken zu Lösungsmittelmolekülen

noch zu anderen Proteinstrukturen beeinflusst wird, sondern hauptsächlich dem Einfluss der geladenen Gruppen in der Nähe ausgesetzt ist. Die deutliche Blauverschiebung der SCN-Absorption unter Beleuchtung und die Beobachtung, dass sich die Schwingungslebensdauer des Sensors in pB der des vollständig wasserexponierten MeSCN annähert, sind eindeutige Zeichen dafür, dass die großräumigen Strukturänderungen während des Photozyklus zu einer Öffnung der Chromophorebindetasche führen und es damit zum Eindringen von Wassermolekülen kommt. Außerdem vergrößert sich der Abstand zur positiven Ladung des R52 erheblich, während der Chromophor protoniert wird und sich ebenfalls vom SCN in M100C* entfernt.

Untersuchung der Photozyklusdynamiken mit zeitaufgelöster IR Spektroskopie

Die transienten Strukturänderungen im Verlauf des Photozyklus wurden mit zeitaufgelöster IR Spektroskopie untersucht. Die Verwendung von sowohl mechanisch als auch elektronisch verzögerten Anregepulsen in den transienten Vis-Pump-IR-Probe Experimenten ermöglichte es die Proteindynamiken bis nahezu einer Millisekunde mit einer hohen Zeitauflösung von hunderten Femtosekunden zu messen und damit einen Großteil des Photozyklus zu untersuchen. Der verfügbare Messbereich wurde durch die zusätzliche Verwendung von zeitaufgelösten Step-Scan FTIR Messungen sogar bis zu 20 ms erweitert. Abhängig von der Position innerhalb des Proteins konnten mit Hilfe des SCN-Sensors unterschiedliche Übergänge des Photozyklus mit hoher Ortsauflösung verfolgt werden. IR-Sensoren, die sich weit vom Chromophor entfernt befinden, reagierten lediglich auf Änderungen auf einer Zeitskala von hunderten Mikrosekunden, wenn Protonentransferprozesse und großräumige Strukturänderungen des Proteins stattfinden. IR-Sensoren in der Nähe des Chromophors oder des Glutamats E46, das in die Stabilisierung der Bindetasche und in Protonentransferprozesse verwickelt ist, erfassten hingegen Veränderungen des Chromophors und der umgebenden Bindetasche, die während des gesamten Photozyklus auftreten. Ein schematisches Photozyklusmodel für WT-PYP sowie die ortsaufgelösten Dynamiken, die anhand des SCN an unterschiedlichen Positionen ermittelt wurden, sind in Abbildung 10.2 zusammen mit einem Strukturmodel von PYP, in dem die fünf untersuchten Positionen farbig markiert sind, dargestellt.

Bei der Untersuchung der frühen Photozyklusdynamik wurden mehrere Lebenszeiten für die Relaxation des elektronisch angeregten Zustands pG* gefunden. Die Isomerisierung des Chromophors und dementsprechend die Bildung des Intermediats I_0, findet wenige Picosekunden nach der Absorption eines blauen Photons statt. Diese frühen Übergänge, welche die Anregung und die Strukturänderungen des Chromophors einschließen, wurden von dem SCN in V57C*, M100C* und V122C* wahrgenommen, die sich alle an unterschiedlichen Positionen in der Chromophorbindetasche befinden. Nach der Isomerisierung des Chromophors wurde für die Mutante M100C* zusätzlich eine deutlich verlangsamte Rückkehr in den Dunkelzustand pG mit etwa 100 ps beobachtet. Dieser Effekt ist vergleichbar zu der verlangsamten Relaxationsdynamik aus dem Signalzustand pB, die schon häufiger nach dem Ersetzen des Methionins durch eine andere Aminosäure in vorangegangenen Studien beobachtet wurde [85, 156–159].

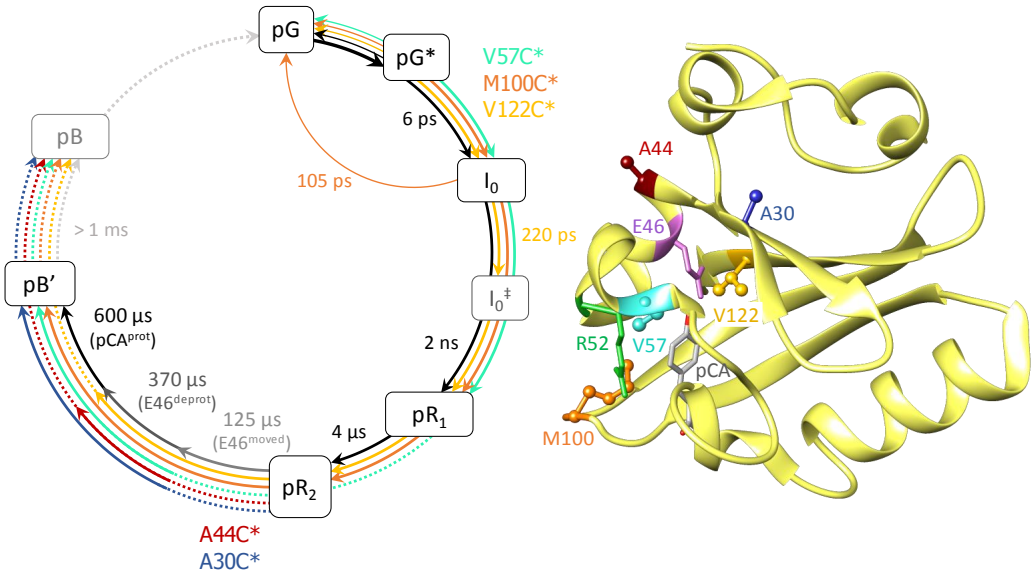

Abbildung 10.2: *Ortsaufgelöstes Photozyklusmodel der SCN-Kinetiken (links) und PYP-Strukturmodel (pdb: 1NWZ) im Dunkelzustand mit den untersuchten Einbauorten (rechts). Die bunten Pfeile markieren die Übergänge im Photozyklus, die anhand des SCN an unterschiedlichen Positionen verfolgt werden konnten. Die schwarzen/grauen Pfeile zeigen den Photozyklus für WT-PYP mit den gemessenen Lebenszeiten der einzelnen Übergänge. In der PYP-Struktur sind die fünf Positionen, an denen das SCN für die zeitaufgelösten Messungen eingebaut wurde, in den Farben passend zum Photozyklusmodel dargestellt. Zusätzlich sind der Chromophor (pCA; grau) und die beiden Aminosäuren E46 (violett) und R52 (grün), die eine wichtige Rolle im Photozyklus spielen, gezeigt.*

Die Untersuchung der Protein- und Chromophordynamik lieferte keinen eindeutigen Hinweis auf die Existenz des $I_0^‡$ Intermediats, das in etwa 220 ps durch Relaxationsprozesse in der Nähe des Chromophors gebildet werden sollte [8, 87]. Die Verschiebung des SCN-Signals in V122C* in 220 ps deutet jedoch auf Veränderungen in der Umgebung des SCN hin, die im gleichen Zeitrahmen, wie für die Entstehung von $I_0^‡$ angenommen, stattfinden. Diese Reaktion des Sensors wird vermutlich durch Änderungen in der Orientierung des nahegelegene E46 ausgelöst, das über eine H-Brücke mit dem Chromophor verknüpft ist und durch Relaxationsprozesse nach Isomerisierung des Chromophors beeinflusst werden könnte. Daher deuten die Änderungen des SCN-Signals mit hoher Wahrscheinlichkeit auf die Existenz des $I_0^‡$ Intermediats hin. Weitere Relaxationsprozesse des Chromophors und des umgebenden H-Brückennetzwerks wurden auf einer Zeitskala von wenigen Nanosekunden beobachtet, die mit der Bildung des pR Intermediats einhergehen. Dieser Übergang wurde ebenfalls von den SCN-Sensoren in V57C*, M100C* und V122C* detektiert.

In den Experimenten, die im Rahmen dieser Arbeit durchgeführt wurden, konnte zum ersten Mal die µs-Dynamik, die in der Literatur der Existenz zweier pR Zustände zugeschrieben wird [70, 73–75, 89, 91, 92], in zeitaufgelösten Infrarot Messungen beobachtet werden. Außerdem war es nicht nur möglich diese Dynamik zu messen, sondern auch die zugehörigen Strukturänderungen zu lokalisieren. Während in den vorangegangenen Studien verschiedene Interpretationen darüber zu finden sind, wo diese Strukturänderungen stattfinden, haben die Vis-Pump-IR-Probe Messungen gezeigt, dass diese auf die Chromophorbindetasche begrenzt werden können, vor allem auf die beiden Aminosäuren E46 und R52, die entweder über H-Brücken oder elektrostatische Wechselwirkungen mit dem

Chromophor verknüpft sind. Diese Beobachtung wird von der Reaktion der SCN-Sensoren in V122C*, nahe E46, und in M100C*, in der direkten Nachbarschaft zu R52, auf einer Zeitskala von wenigen Mikrosekunden unterstützt. Es ist jedoch nicht möglich eindeutig festzustellen, ob die beiden pR Zustände nacheinander gebildet werden und sich pR_1 in wenigen Mikrosekunden in pR_2 umwandelt oder ob beide Zustände gleichzeitig in wenigen Nanosekunden entstehen und anschließend auf unterschiedlichen Zeitskalen in pB' übergehen (pR_1 in wenigen µs und pR_2 in hunderten von µs).

Des Weiteren konnte hier der erste kinetische Nachweis erbracht werden, der die Aminosäure E46 als Protonendonator für den Chromophor ausschließt, da die Deprotonierung des E46 nicht gleichzeitig mit der Protonierung des Chromophors, sondern etwas früher auf der hunderte von µs Zeitskala stattfindet. Daher ist es wahrscheinlicher, dass es eine andere Protonenquelle gibt, eventuell Wassermoleküle, die im Laufe des Photozyklus in die Bindetasche und in die Nähe des Chromophors vordringen können [98]. Während der Austausch von D_2O gegen H_2O kaum Einfluss auf die meisten Photozyklusübergänge hat, scheint sich die Deprotonierung des E46 in H_2O überraschenderweise zu verlangsamen, wohingegen sich die Protonierung des Chromophors beschleunigt hat. Allerdings ist die Zuordnung des Deprotonierungsprozesses in H_2O nicht ganz eindeutig, was die Interpretation erheblich erschwert und keinen endgültigen Schluss über die Rolle als Protondonor für den Chromophor zulässt. Die Blauverschiebung der Carboxylabsorption von E46, die der Bewegung des Glutamats in eine hydrophobere Umgebung zugeschrieben wurde [10, 11], findet in beiden Lösungsmitteln vor den Protonentransferprozessen statt. Aufgrund dieser Beobachtungen lässt sich der allgemein anerkannte Übergang $pR_2 \rightarrow pB'$ in mehrere aufeinanderfolgende Schritte unterteilen, die aus der Bewegung von E46, dessen Deprotonierung und der Protonierung des Chromophors bestehen (im Photozyklusmodel in Abb. 10.2 als $E46^{moved}$, $E46^{deprot}$ und pCA^{prot} bezeichnet).

Mit Hilfe des SCN an verschiedenen Positionen, ist es möglich den einzelnen Schritten dieses Übergangs im Photozyklus zu folgen. Die Bildung von pB' ist der einzige Übergang der von allen fünf untersuchten SCN-Sensoren wahrgenommen wurde. Aufgrund seiner Nähe zu E46, reagiert das SCN in V122C* auf die Deprotonierung und vermutlich die Bewegung des Glutamats in eine hydrophobere Umgebung, da die beiden Prozesse gleichzeitig in dieser Mutante stattfinden. Auch der IR-Sensor in A44C* nimmt die Deprotonierung von E46 wahr. Diese Beobachtung wird von den Experimenten im Gleichgewichtszustand unterstützt, die auf die Entstehung einer geladenen Gruppe in der näheren Umgebung des SCN hindeuteten, wie es bei der Deprotonierung von E46 der Fall ist. Die beschleunigte Kinetik des SCN in H_2O für A44C* deuten daher darauf hin, dass der Deprotonierungsprozess durch den Austausch von D_2O durch H_2O möglicherweise ebenfalls beschleunigt wurde, entsprechend dem zu erwartenden Isotopeneffekt. Diese Schlussfolgerung wäre allein durch die Betrachtung der C=O Schwingung der Carboxylgruppe von E46 in H_2O nicht möglich gewesen. Der SCN-Sensor in A30C* nimmt vermutlich die Konformationsänderungen des N-Terminus wahr, die bereits während der Bildung von pB' in etwa 200 µs auftreten sollten [75, 170, 180] und damit auf einer ähnlichen Zeitskala wie die Änderungen in der SCN-Absorption. In M100C* reagiert das SCN auf die Bewegung der nahegelegenen Aminosäure R52 und vermutlich auf das dadurch verursachte Eindringen von Wassermolekülen in die Chromophorbindetasche. Die Protonierung des Chromophors wird hingegen nicht von dem Sensor detektiert. Auffällig ist die insgesamt deutlich beschleunigte Bildung von pB' in M100C*, die im Gegensatz zum WT-PYP und den anderen Mutanten schon

in etwa 20 µs stattfindet. Für V57C* kann nicht eindeutig unterschieden werden, welche Veränderungen in der Bindetasche letztendlich Einfluss auf das SCN während dieses Photozyklusübergangs haben.

Die zeitaufgelösten Step-Scan FTIR Messungen deuten darauf hin, dass der Signalzustand pB in etwa 7 ms gebildet wird, passend zu der Zeitskala, die in vorangegangenen IR Studien für diesen Übergang gefunden wurde [10, 11]. Mit dieser Methode war es möglich ein winziges SCN-Signal in A44C* (in H_2O) aufzulösen. Die Dynamik des SCN (etwa 100 µs) ist jedoch deutlich schneller als in der Pump-Probe Messung (320 µs) unter ähnlichen Bedingungen, während die Protein- und Chromophordynamik in beiden Experimenten vergleichbar ist. Der deutliche Unterschied in der SCN-Dynamik ist möglicherweise auf das niedrige Signal-Rausch-Verhältnis in den Step-Scan FTIR Messungen zurückzuführen. Trotzdem konnten diese Messungen bestätigen, dass das SCN in A44C* nicht der allgemeinen Proteindynamik während der Bildung des Signalzustands folgt, sondern bereits auf die Änderungen während des $pR_2 \rightarrow pB'$ Übergangs reagiert.

Zusammenfassend lässt sich sagen, dass die Verwendung des IR-Sensors SCN, der an ausgewählten Positionen in PYP eingebaut wird, die Ortsauflösung und Umgebungssensitivität von IR spektroskopischen Messtechniken deutlich erhöht. Dadurch wird die Untersuchung von Proteinstruktur und dynamischen Prozessen während des Photozyklus mit hoher Zeitauflösung und auf dem Level einzelner Seitenketten ermöglicht. Die Informationen, die aus den verschiedenen Observablen im Gleichgewichtszustand und aus der Reaktion des SCN auf die unterschiedlichen Übergänge des Photozyklus gewonnen werden, tragen zu einem besseren Verständnis lokaler, lichtinduzierter Strukturänderungen im Photorezeptor PYP bei. Durch diese umfangreiche Arbeit konnte weiterhin eindrucksvoll demonstriert werden, dass der Einsatz von SCN zur Untersuchung von Proteindynamik eine Möglichkeit darstellt bisher unzugängliche Vorgänge in PYP und potenziell in zahlreichen weiteren Proteinen zu beobachten.

Part VI

Appendix

A UV/vis Spectra of PYP Mutants

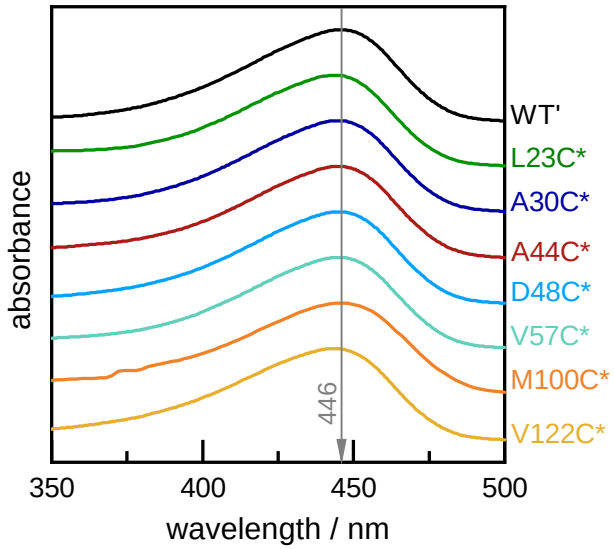

Figure A.1: *UV/vis spectra of PYP-WT' and all SCN-labeled mutants showing the chromophore absorption around 446 nm. All spectra were measured in H_2O with a quartz cuvette of 1 cm path length.*

B Steady-state FTIR Experiments

B.1 FTIR Raw Spectra of SCN Absorption

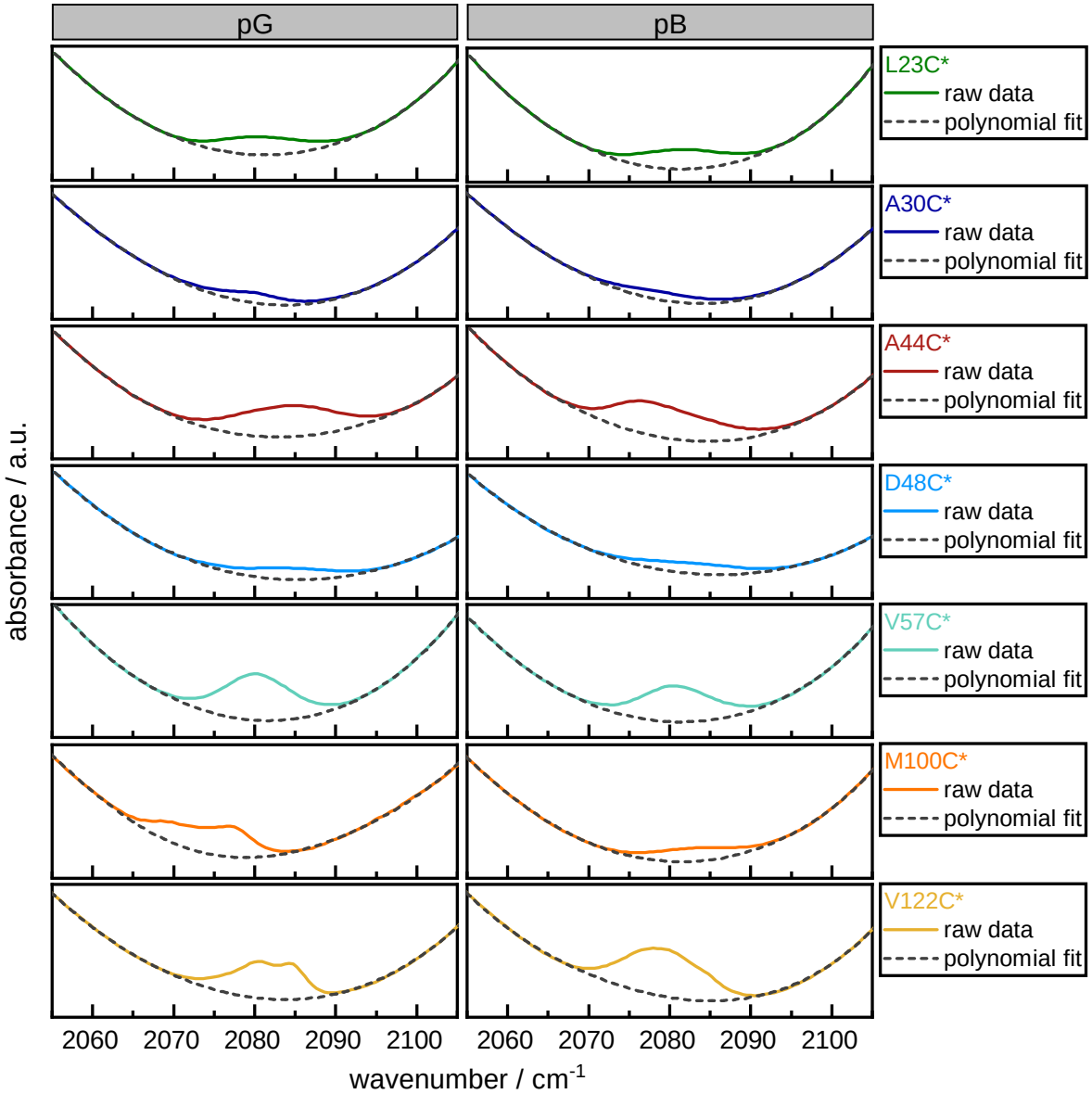

Figure B.1: *Raw FTIR absorption spectra of SCN (colored solid lines) and poylynomial fit for background correction (dark gray dashed lines; the broad underlying water bands were fitted after excluding the wavenumber region where the SCN label absorbs) for all labeled PYP mutants in pG and pB. The 5^{th} order polynomial fit was subtracted from the raw data to obtain the SCN absorption spectra presented in this thesis in chapter 5. For better visualization a linear offset was subtracted from all raw data and the polynomial fits.*

B.2 Second Derivative of SCN Absorption in FTIR Spectra

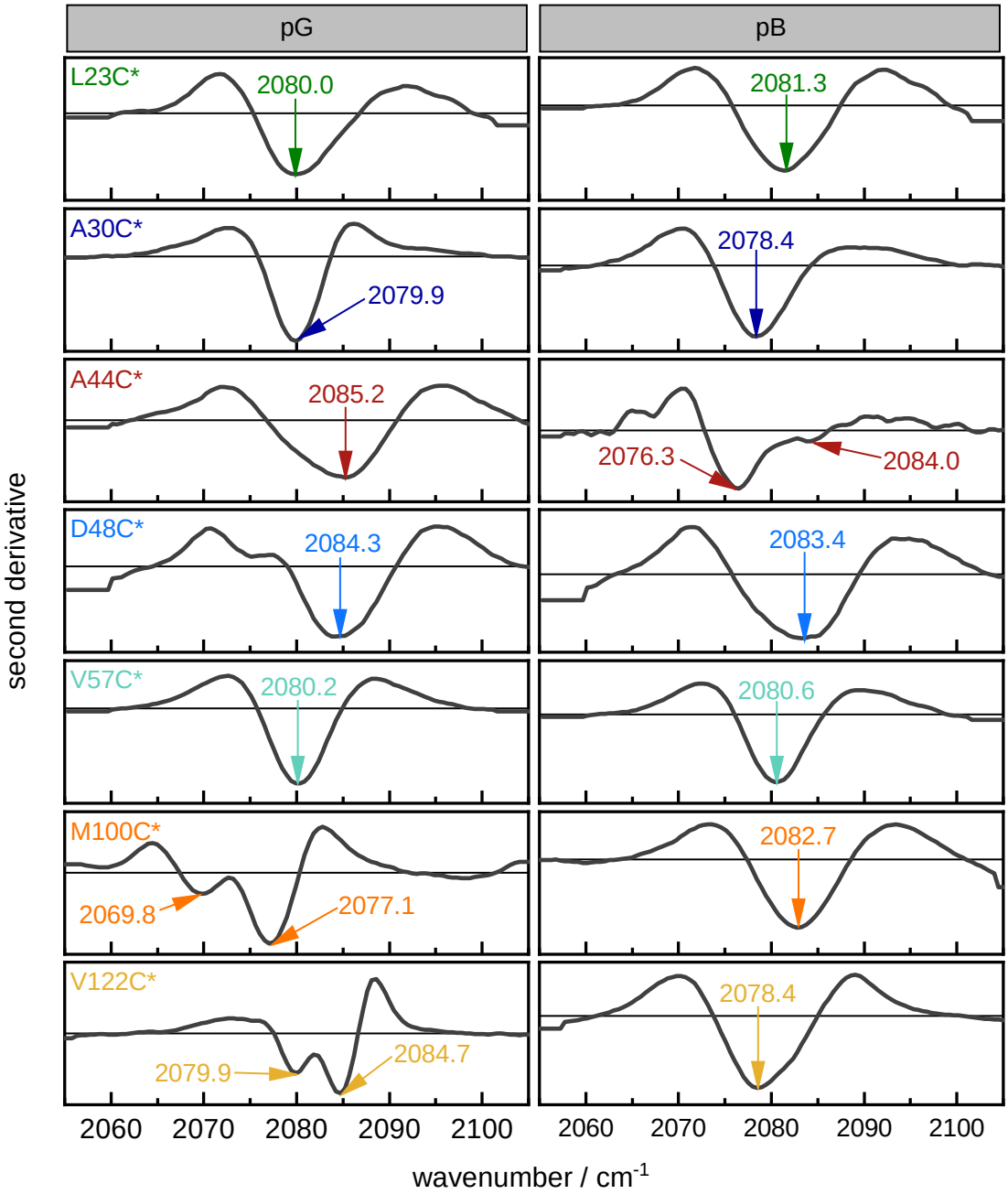

Figure B.2: *Second derivative of FTIR absorption spectra of SCN for all labeled PYP mutants in pG (left row) and pB (right row). The derivative spectra were smoothed with a Savitzky-Golay filter.*[1] *The colored arrows indicate the negative minima of the second derivative that correspond to the wavenumber $\tilde{\nu}_{sd}$ as recorded in table 5.1 on page 58. The appearance of multiple negative minima implies multiple subpopulations for the SCN absorption.*

[1]The second derivative of the spectra was taken by OriginPro 2018 and the implemented smoothing routine was used.

B.3 Temperature-dependent FTIR Absorption Spectra of FTLS Measurements

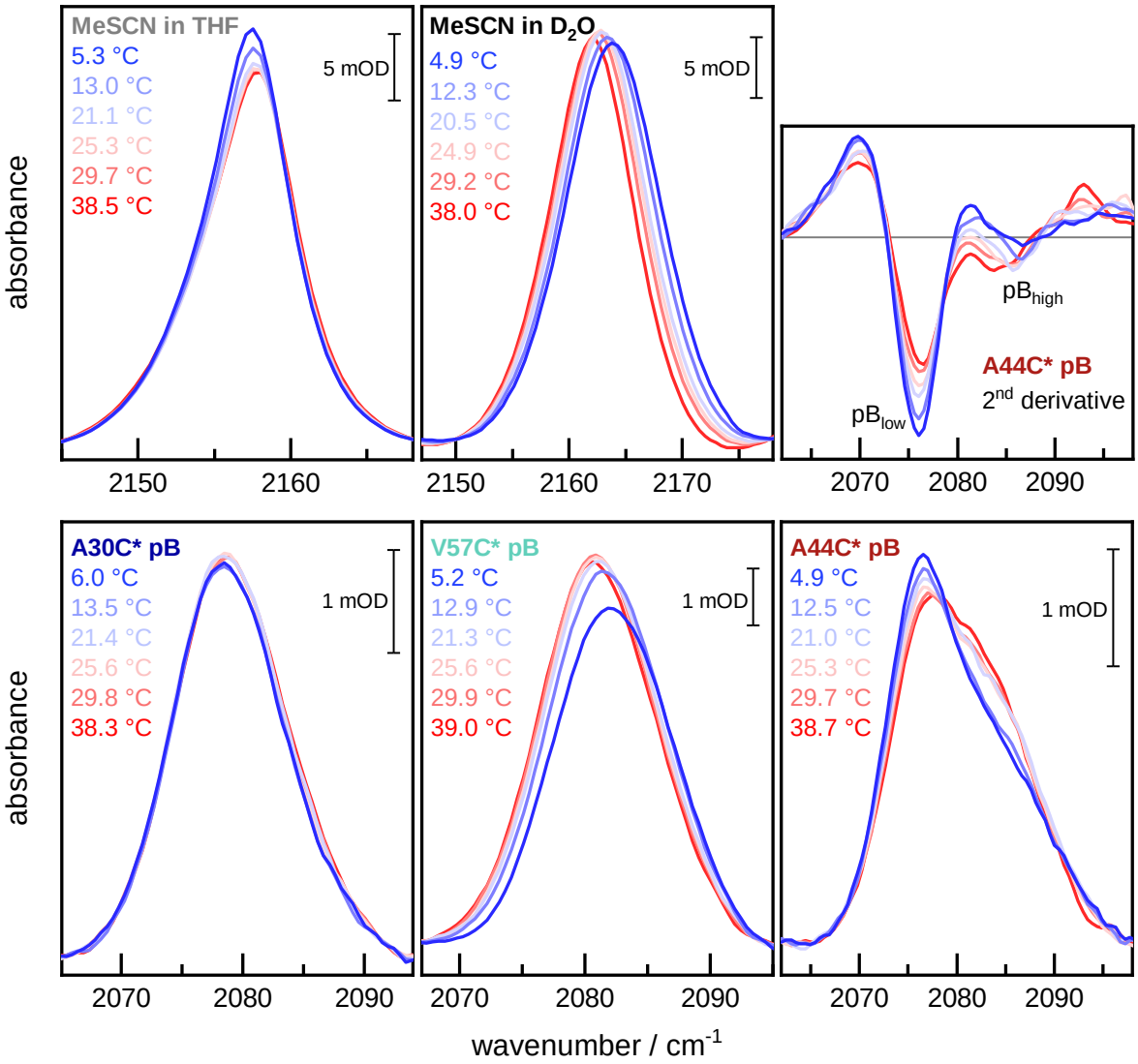

Figure B.3: *Temperature-dependent FTIR absorption spectra of MeSCN in THF and D_2O and SCN in A30C*, V57*, and A44C* (with 2^{nd} derivative) in the pB state. MeSCN was measured at concentrations of 50 mM and a path length of 50 µm, protein samples at a concentration of 8 mM and a path length of 100 µm in D_2O buffer. On the top right the second derivatives (smoothed by a Savitzky-Golay filter) of the absorption spectra of A44C* in the signaling state below are shown. $\tilde{\nu}_{sd}$ for pB_{low} and pB_{high} were obtained by determining the negative minima.*

C MD Simulations of PYP in pG and pB

SASA calculations and WHAM analysis of the average number of hydrogen bonds were performed by Bartosz Błasiak. Details for SASA calculations of the side chains in the wild type are described in [136] and for calculations of the SCN-labeled cysteine residues in [121]. For the dark state pdb-structure 1NWZ was used, for the signaling state pdb-structure 2KX6.

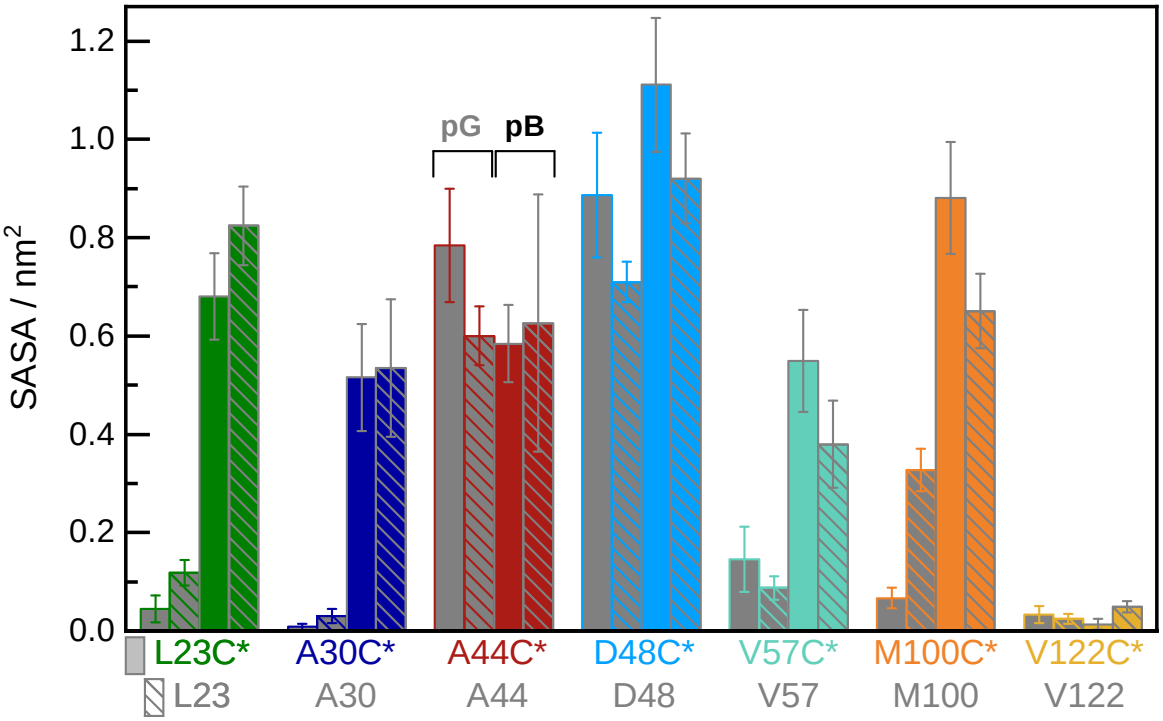

Figure C.1: *SASA calculations of all SCN-labeled cysteine mutants (solid bars) and the corresponding side chains of the amino acids in the wild type (striped bars) for the dark state (gray bars) and the signaling state (colored bars). The side chains in the wild type were normalized relative to alanine to compensate for their different sizes. For the normalization theoretical values for residue X in a tripeptide Gly-X-Gly were used (A = 0.67 nm², L = 1.37 nm², D = 1.06 nm², V = 1.17 nm², M = 1.60 nm²)[193].*

Table C.1: *Average number of hydrogen bonds per SCN residue towards the protein or towards water (bulk and buried in the protein) from MD simulations obtained by WHAM (weighted histogram analysis method) analysis.*

mutant	pG state		pB state	
	Hbond protein	Hbond water	Hbond protein	Hbond water
L23C*	0.0025	0.4192	0.0819	0.8002
A30C*	0.0025	0.2837	0.0274	0.5887
A44C*	0.0025	0.8065	0.0149	0.5736
D48C*	0.0153	0.8197	0.0125	0.7562
V57C*	0.1420	0.6584	0.0614	0.6426
M100C*	0.3132	0.3039	0.0669	0.8136
V122C*	0.0025	0.3384	0.0511	0.3612

D nESI Mass Spectrometry

All nESI mass spectrometry measurements and analysis were performed by Rene Zangl and Jan Hoffmann. nESI mass spectrometry in combination with a time-of-flight analyzer were used to determine the labeling efficiency of the SCN-labeled PYP-mutants. Ion mobility separation under non-illuminated and illuminated conditions allowed to distinguish surface exposure by different patterns of the charge states.

D.1 Labeling Efficiency of PYP Mutants

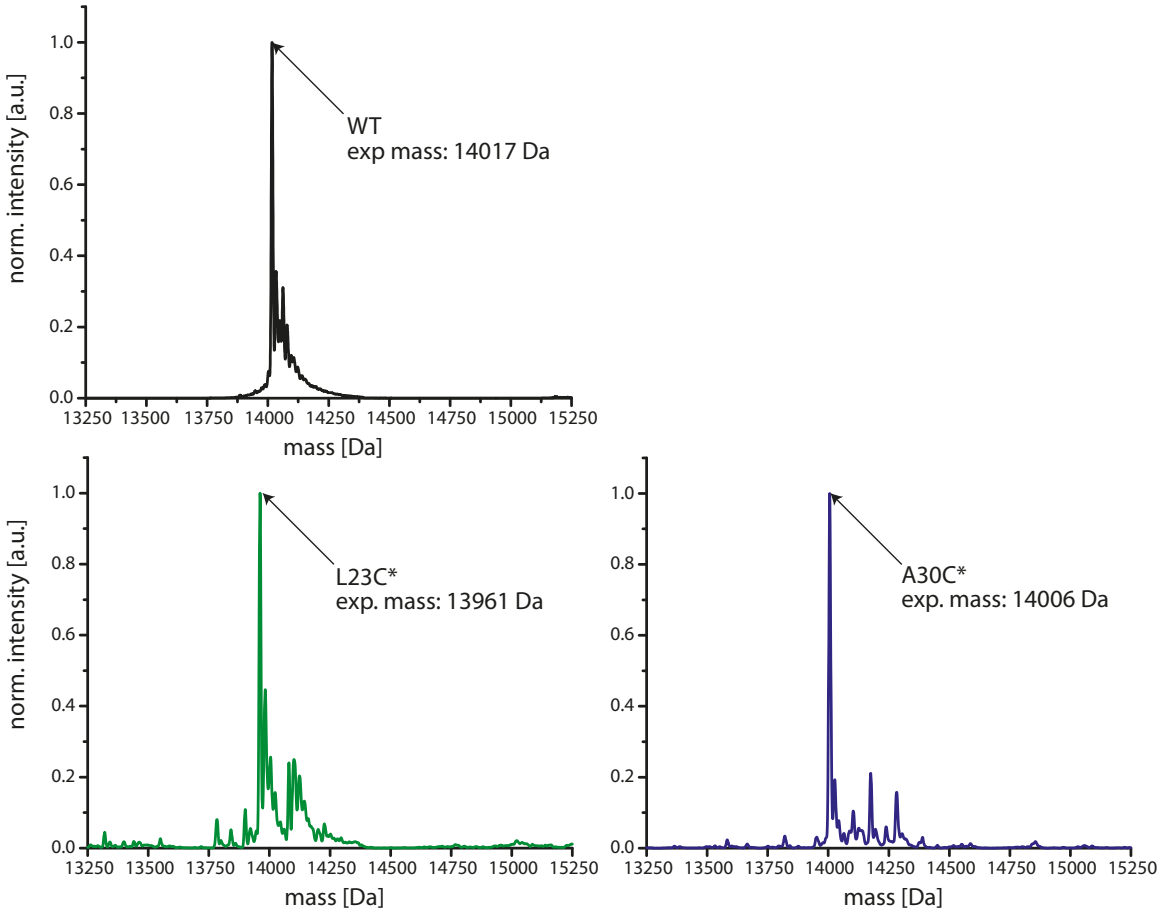

Figure D.1: *Convoluted mass spectra of PYP-WT, L23C*, and A30C*. The experimentally determined masses (given in the spectrum) match the theoretically expected masses (WT = 14020 Da, L23C* = 13963 Da, A30C* = 14005 Da). The $S^{13}C^{15}N$ of the mutants causes an expected shift of +27 Da. The spectra contain no signals at the expected mass for the unlabeled protein indicating labeling with quantitative yield. The signals at higher masses result from sodium or potassium phosphates bound to the proteins.*

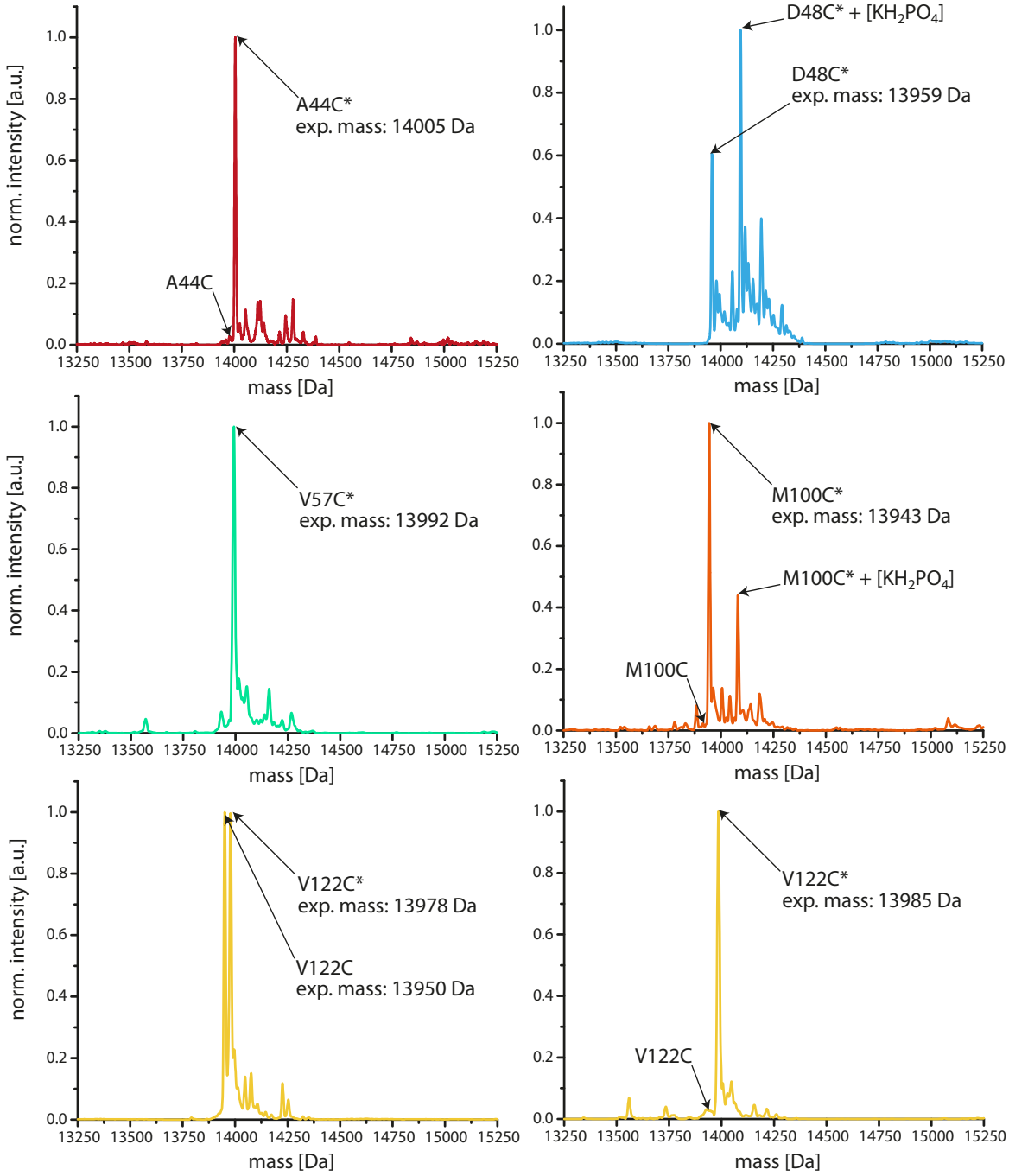

Figure D.2: *Convoluted mass spectra of A44C*, D48C*, V57C*, M100C*, and V122C*. The experimentally determined masses (given in the spectrum) match the theoretically expected masses (A44C* = 14005 Da, D48C* = 13961 Da, M100C* = 13945 Da, V122C* = 13977 Da), except for V57C* and the almost fully labeled V122C* (both with an expected theoretical mass of 13977 Da) which differ by 15 Da and 8 Da, respectively, most likely due to inefficient D-H exchange before the measurement. The $S^{13}C^{15}N$ of the mutants causes an expected shift of +27 Da. The spectra of D48C* and V57C* contain no signals at the expected mass for the unlabeled protein indicating labeling with quantitative yield and also the spectra of A44C*, M100C*, and the second V122C* sample (right spectrum) show only a tiny signal for the unlabeled mutant resulting in labeling efficiencies > 95 %. For one of the two investigated V122C* mutants (left spectrum; used in the transient vis-pump-IR-probe measurements with the electronic delays) only 50 % of the proteins were labeled. The signals at higher masses result from sodium or potassium phosphates bound to the proteins. Especially for D48C* and M100C* the signal of monopotassium phosphate (KH_2PO_4) bound to the labeled mutants is prominent.*

D.2 nESI Ion Mobility Separation

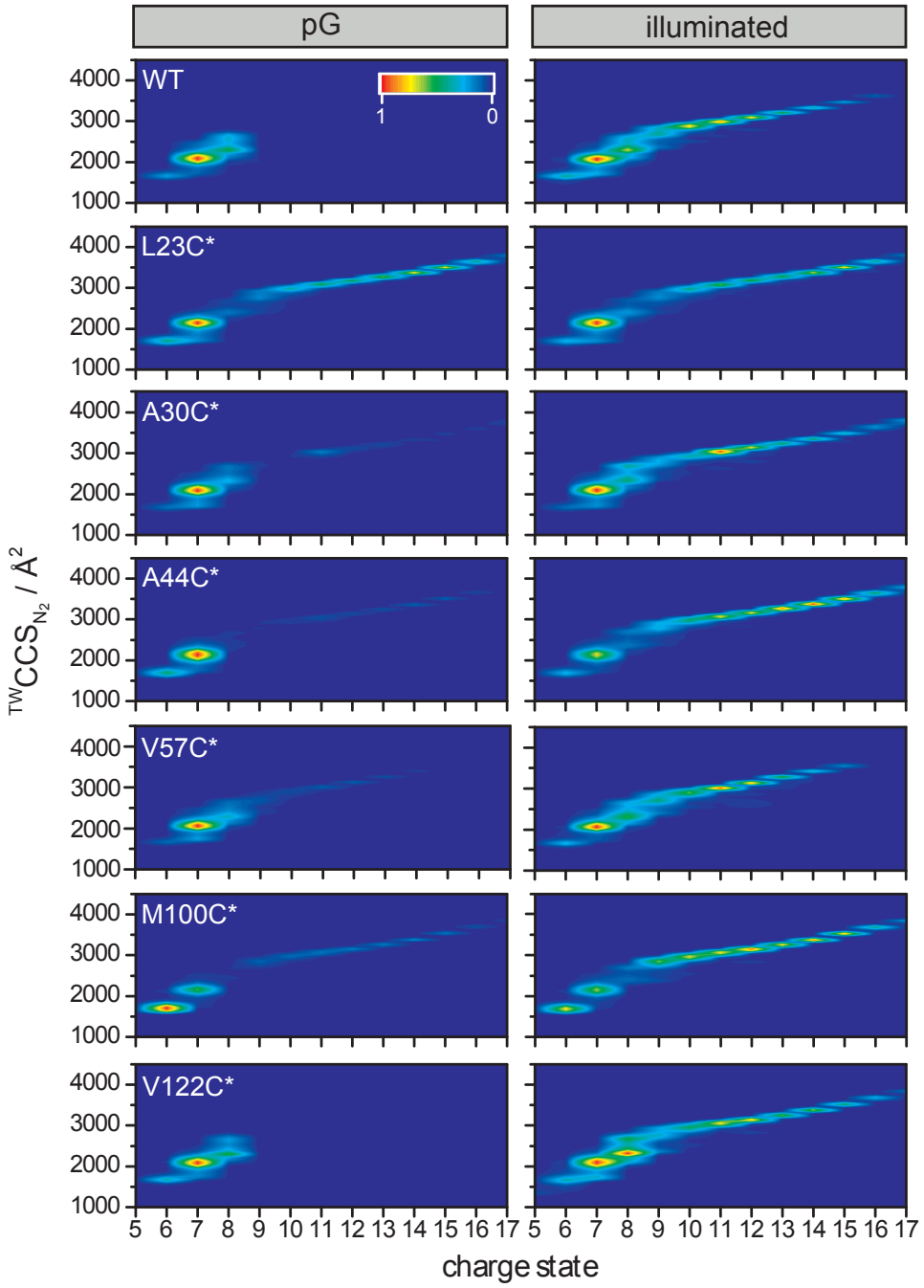

Figure D.3: *Ion mobility data of PYP-WT and selected SCN-labeled mutants in the dark state (left column) and under illumination (right column). All extracted ion mobilograms were normalized. In the dark state signals mainly appear at low charge states with a CCS of about 2000 Å^2, the illuminated samples shift to a distribution of higher charge states with an averaged CCS of about 3000 Å^2. The mutants show similar mobilograms as the WT under both conditions, except for L23C* which exhibits already in pG a distribution of high charge states analogous to the illuminated condition.*

E Ultrafast IR-Pump-IR-Probe Experiments

E.1 FTIR Spectra of MeSCN in H_2O and D_2O

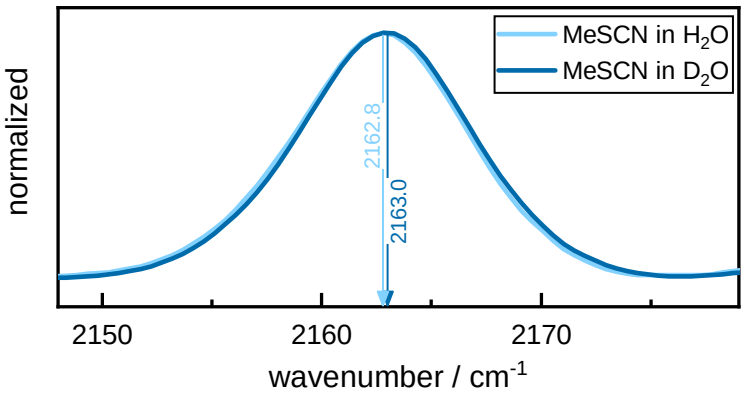

Figure E.1: *FTIR absorption spectra of MeSCN in H_2O (light blue) and D_2O (dark blue) buffer. The MeSCN concentration was 50 mM at 50 µm path length. Both spectra were measured at approximately 21 °C and background corrected by subtraction of a polynomial fit of 5^{th} order.*

E.2 Spectral Position of Pump Pulses for M100C* pG

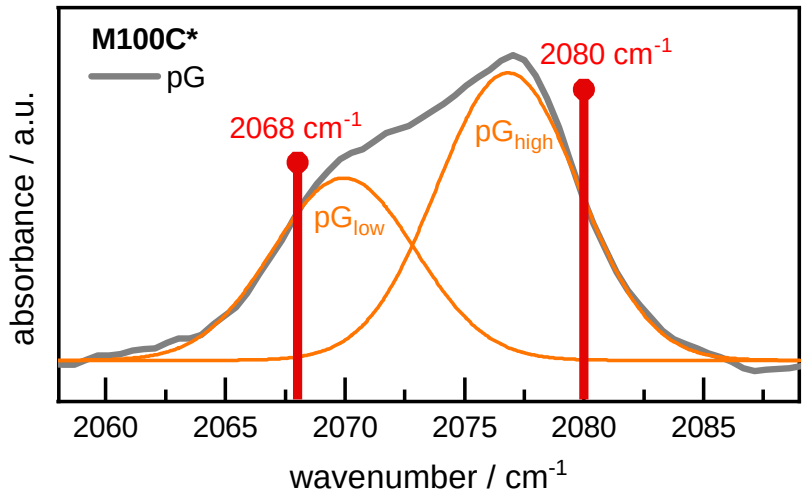

Figure E.2: *FTIR absorption spectrum of M100C* pG (gray) with the spectral position of the two pump pulses (red bars) that were used in the ultrafast IR-pump-IR-probe experiment to excite both subpopulations pG_{low} and pG_{high}, indicated by the two orange Gaussian functions (obtained by fitting the absorption spectrum with two Gaussians), independently. The pump pulses (FWHM 12 cm^{-1}) were centered at 2068 cm^{-1} and 2080 cm^{-1}.*

E.3 Raw Data of IR-Pump-IR-Probe Experiments

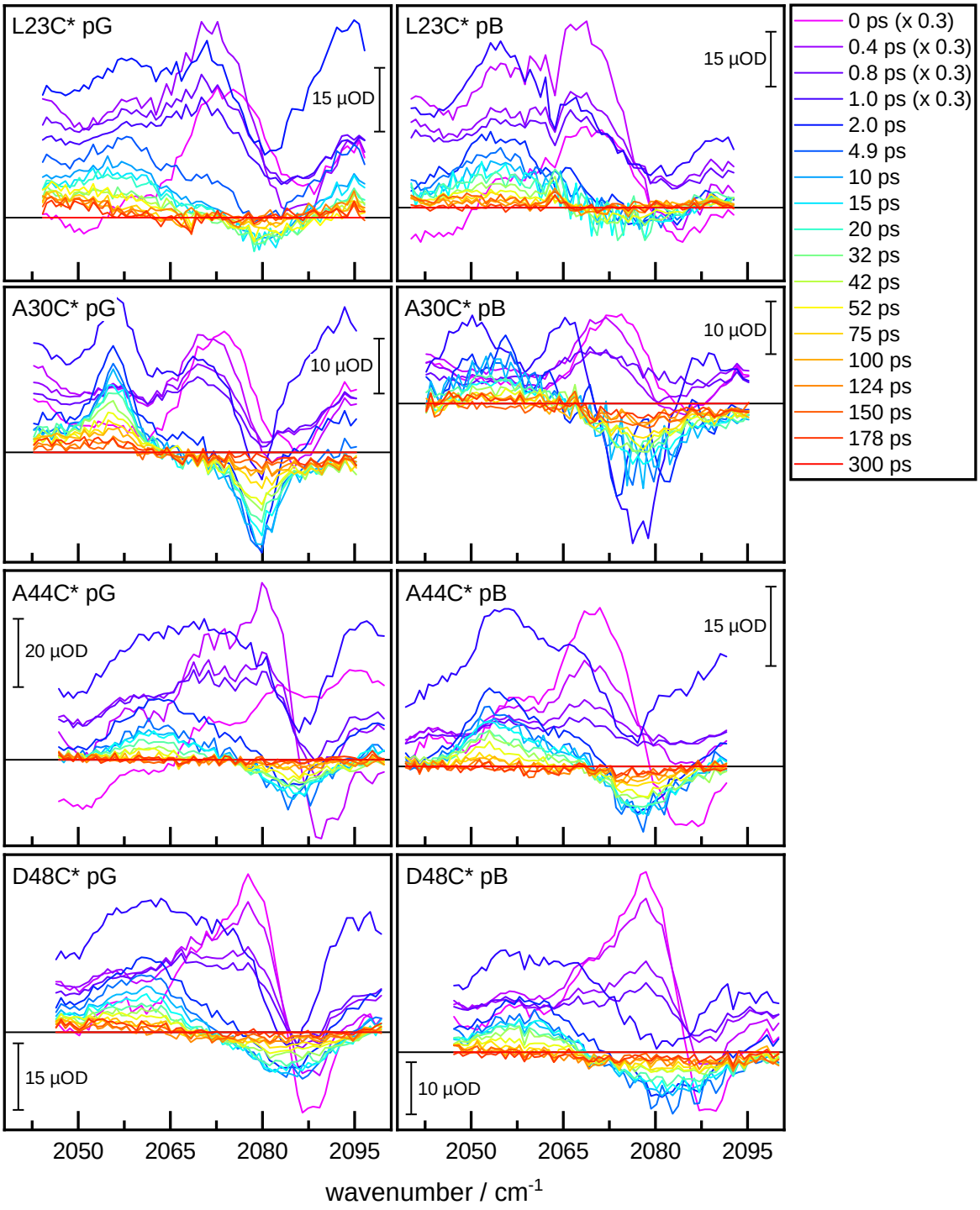

Figure E.3: *Raw difference absorption signals of SCN from ultrafast IR-pump-IR-probe experiment of L23C*, A30C*, A44C*, and D48C* in pG and pB. The background was corrected by subtraction of the spectrum at −40 ps and of the last time point at 300 ps, which was much longer than the lifetime of the SCN vibration. For better visualization only a selection of time points is depicted between 0 ps and 300 ps. The sub-ps spectra that lay within the IRF of the experiment were scaled by a factor of 0.3. The gray vertical line represents y = 0. All data were measured in H_2O buffer with a path length of 100 µm.*

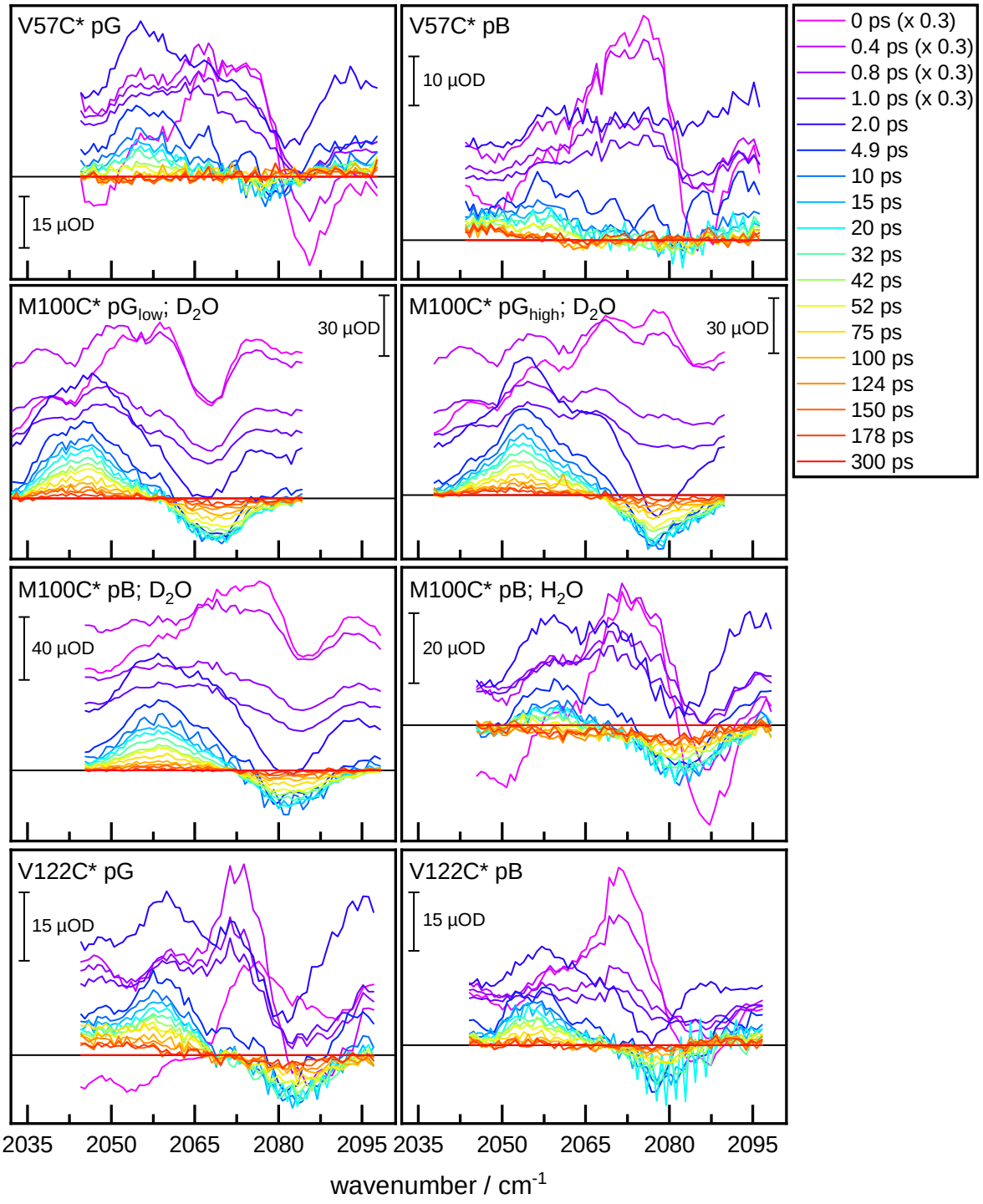

Figure E.4: *Raw difference absorption signals of SCN from ultrafast IR-pump-IR-probe experiment of V57C*, M100C*, and V122C* in pG and pB. The background was corrected by subtraction of the spectrum at −40 ps and of the last time point at 300 ps, which was much longer than the lifetime of the SCN vibration. For better visualization only a selection of time points is depicted between 0 ps and 300 ps. The sub-ps spectra that lay within the IRF of the experiment were scaled by a factor of 0.3. The gray vertical line represents y = 0. Unless stated otherwise, the data were measured in H_2O buffer (D_2O buffer for M100C*) with a path length of 100 µm (150 µm for D_2O).*

E.4 Global Analysis of IR-Pump-IR-Probe Data

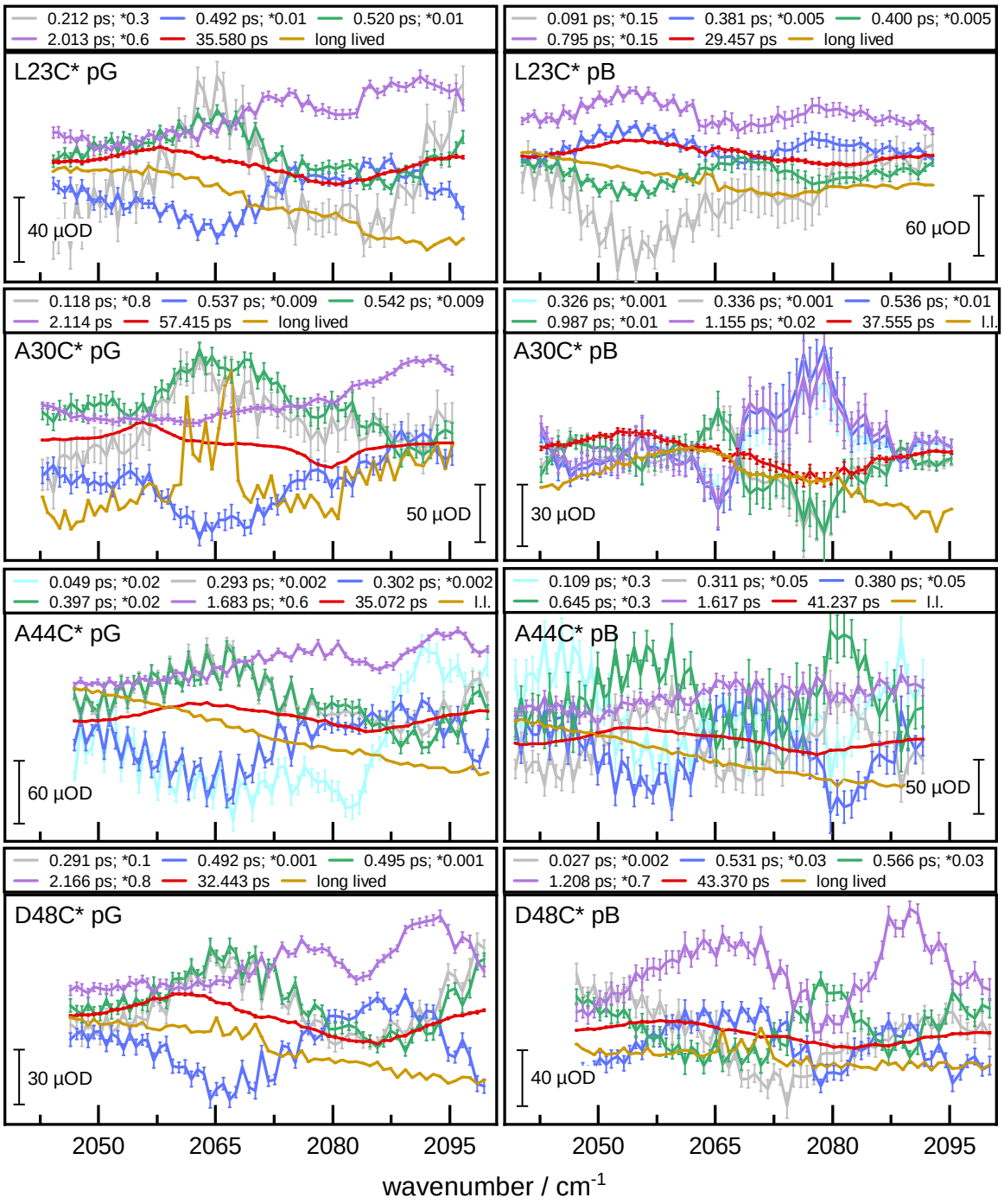

Figure E.5: *Decay-associated difference spectra and error bars from global analysis of ultrafast IR-pump-IR-probe data of L23C*, A30C*, A44C*, and D48C* in pG and pB in H_2O buffer. The data were fitted with a parallel model of either 6 or 7 exponential functions. There are three or four sub-ps components (gray, dark blue, green, light blue) to fit the data during the temporal overlap of pump and probe pulse (< 1 ps after excitation), one fast component (1-7 ps, purple) attributed to solvent excitation, the component corresponding to the vibrational lifetime of the SCN (red) and a "long lived" (l.l.) component (yellow) that exceeds the timescale of the experiment (> 300 ps).*

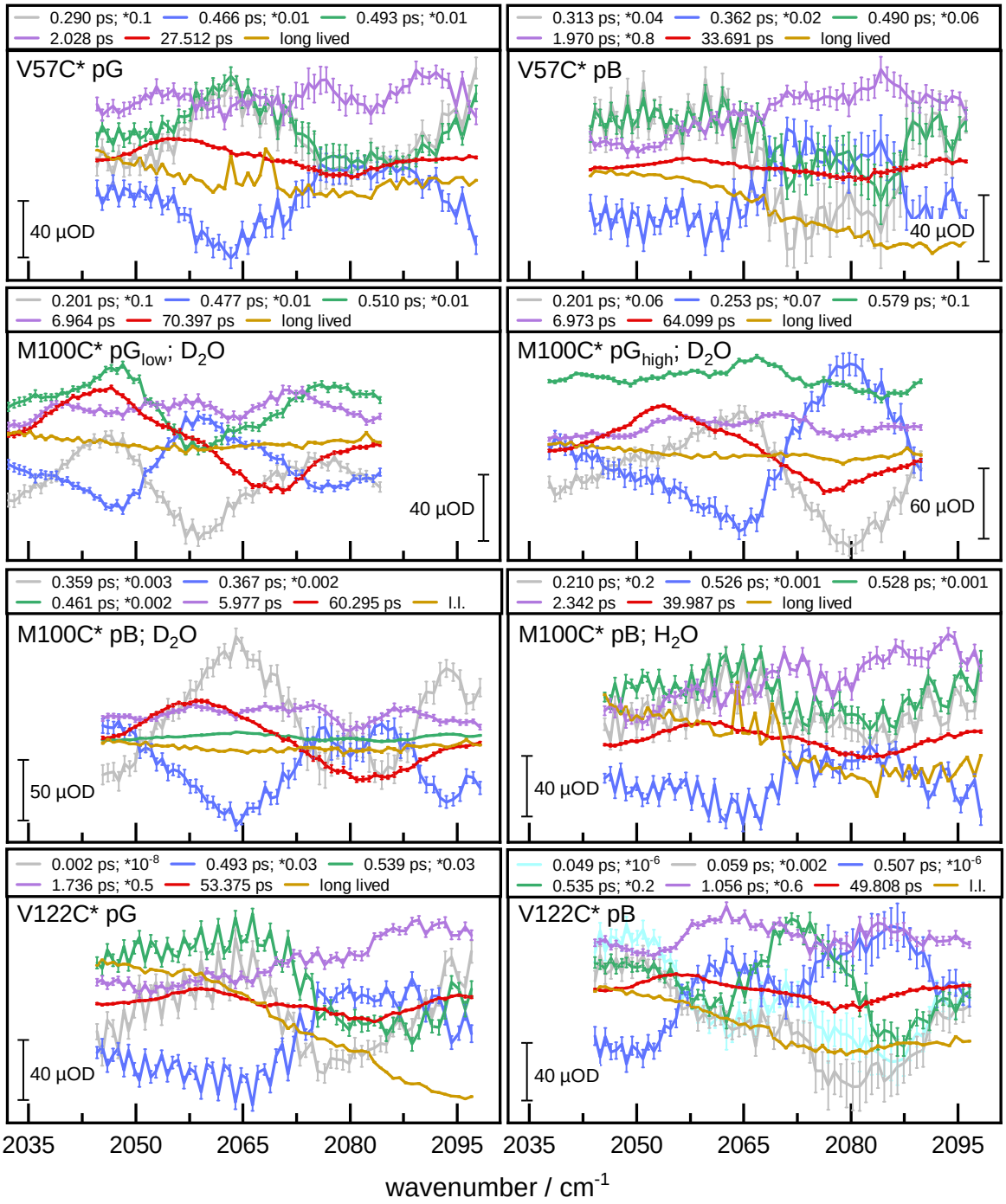

Figure E.6: *Decay-associated difference spectra and error bars from global analysis of ultrafast IR-pump-IR-probe data of V57C*, M100C*, and V122C* in pG and pB in H_2O buffer except for M100C*. The data were fitted with a parallel model of either 6 or 7 exponential functions. There are three or four sub-ps components (gray, dark blue, green, light blue) to fit the data during the temporal overlap of pump and probe pulse (< 1 ps after excitation), one fast component (1-7 ps, purple) attributed to solvent excitation, the component corresponding to the vibrational lifetime of the SCN (red) and a "long lived" (l.l.) component (yellow) that exceeds the timescale of the experiment (> 300 ps).*

F Transient Vis-Pump-IR-Probe Experiments

F.1 Lissajous Scanner

F.1.1 Electronics Circuit

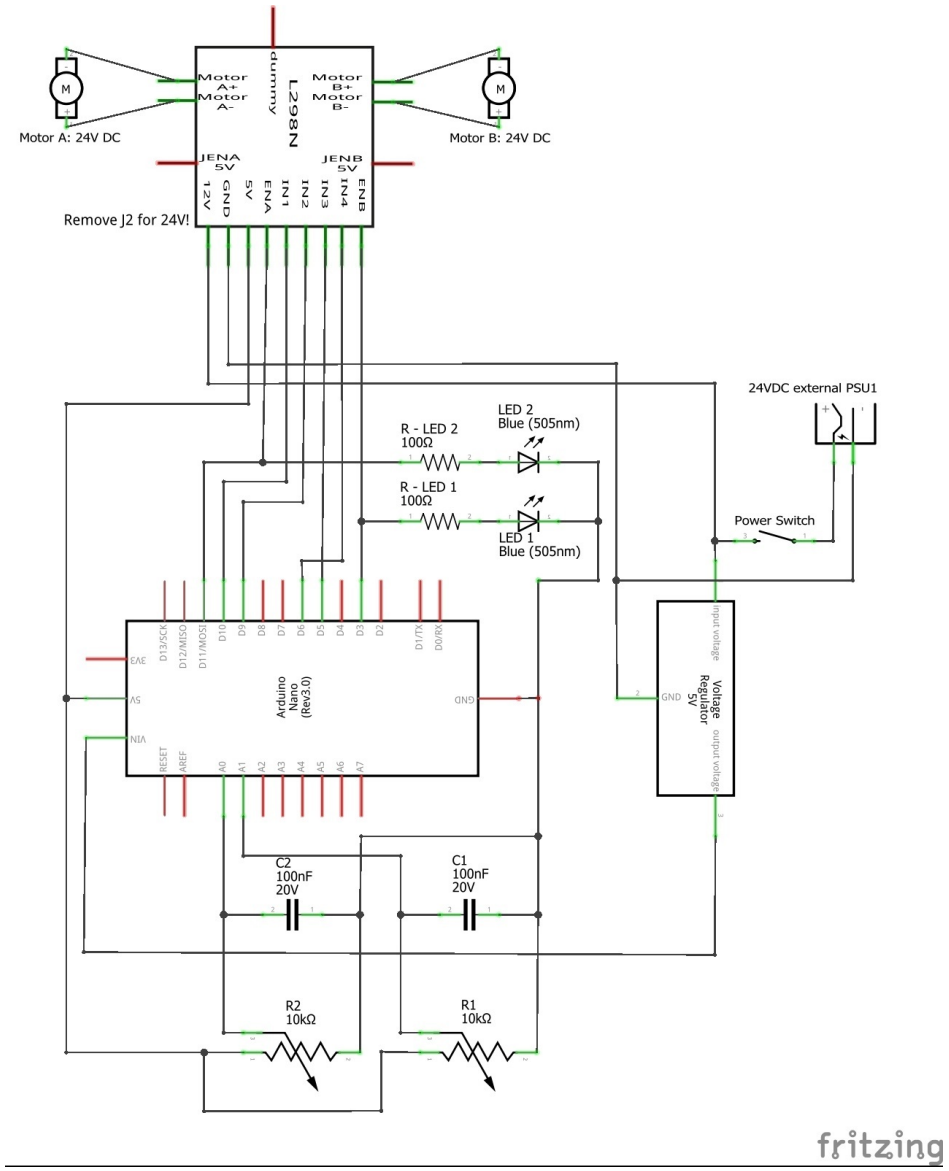

Figure F.1: *A schematic circuit diagram of the electronics that drive the motors of the Lissajous scanner.*[1]

[1]The circuit diagram was drawn with the open source program Fritzing (version 0.9.3., http://fritzing.org/home/, accessed 23/07/19).

F.1.2 Arduino Code

The Arduino Nano code that is used to control the motor driver of the Lissajous scanner is shown on the following three pages. The code is adapted from freely available code published by Tom Igoe (http://www.arduino.cc/en/Tutorial/AnalogInOutSerial, accessed 30/07/19).

```
/*
  Analog input, analog output, serial output

  Reads an analog input pin, maps the result to a range from 0 to 255 and uses
  the result to set the pulse width modulation (PWM) of an output pin.
  Also prints the results to the Serial Monitor.

  The circuit:
  - potentiometer connected to analog pin 0.
    Center pin of the potentiometer goes to the analog pin.
    side pins of the potentiometer go to +5V and ground
  - LED connected from digital pin 9 to ground

  created 29 Dec. 2008
  modified 9 Apr 2012
  by Tom Igoe

  This example code is in the public domain.

  http://www.arduino.cc/en/Tutorial/AnalogInOutSerial
*/

// These constants won't change. They're used to give names to the pins used:
int  analogInPin1 = A1;  // Analog input pin that the potentiometer is attached to
int  analogInPin2 = A0;  // Analog input pin that the potentiometer is attached to
int sensorValue3 = 0;  // variable to store the value coming from the sensor
int outputValue3 = 0;   // variable to send to motor A
int analogInPin3 = A6;    // select the input pin for the Lissajous switch
int sensorValue1 = 0;        // value read from the pot
int outputValue1 = 0;        // value output to the PWM (analog out)
int sensorValue2 = 0;        // value read from the pot
int outputValue2 = 0;        // value output to the PWM (analog out)
int dummy = 0;
int outputValue2_corr = 0;

// connect motor controller pins to Arduino digital pins
// motor one
int enA = 11; // Analog output pin for motor A and pwm activation
int in1 = 10;
int in2 = 9;
// motor two
int enB = 3; // Analog output pin for motor B and pwm activation
int in3 = 5;
int in4 = 6;

void setup() {
  // initialize serial communications at 9600 bps:
  Serial.begin(9600);
  //Set both potis to inputs
  pinMode(analogInPin1, INPUT);
  pinMode(analogInPin2, INPUT);
  // set all the motor control pins to outputs
  pinMode(enA, OUTPUT);
  pinMode(enB, OUTPUT);
  pinMode(in1, OUTPUT);
  pinMode(in2, OUTPUT);
  pinMode(in3, OUTPUT);
  pinMode(in4, OUTPUT);

  //Switch to enter in Lissajous mode
  pinMode(analogInPin3, INPUT_PULLUP);
}
```

```
void demo()
{
  /*To check the functionality of the motor, this demo script can be used.
    Uncomment demoOne in the loop below*/
  analogWrite(enA, 200);
  digitalWrite(in1, LOW);
  digitalWrite(in2, HIGH);
  analogWrite(enB, 200);
  digitalWrite(in3, LOW);
  digitalWrite(in4, HIGH);
}

void Lissajous_fixed_ratio()
{
  //Vertical motor starts consistently running from about 82 of 255 counts on analogInPin2
  //Thus it is chosen to start the motor in the following speed settings: 90, 125, and 160
  //in order to keep the ratio between the two motors constant. The vertical motor is chosen
  //to run a bit faster as it carries less weight.
  //The horizontal motor start running at 67 counts on analogInPin2, thus 15 counts less.
  //The motors are 'calibrated' when taking into account this differences. To get the wanted
  //Lissajous ratio of 34/35, the real motor speed needs to be measured. As a quick hack,
  //it seems that simply using one poti to control both is sufficient to write a nice Lissajous
  //patter on a paper (when taping a pen to the sample cell holder).

  // read the analog in value from a potentiometer (100 kOhm) of Motor A:
  dummy = analogRead(analogInPin2);
  sensorValue2 = analogRead(analogInPin2);
  outputValue2 = map(sensorValue2, 0, 1023, 0, 255);
  // map it to the range of the analog out (the motor board driver only accepts 8-bit input).
  //Write out the poti setting to both motors simultaneously, only if the 'Lissajous switch'
  //is ON.
  analogWrite(enA, outputValue2);
  delay(10);
  analogWrite(enB, outputValue2);

  dummy = analogRead(analogInPin3);
  sensorValue3 = analogRead(analogInPin3);
  if (sensorValue3 < 1000) {
    analogWrite(enA, 0);
    delay(10);
    analogWrite(enB, 0);
    delay(10);
  }
}

void loop() {
  //Activate both motors
  digitalWrite(in1, LOW); //To reverse the speed, set in1 to HIGH, and in2 to LOW
  digitalWrite(in2, HIGH);
  digitalWrite(in3, LOW); //To reverse the speed, set in3 to HIGH, and in4 to LOW
  digitalWrite(in4, HIGH);

  //Check switch to enter Lissajous mode. Inside the Lissajous code the switch is
  //read in again, in order to exit 'Lissajous mode'.
  dummy = analogRead(analogInPin3);
  sensorValue3 = analogRead(analogInPin3);
  Serial.print("sensor Lissajous switch= ");
  Serial.println(sensorValue3);

  //Check switch to enter into 'Lissajous mode'
  if (sensorValue3 > 1000) {
    Lissajous_fixed_ratio();
  }
```

```
  else if (sensorValue3 < 1000) {
    dummy = analogRead(analogInPin1);
    sensorValue1 = analogRead(analogInPin1);
    // map it to the range of the analog out:
    outputValue1 = map(sensorValue1, 0, 1023, 0, 255);
    analogWrite(enA, outputValue1);
    delay(25); //delay between analogreads

    /* //Diagnostics
      // print the results to the Serial Monitor:
      Serial.print("sensor = ");
      Serial.print(sensorValue1);
      Serial.print("\t output = ");
      Serial.println(outputValue1);
      Serial.print("sensor = ");
      Serial.print(sensorValue2);
      Serial.print("\t output = ");
      Serial.println(outputValue2);*/

    dummy = analogRead(analogInPin2); //dummy read to reset
    sensorValue2 = analogRead(analogInPin2);
    // change the analog out value, ie this sets the speed (out of possible range 0~255)
    outputValue2 = map(sensorValue2, 0, 1023, 0, 255);
    analogWrite(enB, outputValue2);

    // wait 2 milliseconds before the next loop for the analog-to-digital
    // converter to settle after the last reading:
    delay(2);
  }

  /* To test the functionaly of the motor, simply uncomment this section:
    demo();
    delay(100);*/
}
```

F.2 Photocycle Dynamics in D_2O

F.2.1 Single Spectra of Selected Delay Times for Mechanical Delays

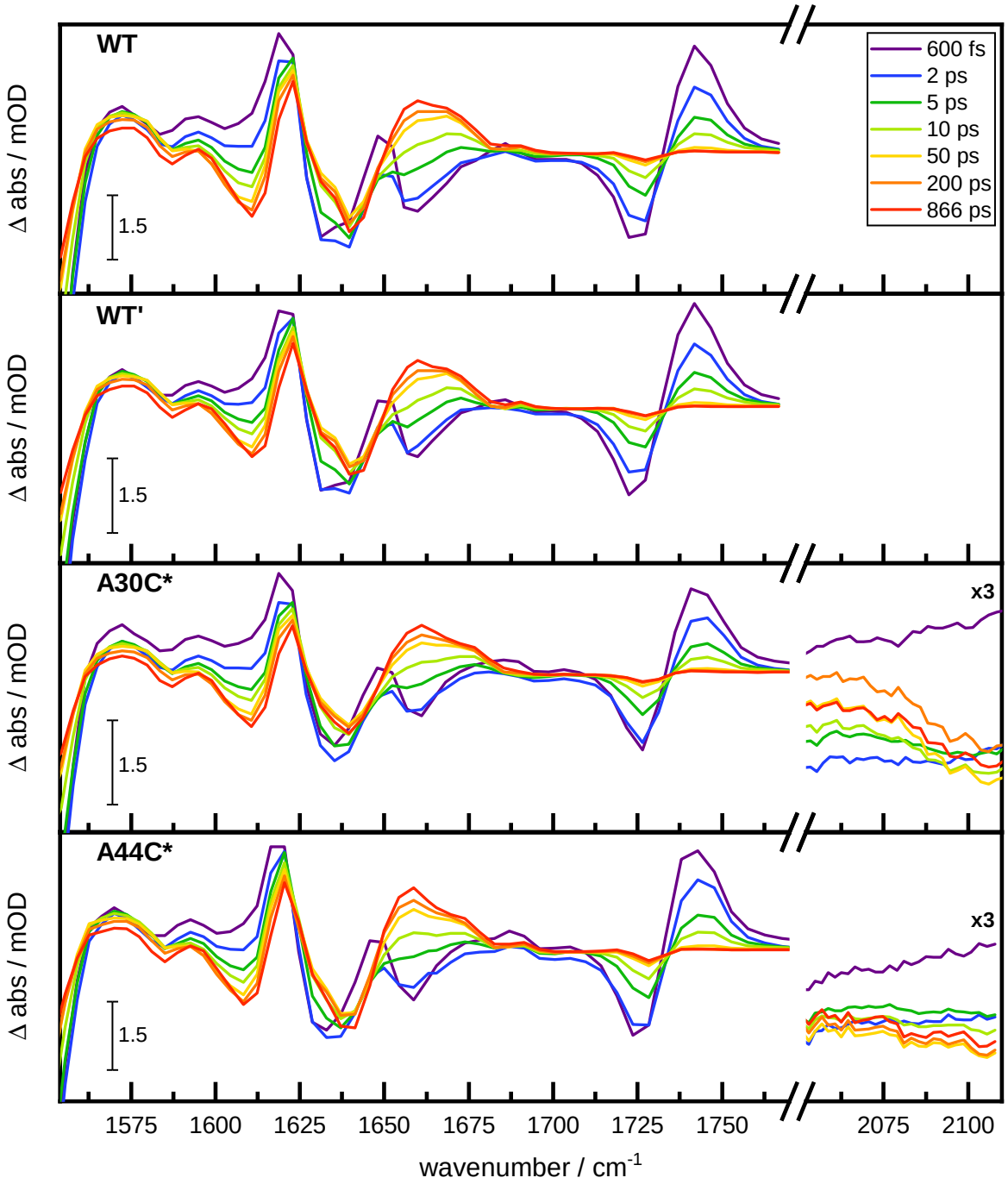

Figure F.2: *Single spectra of raw data for selected delay times of WT, WT', A30C*, and A44C* in the fs-to-ns time range of the CC/CO and SCN region. The overlapping spectral windows of CC and CO region were merged between 1659 cm^{-1} and 1670 cm^{-1}, the CO region was multiplied by a constant factor to adapt the intensity. All spectra were background corrected by subtraction of the spectrum at −20 ps. The SCN region is scaled by the factor given in the graphs for better visualization.*

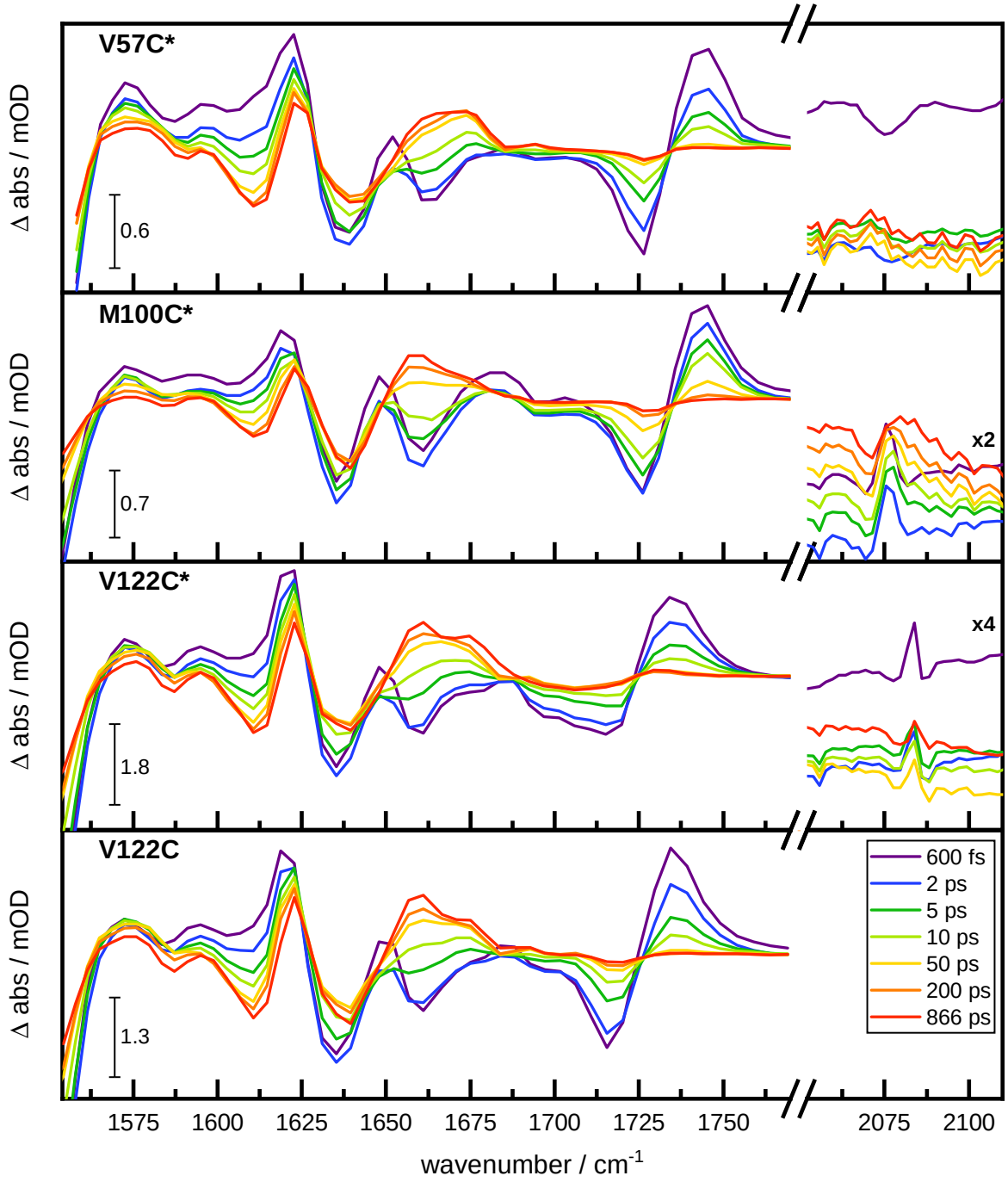

Figure F.3: *Single spectra of raw data for selected delay times of V57C*, M100C*, V122C*, and V122C in the fs-to-ns time range of the CC/CO and SCN region. All spectra were background corrected by subtraction of the spectrum at −20 ps. The overlapping spectral windows of CC and CO region were merged between 1659 cm^{-1} and 1670 cm^{-1}, the CO region was multiplied by a constant factor to adapt the intensity. The SCN region is scaled by the factor given in the graphs for better visualization.*

F.2.2 Single Spectra of Selected Delay Times for Electronic Delays

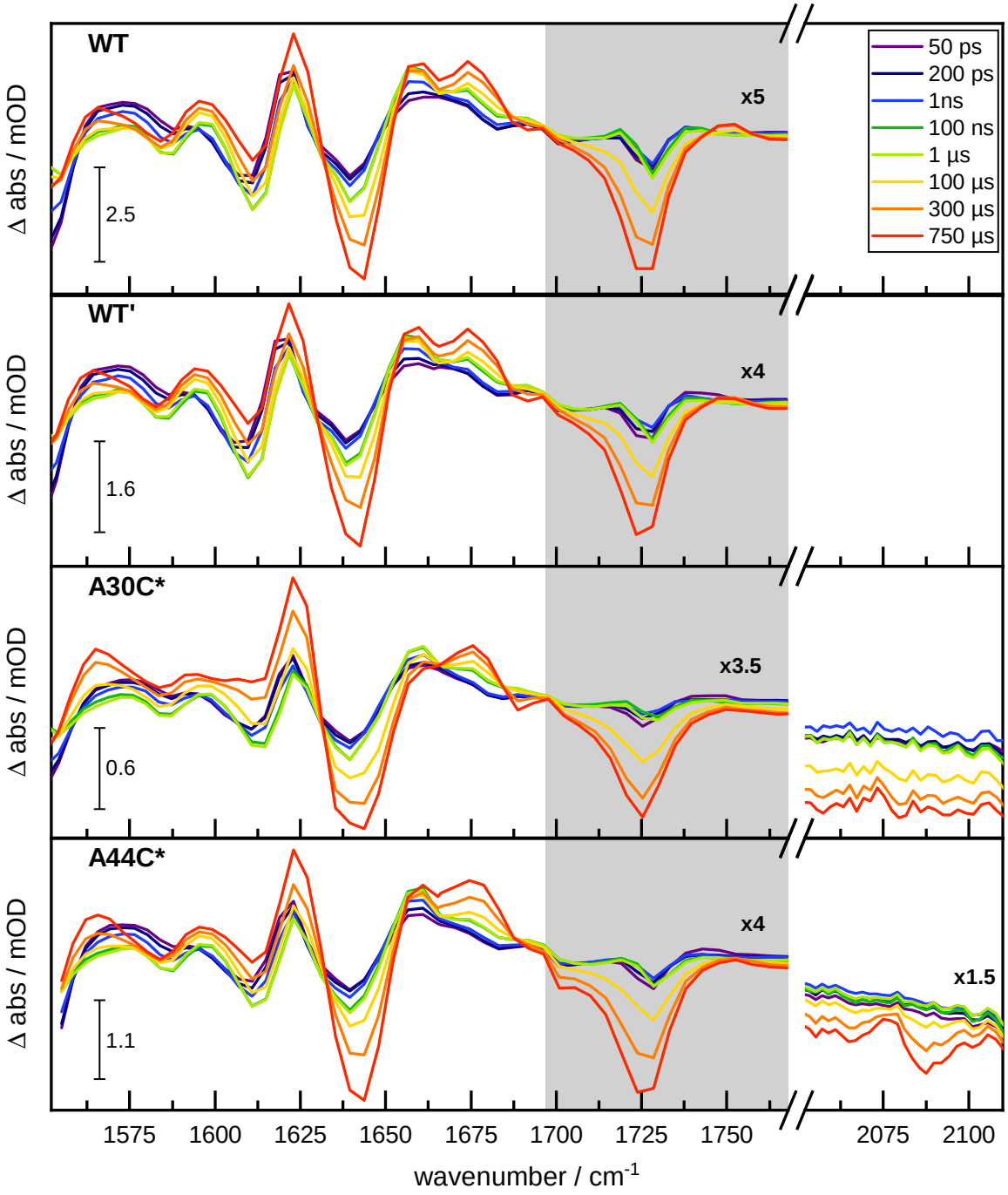

Figure F.4: *Single Spectra of raw data for selected delay times of WT, WT', A30C*, and A44C* in the ps-to-ms time range of the CC/CO and SCN region. All spectra were background corrected by subtraction of the spectrum at −7.5 ns. The overlapping spectral windows of CC and CO region were merged between 1659 cm^{-1} and 1670 cm^{-1}, the CO region was multiplied by a constant factor to adapt the intensity. The CO region of E46 (highlighted in gray) and the SCN region are scaled by the factor given in the graphs for better visualization.*

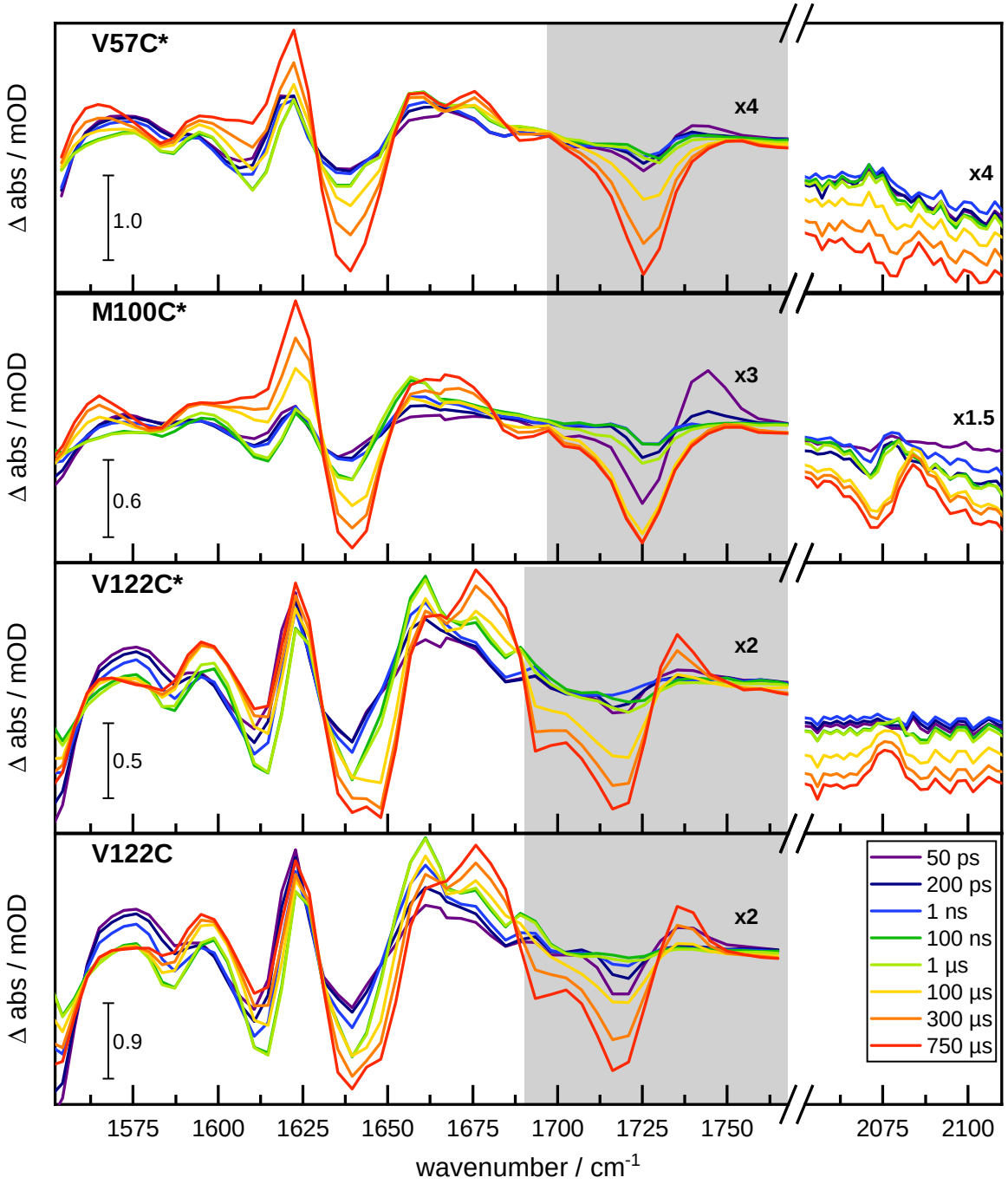

Figure F.5: *Single spectra of raw data for selected delay times of V57C*, M100C*, V122C*, and V122C in the ps-to-ms time range of the CC/CO and SCN region. All spectra were background corrected by subtraction of the spectrum at −7.5 ns. The overlapping spectral windows of CC and CO region were merged between 1659 cm^{-1} and 1670 cm^{-1}, the CO region was multiplied by a constant factor to adapt the intensity. The CO region of E46 (highlighted in gray) and the SCN region are scaled by the factor given in the graphs for better visualization.*

F.2.3 Global Analysis of CC/CO Region for Mechanical Delays

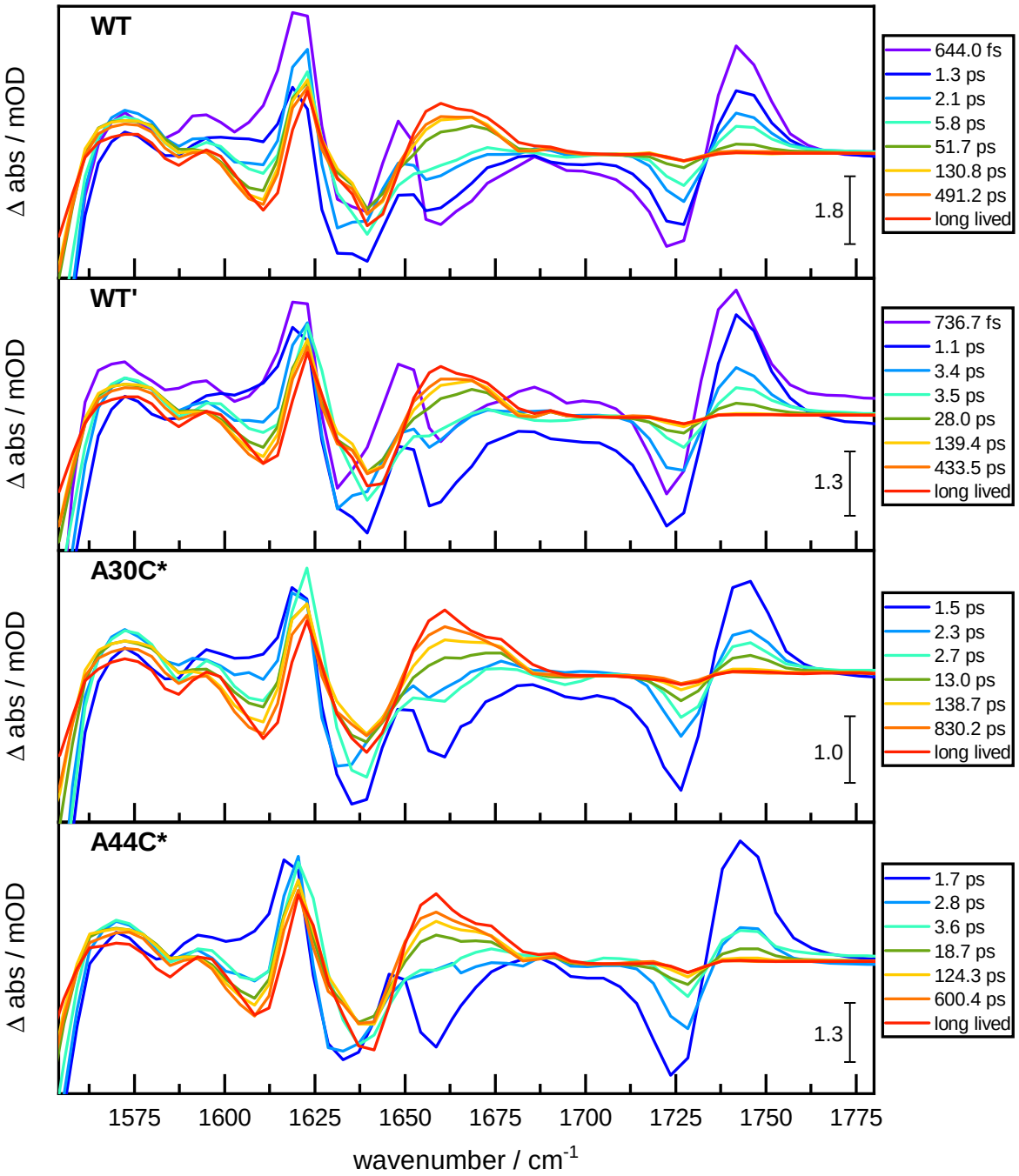

Figure F.6: *SADS obtained by global analysis of WT, WT', A30C*, and A44C* in the fs-to-ns time range of the CC/CO region. For GA of the background corrected data (subtraction of spectrum at −20 ps) a sequential model with 11 components was used. Here only components > 600 fs are shown.*

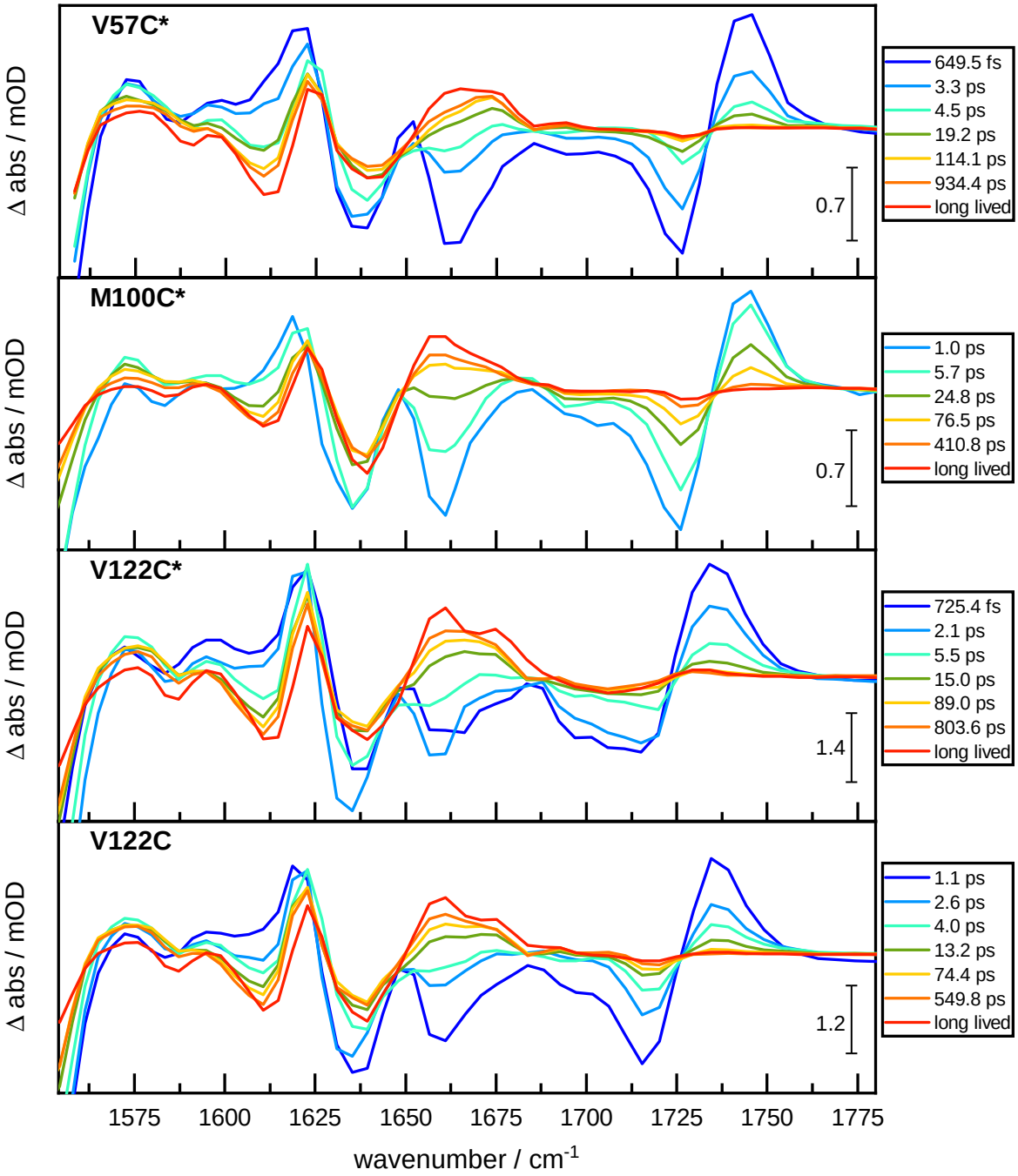

Figure F.7: *SADS obtained by global analysis of V57C*, M100C*, V122C*, and V122C in the fs-to-ns time range of the CC/CO region. For GA of the background corrected data (subtraction of spectrum at −20 ps) a sequential model with 11 components was used. Here only components > 600 fs are shown.*

F.2.4 Global Analysis of CC/CO Region for Electronic Delays

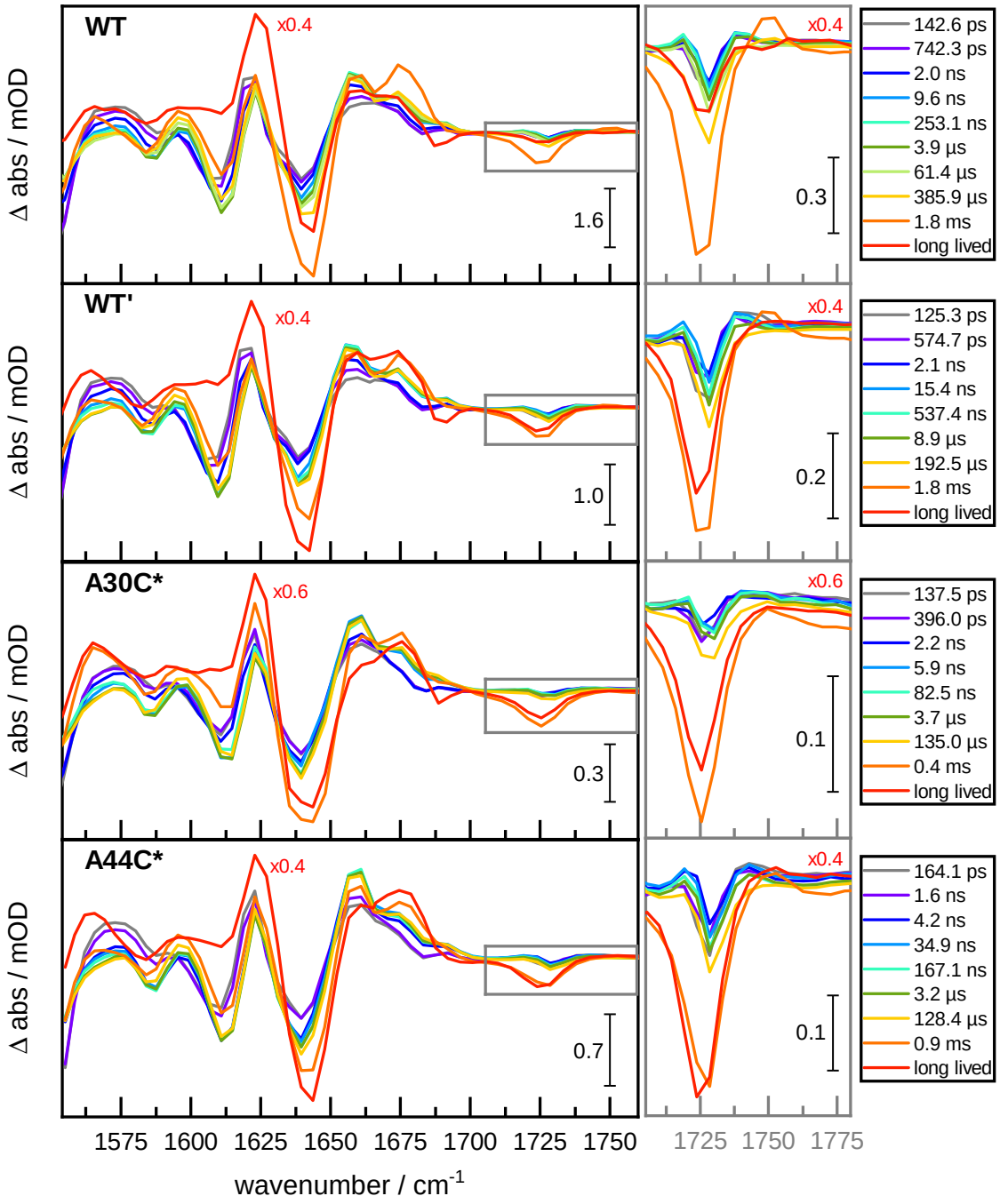

Figure F.8: *SADS obtained by global analysis of WT, WT', A30C*, and A44C* in the ps-to-ms time range of the CC/CO region. For GA of the background corrected data (subtraction of spectrum at −7.5 ns) a sequential model with 11 components was used. Here only components > 50 ps are shown. The long lived spectrum (red) was scaled by the factor given in the respective graph. In the right column a zoom into the CO region of E46 is shown, indicated by a gray box in the graph of the complete spectral region on the left.*

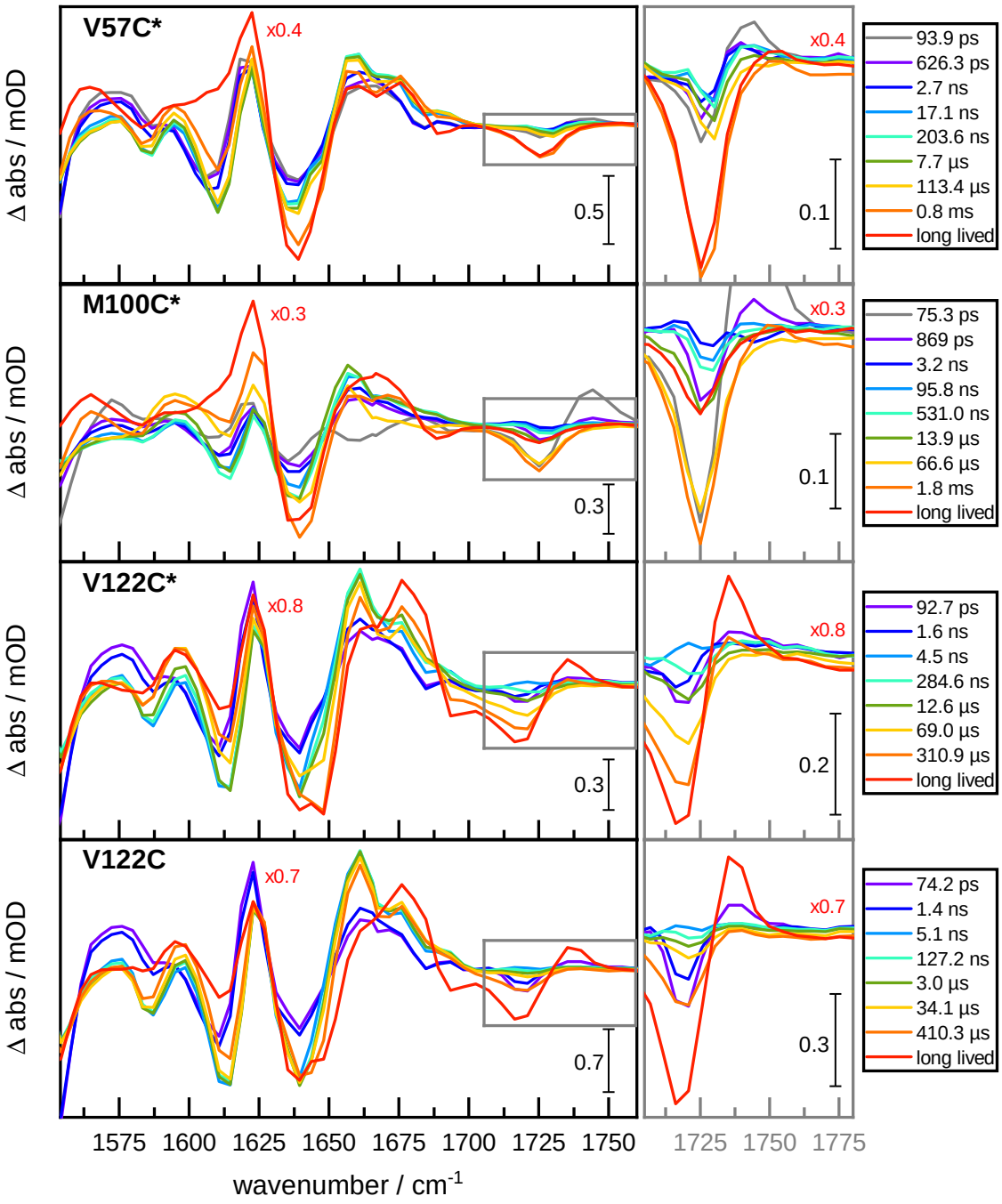

Figure F.9: *SADS obtained by global analysis of V57C*, M100C*, V122C*, and V122C in the ps-to-ms time range of the CC/CO region. For GA of the background corrected data (subtraction of spectrum at −7.5 ns) a sequential model with 11 components was used. Here only components > 50 ps are shown. The long lived spectrum (red) was scaled by the factor given in the respective graph. In the right column a zoom into the CO region of E46 is shown, indicated by a gray box in the graph of the complete spectral region on the left.*

F.2.5 Comparison of Raw and Denoised SCN Data

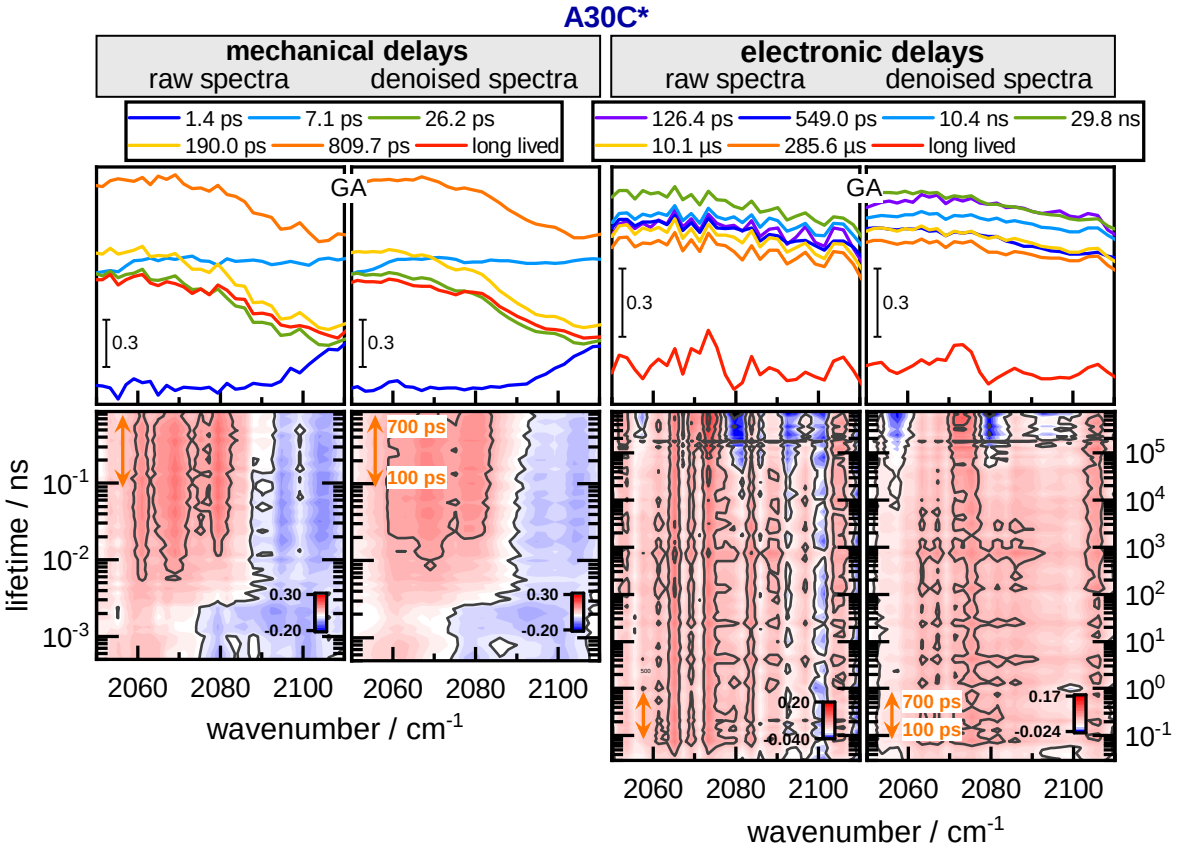

Figure F.10: *Comparison of raw and denoised SCN data of A30C* for mechanical and electronic delays. In the first and second column global analysis (top) and contour plots (bottom) of the raw (left) and denoised SCN spectra (right) for the mechanical delays are depicted. Accordingly the SCN spectra for the electronic delays are shown in the third and fourth column. For the contour plots a linear baseline was subtracted. For the GA spectra only components > 600 fs for the mechanical delays and > 50 ps for the electronic delays are shown. The lifetimes obtained by global analysis are the same for the raw and denoised data.*

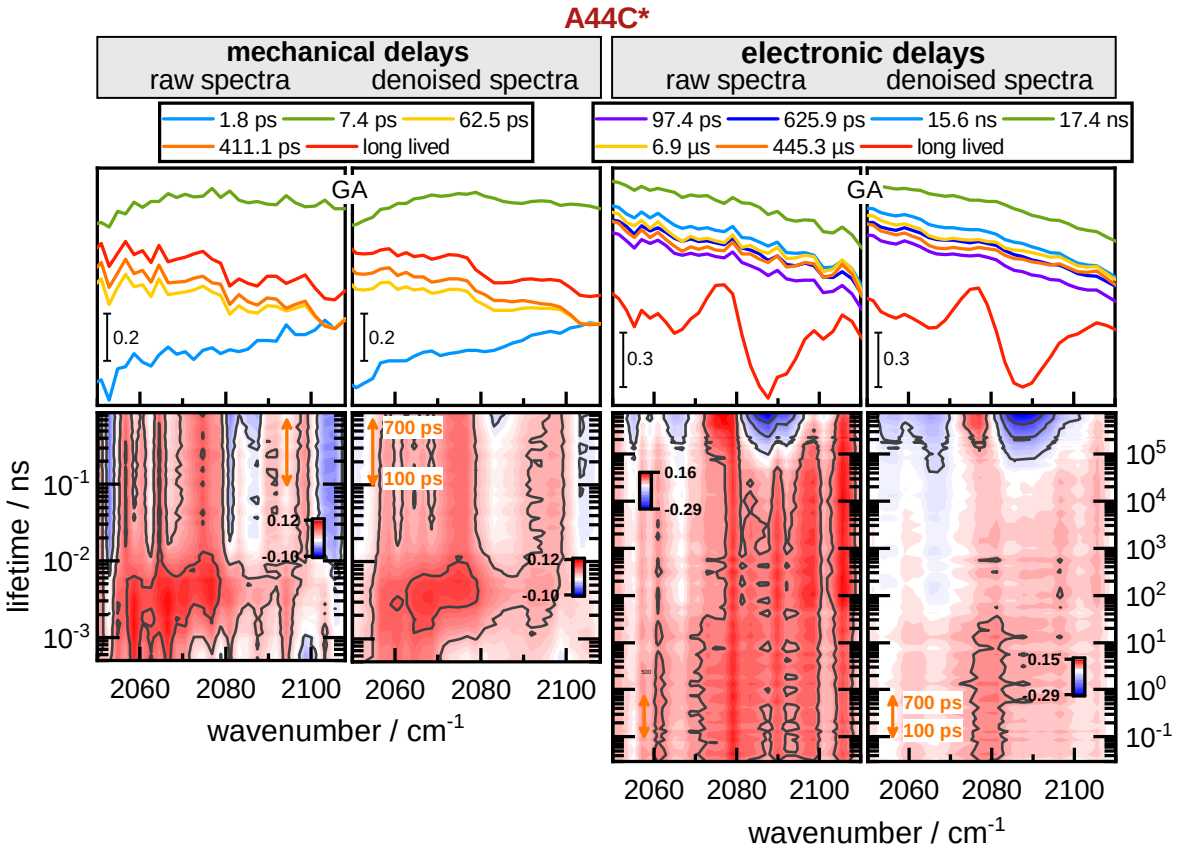

Figure F.11: *Comparison of raw and denoised SCN data of A44C* for mechanical and electronic delays. In the first and second column global analysis (top) and contour plots (bottom) of the raw (left) and denoised SCN spectra (right) for the mechanical delays are depicted. Accordingly the SCN spectra for the electronic delays are shown in the third and fourth column. For the contour plots a linear baseline was subtracted. For the GA spectra only components > 600 fs for the mechanical delays and > 50 ps for the electronic delays are shown. The lifetimes obtained by global analysis are the same for the raw and denoised data.*

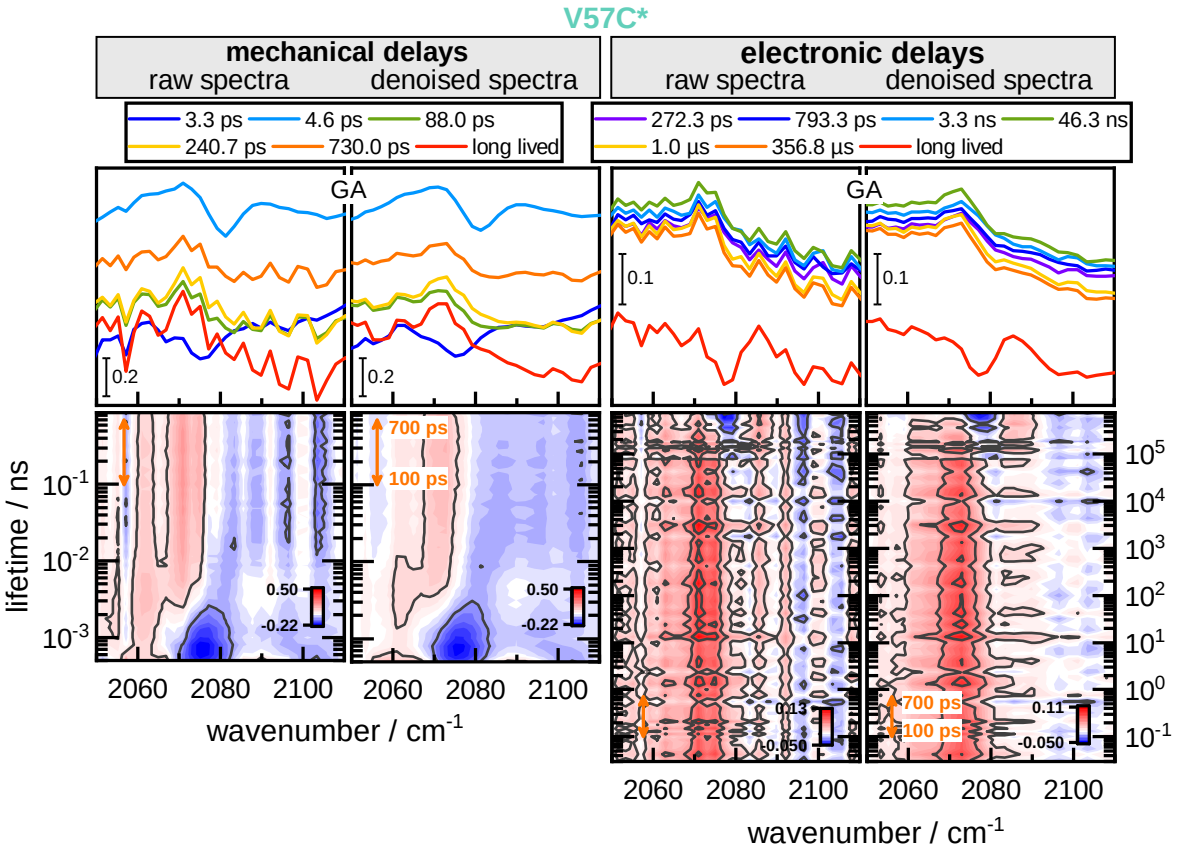

Figure F.12: *Comparison of raw and denoised SCN data of V57C* for mechanical and electronic delays. In the first and second column global analysis (top) and contour plots (bottom) of the raw (left) and denoised SCN spectra (right) for the mechanical delays are depicted. Accordingly the SCN spectra for the electronic delays are shown in the third and fourth column. For the contour plots a linear baseline was subtracted. For the GA spectra only components > 600 fs for the mechanical delays and > 50 ps for the electronic delays are shown. The lifetimes obtained by global analysis are the same for the raw and denoised data.*

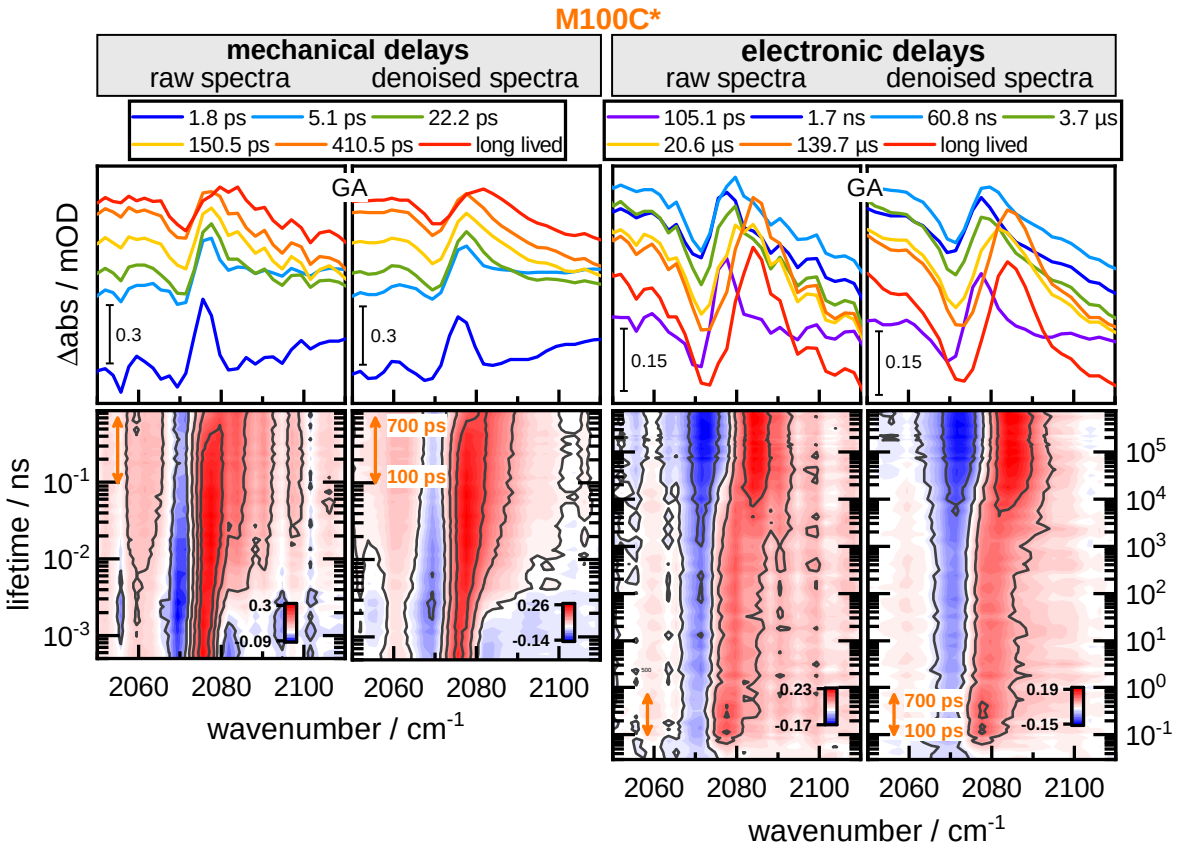

Figure F.13: *Comparison of raw and denoised SCN data of M100C* for mechanical and electronic delays. In the first and second column global analysis (top) and contour plots (bottom) of the raw (left) and denoised SCN spectra (right) for the mechanical delays are depicted. Accordingly the SCN spectra for the electronic delays are shown in the third and fourth column. For the contour plots a linear baseline was subtracted. For the GA spectra only components > 600 fs for the mechanical delays and > 50 ps for the electronic delays are shown. The lifetimes obtained by global analysis are the same for the raw and denoised data.*

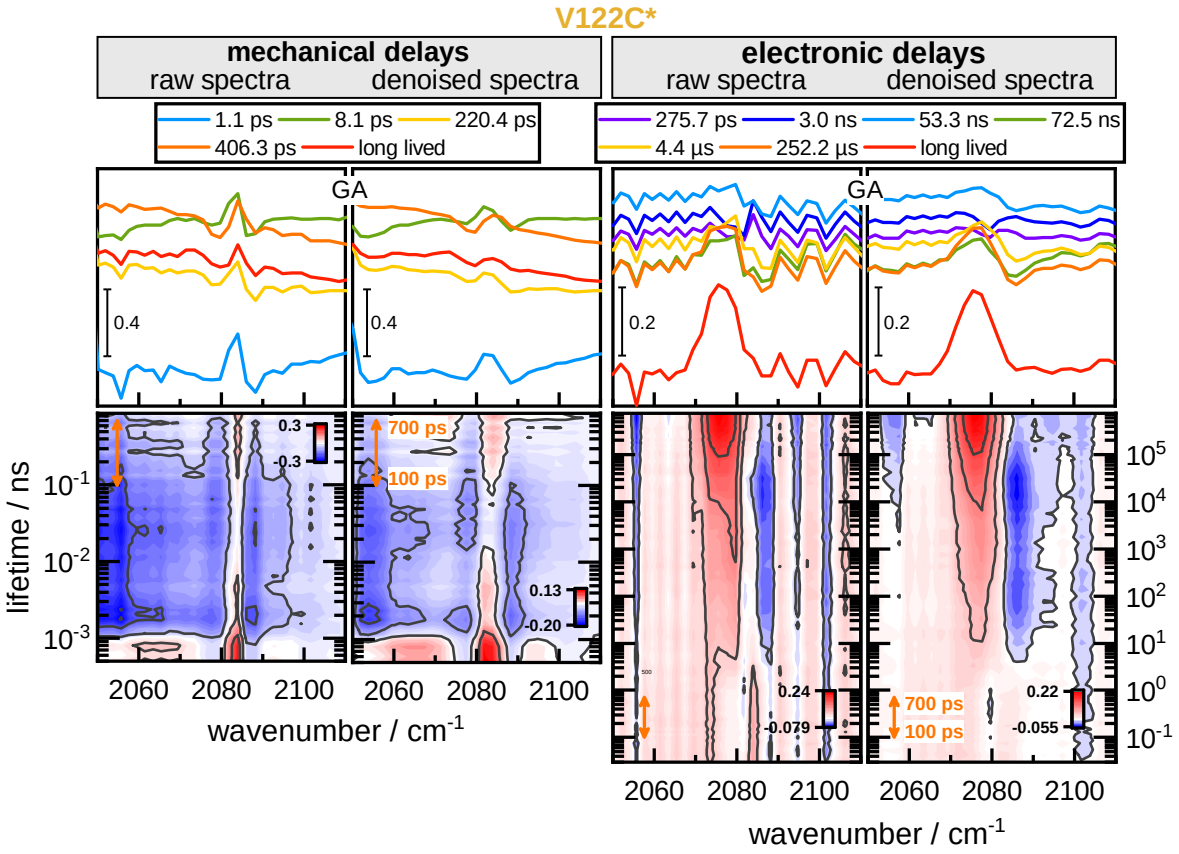

Figure F.14: *Comparison of raw and denoised SCN data of V122C* for mechanical and electronic delays. In the first and second column global analysis (top) and contour plots (bottom) of the raw (left) and denoised SCN spectra (right) for the mechanical delays are depicted. Accordingly the SCN spectra for the electronic delays are shown in the third and fourth column. For the contour plots a linear baseline was subtracted. For the GA spectra only components > 600 fs for the mechanical delays and > 50 ps for the electronic delays are shown. The lifetimes obtained by global analysis are the same for the raw and denoised data.*

F.2.6 All SADS and Errors from Global Analysis

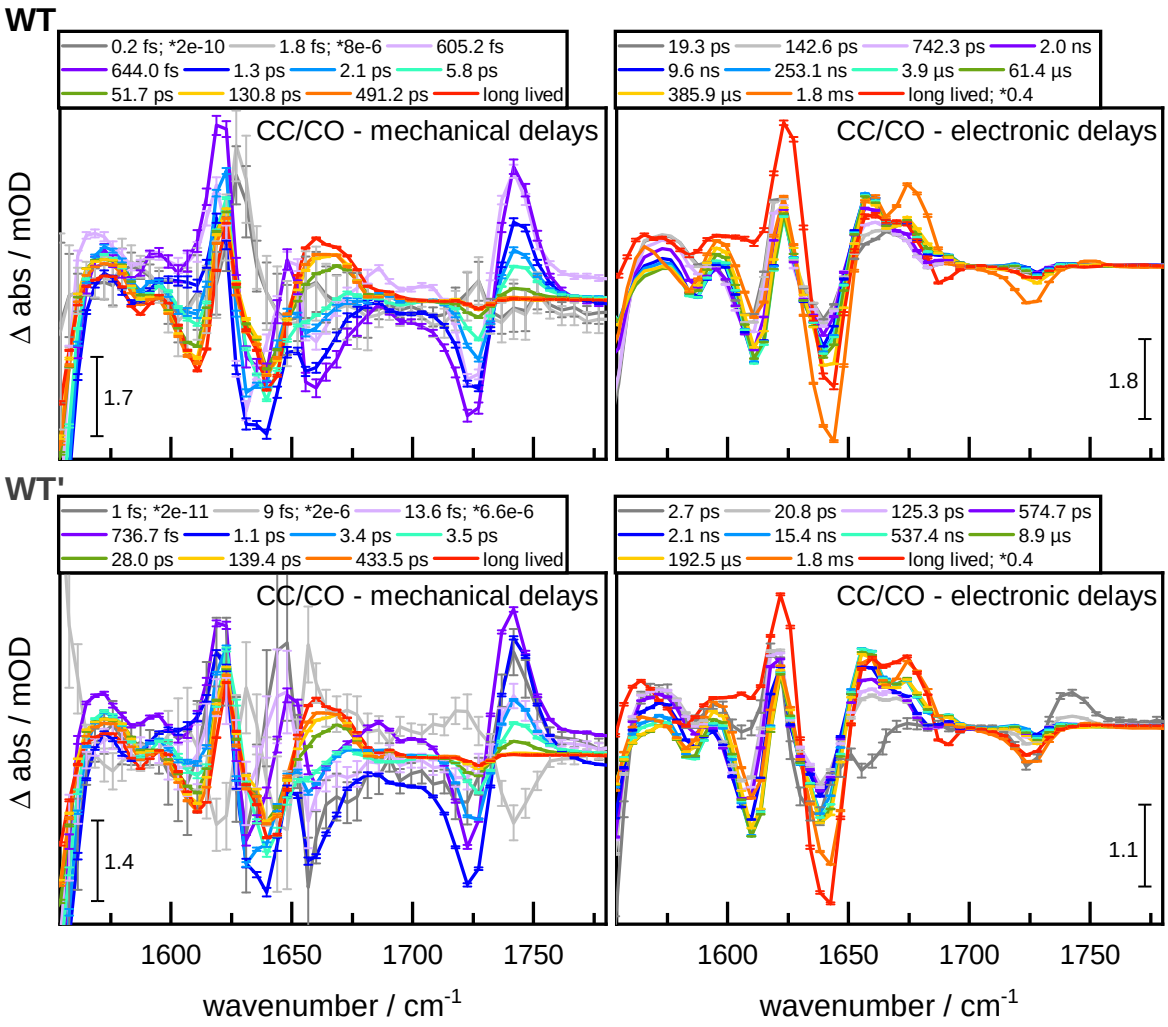

Figure F.15: *SADS with error bars obtained by global analysis of WT (top) and WT′ (bottom) for mechanical delays (left) and electronic delays (right) of the CC/CO region. For GA of the background corrected data (subtraction of spectrum at −20 ps and -7.5 ns, respectively) sequential models with 11 components were used. Some of the components were scaled by the factors given in the corresponding legend.*

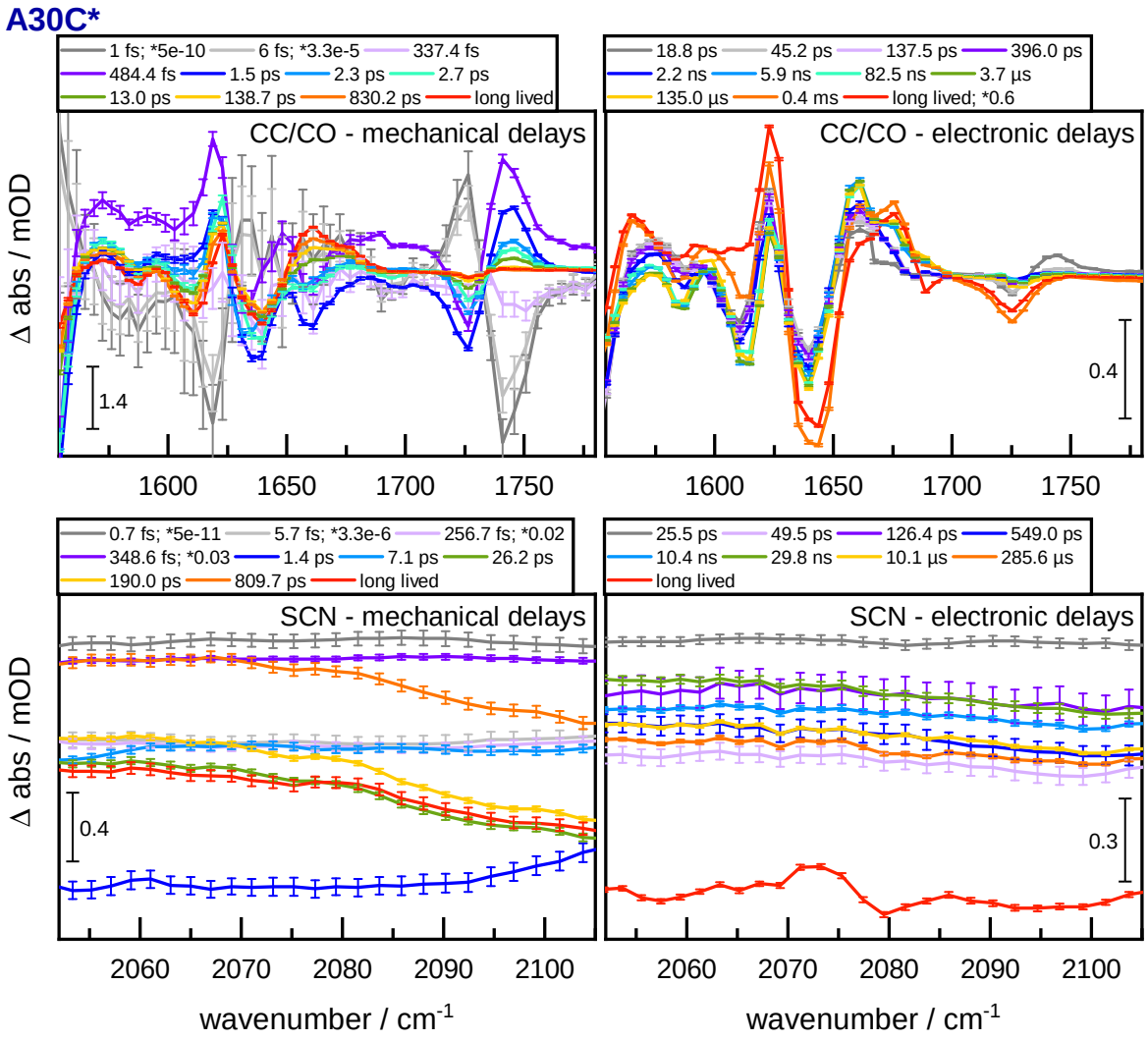

Figure F.16: *SADS with error bars obtained by global analysis of A30C* for mechanical delays (left) and electronic delays (right) of the CC/CO (top) and SCN region (bottom). For GA of the background corrected data (subtraction of spectrum at −20 ps and -7.5 ns, respectively) sequential models with 11 components for the CC/CO regions, 10 components for the SCN region of the mechanical delays and 9 components for the SCN region of the electronic delays were used. Some of the components were scaled by the factors given in the corresponding legend.*

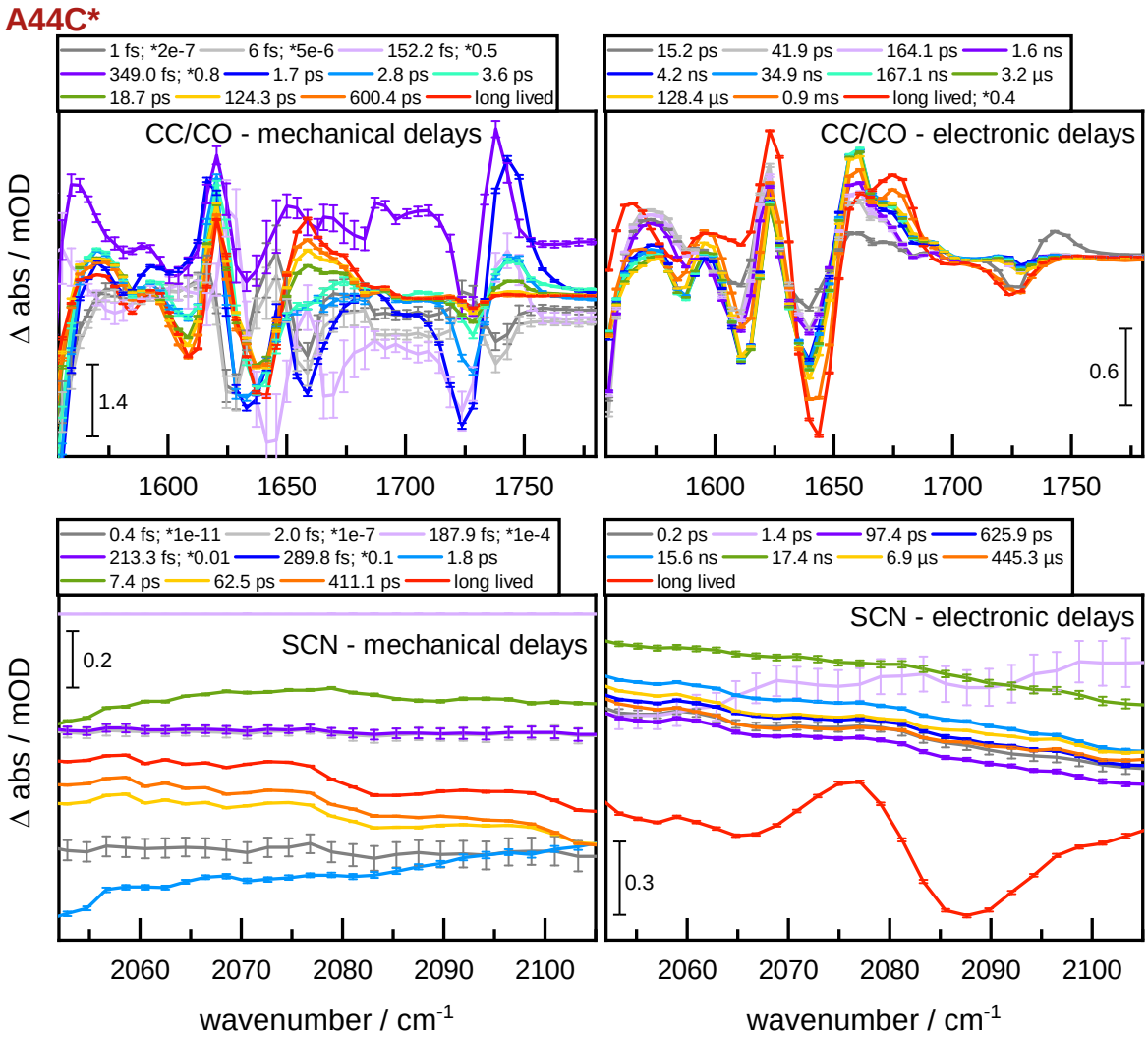

Figure F.17: *SADS with error bars obtained by global analysis of A44C* for mechanical delays (left) and electronic delays (right) of the CC/CO (top) and SCN region (bottom). For GA of the background corrected data (subtraction of spectrum at −20 ps and -7.5 ns, respectively) sequential models with 11 components for the CC/CO regions, 10 components for the SCN region of the mechanical delays and 9 components for the SCN region of the electronic delays were used. Some of the components were scaled by the factors given in the corresponding legend.*

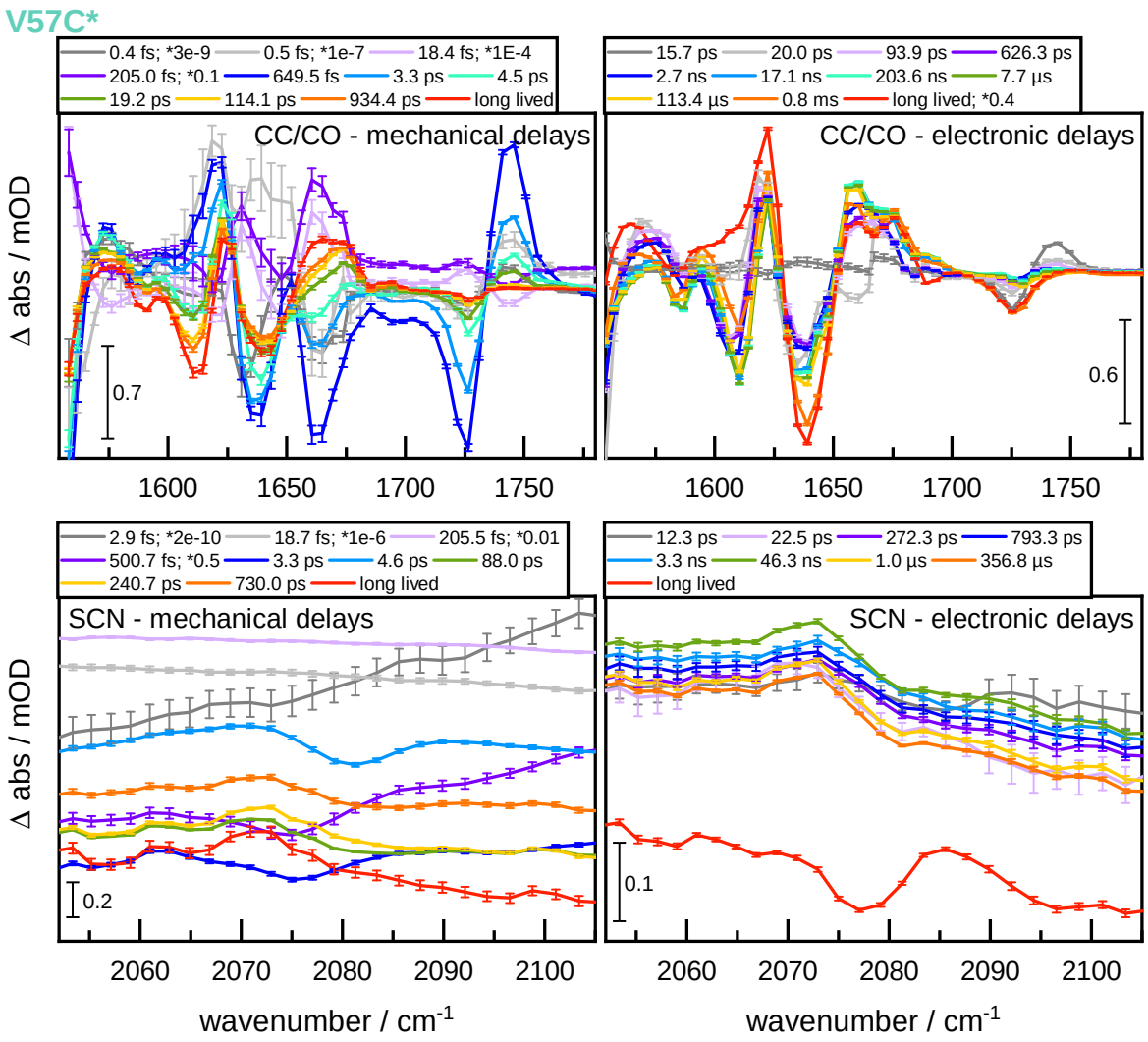

Figure F.18: *SADS with error bars obtained by global analysis of V57C* for mechanical delays (left) and electronic delays (right) of the CC/CO (top) and SCN region (bottom). For GA of the background corrected data (subtraction of spectrum at −20 ps and -7.5 ns, respectively) sequential models with 11 components for the CC/CO regions, 10 components for the SCN region of the mechanical delays and 9 components for the SCN region of the electronic delays were used. Some of the components were scaled by the factors given in the corresponding legend.*

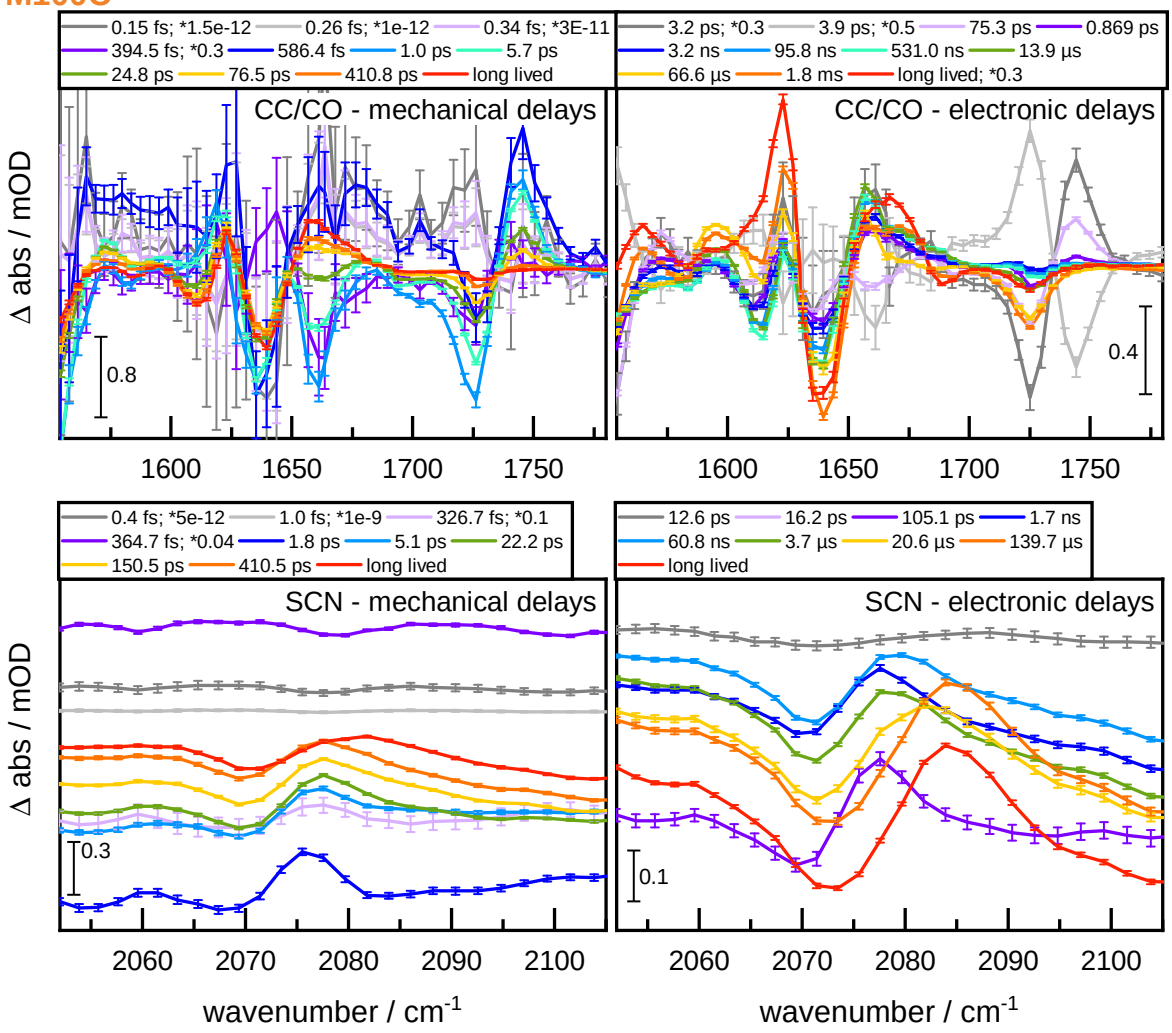

Figure F.19: *SADS with error bars obtained by global analysis of M100C* for mechanical delays (left) and electronic delays (right) of the CC/CO (top) and SCN region (bottom). For GA of the background corrected data (subtraction of spectrum at −20 ps and -7.5 ns, respectively) sequential models with 11 components for the CC/CO regions, 10 components for the SCN region of the mechanical delays and 9 components for the SCN region of the electronic delays were used. Some of the components were scaled by the factors given in the corresponding legend.*

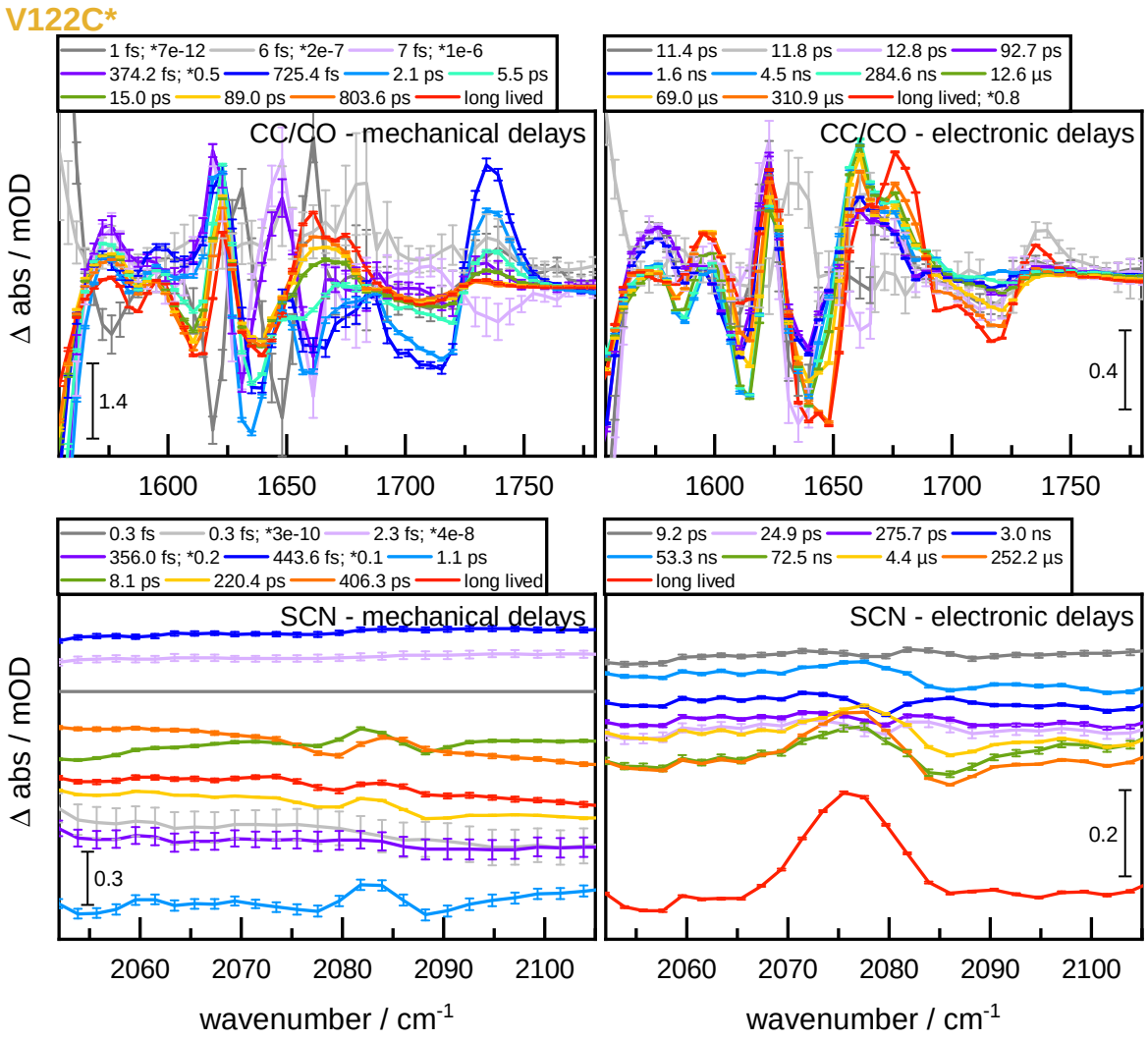

Figure F.20: *SADS with error bars obtained by global analysis of V122C* for mechanical delays (left) and electronic delays (right) of the CC/CO (top) and SCN region (bottom). For GA of the background corrected data (subtraction of spectrum at −20 ps and -7.5 ns, respectively) sequential models with 11 components for the CC/CO regions, 10 components for the SCN region of the mechanical delays and 9 components for the SCN region of the electronic delays were used. Some of the components were scaled by the factors given in the corresponding legend.*

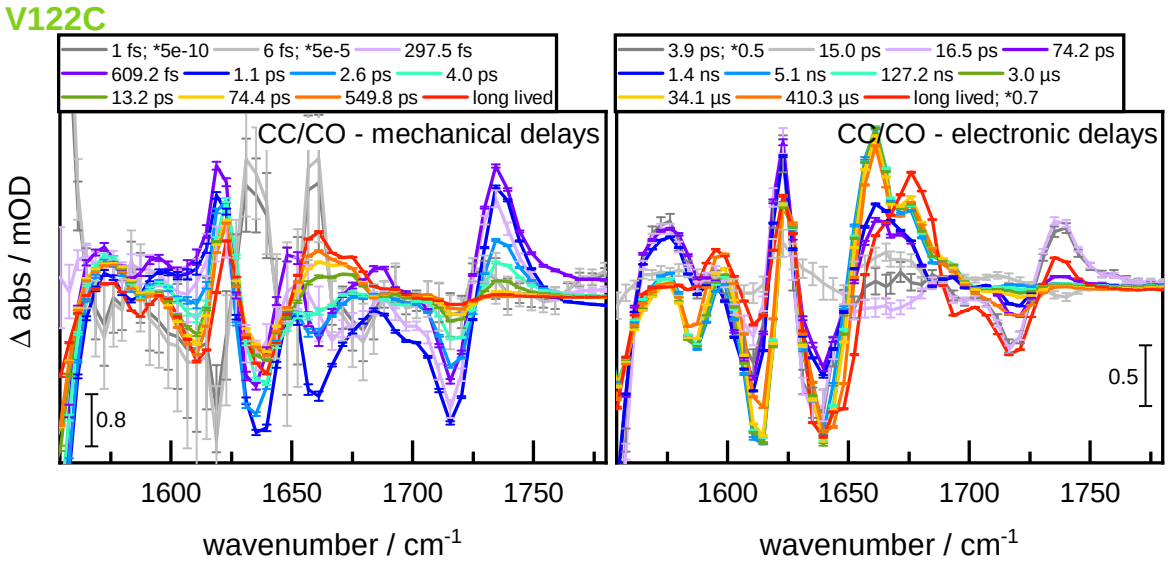

Figure F.21: *SADS with error bars obtained by global analysis of unlabeled V122C for mechanical delays (left) and electronic delays (right) of the CC/CO region. For GA of the background corrected data (subtraction of spectrum at −20 ps and -7.5 ns, respectively) sequential models with 11 components were used. Some of the components were scaled by the factors given in the corresponding legend.*

F.2.7 Time Traces for pCA Protonation and E46 Deprotonation

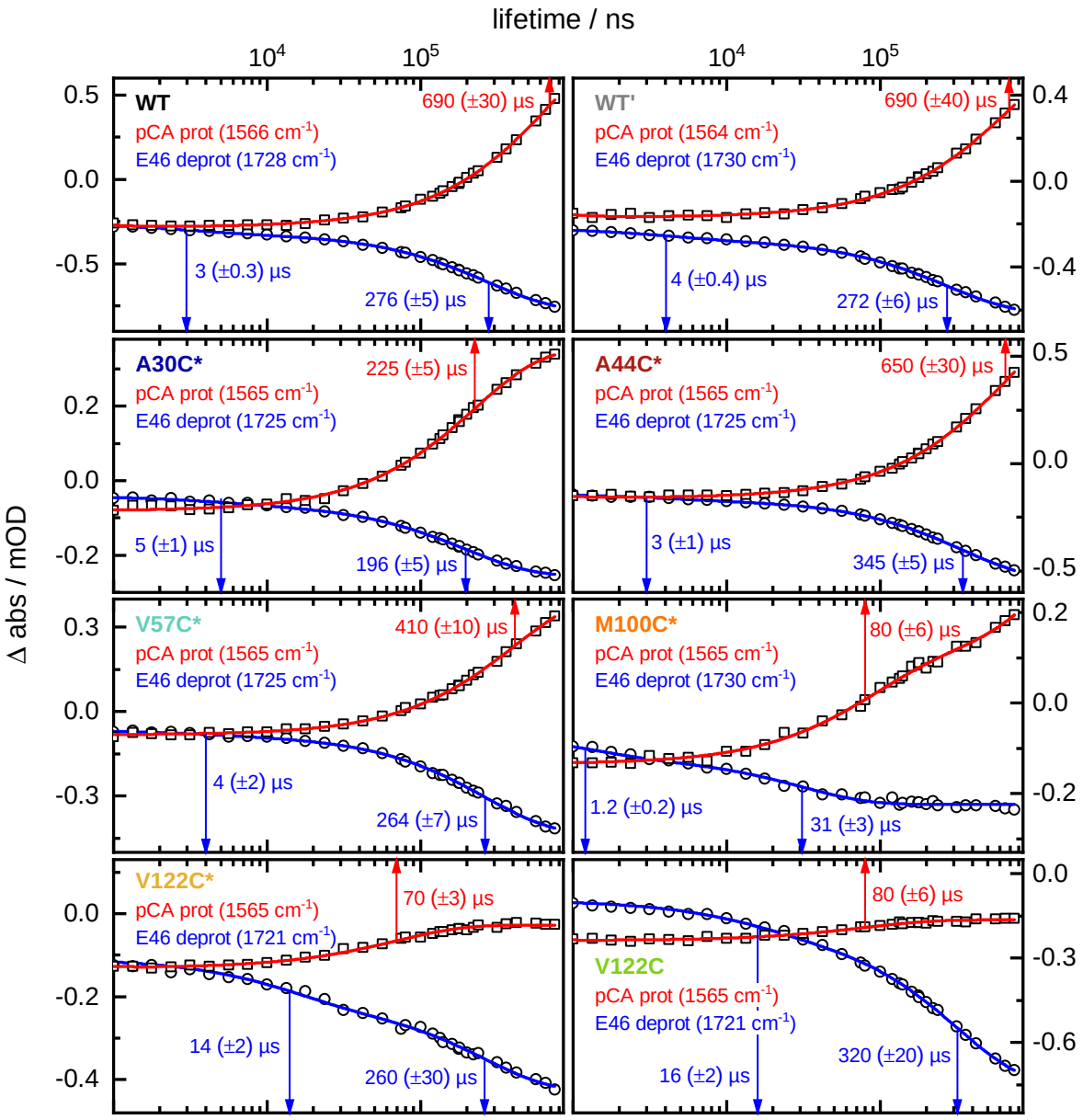

Figure F.22: *Time traces for chromophore protonation (pCA prot) and E46 deprotonation (E46 deprot) on the µs timescale for raw data of all investigated samples. Raw data are depicted in open squares (pCA prot) and open circles (E46 deprot) and corresponding biexponential fits in red and blue, respectively. All data were fitted between 100 ns and 750 µs with two exponential functions. Lifetimes > 1 µs are given in the figures. The fit of the pCA protonation band exhibited a second lifetime < 500 ns for all data except M100C* which revealed a second lifetime ≫ 1 ms. For the biexponential fit the ExpDec2 function of OriginPro 2018G was used.*

F.2.8 Time Slices through ps-to-ms LDMs

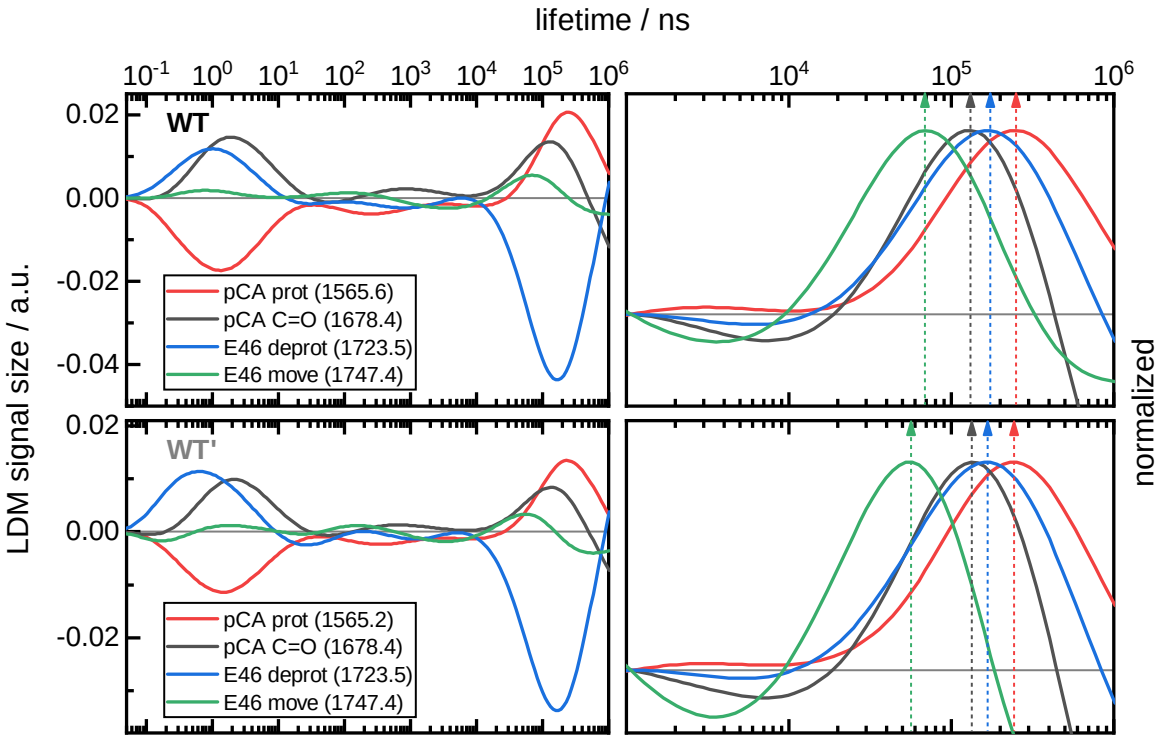

Figure F.23: *Time slices through standardized ps-to-ms LDMs for WT and WT' (figure 7.2 on page 91) for comparison of chromophore protonation (pCA prot, red), changes of chromophore conformation (pCA C=O, gray), E46 deprotonation (E46 deprot, blue) and E46 movement (E46 move, green). Normalized traces (right) are shown in the time range > 1 µs.*

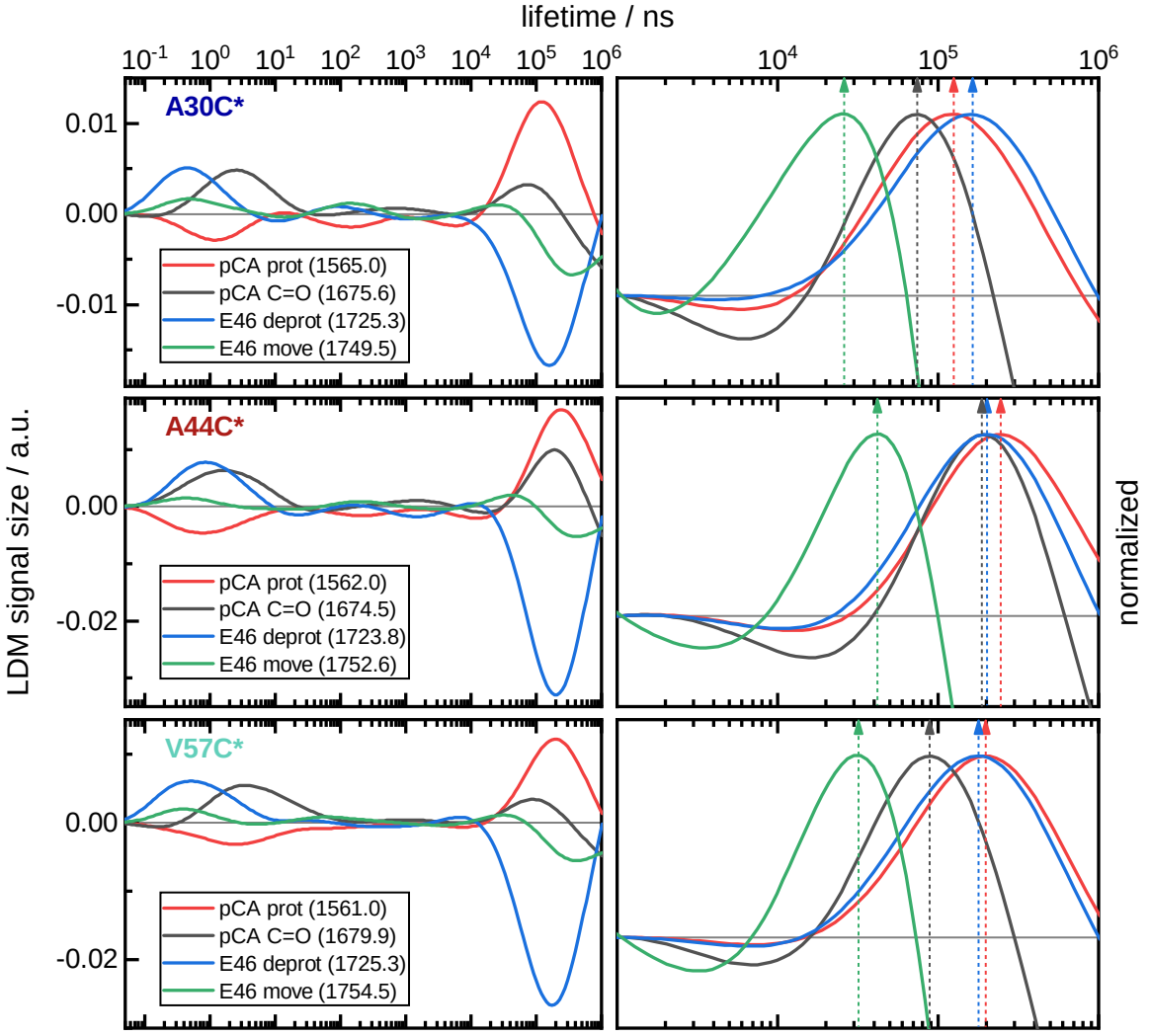

Figure F.24: *Time slices through standardized ps-to-ms LDMs for A30C* (figure 7.7 on page 110), A44C* (figure 7.6 on page 108), and V57C* (figure 7.8 on page 113) for comparison of chromophore protonation (pCA prot, red), changes of chromophore conformation (pCA C=O, gray), E46 deprotonation (E46 deprot, blue) and E46 movement (E46 move, green). Normalized traces (right) are shown in the time range > 1 µs.*

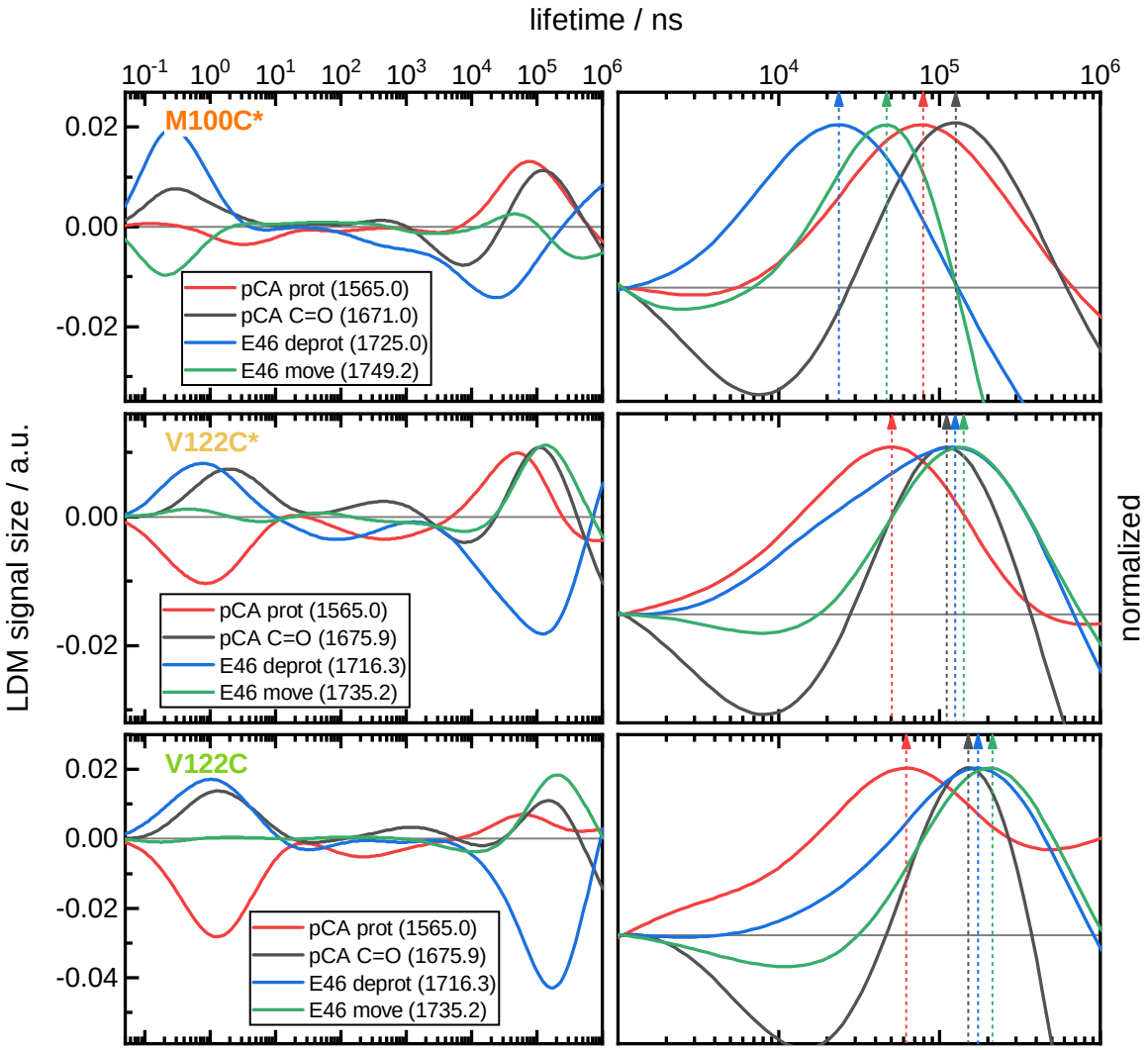

Figure F.25: *Time slices through standardized ps-to-ms LDMs for M100C* (figure 7.9 on page 115), V122C* (figure 7.10 on page 125), and V122C (figure 7.11 on page 130) for comparison of chromophore protonation (pCA prot, red), changes of chromophore conformation (pCA C=O, gray), E46 deprotonation (E46 deprot, blue) and E46 movement (E46 move, green). Normalized traces (right) are shown in the time range > 1 µs.*

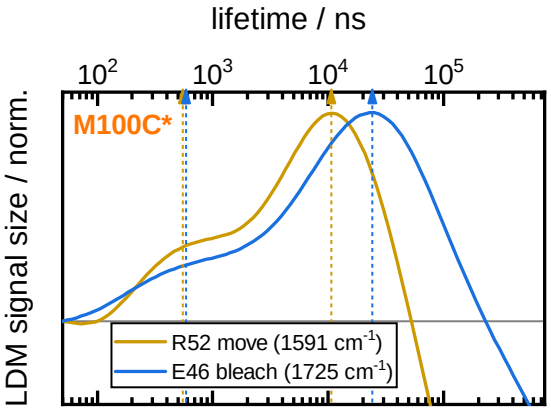

Figure F.26: *Normalized time slices through standardized ps-to-ms LDM for M100C* (figure 7.9 on page 115) for comparison of R52 dynamics (R52 move, yellow) and the dynamics of the E46 bleach (E46 bleach, blue).*

F.2.9 LDMs of SCN Region without Subtraction of Linear Baseline

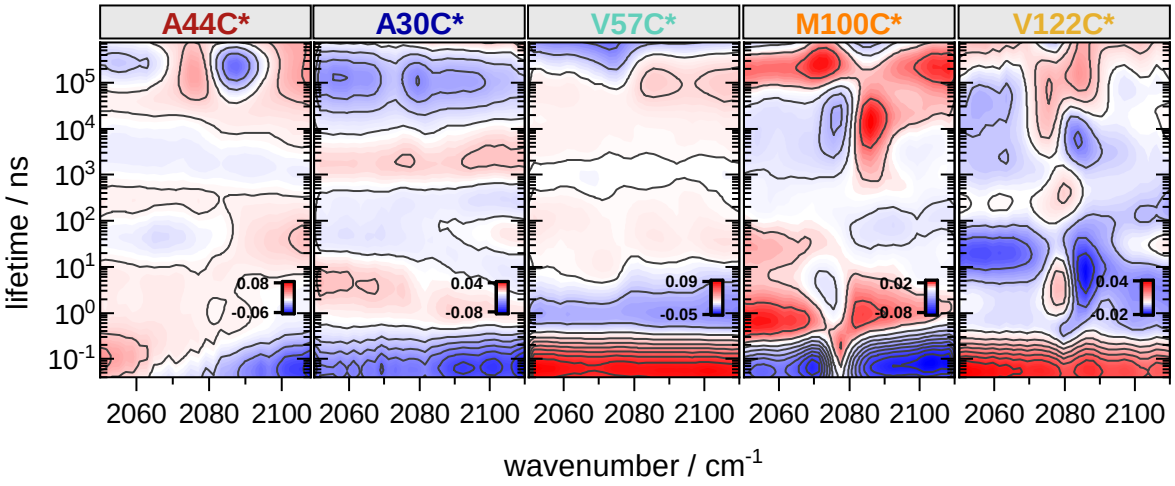

Figure F.27: *Overview of all LDMs in the SCN region for electronic delays without subtraction of a linear baseline between the first and last pixel for each time point. The corresponding LDMs after baseline subtraction are shown in figure 7.5 on page 107.*

F.2.10 LDMs of not-Standardized Data

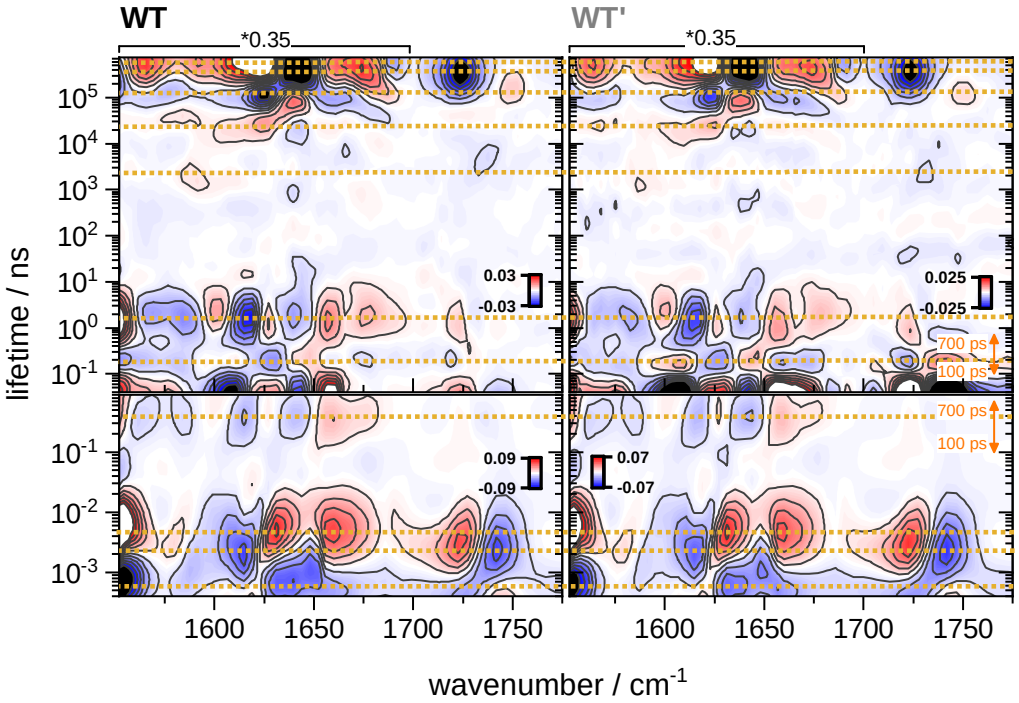

Figure F.28: *LDMs of not-standardized data for WT (left) and WT' (right) in the CC/CO region for mechanical (bottom) and electronic delays (top). All LDMs are plotted with 11 major and 5 minor contour levels. The corresponding L-curves are depicted in figure F.36. The orange arrows display the same time window. For better visualization the intensity of the amide I region in the electronic delay plots is scaled by a factor of 0.35. Yellow dashed lines at 600 fs, 2 ps, 5 ps, 390 ps (mechanical delays) / 180 ps, 2 ns, 2 µs, 24 µs, 130 µs, 390 µs, and 610 µs (electronic delays) highlight prominent features appearing in both samples.*

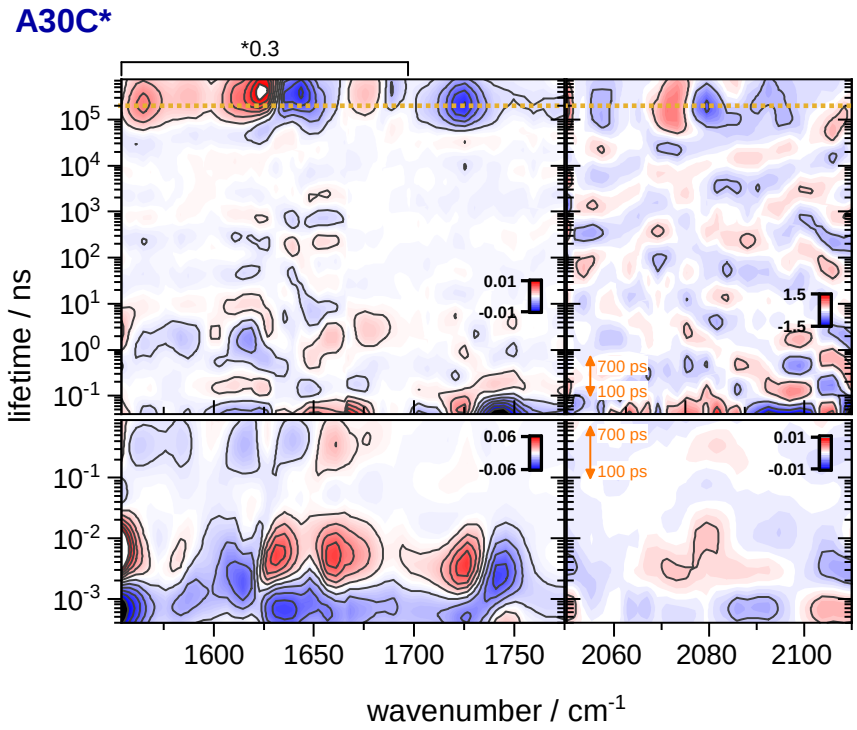

Figure F.29: *LDMs of not-standardized data for A30C* in the CC/CO (left) and SCN region (right) for mechanical (bottom) and electronic delays (top). All LDMs are plotted in the CC/CO region with 11 major and 5 minor contour levels and the SCN region with 5 major and 5 minor contour levels. In the SCN region a linear baseline was subtracted. The corresponding L-curves are depicted in figures F.36 and F.37. The orange arrows display the same time window. The intensity of the amide I region in the electronic delay plot is scaled by a factor of 0.3. The yellow dashed line at 200 µs highlights features that appear simultaneously with changes of the SCN signal.*

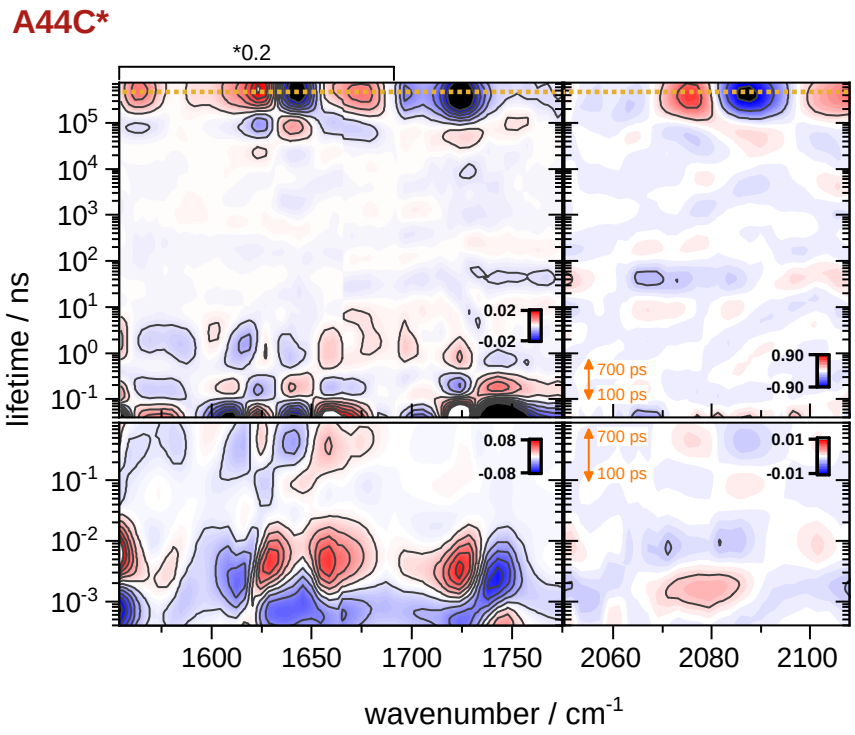

Figure F.30: *LDMs of not-standardized data for A44C* in the CC/CO (left) and SCN region (right) for mechanical (bottom) and electronic delays (top). All LDMs are plotted in the CC/CO region with 11 major and 5 minor contour levels and the SCN region with 5 major and 5 minor contour levels. In the SCN region a linear baseline was subtracted. The corresponding L-curves are depicted in figures F.36 and F.37. The orange arrows display the same time window. The intensity of the amide I region in the electronic delay plot is scaled by a factor of 0.2. The yellow dashed line at 450 µs highlights features that appear simultaneously with changes of the SCN signal.*

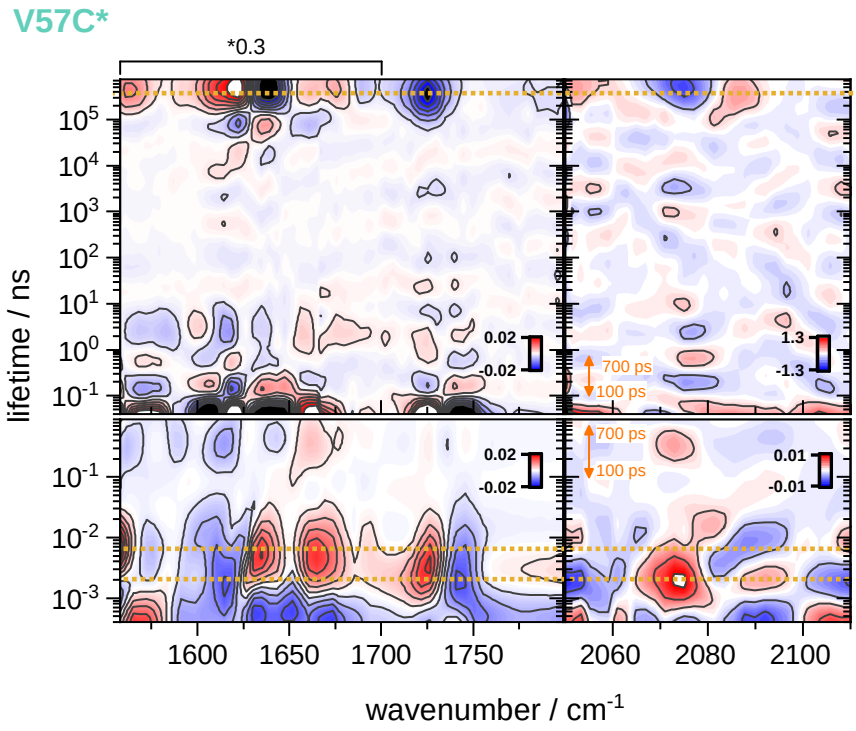

Figure F.31: *LDMs of not-standardized data for V57C* in the CC/CO (left) and SCN region (right) for mechanical (bottom) and electronic delays (top). All LDMs are plotted in the CC/CO region with 11 major and 5 minor contour levels and the SCN region with 5 major and 5 minor contour levels. In the SCN region a linear baseline was subtracted. The corresponding L-curves are depicted in figures F.36 and F.37. The orange arrows display the same time window. The intensity of the amide I region in the electronic delay plot is scaled by a factor of 0.3. The yellow dashed lines at 2 ps, 7 ps / 390 µs highlight features that appear simultaneously with changes of the SCN signal.*

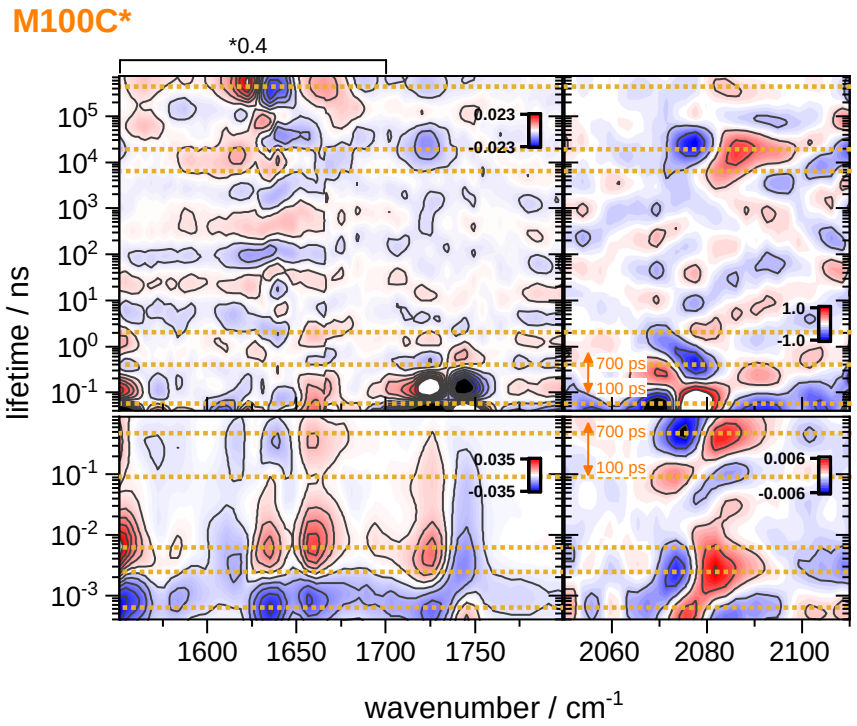

Figure F.32: *LDMs of not-standardized data for M100C* in the CC/CO (left) and SCN region (right) for mechanical (bottom) and electronic delays (top). All LDMs are plotted in the CC/CO region with 11 major and 5 minor contour levels and the SCN region with 5 major and 5 minor contour levels. In the SCN region a linear baseline was subtracted. The corresponding L-curves are depicted in figures F.36 and F.37. The orange arrows display the same time window. The intensity of the amide I region in the electronic delay plot is scaled by a factor of 0.4. The yellow dashed lines at 620 fs, 2 ps, 6 ps, 94 ps, 490 ps / 60 ps, 420 ps, 2 ns, 7 µs, 20 µs, and 440 µs highlight features that appear simultaneously with changes of the SCN signal.*

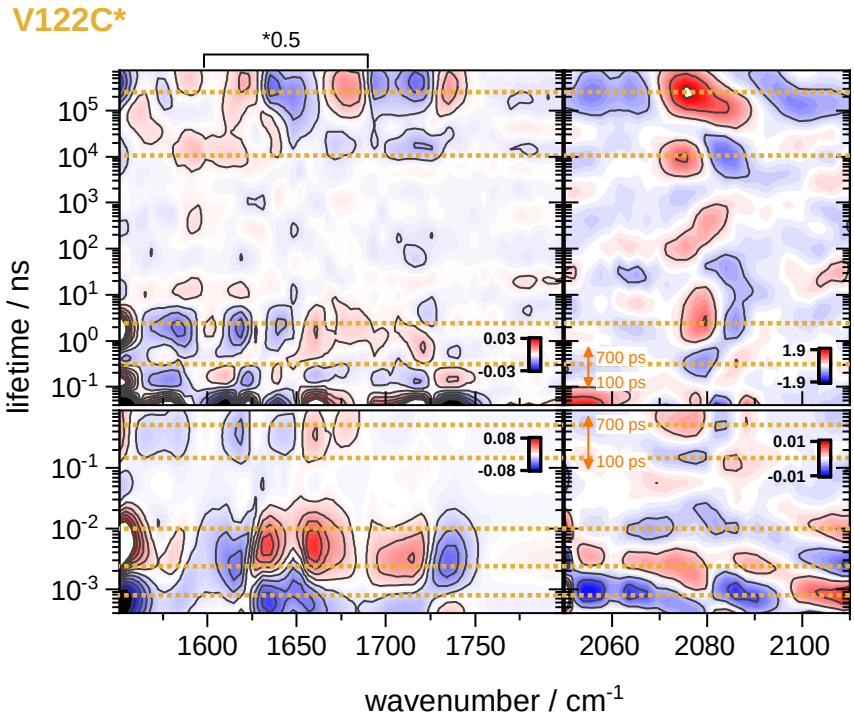

Figure F.33: *LDMs of not-standardized data for V122C* in the CC/CO (left) and SCN region (right) for mechanical (bottom) and electronic delays (top). All LDMs are plotted in the CC/CO region with 11 major and 5 minor contour levels and the SCN region with 5 major and 5 minor contour levels. In the SCN region a linear baseline was subtracted. The corresponding L-curves are depicted in figures F.36 and F.37. The orange arrows display the same time window. The intensity of the amide I region in the electronic delay plot is scaled by a factor of 0.5. The yellow dashed lines at 800 fs, 2 ps, 10 ps, 145 ps, 530 ps / 300 ps, 2 ns, 10 µs, and 270 µs highlight features that appear simultaneously with changes of the SCN signal.*

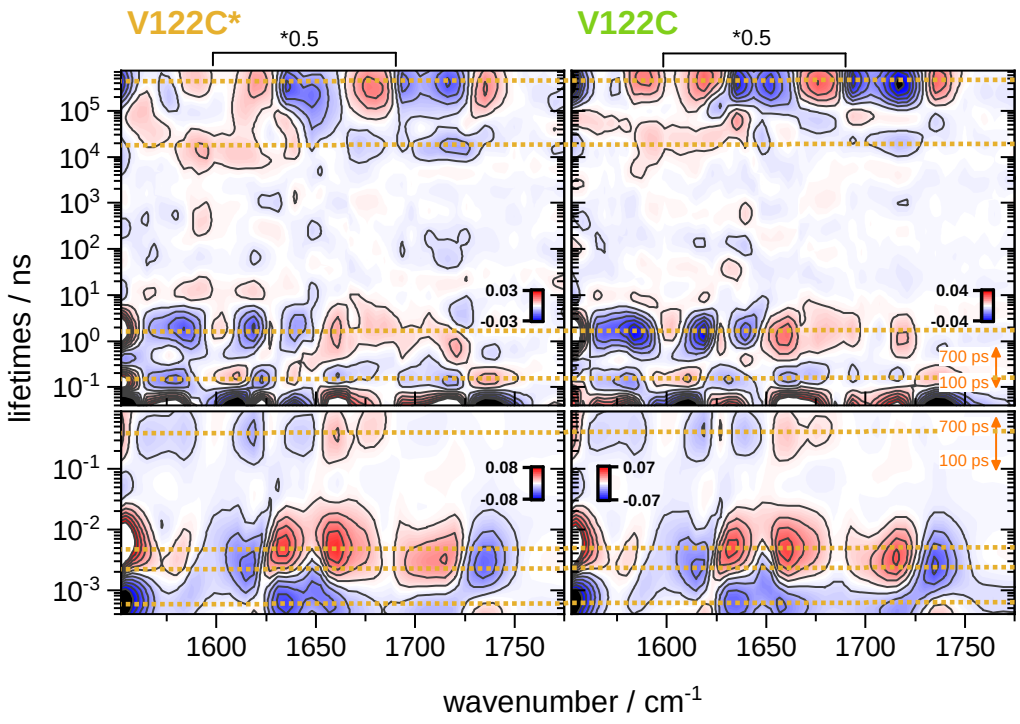

Figure F.34: *Comparison of the LDMs of not-standardized data in the CC/CO region (contour plots with 11 major and 5 minor levels) of V122C* and unlabeled V122C for mechanical (bottom) and electronic delays (top). The corresponding L-curves are depicted in figure F.36. The orange arrows display the same time window. The intensity of the amide I region in the electronic delay plot is scaled by a factor of 0.5. The yellow dashed lines at 650 fs, 2 ps, 5 ps, 410 ps / 160 ps, 2 ns, 19 µs, and 460 µs highlight prominent features.*

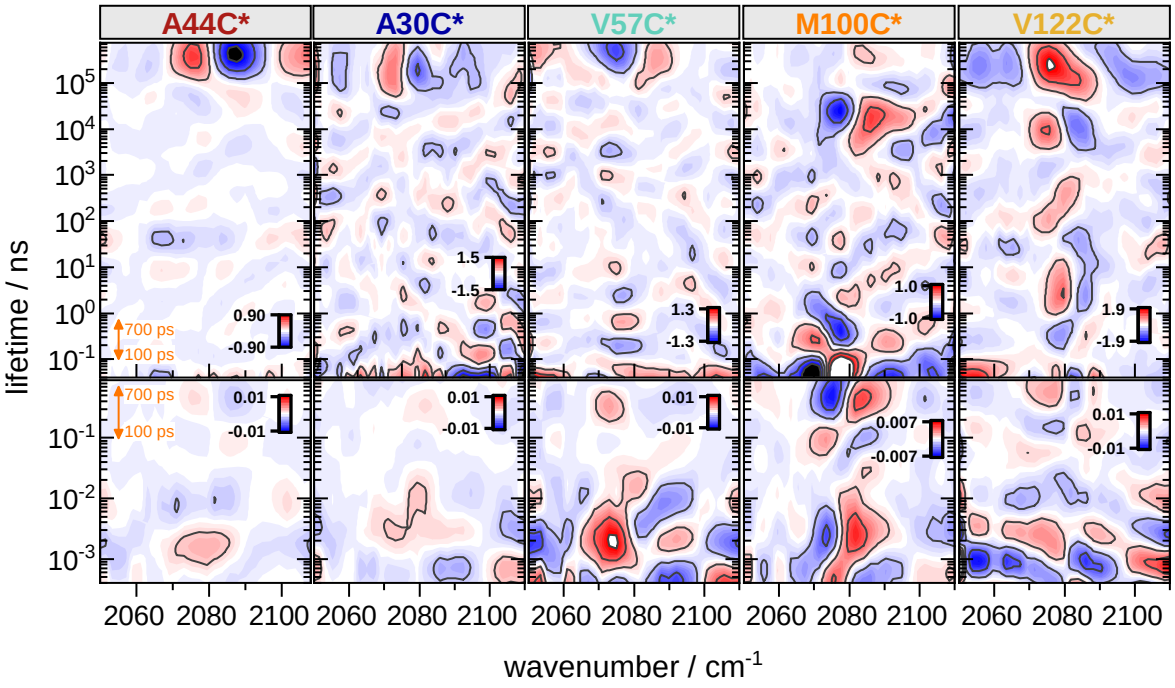

Figure F.35: *Overview of all LDMs of not-standardized data in the SCN region from time-resolved vis-pump-IR-probe measurements with mechanical (bottom) and electronic delays (top). The corresponding L-curves are depicted in figure F.37. The orange arrows display the same time window. A linear baseline between the first and last pixel of each mutant was subtracted for each time point before LDA for mechanical delays and after LDA for electronic delays.*

F.2.11 L-curves from Lifetime Density Analysis

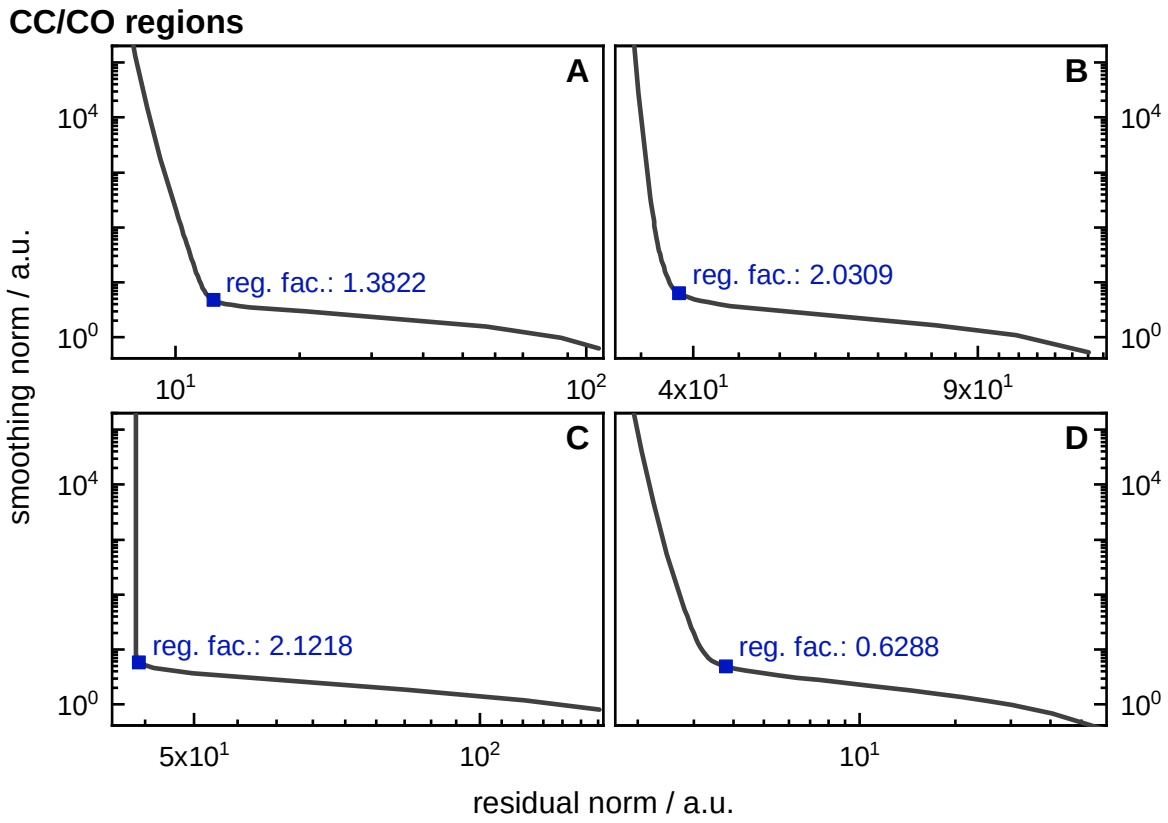

Figure F.36: *L-curves from LDA of the CC/CO regions for mechanical (top) and electronic delays (bottom) of standardized (left) and not-standardized data (right). The CC/CO regions of all investigated samples in D_2O for the respective delays were analyzed simultaneously resulting in one common L-curve. The blue squares mark the regularization factors of the LDMs that were selected. (A) CC/CO region for mechanical delays of standardized data. The corresponding LDMs are shown in figures 7.2, 7.6–7.11 and 7.13. (B) CC/CO region for mechanical delays of not-standardized data. The corresponding LDMs are shown in figures F.28–F.34. (C) CC/CO region for electronic delays of standardized data. The corresponding LDMs are shown in the same figures as for (A). (D) CC/CO region for electronic delays of not-standardized data. The corresponding LDMs are shown in the same figures as for (B).*

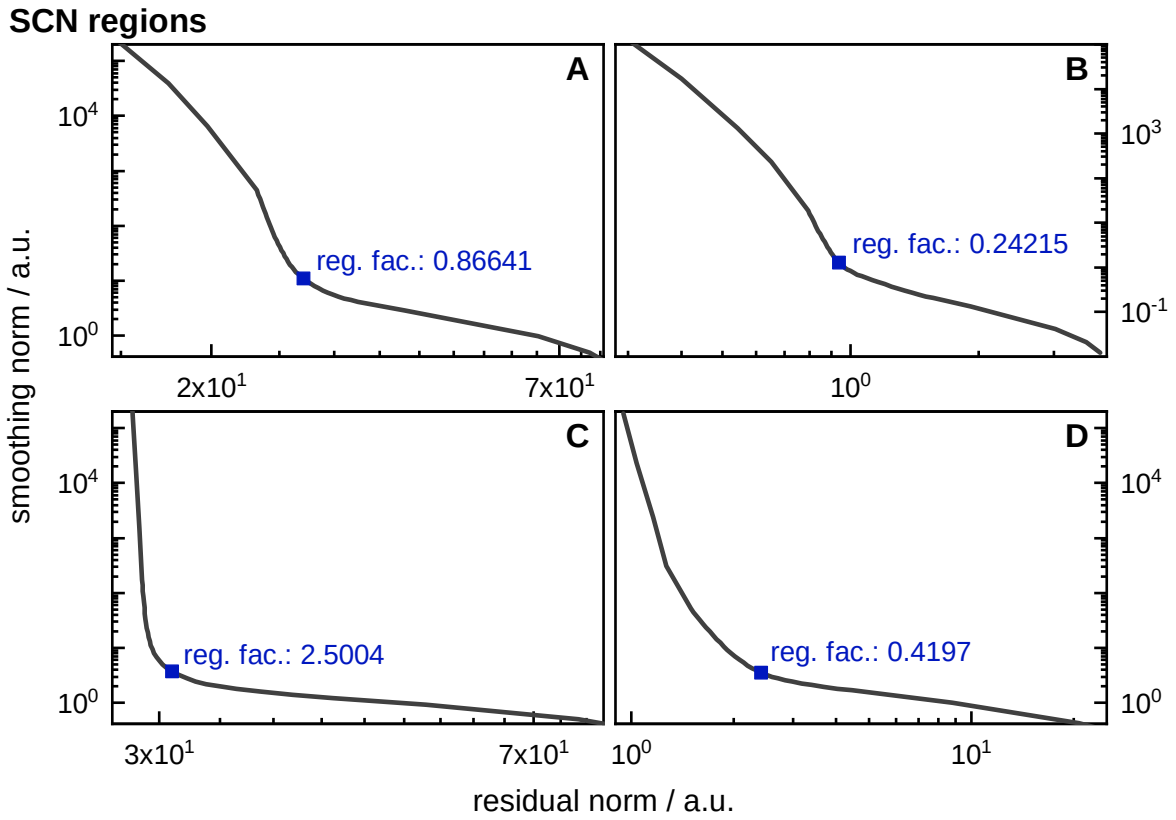

Figure F.37: *L-curves from LDA of the SCN regions for mechanical (top) and electronic delays (bottom) of standardized (left) and not-standardized data (right). The SCN regions of all investigated labeled mutants in D_2O for the respective delays were analyzed simultaneously resulting in one common L-curve. The blue squares mark the regularization factors of the LDMs that were selected. (A) SCN region for mechanical delays of standardized data. The corresponding LDMs are shown in figures 7.5–7.10. (B) SCN region for mechanical delays of not-standardized data. The corresponding LDMs are shown in figures F.29–F.33 and F.35. (C) SCN region for electronic delays of standardized data. The corresponding LDMs are shown in the same figures as for (A) and in figures 7.15, 7.16 and F.27. (D) SCN region for electronic delays of not-standardized data. The corresponding LDMs are shown in the same figures as for (B).*

F.3 Photocycle Dynamics in H_2O

F.3.1 Comparison LDMs of WT′ in H_2O and D_2O

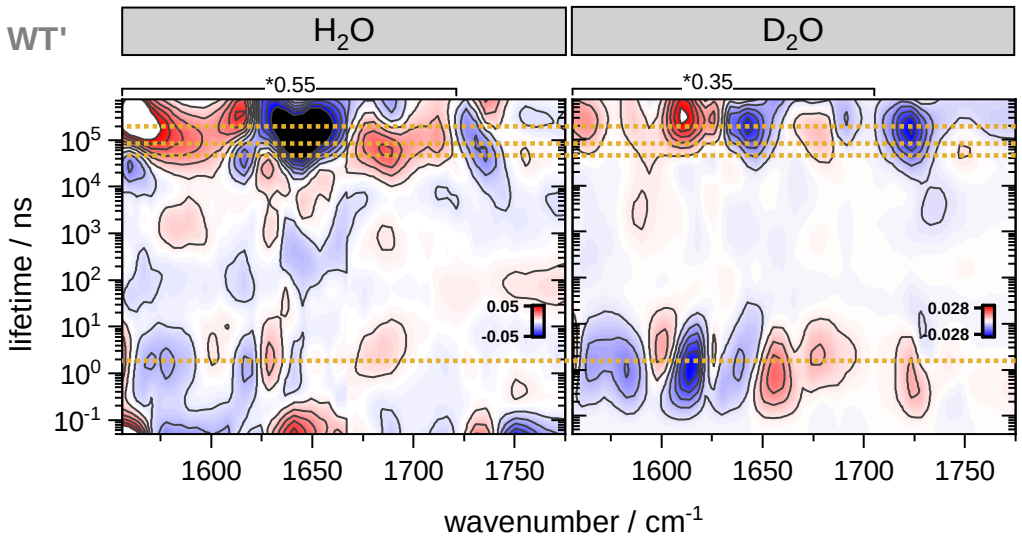

Figure F.38: *Comparison of the LDMs (standardized) for electronic delays of WT′ in the CC/CO region in H_2O (left) and D_2O (right). All LDMs are plotted with 11 major and 5 minor contour levels. The corresponding L-curves are depicted in figures F.36 and F.44. For better visualization the intensity of the amide I region is scaled by a factor of 0.55 in H_2O and 0.35 in D_2O. Yellow dashed lines at 2 ns, 45 µs, 85 µs, and 200 µs highlight prominent features in H_2O.*

F.3.2 Global Analysis of CC/CO Region

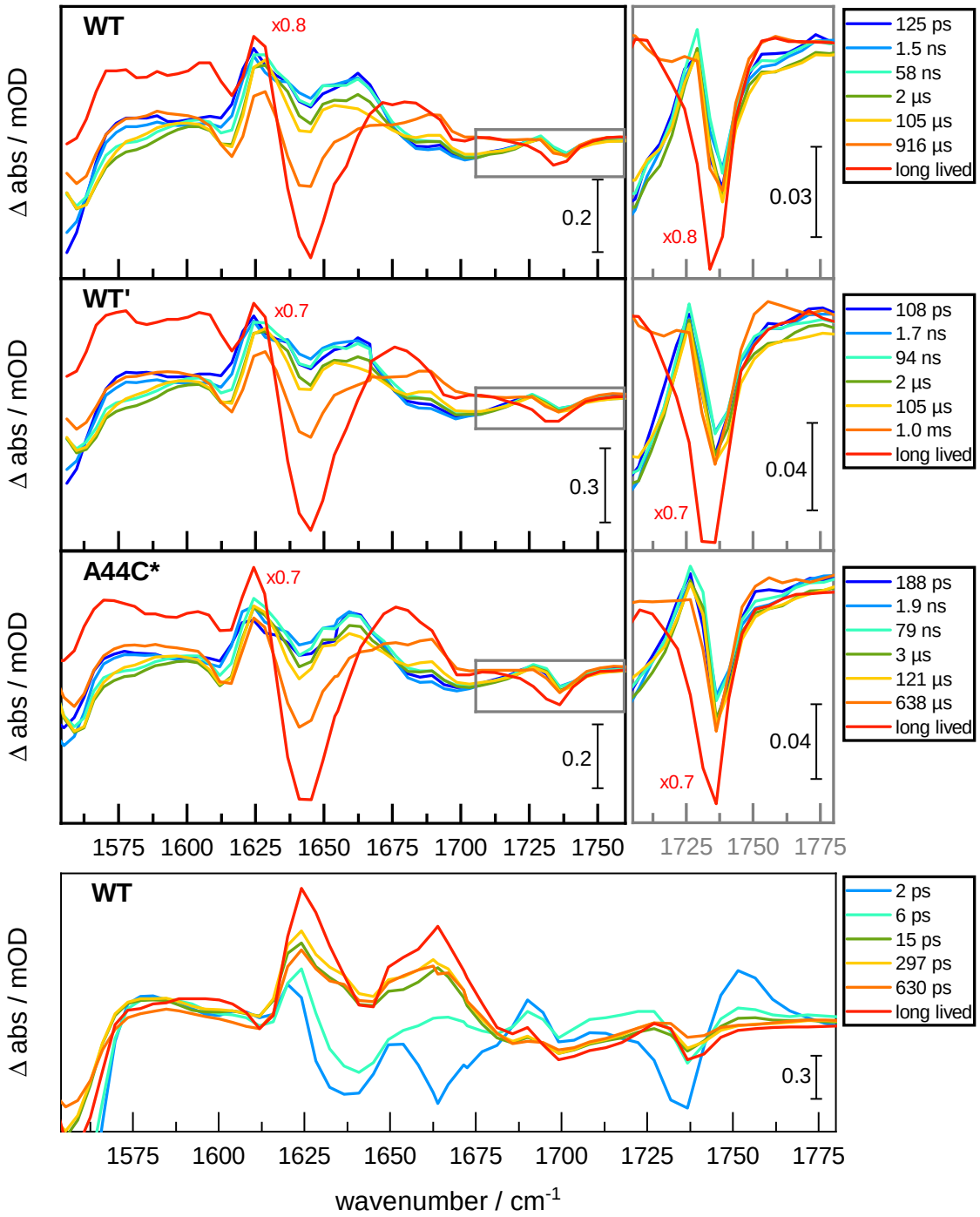

Figure F.39: *SADS obtained by global analysis of WT, WT', and A44C* in H_2O for electronic delays of the CC/CO region (top) and for mechanical delays of WT (bottom). For GA of the background corrected data a sequential model with 10 components was used. Here only components > 600 fs for mechanical delays and > 50 ps for electronic delays are shown. The long lived spectrum (red) was scaled by the factor given in the respective graph. In the right column for the electronic delays a zoom into the CO region of E46 is shown, indicated by a gray box in the graph of the complete spectral region on the left.*

F.3.3 Time Traces for pCA Protonation and E46 Deprotonation in H_2O and D_2O

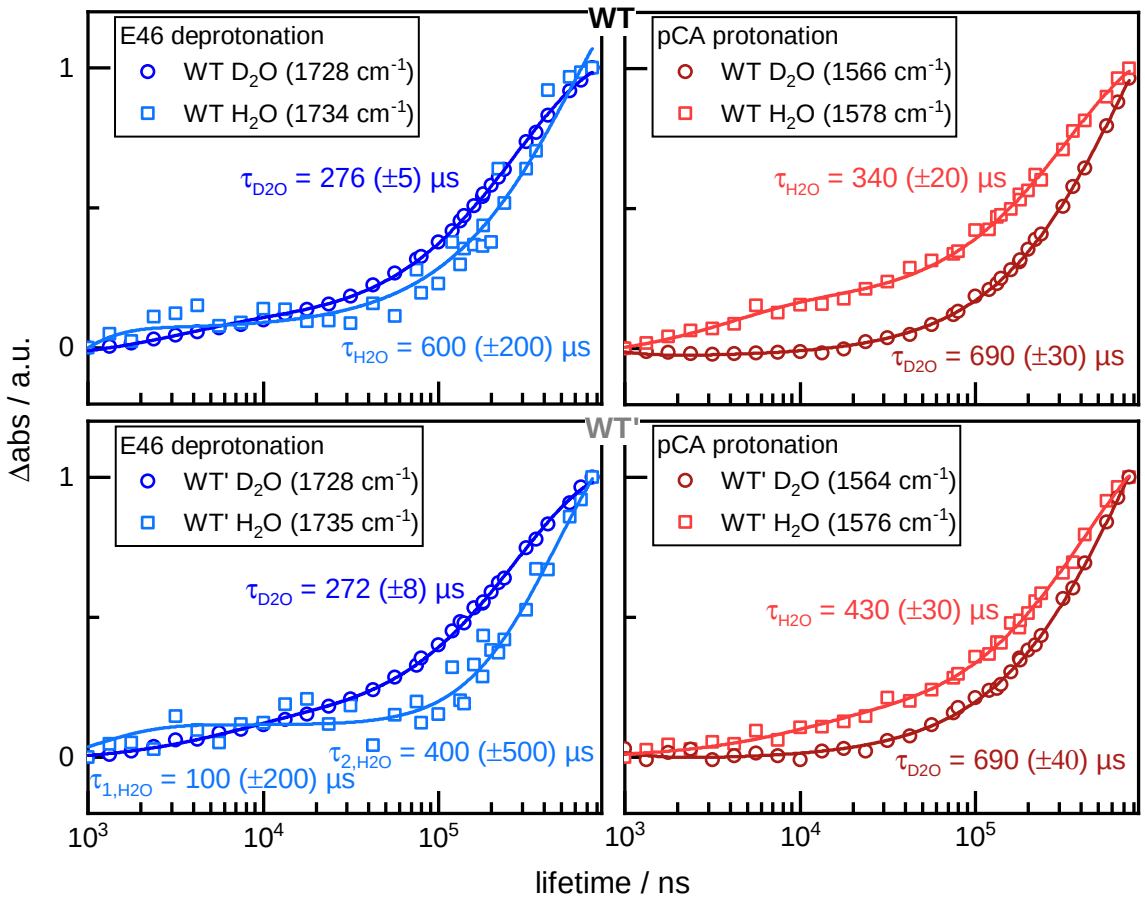

Figure F.40: *Normalized time traces for E46 deprotonation (left) and chromophore protonation (right) in D_2O and H_2O for the raw data of WT (top) and WT′ (bottom) between 1 µs and 750 µs. All data were fitted between 100 ns and 750 µs with two exponential functions (shown as solid lines), but only lifetimes > 10 µs are given in the figure, since the faster ones do most likely not contribute to the (de)protonation processes investigated here. For the biexponential fit the ExpDec2 function of OriginPro 2018G was used.*

F.3.4 Comparison of Raw and Denoised SCN Data

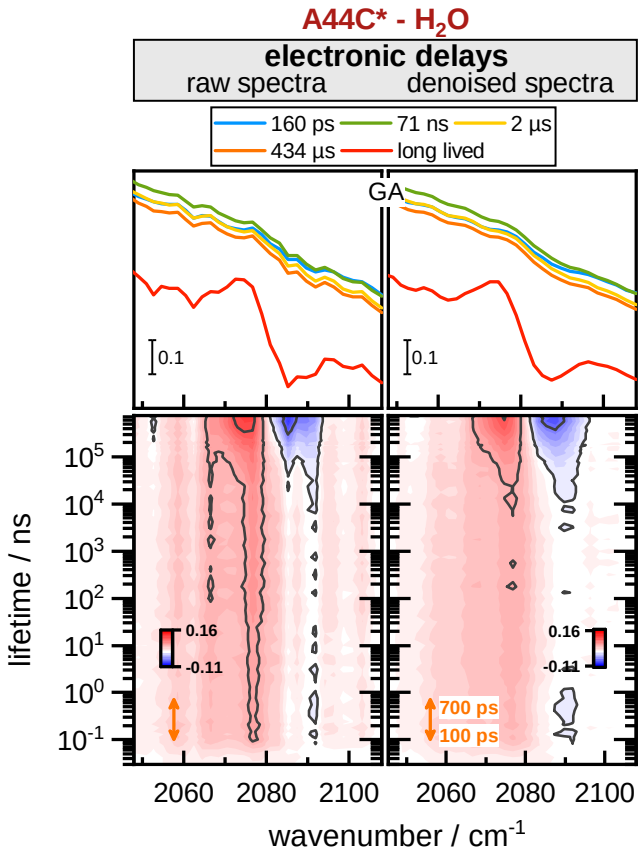

Figure F.41: *Comparison of raw and denoised SCN data of A44C* in H_2O for electronic delays. Global analysis spectra (top) and contour plots (bottom) of the raw (left) and denoised SCN data (right) for the electronic delays are depicted. For the contour plots a linear baseline was subtracted. For the GA spectra only components > 50 ps are shown. The lifetimes obtained by global analysis are the same for the raw and denoised data.*

F.3.5 LDMs of not-Standardized Data

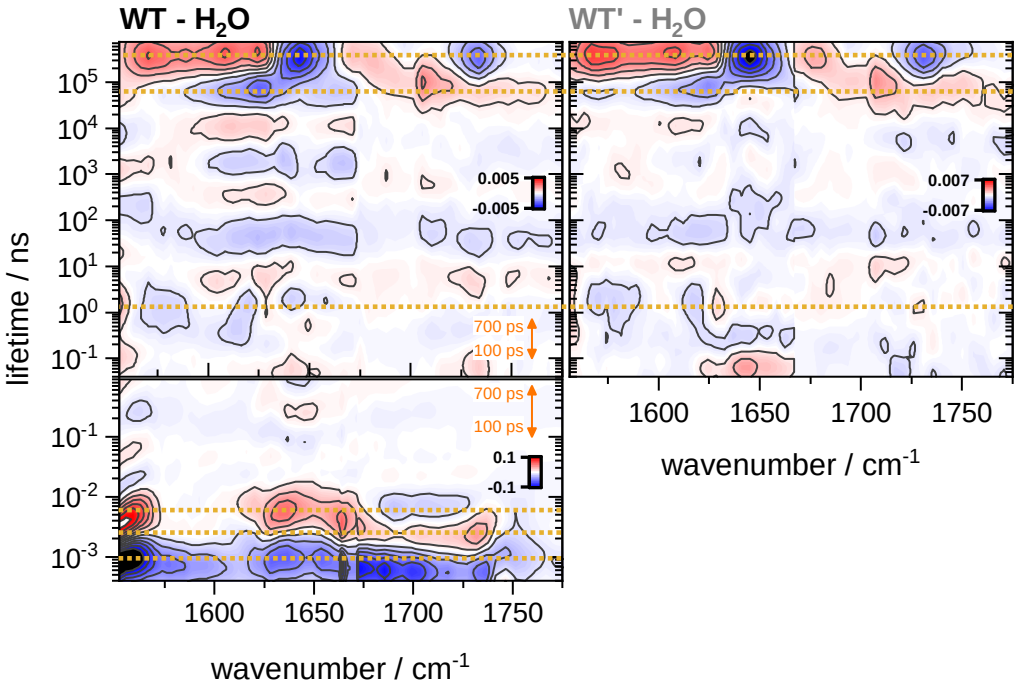

Figure F.42: *LDMs of not-standardized data for WT (left) and WT' (right) in the CC/CO region for mechanical (bottom, only WT) and electronic delays (top). All LDMs are plotted with 11 major and 5 minor contour levels. The corresponding L-curves are depicted in figure F.44. The orange arrows display the same time window. Yellow dashed lines at 930 fs, 3 ps, 6 ps (mechanical delays) / 1 ns, 60 µs, and 390 µs (electronic delays) highlight prominent features.*

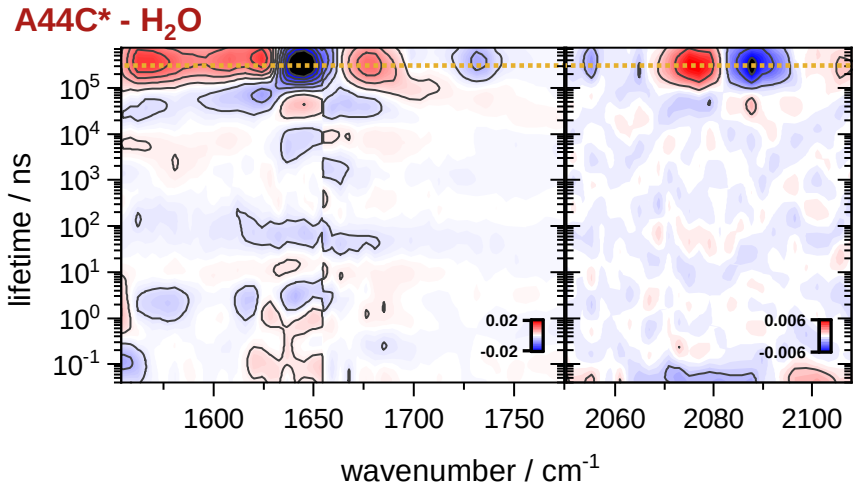

Figure F.43: *LDMs of not-standardized data for A44C* in the CC/CO (left) and SCN region (right) for electronic delays. The LDMs are plotted in the CC/CO region with 11 major levels and 5 minor contour levels and the SCN region with 5 major and 5 minor contour levels. In the SCN region a linear baseline was subtracted. The corresponding L-curves are depicted in figure F.44. The yellow dashed line at 320 µs highlights features that appear simultaneously with changes of the SCN signal.*

F.3.6 L-curves from Lifetime Density Analysis

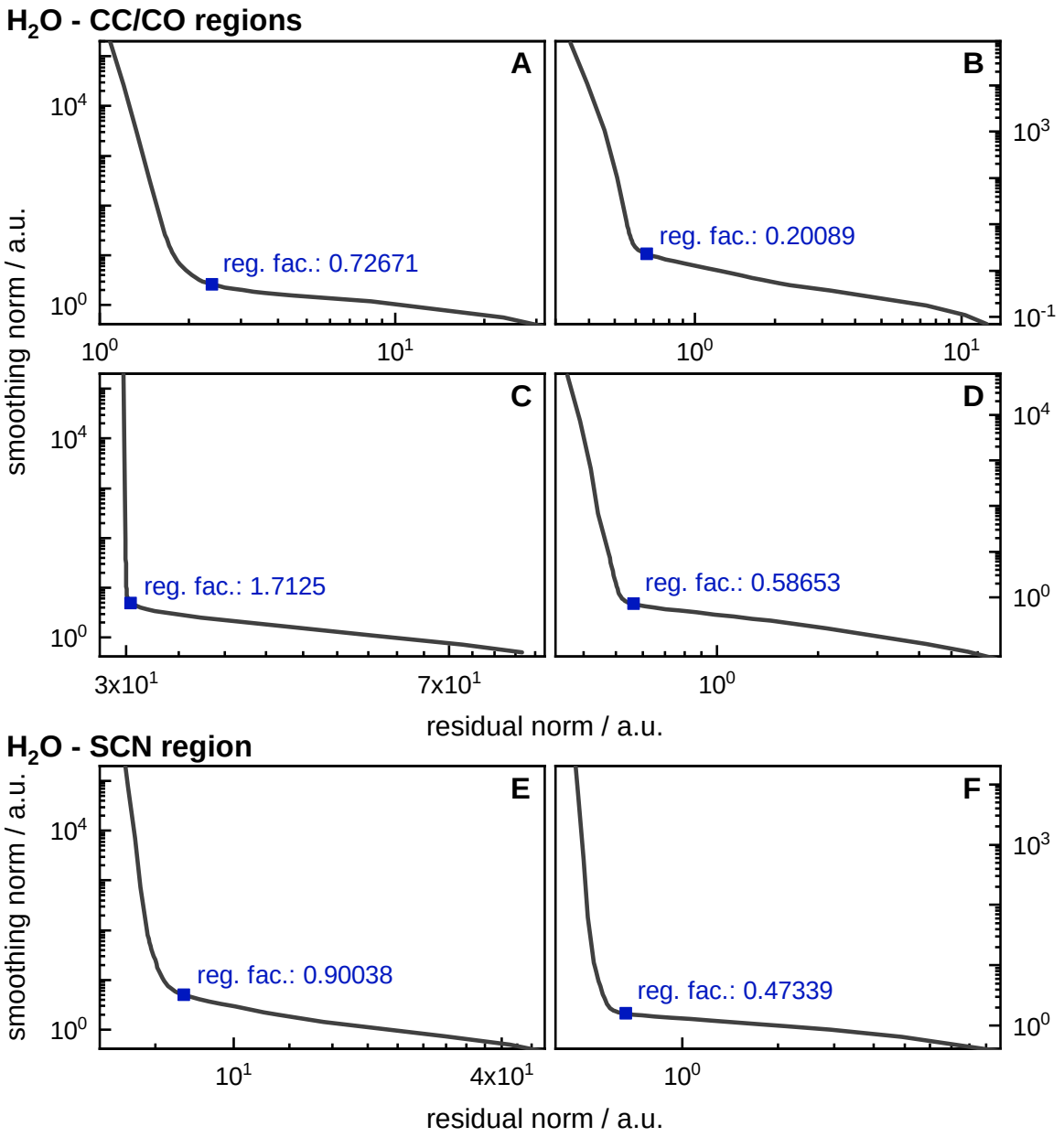

Figure F.44: *L-curves from LDA of the CC/CO regions for mechanical (top) and electronic delays (middle) and the SCN region of electronic delays (bottom) of standardized (left) and not-standardized data (right) in H_2O. The CC/CO regions of WT, WT', and A44C* for electronic delays in H_2O were analyzed simultaneously resulting in one common L-curve. The CC/CO region of WT for mechanical delays and the SCN region of A44C* for electronic delays in H_2O were analyzed separately. The blue squares mark the regularization factors of the LDMs that were selected. (A) CC/CO region of WT for mechanical delays of standardized data. The corresponding LDM is shown in figure 7.13. (B) CC/CO region of WT for mechanical delays of not-standardized data. The corresponding LDM is shown in figure F.42. (C) CC/CO region of WT, WT', and A44C* for electronic delays of standardized data. The corresponding LDMs are shown in figures 7.13, 7.14 and F.38. (D) CC/CO region of WT, WT', and A44C* for electronic delays of not-standardized data. The corresponding LDMs are shown in figures F.42 and F.43. (E) SCN region of A44C* for electronic delays of standardized data. The corresponding LDM is shown in figures 7.14 and 7.15. (F) SCN region of A44C* for electronic delays of not-standardized data. The corresponding LDM is shown in figure F.43.*

F.4 Photocycle Dynamics with Chopper Divider Routine

F.4.1 L-curves from Lifetime Density Analysis

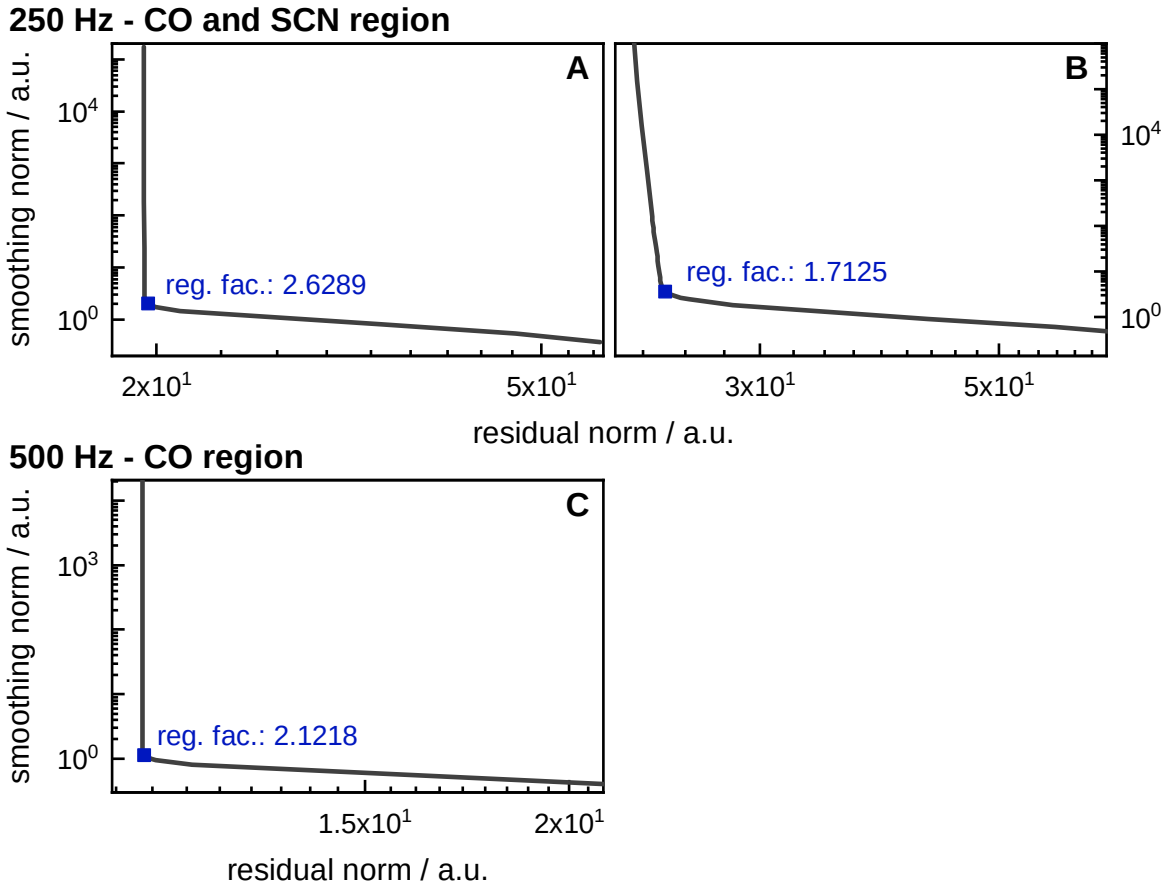

Figure F.45: *L-curves from LDA of the CO region of WT with the chopper divider routine at 250 Hz (A) and at 500 Hz (C) and SCN region of A44C* at 250 Hz and 500 Hz (B) for electronic delays of standardized data. The three bins of the chopper divider routine for the CO region of WT were analyzed simultaneously resulting in one common L-curve. For the SCN region of A44C* the three bins of the chopper divider routine were analyzed simultaneously with the SCN region at 500 Hz resulting in in one common L-curve as well. The CO region of WT at 500 Hz was analyzed separately. The blue squares mark the regularization factors of the LDMs that were selected. The three L-curves correspond to the LDMs shown in figure 7.17.*

G Time-resolved Step-scan FTIR Experiments

G.1 Single Spectra

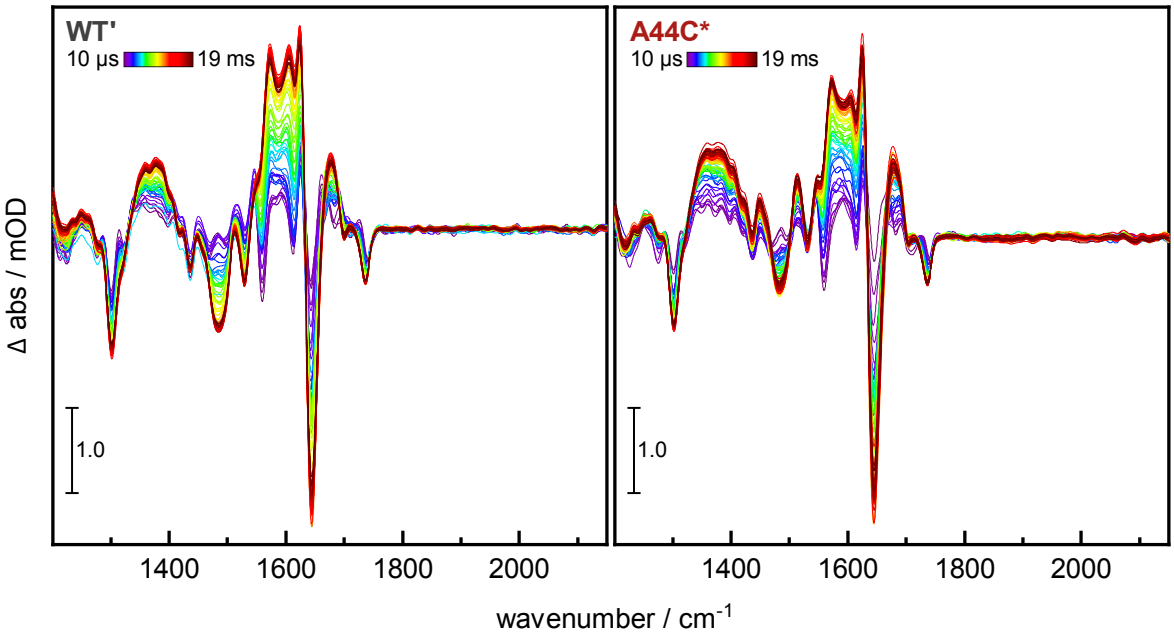

Figure G.1: *Single spectra from time-resolved step-scan FTIR measurements for WT′ (left) and A44C* (right).*

G.2 LDA of Step-scan FTIR Data

G.2.1 LDMs of Standardized Data

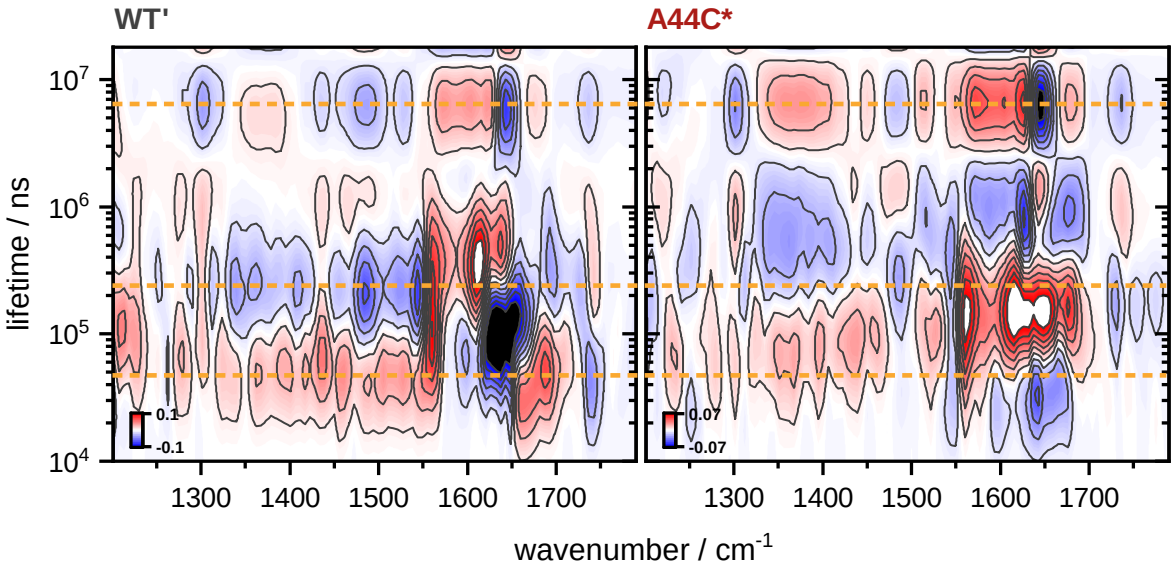

Figure G.2: *LDMs of standardized data for WT′ (left) and A44C* (right) in the CC/CO region from time-resolved step-scan FTIR measurements. The LDMs are plotted with 11 major and 5 minor contour levels. The corresponding L-curve is depicted in figure G.3. The yellow dashed lines at 50 µs, 240 µs, and 6 ms highlight prominent features.*

G.2.2 L-curves from Lifetime Density Analysis

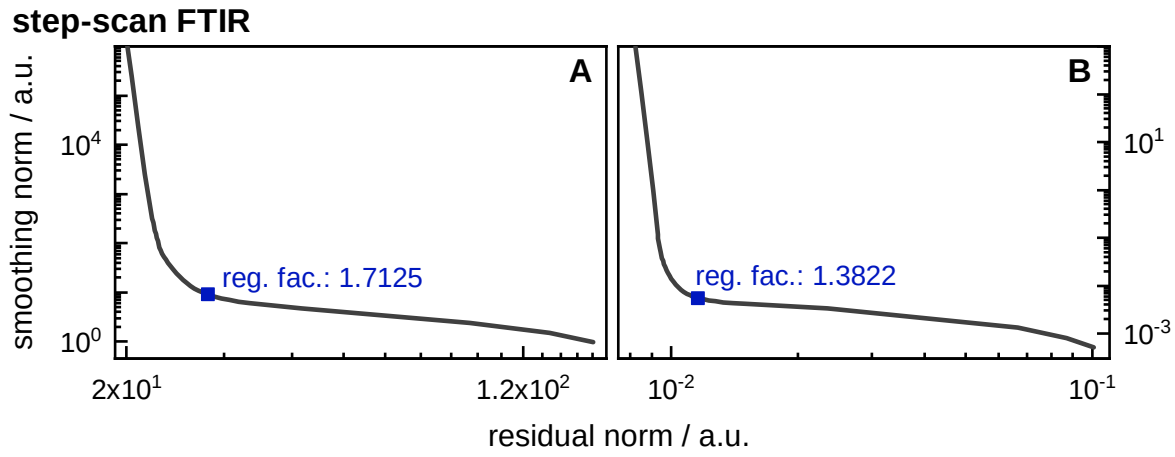

Figure G.3: *L-curves from LDA of step-scan FTIR measurements of WT′ and A44C* for standardized (left) and not-standardized data (right). The entire spectral regions of WT′ and A44C* were analyzed simultaneously resulting in one common L-curve. The blue squares mark the regularization factors of the LDMs that were selected. (A) L-curve of standardized data corresponding to LDMs in figure G.2. (B) L-curve of not-standardized data corresponding to LDMs in figure 8.1.*

Bibliography

[1] I. R. Kleckner and M. P. Foster. An introduction to NMR-based approaches for measuring protein dynamics, *Biochimica et Biophysica Acta* **1814**, no. 8 (2011), pp. 942–968.

[2] D. Ban, C. A. Smith, B. L. de Groot, C. Griesinger, and D. Lee. Recent advances in measuring the kinetics of biomolecules by NMR relaxation dispersion spectroscopy, *Archives of Biochemistry and Biophysics* **628** (2017), pp. 81–91.

[3] M. A. van der Horst and K. J. Hellingwerf. Photoreceptor proteins, "star actors of modern times": a review of the functional dynamics in the structure of representative members of six different photoreceptor families, *Accounts of Chemical Research* **37**, no. 1 (2004), pp. 13–20.

[4] T. E. Meyer, E. Yakali, M. A. Cusanovich, and G. Tollin. Properties of a Water-Soluble, Yellow Protein Isolated from a Halophilic Phototrophic Bacterium That Has Photochemical Activity Analogous to Sensory Rhodopsin, *Biochemistry* **26**, no. 2 (1987), pp. 418–423.

[5] W. D. Hoff, I. H. van Stokkum, H. J. van Ramesdonk, M. E. van Brederode, A. M. Brouwer, J. C. Fitch, T. E. Meyer, R. van Grondelle, and K. J. Hellingwerf. Measurement and global analysis of the absorbance changes in the photocycle of the photoactive yellow protein from Ectothiorhodospira halophila, *Biophysical Journal* **67** (1994), pp. 1691–1705.

[6] T. E. Meyer, M. A. Cusanovich, and G. Tollin. Transient Proton Uptake and Release Is Associated with the Photocycle of the Photoactive Yellow Protein from the Purple Phototrophic Bacterium Ectothiorhodospira halophila, *Archives of Biochemistry and Biophysics* **306**, no. 2 (1993), pp. 515–517.

[7] M. E. van Brederode, W. D. Hoff, I. H. van Stokkum, M. L. Groot, and K. J. Hellingwerf. Protein folding thermodynamics applied to the photocycle of the photoactive yellow protein, *Biophysical Journal* **71** (1996), pp. 365–380.

[8] L. Ujj, S. Devanathan, T. E. Meyer, M. Cusanovich, G. Tollin, and G. H. Atkinson. New Photocycle Intermediates in the Photoactive Yellow Protein from Ectothiorhodospira halophila: Picosecond Transient Absorption Spectroscopy, *Biophysical Journal* **75** (1998), pp. 406–412.

[9] S. Devanathan, A. Pacheco, L. Ujj, M. Cusanovich, G. Tollin, S. Lin, and N. Woodbury. Femtosecond Spectroscopic Observations of Initial Intermediates in the Photocycle of the Photoactive Yellow Protein from Ectothiorhodospira halophila, *Biophysical Journal* **77** (1999), pp. 1017–1023.

[10] R. Brudler, R. Rammelsberg, T. T. Woo, E. D. Getzoff, and K. Gerwert. Structure of the I1 early intermediate of photoactive yellow protein by FTIR spectroscopy, *Nature Structural & Molecular Biology* **8**, no. 3 (2001), pp. 265–270.

[11] A. Xie, L. Kelemen, J. Hendriks, B. J. White, K. J. Hellingwerf, and W. D. Hoff. Formation of a new buried charge drives a large-amplitude protein quake in photoreceptor activation, *Biochemistry* **40**, no. 6 (2001), pp. 1510–1517.

[12] M. L. Groot, L. J. G. W. van Wilderen, D. S. Larsen, M. A. van der Horst, I. H. M. van Stokkum, K. J. Hellingwerf, and R. van Grondelle. Initial steps of signal generation in photoactive yellow protein revealed with femtosecond mid-infrared spectroscopy, *Biochemistry* **42**, no. 34 (2003), pp. 10054–10059.

[13] K. Heyne, O. F. Mohammed, A. Usman, J. Dreyer, E. T. J. Nibbering, and M. A. Cusanovich. Structural Evolution of the Chromophore in the Primary Stages of Trans/Cis Isomerization in Photoactive Yellow Protein, *J. Am. Chem. Soc.* **127**, no. 51 (2005), pp. 18100–18106.

[14] L. J. G. W. van Wilderen, M. A. van der Horst, I. H. M. van Stokkum, K. J. Hellingwerf, R. van Grondelle, and M. L. Groot. Ultrafast infrared spectroscopy reveals a key step for successful entry into the photocycle for photoactive yellow protein, *Proc. Natl. Acad. Sci. USA* **103**, no. 41 (2006), pp. 15050–15055.

[15] V. A. Lorenz-Fonfria. Infrared Difference Spectroscopy of Proteins: From Bands to Bonds, *Chem. Rev.* **120**, no. 7 (2020), pp. 3466–3576.

[16] J. Ma, I. M. Pazos, W. Zhang, R. M. Culik, and F. Gai. Site-specific infrared probes of proteins, *Annu. Rev. Phys. Chem.* **66** (2015), pp. 357–377.

[17] R. Adhikary, J. Zimmermann, and F. E. Romesberg. Transparent Window Vibrational Probes for the Characterization of Proteins With High Structural and Temporal Resolution, *Chem. Rev.* **117**, no. 3 (2017), pp. 1927–1969.

[18] H. Kim and M. Cho. Infrared probes for studying the structure and dynamics of biomolecules, *Chem. Rev.* **113**, no. 8 (2013), pp. 5817–5847.

[19] J. D. Slocum and L. J. Webb. Measuring Electric Fields in Biological Matter Using the Vibrational Stark Effect of Nitrile Probes, *Annu. Rev. Phys. Chem.* **69** (2018), pp. 253–271.

[20] K. J. Hellingwerf, J. Hendriks, M. van der Horst, A. Haker, W. Crielaard, and T. Gensch. "The family of photoactive yellow proteins, the xanthopsins: from structure and mechanism of photoactivation to biological function", *Photoreceptors and Light Signalling*. Ed. by A. Batschauer. Royal Society of Chemistry, 2003.

[21] Y. Degani and A. Patchornik. Cyanylation of sulfhydryl groups by 2-nitro-5-thiocyanobenzoic acid. High-yield modification and cleavage of peptides at cysteine residues, *Biochemistry* **13**, no. 1 (1974), pp. 1–11.

[22] A. T. Fafarman, L. J. Webb, J. I. Chuang, and S. G. Boxer. Site-specific conversion of cysteine thiols into thiocyanate creates an IR probe for electric fields in proteins, *J. Am. Chem. Soc.* **128**, no. 41 (2006), pp. 13356–13357.

[23] M. Maienschein-Cline and C. Londergan. The CN stretching band of aliphatic thiocyanate is sensitive to solvent dynamics and specific solvation, *J. Phys. Chem. A* **111**, no. 40 (2007), pp. 10020–10025.

[24] L. J. G. W. van Wilderen, D. Kern-Michler, H. M. Müller-Werkmeister, and J. Bredenbeck. Vibrational dynamics and solvatochromism of the label SCN in various solvents and hemoglobin by time dependent IR and 2D-IR spectroscopy, *Phys. Chem. Chem. Phys.* **16**, no. 36 (2014), pp. 19643–19653.

[25] L. J. G. W. van Wilderen, D. Kern-Michler, H. M. Müller-Werkmeister, and J. Bredenbeck. Correction: Vibrational dynamics and solvatochromism of the label SCN in various solvents and hemoglobin by time dependent IR and 2D-IR spectroscopy, *Phys. Chem. Chem. Phys.* **19**, no. 14 (2017), pp. 9676–9678.

[26] N. B. Colthup. *Introduction to Infrared and Raman Spectroscopy*. 2nd ed. Elsevier Science, 2014.

[27] P. Larkin. *IR and Raman Spectroscopy: Principles and Spectral Interpretation*. 1st ed. Elsevier, 2011.

[28] W. Mäntele and E. Deniz. UV-VIS absorption spectroscopy: Lambert-Beer reloaded, *Spectrochimica Acta Part A* **173** (2017), pp. 965–968.

[29] A. H. Zewail. Laser Femtochemistry, *Science* **242** (1988), pp. 1645–1653.

[30] S. Mukamel. Femtosecond Optical Spectroscopy: A Direct Look at Elementary Chemical Events, *Annu. Rev. Phys. Chem.* **41** (1990), pp. 647–681.

[31] H. Abramczyk. *Introduction to Laser Spectroscopy*. 1st ed. Elsevier Science, 2005.

[32] T. Karabencheva-Christova, ed. *Dynamics of Proteins and Nucleic Acids*. Vol. 92. Advances in Protein Chemistry and Structural Biology. Academic Press, 2013.

[33] P. R. Markwick, T. Malliavin, and M. Nilges. Structural biology by NMR: structure, dynamics, and interactions. *PLoS Comput. Biol.* **4**, no. 9 (2008), e1000168.

[34] H. Ode, M. Nakashima, S. Kitamura, W. Sugiura, and H. Sato. Molecular dynamics simulation in virus research, *Frontiers in Microbiology* **3**, no. 258 (2012), pp. 1–9.

[35] R. Berera, R. van Grondelle, and J. T. M. Kennis. Ultrafast transient absorption spectroscopy: principles and application to photosynthetic systems, *Photosynthesis Research* **101**, no. 2-3 (2009), pp. 105–118.

[36] E. T. J. Nibbering, H. Fidder, and E. Pines. Ultrafast chemistry: using time-resolved vibrational spectroscopy for interrogation of structural dynamics, *Annual review of physical chemistry* **56** (2005), pp. 337–367.

[37] K. T. Munson, E. R. Kennehan, and J. B. Asbury. Structural origins of the electronic properties of materials via time-resolved infrared spectroscopy, *Journal of Materials Chemistry C* **7**, no. 20 (2019), pp. 5889–5909.

[38] W. Uhmann, A. Becker, C. Taran, and F. Siebert. Time-Resolved FT-IR Absorption Spectroscopy Using a Step-Scan Interferometer, *Applied Spectroscopy* **45**, no. 3 (1991), pp. 390–397.

[39] R. A. Palmer, J. L. Chao, R. M. Dittmar, V. G. Gregoriou, and S. E. Plunkett. Investigation of Time-Dependent Phenomena by Use of Step-Scan FT-IR, *Applied Spectroscopy* no. 47 (1993), pp. 1297–1310.

[40] J. Bredenbeck, J. Helbing, and P. Hamm. Continuous scanning from picoseconds to microseconds in time resolved linear and nonlinear spectroscopy, *Rev. Sci. Instr.* **75**, no. 11 (2004), pp. 4462–4466.

[41] J. P. Kraack. Ultrafast structural molecular dynamics investigated with 2D infrared spectroscopy methods, *Topics in Current Chemistry* **375**, no. 86 (2017), pp. 1–93.

[42] J. M. Anna, C. R. Baiz, M. R. Ross, R. McCanne, and K. J. Kubarych. Ultrafast equilibrium and non-equilibrium chemical reaction dynamics probed with multi-dimensional infrared spectroscopy, *International Reviews in Physical Chemistry* **31**, no. 3 (2012), pp. 367–419.

[43] D. Czurlok, J. Gleim, J. Lindner, and P. Vöhringer. Vibrational Energy Relaxation of Thiocyanate Ions in Liquid-to-Supercritical Light and Heavy Water. A Fermi's Golden Rule Analysis, *J. Phys. Chem. Lett.* **5**, no. 19 (2014), pp. 3373–3379.

[44] S. A. Egorov and J. L. Skinner. A theory of vibrational energy relaxation in liquids, *J. Chem. Phys.* **105**, no. 16 (1996), pp. 7047–7058.

[45] J. L. Skinner. Vibrational energy relaxation of small molecules and ions in liquids, *Theoretical Chemistry Accounts* **128**, no. 2 (2011), pp. 147–155.

[46] K. J. Hellingwerf, J. Hendriks, and T. Gensch. Photoactive Yellow Protein, A New Type of Photoreceptor Protein: Will This "Yellow Lab" Bring Us Where We Want to Go?, *J. Phys. Chem. A* **107**, no. 8 (2003), pp. 1082–1094.

[47] M. Schmidt. A short history of structure based research on the photocycle of photoactive yellow protein, *Structural Dynamics* **4**, no. 3 (2017), p. 032201.

[48] W. W. Sprenger, W. D. Hoff, J. P. Armitage, and K. J. Hellingwerf. The eubacterium Ectothiorhodospira halophila is negatively phototactic, with a wavelength dependence that fits the absorption spectrum of the photoactive yellow protein, *Journal of Bacteriology* **175**, no. 10 (1993), pp. 3096–3104.

[49] M. A. van der Horst, T. P. Stalcup, S. Kaledhonkar, M. Kumauchi, M. Hara, A. Xie, K. J. Hellingwerf, and W. D. Hoff. Locked chromophore analogs reveal that photoactive yellow protein regulates biofilm formation in the deep sea bacterium Idiomarina loihiensis, *J. Am. Chem. Soc.* **131**, no. 47 (2009), pp. 17443–17451.

[50] W. R. Briggs and J. L. Spudich. *Handbook of Photosensory Receptors*. Wiley, 2005.

[51] E. D. Getzoff, K. N. Gutwin, and U. K. Genick. Anticipatory active-site motions and chromophore distortion prime photoreceptor PYP for light activation, *Nature Structural & Molecular Biology* **10**, no. 8 (2003), pp. 663–668.

[52] J. A. Kyndt, T. E. Meyer, M. A. Cusanovich, and J. J. van Beeumen. Characterization of a bacterial tyrosine ammonia lyase, a biosynthetic enzyme for the photoactive yellow protein, *FEBS Letters* **512**, no. 1-3 (2002), pp. 240–244.

[53] J. A. Kyndt, F. Vanrobaeys, J. C. Fitch, B. V. Devreese, T. E. Meyer, M. A. Cusanovich, and J. J. van Beeumen. Heterologous Production of Halorhodospira halophila Holo-Photoactive Yellow Protein through Tandem Expression of the Postulated Biosynthetic Genes, *Biochemistry* **42**, no. 4 (2003), pp. 965–970.

[54] A. P. Gamiz-Hernandez and V. R. I. Kaila. Conversion of light-energy into molecular strain in the photocycle of the photoactive yellow protein, *Phys. Chem. Chem. Phys.* **18**, no. 4 (2016), pp. 2802–2809.

[55] H. S. Cho, F. Schotte, N. Dashdorj, J. Kyndt, R. Henning, and P. A. Anfinrud. Picosecond Photobiology: Watching a Signaling Protein Function in Real Time via Time-Resolved Small- and Wide-Angle X-ray Scattering, *J. Am. Chem. Soc.* **138**, no. 28 (2016), pp. 8815–8823.

[56] P. Changenet-Barret, A. Espagne, P. Plaza, K. J. Hellingwerf, and M. M. Martin. Investigations of the primary events in a bacterial photoreceptor for photomotility: photoactive yellow protein (PYP), *New Journal of Chemistry* **29**, no. 4 (2005), pp. 527–534.

[57] T. Matsuhira, K. Tsuchihashi, H. Yamamoto, T.-a. Okamura, and N. Ueyama. Novel photosystem involving protonation and deprotonation processes modelled on a PYP photocycle, *Organic & Biomolecular Chemistry* **6**, no. 17 (2008), pp. 3118–3126.

[58] M. Kim, R. A. Mathies, W. D. Hoff, and K. J. and Hellingwerf. Resonance Raman evidence that the thioester-linked 4-hydroxycinnamyl chromophore of photoactive yellow protein is deprotonated, *Biochemistry* **34**, no. 39 (1995), pp. 12669–12672.

[59] R. Kort, H. Vonk, X. Xu, W. D. Hoff, W. Crielaard, and K. J. Hellingwerf. Evidence for trans-cis isomerization of the p-coumaric acid chromophore as the photochemical basis of the photocycle of photoactive yellow protein, *FEBS Letters* **382** (1996), pp. 73–78.

[60] Y. Imamoto and M. Kataoka. Structure and photoreaction of photoactive yellow protein, a structural prototype of the PAS domain superfamily, *Photochemistry and Photobiology* **83**, no. 1 (2007), pp. 40–49.

[61] A. Baltuška, I. H. M. van Stokkum, A. Kroon, R. Monshouwer, K. J. Hellingwerf, and R. van Grondelle. The primary events in the photoactivation of yellow protein, *Chemical Physics Letters* **270** (1997), pp. 263–266.

[62] D. S. Larsen, I. H. M. van Stokkum, M. Vengris, M. A. van der Horst, F. L. de Weerd, K. J. Hellingwerf, and R. van Grondelle. Incoherent manipulation of the photoactive yellow protein photocycle with dispersed pump-dump-probe spectroscopy, *Biophysical Journal* **87**, no. 3 (2004), pp. 1858–1872.

[63] R. Nakamura, N. Hamada, H. Ichida, F. Tokunaga, and Y. Kanematsu. Coherent oscillations in ultrafast fluorescence of photoactive yellow protein, *J. Chem. Phys.* **127**, no. 21 (2007), p. 215102.

[64] C. N. Lincoln, A. E. Fitzpatrick, and J. J. van Thor. Photoisomerisation quantum yield and non-linear cross-sections with femtosecond excitation of the photoactive yellow protein, *Phys. Chem. Chem. Phys.* **14**, no. 45 (2012), pp. 15752–15764.

[65] M. Creelman, M. Kumauchi, W. D. Hoff, and R. A. Mathies. Chromophore Dynamics in the PYP Photocycle from Femtosecond Stimulated Raman Spectroscopy, *J. Phys. Chem. B* **118**, no. 3 (2014), pp. 659–667.

[66] K. Pande, C. D. M. Hutchison, G. Groenhof, A. Aquila, J. S. Robinson, J. Tenboer, S. Basu, S. Boutet, D. P. DePonte, M. Liang, T. A. White, N. A. Zatsepin, O. Yefanov, D. Morozov, D. Oberthuer, C. Gati, G. Subramanian, D. James, Y. Zhao, J. Koralek, J. Brayshaw, C. Kupitz, C. Conrad, S. Roy-Chowdhury, J. D. Coe, M. Metz, P. Lourdu Xavier, T. D. Grant, J. E. Koglin, G. Ketawala, R. Fromme, V. Šrajer, R. Henning, J. C. H. Spence, A. Ourmazd, P. Schwander, U. Weierstall, M. Frank, P. Fromme, A. Barty, H. N. Chapman, K. Moffat, J. J. van Thor, and M. Schmidt. Femtosecond structural dynamics drives the trans/cis isomerization in photoactive yellow protein, *Science* **352**, no. 6286 (2016), pp. 725–729.

[67] H. Kuramochi, S. Takeuchi, K. Yonezawa, H. Kamikubo, M. Kataoka, and T. Tahara. Probing the early stages of photoreception in photoactive yellow protein with ultrafast time-domain Raman spectroscopy, *Nature Chemistry* **9**, no. 7 (2017), pp. 660–666.

[68] D. Hoersch, H. Otto, M. A. Cusanovich, and M. P. Heyn. Distinguishing chromophore structures of photocycle intermediates of the photoreceptor PYP by transient fluorescence and energy transfer, *J. Phys. Chem. B* **112**, no. 30 (2008), pp. 9118–9125.

[69] Y. O. Jung, J. H. Lee, J. Kim, M. Schmidt, K. Moffat, V. Srajer, and H. Ihee. Volume-conserving trans-cis isomerization pathways in photoactive yellow protein visualized by picosecond X-ray crystallography, *Nature Chemistry* **5**, no. 3 (2013), pp. 212–220.

[70] H. Ihee, S. Rajagopal, V. Srajer, R. Pahl, S. Anderson, M. Schmidt, F. Schotte, P. A. Anfinrud, M. Wulff, and K. Moffat. Visualizing reaction pathways in photoactive yellow protein from nanoseconds to seconds, *Proc. Natl. Acad. Sci. USA* **102**, no. 20 (2005), pp. 7145–7150.

[71] S. Yeremenko, I. H. M. van Stokkum, K. Moffat, and K. J. Hellingwerf. Influence of the crystalline state on photoinduced dynamics of photoactive yellow protein studied by ultraviolet-visible transient absorption spectroscopy, *Biophysical Journal* **90**, no. 11 (2006), pp. 4224–4235.

[72] C. P. Joshi, B. Borucki, H. Otto, T. E. Meyer, M. a. Cusanovich, and M. P. Heyn. Photoreversal kinetics of the I1 and I2 intermediates in the photocycle of photoactive yellow protein by double flash experiments with variable time delay, *Biochemistry* **44**, no. 2 (2005), pp. 656–665.

[73] K. Takeshita, Y. Imamoto, M. Kataoka, K. Mihara, F. Tokunaga, and M. Terazima. Structural Change of Site-Directed Mutants of PYP: New Dynamics during pR State, *Biophysical Journal* **83**, no. 3 (2002), pp. 1567–1577.

[74] J. Hendriks, I. H. van Stokkum, and K. J. Hellingwerf. Deuterium Isotope Effects in the Photocycle Transitions of the Photoactive Yellow Protein, *Biophysical Journal* **84**, no. 2 (2003), pp. 1180–1191.

[75] T. W. Kim, J. H. Lee, J. Choi, K. H. Kim, L. J. G. W. van Wilderen, L. Guerin, Y. Kim, Y. O. Jung, C. Yang, J. Kim, M. Wulff, J. J. van Thor, and H. Ihee. Protein structural dynamics of photoactive yellow protein in solution revealed by pump-probe X-ray solution scattering, *J. Am. Chem. Soc.* **134**, no. 6 (2012), pp. 3145–3153.

[76] G. Rubinstenn, G. W. Vuister, F. A. A. Mulder, P. E. Düx, R. Boelens, K. J. Hellingwerf, and R. Kaptein. Structural and dynamic changes of photoactive yellow protein during its photocycle in solution, *Nature Structural & Molecular Biology* **5**, no. 7 (1998), pp. 568–570.

[77] W. D. Hoff, A. Xie, I. H. van Stokkum, X. J. Tang, J. Gural, A. R. Kroon, and K. J. Hellingwerf. Global conformational changes upon receptor stimulation in photoactive yellow protein, *Biochemistry* **38**, no. 3 (1999), pp. 1009–1017.

[78] C. J. Craven, N. M. Derix, J. Hendriks, R. Boelens, K. J. Hellingwerf, and R. Kaptein. Probing the nature of the blue-shifted intermediate of photoactive yellow protein in solution by NMR: hydrogen-deuterium exchange data and pH studies, *Biochemistry* **39**, no. 47 (2000), pp. 14392–14399.

[79] B. C. Lee, P. A. Croonquist, T. R. Sosnick, and W. D. Hoff. PAS domain receptor photoactive yellow protein is converted to a molten globule state upon activation, *J. Biol. Chem.* **276**, no. 24 (2001), pp. 20821–20823.

[80] M. Harigai, Y. Imamoto, H. Kamikubo, Y. Yamazaki, and M. Kataoka. Role of an N-terminal loop in the secondary structural change of photoactive yellow protein, *Biochemistry* **42**, no. 47 (2003), pp. 13893–13900.

[81] G. Fuentes, A. J. Nederveen, R. Kaptein, R. Boelens, and A. M. J. J. Bonvin. Describing partially unfolded states of proteins from sparse NMR data, *Journal of Biomolecular NMR* **33**, no. 3 (2005), pp. 175–186.

[82] U. K. Genick, G. E. 0. Borgstahl, K. Ng, Z. Ren, C. Pradervand, M. Burke, V. Srajer, T. Y. Teng, W. Schildkamp, D. E. McRee, K. Moffat, and E. D. Getzoff. Structure of a Protein Photocycle Intermediate by Millisecond Time – Resolved Crystallography, *Science* **275** (1997), pp. 1471–1475.

[83] P. L. Ramachandran, J. E. Lovett, P. J. Carl, M. Cammarata, J. H. Lee, Y. O. Jung, H. Ihee, C. R. Timmel, and J. J. van Thor. The Short-Lived Signaling State of the Photoactive Yellow Protein, *J. Am. Chem. Soc.* **133** (2011), pp. 9395–9404.

[84] N. Shimizu, Y. Imamoto, M. Harigai, H. Kamikubo, Y. Yamazaki, and M. Kataoka. pH-dependent equilibrium between long lived near-UV intermediates of photoactive yellow protein, *J. Biol. Chem.* **281**, no. 7 (2006), pp. 4318–4325.

[85] A. F. Philip, M. Kumauchi, and W. D. Hoff. Robustness and evolvability in the functional anatomy of a PER-ARNT-SIM (PAS) domain, *Proc. Natl. Acad. Sci. USA* **107**, no. 42 (2010), pp. 17986–17991.

[86] J. Hendriks, I. H. M. van Stokkum, W. Crielaard, and K. J. Hellingwerf. Kinetics of and intermediates in a photocycle branching reaction of the photoactive yellow protein from Ectothiorhodospira halophila, *FEBS Letters* **458** (1999), pp. 252–256.

[87] T. Gensch, C. C. Gradinaru, I. van Stokkum, J. Hendriks, K. J. Hellingwerf, and R. van Grondelle. The primary photoreaction of photoactive yellow protein (PYP): anisotropy changes and excitation wavelength dependence, *Chemical Physics Letters* **356** (2002), pp. 347–354.

[88] Y. Zhou, L. Ujj, T. E. Meyer, M. A. Cusanovich, and G. H. Atkinson. Photocycle Dynamics and Vibrational Spectroscopy of the E46Q Mutant of Photoactive Yellow Protein †, *J. Phys. Chem. A* **105**, no. 23 (2001), pp. 5719–5726.

[89] E. Chen, T. Gensch, A. B. Gross, J. Hendriks, K. J. Hellingwerf, and D. S. Kliger. Dynamics of protein and chromophore structural changes in the photocycle of photoactive yellow protein monitored by time-resolved optical rotatory dispersion, *Biochemistry* **42**, no. 7 (2003), pp. 2062–2071.

[90] M. Unno, M. Kumauchi, N. Hamada, F. Tokunaga, and S. Yamauchi. Resonance Raman evidence for two conformations involved in the L intermediate of photoactive yellow protein, *J. Biol. Chem.* **279**, no. 23 (2004), pp. 23855–23858.

[91] S. Rajagopal, S. Anderson, V. Srajer, M. Schmidt, R. Pahl, and K. Moffat. A structural pathway for signaling in the E46Q mutant of photoactive yellow protein, *Structure* **13**, no. 1 (2005), pp. 55–63.

[92] T. W. Kim, C. Yang, Y. Kim, J. G. Kim, J. Kim, Y. O. Jung, S. Jun, S. J. Lee, S. Park, I. Kosheleva, R. Henning, J. J. van Thor, and H. Ihee. Combined probes of X-ray scattering and optical spectroscopy reveal how global conformational change is temporally and spatially linked to local structural perturbation in photoactive yellow protein, *Phys. Chem. Chem. Phys.* **18**, no. 13 (2016), pp. 8911–8919.

[93] D. Pan, A. Philip, W. D. Hoff, and R. A. Mathies. Time-Resolved Resonance Raman Structural Studies of the pB′ Intermediate in the Photocycle of Photoactive Yellow Protein, *Biophysical Journal* **86**, no. 4 (2004), pp. 2374–2382.

[94] Y. Imamoto, K. Mihara, O. Hisatomi, M. Kataoka, F. Tokunaga, N. Bojkova, and K. Yoshihara. Evidence for proton transfer from Glu-46 to the chromophore during the photocycle of photoactive yellow protein, *J. Biol. Chem.* **272**, no. 20 (1997), pp. 12905–12908.

[95] A. Sergi, M. Grüning, M. Ferrario, and F. Buda. Density Functional Study of the Photoactive Yellow Protein's Chromophore, *J. Phys. Chem. B* **105** (2001), pp. 4386–4391.

[96] B. Borucki, S. Devanathan, H. Otto, M. a. Cusanovich, G. Tollin, and M. P. Heyn. Kinetics of proton uptake and dye binding by photoactive yellow protein in wild type and in the E46Q and E46A mutants, *Biochemistry* **41**, no. 31 (2002), pp. 10026–10037.

[97] A. Xie, W. D. Hoff, A. R. Kroon, and K. J. Hellingwerf. Glu46 Donates a Proton to the 4-Hydroxycinnamate Anion Chromophore During the Photocycle of Photoactive Yellow Protein, *Biochemistry* **35**, no. 47 (1996), pp. 14672–14678.

[98] B. Borucki. Proton transfer in the photoreceptors phytochrome and photoactive yellow protein, *Photochemical & Photobiological Sciences* **5**, no. 6 (2006), pp. 553–566.

[99] B. Honig and A. Nicholls. Classical Electrostatics in Biology and Chemistry, *Science* **268** (1995), pp. 1144–1149.

[100] E. Demchuk, U. K. Genick, T. T. Woo, E. D. Getzoff, and D. Bashford. Protonation states and pH titration in the photocycle of photoactive yellow protein, *Biochemistry* **39**, no. 5 (2000), pp. 1100–1113.

[101] A. L. Le Sueur, R. E. Horness, and M. C. Thielges. Applications of two-dimensional infrared spectroscopy, *The Analyst* **140**, no. 13 (2015), pp. 4336–4349.

[102] A. T. Fafarman and S. G. Boxer. Nitrile bonds as infrared probes of electrostatics in ribonuclease S, *J. Phys. Chem. B* **114**, no. 42 (2010), pp. 13536–13544.

[103] J. Ma, I. M. Pazos, and F. Gai. Microscopic insights into the protein-stabilizing effect of trimethylamine N-oxide (TMAO), *Proc. Natl. Acad. Sci. USA* **111**, no. 23 (2014), pp. 8476–8481.

[104] R. E. Horness, E. J. Basom, and M. C. Thielges. Site-selective Characterization of Src Homology 3 Domain Molecular Recognition with Cyanophenylalanine Infrared Probes, *Analytical Methods* **7** (2015), pp. 7234–7241.

[105] S. Ramos, R. E. Horness, J. A. Collins, D. Haak, and M. C. Thielges. Site-specific 2D IR spectroscopy: A general approach for the characterization of protein dynamics with high spatial and temporal resolution, *Phys. Chem. Chem. Phys.* **21**, no. 2 (2019), pp. 780–788.

[106] H. Mohrmann, I. Kube, V. A. Lorenz-Fonfria, M. Engelhard, and J. Heberle. Transient Conformational Changes of Sensory Rhodopsin II Investigated by Vibrational Stark Effect Probes, *J. Phys. Chem. B* **120**, no. 19 (2016), pp. 4383–4387.

[107] D. E. Levin, A. J. Schmitz, S. M. Hines, K. J. Hines, M. J. Tucker, S. H. Brewer, and E. E. Fenlon. Synthesis and Evaluation of the Sensitivity and Vibrational Lifetimes of Thiocyanate and Selenocyanate Infrared Reporters, *RSC Adv.* **43**, no. 6 (2016), pp. 36231–36237.

[108] L. J. G. W. van Wilderen, H. Brunst, H. Gustmann, J. Wachtveitl, J. Broos, and J. Bredenbeck. Cyano-tryptophans as dual infrared and fluorescence spectroscopic labels to assess structural dynamics in proteins, *Phys. Chem. Chem. Phys.* **20**, no. 30 (2018), pp. 19906–19915.

[109] S. Ye, E. Zaitseva, G. Caltabiano, G. F. X. Schertler, T. P. Sakmar, X. Deupi, and R. Vogel. Tracking G-protein-coupled receptor activation using genetically encoded infrared probes, *Nature* **464**, no. 7293 (2010), pp. 1386–1389.

[110] H. M. Müller-Werkmeister, Y.-L. Li, E.-B. W. Lerch, D. Bigourd, and J. Bredenbeck. Ultrafast hopping from band to band: Assigning infrared spectra based on vibrational energy transfer, *Angew. Chem. Int. Ed.* **52**, no. 24 (2013), pp. 6214–6217.

[111] R. Bloem, K. Koziol, S. A. Waldauer, B. Buchli, R. Walser, B. Samatanga, I. Jelesarov, and P. Hamm. Ligand binding studied by 2D IR spectroscopy using the azidohomoalanine label, *J. Phys. Chem. B* **116**, no. 46 (2012), pp. 13705–13712.

[112] H. M. Müller-Werkmeister and J. Bredenbeck. A donor-acceptor pair for the real time study of vibrational energy transfer in proteins, *Phys. Chem. Chem. Phys.* **16**, no. 7 (2014), pp. 3261–3266.

[113] M. C. Thielges, J. Y. Axup, D. Wong, H. S. Lee, J. K. Chung, P. G. Schultz, and M. D. Fayer. Two-dimensional IR spectroscopy of protein dynamics using two vibrational labels: a site-specific genetically encoded unnatural amino acid and an active site ligand, *J. Phys. Chem. B* **115**, no. 38 (2011), pp. 11294–11304.

[114] D. Kossowska, K. Park, J. Y. Park, C. Lim, K. Kwak, and M. Cho. Rational Design of an Acetylenic Infrared Probe with Enhanced Dipole Strength and Increased Vibrational Lifetime, *J. Phys. Chem. B* **123**, no. 29 (2019), pp. 6274–6281.

[115] K.-H. Park, J. Jeon, Y. Park, S. Lee, H.-J. Kwon, C. Joo, S. Park, H. Han, and M. Cho. Infrared Probes Based on Nitrile-Derivatized Prolines: Thermal Insulation Effect and Enhanced Dynamic Range, *J. Phys. Chem. Lett.* **4**, no. 13 (2013), pp. 2105–2110.

[116] A. T. Fafarman, P. a. Sigala, J. P. Schwans, T. D. Fenn, D. Herschlag, and S. G. Boxer. Quantitative, directional measurement of electric field heterogeneity in the active site of ketosteroid isomerase, *Proc. Natl. Acad. Sci. USA* **109**, no. 6 (2012), E299–308.

[117] C. H. Londergan, R. Baskin, C. G. Bischak, K. W. Hoffman, D. M. Snead, and C. Reynoso. Dynamic asymmetry and the role of the conserved active-site thiol in rabbit muscle creatine kinase, *Biochemistry* **54**, no. 1 (2015), pp. 83–95.

[118] C. T. Liu, J. P. Layfield, R. J. 3. Stewart, J. B. French, P. Hanoian, J. B. Asbury, S. Hammes-Schiffer, and S. J. Benkovic. Probing the electrostatics of active site microenvironments along the catalytic cycle for Escherichia coli dihydrofolate reductase, *J. Am. Chem. Soc.* **136**, no. 29 (2014), pp. 10349–10360.

[119] J. P. Layfield and S. Hammes-Schiffer. Calculation of vibrational shifts of nitrile probes in the active site of ketosteroid isomerase upon ligand binding, *J. Am. Chem. Soc.* **135**, no. 2 (2013), pp. 717–725.

[120] K. L. Kelly, S. R. Dalton, R. B. Wai, K. Ramchandani, R. J. Xu, S. Linse, and C. H. Londergan. Conformational Ensembles of Calmodulin Revealed by Nonperturbing Site-Specific Vibrational Probe Groups, *J. Phys. Chem. A* **122**, no. 11 (2018), pp. 2947–2955.

[121] J. M. Schmidt-Engler, L. Blankenburg, B. Błasiak, L. J. G. W. van Wilderen, M. Cho, and J. Bredenbeck. Vibrational Lifetime of the SCN Protein Label in H2O and D2O Reports Site-Specific Solvation and Structure Changes During PYP's Photocycle, *Analytical Chemistry* **92** (2020), pp. 1024–1032.

[122] A. J. Stafford, D. M. Walker, and L. J. Webb. Electrostatic effects of mutations of Ras glutamine 61 measured using vibrational spectroscopy of a thiocyanate probe, *Biochemistry* **51**, no. 13 (2012), pp. 2757–2767.

[123] D. M. Walker, R. Wang, and L. J. Webb. Conserved electrostatic fields at the Ras-effector interface measured through vibrational Stark effect spectroscopy explain the difference in tilt angle in the Ras binding domains of Raf and RalGDS, *Phys. Chem. Chem. Phys.* **16**, no. 37 (2014), pp. 20047–20060.

[124] A. W. Ritchie and L. J. Webb. Understanding and Manipulating Electrostatic Fields at the Protein-Protein Interface Using Vibrational Spectroscopy and Continuum Electrostatics Calculations, *J. Phys. Chem. B* **119**, no. 44 (2015), pp. 13945–13957.

[125] R. Adhikary, J. Zimmermann, P. E. Dawson, and F. E. Romesberg. Temperature Dependence of CN and SCN IR Absorptions Facilitates Their Interpretation and Use as Probes of Proteins, *Analytical Chemistry* **87**, no. 22 (2015), pp. 11561–11567.

[126] Y. Gao, Y. Zou, Y. Ma, D. Wang, Y. Sun, and G. Ma. Infrared Probe Technique Reveals a Millipede-like Structure for Abeta(8-28) Amyloid Fibril, *Langmuir* **32**, no. 4 (2016), pp. 937–946.

[127] S. D. Fried and S. G. Boxer. Measuring electric fields and noncovalent interactions using the vibrational stark effect, *Accounts of Chemical Research* **48**, no. 4 (2015), pp. 998–1006.

[128] B. Błasiak, C. H. Londergan, L. J. Webb, and M. Cho. Vibrational Probes: From Small Molecule Solvatochromism Theory and Experiments to Applications in Complex Systems, *Accounts of Chemical Research* **50**, no. 4 (2017), pp. 968–976.

[129] N. M. Levinson, S. D. Fried, and S. G. Boxer. Solvent-induced infrared frequency shifts in aromatic nitriles are quantitatively described by the vibrational Stark effect, *J. Phys. Chem. B* **116**, no. 35 (2012), pp. 10470–10476.

[130] B. Błasiak, A. W. Ritchie, L. J. Webb, and M. Cho. Vibrational solvatochromism of nitrile infrared probes: beyond the vibrational Stark dipole approach, *Phys. Chem. Chem. Phys.* **18**, no. 27 (2016), pp. 18094–18111.

[131] S. Bagchi, S. D. Fried, and S. G. Boxer. A solvatochromic model calibrates nitriles' vibrational frequencies to electrostatic fields, *J. Am. Chem. Soc.* **134**, no. 25 (2012), pp. 10373–10376.

[132] J. T. First, J. D. Slocum, and L. J. Webb. Quantifying the Effects of Hydrogen Bonding on Nitrile Frequencies in GFP: Beyond Solvent Exposure, *J. Phys. Chem. B* **122**, no. 26 (2018), pp. 6733–6743.

[133] J. Hendriks. "Shining light on the Photoactive Yellow Protein from Halorhodospira halophila". PhD thesis. Amsterdam: University of Amsterdam, 2002.

[134] S. R. Dalton, A. R. Vienneau, S. R. Burstein, R. J. Xu, S. Linse, and C. H. Londergan. Cyanylated Cysteine Reports Site-Specific Changes at Protein-Protein-Binding Interfaces Without Perturbation, *Biochemistry* **57**, no. 26 (2018), pp. 3702–3712.

[135] T. E. Meyer, G. Tollin, J. H. Hazzard, and M. A. Cusanovich. Photoactive yellow protein from the purple phototrophic bacterium, Ectothiorhodospira halophila. Quantum yield of photobleaching and effects of temperature, alcohols, glycerol, and sucrose on kinetics of photobleaching and recovery, *Biophysical Journal* **56**, no. 3 (1989), pp. 559–564.

[136] L. Blankenburg, L. Schroeder, F. Habenstein, B. Błasiak, T. Kottke, and J. Bredenbeck. Following local light-induced structure changes and dynamics of the photoreceptor PYP with the thiocyanate IR label, *Phys. Chem. Chem. Phys.* **21**, no. 12 (2019), pp. 6622–6634.

[137] M. M. Gromiha. *Protein Bioinformatics*. Academic Press, 2010.

[138] G. Ben-Nissan and M. Sharon. The application of ion-mobility mass spectrometry for structure/function investigation of protein complexes, *Current Opinion in Chemical Biology* **42** (2018), pp. 25–33.

[139] P. Hamm, R. A. Kaindl, and J. Stenger. Noise suppression in femtosecond mid-infrared light sources, *Optics Letters* **25**, no. 24 (2000), pp. 1798–1800.

[140] M. Bradler, P. Baum, and E. Riedle. Femtosecond continuum generation in bulk laser host materials with sub-μJ pump pulses, *Applied Physics B* **97**, no. 3 (2009), pp. 561–574.

[141] G. Cerullo and S. de Silvestri. Ultrafast optical parametric amplifiers, *Rev. Sci. Instr.* **74**, no. 1 (2003), pp. 1–18.

[142] J. Helbing and P. Hamm. Compact implementation of Fourier transform two-dimensional IR spectroscopy without phase ambiguity, *Journal of the Optical Society of America B* **28**, no. 1 (2011), pp. 171–178.

[143] E. Deniz, K. B. Eberl, and J. Bredenbeck. Note: An automatic liquid nitrogen refilling system for small (detector) Dewar vessels, *Rev. Sci. Instr.* **89**, no. 11 (2018), e116101.

[144] L. J. G. W. van Wilderen, C. N. Lincoln, and J. J. van Thor. Modelling multi-pulse population dynamics from ultrafast spectroscopy, *PLoS One* **6**, no. 3 (2011), e17373.

[145] M. Pescher. "Moleküldynamik von ps bis ms: Aufbau, Charakterisierung und Anwendung eines Systems synchronisierter Femtosekundenlaser". PhD thesis. Frankfurt am Main: Johann Wolfgang Goethe-University Frankfurt, 2014.

[146] C. Slavov, H. Hartmann, and J. Wachtveitl. Implementation and evaluation of data analysis strategies for time-resolved optical spectroscopy, *Analytical Chemistry* **87**, no. 4 (2015), pp. 2328–2336.

[147] V. A. Voelz and V. S. Pande. Calculation of rate spectra from noisy time series data, *Proteins* **80**, no. 2 (2012), pp. 342–351.

[148] A. Siemiarczuk, B. D. Wagner, and W. R. Ware. Comparison of the Maximum Entropy and Exponential Series Methods for the Recovery of Distributions of Lifetimes from Fluorescence Lifetime Data, *J. Phys. Chem.* **94** (1990), pp. 1661–1666.

[149] D. R. James and W. R. Ware. Recovery of underlying distributions of lifetimes from fluorescence decay data, *Chemical Physics Letters* **126**, no. 1 (1986), pp. 7–11.

[150] V. I. Prokhorenko, D. B. Steensgaard, and A. R. Holzwarth. Exciton Dynamics in the Chlorosomal Antennae of the Green Bacteria Chloroflexus aurantiacus and Chlorobium tepidum, *Biophysical Journal* **79**, no. 4 (2000), pp. 2105–2120.

[151] R. Croce, M. G. Müller, R. Bassi, and A. R. Holzwarth. Carotenoid-to-Chlorophyll Energy Transfer in Recombinant MajorLight-Harvesting Complex (LHCII) of Higher Plants. I. Femtosecond Transient Absorption Measurements, *Biophysical Journal* **80**, no. 2 (2001), pp. 901–915.

[152] J. García, R. Salmerón, C. García, and M. d. M. López Martín. Standardization of Variables and Collinearity Diagnostic in Ridge Regression, *International Statistical Review* **84**, no. 2 (2016), pp. 245–266.

[153] C. Thöing, S. Oldemeyer, and T. Kottke. Microsecond Deprotonation of Aspartic Acid and Response of the α/β Subdomain Precede C-Terminal Signaling in the Blue Light Sensor Plant Cryptochrome, *J. Am. Chem. Soc.* **137**, no. 18 (2015), pp. 5990–5999.

[154] R. Brudler, C. R. Gessner, S. Li, S. Tyndall, E. D. Getzoff, and V. L. Woods. PAS domain allostery and light-induced conformational changes in photoactive yellow protein upon I2 intermediate formation, probed with enhanced hydrogen/deuterium exchange mass spectrometry, *Journal of Molecular Biology* **363**, no. 1 (2006), pp. 148–160.

[155] M. Harigai, M. Kataoka, and Y. Imamoto. Interaction between N-terminal loop and beta-scaffold of photoactive yellow protein, *Photochemistry and Photobiology* **84**, no. 4 (2008), pp. 1031–1037.

[156] M. Kumauchi, N. Hamada, J. Sasaki, and F. Tokunaga. A role of methionine 100 in facilitating PYP(M)-decay process in the photocycle of photoactive yellow protein, *Biochemistry* **132**, no. 2 (2002), pp. 205–210.

[157] S. Devanathan, U. K. Genick, I. L. Canestrelli, T. E. Meyer, M. Cusanovich, E. D. Getzoff, and G. Tollin. New insights into the photocycle of Ectothiorhodospira halophila photoactive yellow protein: photorecovery of the long-lived photobleached intermediate in the Met100Ala mutant, *Biochemistry* **37**, no. 33 (1998), pp. 11563–11568.

[158] J. Sasaki, M. Kumauchi, N. Hamada, T. Oka, and F. Tokunaga. Light-induced unfolding of photoactive yellow protein mutant M100L, *Biochemistry* **41**, no. 6 (2002), pp. 1915–1922.

[159] J. A. Kyndt, S. N. Savvides, S. Memmi, M. Koh, J. C. Fitch, T. E. Meyer, M. P. Heyn, J. J. van Beeumen, and M. A. Cusanovich. Structural Role of Tyrosine 98 in Photoactive Yellow Protein: Effects on, *Biochemistry* **46**, no. 1 (2007), pp. 95–105.

[160] J. T. Pelton and L. R. McLean. Spectroscopic methods for analysis of protein secondary structure, *Analytical Biochemistry* **277**, no. 2 (2000), pp. 167–176.

[161] S. M. Kelly, T. J. Jess, and N. C. Price. How to study proteins by circular dichroism, *Biochimica et Biophysica Acta* **1751**, no. 2 (2005), pp. 119–139.

[162] L. Whitmore and B. A. Wallace. Protein secondary structure analyses from circular dichroism spectroscopy: methods and reference databases, *Biopolymers* **89**, no. 5 (2008), pp. 392–400.

[163] S. Kelly and N. Price. The Use of Circular Dichroism in the Investigation of Protein Structure and Function, *Current Protein & Peptide Science* **1**, no. 4 (2000), pp. 349–384.

[164] B. Borucki, H. Otto, T. E. Meyer, M. a. Cusanovich, and M. P. Heyn. Sensitive circular dichroism marker for the chromophore environment of photoactive yellow protein: assignment of the 307 and 318 nm bands to the n – pi* transition of the carbonyl, *J. Phys. Chem. B* **109**, no. 1 (2005), pp. 629–633.

[165] G. E. 0. Borgstahl, D. R. Williams., and E. D. Getzoff. 1.4 A Structure of Photoactive Yellow Protein, a Cytosolic Photoreceptor: Unusual Fold, Active Site, and Chromophore, *Biochemistry* **34**, no. 19 (1995), pp. 6278–6287.

[166] Jack Kyte and Russel F. Doolittle. A Simple Method for Displaying the Hydropathic Character of a Protein, *Journal of Molecular Biology* **152** (1982), pp. 105–132.

[167] Nozomi Nagano, Motonori Ota, and Ken Nishikawa. Strong hydrophobic nature of cysteine residues in proteins, *FEBS Letters* **458** (1999), pp. 69–71.

[168] D. M. Alessi and S. M. Decatur. Temperature Dependence of the Amide I Frequency as a Probe of Solvent Accessibility of the Protein Backbone, *Biophysical Journal* **98**, no. 3 (2010), pp. 629–630.

[169] M. Unno, M. Kumauchi, J. Sasaki, F. Tokunaga, and S. Yamauchi. Resonance Raman spectroscopy and quantum chemical calculations reveal structural changes in the active site of photoactive yellow protein, *Biochemistry* **41**, no. 17 (2002), pp. 5668–5674.

[170] Y. Hoshihara, Y. Imamoto, M. Kataoka, F. Tokunaga, and M. Terazima. Conformational changes in the N-terminal region of photoactive yellow protein: a time-resolved diffusion study, *Biophysical Journal* **94**, no. 6 (2008), pp. 2187–2193.

[171] P. Changenet, H. Zhang, M. J. van der Meer, K. J. Hellingwerf, and M. Glasbeek. Subpicosecond fluorescence upconversion measurements of primary events in yellow proteins, *Chemical Physics Letters* **282** (1998), pp. 276–282.

[172] Z. Ren, B. Perman, V. Srajer, T. Y. Teng, C. Pradervand, D. Bourgeois, F. Schotte, T. Ursby, R. Kort, M. Wulff, and K. Moffat. A molecular movie at 1.8 A resolution displays the photocycle of photoactive yellow protein, a eubacterial blue-light receptor, from nanoseconds to seconds, *Biochemistry* **40**, no. 46 (2001), pp. 13788–13801.

[173] Y. N. Chirgadze, O. V. Fedorov, and N. P. Trushina. Estimation of amino acid residue side-chain absorption in the infrared spectra of protein solutions in heavy water, *Biopolymers* **14**, no. 4 (1975), pp. 679–694.

[174] S. Venyaminov and N. N. Kalnin. Quantitative IR spectrophotometry of peptide compounds in water (H2O) solutions. I. Spectral parameters of amino acid residue absorption bands, *Biopolymers* **30**, no. 13-14 (1990), pp. 1243–1257.

[175] G. Groenhof, M. F. Lensink, H. J. C. Berendsen, J. G. Snijders, and A. E. Mark. Signal transduction in the photoactive yellow protein. I. Photon absorption and the isomerization of the chromophore, *Proteins* **48** (2002), pp. 202–211.

[176] J. N. Onuchic, Z. Luthey-Schulten, and P. G. and Wolynes. Theory of Protein Folding: The Energy Landscape Perspective, *Annu. Rev. Phys. Chem.* **48** (1997), pp. 545–600.

[177] J. N. Onuchic, P. G. Wolynes, Z. Luthey-Schulten, and N. D. Socci. Toward an outline of the topography of a realistic protein- folding funnel, *Proc. Natl. Acad. Sci. USA* **92** (1995), pp. 3626–3630.

[178] S. Anderson, V. Srajer, R. Pahl, S. Rajagopal, F. Schotte, P. Anfinrud, M. Wulff, and K. Moffat. Chromophore conformation and the evolution of tertiary structural changes in photoactive yellow protein, *Structure* **12**, no. 6 (2004), pp. 1039–1045.

[179] M. Unno, M. Kumauchi, J. Sasaki, F. Tokunaga, and S. Yamauchi. Evidence for a Protonated and cis Configuration Chromophore in the Photobleached Intermediate of Photoactive Yellow Protein, *J. Am. Chem. Soc.* **122**, no. 17 (2000), pp. 4233–4234.

[180] D. Hoersch, H. Otto, M. Cusanovich, and M. P. Heyn. Time-resolved spectroscopy of dye-labeled photoactive yellow protein suggests a pathway of light-induced structural changes in the N-terminal cap, *Phys. Chem. Chem. Phys.* **11**, no. 26 (2009), pp. 5437–5444.

[181] Y. Imamoto, M. Harigai, T. Morimoto, and M. Kataoka. Low-temperature Spectroscopy of Met100Ala Mutant of Photoactive Yellow Protein, *Photochemistry and Photobiology* **84** (2008), pp. 970–976.

[182] L. L. Premvardhan, M. A. van der Horst, K. J. Hellingwerf, and R. van Grondelle. Stark Spectroscopy on Photoactive Yellow Protein, E46Q, and a Nonisomerizing Derivative, Probes Photo-Induced Charge Motion, *Biophysical Journal* **84**, no. 5 (2003), pp. 3226–3239.

[183] A. Barth. The infrared absorption of amino acid side chains, *Progress in Biophysics & Molecular Biology* **74** (2000), pp. 141–173.

[184] T. Lian, B. Locke, Y. Kholodenko, and R. M. Hochstrasser. Energy Flow from Solute to Solvent Probed by Femtosecond IR Spectroscopy: Malachite Green and Heme Protein Solutions, *J. Phys. Chem.* **98** (1994), pp. 11648–11656.

[185] C. M. Phillips, Y. Mizutani, and R. M. Hochstrasser. Ultrafast thermally induced unfolding of RNase A, *Proc. Natl. Acad. Sci. USA* **92** (1995), pp. 7292–7296.

[186] S. A. Petty and M. Volk. Fast folding dynamics of an α-helical peptide with bulky side chains, *Phys. Chem. Chem. Phys.* **6**, no. 5 (2004), pp. 1022–1030.

[187] S. Scheiner. Calculation of effects from first principles, *Biochimica et Biophysica Acta* **1458** (2000), pp. 28–42.

[188] M. Ibrahim, A. Nada, and D. E. Kamal. Density functional theory and FTIR spectroscopy study of carboxyl group, *Indian J. of Pure & Appl. Phys.* **43** (2005), pp. 911–917.

[189] M. Azadbakht, C. Fraser, and K. Khoshelham. A Sparsity-Based Regularization Approach for Deconvolution of Full-Waveform Airborne Lidar Data, *Remote Sensing* **8**, no. 648 (2016), pp. 1–26.

[190] D. A. Smith, G. McKenzie, A. C. Jones, and T. A. Smith. Analysis of TCSPC data: a comparative evaluation of deterministic and probabilistic approaches, *Methods Appl. Fluoresc.* **5**, no. 4 (2017), pp. 1–20.

[191] R. J. Xu, B. Blasiak, M. Cho, J. P. Layfield, and C. H. Londergan. A Direct, Quantitative Connection between Molecular Dynamics Simulations and Vibrational Probe Line Shapes, *J. Phys. Chem. Lett.* **9**, no. 10 (2018), pp. 2560–2567.

[192] J. M. Schmidt-Engler, R. Zangl, P. Guldan, N. Morgner, and J. Bredenbeck. Exploring the 2D-IR repertoire of the -SCN label to study site-resolved dynamics and solvation in the calcium sensor protein calmodulin, *Phys. Chem. Chem. Phys.* **22**, no. 10 (2020), pp. 5463–5475.

[193] S. Miller, J. Janin, A. M. Lesk, and C. Chothia. Interior and surface of monomeric proteins, *Journal of Molecular Biology* **196**, no. 3 (1987), pp. 641–656.

List of Abbreviations

4CzIPN	2,4,5,6-tetra(carbazol-9-yl)benzene-1,3-dicarbonitrile
µs	microsecond
E.coli	*Escherichia coli*
AGS	silver thiogallate, $AgGaS_2$
Ala, A	alanine
AR	anti-reflective
Arg, R	arginine
Asp, D	aspartic acid
BaF_2	barium fluoride
BBO	β-barium borate, β-BaB_2O_4
BS	beamsplitter
CaF_2	calcium fluoride
CCS	collision cross section
CD	circular dichroism
CDI	1,1'-carbonyldiimidazole
CP	calcite plate
cw	continuous wave
Cys, C	cysteine
DADS	decay associated difference spectra
DCM	dichloromethane
DEER	double electron electron resonance
DFG	difference frequency generation
DM	dichroic mirror
DMF	N,N-dimethylformamide
DMSO	dimethyl sulfoxide
DNA	deoxyribonucleic acid
DTE	dithioerythritol
DTNB	5,5'-dithiobis(2-nitrobenzoic acid)
fs	femtosecond
FTIR	Fourier transform infrared
FTLS	frequency-temperature line slope
FWHM	full width at half maximum
GA	global analysis

GaAs ..... gallium arsenide
Gdm-HCl ..... guanidinium chloride
Glu, E ..... glutamic acid
HCl ..... hydrochloride
His, H ..... histidin
HR ..... high reflective
IMS ..... ion mobility separation
IPTG ..... isopropyl-β-D-thiogalactopyranoside
IR ..... infrared
IRF ..... instrument response function
KCN ..... potassium cyanide
LB ..... lysogeny broth
LDA ..... lifetime density analysis
LDM ..... lifetime density map
Leu, L ..... leucine
LPF ..... long pass filter
MCT ..... mercury cadmium telluride, HgCdTe
MeSCN ..... methyl thiocyanate
Met, M ..... methionine
ms ..... millisecond
NaCl ..... sodium chloride
NaPi ..... sodium phosphate
Nd:YAG ..... neodymium-doped yttrium aluminum garnet, Nd:$Y_3Al_5O_{12}$
Nd:YLF ..... neodymium-doped yttrium lithium fluoride, Nd:$LiYF_4$
nESI ..... nano electrospray ionization
Ni-NTA ..... Ni^{2+}-nitrilotriacetic acid
NMR ..... nuclear magnetic resonance
ns ..... nanosecond
OD ..... optical density
OPA ..... optical parametric amplifier
OPO ..... optical parametric oscillator
PAGE ..... polyacrylamide gel electrophoresis
pCA ..... p-coumaric acid
PCR ..... polymerase chain reaction
PGM ..... parabolic gold mirror
ps ..... picosecond
PSU ..... power supply unit
PTFE ..... polytetrafluoroethylene
PYP ..... Photoactive Yellow Protein
SADS ..... species associated difference spectra

SASA ..... solvent accessible surface area
SAXS ..... small angle X-ray scattering
SCN ..... thiocyanate
SFG ..... sum frequency generation
SGM ..... spherical gold mirror
SHG ..... second harmonic generation
TCEP ..... tris(2-carboxyethyl)phosphine
TEV ..... Tobacco Etch Virus
TFP ..... thin film polarizer
THF ..... tetrahydrofuran
Thr, T ..... threonine
Ti:Sapphire ..... titanium-sapphire, Ti:Al_2O_3
TNB 2-nitro-5-thiobenzoate
tr ..... time resolved
Tris ..... tris(hydroxymethyl)aminomethane
Tyr, Y ..... tyrosine
UV ..... ultraviolet
Val, V ..... valine
vis ..... visible
WAXS ..... wide angle X-ray scattering
WS ..... wavelength separator
WT ..... wildtype
YAG ..... yttrium aluminum garnet, $Y_3Al_5O_{12}$
ZeSn ..... zinc selenide

List of Figures

List of Tables

Collaborative Research

Part of the work presented in this thesis was obtained in close collaboration with external research groups. The contributions of these people are much appreciated and shortly listed in the following:

The umbrella sampling MD simulations of PYP and the SCN-labeled mutants as well as detailed analyses of the results, *e.g* by SASA calculations or WHAM analysis of the hydrogen-bonding contributions of SCN, were performed by *Bartosz Błasiak*, currently Wrocław University of Science and Technology, Department of Physical and Quantum Chemistry, Poland.

The nESI mass spectrometry measurements for determination of the labeling efficiency and the IMS MS experiments under dark and illuminated conditions of PYP-WT and the SCN-labeled mutants were performed and analyzed by *Rene Zangl* and *Jan Hoffmann* from the research group of *Nina Morgner*, Institute of Physical and Theoretical Chemistry, Goethe University, Frankfurt am Main.

The time-resolved step-scan FTIR data for WT' and the SCN-labeled A44C* were measured in collaboration with *Lea Schröder* and *Tilman Kottke*, Physical and Biophysical Chemistry, Bielefeld University. They also performed the postprocessing of the obtained data sets including averaging of the data and correction for the water background.

Publications and Conference Contributions

List of Publications

Following local light-induced structure changes and dynamics of the photoreceptor PYP with the thiocyanate IR label
Larissa Blankenburg, Lea Schroeder, Florian Habenstein, Bartosz Błasiak, Tilman Kottke, and Jens Bredenbeck
Phys. Chem. Chem. Phys., 2019, **21**, 6622–6634, DOI: 10.1039/c8cp05399e

Vibrational Lifetime of the SCN Protein Label in H_2O and D_2O Reports Site-Specific Solvation and Structure Changes During PYP's Photocycle
Julian M. Schmidt-Engler*, **Larissa Blankenburg***, Bartosz Błasiak, Luuk J. G. W. van Wilderen, Minhaeng Cho, and Jens Bredenbeck
Anal. Chem., 2020, **92**, 1024-1032, DOI: 10.1021/acs.analchem.9b03997

Working title: **Local Conformational Dynamics of the Photo-Switchable Protein PYP Probed by the –SCN Label using 2D-IR Spectroscopy**
Julian M. Schmidt-Engler*, **Larissa Blankenburg***, Rene Zangl, Jan Hoffmann, Nina Morgner, and Jens Bredenbeck
in preparation

Working title: **Uncovering local site-specific dynamics during the photocycle of the photoreceptor Photoactive Yellow Protein on a femtosecond-to-millisecond timescale *via* the vibrational label SCN**
Larissa Blankenburg*, Luuk J. G. W. van Wilderen*, and Jens Bredenbeck
in preparation

*Authors contributed equally.

List of Conference Contributions

Femtosecond to millisecond dynamics of photoactive yellow protein revealed by the vibrational label –SCN
Luuk J. G. W. van Wilderen, **Larissa Blankenburg**, and Jens Bredenbeck
Talk, 119th General Assembly of the German Bunsen Society for Physical Chemistry
01. – 03.04.2020, Giessen, Germany. — *canceled by organizer*

Following the formation of PYP's photocycle intermediates on a femtosecond to millisecond timescale with a site-specific IR label
Larissa Blankenburg, Luuk J. G. W. van Wilderen, and Jens Bredenbeck
Talk, DPG Frühjahrstagung, Sektion Kondensierte Materie
15. – 20.03.2020, Dresden, Germany. — *canceled by organizer*

Adding Another Dimension to Our Understanding of Proteins: 2D-IR Spectroscopy of the IR Label -SCN
Julian M. Schmidt-Englert, **Larissa Blankenburg**, and Jens Bredenbeck
Talk, 18th European Conference on Spectroscopy of Biological Molecules (ECSBM)
19. – 22.08.2019, Dublin, Ireland.

Following the conformational diversity of the PYP photoreceptor with native Ion-Mobility MS
Jan Hoffmann, Rene Zangl, **Larissa Blankenburg**, Jens Bredenbeck, and Nina Morgner
Poster, 52. DGMS-Jahrestagung, Deutschen Gesellschaft für Massenspektrometrie
10. -– 13.03.2019, Rostock, Germany.

Cyanylated cysteines as infrared labels to unravel the vibrational dynamics along the photocycle of the photo-switchable protein PYP by mid infrared pump-probe spectroscopy
Julian M. Schmidt-Engler, **Larissa Blankenburg**, Bartosz Błasiak, Luuk J. G. W. van Wilderen, Minhaeng Cho, and Jens Bredenbeck
Poster, XXI. International Conference on Ultrafast Phenomena
15. – 20.07.2018, Hamburg, Germany.

Photoreceptor Studied by Steady-State and Step-Scan FTIR Spectroscopy of Thiocyanate Labels
Larissa Blankenburg, Lea Schröder, Florian Habenstein, Tilman Kottke, and Jens Bredenbeck
Poster, XVIII. Time Resolved Vibrational Spectroscopy Meeting (TRVS)
16. – 21.07.2017, Cambridge, UK.

Vibrational dynamics of the thiocyanate label in the resting and signalling state of a photoreceptor
Julian M. Schmidt-Engler, **Larissa Blankenburg**, Florian Habenstein, Luuk J. G. W. van Wilderen, and Jens Bredenbeck
Poster, XVIII. Time Resolved Vibrational Spectroscopy Meeting (TRVS)
16. – 21.07.2017, Cambridge, UK.

Following the photo-induced structure changes and dynamics of the photoreceptor PYP with an IR label
Larissa Blankenburg, Florian Habenstein, Lea Schröder, Tilman Kottke, and Jens Bredenbeck
Poster, 116th General Assembly of the German Bunsen Society for Physical Chemistry
25. – 27.05.2017, Kaiserslautern, Germany.

Vibrational dynamics of cyanylated cysteins in a photosensor protein
Julian M. Schmidt-Engler, **Larissa Blankenburg**, Florian Habenstein, Luuk J. G. W. van Wilderen, and Jens Bredenbeck
Poster, 116th General Assembly of the German Bunsen Society for Physical Chemistry
25. – 27.05.2017, Kaiserslautern, Germany.

IR-Spectroscopy and Artificial Amino Acids: A Great Couple for Protein Biophysics
Larissa Blankenburg, Jens Bredenbeck, Katharina Eberl, Martin Essig, Daniela Kern-Michler, and Henrike M. Müller-Werkmeister
Poster, 16. Deutsche Physikerinnentagung
25. – 28.10.2012, Freiburg, Deutschland.